Role of AGN feedback in galaxy evolution at high-redshift

Cédric Collet

To cite this version:

Cédric Collet. Role of AGN feedback in galaxy evolution at high-redshift. Cosmology and Extra-Galactic Astrophysics [astro-ph.CO]. Université Paris Sud - Paris XI, 2014. English. NNT : 2014PA112074 . tel-01061155

HAL Id: tel-01061155
https://theses.hal.science/tel-01061155

Submitted on 5 Sep 2014

Institut d'Astrophysique Spatiale

Université Paris-Sud

École Doctorale d'Astronomie et Astrophysique d'Île de France

Thèse de Doctorat

Spécialité Astrophysique et instrumentations associées

soutenue le 28/04/2014

par

Cédric Collet

The role of AGN feedback in galaxy evolution

Directrice de thèse :	Nicole Nesvadba	Chargée de Recherche (Institut d'Astrophysique Spatiale)
Président du jury :	Guilaine Lagache	Astronome (Institut d'Astrophysique Spatiale)
Rapporteurs :	Philippe Amram	Professeur (Laboratoire d'Astrophysique de Marseille)
	Thierry Contini	Chargé de Recherche (Institut de Recherche en Astrophysique et Planétologie, Toulouse)
Examinateurs :	Marta Volonteri	Directeur de Recherche (Institut d'Astrophysique de Paris)
	Clive Tadhunter	Professor (Sheffield University)

Remerciements

Les remerciements étant la partie la plus lue d'un manuscrit de thèse, je vais faire de mon mieux pour n'oublier personne. Mais j'en oublierai forcément, aussi je voudrais commencer par remercier tous ceux et celles que j'ai croisé au cours de ma thèse mais qui n'apparaissent pas ici, quand ils mériteraient d'y être.

Mes premières pensées vont à mes amis et collègues qui m'ont accompagné pendant mes études et en particulier à mes colocataires successifs. À Romain et Bastien, merci pour ces trois années à l'Hay, pour les parties de Carcassonne et de DotA, pour les découvertes culinaires et nos soirées Californication, pour la Kappa Haus qui restera la meilleure colocation où j'ai vécu, puisque la première. À Long, merci pour les Banh Xeo, de m'avoir donné un aperçu en avant première de ce que peut être la période de rédaction et, surtout, de m'avoir montré qu'à force de courage et d'obstination, on finit toujours par y arriver. À Kévin, merci pour ta bonne humeur permanente, d'avoir été un compagnon de rédaction indéfectible et pour toutes ces discussions sur ce qui pouvait bien nous attendre après la thèse.

Mais je n'ai pas eu que des coloc' ! L'IAS est connu pour être un laboratoire où il fait bon travailler et cette réputation est amplement justifiée. Un grand merci à Mathieu, Alex, Ju, Rosario, Nabila, Eddy, Sébastien, Aurélie, Léo, Pierre, Ben, Alexandre et les autres. L'équipe des thésards n'a jamais été en reste non plus et je voudrais remercier mes compagnons qui sont entrés en thèse à l'IAS en même temps que moi : Sté, Fab, Sihane, Chloé, et bien sûr Morgan, avec qui j'ai tant discuté. Je souhaite tout le succès possible aux ptits jeunes, David, Marco, Lapo, JB, Raoul, Martinache, Vincent et les autres, avec une mention spéciale pour Agnès — tu vas me manquer co-bureau ! Finally, a big "thank you" to Dan, it was good to discuss with you on our way to the swimming pool. Si je suis si souvent venu à Orsay le sourire aux lèvres, c'est grâce à vous tous !

Je voudrais également remercier tous mes camarades qui m'ont accompagné, de la L3 au M2 : Soso la princesse, Lucie, Marina, Alice, Élo, Clément (avec qui j'ai eu la chance de partager mon premier stage en astro, déjà à l'IAS), Bruno, Clotilde, Amélie, Anne-Lise, Lionel, Stefano, Shan, John, David, Céline et bien sûr Loulou !

Mon mandat de représentant doctorant, aux côtés de Mélanie, Étienne, Alexis et Kévin a aussi été riche en enseignements, notamment sur le fonctionnement du monde de la recherche et ses évolutions en cours. Nous avons vraiment fait de notre mieux et je pense que nous nous en sommes plutôt bien sortis. Et c'était un vrai plaisir de se retrouver tous les cinq dans la salle du sixième étage de l'Observatoire pour nos réunions !

Mon engagement au GENEPI a été une autre occupation qui m'a énormément apporté à cette même période. Outre les rencontres, toutes plus enrichissantes les unes que les autres et que je n'aurais jamais faites en temps normal, cela m'a permis de découvrir un autre univers, que je connaissais encore moins bien que celui de ma thèse. Heureusement Joseph, Alix, Clarisse, Anne et Derek, Jeanne, Anne, Gaetano et une foule de bénévoles surmotivés m'ont permis de vite combler toutes mes lacunes. Et mon année à animer le groupe de Fresnes aux côtés d'Alexis, Pauline, Vincent, Bastien, Manon et Élodie a été la cerise sur le gateau !

J'ai également eu la chance de passer deux mois à l'ESO à Munich en début de troisième année. Cela a été une excellente expérience et je voudrais remercier Carlos et Guillaume pour m'avoir accueilli si chaleureusement là-bas. L'ambiance qui règne à Garching est aussi bonne que celle d'Orsay, et c'est grâce à tous ceux que j'ai pu y rencontrer : Alvaro, Mathias, Bitten, Fei, Tim, Mez, Grant, Nora, Laeticia, Graine, Anna, Leo, Neale, Laura, Peter . . .

Enfin, mes amis de toujours, vous n'imaginez pas à quel point cela me faisait du bien de vous retrouver. Ce n'était pas très souvent, ni jamais très longtemps, mais le temps d'un festival ou d'un week-end, je ne parlais ni de thèse ni de physique et c'était tout ce dont j'avais besoin ! Le Xi, Skaven, les deux Vince, Tata, Flo, Arthur, Jé et Paul, vous êtes les meilleurs !

Et le mot de la fin sera pour ma famille. Papa, Maman, Antoine et Mathilde, simplement, merci pour tout !

Résumé

Durant cette thèse, je me suis intéressé à la rétroaction des noyaux actifs de galaxie sur leur galaxie hôte, à haut décalage spectral vers le rouge[1]. Derrière ce nom se cache un des ingrédients-clé de la recette qui permet d'obtenir des galaxies telles que nous les observons aujourd'hui, dans l'Univers local.

Contexte

Modèles de formation et d'évolution des galaxies

Les grandes lignes de la formation et de l'évolution des galaxies sont connues depuis des décennies. Le cadre général est celui du modèle cosmologique ΛCDM, qui est capable d'expliquer au mieux la forme des fluctuations observées dans le fond diffus cosmologique et dans lequel la majorité de la matière est dite *noire*, car elle n'interagit que gravitationnellement avec la matière classique[2]. Alors que l'Univers était extrêmement homogène juste après le Big-Bang, comme le révèle l'observation du fond diffus cosmologique, la matière noire se structure peu à peu sous l'effet de la gravitation, jusqu'à prendre la forme d'une toile cosmique, faite de filaments de matière noire qui se croisent en des nœuds. Cette évolution est visible sur la partie gauche de la Figure 1.1, qui représente la densité de matière noire dans une simulation basée sur le modèle ΛCDM à différentes époques. À droite de cette figure, on trouve une observation de cette structuration en filaments, faite par le Sloan Digital Sky Survey (SDSS, York et al., 2000). La structuration de la matière noire sert de squelette à la formation des galaxies : en effet, au premier ordre, la matière baryonique suit le potentiel gravitationnel créé par la matière noire. Le gaz se condense donc dans les halos de la toile cosmique pour former des galaxies.

Ce scenario, malgré sa simplicité, permet d'expliquer relativement bien la plupart des observations, notamment la fonction de luminosité des galaxies. Celle-ci est visible sur la Figure 1.3 et représente la densité comobile de galaxies par intervalle de luminosité, en fonction de leur luminosité (exprimée ici en magnitude, en bande K pour le graphique de gauche et en bande b_J pour celui de droite). Les prédictions de ce modèle sont données par la droite tiretée et les observations par les points bleus. Il se trouve que la fonction de luminosité des galaxies a une forme bien connue, dont l'expression analytique a été donnée par Press & Schechter (1974); Schechter (1976) : elle suit une loi de puissance jusqu'à une luminosité caractéristique $\mathcal{L}_\star$, suivie d'une décroissance exponentielle pour les galaxies les plus lumineuses. On observe que le modèle simple décrit ci-dessus reproduit bien les observations pour les galaxies moyennes, dont la luminosité est plus petite que $\mathcal{L}_\star$, mais qu'il prédit trop de galaxies ayant une forte luminosité. Cette dernière étant reliée à sa masse stellaire, cela se traduit par le fait que le modèle, tel que décrit jusqu'à présent, permet la formation de trop de galaxies massives.

Ce problème est connu sous le nom de *sur-refroidissement*. La masse d'une galaxie est en effet principalement déterminée par sa masse stellaire, notamment dans l'Univers local, où une part importante du gaz de la galaxie a eu le temps d'être converti en étoiles. Pour résoudre ce problème et réconcilier le modèle avec les données, on doit trouver un mécanisme supplémentaire, qui permettra d'empêcher une partie du gaz des galaxies les plus massives de former des étoiles. Une des possibilités consiste en la rétroaction du noyau actif de galaxie sur la galaxie hôte, dont j'ai caractérisé les effets observationnels durant cette thèse.

---

[1] Afin d'en alléger la lecture, je me permettrai d'utiliser l'anglicisme *redshift* dans la suite de ce résumé, à la place du terme *décalage spectral vers le rouge*. Il s'agira de la seule entorse à la langue de Molière.

[2] D'après les derniers résultats du satellite Planck, plus de 80% de la matière de l'Univers est de la matière noire.

La rétroaction du noyau actif de galaxie

Avant d'exposer les résultats de cette thèse, je voudrais brièvement rappeler quelques caractéristiques des noyaux actifs de galaxie[3], qui sont au cœur de mon travail. Ceux-ci sont des trous noirs massifs, dont la masse peut atteindre plusieurs milliards de masses solaires : $\mathrm{M}_{\mathrm{TN}} \sim 10^{6-10}\ \mathrm{M}_{\odot}$. Ils sont situés au centre de leur galaxie hôte (d'où le terme de *noyau de galaxie*) et, d'après le modèle classique d'AGN, ils sont entourés d'un disque de matière, qui est lui-même alimenté par un tore de gaz et de poussières, situé à plus grande distance. C'est ce disque qui rend le noyau *actif*, par le mécanisme d'accrétion-éjection : l'énergie potentielle de la matière du disque qui "tombe" sur le trou noir central est convertie en énergie radiative, ce qui rend le disque d'accrétion très brillant sur une grande partie du spectre électromagnétique, et cinétique, sous forme de deux jets relativistes de matière qui s'échappent dos à dos du système. Ces jets portent également un champ magnétique autour duquel spiralent des électrons, ceux-ci émettent alors un rayonnement synchrotron qui est détecté dans le domaine radio, ce qui leur donne le nom de *jets radio*. Un schéma représentant la structure typique d'un noyau actif de galaxie est donné Figure 1.4. L'énergie émise par un AGN peut être colossale et facilement atteindre l'énergie potentielle gravitationnelle de la galaxie hôte. Les signatures observationnelles des AGN peuvent beaucoup varier, notamment en fonction de la visibilité ou de l'obscuration de la partie centrale de l'AGN[4] et de la présence ou de l'absence de jets radio. Cette variété de signatures observationnelles a mené à autant de classes d'objets. Nous distinguerons ici deux grandes catégories :

- Si la partie centrale de l'AGN est dégagée, selon notre ligne de visée, on parlera d'AGN de type-I. Historiquement, on appelle *quasar* un AGN de type-I avec une forte émission radio, ou *QSO*[5] s'il n'est pas (fortement) détecté en radio. Cependant, l'usage a fait que ces deux termes sont devenus synonymes et on parlera plutôt de *Radio-Loud Quasar* (RLQ) ou de *Radio-Quiet Quasar* (RQQ) si on veut faire une distinction claire entre ces deux classes d'objet.

- Par contre, si on ne voit pas la partie centrale de l'AGN, c'est à dire que le disque d'accrétion et la BLR sont cachés depuis la Terre, on parlera d'AGN de type-II ou d'AGN obscurci. Les radio galaxies à haut redshift[6] en sont un exemple, ayant, en plus, des jets radio. Les AGN de type-II et n'ayant pas (ou que peu) d'émission radio sont plus difficiles à détecter, mais ils existent et ils pourraient même être relativement courant dans l'Univers lointain (par exemple Sajina et al., 2007b, 2008, trouvent qu'une fraction importante de leur échantillon de galaxies lointaines obscurcies et à flambée d'étoile ont un AGN).

Il parait de plus en plus probable que toutes les galaxies, au delà d'une certaine masse, abritent un trou noir supermassif en leurs centres (Kormendy & Richstone, 1995). Dès lors, toutes ces galaxies peuvent connaitre une phase d'activité de leur noyau, pour peu qu'un disque se forme autour du trou noir central et que le processus d'accrétion-éjection se mette en place. Or, la quantité d'énergie qu'il émet est colossale et pourrait donc fortement perturber la galaxie hôte, *à condition* que cette énergie soit capable de se coupler au milieu interstellaire pour perturber le gaz. Il est difficile de répondre à cette question de manière théorique, aussi des observations détaillées des possibles effets de l'AGN sur le gaz de la galaxie hôte sont nécessaires afin de trancher. C'est justement l'objet de cette thèse. On étudiera en détail les possibles mécanismes de couplage entre l'énergie émise par l'AGN et le gaz du milieu interstellaire dans la partie 1.4.2 et on se contentera ici de les résumer en deux mots. L'AGN pourrait perturber le milieu interstellaire de sa galaxie hôte, et ainsi y freiner — voire y stopper — la formation d'étoiles, de deux manières : d'une part, la forte luminosité de l'AGN peut, dans son environnement immédiat, accélérer des vents jusqu'à des vitesses quasi-relativistes (Crenshaw et al., 2003), soit directement par pression de radiation, soit par l'intermédiaire de

---

[3] qui sera souvent abrégé en AGN, pour *active galactic nuclueus* en anglais.

[4] qui comprend le disque d'accrétion et la *broad line region*, BLR, faite de nuages de gaz dense en rotation rapide autour du trou noir, voir §6.2 pour plus de détails.

[5] pour *Quasi-Stellar Object* en anglais.

[6] que nous abrégerons souvent en *HzRG*, pour l'anglais *High-Redshift Radio Galaxy*.

diffusions Compton, ce qui a pour effet de chauffer les électrons à haute température (de l'ordre de 10^{7-8} K). D'autre part, les jets radio, qui sont moins denses que le milieu interstellaire, peuvent gonfler un "cocon" de plasma chaud après qu'ils aient frappé le milieu environnant au niveau d'une surface de contact, ce qui fait revenir en arrière la matière qui composait le jet radio. à mesure que les jets radio heurtent le milieu ambiant, faisant avancer la surface de contact, le cocon de plasma continue de gonfler et peut entrainer des nuages de gaz plus denses dans son expansion. Son expansion étant généralement supersonique, une onde de choc se crée tout autour de l'AGN (voir la Figure 1.4 pour avoir une représentation schématique de ce modèle) et peut donc aussi perturber le milieu interstellaire de la galaxie hôte dans son ensemble. Ce sont ces deux modes de rétroaction de l'AGN que nous chercherons à étudier dans cette thèse (au chapitre 4 pour l'effet mécanique des jets radio et au chapitre 6 pour les effets de la forte luminosité de l'AGN).

Autres motivations pour l'étude des effets de l'AGN sur la galaxie hôte

Au delà de la validation observationnelle du mécanisme de rétroaction AGN comme élément-clé du modèle actuel de formation et d'évolution des galaxies, ce qui constitue la motivation majeure de mon travail ; d'autres observations actuellement mal comprises pourraient être expliquées par la même occasion. Je voudrais en dire quelques mots dans les prochains paragraphes.

Mesure de la masse du trou noir central

Grâce à la dynamique de la BLR, constituée de nuages de gaz a priori en rotation káplérienne autour du trou noir central, il est possible d'en mesurer la masse à partir de la distance r entre ce dernier et le gaz émettant une raie donnée[7] et de la vitesse de rotation v de ces nuages de gaz :

$$\mathrm{M_{TN}} = \frac{r\ v^2}{G}$$

Sous l'hypothèse que le disque d'accrétion soit aux environs immédiats du trou noir, alors que les nuages de gaz donnant lieu aux raies larges[8] de la BLR sont plus éloignés et sont ionisés par les radiations émises par le disque d'accrétion, il suffit de mesurer le décalage temporel entre les variations d'intensité du continuum et celles des raies d'émission de la BLR pour connaitre la distance les séparant, la vitesse de la lumière étant connue. Cette technique pour estimer la taille de la BLR est connue sous le nom de *reverberation mapping* (voir par exemple Kaspi et al., 2000). La vitesse de rotation des nuages de gaz autour du trou noir est estimée à partir de la largeur des raies d'émission, puisque la région de l'AGN n'est pas résolue dans la grande majorité des observations. Il faut également prendre en compte l'angle ϕ sous lequel l'AGN est vu puisque cela diminue d'un facteur $\sin(\phi)$ la vitesse de rotation observée par rapport à la réelle.

Corrélations entre la masse du trou noir central et des propriétés de la galaxie hôte

Grâce à la méthode présentée ci-dessus, la masse du trou noir central peut être estimée et ensuite comparée à d'autres propriétés de la galaxie hôte. De fortes corrélations peuvent alors être observées, par exemple entre la masse du trou noir central et la dispersion de vitesse des étoiles du bulbe de la galaxie (Magorrian et al., 1998; Gebhardt et al., 2000; Ferrarese & Merritt, 2000) ou avec la masse du bulbe de la galaxie (Marconi & Hunt, 2003; Häring & Rix, 2004; Gültekin et al., 2009). Des illustrations de ces corrélations sont présentées sur la Figure 1.2.

De telles corrélations sont intrigantes. En effet, la masse du trou noir central est négligeable par rapport à la masse globale de la galaxie (d'un facteur 1 000 en moyenne). De même, le rayon de Schwarzschild du trou noir super massif de l'AGN est beaucoup plus petit que la taille typique d'une galaxie (en dessous du parsec pour le premier, comparé à la dizaine de kiloparsecs pour la seconde). Vu ces différences d'échelles, une question se pose alors naturellement : Comment l'AGN peut-il contrôler des propriétés globales de la

---

[7] en gardant en mémoire que les raies d'émission les plus énergétiques sont émises plus proches du trou noir

[8] avec des largeurs à mi-hauteur de l'ordre de FWHM $\sim 1\,000 - 10\,000$ km s^{-1}.

galaxie hôte ? Ou, inversement, comment se fait-il que la galaxie sache comment faire évoluer l'AGN qu'elle abrite pour que sa masse suive certaines de ses propriétés ? La rétroaction AGN, en couplant ces deux échelles, peut éventuellement servir de lien entre AGN et galaxie et être la cause de ces corrélations.

SINFONI et notre stratégie d'observation

SINFONI, un spectro-imageur dans l'infrarouge

La plupart des résultats de ma thèse viennent d'observations réalisées avec l'instrument SINFONI, qui se trouve sur le téléscope Yepun du VLT. SINFONI est décrit en détail au chapite 2 et je n'en donne ici que les caractéristiques essentielles. Il s'agit d'un spectro-imageur, c'est à dire qu'il fournit à la fois une information spatiale et spectrale sur l'objet observé. Schématiquement, au lieu de l'intensité intégrée sur la bande d'observation, comme sur une image classique, chaque "pixel" d'une observation de SINFONI est en fait un spectre. On travaille donc avec un cube de données, ayant deux dimensions spatiales et une dimension spectrale. SINFONI fonctionne dans l'infrarouge, dans l'une des trois bandes spectrales pour lesquelles l'atmosphère est relativement transparente, et avec un bon pouvoir de résolution spectrale $\mathcal{R}$: la bande J (1.1−1.4 μm ; $\mathcal{R} \sim 2000$), la bande H (1.45−1.85 μm ; $\mathcal{R} \sim 3000$) et la bande K (1.95−2.45 μm ; $\mathcal{R} \sim 4000$). Une quatrième bande d'observation est offerte, il s'agit d'une combinaison des bandes H et K (1.45−2.45 μm ; $\mathcal{R} \sim 1500$). Le champ de vue de nos observations vaut $8'' \times 8''$, ce qui correspond au plus grand champ de vue possible. les observations de SINFONI peuvent être assistées par optique adaptative, ce qui donne une résolution spatiale meilleure que la seconde d'arc (typiquement $\sim 0.2''$, voir le chapitre 6 sur les quasars par exemple). Si le module d'optique adaptative n'est pas utilisé, la résolution spatiale est donnée par le seeing et est alors généralement de l'ordre de la seconde d'arc.

Stratégie d'observation

Pour tester les différents mécanismes qui pourraient être à l'origine de la rétroaction AGN et par lesquels le problème de sur-refroidissement pourrait être résolu, les cibles de nos observations sont des AGN à haut redshift. En effet, les galaxies massives ont formé le gros de leurs étoiles à haut redshift et sur une courte période, qui s'est terminée abruptement (vers $z \sim 1-3$ Thomas et al., 2010). C'est donc pendant cette période qu'il faut stopper la formation d'étoiles dans les galaxies massives et que la rétroaction AGN, si elle est effectivement efficace, doit se produire. D'où l'observation de radio galaxies et de quasars qui sont pour la plupart à des redshift $z \sim 2.0-2.5$.

À ces redshifts, ce sont les raies d'émission initialement émises dans le visible qui sont observées avec SINFONI. Les raies les plus intenses que nous détecterons dans nos observations sont donc Hβ, le doublet [OIII] à 4959Å et 5007Å, Hα et le doublet [NII] à 6548Å et 6583Å. Dans quelques sources, nous détectons aussi le doublet [SII] à 6716Å et 6731Å. Ces raies d'émission sont émises par du gaz ionisé chaud (à des températures de l'ordre de 10^4 K) dont la source d'ionisation peut être facilement déterminée grâce à des diagnostics impliquant les rapports de flux des quatre raies d'émission mentionnées ci-dessus (Baldwin et al., 1981). D'autre part, la luminosité de la raie d'émission Hα permet d'estimer la masse de gaz ionisé que l'on observe dans nos sources, moyennant certaines hypothèses (voir le §1.6.2 pour les détails). Le rapport entre les flux des raies d'émission Hβ et Hα permet d'estimer l'extinction que subit la lumière visible à cause de la poussière dans les galaxies observées. Enfin, lorsqu'il est détecté, le doublet [SII] permet d'estimer la densité d'électrons dans le gaz ionisé.

Grâce à SINFONI, nous sommes aussi capables d'étudier la cinématique du gaz ionisé dans toute la région de la galaxie hôte où il est détecté : le décalage Doppler des raies d'émission permet d'observer ses mouvements ordonnés et à grande échelle, la largeur à mi hauteur des raies d'émission permet d'estimer son degré de turbulence et l'intensité des raies d'émission donne accès à sa brillance de surface, le tout à travers toute la galaxie. Si l'on a réussi à déterminer sa masse, on est donc capable d'estimer les énergies cinétique et turbulente du gaz ionisé dans la galaxies.

ATCA pour les observations radio

Avec SINFONI, nous avons accès à beaucoup d'informations sur le gaz ionisé, mais pour vérifier que ses caractéristiques peuvent être expliquées par les effets des jets radio sur le milieu interstellaire, il nous reste à observer et étudier ces jets. Pour cela, j'ai utilisé l'*Australian Telescope Compact Aarray* (ATCA), dont la résolution spatiale, pour des observations à 5.5−9.0 GHz, est comparable à celle de SINFONI. l'ATCA est décrit est détail au §2.3 et je me limiterai ici au fait que les observations radio permettent d'observer la morphologie du jet radio, qui peut donc être comparée à celle du gaz ionisé, et permettent aussi d'estimer la puissance des jets radio, qui peut alors être comparé aux énergies cinétique et turbulente du gaz inisé. Ces deux comparaisons permettent d'estimer si les jets radio sont responsables de l'état du gaz ionisé, tel qu'observé avec SINFONI.

Arrêt brutal de la formation d'étoiles par les radio-jets

Résultats préliminaires concernant les radio galaxies les plus puissantes

Les radio galaxies ont pendant longtemps été les objets les plus lointains connus et, en tant que telles, elles ont été l'objets de nombreuses études (à ce sujet, on pourra se référer à la revue de Miley & De Breuck, 2008). Ainsi, les radio galaxies à haut redshift font déjà l'objet d'une littérature abondante et nous pouvons leur trouver quelques caractéristiques communes : Ces galaxies sont parmi les plus massives de leur époque (Rocca-Volmerange et al., 2004; Seymour et al., 2007; De Breuck et al., 2010) et forment des étoiles à un rythme effréné, avec un taux de formation d'étoiles de plusieurs centaines, voire d'un millier, de masses solaires par an (par exemple, cf. Archibald et al., 2001; Reuland et al., 2004). De plus, nous les trouvons préférentiellement dans des régions sur-denses de l'Univers, comme l'ont montré, entre autres, Best et al. (2003b); Kurk et al. (2004b); Venemans et al. (2007); Matsuda et al. (2010); Galametz et al. (2013). Cette tendance à se trouver dans des régions denses de l'Univers nous fait penser qu'elles pourraient être les précurseurs des galaxies se trouvant au centre des amas locaux de galaxies, avec qui elles ont d'ailleurs une forte ressemblance morphologique (voir, par exemple, Pentericci et al., 1997; Hatch et al., 2009).

La puissance (10^{45-47} erg s^{-1}) et la durée d'activité (10^{6-7} ans) de leurs jets font qu'ils peuvent founir assez d'énergie pour perturber une partie importante du gaz de la galaxie hôte, voire pour l'en dissocier gravitationnellement. Le mécanisme par lequel les jets radio peuvent se coupler au milieu interstellaire a déjà été rapidement introduit et sera expliqué en détail au §1.4.2. Des signatures observationnelles de ce mécanisme existent déjà. Par exemple, Nesvadba et al. (2006, 2008) ont étudié la dynamique et l'énergétique du gaz ionisé dans quatre HzRGs, qui ont des jets radio parmi les plus puissants de l'Univers. Ils ont observé l'émission de gaz ionisé sur de grandes régions, recelant d'importantes quantités de gaz ionisé (jusqu'à 10^{10} M$_\odot$). Ce gaz est très perturbé (avec des raies d'émission dont la largeur à mi-hauteur est de l'ordre de 1000 km s^{-1}) et présente d'importants gradients de vitesse, comparable avec la vitesse de libération de la galaxie hôte. Ces régions d'émission du gaz ionizé, ainsi que le gradient de vitesse qu'elles présentent, sont alignés avec la direction des jets radio, mais moins étendus que ceux-ci (voir la Figure 1.7 qui présente le cas typique de la radio galaxie MRC 0406−244). De plus, l'énergie cinétique et turbulente du gaz ionizé sont de l'ordre du pourcent de l'énergie du jet. Tous ces constats pointent fortement du doigt les radio jets comme étant les responsables de la dynamique extrême du gaz ionizé dans ces radio galaxies très puissantes.

Mes résultats pour des radio galaxies de puissance plus modérée

La capacité des jets radio très puissants à perturber fortement une importante fraction du gaz interstellaire, voire à en entrainer une part non-négligeable en dehors du potentiel gravitationnel de la galaxie hôte, est donc démontrée. Néanmoins, ce type de radio galaxie reste extrêmement rare, bien que la fonction de luminosité radio croit très rapidement avec le redshift, notamment dans sa partie la plus lumineuse (comme observé par Willott et al., 2001; Gendre et al., 2010, et illustré par la Figure 1.9). Le mécanisme d'arrêt de la formation d'étoiles par les radio jets étant validé dans le cas le plus évident (c'est à dire avec les jets radio les plus puissants connus) et ses signatures observationnelles étant également identifiées, l'idée de la première partie de ma thèse a alors été d'étendre les études précédentes à un échantillon de radio galaxies moins puissantes (d'un facteur 10 à 100) et par conséquent plus communes que leurs cousines extrêmement puissantes. Nous avons ainsi observé douze radio galaxies dont les jets radio sont environ dix fois moins puissants que ceux des galaxies étudiées par Nesvadba et al. (2006, 2008), et six autres radio galaxies dont la puissance des jets radio est cent fois moins puissante. Tout comme leurs cousines les plus puissantes, ces HzRGs présentent elles aussi de grandes régions d'émission de raies du gaz ionizé. Ce gaz est également très perturbé (avec des largeurs de raies à mi hauteur de l'ordre de $500-1000$ km s^{-1}). Par contre, les gradients de vitesse observés sont plus modérés (de l'ordre de $100-700$ km s^{-1}) et n'atteignent pas, par exemple, la vitesse de libération de leur galaxie hôte. Par analogie avec les études précédentes, l'entrainement du gaz ionisé par les jets radio est à nouveau le mécanisme le plus plausible.

Arrêt brutal de la formation d'étoiles par la luminosité de l'AGN

L'autre mécanisme par lequel l'AGN pourrait perturber le milieu interstellaire, freinant ou stoppant ainsi la formation d'étoiles de sa galaxie hôte et résolvant le problème du sur-refroidissement, implique sa grande luminosité. J'ai donc travaillé sur les données d'observations par SINFONI de onze quasars, dont six sont bien détectés en radio (ce sont donc des RLQ), les cinq autres étant des RQQ. La difficulté de ce travail réside dans la soustraction précise de la composante large de la raie d'émission Hα, qui est due à la rotation rapide de nuages denses à proximité du trou noir super-massif central, et qui domine largement la raie d'émission Hα. Notre technique de soustraction est décrite au §6.2 et ne requiert que l'hypothèse que la composante étroite de la raie d'émission, due à la région étendue d'émission de raie du gaz ionisé, est gaussienne. Le continu dû au disque d'accrétion est quant à lui décrit par une loi de puissance. Les résultats de cette soustraction sont présentés aux Figures 6.5(a), 6.6, 6.11(a) et 6.12.

Deux sources intrigantes

Dans notre échantillon d'une cinquantaine de radio galaxies (dont font partie celles présentées dans cette thèse, voir Nesvadba et al., 2014, en préparation, pour l'échantillon complet) il y en a deux qui semblent être différentes des autres : Leurs régions d'émission de raie du gaz ionisé ne sont pas du tout alignées avec leurs jets radio, comme c'est le cas pour le reste de l'échantillon. Afin d'en savoir plus, j'ai proposé, et obtenu, d'observer ces deux galaxies avec l'imageur proche infra-rouge ISAAC, monté sur un des téléscopes du VLT, pour essayer de comprendre l'origine de leur particularité. Le principal avantage d'ISAAC par rapport à SINFONI réside dans son grand champ de vue ($152'' \times 152''$ par rapport à $8'' \times 8''$) et dans la disponibilité d'un filtre étroit[9] centré sur la raie d'émission *redshiftée* Hα de l'une de ces deux galaxies. Cela nous permettra donc d'étudier la répartition du gaz ionisé (tracé par l'émission de la raie Hα) à de plus grandes distances que ce que permet SINFONI, et notamment de chercher des galaxies présentant un excès de flux dans l'image en bande étroite par rapport à leur flux en filtre large et qui peuvent être des émetteurs Hα (Hα *emitters* en anglais, abrégé en *HAE*). Les images de ces deux galaxies avec des filtres larges permettront d'étudier leurs morphologies stellaires et par exemple d'observer des signatures d'interaction (ou fusion) de la radio galaxie avec un partenaire, ce qui pourrait peut être causer le non-alignement des régions d'émission de raie du gaz ionizé. Notons tout de même que ce scénario parait peu probable : dans l'Univers local, les régions d'émission de raies par le gaz ionizé qui sont dues à la fusion de galaxies sont moins brillantes que ce que nous observons dans le cas de ces deux radio galaxies à haut redshift (voir, par exemple, Stockton et al., 2002; Fu & Stockton, 2007b).

Les observations ont été conduites sous d'excellentes conditions atmosphériques, donnant une résolution spatiale de $\sim 0.5''$ (ou ~ 4 kpc aux redshifts de ces galaxies). Pour les deux galaxies, ces nouvelles observa-

---

[9] d'une largeur à mi-hauteur de 250Å, ce qui correspond à une dispersion de vitesse de ±2300 km s^{-1} autour du redshift de la radio galaxie.

tions confirment ce que nous avions déjà observé avec SINFONI. Nous avons donc été capable d'étudier de manière précise la morphologie de ces deux radio galaxies. Contrairement à ce qui est généralement observé pour les galaxies à haut redshift, qui ont tendance à être plus compactes que les galaxies elliptiques locales (Daddi et al., 2005; van Dokkum et al., 2008), ces deux radio galaxies montrent des signes d'enveloppes stellaires étendues. Ceci constitue un signe d'évolution avancée, puisqu'elles ont eu le temps de constituer le halo stellaire habituellement observé à plus bas redshift. L'image centrée sur la raie d'émission Hα (voir la Figure 5.11) de l'une des deux galaxies confirme les observations de SINFONI et la présence de gaz ionisé selon une direction quasiment perpendiculaire à la direction des jets radio. Comme indiqué précédemment, les HzRGs ont tendance à se trouver dans des régions sur-denses de l'Univers et, pour cette raison, sont suspectées d'être les ancêtres des galaxies centrales (ou dominantes) et massives des amas de galaxies locaux. Or, les amas de galaxies sont entourés d'une atmosphère de plasma très chaud (avec des températures de l'ordre de 10^{7-8} K, voir McNamara & Nulsen, 2007, pour une revue sur le sujet) dans lesquels on observe des filaments de gaz ionisé, dont l'origine est toujours débattue (voir Conselice et al., 2001, pour le cas frappant de l'amas de Persée). Un scénario pouvant expliquer les étranges régions d'émission de raie du gaz ionisé dans ces deux galaxies consiste donc à supposer qu'elles sont des analogues, à haut redshift, de ces filaments de gaz ionisé observé autour d'environ un tiers des amas de galaxies locaux (McDonald et al., 2010). Ce scénario est conforté par l'observation de treize émetteurs Hα autour de la radio galaxie observée en bande étroite, ce qui correspond à une sur-densité du nombre de sources détectées d'un facteur ~ 30 par rapport à des observations d'un champ quelconque (Sobral et al., 2012) à la même époque.

Contents

Chapter 1

AGN feedback: an important piece of galaxy evolution models

Contents

We study in this thesis an important component of current models of galaxy formation and evolution: the feedback from the Active Galactic Nucleus (AGN). In this introduction, we will, in a first part, present the underlying cosmological model, the framework in which galaxy formation and evolution occur. We will then give some details on models of structure formation and notably on their difficulties to reproduce some key observations. In the following section, we will introduce the AGN feedback mechanism and show how it can address the problems encountered by these models. We conclude this introduction by giving some observational examples of AGN feedback and by outlining the approach of this thesis.

1.1 The underlying cosmological paradigm: the ΛCDM model

Similarly to all models in physics, the ΛCDM model is based on a theory, the General Relativity, and requires some assumptions, the spatial homogeneity and the isotropy of the Universe, collectively called the cosmological principle.

1.1.1 What is the ΛCDM model?

This model is the simplest one that can explain most of the available observations of our Universe, even though its main components are of unknown nature:

- Λ, called the cosmological constant, represents the "dark energy", responsible for the observed acceleration of the expansion of the Universe. According to the observation of the Cosmic Microwave Background (CMB) by the Planck satellite, the dark energy represents about 68% of the energy content of the Universe today (Planck Collaboration, XVI, 2013).
- CDM stands for "Cold Dark Matter", *i.e.*, matter that interacts only gravitationally, not electromagnetically, and therefore does not emit light, hence the adjective "dark". It is also called "cold" because it is supposed to be non-relativistic. Currently, dark matter represents about 27% of the energy content of the Universe, *i.e.*, more than 80% of the matter of the Universe.
- Baryonic (or ordinary) matter, of which stars, planets, dust, ... are made, represents only about 5% of the energy content of the Universe today, or about 20% of the matter of the Universe.

1.1.2 Evidence in favor of this model

The ΛCDM model is able to explain various available observations of our Universe: the fact that it is expanding (Hubble, 1929), its homogeneity on large scales (larger than $\sim$ 100 Mpc, see Gott et al., 2005, for an observational illustration), the properties of the structures observed at smaller scales, such as galaxies or clusters of galaxies (probed by surveys, *e.g.*, the Sloan Digital Sky Survey, York et al., 2000), the primordial chemical enrichment (Steigman, 2007), the acceleration of the expansion of the Universe (Perlmutter et al., 1999), etc.

Hubble's observation that galaxies are receding from us and the fact that the further they are, the more rapid is their recession, must be translated into an expanding Universe. Indeed, according to the cosmological principle, there is no reason that our position is special, meaning that galaxies are not only receding from us, they are receding from one another as well. Conversely, this means that the Universe was denser and denser as we go back in time. Up to the point when the Universe was so dense, *i.e.*, so hot, that our usual theories (general relativity and quantum mechanics) do not hold anymore and that is called the "Big Bang". Soon after this, all the matter must have been under the form of a plasma, whose temperature was decreasing with the expansion of the Universe. The primordial nucleosynthesis of some isotopes of hydrogen, helium, lithium and beryllium occured at that time, when the temperature was high enough to allow the production of these nuclei from individual protons and neutrons, but not too high so that their destruction rate by energetic photons was lower than their production rate. The relative abundance of each species depends on the duration of this period (about 10 minutes), *i.e.*, on the expansion rate of the Universe which itself depends on the quantity of matter: the greater the matter density of the Universe is, the slower is the expansion. Note that stellar nucleosynthesis, *i.e.*, the production of heavier elements by the fusion of light elements in cores of stars or in the explosion of supernovae, does not produce enough helium and actually destroys lithium and beryllium. Therefore, it cannot explain the abundance of these three species.

After the primordial nucleosynthesis, the temperature of the expanding Universe was still high enough to keep the newly formed atoms ionized. The photons were therefore continuously Compton scattered on free electrons of this plasma. Eventually, the Universe became too cold to prevent the combination of electrons with protons and the formation of hydrogen atoms. The mean free path of photons suddenly increased strongly and the Universe became transparent. Photons from this last scattering surface are still observable: they form the Cosmic Microwave Background (CMB), observed today as a black body at ~ 2.7 K. From the observation of the CMB, it is therefore possible to obtain information about the state of the Universe in its very early stages, since it was emitted only 380,000 yrs after the Big-Bang. It appears that the Universe was very homogeneous at that time, with relative variations of density from one place to another of the order of 10^{-5}.

In this thesis, the cosmological parameters are chosen in agreement with the concordance ΛCDM model that we described previously: the Universe is flat, *i.e.*, the space curvature $\Omega_k = 0$; the energy content is dominated by dark energy $\Omega_\Lambda = 0.7$; the rest of the energy content is constituted of (mostly dark) matter $\Omega_M = 0.3$ and the expansion rate of the Universe is given by $\mathrm{H}_0 = 70$ km s^{-1} Mpc^{-1}, the current value of the Hubble constant.

1.2 Structure formation

In contrast with the homogeneity of the CMB, the local Universe, as we observe it 13.8 Gyr after the Big Bang, is strongly inhomogeneous and structured, from stellar systems to galaxies and clusters of galaxies, representing dramatic variations of density from one place in the Universe to another.

1.2.1 The CMB anisotropies as the seeds of today large scale structures

According to the ΛCDM model, today large scale structures of dark matter originate from the tiny inhomogeneities observed in the CMB, making them the seeds from which galaxies and clusters of galaxies formed under the action of gravity.

From primordial inhomogeneities visible in the CMB, gravity leads to the formation of halos of dark matter, as illustrated in Fig. 1.1 (*left*). This means that structures formed in a *hierarchial* way, from the smallest to the biggest, by a succession of mergers. N-body simulations, performed in the ΛCDM framework and taking the CMB anisotropies as initial conditions, allow us to follow the evolution of the dark matter structures. Statistically, they reproduce the observed distribution of galaxies, that traces the distribution of dark matter with a certain level of fidelity. This is illustrated by Fig. 1.1 which shows an example of a N-body numerical simulation on the left and the actual distribution of galaxies in a slice of sky around the Milky Way as observed by the Sloan Digital Sky Survey[1] on the right. These dark matter halos constitute the skeleton in which baryons are gravitationally trapped and form galaxies.

1.2.2 Baryonic processes become important at galaxy scales

The validity of these dark matter simulations stops at the galaxy cluster scale though. Indeed, contrary to larger structures, gravity is not any more the only process driving the evolution of galaxies or clusters of galaxies: processes involving gas cooling and heating start being as important as gravity and must be taken

---

[1] shortened as “SDSS” thereafter. It has surveyed a quarter of the sky in 5 photometric bands in the visible and has followed up subsets of bright objects with spectroscopy, thus detecting millions of galaxies and about one million of quasars (York et al., 2000).

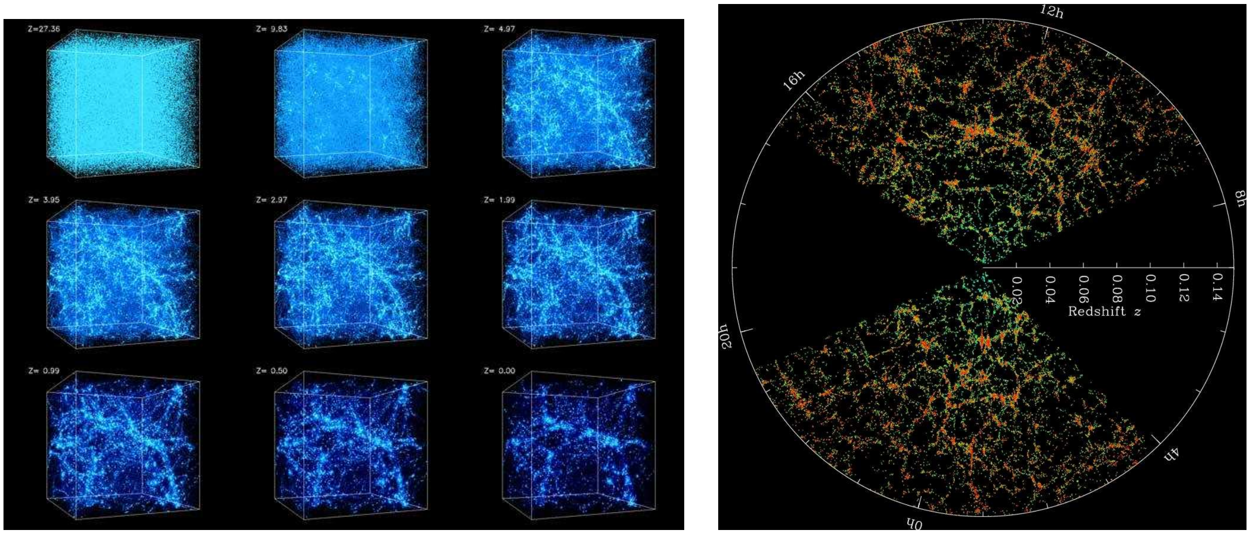

Figure 1.1: *Left*: Evolution of the dark matter structures in the standard ΛCDM model. The first image is at redshift z = 27, corresponding to a Universe about 100 Myr old, the sixth one is at redshift z = 2, when the Universe was 3.5 Gyr old and the last one correspond to the Universe today (z = 0) — Credit: University of Chicago. *Right*: Structure of the local Universe, as observed by the SDSS and traced by galaxies in a slice of sky around us — Credit: SDSS

into account. However, all of these mechanisms are complex to model: they depend on many parameters (*e.g.*, the star formation rate, the metallicity, . . .), are interdependent and based on non-linear equations (*e.g.*, of (magneto)hydrodynamics). Because of their complexity, they can presently be numerically simulated only on the scale of individual galaxies and it is impossible to include them in the cosmological simulations. Simplified analytical relations must therefore be used in order to mimic baryonic processes in the output of cosmological simulations. These models, called semi-analytic, take advantage of either empirical laws or theoretical expectations to simulate the evolution of baryons in dark matter haloes.

1.2.3 Discrepancies between observations and model predictions and unexplained observations

Thus, to recover the formation and evolution of galaxies, semi-analytic models apply simplified relations instead of directly modelling complex processes. For example, the Schmidt-Kennicutt law (Schmidt, 1959; Kennicutt, 1998) is an empirical law based on the observed tight correlation between star formation rate surface density and molecular gas mass surface density. It is commonly adopted to quantify how gas is turned into stars in galaxies. These empirical relations are governed by some free parameters (*e.g.*, the index of the Schmidt-Kennicutt law), tuned to reproduce available observations and then applied to the results of dark matter simulations in order to study the formation and evolution of galaxy populations. Their results can then be statistically compared to observations and we can test the validity of modelled mechanisms.

Luminosity and mass functions of galaxies

A common observation that semi-analytical models try to reproduce is the luminosity function (LF) of galaxies that gives the comoving number density of galaxies per luminosity bin, as a function of their luminosity (*i.e.*, their absolute magnitude). An example of a luminosity function is given in Fig. 1.3, in two different photometric bands.

The mass function of galaxies can be constructed from the luminosity function, provided that some mass-to-light ratio is assumed in order to convert the luminosity of a galaxy into its mass. Similarly to the LF, the mass function gives the number of galaxies per comoving volume and per stellar mass bin as a function of their stellar mass and can be compared to predictions of semi-analytical models.

The overcooling problem

When comparing the predictions of semi-analytic models with observations, an important discrepancy appears: models predict too many massive galaxies and too many dwarf galaxies. This phenomenon is known as the "overcooling problem" (White & Rees, 1978). Indeed, stars form from gas, that first has to cool in order to condense. In models, this cooling is too efficient and gas is converted into stars at too high rates (*e.g.*, White & Frenk, 1991; Benson et al., 2003). Unless something is fundamentally wrong about our understanding of how the gas cools and collapses in galaxies, some mechanism able to heat the gas must be found in order to slow down the star formation rate and to reconcile the predictions of models with observations.

In low-mass systems, this problem is solved by including the photoionization caused by UV radiation coming from massive stars or the kinetic energy coming from supernovae explosions. Indeed, their potential wells are not deep enough to detain galactic winds induced by these explosions of massive stars (*e.g.*, Efstathiou, 1992; Silk, 1997). But it appears that this solution is not sufficient for the most massive galaxies and their much deeper gravitational wells, and another source of energy has to be found (*e.g.*, Thoul & Weinberg, 1995).

Empirical relations between supermassive black holes and host galaxies

At the center of virtually all galaxies there is a supermassive black hole (*e.g.*, Kormendy & Richstone, 1995; Kormendy & Gebhardt, 2001; Ferrarese & Ford, 2005). We will describe them in detail in §1.4.1, here we simply need to recall that an astrophysical black hole is characterized by only two quantities: its mass and its angular momentum[2] (*e.g.*, Robinson, 1975). While its angular momentum is difficult to measure since it affects only the close environment of the black hole (*e.g.*, Done et al., 2013), its mass can be estimated more easily (*e.g.*, by reverberation mapping, Kaspi et al., 2000). When doing so, correlations are observed between the mass of the black hole $\mathrm{M_{BH}}$ and some properties of the bulge of the host galaxy (such as the velocity dispersion of the stars in the bulge σ, or the bulge mass $\mathrm{M_{bulge}}$). The observations of Magorrian et al. (1998); Gebhardt et al. (2000); Ferrarese & Merritt (2000) showed that $\mathrm{M_{BH}}$ and σ_{bulge} are correlated: it is the so-called $\mathrm{M}-\sigma$ relation. Marconi & Hunt (2003); Häring & Rix (2004) showed that $\mathrm{M_{BH}}$ is correlated to $\mathrm{M_{bulge}}$: it is the $\mathrm{M_{BH}} - \mathrm{M_{bulge}}$ relation. These two relations are illustrated in Fig. 1.2. A third correlation between the supermassive black hole mass and a property of the host galaxy exists: it implies the luminosity of the bulge (*e.g.*, Gültekin et al., 2009).

These correlations are puzzling because, despite of orders of magnitude of difference in the masses or sizes of the black hole and the galaxy bulge, these two objects are somehow "aware" of each other. This is enigmatic since, according to the $\mathrm{M_{BH}} - \mathrm{M_{bulge}}$ relation, the supermassive black hole is $\sim 1000\times$ less massive than the galaxy bulge. The ratio between their sizes is even more important: the Schwarzschild radius of a black hole is given by $R_S \simeq 3\ M_{BH}/M_\odot$ km, *i.e.*, 10^{-4} pc for a $10^9\ \mathrm{M_\odot}$ supermassive black hole, while the typical size of the bulge is ~ 10 kpc. Given these differences, it is difficult to imagine that there is some causal link between the supermassive black hole and its host galaxy, however these observed correlations clearly call for some mechanism(s) able to link them one to another.

---

[2] its charge can be neglected in an astophysical context.

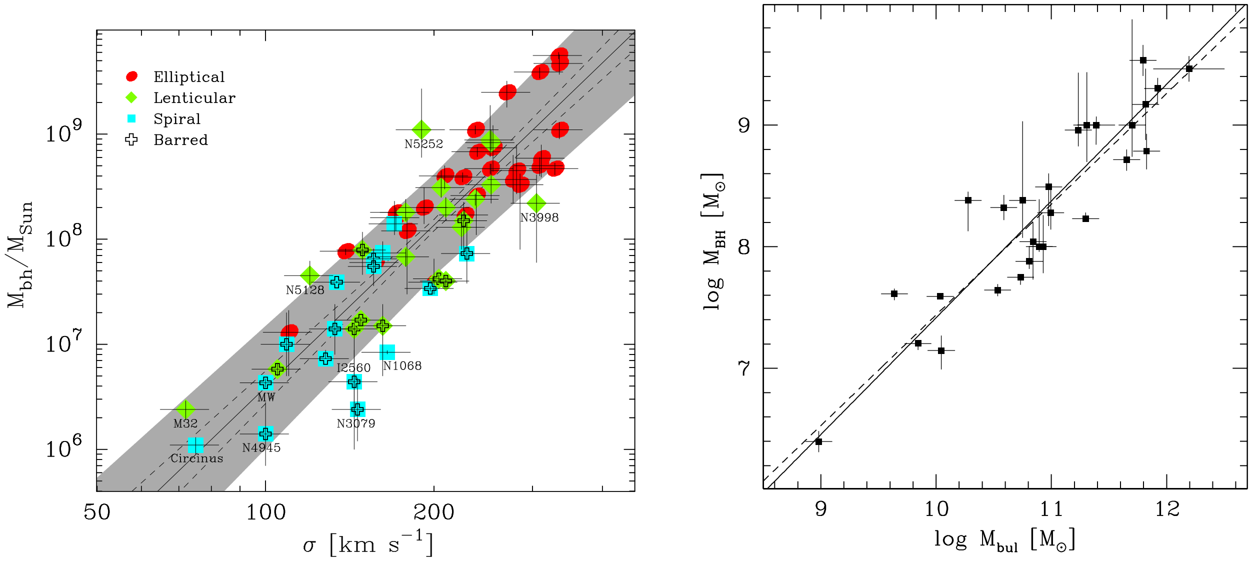

Figure 1.2: Illustration of the observed correlations between the mass of the supermassive black hole and two properties of their host galaxies. *Left*: $M_{\rm BH} - \sigma$ relation from Graham et al. (2011). *Right*: $M_{\rm BH} - M_{\rm bulge}$ from Marconi & Hunt (2003).

1.3 Feedback loops as a solution to the overcooling problem

Feedback mechanisms, when applied to models of galaxy formation and evolution, are used to control the star formation rate and are therefore potential solutions to the overcooling problem. All of these mechanisms act on the interstellar medium (ISM) with the aim of keeping it unsuitable for star formation, *i.e.*, preventing it from reaching the state of a self-gravitating cloud of cold dense molecular gas. Therefore, feedback mechanisms can a priori act on all phases of the ISM: the dense cold molecular gas (T $\sim$ 10 K) and the warmer neutral atomic phase (T $\sim 100 - 1000$ K), from which star formation is more likely to occur on short timescales. Other phases of the ISM, the warm ionized phase (with T $\sim 10^4$ K) and the hot and diffuse gas phase (with T $\sim 10^7$ K), although unsuitable for star formation as they are, can also trace the effect of feedback mechanism and can be easier to observe than the cold gas.

1.3.1 Starburst and supernovae feedback

Feedback through the energy injection from starburst and supernovae into the interstellar gas was rapidly introduced in semi-analytical models in order not to overpredict the number of faint galaxies (*e.g.*, Efstathiou, 1992; Cole et al., 1994; Silk, 1997). This is a feedback loop in the sense that stars form from the cold clouds of molecular gas of the interstellar medium. But, in turn, these clouds are heated and ionized by the radiation and stellar winds coming from the most massive stars and then disrupted when these massive stars explode as supernovae, therefore limiting star formation. Assuming a Salpeter initial mass function (IMF, Salpeter, 1955), supernovae emit $\sim 10^{49}$ erg per solar mass of star formed. De Young & Heckman (1994) investigated the effect of central starburts on the instellar medium of dwarf and normal galaxies, with stellar masses in the range $\rm M = 10^7 - 10^{11}\ M_\odot$. They assume that star formation happen in a single starburst and that there is no dark matter halo surrounding the galaxies, which implies that the energy from supernovae explosions is released on short timescales, typically $\sim 10^7$ yrs (*i.e.*, the lifetime of massive stars). Star formation histories more realistic than this single starburst model give longer timescales for the release of supernovae energy, typically $\lesssim 10^8$ yrs (*e.g.*, Marcolini et al., 2004). De Young & Heckman (1994) calculated the fraction of the ISM that escape from the galaxy under the form of winds caused by the large quantities of energy emitted by the starburst, depending on the gas geometry, the gas density, the mass of the host galaxy and the energy of starburst. They found that most of the interstellar gas of small dwarf galaxies (with $\mathrm{M} \sim 10^7\ \mathrm{M}_\odot$) escape from the potential well of the galaxy, irrespective of the other parameters. On the other hand, normal galaxies (with $\mathrm{M} \sim 10^{11}\ \mathrm{M}_\odot$) have potential wells deep enough to retain their ISM in most cases. The interstellar gas of typical dwarf galaxies (with $\mathrm{M} \sim 10^9\ \mathrm{M}_\odot$) show more diverse behaviours.

Observations of local starburst galaxies, for example by Heckman et al. (1990); Lehnert & Heckman (1995, 1996a,b), showed that starbursts, because of the stellar winds and supernovae they imply, are indeed able to drive winds along the minor axis of galaxies out to large distances (up to ~ 10 kpc). A nearby example is the M82 starburst galaxy: Lehnert et al. (1999a) showed that a significant part of the "superwind" is energetic enough to eventually leave the galaxy potential well. One consequence of these galactic winds is the enrichment of the intergalactic medium in metals. This enrichment can be observed by chance alignments between galaxies and background quasars (*i.e.*, very luminous sources). This leads to observed superimposed metal absorption lines, associated with the foreground galaxy, in the quasar spectrum (*e.g.*, Kacprzak et al., 2011b). The impact parameter between the quasar and the galaxy is typically in the range $10-100$ kpc, meaning that metals have indeed been driven from their production place out to large distances, potentially by galactic winds due to a previous starburst.

Given these theoretical predictions and these observations, starburst feedback, through stellar winds and supernovae explosions, is efficiently able to unbind significant fractions of the interstellar gas from the potential well of dwarf galaxies. Larger escape velocities of normal galaxies imply that these galaxies could detain large fractions of their ISM. Only massive galactic winds due to intense starbursts (triggered by major galaxy mergers for instance) could blow away all the gas from normal galaxies. The overcooling problem can therefore be solved in dwarf galaxies by taking into account the effects of supernovae and stellar winds feedback.

1.3.2 The need for an additional source of energy in massive galaxies

In massive galaxies, the energy emitted by supernovae is far from being sufficient to drive galactic winds because of their deep potential wells (*e.g.*, Thoul & Weinberg, 1995). The overcooling problem therefore subsists in massive systems, unless an additional source of energy is found (*e.g.*, Kauffmann et al., 1999). Silk & Rees (1998) introduced such a potential source of energy: accretion onto the supermassive black hole, found at the center of most galaxies (see §1.2.3), that can emit, under certain conditions, large quantities of energy and drive outflows even in the most massive galaxies. Potential mechanisms leading to the release of energy by the supermassive black hole will be extensively discussed in the next section 1.4. In order to see the effects of this mechanism, called AGN feedback, one can run hydrodynamical simulations that take the energy emitted by the supermassive black hole into account. These simulations resolve the equations of the hydrodynamics for a large number of particles, that can represent dark matter, stars or interstellar gas. Heating and cooling processes are usually also taken into account. However, the spatial resolution of these simulations (typically $\sim 5-50$ pc) is too large to resolve phenomena such as star formation or accretion onto the central supermassive black hole and "sub-grid" recipes must be used in order to take them into account. For instance, Springel et al. (2005); Di Matteo et al. (2005) simulated the impact of AGN feedback during and after the merger of two spiral galaxies[3]. They suggested that gravitational interactions induced by the merger lead to intense star formation but also provoke the activity of the central supermassive black hole. This activity rapidly quenches the episode of star formation (on timescale of typically 10^7 yrs) and expels a fraction of the interstellar medium out of the remnant galaxy. Semi-analytic models also took into account prescriptions that supposedly model AGN feedback (*e.g.*, Kauffmann & Haehnelt, 2000; Benson et al., 2003) and could thus abruptly stop the star formation and solve the overcooling problem in the massive galaxies. This is known as the "quenching phase" of AGN feedback.

---

[3] Mergers of galaxies are thought to drive large amounts of gas towards the center of galaxies (*e.g.*, Mihos & Hernquist, 1996), a necessary step before the supermassive black hole can emit energy.

1.3.3 Keeping the gas hot

However, quenching the star formation is only the first step. Indeed, given the deep potential wells of massive galaxies, it is difficult to expel all of their ISM and the gas perturbed by the quenching phase of AGN feedback will eventually cool and fall back on its host galaxy if it has not escaped. Moreover, evolved stellar populations also return large quantities of gas into the interstellar medium (up to about half of the initial stellar mass in a Hubble time, *e.g.*, Jungwiert et al., 2001) and accretion onto the galaxy also replenishes its interstellar medium in gas (*e.g.*, Bouché et al., 2013). All of this gaseous content will eventually cool and form stars: the quenching phase of AGN feedback only delays the overproduction of stars. Croton et al. (2006); Somerville et al. (2008) therefore included a "maintenance phase" of AGN feedback in their models, which is able to keep this gas hot and unsuitable for star formation.

The usefulness of this mechanism in massive systems is illustrated in Fig. 1.3. The observed luminosity function (in the $K-$band in the left panel, in the b_J-band in the right panel) is given by the blue points. The luminosity function predicted by the model that does not include the "maintenance phase" AGN feedback is represented by the dashed line (but feedback from starburst, supernovae and the "quenching phase" from AGN are included). The predicted number of very luminous systems, *i.e.*, the most massive galaxies[4], is clearly overestimated (dashed line). The model is in better agreement with the data when this additional and long-term source of energy (namely the "maintenance phase" AGN feedback) is taken into account, as shown by the solid curve.

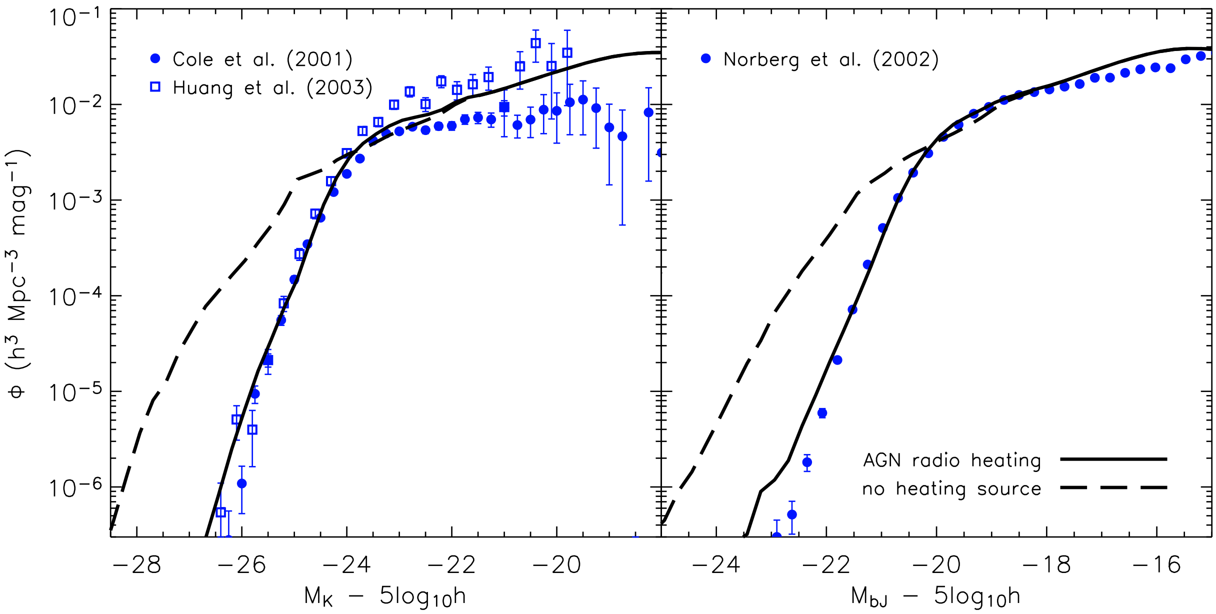

Figure 1.3: Illustration of the effect of energy injected in massive galaxies by the AGN in the model of Croton et al. (2006) during the "maintenance phase" (that they call "AGN radio heating"). When it is turned off (dashed lines), the number of very luminous galaxies is dramatically over-predicted compared to observations: this is the overcooling problem. This is resolved by adding a "maintenance phase" of AGN feedback in the model (solid line), which keeps the gas hot and unsuitable for star formation in the most massive systems.

---

[4] the $K-$band magnitude is a good proxy for the stellar mass, since most of the stellar mass lies in low-mass stars (with $M \lesssim 2M_\odot$), which emission peaks in the visible-NIR. On the contrary, the radiation emitted by massive stars peaks in the UV-visible and is, relatively to their integrated mass, very large, as illustrated by the mass-luminosity relation $\frac{\mathcal{L}}{\mathcal{L}_\odot} = (\frac{M}{M_\odot})^{3.5}$. Therefore, NIR luminosities probe the bulk of the stellar mass and is not very sensitive to the emission of massive stars, which makes it a good proxy for stellar mass.

1.4 AGN feedback, a solution to the overcooling problem in massive galaxies

The solution usually invoked to solve the overcooling problem in massive galaxies involves the Active Galactic Nucleus (AGN), which is thought to be able to heat the interstellar gas of massive galaxies more efficiently than starburst and supernovae feedbacks. In some cases, it might even unbind a significant fraction of this gas from the potential well of the host galaxy. Furthermore, if it can keep the gas hot as postulated in some models (*e.g.*, Croton et al., 2006; Somerville et al., 2008) it could also prevent subsequent star formation on long time scales. In this section, we give the big picture of what an active galactic nucleus is ; and we discuss the potential mechanisms of AGN feedback in more detail.

1.4.1 What is an "Active Galactic Nucleus"?

As indicated by its name, the AGN is found at the center of galaxies. It is a supermassive black hole (SMBH), with $\mathrm{M_{SMBH}}$ of-order $\sim 10^{6-10}$ $\mathrm{M_\odot}$(Wandel et al., 1999; Kaspi et al., 2000). In the standard scenarios, it is immediately surrounded by a disk of matter accreting onto it, and a torus of gas and dust at larger radii, that is a reservoir of material for the accretion disk (Antonucci, 1993). It is called "active" because of the tremendous quantities of energy emitted from this region, as matter from the accretion disk falls onto the supermassive black hole. In this process, gravitational energy is usually converted into radiative and/or kinetic energy very efficiently. From this, it appears that the accretion rate onto the SMBH is one of the important parameters that will govern the quantity of energy emitted by the AGN.

As theorized by Shakura & Sunyaev (1973), the accretion disk is made of different layers, orbiting the central black hole with Keplerian motions. Because of turbulence and friction between the material in these different layers, angular momentum is transfered outwards and the material flows towards the central black hole. The decrease in its gravitational energy translates into an increase of its kinetic energy, along with an increase of its thermal energy, that is radiated away. The temperature of the accretion disk therefore depends on the distance from the central black hole, from very hot close to it (T $\sim 10^{8-9}$ K at a few gravitational radii) to more moderate temperatures further out (T $\sim 10^5$ K at some 10^{2-3} gravitational radii). The disk therefore emits from the hard X-ray to the UV, although some of this radiation can be reproccessed by the surrounding environment. Extraction of angular momentum can also occur through the formation of two back-to-back jets of relativistic material, escaping from the AGN (*e.g.*, Scheuer, 1974; Blandford & Rees, 1974; Blandford, 1976; Blandford & Znajek, 1977; Begelman et al., 1984).

In the classical scenario, at radii larger than the accretion disk, we find the broad line region (BLR). This region probably consists of dense clouds of gas (with $n_H \sim 10^{10-11}$ $\mathrm{cm^{-3}}$, Snedden & Gaskell, 1999) under the gravitational influence of the supermassive black hole. They reach relativistic velocities as they rotate within the deep gravitational potential well of the black hole, giving rise to the characteristic broad line emissions (FWHM $\sim$ 1,000−10,000 km $\mathrm{s^{-1}}$) that explain the name of this region. They are ionized by the radiation coming from the accretion disk (*e.g.*, Kaspi & Netzer, 1999). Other models exist to explain the formation and the confinement of these clouds that give rise to the broad lines, since, under the physical conditions of this region, these clouds should be quickly destroyed (whether because of rapid desintegration or of cloud-cloud collisions). For instance, Emmering et al. (1992) proposed that these clouds could be confined by magnetic pressure, while Murray et al. (1995) proposed that a continuous, optically thick and radiatively driven outflow from the accretion disk could also explain the broad emission lines observed in some AGN (see also Chajet & Hall, 2013).

At radii larger than the dusty torus, we find the narrow line region (NLR). It consists of clouds much less dense than those of the BLR (*e.g.*, electron densities of $\sim 10^{2-3}$ $\mathrm{cm^{-3}}$ are measured by Groves, 2007; Ludwig et al., 2012). These lower densities allow the observation of lines such as the [OIII]$\lambda4959, 5007$ or the [NII]$\lambda6548, 6583$ doublets, that are predominantly collisionnally de-excited in denser environments. These clouds are far from the black hole, so their kinematics is not dominated by it and their velocity dispersions are therefore more quiescent (FWHM $\sim$ 100−1,000 km $\mathrm{s^{-1}}$).

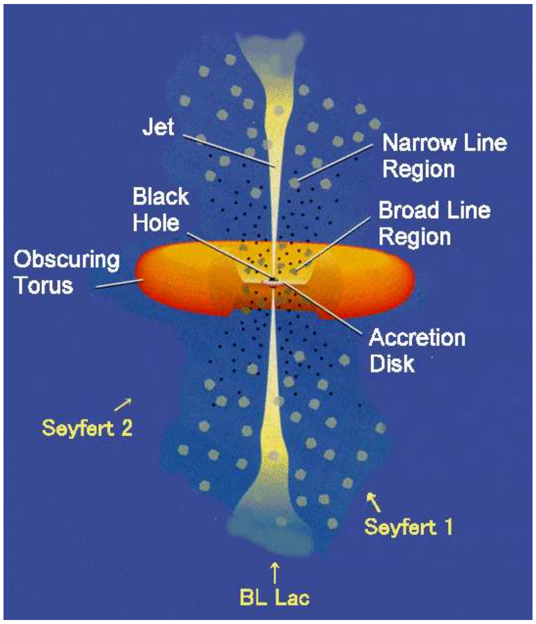

Figure 1.4: Schematic view of an AGN: a supermassive black hole ($M_{SMBH} = 10^{6-10} M_{\odot}$) is surrounded by an accretion disk, being fueled by a dusty, obscuring torus that lies further from the SMBH. When seen sufficiently edge-on, this torus obscurs the central part of the AGN, especially the broad line region (BLR). The BLR is thought to originate from fast moving gas in the accretion disk or in the close vicinity of the SMBH, leading to velocity dispersions of several × 1,000−10,000 km $s^{-1}$and giving broad emission lines in the spectra of these sources (hence their name). In contrast, the narrow line region (NLR) is thought to be due to gas clouds further away from the central engine and being less perturbed (velocity dispersions of few × 100−1,000 km s^{-1}).

AGN can be observed under various forms, each of which has its own name. The main observational differences involve:

- the presence or the absence of radio emission. It originates from synchrotron emission of electrons spiraling along the magnetic field of back-to-back jets that are sometimes observed in AGN (*e.g.*, Begelman et al., 1984).
- The presence or the absence of a clear line of sight to the central part of the AGN. Indeed, a clear view of the accretion disk will lead to the observation of a bright, non-thermal, nuclear continuum. The visibility of the BLR, if present, also has an important impact on the observed spectrum of the AGN. The relative inclination of the AGN with its line of sight and hence the potential obscuration of its central parts by the torus of dusty material, or obscuration by dust lanes further out from the nucleus (*e.g.*, Smajić et al., 2012), is the usual explanation of these different possible observations.

This second point led to the unified model of AGN (Antonucci, 1993). According to this model, the different forms that can take the observation of an AGN mainly depend on its orientation. Thus, a quasar (also called a type−I AGN) is an object with a clear line of sight into its AGN, which is so bright that it outshines its host galaxy, and that is also detected in the radio[5]. Its counterpart that has a hidden AGN, whether because of a dusty torus or because of galactic dust lanes at larger scales, is an obscured (or type−II) AGN. On the other hand the counterpart of a quasar that lacks radio emission is called a quasi-stellar object (QSO). Seyfert galaxies are objects in which the AGN is not bright enough to outshine its host galaxy, which usually

---

[5] This is correct from an historical point of view, given that "quasar" stands for "quasi-stellar radio source". However, nowadays, quasar can designate any AGN with a clear line of sight, irrespective of its radio emission.

also experiences a nuclear starburst. Some observations are in favor of this unified model of AGN, such as the detection of broad line regions, normaly "hidden" from direct observation, but which are reflected on the dust surrounding the central engine and therefore more easily seen in polarized light (*e.g.*, Cohen et al., 1999; Vernet et al., 2001). This supports the existence of an obscuring torus, leading to observe objects that appear different from one another, but that are in fact similar sources, seen differently only because of the line of sight along which it is observed. However, other observations tend to show that this simple model of obscuring material is sometimes not sufficient: some sources seem to really lack broad line regions (*e.g.*, Bianchi et al., 2008). Alternatively, the variations in the observed forms of AGN can also reflect temporal evolutions of the AGN and of its environment, as suggested by Hopkins et al. (2006a).

Finally, some AGN do not seem to have any accretion disk. The origin of the energy it emits is still gravitational, but matters accretes onto the black hole according to another mechanism: an advection dominated accretion flow (Ichimaru, 1977; Rees et al., 1982; Blandford & Begelman, 1999). In this model, the accretion is thought to happen quasi-spherically onto the black hole and at very small rates, compared to what a similarly massive black hole can experience with the mechanism proposed by Shakura & Sunyaev (1973). Because gravitational energy cannot be radiated away, jets become the main way to carry away energy and angular momentum from the accreting matter. Local radio galaxies are thought to be powered by this mechanism.

1.4.2 Two possible modes of AGN feedback

The emission of large quantities of energy by the AGN is necesary if AGN feedback is to solve the overcooling problem in the most massive galaxies. But this is not necessarily sufficient: this energy must be efficiently coupled to the gas of the interstellar medium in order to heat it and possibly drive it out of the galaxy and therefore stop the star formation in the host galaxy. Given the functioning of an AGN, explained in §1.4.1, we can think of two distinct mechanisms for the AGN feedback: in presence of radio jets, it can occur from the deposition of mechanical energy from the jet into the ISM (*e.g.*, Wagner et al., 2012) ; or it can come from the radiative output of the accretion disk that can ionize and drive winds because of radiation pressure and Compton heating (*e.g.*, Crenshaw et al., 2003). Both mechanisms are explored in more detail in the following.

Mechanical feedback from radio jets

The presence of jets of charged particles (mainly electrons) accelerated to relativistic speeds is a characteristic of some AGN. These jets are made of magnetized plasma, with magnetic field magnitudes of $\sim 10\,\mu$G (*e.g.*, Carilli & Taylor, 2002), around which electrons spiral and emit synchrotron radiation, which is detected in the radio. These jets can be strongly collimated, both because they are less dense than the surrounding medium and because of their magnetic field (Begelman et al., 1984). As it advances, the collimated jet eventually hits the gas of the ambient interstellar medium: this region is called the working surface. It is visible in Fig. 1.5, which gives the results of hydrodynamical simulations of Wagner & Bicknell (2011): the working surface is the transition between the light, relativistic, collimated jet in blue and the material from the ambient interstellar gas that is shocked by the jet in red. Once it has hit the ISM, jet material flows backwards and mixes with the ambient medium through Kelvin-Helmholtz instabilities[6] (visible in the late stages of the simulation of Wagner & Bicknell (2011) in Fig. 1.5). This material accumulates around the jet and forms a cocoon of hot material (in greenish colors in Fig. 1.5), because of the transfer of a part of the kinetic energy from the jet to thermal energy. The pressure of the cocoon is greater than the one of the ambient interstellar medium, it therefore expands, although at more moderate speed than the head of the jet (Blandford & Rees, 1974). Based on this mechanism and depending on its lifetime, the jet can reach large distances, up to Mpc scales (Saripalli et al., 2005).

---

[6] This instability happens at the interface between two fluids with a velocity shear between them, for instance because they propagate in different directions or have different speeds.

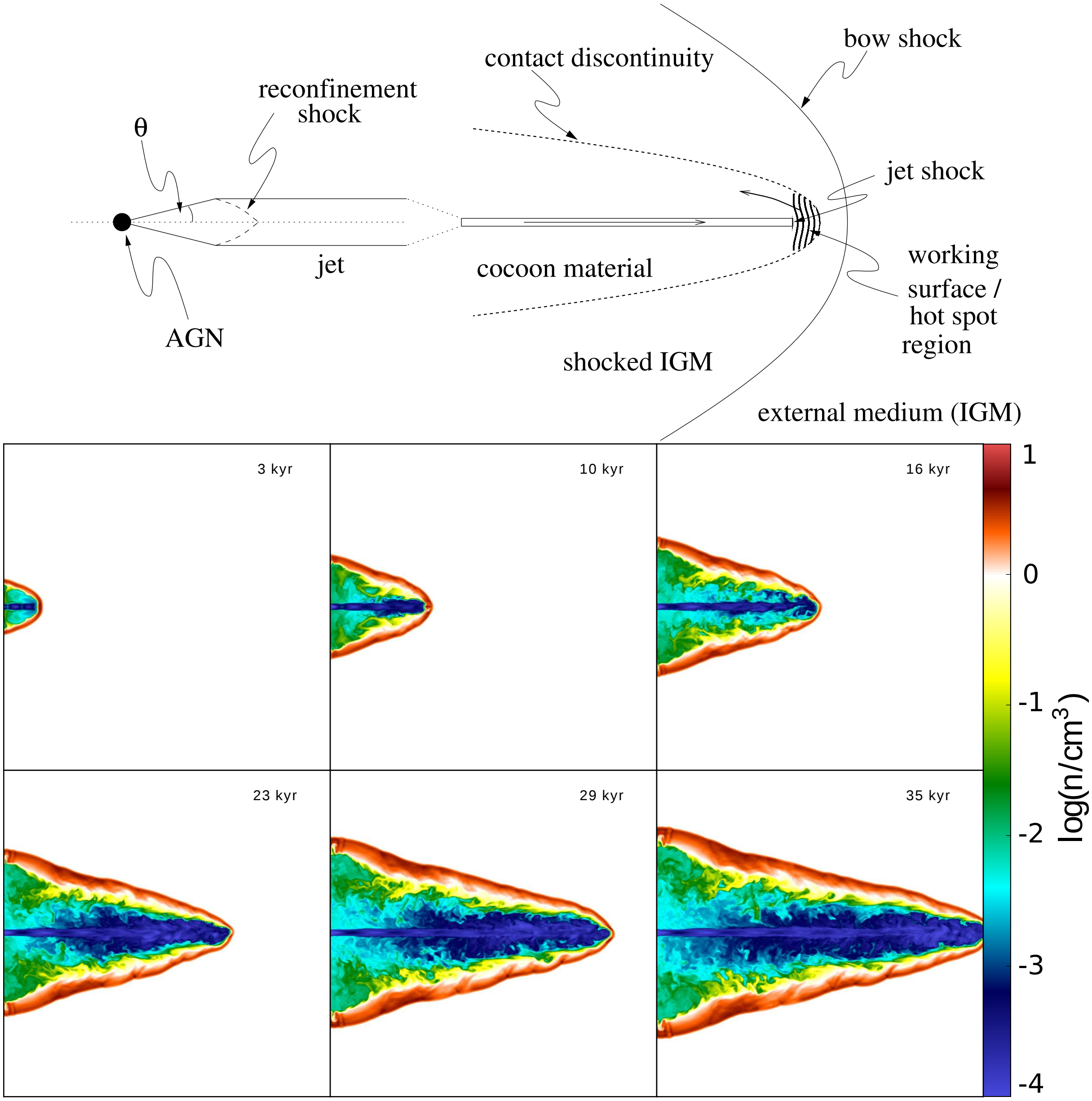

Figure 1.5: *Top*: Schematic of the effects of the radio jet on the surrounding medium: the working surface, *i.e.*, the region where the jet impacts the interstellar medium, can be observed as a radio "hot spot" ; and the expansion of the cocoon, made of hot wasted material of the jet, because of it is overpressurized compared to the surrounding medium (adapted from Kaiser & Alexander, 1997). *Bottom*: Density of the interstellar gas perturbed by a jet, as determined by the hydrodynamical simulations of Wagner & Bicknell (2011). The growth of the cocoon of hot, overpressurized gas is obvious on these simulations. It is also clear that the jet does not impact the galaxy only around the working surface. Each box is 1 kpc wide and the spatial resolution of the simulation is at most 2 pc.

Estimating the kinetic energy carried by radio jets from observations is a challenging task. A reliable tool to estimate the mechanical energy of the jet is to calculate the work required to inflate cavities, observed in the halos of hot plasma embedding local clusters of galaxies. These cavities, seen in X-rays observations, are filled with radio emitting plasma (*e.g.*, Böhringer et al., 1993; Carilli et al., 1994, for early results) and are strong evidence that radio jets interact with atmospheres of clusters, and may therefore be able to keep them hot. If one assumes that these X-rays cavities are solely inflated by the radio jets and is able to calculate the PdV work required for this and the internal energy of the cavity, then the mean mechanical power of the radio jet is accessible (and is simply the sum of the two previous terms, see McNamara & Nulsen, 2007, 2012, for a review on this subject). Since X-ray observations become tricky at high redshift z $\gtrsim 1$, an empirical relation between the jet power and its radio luminosity can be a useful tool to rapidly assess the kinetic power of the jet of any radio galaxy lacking X-ray observations, although this estimate would expectably be less acurate. Many studies (*e.g.*, Bîrzan et al., 2004, 2008; Cavagnolo et al., 2010) provide such scaling relationships. The kinetic power of the jet is derived from X-ray observations and is then plotted against the radio luminosity (whether the bolometric or at different frequencies) of the source. An example of such a study is presented in Fig. 1.6. Willott et al. (1999) also proposed this kind of scaling relation, but they based their analysis on a different estimate of the kinetic power of the radio jet: it is derived from the luminosity of the [OII]λ3727 emission line rather than X-ray observations. Despite its less strong physical justification, this relation has proved itself quite acurate, provided that their factor f, which accounts for systematic errors and astrophysical uncertainties, is taken around values of $f \sim 10$.

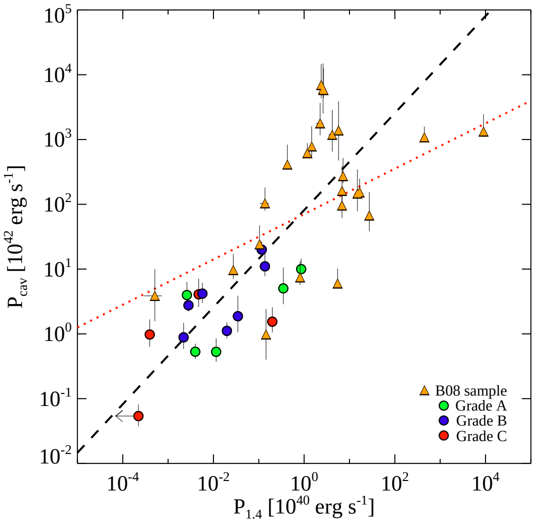

Figure 1.6: Scaling relation between the mechanical power of the jet (derived from X-ray observations) and its radio luminosity (in this case the 1.4 GHz radio luminosity), as observed by Cavagnolo et al. (2010). The relation of Willott et al. (1999) is also represented, with a value $f = 1$, which is much smaller than the value of $f \sim 10$ that can reproduce similar scaling relation.

Current (magneto)hydrodynamical simulations can take into account many properties of the interstallar medium or of the jet, for example magnetic fields are included in Gaibler et al. (2009). Other simulations take into account the inhomogeneity of the ISM, whether by considering a single denser cloud in an otherwise homogeneous medium (Antonuccio-Delogu & Silk, 2008), or a more complex two-phase medium, with one hot and diffuse phase and one of embedded warm and dense clouds (Saxton et al., 2005; Wagner et al., 2012). The particularly complete set of simulations of Wagner et al. (2012) shows how the jet can disrupt clouds of warm dense gas, or radially drive these clouds outside of the galaxy, at velocities v $\sim 10^{2-3}$ km s^{-1}. Some parameters are critical for the effeciency of radio jet feedback, such as the filling factor of the dense clouds, the density or the typical size of the clouds. Indeed, by changing the geometry and the distribution of the dense clouds, one also changes the volume through which the jet can flow. Wagner et al. (2012) also show that smaller clouds are more subject to ablation, *i.e.*, their material is progressively removed and transfered into the hot gas phase under the continous impact of the wind against them. The jet also needs more time before escaping from the interstellar medium of the galaxy and reaching the diffuse intergalactic medium.

These theoretical arguments drawn from (magneto)hydrodynamical simulations suggest that radio jets produced by some AGN can perturb the interstellar medium of the host galaxy and drive outflows. In such a perturbed interstellar medium, gas should not be able to cool, meaning that star formation is unlikely to happen. This makes radio jets an efficient mechanism for the "quenching-phase" AGN feedback.

Radiative feedback

The large bolometric luminosity of AGN is the source of energy of other possible feedback mechanisms. For example, radiation pressure could drive important parts of the interstellar medium out of the galaxy. The efficiency of radiation pressure depends mainly on the opacity of the medium, *i.e.*, on the content of the medium in dust since dust has the greatest opacity to the radiation of the black hole (*e.g.*, Draine & Lee, 1984). If the interstellar gas is hydrodynamically coupled to the dust, then it can be dragged out of the galaxy along with it, with efficiencies up to a thousand times of what could be expected from Thomson scattering alone (*e.g.*, Fabian et al., 2008). However, production of dust happens on timescales longer or at least as long as the starburst timescale: *e.g.*, if dust is produced in AGB stars, it typically requires $\sim 10^9$ yrs, if it is produced by supernovae, it requires $\sim 10^6$ yrs after the explosions of the first supernovae. Moreover, dust must be able to survive to the radiation of the AGN and to the temperature close to the nucleus if the mechanism is to work. But, given that the temperature of dust sublimation is $\mathrm{T_{subli}} \gtrsim 10^3$ K (*e.g.*, Barvainis, 1987), it is very unlikely to be present in the central regions. Other mechanisms, such as bound-bound and bound-free transitions, could be efficient to drive winds in these central regions (*e.g.*, Arav & Li, 1994; Arav et al., 1994).

Compton scattering can also heat the gas and possibly produce high velocity winds in the nucleus of the galaxy. Indeed, scattering of photons by free electrons acts to thermalize the electrons with the radiation coming from the AGN: if photons are energetic (X-ray, UV), the temperature of the electrons increases and the scattered photons are less energetic than initially ; on the contrary, the energy transfer can also go from the electron to the photon and then the electron temperature decreases. Given the typical spectrum of an AGN, the electron can typically reach temperatures of 10^{7-8} K because of the Compton scattering. These winds are both predicted in hydrodynamical simulations (*e.g.*, Wada, 2012) and observed in a significant fraction of AGN as blueshifted absorption features in the spectrum of the central source, with high ionization potentials (*e.g.*, Crenshaw et al., 2003; Tombesi et al., 2010). However, these large velocity winds, typically $\sim 0.1 \times c$, remain nuclear and are not observed at large radii. What could happen, according to hydrodynamical simulations of Wagner et al. (2013), is that, due to the high velocity of these winds, they could in turn perturb the ISM at larger scales and give rise to winds similar to what is expected from radio jets. However, to our knowledge, there is not any observationnal confirmation of this phenomenon yet.

The "maintenance" phase

Heating the gas through starbursts or AGN feedback is important to stop the star formation and therefore avoid the overcooling problem. But it is equally important to prevent this hot gas from any subsequent cooling, and to heat gas released in the galaxy by stellar winds, or gas arriving because of secular accretion, because it would eventually lead to new episodes of star formation and to the reappearance of the overproduction of massive galaxies. Croton et al. (2006); Somerville et al. (2008) introduced a second step in AGN feedback, called "maintenance phase", which keeps the gas hot and unsuitable for star formation. In these models, the maintenance phase is thought to be due to the impact of radio jets. Indeed, they can be produced even with low accretion rates onto the black hole (*e.g.*, Blandford & Begelman, 1999) but still have an important impact on the interstellar gas of the host galaxy. Best et al. (2005) find that about a third of local massive elliptical galaxies are radio-loud and Best et al. (2006) show that their radio jets can indeed account for gas cooling over time. Another observational evidence for this maintenance phase is brought by Lehnert et al. (2011). Their study is based on the absorption line caused by the Na I doublet in local radio galaxies. This absorption line traces the warm atomic interstellar medium since its ionization potential is smaller than the one of hydrogen (5.1 against 13.6 eV), meaning that it must be shielded by dust from most of the UV radiation if it is to be observed in absorption. Sodium is also present in stellar photospheres, so that the absorption line due to the Na D is an usual feature of spectra of galaxies. Lehnert et al. (2011) modelled the spectra of nearly 700 local radio galaxies and observed that, for about half of them, there is an additional Na D absorption, *i.e.*, which cannot be accounted for only by the sodium in stellar photospheres. These additional absorption features are moderately blueshifted compared to the systematic redshift and show large velocity dispersions. Lehnert et al. (2011) interpreted these as outflows of warm neutral gas, with rates of $\sim 10\ \mathrm{M_\odot yr^{-1}}$ and which require about 1−10% of the jet mechanical power to happen.

In this thesis, we focus only on the "quenching phase", not on the maintenance phase.

1.5 Observational examples of AGN driven winds

Observations of AGN driven winds, a direct consequence of AGN feedback, are numerous nowadays, at both low and high redshift and accross the whole wavelength range. We give here some examples of such observations.

1.5.1 At low redshift

Blueshifted absorption lines, seen against the emission from the background source (whether the AGN or the galaxy), are usually interpreted as arising from gas moving towards us, therefore tracing outflows. This outflow signature has been used at all wavelengths: For instance, Tombesi et al. (2010) observed ultra-fast outflows (with $\mathrm{v} \gtrsim 10^4$ km $\mathrm{s^{-1}}$) in radio-quiet AGN with the X-ray satellite XMM-Newton. These outflows are probed by absorption lines of highly ionized iron and are located in the direct environment of the accretion disk. Optical long-slit spectroscopy of local radio galaxies by Holt et al. (2008) also show evidence for outflows of warm ionized gas, probed by broad, blueshifted [OIII] emission lines and driven by the radio jets (see also Tadhunter et al., 2001). Most of these sources also show blueshifted absorption in the HI line, seen in the radio, suggesting that the outflow also encompasses an important atomic gas phase (of up to $\sim 50\ \mathrm{M_\odot yr^{-1}}$, *e.g.*, Morganti et al., 2005).

Regarding the observational evidence of radiative AGN feedback in the local Universe, results are more contrasted than mechanical feedback due to radio jets: Husemann et al. (2013) observed 31 low-redshift QSOs and found extended emission line regions due to the AGN illumination around about half of their sources. However, only few of them (3/31) display extreme kinematics, the kinematics of the rest of the EELR can be explained by gravitation. Sources that have very perturbed ionized gas kinematics also have radio jets, suggesting jet-cloud interactions (see also Greene et al., 2011).

1.5.2 At high redshift

Similarly to observations at low redshift, blueshifted absorption lines are also observed in high redshift AGNs. Moe et al. (2009) observed broad absorption lines in many restframe UV lines in a high redshift QSO ($z = 2.0$), which they interpret as evidence for an outflow. These absorption lines allowed them to model the physical properties of the outflow and to find that one of the three absorption components was quite far from the AGN (~ 3 kpc) and important, with an outflowing mass rate of $\sim 500\ \mathrm{M_\odot yr^{-1}}$ and with a speed of $\sim 5,000$ km $\mathrm{s^{-1}}$. According to these values, it means that about $1 - 2\%$ of the bolometric energy of the QSO is converted into kinetic energy of the outflow. Moe et al. (2009) therefore suggest that their observations can be interpreted these as evidence for radiative AGN feedback. Another example of radiative AGN feedback is brought by Cano-Díaz et al. (2012), who observed a luminous quasar at $z = 2.4$ with the integral field spectrograph SINFONI on the VLT. They interpreted the observation of a blueshifted component of the asymetric [OIII] emission line as ionized gas outflowing due to radiative AGN feedback, with a claimed outflow rate of $\sim 200\ \mathrm{M_\odot yr^{-1}}$ and with a speed of $\sim 2,000$ km $\mathrm{s^{-1}}$, which represents about

0.1% of the AGN bolometric luminosity. However, the mass estimate of Cano-Díaz et al. (2012) is based on the [OIII] emission line, which is known to be a poor mass proxy, and the kinematic of the [OIII] emission line is not seen in the narrow component of the Hα emission line, which is though a much better proxy for the ionized gas mass. Finally, their velocity map based on the [OIII] emission line shows much more quiescent kinematics (with $v_{\rm ion}$ in the range -390; $+260$ km s^{-1}) than the claimed outflow velocity of $\sim 2,000$ km s^{-1}.

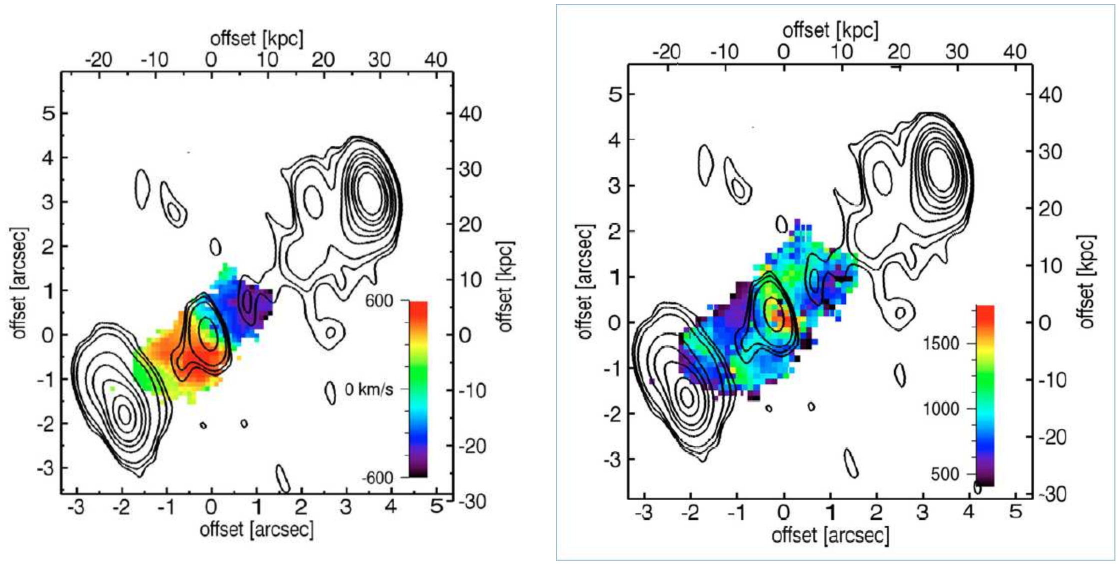

Figure 1.7: Dynamics of the ionized gas in MRC 0406−244 infered by Nesvadba et al. (2008) from SINFONI observations. *Left*: Velocity map. *Right*: Velocity dispersion (FWHM). Both maps are given in units of km s^{-1}. Radio emission at 1.4 GHz, with similar spatial resolution (Carilli et al., 1997), is superimposed as contours. This source is an archetype of jet driven winds, which are a clear signature of AGN feedback in a high-redshift radio galaxy.

Clear examples of AGN feedback at high redshift exist nonetheless, and are observed in very powerful radio galaxies (Nesvadba et al., 2006, 2007a, 2008). They observed 6 high redshift radio galaxies (HzRGs) that show spectacular outflows of ionized gas, driven by their radio jets, as illustrated in Fig. 1.7 in the case of MRC 0406−244 at z = 2.42. Generally speaking, these outflows contain large quantities of ionized gas, with $M_{\rm ion} \lesssim 10^{10}$ $M_\odot$, present large velocity gradients, with $v_{\rm ion} \lesssim 1500$ km s^{-1} and large velocity dispersions, with $\mathrm{FWHM}_{\rm ion} \sim 1000$ km s^{-1}. They can be very extended as well, with projected sizes of up to 50 kpc. Given their extension and their high bulk velocity, these outflows are quite young, with dynamical timescales of $\sim 10^7$ yrs. Finally, and more importantly, these outflows are aligned with the radio emission coming from the jets of the galaxies, as illustrated by Fig. 1.7. The kinetic power of these outflows can be estimated and is found to be $\sim 10^{45}$ erg s^{-1}, *i.e.*, a few percent of the power of the jet, estimated to be $\sim 10^{46-47}$ erg s^{-1}. The combination of all these observations strongly favor the scenario of outflows driven by radio jets.

1.6 Approach of this thesis: looking for observational signatures of AGN feedback at high redshift

With the mechanisms of AGN feedback and the motivations to invoke such processes at hand, we can now turn to the subject of this thesis: looking for observational signatures of AGN feedback in the early Universe. In a first part, we will focus on extending the work of Nesvadba et al. (2006, 2008) towards radio galaxies of lower and lower power. The idea is to test whether less powerful jets — but with still very powerful jets by local standards — are still able to drive winds as those already observed in the few most powerful radio galaxies. If not, we want to study if the moderately powerful radio jets are able to quench the star formation, by depositing large amounts of energy in the interstellar medium. Our goal is to obtain the efficiency of mechanical AGN feedback as a function of the power of the radio jets. Then, in a second part, we want to study the effects of the bolometric luminosity of high redshift radio-quiet QSOs on their interstellar medium and to test whether the radiative AGN feedback is efficent in quenching the star formation. We will finish by studying the interstellar medium of high redshift radio-loud quasars that have similar bolometric luminosities as the radio-quiet sample and similar radio jets powers as the high reshift radio galaxies sample. By contrasting these samples, we should therefore be able to disentangle the contributions of mechanical and radiative AGN feedback. But before turning to the core of our work, we want to justify our observational methods, namely probing the warm ionized phase of the interstellar medium of high redshift galaxies.

1.6.1 Why focusing at z $\sim 2-3$?

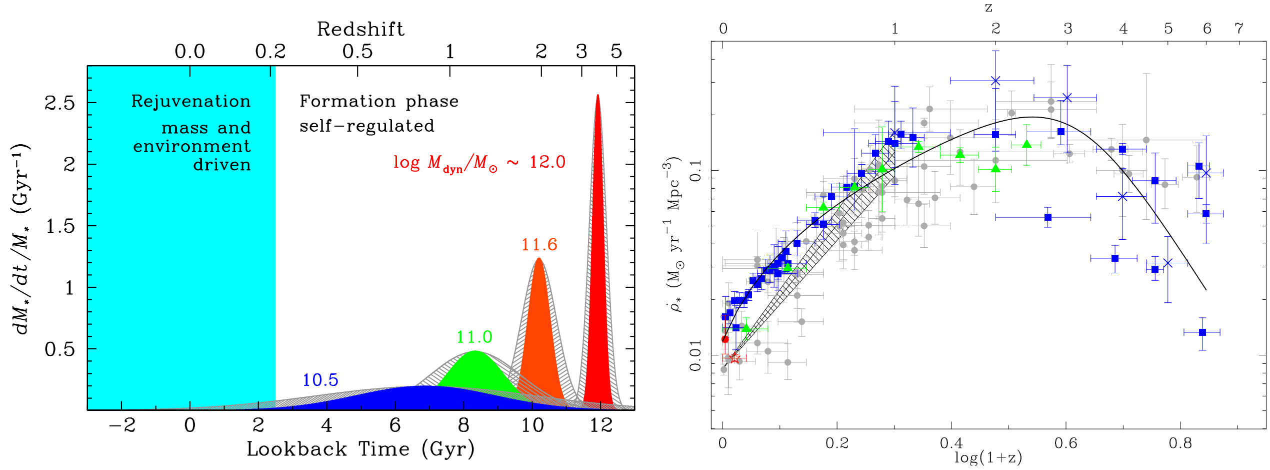

Figure 1.8: *Left*: Specific star formation rate against redshift for different typical galaxy masses, as inferred by of Thomas et al. (2010). This schematic reproduces average stellar properties of local early-type galaxies observed by the SDSS. The most massive galaxies formed all of their stars on very short timescales, less than 1 Gyr. *Right*: Evolution of the star formation density as a function of the redshift, as modeled by Hopkins & Beacom (2006).

The formation epoch of the most massive galaxies was brief and happened early in the history of the Universe (at z $\sim 2-3$, Cowie et al., 1996; Heavens et al., 2004; Panter et al., 2007). The observations of Thomas et al. (2005, 2010) confirm this idea, as illustrated by the schematic on the *left* in Fig. 1.8. Their observations are based on the chemical enrichment of stellar populations that itself traces the chemical enrichment of the interstellar medium at the epoch of stars formation. The chemical enrichment of the interstellar medium depends mainly on the rate and type of supernovae. Type-II supernovae are the main producers of "α-elements", made from the helium nucleus: O (built from 4 nuclei of He), Mg, Si, Ca, Ti, . . . The short lifetime of massive stars and their explosions as supernovae leads to a rapid enrichment of the ISM in α-elements, on timescales shorter than the typical timescale of a starburst, meaning that stars formed at this epoch will show features from these α-elements in their spectra for their whole lifetime. On the other hand, the main producers of Fe are type-Ia supernovae, that happen at much later times than type-II supernovae (typically after a few 10^8 yrs and up to 1 Gyr for massive elliptical galaxies, *e.g.*, Matteucci & Recchi, 2001). The enrichment of the ISM in iron is therefore done at later times than the enrichment in α-elements, making the α-to-Fe abundance ratio a natural clock of star formation. Observations of local early-type galaxies with the SDSS by Thomas et al. (2005, 2010) show that their stellar [α/Fe] ratios are enhanced compared to solar values. This can be interpreted as the fact that the star formation in these systems occured on timescales short enough so that type-Ia supernovae had not yet enriched the ISM with iron. In other words, the star formation is truncated early enough after the beginning of the starburst so that type-Ia supernovae had not happened yet, *i.e.*, local massive elliptical galaxies formed their stars early (at $z \sim 2-3$) and on a short timescale (in $\lesssim 10^8$ yrs) and any subsequent episode of star formation in these systems must have been very weak.

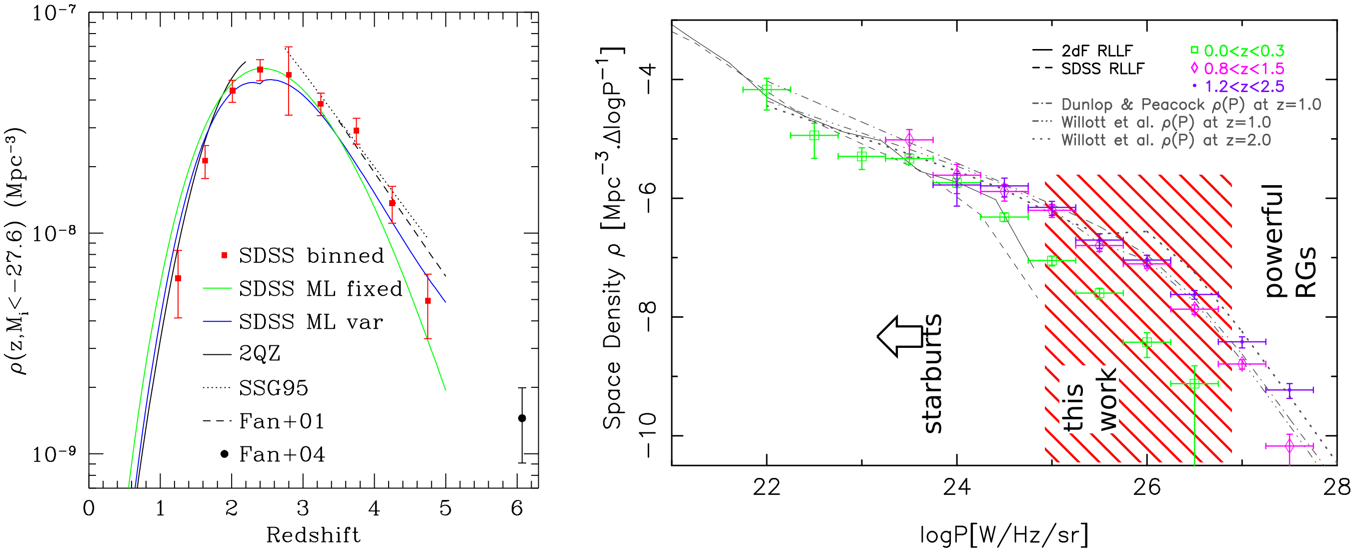

Figure 1.9: *Left*: Evolution of the QSO density in the Universe as a function of time, observed from SDSS data by Richards et al. (2006). *Right*: Radio luminosity function in different redshift bins found by Gendre et al. (2010). Its evolution in redshift is very important, especially for the most powerful sources. The density of radio galaxies also decreases rapidly with increasing power. The combination of these two effects means that moderately powerful radio galaxies were much more numerous in the early Universe than they are locally.

This picture agrees quite well with the history of star formation on cosmic scales, which peaks at $z \sim 2-3$ (*e.g.*, Hopkins & Beacom, 2006, see the *right* panel in Fig. 1.8). The observations of a population of massive galaxies, with extremely high star formation rates (*e.g.*, Magnelli et al., 2012; Rocca-Volmerange et al., 2013), also confirms the idea that the most massive galaxies formed their stars very quickly in the early Universe. The cosmic density of AGN peaks at the same epoch, as illustrated in Fig. 1.9. The *left* panel shows the evolution of the comoving quasar density brighter than a given threshold against redshift (Richards et al., 2006). It clearly peaks around $z \sim 2-3$, like the star formation history (see also Croom et al., 2009; Ross et al., 2013). The same holds for the density of radio galaxies: the most powerful of them were more numerous than in the local Universe by up to two orders of magnitude, as illustrated by the evolution of the radio luminosity function against redshift (*e.g.*, Willott et al., 2001; Gendre et al., 2010).

1.6.2 The restframe visible emission lines from the ionized gas as interesting proxies of AGN feedback

Since massive galaxies experience the bulk of their star formation at high redshift ($z \sim 2-3$) and because AGN feedback may be an effective mechanism to regulate star formation in these same massive galaxies, it is natural to search for its observational evidence in the early Universe. However, observing at high redshift is notoriously difficult. We decide to observe the restframe visible emission lines of the ionized gas (*i.e.*, mainly Hβ, [O III]$\lambda4959, 5007$, Hα and [N II]$\lambda6548, 6583$) to probe the kinematics and energetics of the warm phase ($T \sim 10^4$ K) of the interstellar gas that are redshifted into the near infrared at $z \sim 2-3$. Optical lines from the ionized gas indeed allow to estimate crucial physical properties of the host galaxy. For instance, the ratio of the two lines of the [SII]$\lambda6716, 6731$ doublet is sensitive to a wide range of electron densities and we use this ratio (when both lines are well detected) to estimate the electron density (Osterbrock, 1989). This doublet is sensitive to the electron density because both transitions have similar excitation energies, meaning that both levels are equally populated by free electrons. However, their statistical weights are different (6 for [SII]λ6716 and 4 for [SII]λ6731) as well as their probabilities of radiative de-excitation (the level lifetime is equal to 3846 sec for [SII]λ6716 and to 1136 sec for [SII]λ6731). In the two limit regimes, at very high and very low densities, the ratio between the two levels [SII]λ6716/[SII]λ6731 is respectively dictated by the ratio of the level lifetimes times the ratio of statistical weights (which is equal to $6/4 \times 1136/3846 \simeq 0.44$), or by simply the ratio of statistical weights (which is equal to $6/4 = 1.5$). Between these two regimes, and particularly between $n_e = 10^2$ cm^{-3} and $n_e = 10^4$ cm^{-3} the ratio of the two levels is between these two limit values and depends on the electron density (and also slightly on temperature, since it has a small impact on the population of the two levels, which is assumed equal in our previous explanations). This is illustrated by Fig. 1.10, which gives the ratio of the two emission lines as a function of the electron density, and temperature to a lesser extend. Since the dependance on temperature is weak, assuming a typical temperature for the ionized gas, instead of measuring it properly, does not imply large errors.

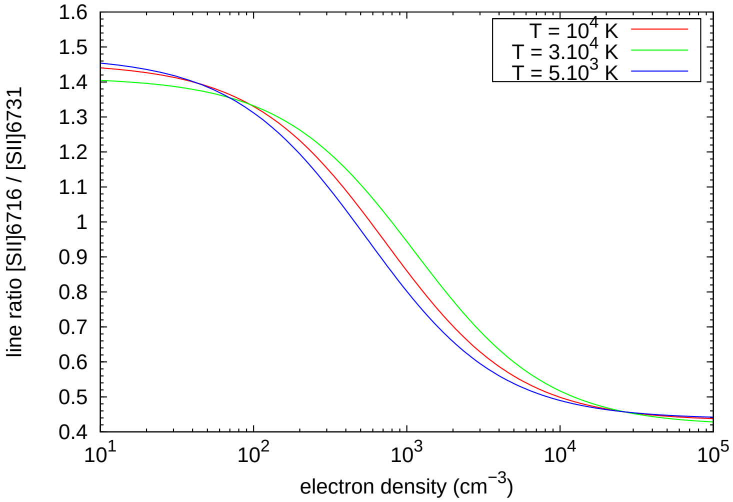

Figure 1.10: [SII]λ6716/[SII]λ6731 emission lines ratio as a function of electron density, for three typical temperature of the ionized gas. The dependance on temperature is weak, meaning that this line ratio is a good proxy for electron density over a large range of density, from $n_e = 10^2$ cm^{-3} to $n_e = 10^4$ cm^{-3}.

Another possibility offered by restframe visible emission lines is to estimate the extinction in the host galaxy, assuming a galactic extinction law (Cardelli et al., 1989). The extinction is caused by the presence of dust in the ISM, that easily reprocesses UV and blue light into infra-red emission, causing a "reddening" of the observations. In order to account for extinction, the usual method is based on comparing the ratio of observed Hβ-to-Hα lines to its expected value, from the Balmer decrement. The Balmer decrement is the theoretical value of the ratio of two Balmer emission lines, depending on the radiation field and the electron density of the medium (because of potential collisional excitations) to which it is exposed, *i.e.*, roughly speaking, whether ionization source are massive stars (and then Hα/Hβ=2.85) or a quasar (and then Hα/Hβ=3.1).

Another advantage of these emission lines coming from the warm ionized gas is that they have been studied for decades. Physical processes that govern their emission are therefore well-understood and can be used in many diagnostics to understand what happens to the ionized gas. For instance, some line ratios, such as [OIII]/Hβ plotted against [NII]/Hα, originally introduced by Baldwin, Phillips, & Terlevich (1981) and therefore often refered to as “BPT diagrams”, are commonly used to determine the source of the ionizing photons. The [OIII]/Hβ vs. [NII]/Hα diagram is particularly widely used: it is made of two sequences, which give it the shape of a seagull wings, each wing corresponding to a different source of ionization. These diagrams can notably discriminate between ionization of the gas due to star forming regions — the so-called HII regions — or due to the harder spectrum coming from an AGN. Indeed, the ionizing radiation of HII regions is dominated by the emission of young massive hot star, that have a small scatter in effective temperature (stars of spectral types B and O, with effective temperatures $T_{\rm eff} \geq 10,000$ K). Given the similarity of the ionizing sources in all HII regions, then their emitted radiation should always have the same spectral characteristics and the intensity of the emission lines coming from the photoionized species (typically [OIII]λ5007 and [NII]λ6583) should depends only on the metallicity of the interstellar medium. In the case of heating of the ISM by the harder spectrum of an AGN, the emission from species with higher ionization potential should be higher, *i.e.*, we should observe higher [OIII]λ5007 fluxes compared to [NII]λ6583 fluxes. If these fluxes were directly compared, large uncertainties would be introduced because bluer emission lines (such as [OIII]λ5007) suffer more from extinction than redder ones. In order to cope with extinction, these fluxes are “normalized” to spectrally close Balmer transitions: [OIII]λ5007 flux is divided by the Hβ flux and [NII]λ6583 flux is divided by the Hα flux.

Finally, the Hα luminosity is a good proxy for the total mass of ionized gas, assuming the “case B” recombination of Osterbrock (1989). This limit model assumes that the energy of excited, newly recombined hydrogen atoms cannot be radiated away by Lyman photons because of the too high optical depth of the ISM to ionizing photons and to the Lyman lines of neutral hydrogen. Lyman photons are therefore continuously emitted and reabsorbed by the hydrogen of the ISM, until these photons are “converted” to lower-series photons, which happens with a branching probability given by Quantum Mechanics. Thus, this case B recombination model assumes that the energy emitted through the Hα line is proportional to the total number of ionized hydrogen atoms and hence to the total mass of ionized gas, which is dominated by ionized hydrogen atoms. Applying this formalism, Nesvadba et al. (2006, 2008) found that large amounts of the gas of the most powerful high redshift radio galaxies can be in the ionized phase, with $M_{\rm gas}^{\rm ion} \lesssim 10^{10}$ M$_\odot$. Although this gas is neither the fuel of star formation, nor the main phase of the cocoon inflated by radio jets, it is a good proxy for the impact that radio jets have on the interstellar medium. This was shown by Wagner et al. (2012) who introduced dense clouds in their hydrodynamical simulations and found that these clouds were accelerated within the cocoon to velocities of few $\times 10^2$ km s^{-1}and up to $\sim 10^3$ km s^{-1}.

1.7 High-redshift galaxies

1.7.1 High-redshift radio galaxies

A large part of this thesis is devoted to the study of high-redshift radio galaxies (that we abbreviate in “HzRG”) and we would like to introduce some general features of this class of objects.

Massive and actively star forming systems

HzRGs are amongst the most massive galaxies observed at all redshifts (*e.g.*, Rocca-Volmerange et al., 2004; Seymour et al., 2007; De Breuck et al., 2010), with typical stellar masses of $M_* \simeq 10^{11-12}$ M$_\odot$. As most massive galaxies, they have assembled the bulk of their stellar mass in only a few Gyr in the early Universe. This view is supported by the high star formation rates detected in some of these systems. For example, Archibald et al. (2001); Reuland et al. (2004) observed 47 and 24 HzRGs (respectively, with 2 objects of the sample of Reuland et al. being also in the sample of Archibald et al.) in the submillimeter down to the mJy level and detected 14 and 12 of them, respectively. In this wavelength range, the continuum of the cold dust emission ($T \sim 10-50$ K) is observed. This dust is heated by star formation and is therefore a good estimate of the SFR in these systems. Observations of Archibald et al. (2001); Reuland et al. (2004) lead to star formation rates of SFR $\sim 100-1000$ M$_\odot$ yr^{-1}. Large reservoirs of molecular gas (with $M_{H_2} \sim 10^{10-11}$ M$_\odot$), the raw material for star formation, are also detected in some HzRGs (*e.g.*, Papadopoulos et al., 2000; Ivison et al., 2012; Emonts et al., 2011b,a, 2013). This kind of study will presumably become common with the advent of ALMA.

We have seen that HzRGs are actively star forming systems, but is the inverse true? Yan et al. (2005); Sajina et al. (2007a) observed ultra-luminous infra-red galaxies (with $\mathcal{L}_{\rm IR} \sim 10^{12-13}\mathcal{L}_\odot$) at high-redshift (z $\sim$ 2) with the satellite Spitzer (Werner et al., 2004). These systems are also actively star forming, although, in some cases, a significant part of their IR luminosity can come from an AGN. Sajina et al. (2007b, 2008) studied the radio-emission of these high-redshift dusty starbursts and obtained optical and near IR spectra for nearly half of their sources. They found that $\sim 2/3$ of their sample of 48 ULIRGs is detected at 1.4 GHz and/or at 610 MHz and have high luminosities ($\mathcal{L}_{1.4\,\rm GHz} \gtrsim 10^{24}$ W Hz^{-1}). In a couple of these sources, the morphology of the radio emission clearly indicates radio jets. The radio luminosities of the radio-loud sources (defined as $\mathcal{L}_{1.4\,\rm GHz} \geq 10^{25}$ W Hz^{-1}) at 610 MHz and 1.4 GHz reveal that they have steep radio spectra, with a mean index ~ -1. The optical and near IR spectroscopy also reveals that a large fraction of their sources host obscured quasars. These high radio luminosities, morphologies and radio spectral indexes are hard to explain by any other mechanism than by the presence of an AGN. They concluded that more than half[7] of their 35 sources at $z > 1.5$ host an AGN, among which many are radio-loud. This shows that a significant fraction of high-redshift star-forming systems can experience a period of AGN activity, including under the form of radio-jets, proving that AGN feedback can be a generic mechanism of galaxy evolution.

In overdense regions of the Universe

The rapid and early formation and evolution of HzRGs requires that they are part of the first dark matter structures to collapse, which are also the most massive. Large quantities of gas should therefore be available to allow the high rates of star-formation detected. This also raises the suspicion that HzRGs tend to lie in environments denser than the average since the densest dark matter halos are the precursors of galaxy clusters.

Taking advantage of this theoretical prediction and of the known redshift of the radio galaxy, many authors successfully searched for galaxies associated with the HzRG in deep narrow-band imaging centered on important emission lines at the redshift of the radio galaxy. Most of these studies used the bright Lyα emission line to detect over-densities of Lyα emitters around the radio galaxy. They used narrow-band filters centered on the adequate wavelength given the redshift of the HzRG, which is normally in the visible and relatively easy to observe (*e.g.*, Pentericci et al., 2000b; Venemans et al., 2004, 2005; Kurk et al., 2000; Matsuda et al., 2009, 2010). Other studies used the Hα line, redshifted into the infra-red, to search for Hα emitters associated with the radio galaxy (*e.g.*, Kurk et al., 2004c; Matsuda et al., 2011). Emission line candidates found with these methods are generally spectroscopically confirmed to be at the same redshift as the HzRG (*e.g.*, Stern et al., 2003; Kurk et al., 2004b; Venemans et al., 2002, 2007; Tanaka et al., 2011). We use this approach in Chapter 5. Finally, simple deep broad-band, or more complete multi-band observations, can be sufficient to assess, in a more circumstantial way, based on colors, if a radio galaxy lies in a dense environment (*e.g.*, Best, 2000; Best et al., 2003b; Miley et al., 2006; Galametz et al., 2010, 2012; Mayo et al., 2012).

Precursors of local Brightest Cluster Galaxies?

At, or close to the center of dense clusters of galaxies, there is, in many cases, one galaxy that is brighter and larger than the rest of the cluster members and that is called the "brightest cluster galaxy" (abbreviated in BCG, *e.g.*, Jones & Forman, 1984). It often shows an extended stellar halo, in which case it is also classified as a "cD galaxy" (*e.g.*, Fasano et al., 2010) ; however, all cD galaxies are not BCGs and vice-versa. BCGs are most of the time elliptical galaxies that have assembled the bulk of their stellar mass at high-redshift (*e.g.*, Collins et al., 2009). They usually do not exhibit much star formation (*e.g.*, von der Linden et al.,

---

[7] they can only give a lower limit because optical spectroscopy was not obtained for the whole sample

2007), despite the large quantities of gas available around them (with masses of this gas of about 10% of the total mass of the cluster, *e.g.*, Vikhlinin et al., 2006), but this gas is in a hot phase (T $\sim 10^7$ K, it therefore mostly emits in the X-rays) and is not self-gravitating, so that it is unsuitable for star formation. In a small fraction of BCGs (less than 1% of them), hints of current star formation activity is nonetheless detected, although these late episodes of star formation contribute to a small fraction of their stellar content (less than 1%, *e.g.*, Liu et al., 2012). BCGs tend to have morphologies similar to elliptical galaxies, with luminosity profiles usually well fitted by a de Vaucouleurs' law[8], *i.e.*, their intensity I decreases with their radius r as $I(r) \propto \exp\left(-(r/r_e)^{1/n} - 1\right)$, where n and r_e are free parameters, respectively called Sérsic index and effective radius (*e.g.*, Donzelli et al., 2011). However, local BCGs tend to have a Sérsic index slightly greater than the de Vaucouleurs value $n = 4$, typical for elliptical galaxies (*e.g.*, Graham et al., 1996). They also show radio activity more frequently than galaxies with similar masses and that are not found at the center of clusters (*e.g.*, Burns, 1990; Best et al., 2007). As explained before, high redshift radio galaxies tend to lie in environments denser than the average. Then, could they be the ancestors of local BCGs?

We will study this hypothesis further in Chapter 5. Here we recall that one of the best studied high redshift radio galaxies, MRC 1138−262, indeed shows many properties that are typical of local BCGs: it is surrounded by numerous satellite galaxies (Pentericci et al., 1997, 1998; Miley et al., 2006), including Lyα emitters (Kurk et al., 2000; Pentericci et al., 2000b) and Hα emitters (Kurk et al., 2004a,c). It is also embedded in a large Lyα halo (Pentericci et al., 1997). Radio observations of MRC 1138−262 (Carilli et al., 1997) show large rotation measures, also indicative of large quantities of hot ionized gas around the galaxy. The structure of the radio galaxy itself also shows similarities to local BCGs: its luminosity profile is well fitted by a de Vaucouleurs profile (Pentericci et al., 1997), which is typical of elliptical galaxies and close to values usually found for BCGs.

1.7.2 High-redshift quasars

The discovery of the nature of quasars about fifty years ago (Schmidt, 1963; Matthews & Sandage, 1963) has been one of the milestones of the study of galaxy formation and evolution: for instance, the research of mechanisms able to explain their high luminosities led to the development of the accretion-ejection mechanism, while their cosmological distances make them unique tools to study the high redshift Universe. They can notably be used as bright background sources to probe intervening matter or galaxies found along the line of sight (*e.g.*, Kacprzak et al., 2011a), they can be used in cosmology (*e.g.*, to detect the Baryonic Acoustic Oscillations Busca et al., 2013) and they can even be used to test questions of fundamental physics (such as "Are constants of Physics really constant?" Murphy et al., 2003; Uzan, 2011).

Quasars are interesting objects in themselves and they gained even more attention during the last decade when it was realized that they could solve the overcooling problem in massive galaxies (see §1.2.3). Indeed, quasars are thought to be powered by an accretion-ejection mechanism onto the central supermassive black hole found at thair center, which allows them to emit so large quantities of radiation that they can outshine the rest of their host galaxy. This mechanims is well motivated by observations: quasars are known to be variable sources, on time-scales from weeks to years, meaning that the emitting region has to be smaller than the corresponding speed of light crossing size. This puts stringent lower limit on the efficiency of the mechanism that can lead to the emission of so quantities of energy from so small regions, and accretion onto a massive object (such as a black hole with mass M$\sim 10^{6-10}$ M$_\odot$) is the most widely accepted mechanism to explain this. A convenient upper luminosity, called the Eddington luminosity, $\mathcal{L}_{\mathrm{Edd}}$, can be defined for any radiating and spherically accreting object, as the luminosity at which the radiation pressure on the plasma

---

[8] see §5.3.1 to have more details about the de Vaucouleurs, and more generally about Sérsic, luminosity profiles.

around the central object equals gravitational forces that drive it onto it. This leads to the expression:

$$\begin{aligned}\mathcal{L}_{\mathrm{Edd}} &= \frac{4\pi G m_p c}{\sigma_T} \mathrm{M_{BH}} \\ &\simeq 1.26\,\frac{\mathrm{M_{BH}}}{\mathrm{M_\odot}} \times 10^{38}\ \mathrm{erg\ s^{-1}}\end{aligned}$$

where G is the gravitational constant, m_p is the proton mass, c is the speed of light, σ_T is the Thomson cross-section and $\mathrm{M_{BH}}$ is the mass of the central object, a super-massive black hole here. The Eddington luminosity is an interesting typical quantity against which observations can be compared and it is common to express observed quasars luminosities as a fraction of their Eddington luminosity.

1.8 Thesis outline

We begin by presenting the tools that we have used in this thesis, focusing first on telescopes and instruments from which our data come (SINFONI on the VLT and the ATCA, Chapter 2) and then presenting the algorithms that we used, notably the limits under which they cannot give reliable results (Chapter 3).

In Chapter 4, we analyse the effect of moderately strong radio jets on the ISM of high-redshift radio galaxies (HzRGs). Results for the most powerful radio galaxies already exist (*e.g.*, Nesvadba et al., 2006, 2007a, 2008) and show spectacular outflows of ionized gas driven by their radio jets. The question is whether this result holds for radio galaxies less powerful than the few extreme radio galaxies already observed. Radio galaxies studied in this Chapter are one to two orders of magnitude less powerful. At these radio powers, we know that we probe a much larger part of the galaxy population, as shown by the radio luminosity function (see Fig.1.9), but in systems whose energetics is still largely dominated by the radio jets, which will greatly help us in unambiguously determining the source of energy needed to explain the observations.

In Chapter 5, we focus on two objects that display atypical features when compared to the rest of our sample of HzRG. We include in this chapter additional observations of these two galaxies with the near-infrared imager ISAAC on the VLT that allow us to probe their environment out to large distances. We explore different scenarios that could explain these observations and argue that they could be high-redshift analogs to central galaxies of local clusters.

Finally, in Chapter 6, we study the impact of radio-quiet QSOs on the ionized gas of their host galaxy. As a transition between these two classes of objects, we also study radio-loud quasars, in which both mechanisms of AGN feedback, namely mechanical from the radio jet and radiative from the high luminosity accretion disk, can play a role.

Chapter 2

VLT and ATCA: Tools of choice to study galaxy evolution

Contents

2.1 SINFONI

Techniques of IFU spectroscopy allow one to obtain, in a single observation, both spatial and spectroscopic information about the observed object.

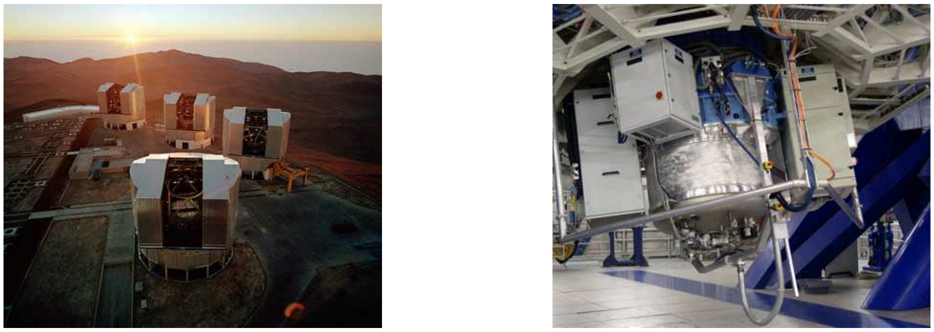

Figure 2.1: SINFONI (on the right) at VLT/UT4 (Yepen) Cassegrain focus (the foreground telescope on the photo of the left).

The Spectrograph for INtegral Field Observations in the Near Infrared (SINFONI, see Fig. 2.1) of ESO is an integral-field spectrograph (IFS) that saw first light at the VLT in July 2004. We will describe the instrument and data reduction to the extent needed for this thesis, complete information can be found in Eisenhauer et al. (2003) and Bonnet et al. (2004), for the description of the adaptive optics (AO) module. Interested readers can also refer to the issue of September 2004 of the ESO Messenger that presented SINFONI to the astrophysical community.

2.1.1 Working principle of SINFONI

Before getting into the technical details of SINFONI, let us briefly recall the working principle of IFS such as SINFONI or similar instruments that came into service on other 10 m-class telescopes around the same time: OSIRIS at Keck II in February 2005 and NIFS at Gemini-North in October 2005.

Fig. 2.2 illustrates the principle of IFS in a simple way: the two-dimensional image of the observed object is divided into slices with plane mirrors. Those slices are then re-arranged next to another to form a long, one-dimensional 'pseudoslit'. This 'pseudoslit' is then dispersed with a grism similar to a long-slit spectrograph. Afterwards, all spectra are arranged into a data cube at their initial spatial position.

Fig. 2.3 shows the image slicer of SINFONI on the left. The different direction of each of the 32 slicing mirrors is clearly identifiable. On the right, the mirrors that arrange each slice of the image along a 'pseudo-longslit' can be seen. The light initially comes through the hole in the middle of it .

2.1.2 Integral Field Units (IFU) spectroscopy

Other types of IFU exist and here we give a brief overview of these.

Lenslet arrays

In this case, the focal plane of the telescope is not equiped with a camera, as if imagery were being performed, but instead with an array of small lenses (the so-called lenslet). Behind these lenses, each corresponding to a spatial pixel, there is a grism that disperses the light of each of the reduced pixels. Offsets between spectra coming from pixels that are spatially adjacent along the spectral direction are necessary to avoid the superimposition of their spectra. TIGER (Bacon et al., 1995) is an example of an IFU working according to this technique.

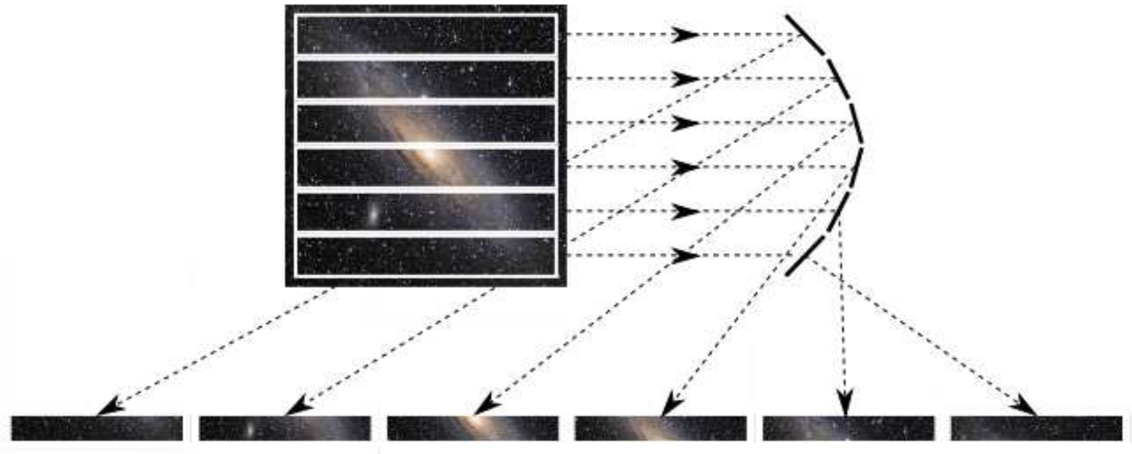

Figure 2.2: Simplified working principle diagram of IFUs: the observed object is divided into 32 slices, that are then put next to one another by a set of mirrors in order to be dispersed through a long-slit spectrograph.

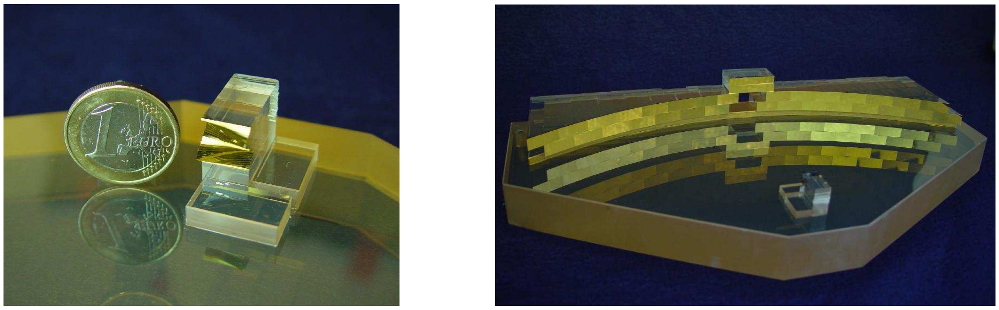

Figure 2.3: The actual image slicer (*left*) that cuts the image in 32 slices, and set of mirrors of SINFONI (*right*) that arrange these slices along a 'pseudo-longslit'.

Optical fibers arrays

This technique is similar to the one used for lenslet arrays, the difference lies in the use of optical fibers instead of an array of lenslets. These optical fibers are brought in front of a long-slit spectrograph that disperses the light coming from each pixel, corresponding to a fiber.

The main drawback of this technique is the partial coverage of the field of view (usually around 70%), in contrast to the lenslets array, that can have a full coverage if the lenses are square or hexagonal. However, Optical fibers allow great flexibility on where to place them on the field of view, therefore selecting objects of interest easily (the Sloan Digital Sky Survey took full advantage of this possibility York et al., 2000). For instance, this is achieved for the SAMI instrument (Croom et al., 2012) which is made of several "hexabundles" (name given to a group of optical fibers, analogous to a single IFU) that can be placed whereever wanted on the field of view of the instrument.

Fabry-Pérot and Michelson spectrographs

The first integral field spectrometers took advantage of Michelson or Fabry-Pérot spectroscopy: the field of view was imaged in a first wavelength window, which was then shifted[1] to following wavelengthes in order to cover the whole needed range.

---

[1] whether by moving the second mirror of the Michelson or by changing the space between the two mirrors of the Fabry-Pérot

The main issue with this technique is the delay between the first and the last wavelength windows imaged, since conditions of observations could change and make the reassembly difficult for these different images into a single coherent data cube.

2.1.3 Description of the instrument and observation strategies

SINFONI operates in the near infrared wavebands, from 1.1μm to 2.5μm. Observations can be made using one of the four available gratings, matching the infrared windows of the atmosphere: the $J-$band (1.1$-$1.4 μm), $H-$band (1.45$-$1.85 μm) and $K-$band (1.95$-$2.45 μm). The fourth grating is a combination of the $H-$ and $K-$bands. Spectral resolutions reached with each of these gratings are about 2000 (or FWHM $\sim$ 150 km s^{-1}), 3000 (or FWHM $\sim$ 100 km s^{-1}), 4000 (or FWHM $\sim$ 75 km s^{-1}) and 1500 (or FWHM $\sim$ 200 km s^{-1}) for the $J-$, $H-$, $K-$ and $H+K$ bands respectively. These spectral resolutions are sufficient to study the kpc-scale motion of the ionized gas in high-redshift galaxies.

The field of view of SINFONI is divided into 32 slices, which can have an aperture on the sky of 0.25$''$, 0.10$''$ or 0.025$''$, depending on the observer's choice. These lead to possible fields of view of 8$''\times$8$''$, 3$''\times$3$''$ or 0.8$''\times$0.8$''$, respectively. The two smallest fields of view are best used in diffraction-limited observations, thanks to adaptive optics, whether coming from a natural guide star or a laser guide star, in order to take full advantage of the fine spatial sampling offered. The largest field of view is more often used during seeing-limited observations. The other advantage of this mode is its "large" field of view, that assures us that, at least, a large part of the target will be observed (and most often its whole extend), which will be a crucial condition for the work presented in this thesis. Indeed, at z $\sim$ 2$-$3, 1$''$ represents roughly 8 kpc, which gives a field of view of $\sim$ 64 kpc$\times$64 kpc, comparable to the largest emission lines regions detected to this date[2]. Finally, this large pixel scale maximises the number of photons collected per pixel, which is essential to observe high-redshift objects down to low surface brightness

The detector of SINFONI is a 2048×2048 pixels Hawaii 2RG. It receives each of the 32 slitlets on 64 pixels. They are put one next to another, along the horizontal axis, to be dispersed by the slit. The dispersion is done along the whole (2048 pixels) vertical axis. Fig. 2.4 gives an example of a raw frame of SINFONI.

In order to limit electronics noise, thermal expansion and thermal emission of the instrument, it is entirely cooled with liquid nitrogen at 77 K. The most troublesome source of noise in NIR spectroimaging are the emission lines coming from the OH radical, that forms in the upper layers of the atmosphere (between altitudes of 80 and 90 km) from a reaction between atomic hydrogen and ozone. These emission lines are seen as bright horizontal lines on the raw frame in Fig. 2.4. OH lines are particularly problematic because they are a non-Gaussian source of noise, because their intensity is time and wavelength dependent. At the red end of the $K-$band, the thermal emission from the atmosphere and the telescope also begin to be important. This can also be guessed from Fig. 2.4, as a slightly brighter background at the bottom of the raw frame than at the top of it.

Although instrumental noise is less important than those coming from OH lines or thermal emission, it is not negligible: read-out noise and dark current are important in infrared detectors. In the optical, this is usually balanced by longer intregration times. But the atmospheric properties in the infrared (OH lines intensities, sky brightness) change on timescales of a few minutes, we must therefore use exposure times shorter than 5 minutes, typically, to be able to do the "sky subtraction" correctly.

Indeed, high-redshift objects, as those studied in this thesis, are faint targets (typically H $\sim$ K$_S$ $\sim$ 19$-$20), *i.e.*, several magnitudes fainter than the sky in the infrared (H$_{\rm sky}$ $\sim$ 14, K$_{S,\,\rm sky}$ $\sim$ 13). As it is usual in IR imaging, we will have to "subtract the sky" in each science frame to account for sky emission. This is usually done by observing an "empty" part of the sky close to the science target before or after each observation of the object of interest, usually following a pointing strategy of the type AB$-$BA$-$AB$-$... (where A is the science target and B is an empty part of the sky). By doing so, at least half of the telescope time is spent in observing something else than the target we are interested in. This has another undesirable effect:

---

[2] but smaller than diffuse blobs surrounding some HzRG

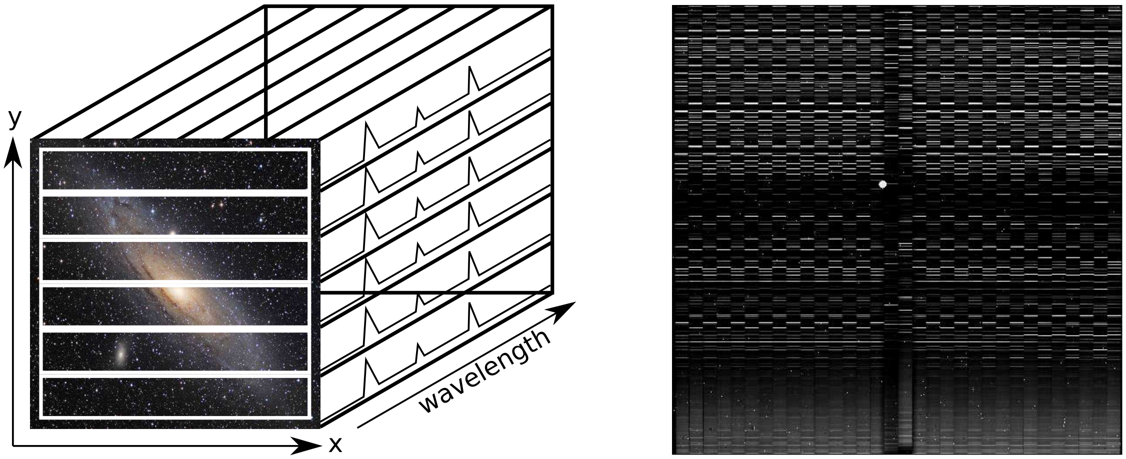

Figure 2.4: *Left:* Representation of a datacube: $x-$ and $y-$axis denote spatial dimensions, which can be as wide as $8'' \times 8''$ in the case of SINFONI. The third axis corresponds to the spectral dimension, which can be chosen in a combination of the $J-$, $H-$ or $K-$bands. *Right:* Example of a raw frame of SINFONI. The 32 slitlets can be seen next to one another horizontally while the dispersion direction is along the vertical axis, slightly shifted from one slitlet to another. We can clearly identify the bright night sky lines along the dispersion axis. The hole in the middle of the detector is the place where the read-out electronics leaves the camera.

since atmospheric properties change on timescales of a few minutes, we must use integration times short enough to be sure that the observed sky has the same properties as in the corresponding science frame and to correctly account for the sky emission.

This necessity can be circumvented if the field of view of the instrument is large enough, because empty parts of the sky are then naturally present within the observed field and can be used as estimates of the sky emission[3]. However, as explained at the beginning of this section, the field of view of SINFONI is small ($8'' \times 8''$ at the maximum). If we use the same technique, we must be sure that the observed object is small enough to fit in half of the field of view. It is also necessary that the detector sensitivity does not dramatically change across the field of view. Finally, this techniques requires extremely precise pointings of the telescope. Given that the absolute pointing precision of the VLT is too low (about $1''$) for our purpose, we have to first point a bright object close to the target and then offset the telescope by the relevant amount.

2.1.4 Data reduction

Due to the nature of IFS, the way data are reduced naturally borrows from techniques of both imaging and spectroscopy.

As part of the calibration procedures of ESO, 3 dark frames and 10 flatfield frames are taken during the subsequent day of the science observations. The 3 dark frames are taken, with the same exposure time as the science observations, in order to account for the dark current and "hot" and "dark" pixels. The combined dark frame that we subtract from science frames is the median of these 3 frames (an example of such a combined dark frame can be seen on the left of Fig. 2.5). Flatfield frames are made by a uniform illumination of the detector with a lamp, in order to account for differences in sensitivity across the detector. They are therefore taken with the same grating and pixel scale as the science frames. Among the 10 flatfield frames taken, the lamp is turned on for 5 of them and turned off for the 5 others, usually in the order AB−BA−AB−… We subtract the corresponding "off" frame from each "on" flatfield[4], add together these

---

[3] This technique also has the advantage of *simultaneously* estimating the sky emission

[4] but note that we do not subtract any dark frame from any of these flatfield frames

5 subtracted flatfields and finally divide it by its clipped mean. Each science frame is divided by the result of previous steps (a typical combined flatfield can be seen on the middle of Fig. 2.5).

Figure 2.5: Examples of dark (*left*), flat (*middle*) and distortion (*right*) combined frames.

The next step in the data reduction is to precisely localize edges of each slitlet and to account for the distortion that affects all frames. This last effect is quite subtle at the scale of the whole image, but can be guessed when looking carefully at raw frames: for example, in Fig. 2.5, it is notable that the last slitlet (on the right of the detector) is bent from the top-right to the bottom-left. This effect can also be seen for the first slitlet (on the left of the detector) but in the opposite direction. All slitlets are bent and we must correct for this effect before the wavelength-calibration of our data (again, as is normally done for spectroscopic data). To these ends, distortion frames are taken about once a month: The center of each slitlet is individually lit by a white point source. Usually 75 of these distortion frames are taken[5], we have to add them, one to another, in order to produce the frame that can be seen on the right of Fig. 2.5. From this frame, we can localise the centre of each slitlet and study how it moves along the dispersion direction, to then correct the science frames.

Once slitlet frames have been localised and corrected from distortion, we can estimate the wavelength calibration solution. As part of the calibration procedures of ESO, two wavelength calibrating frames with the same grating and pixel scale as the science setup are taken during the day following observations. One of these two frames is taken with an arc-lamp (usually a xenon lamp) switched on in front of the instrument. The other one is done with the laser-lamp switched off. As for the flats, the lamp-off frame is subtracted from the the lamp-on frame. Slitlets of the result are localised and corrected for distortion, so that we can estimate the wavelength solution for each of them. Typical residuals between the wavelength calibration found and the theoritical wevelengths of the arc-lamp are between ± 1Å. Once this step is completed, the calibration is enhanced based on the OH lines: their wavelengthes are well-known (*e.g.*, Rousselot et al., 2000) and they are unresolved spectrally.

The next step in the data reduction is to subtract the sky in the science frames. Each of them is associated with one observed just after, that is usually another science frame. Indeed, most of the observed galaxies are smaller than the field of view of SINFONI. We therefore adopt a dither pattern where the object is shifted between two opposite corners of the field of view, which allows us to use two subsequent frames for the sky subtraction and makes dedicated sky frames unnecessary. This is illustrated by Fig. 2.6.

However, because of the presence of the observed object in each "sky" frame, we systematically oversubtract the sky contribution in some part of the combined image, as illustrated by the two negative images of the galaxy in Fig. 2.6. In order to circumvent this effect, when these first images are obtained, we combine them into a datacube and use it to estimate the morphology of the source (usually using a line image, that would slightly overestimate the size of the source). Its morphology is translated back into frames , so that the object can be masked in individual frames before performing the sky subtraction again.

---

[5] meaning that 11 slitlets have 3 such frames, while the others have 2 of them

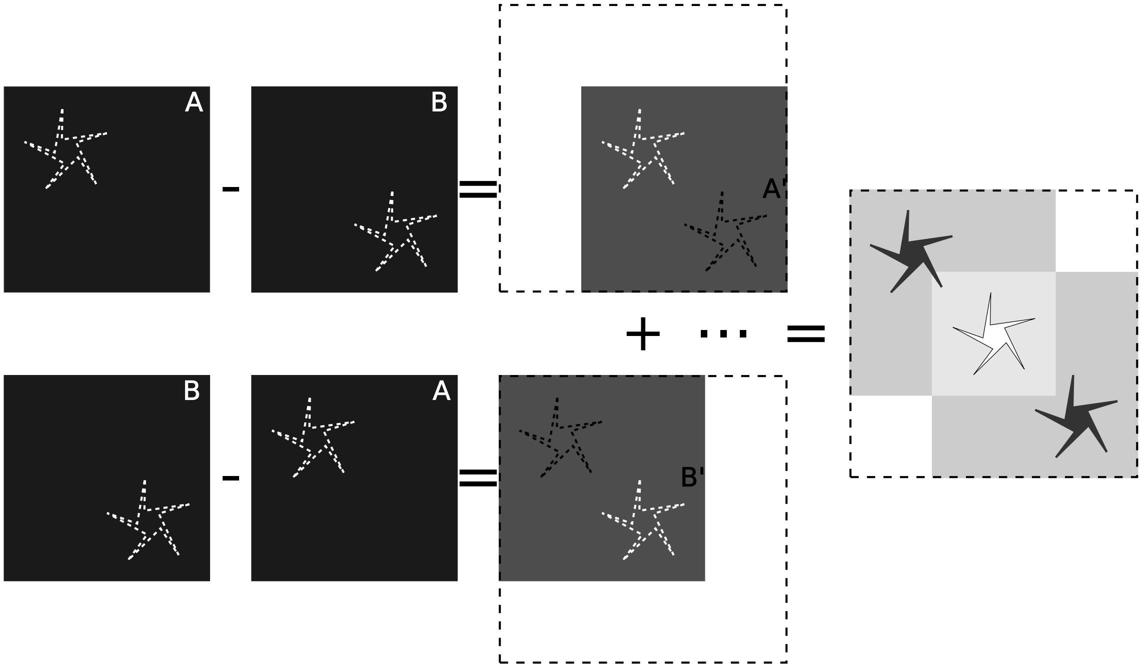

Figure 2.6: Principle of sky subtraction: Two consecutive science frames A and B have slightly different pointings that put the observed galaxy in two opposite corners. Each frame is used as the sky frame of the other and the results are added together. As illustrated here, this method will lead to a systematic oversubtraction where the galaxy is. That is why, after a first iteration that gives the size and the morphology of the object, a second sky subtraction is performed in which the object is masked accordingly in frames that are used as the sky.

The same reduction procedure is followed for the standard star(s) observed during each 1-hour observing sequence (see observing logs for details about when they were observed). Standard stars are usually massive stars because they have a spectrum with few features imprinted in it ; or Vega or solar type stars since we know their parent spectrum very well, so that we can again account for absorption or emission lines due to the star. The important criterion being that we know the theoretical spectrum of the observed standard star, so that we can estimate and account for telluric absorptions and variations in atmosphere transmission in the spectrum of our science target. Fig. 2.7 present a sprectrum of a typical standard star, on which absorption lines due to elements in the atmosphere of the star are indicated (bottom arrows), along with telluric absorptions (upper arrows), due to our atmosphere. We fit the spectral features coming from the atmosphere of the star by a Gaussian in order to remove it before dividing the observed standard star spectrum by the theoretical spectrum (*i.e.*, a black body) in order to obtain only the effects of our atmosphere on the observations.

The other utility of standard stars is to provide the flux calibration of our observations, since these stars already have well-known fluxes in catalogues, 2−MASS for our purpose. We calibrate the $H-$ and $K-$bands separately since magnitudes are given for each of these two bands. Calibration factors given by each band usually agree within 20%, and are around 10^{-17} erg s^{-1} cm^{-2} Å^{-1} $\#^{-1}$. We use the calibration based on the $K-$band. Finally, the standard star gives us the seeing of our observation, since it is observed the same night, at similar elevation (air mass) and can be considered as a point-source.

2.1.5 Advantages and drawbacks of IFS

The advantages of IFS comes from the complete view that we have, in one observation, of the observed field, both spectroscopically and morphologically.

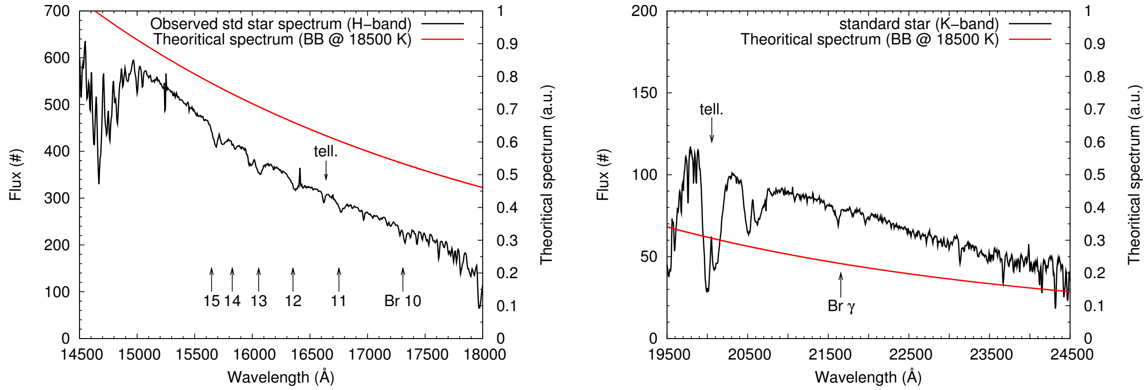

Figure 2.7: Example of a standard star spectrum (Hip070506 — spectral type B3IV). The main spectral features due to the atmosphere of the star are indicated by the bottom arrows while telluric absorptions are indicated by upper arrows. The theoritical spectrum of this type of star (*i.e.*, a black body at 18500 K) is indicated by the red curve. Note that the normalization between the observed and the theoritical spectra are different.

Advantages over long-slit spectroscopy

The traditional long-slit method implies the definition of a preferred direction *a priori*, along which the slit will be placed (*e.g.*, along the direction defined by radio jets, or along the morphological major/minor axis). This raises two difficulties: First, if the object is larger than the width of the slit, a (potentially large) fraction of the flux is lost. Second, this partial information complicates the subsequent interpretation since some assumptions about the geometry of the source have to be made to extend properties found along the slit to results valid for the whole galaxy. Integral field spectroscopy does not have this problem: the kinematics of the gas can be followed across the whole object, leading to an understanding that would have been difficult to reach with long-slit spectroscopy (*e.g.*, in the case of high-redshift galaxies, that appear clumpy, or for the observation of mergers). The second difficulty also disappears since we make sure that all the flux from lines is directly measured, and not extrapolated from a partial view of the source. However, the spectral resolution reached, although sufficient for our purpose, is not as high as those available with long-slit spectrographs

Advantages over classical imaging

Regarding imaging, the main advantage is to observe simultaneously morphologies of emission lines and of continuum. No issue due to relative alignment can come into play. Compared to narrow-band imaging, IFS gives access to a large wavelength coverage. When long-slit spectroscopy restrains itself spatially, narrow-band imaging restrains itself spectrally. IFS has none of these restrictions. While objects detected in narrow-band images can be interlopers due to other strong emission lines at different redshiftshis, IFS offers a much better estimation of the redshift of objects in the field of view, due to its large spectral coverage. However, the field of view of IFS is generally small compared to the one of imaging camera, even though some techniques[6] can have large fields of view. The last generation of IFS, such as KMOS or MUSE will also give access to large field of view. But, as far as SINFONI is concerned, studies are limited to the close vicinity of a galaxy (in some cases, we may even not probe the whole extent of the gas associated with a galaxy).

---

[6] as those using Fabry-Pérot or Michelson spectrographs, which are basically a succession of narrow-band images

2.2 ISAAC

2.2.1 Description of the instrument

The Infrared Spectrometer And Array Camera (ISAAC, Moorwood et al., 1999) is a near-infrared camera capable of imaging (with both broad- and narrow-bands filters), imaging polarimetry and spectroscopy (at a low-resolution level, $R \sim 500$, or at a high-resolution level, $R \sim 3000$). It was offered to the community on April 1999 and should be decommissioned soon to leave its place for SPHERE. It can work from 0.9 μm to 5.0 μm and has two cameras: the 1024×1024 pixels Hg:Cd:Te array is optimized for the shortest wavelengthes (from 0.9 μm to 2.5 μm) and was manufactured by the Rockwell International Science Center ; the 256×256 pixels InSb array is used for longer wavelengthes (from 2.5 μm to 5.0 μm) and comes from the Santa Barbara Research Center. The whole instrument is cryogenically cooled.

We used only the imaging capabilities at shortest wavelengthes of ISAAC during this thesis (see chapter 5) so we won't discuss its other modes here, the interested reader is referred to the article of the ESO Messenger presenting ISAAC. The field of view of ISAAC at these wavelengthes is $2.5' \times 2.5'$, with a pixel scale of $0.147''$/pixel. The three usual NIR broad-band filters are available ($J-$, $H-$ and K_s- windows) and several narrow-band filters[7], with a typical spectral width of 100−300Å.

2.2.2 Observation strategy & Data reduction

Similarly to observations with SINFONI, the object is usually not detected in single science frames. The integration time is chosen as long as possible, so as to reduce the read-out noise without saturating the detector. It is typically around 10−15 sec for broad-bands imaging and around 100 sec for narrow-bands imaging. Between each integration, the pointing is slightly shifted (by a few arcseconds). This dithered pattern avoid the systematic addition of bad-pixels at the same positions of the image (and therefore ease the subsequent sky subtraction), as well as the phenomenon of persistence where the brightest stars were (the field of view of ISAAC is large enough to have several objects with $\mathrm{J} \sim \mathrm{H} \sim \mathrm{K}_s \sim 14{-}15$).

We used IRAF to reduce the data. The three darks taken as part of the calibration procedures of ESO are combined with the `imcombine` task, by taking their median. The flat is produced from the science frames, by taking their normalized median, with the procedure `imcombine` again. This is possile because enough of them were taken, so that their median cancel out the contribution of bright objects, that occupy different positions during each integration. We checked that the flatfield produced with the dedicated calibration frames is near identical (variations of less than 1%). The combined dark is subtrated from each science frame, which are then divided by the combined flat. At this point, an effect due to the read-out of the detector has to be accounted for: two read-out are done, one for the top half part of the detector and one for the bottom half, leading to systematically higher values for the first ∼20 rows of each half. To correct for this effect, we follow the recipe given by Labbé et al. (2003) and replaced the median value of these first 20 rows by the median value of pixels on the rest of the half detector.

The task `xdimsum` is used for the rest of the data reduction. Bad pixels and cosmic rays maps are created and values of pixels at these positions are replaced the median value of neighboring pixels. A first pass of sky subtraction is performed by using as sky value the mean value of up to the 6, with a minimum of 3 frames closest in time with the frame being sky-subtracted. Sky frames that have pixel values differing by more than 5σ from the mean value are rejected from the calculation of the mean and this proccess is repeated up to 10 times if necessary. Once all frames are sky-subtrated, a source-detection algorithm creates a mask frames that will be used in the second pass of sky subtraction, in order to avoid using frames with an object at the point of interest in the proccess of sky-subtraction.

Sky-subtracted frames are co-added accordingly, depending of their relative shift with the first frame, taken as the reference. To calculate the relative shift between each science frame, some bright objects (typically 3−4) are located by hand on all of the individual frames. Individual frames are then cross-correlated with the first one in order to obtain precise (at the sub-pixel scale) shifts between individual

---

[7] The list is available online.

frames, our object location being the first guess from which this is done. This gives the final image, that still needs to be flux-calibrated and astrometry-calibrated. Standard stars are observed at similar airmass as part of the calibration plans of ESO and can be used for the flux calibration. There are usually several stars detected in 2−MASS (Skrutskie et al., 2006) in the field of view of our observations and we can also use these stars to calibrate in flux our image. These two techniques usually agree to $\lesssim 10\%$ and we used the flux-calibration solution based on the 2−MASS stars. The astrometry of the final image is usually good (offsets $\lesssim$ few arcseconds) but can still be enhanced. To this end, we used the software `gaia`, distributed in the ESO Scisoft package [8]. `Gaia` allows one to query the public catalogues, such as 2−MASS, and to locate objects (at least 3) in order to correct the astrometry of the image by placing these objects at the positions given in the catalogue. The new astrometry usually presents a RMS of $\sim 0.1''$.

2.3 The Australian Telescope Compact Array (ATCA)

Figure 2.8: View of 5 of the 6 antennas forming the ATCA, in a compact configuration: the three antennas on the right are on the East-West tracks while the the two on the left are on the North-South track.

2.3.1 The radio telescope

The ATCA is a radio interferometer composed of six 22-meters antennas, situated in Narrabri, New South Wales, Australia, about 500 km north-west of Sydney. The configuration of the array can be changed thanks to tracks on which 5 of the 6 antennas can be moved, the sixth antenna being fixed, at 3 km to the west of the station. The 17 possible configurations of the array can be gathered into two groups: extended configurations, where the array is along a east-west axis and with the largest baseline being as long as 6 km ; whereas compact configurations usually involve a couple of antennas being shifted to the North, as it is the case in Fig. 2.8.

Each antenna is equiped with recent receptors, the Compact Array Broadband Backend (CABB, Wilson et al., 2011), since April 2009, allowing for 2×2048 MHz bandwidth observations, with a resolution of up to 1 MHz and over a window of up to 8 GHz. The position of the subreflectors, situated at the prime focus of the main dish, can be adapted according to the observed frequency in order to obtain a focus at the entry of the corresponding feedhorn. Indeed, the different bands offered correspond to the 5 available feedhorns: the largest one is used for observations from 1.1 to 3.1 GHz (the “16 cm” band), the second one for observations from 3.9 to 11.0 GHz (the “6 cm” and “3 cm” bands) and the three smallest ones are used for millimeter observations, spanning 16.0 to 25.0 GHz (the “15 mm” band), 30.0 to 50.0 GHz (the “7 mm” band) or 83.0

---

[8] For more information, see the Scisoft webpage

to 105.0 GHz (the “3 mm” band). These feedhorns are located in a turret at the center of the main dish, that can rotate in order to use the desired receptor. Each feedhorn is coolded and measures the intensity of the signal in its two linear polarizations, leading to a full knowledge (*i.e.*, the four Stokes parameters) of the observed radio wave. The frequency f of the signal has to be shifted into the 4−12 GHz range in oder to be readable by the subsequent electronics. This can be achieved by multiplying the signal with a local oscillator, *i.e.*, a pure sinusoidal signal, whose frequency f_{lo} is well chosen as to bring $f \pm f_{lo}$ into the range in which the electronics works.

For further information about ATCA, the interested reader is referred to the user guide of the telescope.

2.3.2 Observations and data reduction

Preliminary precautions

Since we directly observe an object in its Fourier plane in radio, observations have to be as long as possible in order to obtain the best coverage of the (u, v) plane[9]. Indeed, in order to obtain the final image of the observed object, we will have to take the inverse Fourier transform of the data. However, the sampling in the Fourier plane is far from complete: we only have a certain number of baselines (15 in the case of ATCA), each probing a given spatial scale (also called *spatial frequency*) and a given direction. The first issue can be solved by observing the same object with another configuration of the array, giving access to different spatial scales. In practice, this is rarely needed and the sampling of the Fourier plane with one well-chosen array configuration is, most of the time, sufficient. The second issue is simply solved by letting the Earth rotate, changing the relative orientation of the array compared to the observed source. This is achieved when the source has travelled 180° in the sky, *i.e.*, in 12 hours.

The first thing to do before observing, once the array is set up as desired[10], is to calibrate the delays between signals coming from each antenna in order to make them interfere. Then, at least three kinds of calibrations have to be made during the observing run:

Bandpass calibration is needed to determine the response of the array as a function of the frequency, which is not exactly constant. Some standard bright sources can be used for this purpose and are usually also used to perform the calculation of the delays.

Flux calibration is necessary to obtain a meaningful scale of intensity. To be as accurate as possible, the flux-calibrator should be observed in conditions (elevation, time of observation) similar to the science target. Few well-studied sources are used as flux-calibrators: PKS1934-638 at low frequency ($f \lesssim 10$ GHz) or planets (Uranus, Neptune, Mars) at higher frequency.

Phase calibration (or gain calibration) is required to follow and account for changes in the observing conditions accross the run. A good phase calibrator is a point source object (since it has the same aspect for all baselines) with a flux constant in time (so that gain of the array can be corrected) and close enough to the science object (in order to sample the same conditions of atmosphere). While bandpass and flux calibrators need to be observed only once or twice during the run, the phase calibrator has to be observed every 5−15 minutes, depending on the frequency of the observations and the weather.

Pointing calibration is needed for millimeter observations. Indeed, the size of the primary beam of antennas is inversely propotionnal to the frequency of the observation and becomes of the same order of magnitude as the pointing accuracy of the telescope at millimeter wavelength, potentially leading to significant flux losses because the array does not exactly point at the wanted position. This issue is overcome by observing a bright point-source in the vicinity of the science target. Pointing solutions of each antenna is corrected as to maximise the flux of this point-source. This procedure has to be repeated once the telescope has scanned more than $\sim 20°$, *i.e.*, every hour or when changing of target.

---

[9] The (u, v) plane is simply the Fourier transform of the image of the observed object.

[10] Everything is explained in details on the ATCA website.

Calibrations

The data reduction is done with `Miriad` (Sault et al., 1995), which is also extensively described on the dedicated website. `Miriad` is able to read the raw data delivered by the array, to separate them into the several objects and frequencies that were used and to apply calibrations discussed above to science data in order to produce meaningful scientific data.

First, some frequencies at some periods of the observation have to be discarded ("flagged") because of radio-frequency interferences (RFI) due to FM radio stations, cell-phones communications, microwave ovens, … Some frequencies are nearly always contaminated with emissions related to human activities and can be automatically flagged when loading the data in `Miriad` with the task `atlod`, but some others require visual inspection because RFI are not always present and can be fagged by using tasks `uvflag`, `blflag`, `pgflag` or `mirflag`. Finally, some self-generated interferences also have to be flagged.

Once datasets have been divided into the different observed objects at the different frequencies with `uvsplit` and these data cleaned from RFI, the bandpass calibration is determined by using the task `mfcal` on the relevant calibrator. Note that it is possible to determine a time-dependant bandpass solution if the relevant calibrator has been observed often enough. The solution is applied ("copied") to the rest of the data, using `gpcopy` afterwards. The task `gpcal` is then used to perform the flux calibration. This task has models for sources frequently used as flux calibrators and it is not necessary to provide a flux scale in this case. If an unusual flux calibrator was observed, more care must be paid at this step of the data reduction. At this stage, as a sanity check, we verify that real and imaginary parts of Stokes parameters of the flux calibrator have consitent values. Should it not be the case, extra flagging is performed.

Phase calibration is then done, again using `gpcal`, but not solving for flux (this was the previous step), only for Q and U Stokes parameters. The time-dependent flux calibration of the phase calibrator, observed throughout the run, is performed with `gpboot` in order to take into account variations in the absolute flux scale, *e.g.*, due to changes in system gain or in atmospheric conditions. The same is done for the bandpass calibration of the phase calibrator, using `mfboot`. Finaly, the calibrations are applied to science sources with `gpcopy`.

Image inversion

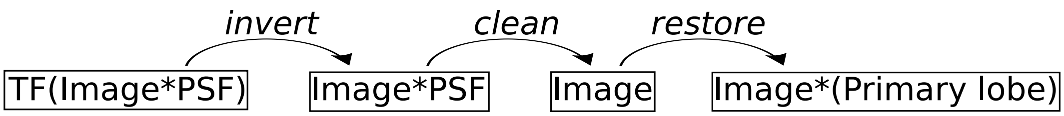

Figure 2.9: Schematic view of the imaging process in radio: The first step is to bring the observations in the real space (since they naturally occur in the Fourier space in radio), which is performed with the inverse task of MIRIAD. Then, this image needs to be deconvolved from the "dirty beam" — a consequence of the incomplete sampling of the (u, v) plane — which is performed thanks to the clean algorithm. Finally, the collection of point sources found in the previous step are convolved with the primary beam of the radio telescope (with the task restore) in order to give the final result.

As already mentionned, radio observations are directly made in Fourier space. However, only a few portions of the (u, v) plane are sampled: those with spatial frequencies between the largest baseline and the size of a single dish, and at angles determined by the relative orientation of the array compared to the source at the time of observations. The data we obtain from the telescope ($\widehat{I}_{\text{obs}}$ is therefore the multiplication of the Fourier transform of the source ($\widehat{I}_{\text{real}}$ with the sampling function (S) of the (u, v) plane of the observations. When observed from the real space, this is equivalent to convolving the observations with a "dirty beam" (B), although it has nothing to do with the beam of the dishes of the interferometer, but only comes from the partial covering of the Fourier plane:

$$\widehat{I}_{\text{obs}}(u,v) = \widehat{I}_{\text{real}}(u,v) \times S(u,v)$$
$$I_{\text{obs}}(x,y) = I_{\text{real}}(x,y) \star B(x,y)$$

The problem with the observations is that we obtain $\widehat{I}_{\text{obs}}$ and we are interested in I_{real}. We will therefore have to:

1. Fourier transform our observations back into the real space. This is performed with the task `invert`.
2. Deconvolve the result from the term B. This is done by the task `CLEAN` , based on the algorithm of Högbom (1974).

Note also, in the case of continuum images, that the size of the beam of the array can significantly change over the large bandwidth of the observations. It is therefore a better option to perform the inversion frequency by frequency and add all these images together to create the continuum image only afterwards.

The most important option of the `invert` task regards the weight given to the signal coming from each baseline. Depending on our choice, the noise can be increased or the sidelobes can be more important. We use a `robust` weighting of 0.5 and ask the `invert` task to produce a continuum image, by activating the options `mfs` and `sdb`.

The next step of the formation of the image calls the `CLEAN` algorithm (Högbom, 1974). It deconvolves the image I_{obs} from the contribution of the "dirty beam" B in order to give what interests us: I_{real}. It procedes iteratively, looking for the extremum value in the convolved image and subtracting a fraction (set to 0.1 in our case) of the " dirty beam" B, centered on this pixel, from the image. This proccess is repeated on the residual image, until the extremum pixel in the residual image has a negative value. The loop can also be stopped by other conditions (*e.g.*, once the extremum value is lower than a threshold or after a given number of iterations), but we do not use them. Variants of the `CLEAN` algorithm exist, *e.g.*, Clark (1980); Steer et al. (1984), and `Miriad` can use any one of these three implementations at each iteration step, depending on the nature of the residual image.

Finally, since the "cleaned" image, obtained from the previous step, is merely a collection of point sources, it contains information that is actually not accessible to the observations: observing a point source would require an infinitely small beam[11], *i.e.*, infinitely large telescope/dishes. This is due to the nature of the algorithm itself, so that we have to bring the cleaned image back into the interval of spatial scales actually accessible with the ATCA. This is done by convolving the cleaned image with the "cleaned beam", a Gaussian which fits the PSF of the telescope. The task `restor` performes this step. Finally, the last residual image from the `CLEAN` algorithm is added to this image. All the steps leading to the formation of an image in radio are schematically summurized in Fig. 2.9.

---

[11] the "real" beam here, due to the finite size of the dishes of the array

Chapter 3

Monte Carlo simulations: How to reach a deep understanding of our data?

Contents

A large part of the results presented in this thesis originate from fits to spectral lines that have, most of the time, complex profiles. In order to obtain reliable conclusions, it is necessary to estimate relevant uncertainties of derived parameters and study systematic effects that affect our observations. For these reasons, we run Monte-Carlo simulations by creating sets of artificial cubes with different characteristics (signal-to-noise ratio, seeing size, ...) and then applying our routines on them. By comparing results given by our analysis tools with input parameters, we can estimate the minimum signal-to-noise ratio required to obtain reliable conclusions, the associated uncertainties and, in some cases, correction factors that can be applied to results.

In this chapter, we begin with reviewing the effects that can be addressed by these simulations: presence of the night sky lines and effect of the seeing on the emission lines. Then, we explain how we create the artificial cubes. Finally, we give the results of these simulations.

3.1 Effects affecting our observations and expectations from these simulations

Before exploring the results of our simulations, we first review the phenomena that can affect our observations and, more importantly, detail how we define the SNR thresholds that will be used later on real observations.

3.1.1 Night sky residuals

The first issue comes from night sky residuals, due to unperfectly subtracted night sky lines, mainly OH emission lines. Indeed, the intensity of these lines vary on timescales of a few minutes, comparable with the integration time that we use in our observations. The wavelength calibration might also not be perfect and that would lead to typical features in spectra, that look like P-cygni profiles. Indeed, if the night sky lines are not exactly at the same spectral position, the red (resp. blue) wing of the line can be oversubtracted (resp. undersubtracted) ; or vice-versa. Note that this effect tend to be systematic, averaging over several spatial pixels usually does not help much to attenuate night sky residuals.

Since the spectral position and intensity of the night sky lines is well-known, we have all the information we need to tackle this problem. Night sky lines residuals can be not taken into account if the main emission lines from the observed objects are at wavelengthes relatively free of strong night sky lines residuals. However, in some cases, faint — but interesting — emission lines are blended with stong night sky lines (*e.g.*, Hβ in NVSS J1449 or in NVSS J2046, see chapter 4), it is therefore important to study if it is possible to recover reliable fluxes from a line blended with night sky residuals and, if it is, under which assumptions.

There is another particular but troublesome problem caused by night sky residuals: If they are just blueward or redward of a strong emission line from the ionised gas that we use to trace kinematics, our results can be affected by this night sky residual since it will systematically stretch the centroid of the fitted line. Again, our Monte-Carlo simulations should allow us to quantify this effect.

3.1.2 Seeing

The effect of the atmosphere on astronomical observations can be dramatic: turbulent motions of atmospheric layers imprint random pathway differences in the wavefront, resulting in observing speckles instead of the expected Airy disk. These motions are rapid and these speckles can be seen only for exposure times shorter than ~ 10 ms. For integration times much longer than this, as it is the case for our observations, these speckles add together to give the seeing disk (if a point source is observed), that gives the actual spatial resolution, usually given as the FWHM of this seeing disk. From one night to another, or even accross a single night, atmospheric conditions can vary a lot and therefore have a large impact on the quality of our observations.

The seeing disk also depends on the wavelength of the observations. The Fried parameter r_0 illustrates this: it corresponds to the aperture of a telescope that would be limited only by diffraction and that would have the same resolution as the seeing disk:

$$\frac{\lambda}{r_0} \sim FWHM$$

It can be shown (see, *e.g.*, Léna et al., 2008, chapter 6) that:

$$r_0 \propto \lambda^{6/5}$$

We can therefore see that the effect of the seeing is more important in the optical than in the NIR.

The seeing obviously impacts our observations spatially, by limiting the spatial resolution, but it can also have an impact on the spectral information that we measure. Indeed, if two regions of the galaxy are within the same spatial resolution (*i.e.*, less separated than a seeing disk) but are sampled on two different spaxels and have very different kinematics, the seeing will cause information from one spaxel to leak into its neighboor, leading to observed kinematics that is attenuated compared to reality. Note that these conditions are (unfortunately) easily met: typical seeing in our observations is $0.5 - 1.0''$. At the redshifts of our observations ($z = 1 - 3$), this roughly corresponds to $4 - 8$ kpc, *i.e.*, a significant fraction of the typical size of a galaxy. The spatial sampling of SINFONI is, at worst, $0.25''$. So, if the object that we observe presents sharp variations in its kinematics (*e.g.*, back-to-back outflows, mergers, ...) the seeing will likely attenuate its observation. As an associated effect, the velocity dispersion will be increased in these two spaxels, due to the leakage of lines in its neighboring spaxels that are at a different velocity. This effect is perfectly illustrated in Fig. 3.2 that show the spectrum integrated in the central 5×5 spaxels before convolution (in red), after convolution (in green) and after addition of low level noise (in blue). The last effect of the seeing is to make the observed object appear larger than it actually is.

3.2 Simulation of a cube

3.2.1 Modelling a galaxy

The galaxy emission that we model consist simply in two emission lines coming from the ionized gas and that represent the [OIII] doublet, the line at the basis of most of our studies. We do not include any continnum (coming from the stars) since it is usually faint compared to the emission lines and, in case it is not, it can easily be subtracted in the first step. The morphology of the galaxy is also very simple since it is chosen to be Gaussian[1]. This morphology depicts quite accurately most of the galaxies that we observed and, in the same time, it allows easy comparisons with analytical predictions.

In the following, x and y will represent the two spatial variables and we use λ to denote the spectral dimension of the cube (see Fig. 2.4). We will note L the number of pixels along the $x-$ and $y-$axis directions.

The mock cube is modeled as described below:

1. We create a data cube of the size $L \times L \times 2048$. We keep the spectral size of SINFONI in our simulated cube for reasons of simplicity and compatibility with analysis routines designed for real cubes.
2. Each spaxel of the cube, according to its position (x, y), receives the appropriate spectrum, that mimics the [OIII] doublet: the line core of the line is set to $F(x, y)$ and its relative velocity is set to $V \times v(x)$. We also choose the FWHM of the line, typically FWHM ~ 800 km s^{-1}.
3. The line core $F(x, y)$ of the extended emission line region of the galaxy at the position (x, y) has a Gaussian morphology, parametrized by σ_x, σ_y (entension along $x-$ and $y-$axis respectively) and I:

$$F(x,y) = I \times \exp\Big(- \frac{(\frac{x}{L} - \frac{1}{2})^2}{2\sigma_x^2} - \frac{(\frac{y}{L} - \frac{1}{2})^2}{2\sigma_y^2} \Big)$$

---

[1] *i.e.*, in a more astronomical way, it has a Sérsic profile with $n = 0.5$, see section 5.3 to have a more complete description of Sérsic profiles.

4. The velocity field varies only along the $x-$axis, according to $V \times v(x)$, where $v(x)$ is:

$$v(x) = \tanh\left\{a \times \left(\frac{x}{L} - \frac{1}{2}\right)\right\} - b \times \left(\frac{x}{L} - \frac{1}{2}\right)$$

   a is linked to the distance between the two "turning points" in the velocity field: the greater it is, the smaller this distance. The parameter b gives the strength with which the `tanh` function is attenuated at the edges of the cube. Typical velocity fields are on Fig. 3.1. This figure is also useful to see how parameters a and b influence its shape. V is the intensity of the velocity gradient, usually chosen to be $V = 800$ km s^{-1}, giving a velocity offset of ±600 km s^{-1}, slightly larger than what is typically observed, but not unknown of some HzRGs (*e.g.*, Nesvadba et al., 2008).

   The distance D between the two turning points of the velocity field can be expressed as:

$$D = \frac{L}{a} \times \text{acosh}\left(\frac{2a}{b} - 1\right)$$

5. The velocity dispersion of the line is chosen to be equal to 40Å, which corresponds to FWHM $\sim$ 800 km s^{-1}, depending on the spectral position of the line. In order to model different ratios of velocity gradient-to-velocity dispersions, we also used values of velocity dispersions of FWHM = 400 km s^{-1} and FWHM = 1200 km s^{-1}. This will allow us to study the impact of the ratio of bulk motions to turbulent motions on what is observed. Indeed, velocity gradients can be expected to be less visible if the velocity dispersion is high.

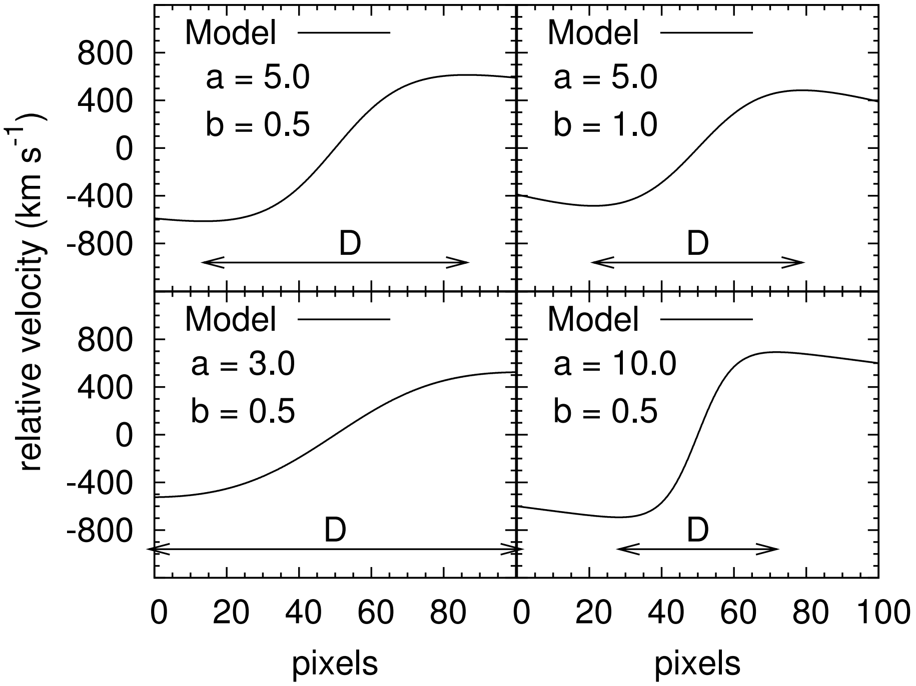

Figure 3.1: Examples of velocity fields along a cut in the $x-$axis, with typical values of a and b. In all panels, $V = 800$ km s^{-1}. The distance D between the two turning points of the velocity field is indicated by the horizontal arrow.

3.2.2 Modelling atmospherical effects

On top of emission from the galaxy, we must include effects caused by the atmosphere and the telescope: convolution of the observed object by the seeing and night sky line residuals. The seeing is due to the turbulence of the atmosphere, which perturbes the wave front coming from the observed source. What is observed is then the convolution of the source with the seeing disk, under the conditions of observation. The night sky residuals are mainly due to the NIR emission lines of the OH radical that cannot perfectly be accounted for during data reduction. Therefore, we have to include these effects in our simulations of datacubes.

1. The cube is convolved with the seeing disk, that we consider Gaussian. It is characterized by its standard deviations $\sigma_{PSF,x}$ and $\sigma_{PSF,y}$, which are a fraction f of the flux width:

   $$\sigma_{PSF,x} = f \times \sigma_x$$

   (the definition is analogue for $\sigma_{PSF,y}$).

2. Finally, we add Gaussian distributed noise to each element of the simulated cube, according to the desired signal-to-noise ratio. To account for night sky residuals, we add constant quantity in all spaxels and at fixed spectral positions. The width of these features is set to two spectral pixels.

Note that, because of the convolution, the width of the source in the mock cube is increased by a factor $\sqrt{1+f^2}$, which makes the source looks bigger. But, as the flux must be conserved in the convolution process, that also means that, in a given spaxel, the lines seem weaker. If there are some velocity shifts in the source on scales smaller than the seeing, it also makes the line appear wider and attenuates the velocity shifts. The results of these different steps can be seen on Fig. 3.2: it shows the spectrum of the simulated cube integrated over the central 5×5 pixels, where the velocity shifts are important.

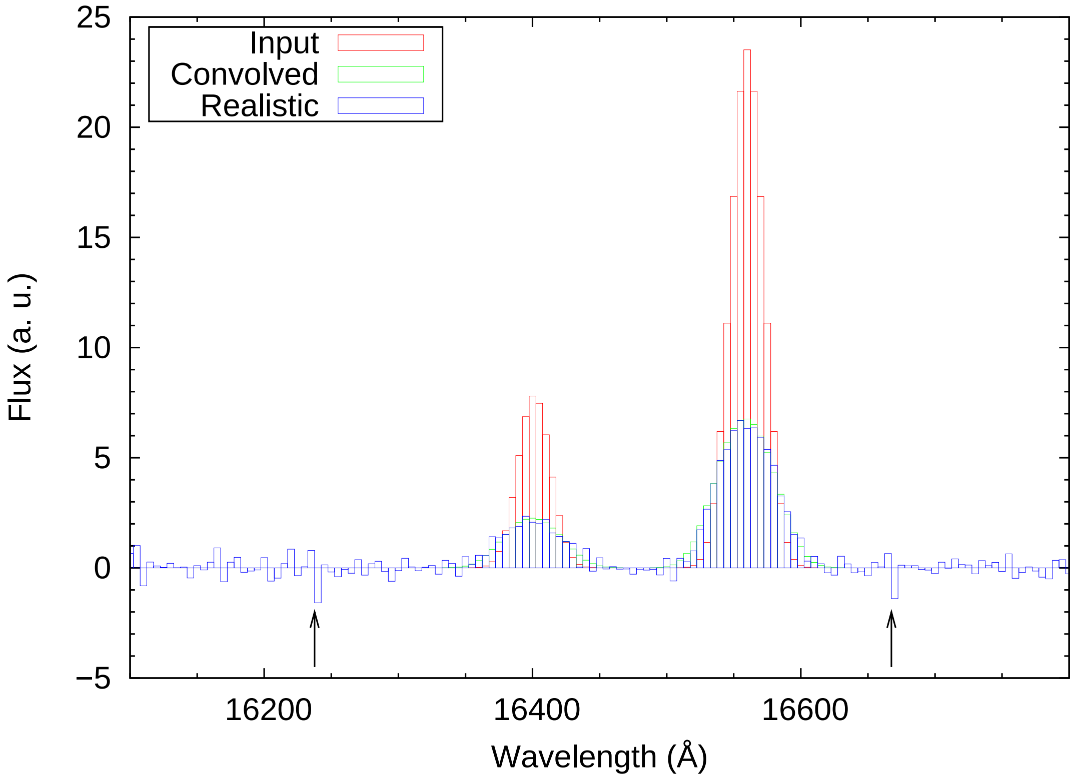

Figure 3.2: Spectrum at the mock cube at different steps of its creation: *red:* the “perfect” cube of the input ; *green:* the perfect cube convolved with a seeing disk of $f = 1$; *blue:* the cube with some noise added. Two examples of night sky residuals are indicated by the arrows.

3.2.3 Inputs spectra: from idealistic to realistic cases

Gaussian emission line and Gaussian distributed noise

The first set of simulations corresponds to a simple situation: emission lines are modelled with Gaussian profiles, and described by the three usual parameters λ_0 (the centroid position of the line), σ (the width of the line — in the standard deviation sense) and I_C (the line core):

$$\mathrm{Line}_{\mathrm{Gauss}}(\lambda) = I_C \times \exp - \Big(\frac{(\lambda - \lambda_0)^2}{2\sigma^2} \Big)$$

To this spectrum, Gaussian noise is added, using the IDL procedure `randomN`, which produces normally-distributed pseudo-random numbers with a mean of zero and a standard deviation of one, to create it. So, by simply scaling the sequence given by `randomN`, we can test different relative levels of the noise, that we describe in this case by the ratio I_C/RMS, where I_C is the line core and RMS is the root mean square of the intensity of the noise, estimated on the spectral range not dominated by the line:

$$\mathrm{RMS} = \sqrt{\sum_{\mathrm{pix}} (I(\mathrm{pix}) - \overline{I})^2}$$

where $\overline{I}$ is the mean intensity on the considered spectral range (*i.e.*, $\overline{I} \simeq 0$ here since the line is not considered and the noise we choose has a mean of zero). Night sky residuals are also modelled by adding in all spaxel, at a fixed spectral position, a random quantity on two contiguous spectral pixels.

Gaussian profile and real noise

This set of simulations is designed to test the fitting algorithm that we use under more realistic conditions but still with a perfect knowledge of our input parameters to keep comparisons between input and fitted parameters straightfoward. The noise comes from our data, randomly chosen in a spatial 3×3 pixel box of some of our datacube, and in spectral regions of ~ 500.0 Å, free from emission lines (which positions are different enough from one cube to another so that all spectral ranges are used as noise). We also substract the noise from its mean value, in order to avoid effects induced by the presence of the continuum of the galaxy that stands in the datacube.

This noise differs from the previous one, mainly because of night sky residuals that are not Gaussian, since they are at fixed spectral position and tend to have the same sign over large regions of the data cube. We also distinguish $H-$band and $K-$band noises, since night sky lines are much more intense in the former. The line has still a Gaussian profile of known parameters λ_0, FWHM and I_C. The centroid of the line is the center of the spectral range chosen for the noise and therefore changes for all realisations. We keep the values of FWHM = 40Å and $I_C = 10^{-18}$ erg s^{-1} cm^{-2} Å^{-1} from previous simulations. We chose a spectral binning of 5.0Å, which is very close to the one in real data. We still use the same definition of signal-to-noise ratio, namely SNR = I_C/RMS, where I_C is the line core of the Gaussian line and is well-defined ; and where RMS is the root mean square of the chosen spectral portion of data.

Real emission line profile and real noise

Now that we better understand how real noise extracted from datacubes can affect the fit of a Gaussian line profile, the last step for our simulations is to introduce realistic line profiles. Since most of our studies rely on the [OIII]λ5007 line, we extract this line in each of our datacubes, corrected for possible blueshift or redshift with respect to the systemic redshift[2]. We extract the [OIII]λ5007 line on a width of $\pm 3\sigma$, where σ is the standard deviation of the Gaussian fit to the line. We are then able to recover most of the line, with all its non-Gaussiannities (broad blue wings, ...), without being too polluted by the strong night sky residuals that may fall in this spectral range.

---

[2] see section 4.2 for more details about how we make these corrections

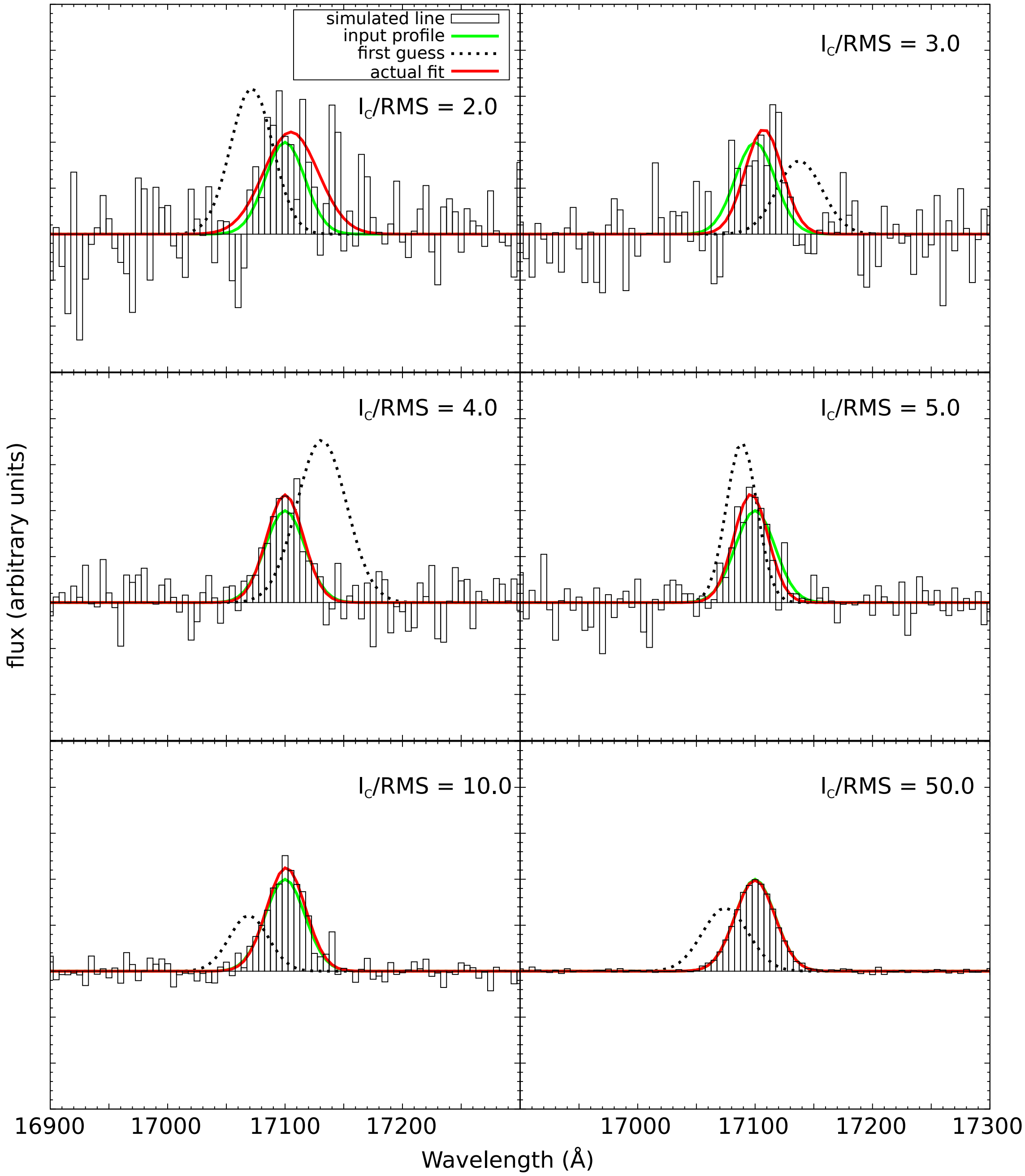

Figure 3.3: Examples of realisations of Gaussian line with Gaussian noise, under various conditions: I_C/RMS = 2.0 (top left) ; 3.0 (top right) ; 4.0 (middle left) ; 5.0 (middle right) ; 10.0 (bottom left) and 50.0 (bottom right).

The noise we use is the same as in the previous set of simulations "Gaussian line and real noise". It is also scaled to match the desired I_C/RMS ratio, which is still the value we use to parametrize our simulations. We adapt the definition of I_C to be the maximum value of the extracted line.

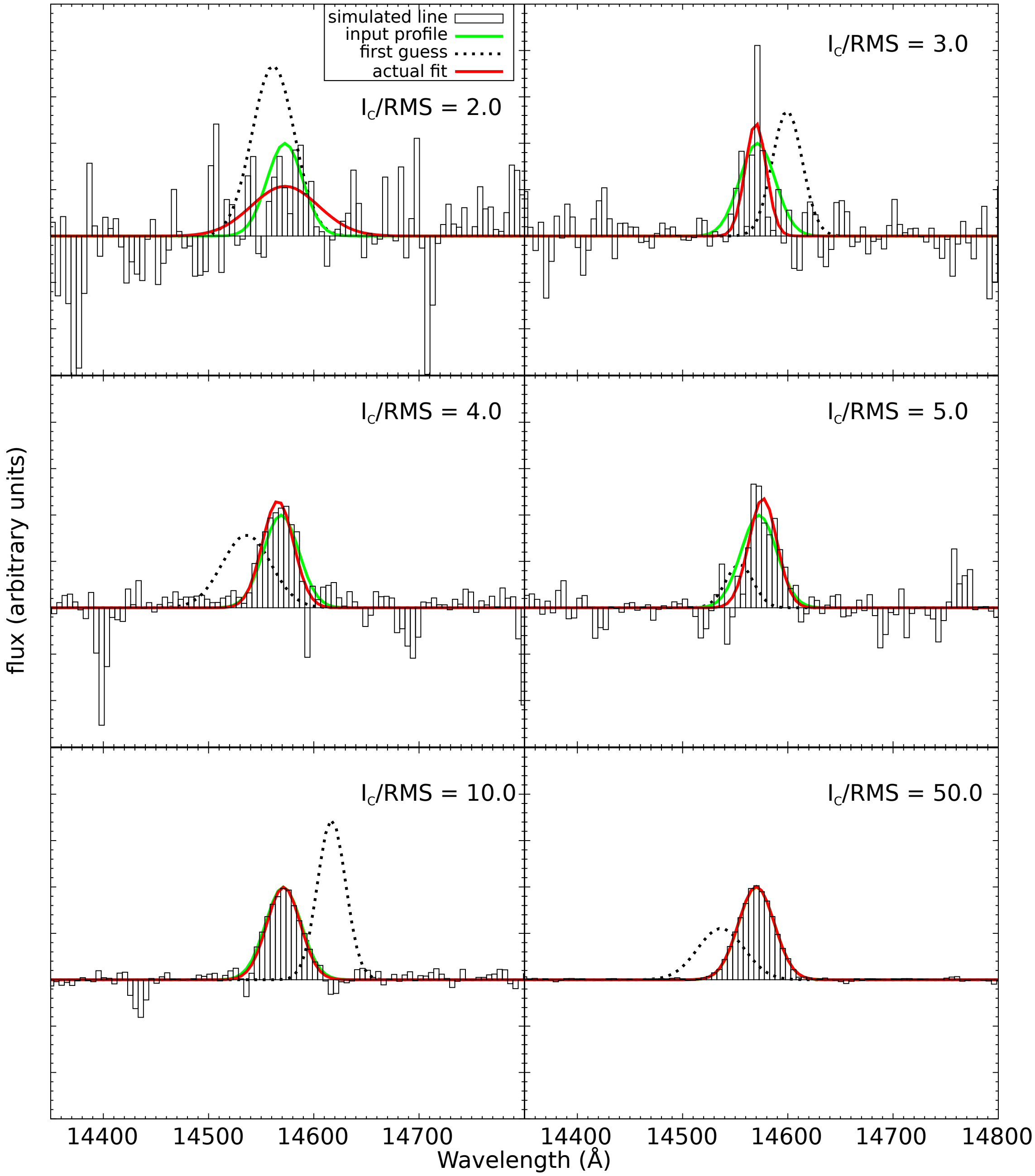

Figure 3.4: Examples of realisations of Gaussian lines with real noise (coming from the $H-$band here), under various conditions: $I_C/\mathrm{RMS} = 2.0$ (top left) ; 3.0 (top right) ; 4.0 (middle left) ; 5.0 (middle right) ; 10.0 (bottom left) and 50.0 (bottom right).

3.2.4 Expected results

Before running all these simulations, let's see what we can expect from them, that will give us first benchmarks. First, the flux F is convolved with the PSF to give F_c:

$$\begin{aligned} F_c(x,y) &= F(x,y) * PSF(x,y) \\ &= I_c \times \exp\Big(-\frac{(\frac{x}{L}-\frac{1}{2})^2}{2\sigma_{x,c}^2} - \frac{(\frac{y}{L}-\frac{1}{2})^2}{2\sigma_{y,c}^2}\Big) \end{aligned}$$

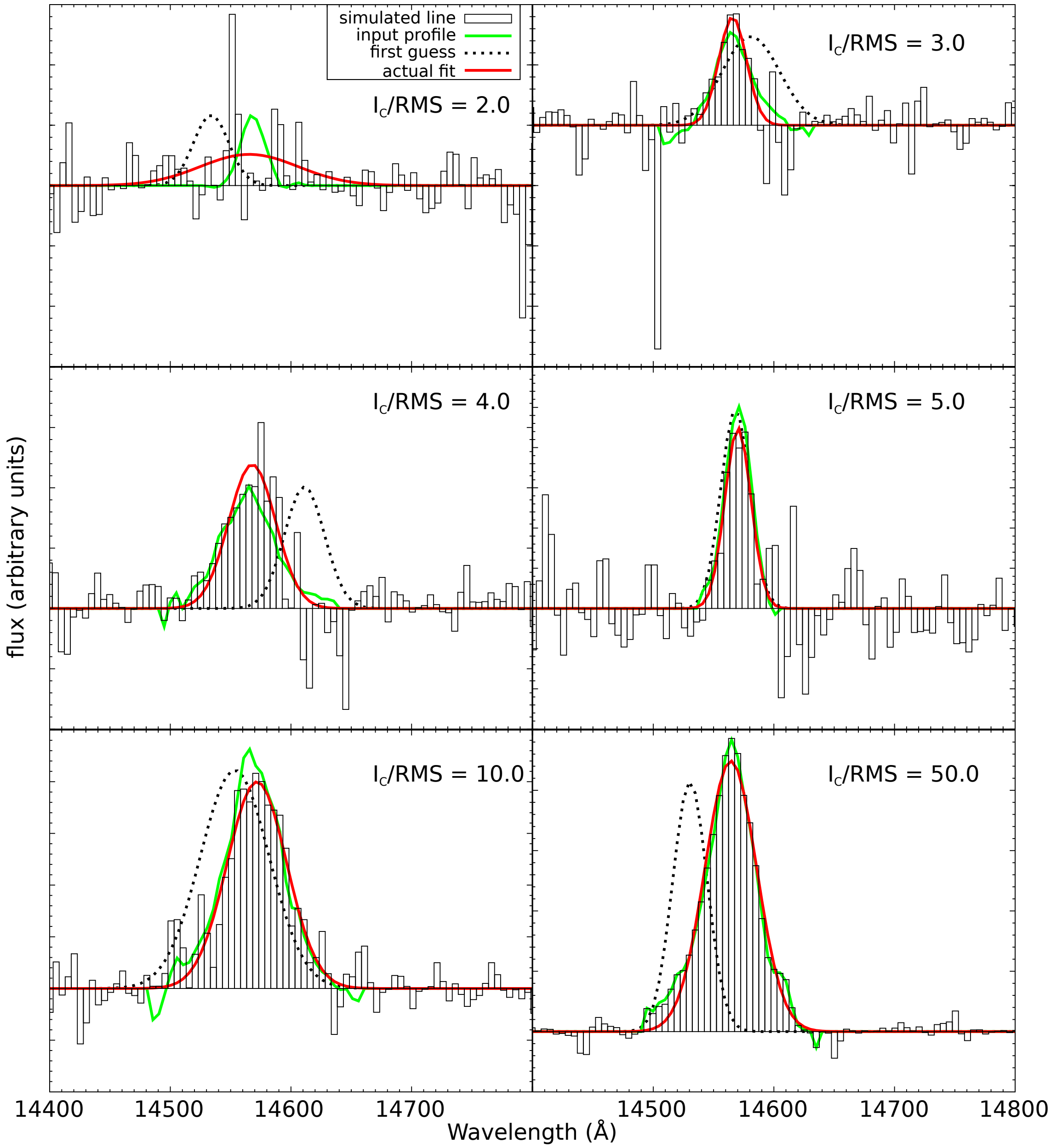

Figure 3.5: Examples of realisations under various conditions: $I_C/\text{RMS} = 2.0$ (top left) ; 3.0 (top right) ; 4.0 (middle left) ; 5.0 (middle right) ; 10.0 (bottom left) and 50.0 (bottom right).

Indeed, the convolution of two 2-D Gaussians is also a 2-D Gaussian. Furthermore, since these two 2-D Gaussians have the same orientation, the expression of the parameters I_c, $\sigma_{x,c}$ and $\sigma_{y,c}$ of their convolution is rather simple:

$$I_c = \frac{I}{1+f^2}$$

$$\sigma_{x,c} = \sqrt{1+f^2}\,\sigma_x$$

$$\sigma_{y,c} = \sqrt{1+f^2}\,\sigma_y$$

The simulated object should therefore look more extended than the input object by a factor $\sqrt{1+f^2}$ and the flux should be reduced by a factor $1+f^2$.

3.3 Analysis of the simulated cubes: Signal-to-noise threshold

In this section, the aim is to test the behavior of `MPFIT`[3], the fitting algorithm that we use. We test it under various conditions, namely $I_C/\mathrm{RMS} = 2.0; 3.0; 4.0; 5.0; 10.0$ and 50.0. The first guess for each parameter is randomly chosen around the input values that were used to create the "real" line.

All results in this section originate from simulations with the following parameters: $a = 5.0$, $b = 0.5$, $V = 800$ km s^{-1}, FWHM = 800 km s^{-1} and a spectral binning of 5.0Å, which are values representative of our real observations. We simulate only emission lines, *i.e.*, we do not create a cube and there is no convolution step in the simulations analysed in this section because we focus here on the determination of the signal-to-noise threshold that we will use in the analysis of our observations and on the associated uncertainties (*i.e.*, random errors). The effects of the variations of these parameters and, more importantly, of the convolution by the seeing disk will be explored in the next section, along with the systematic errors that they can bring.

3.3.1 Gaussian line and Gaussian noise

We begin with our simplest set of simulations. Some examples of the 10,000 realisations of each SNR are displayed on Fig. 3.3.

Results of these simulations are summed up in Table 3.1. For illustration, we also present some distributions of the parameters of the fitted lines, with respect to the input I_C/RMS ratio, on Fig. 3.6. To characterize these distributions, we fitted them with Gaussians, which are also dispayed. The parameters of these fits allow us to estimate the typical uncertainty and systematic error at a given SNR.

For this set of simulations, it appears that the centroid of the line is, on average, well recovered by `MPFIT`: the distribution of the parameter of the fit $\lambda_{0,\mathrm{fit}}$ is centered on 0 at all signal-to-noise ratios, even at its lowest value $I_C/\mathrm{RMS} = 2.0$. As expected, the width of this distribution narrows as the SNR becomes larger: from a typical uncertainty of 5.4Å (*i.e.*, nearly 100 km s^{-1}) for $I_C/\mathrm{RMS} = 2.0$, it is divided by more than a factor 2 when $I_C/\mathrm{RMS} = 5.0$ with an uncertainty of 2.5Å (or ~ 40 km s^{-1}) and it becomes negligeable for $I_C/\mathrm{RMS} \geq 10.0$, with an uncertainty of less than 1.5Å (or 25 km s^{-1}).

Regarding the velocity dispersion, *i.e.*, the width of the line, it tends to be systematically lower than the input value at low signal-to-noise ratios: for $I_C/\mathrm{RMS} = 2.0$, it is on average reduced of 2.5Å (or ~ 40 km s^{-1}, *i.e.*, 5% of the input value). For $I_C/\mathrm{RMS} \geq 5.0$ this effect becomes negligeable, with a systematic narrowing of only 0.3Å (or ~ 5 km s^{-1}). The typical uncertainty on the fitted value is large at low signal-to-noise ratios: it reaches 12.3Å (*i.e.*, more than 200 km s^{-1}) at $I_C/\mathrm{RMS} = 2.0$ and becomes smaller than 100 km s^{-1} (4.9Å) only for $I_C/\mathrm{RMS} \geq 5.0$.

On average, the fitted line core is close to the input value at all SNR: it is larger by only 6% for $I_C/\mathrm{RMS} = 2.0$ and is correct within 1% for $I_C/\mathrm{RMS} \geq 5.0$. The typical error on the fit of the line core is as important as 30% of the input value for $I_C/\mathrm{RMS} = 2.0$, it reduces to $\sim$ 10% at $I_C/\mathrm{RMS} = 5.0$ and it still amounts to 6% at $I_C/\mathrm{RMS} = 10.0$

From this first set of simulations, a threshold at $I_C/\mathrm{RMS} = 5.0$ appears as the minimum SNR value to recover parameters of the line that do not suffer fom systematic biases (this is especially true for the width of the line and the value of the line core) and that have typical uncertainties that are acceptable, *i.e.*, whose value is (much) smaller than what is typically observed in real data. And we observe typical offsets in the bulk velocity of the gas of a few times 100 km s^{-1} (see chapter 4), compared to an uncertainty of $\sim$ 40km s^{-1} at $I_C/\mathrm{RMS} = 5.0$. Typical velocity dispersions are in the range 400−1000 km s^{-1}, compared to an uncertainty of 100 km s^{-1} at $I_C/\mathrm{RMS} = 5.0$. Finally, at this SNR, the uncertainty on the fit of the line core is $\sim$ 10%, comparable to the uncertainty in flux calibration.

---

[3] see http://www.physics.wisc.edu/ craigm/idl/fitting.html

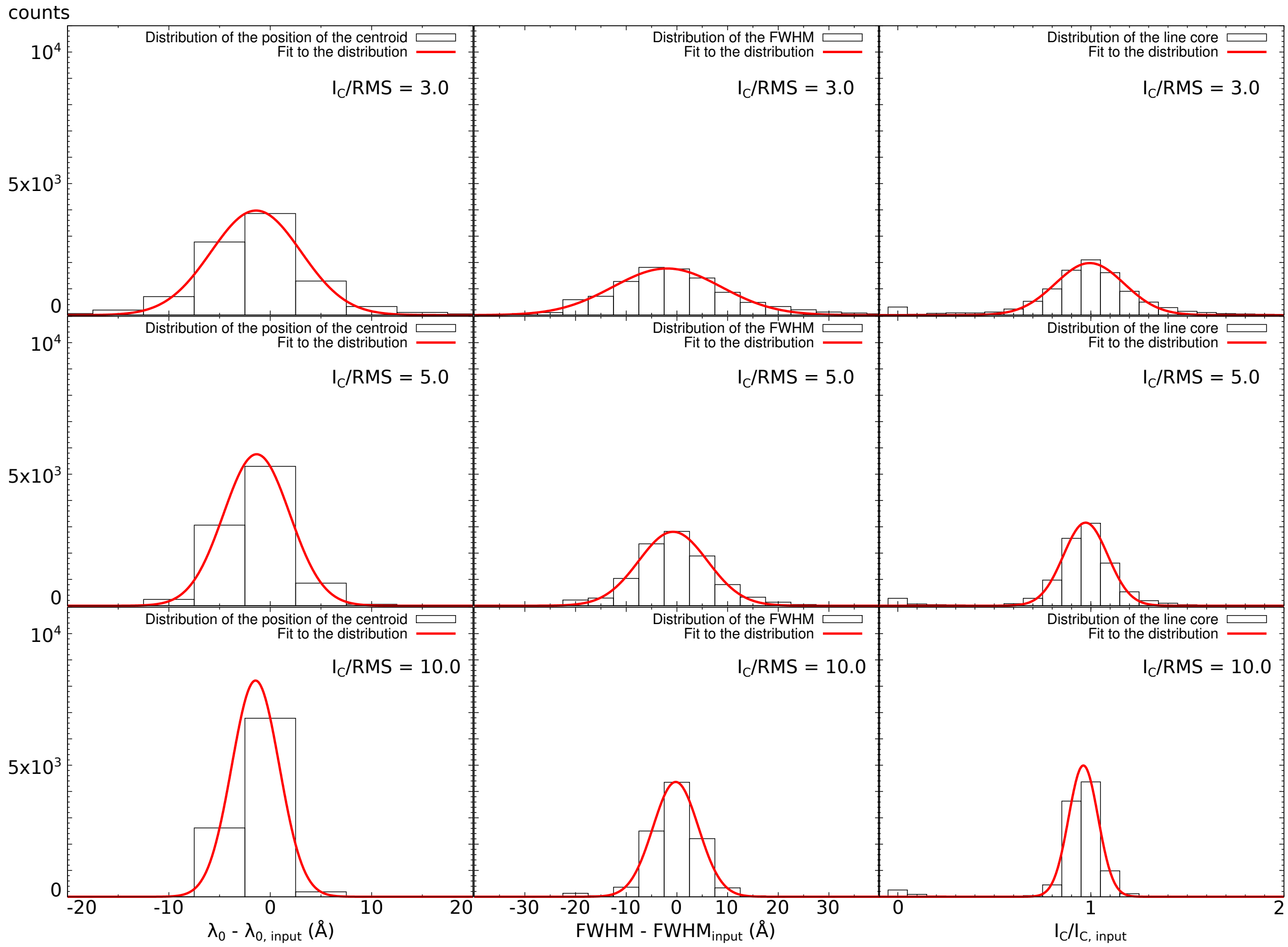

Figure 3.6: Distributions of the fitted parameters for the "Gaussian line and Gaussian noise" set of simulations: λ_0 (left), FWHM (middle) and I_C (right) for $I_C/\mathrm{RMS} = 3.0$ (top) ; 5.0 (middle) and 50.0 (bottom). We fit these distributions with Gaussians to characterize them. Parameters of these fits can be found in Table 3.1.

3.3.2 Gaussian line and real noise

We test again the `MPFIT` procedure under different conditions, using noise coming from actual observations. They are still parameterized with the same quantity I_C/RMS and the extracted noise is scaled to the appropriate value, as before. We present some examples in Fig. 3.4.

We analyse the results of this set of simulation the same way as before: distributions of the fitted parameters are adjusted by Gaussians to characterize them. The results, given in Table 3.2 are similar to the first ones, obtained with a Gaussian line profile and Gaussian noise, but distributions are somewhat broader, notably for the estimation of the width of the line.

Regarding the centroid of the line found by `MPFIT`, it is still on average unbiased, at all signal-to-noise ratios. The uncertainty associated with this parameter is slightly larger than with the previous set of simulations at low SNR, but becomes slightly smaller et larger SNR. Therefore it appears that the non-Gaussianity of the noise does not have an important impact on the determination and the uncertainty of the position of the line centroid.

The fit of the velocity dispersion still shows a systematic reduced value at low signal-to-noise ratios, but this effect is increased compared to the previous set of simulations: at $I_C/\mathrm{RMS} = 2.0$, the fitted velocity dispersion tends to be smaller by 4.4Å (or ~ 80 km s^{-1}), *i.e.*, nearly twice as much as with the previous

	I_C/RMS					
	2.0	3.0	4.0	5.0	10.0	50.0
$\lambda_{0,\text{fit}} - \lambda_{0,\text{input}}$ (Å)	-0.033	0.044	0.064	0.019	-0.014	-0.342
σ_{λ_0} (Å)	5.397	3.686	2.916	2.488	1.546	1.083
I_{λ_0}	3321	5102	6534	7585	9631	10356
$\text{FWHM}_{\text{fit}} - \text{FWHM}_{\text{input}}$ (Å)	-2.525	-1.13	-0.637	-0.274	0.036	-0.105
σ_{FWHM} (Å)	12.317	7.986	5.888	4.887	2.795	1.437
I_{FWHM}	1522	2393	3269	3980	6994	9907
$I_{C,\text{fit}}/I_{C,\text{input}}$	1.062	1.029	1.017	1.001	1.002	1.008
σ_{I_C}	0.284	0.174	0.131	0.106	0.058	0.021
I_{I_C}	1328	2174	2918	3593	6652	10486

Table 3.1: Results of the fits to the parameter distributions, with respect to the input I_C/RMS, for the "Gaussian line and Gaussian noise" set of simulations. $\lambda_{0,\text{fit}} - \lambda_{0,\text{input}}$ is the position of the centroid of the distribution of the parameter λ_0 of the fit (in Å), *i.e.*, indicating possible systematic errors in the fit of the centroid of the line. σ_{λ_0} is its standard deviation (in Å), giving an idea of the typical uncertainty on the fit of the centroid of the line and I_{λ_0} is the intensity of the distribution. The same apply for the two others parameters, FWHM (for which results are also expressed in Å) and I_C (for which results are normalized to the input value).

simulation set. However, this systematic reduction is rapidly reduced at higher SNR and reaches negligeable values (0.4Å or less than 10 km s^{-1}) for $I_C/\text{RMS} \geq 5.0$. The uncertainty on the width of the line is also increased, especially at low SNR: it reaches 9.6Å (or $\sim$ 170 km s^{-1}), compared to 8.0Å, at $I_C/\text{RMS} = 3.0$ and 7.0Å (or $\sim$ 120 km s^{-1}), compared to 5.9Å, at $I_C/\text{RMS} = 4.0$. For $I_C/\text{RMS} \geq 5.0$, the uncertainty becomes comparable to values found with the previous set of simulations (5.3Å compared to 4.9Å, or nearly 100 km s^{-1}).

The fitted value of the line core tends to be overestimated, again, but this effect is comparable in both "Gaussian noise" and "real noise" sets of simulations. The same is true with the uncertainty associated with the line core: it is very similar to what is found in the previous set of simulations.

This can be understood since night sky lines residuals, which are an important source of noise in our datacubes, are usually broader than the spectral sampling. This causes some correlated noise on a few (typically $3-4$) consecutive spectral pixels. Then, if a relatively strong night sky residual falls at the edge of the simulated line, it will tend to either broaden or shrink the line, depending if it is positive or negative.

3.3.3 Real line and real noise

While we previously always used Gaussians lines with FWHM = 40Å (or FWHM $\simeq$ 700 km s^{-1}), the line profiles, and hence the velocity dispersions, in each observed galaxy are all different. In order to compare widths fitted on these different lines with previous sets of simulations, we scale them to the value we used in all previous simulations, namely 40.0Å. This means that figures given in Table 3.3 for the FWHM have been transformed as:

$$\text{FWHM}_{\text{fit}} - \text{FWHM}_{\text{input}} = (\text{FWHM}_{\text{fit,real}} - \text{FWHM}_{\text{intrisic}}) \times 40.0/\text{FWHM}_{\text{intrisic}}$$

All results are given in Table 3.3 and some distributions of the fitted parameters, along with their Gaussian fit, are presented in Fig. 3.8 for $I_C/\text{RMS} = 3.0$; 5.0 and 10.0, as previously.

Specifically, we observe that the centroid of the fit is systematically blueshifted compared to the reference value, which is the wavelength of the maximum in the integrated spectrum of the galaxy (the explanation of how we construct this integrated spectrum is given in §4.2). This is something new, since we did not observe any systematic shift in the fitted central wavelength in the two previous sets of simulations. This

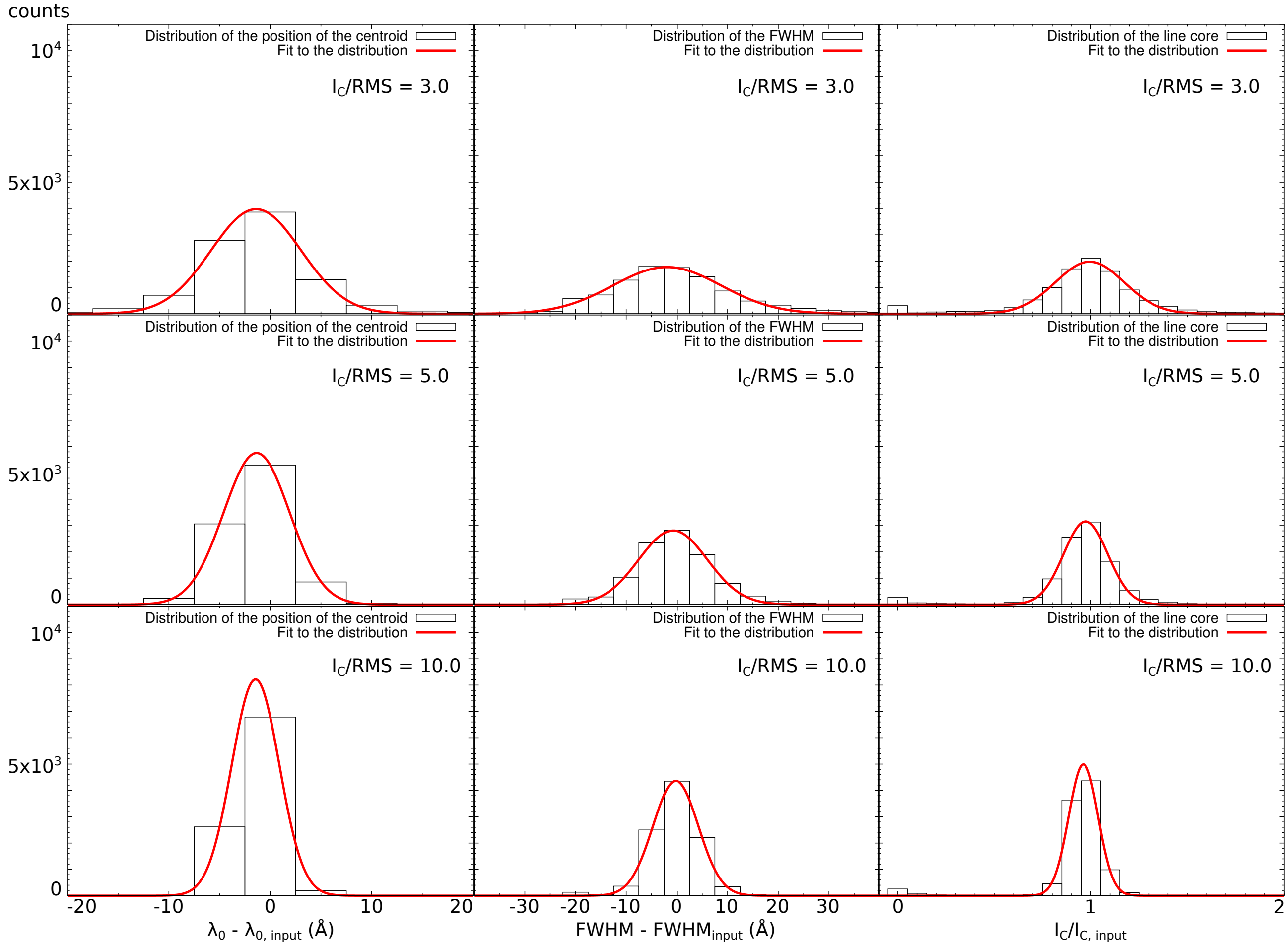

Figure 3.7: Distributions of the fitted parameters for the "Gaussian line + real H-noise" simulations: λ_0 (left), FWHM (middle) and I_C (right) for $I_C/\text{RMS} = 3.0$ (top) ; 5.0 (middle) and 10.0 (bottom). We fit these distributions with a Gaussian to characterize them.

effect can therefore be attributed to the use of real lines, which do not have a rigorously Gaussian profile. The main deviation from Gaussianity are the blue wings that some galaxies present (*e.g.*, NVSS J2342, see §4.3.4). The presence of a blue wing will indeed make the centroid of the fitted line lie at lower wavelength and can cause the systematic shift that we observe. The fact that this effect remains at high SNR confirms the explanation that the origin of this effect is in the profile of the line.

However, this effect, although not negligeable, is not very important: it is of ~ 1.5Å at all SNR, or $\sim$ 30 km s^{-1}. This is well within the uncertainties, which are slightly larger than in the two previous sets of simulations. Indeed, we find uncertainties of 6.2Å (or 130 km s^{-1}) at $I_C/\text{RMS} = 2.0$ and they decrease to 3.3Å (or 70 km s^{-1}) at $I_C/\text{RMS} = 5.0$. At very high SNR, they are down to values found before, *i.e.*, uncertainties of 1.3Å. Finally, a last note regarding the systematic blueshift: in our studies, we are more interested in the relative variations of the gas velocity, making the definition of the origin (*i.e.*, the redshift of the galaxy) not of crucial importance.

Regarding the velocity dispersion, we still observe a systematic under-estimation at low SNR, coherent with previous sets of simulations. This offset is strongly reduced at higher SNR and for $I_C/\text{RMS} \geq 5.0$, it is smaller than 0.7Å (or less than 15 km s^{-1}). The associated uncertainties are slightly larger than those found previously, from 15.0Å (or 300 km s^{-1}) at $I_C/\text{RMS} = 2.0$ to 6.8Å (or less than 150 km s^{-1}) at $I_C/\text{RMS} =$ 5.0.

It appears that the estimation of the line core is the other parameter affected by non-Gaussianities in

	I_C/RMS					
	2.0	3.0	4.0	5.0	10.0	50.0
$\lambda_{0,\text{fit}} - \lambda_{0,\text{input}}$ (Å)	-0.148	0.043	-0.008	0.005	0.034	-0.052
σ_{λ_0} (Å)	5.594	3.767	3.129	2.761	1.917	1.351
I_{λ_0}	3019	4680	5902	6866	9085	9750
$\text{FWHM}_\text{fit} - \text{FWHM}_\text{input}$ (Å)	-4.381	-1.688	-0.669	-0.410	0.036	-0.105
σ_FWHM (Å)	12.028	9.644	7.009	5.344	3.057	1.343
I_FWHM	1538	2005	2697	3492	6283	9808
$I_{C,\text{fit}}/I_{C,\text{input}}$	1.063	1.036	1.022	1.017	1.004	1.002
σ_{I_C}	0.262	0.168	0.131	0.104	0.059	0.034
I_{I_C}	1367	2132	2785	3518	6339	5794

Table 3.2: Results of the fits to the parameter distributions, with respect to the input I_C/RMS, for the "Gaussian line + real H-noise" set of simulations. $\lambda_{0,\text{fit}} - \lambda_{0,\text{input}}$ is the position of the centroid of the distribution of the parameter λ_0 of the fit (in Å), σ_{λ_0} its standart deviation (in Å) and I_{λ_0} its intensity. The same signification stands for the two others parameters, FWHM (for which results are also expressed in Å) and I_C (for which results are normalized to the input value).

the line profile: it is systematically lower than the observed maximum of the line, up to 5% at high SNR, while this parameter tended to be slightly over-estimated in previous sets of simulations. Indeed, if the fit tries to "catch" deviations in the line profile (*e.g.*, the blue wing) we can see that the line core will tend to be lowered. The uncertainty associated with the estimation of the line core remains comparable to the previous set of simulation and becomes lower than $\sim 10\%$ for $I_C/\text{RMS} \geq 5.0$.

	I_C/RMS					
	2.0	3.0	4.0	5.0	10.0	50.0
$\lambda_{0,\text{fit}} - \lambda_{0,\text{input}}$ (Å)	-1.491	-1.401	-1.403	-1.342	-1.452	-1.723
σ_{λ_0} (Å)	6.157	4.441	3.787	3.266	2.345	1.697
I_{λ_0}	2710	3973	4880	5756	8216	12830
$\text{FWHM}_\text{fit} - \text{FWHM}_\text{input}$ (Å)	-3.946	-1.944	-1.060	-0.747	-0.232	-0.456
σ_FWHM (Å)	15.111	10.681	8.290	6.789	4.484	3.264
I_FWHM	1266	1772	2295	2809	4363	6047
$I_{C,\text{fit}}/I_{C,\text{input}}$	1.018	0.994	0.981	0.973	0.961	0.953
σ_{I_C}	0.266	0.178	0.138	0.115	0.076	0.043
I_{I_C}	1325	1978	2597	3156	4988	9563

Table 3.3: Results of the fits to the parameter distributions, with respect to the input I_C/RMS, for the "real line + real $H-$noise" simulations. $\lambda_{0,\text{fit}} - \lambda_{0,\text{input}}$ is the position of the centroid of the distribution of the parameter λ_0 of the fit (in Å), σ_{λ_0} its standart deviation (in Å) and I_{λ_0} its intensity. The same signification stands for the two others parameters, FWHM (for which results are also expressed in Å) and I_C (for which results are 'normalized' to the input value).

To sum up, we find here slightly larger uncertainties than with the previous sets of simulations and this can largely be attributed to the non-Gaussiannities of real lines profiles, coming mainly from the relatively strong blue wings that are seen in some galaxies. However, the most striking impact of the non-Gaussian line profiles lies in systematic shifts of the fitted parameters: the estimated line core tends to be lower than the maximum of the line and the centroid of the line is blueshifted. These effects remain at high SNR, where the intrinsic profile of the line dominates, confirming this explanation.

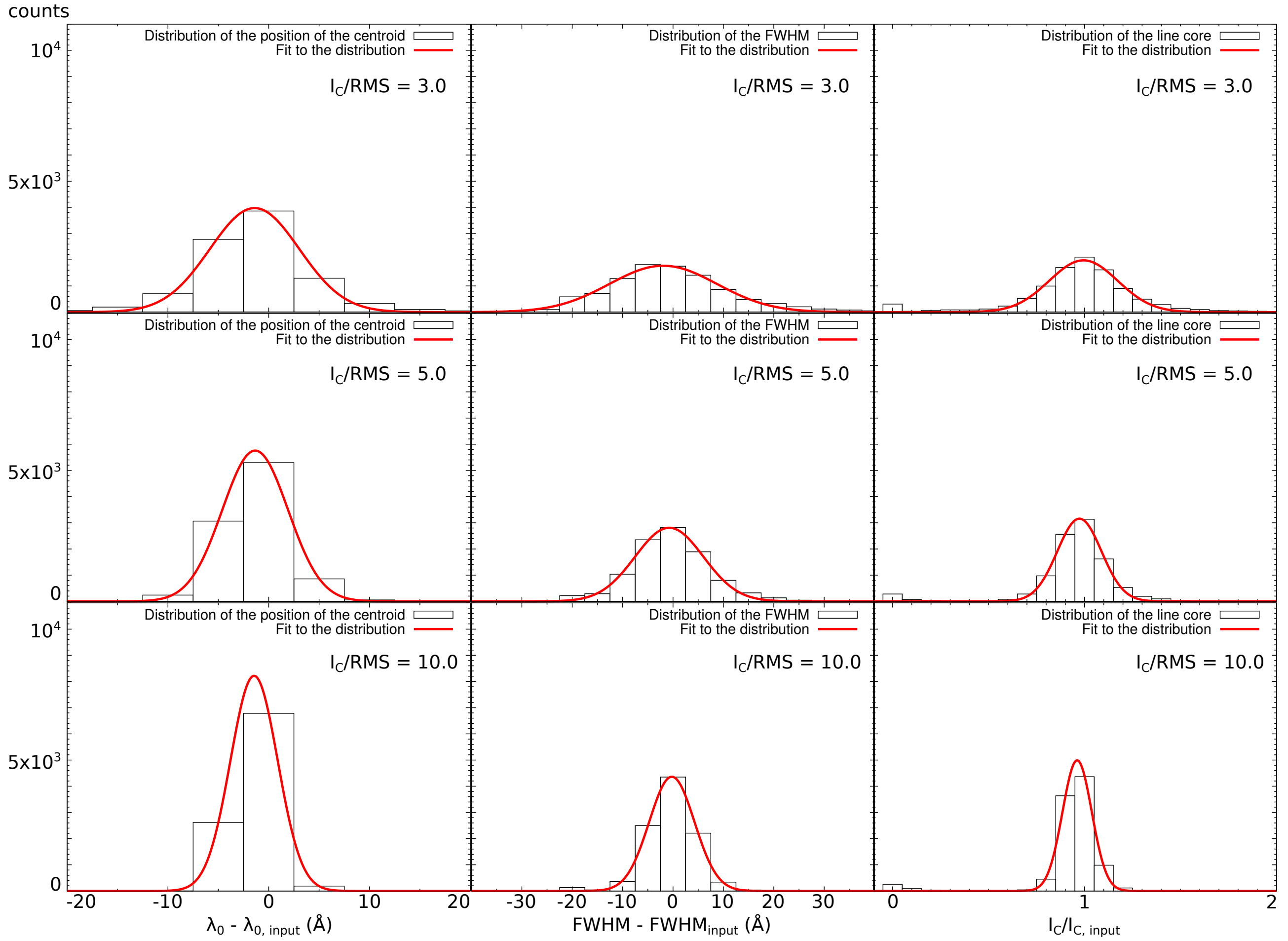

Figure 3.8: Distributions of the fitted parameters for the "real line and real $H-$noise" simulations: λ_0 (top), FWHM (middle) and I_C (bottom), for I_C/RMS = 3.0 (left) ; 5.0 (middle) and 10.0 (right). We fit these distributions with a Gaussian to characterize them.

As previously, a threshold at I_C/RMS = 5.0 appears as a reasonnable choice: some systematic effects (*e.g.*, regarding the estimation of the line width and of the line core) become negligeable at this signal-to-noise ratio. As illustrated by Fig. 3.9, uncertainties are also reduced to reasonnable values for I_C/RMS $\geq$ 5.0, in the sense that they become lower than typical values observed in our observations: they are $\lesssim$ 50 km s^{-1} for the line centroid, compared to velocity gradients of up to 800 km s^{-1} ; they are $\lesssim$ 150 km s^{-1} for the velocity dispersion, compared to typical values of 500 – 1000 km s^{-1} and they are $\lesssim$ 10% for the estimation of the line core, comparable to the uncertainty in flux calibration.

3.4 Analysis of the simulated cubes: Beam smearing effects

In the previous section, we estimated the signal-to-noise threshold that we should apply to our data in order to obtain unbiased fits to the emission found in our data, along with uncertainties small enough as to be able to obtain meaningful conclusions. Here we focus on the effects of beam-smearing, already anticipated on a theoritical basis in §3.1.2. We explained how the mixing of different spatial elements holding different spectral information would lead to an attenuation of velocity gradients and an increase of the observed velocity dispersions. This is now explored quantitativaly, based on simulated cubes in which the input velocity gradients and velocity dispersions are well known since we model the emission line by a Gaussian,

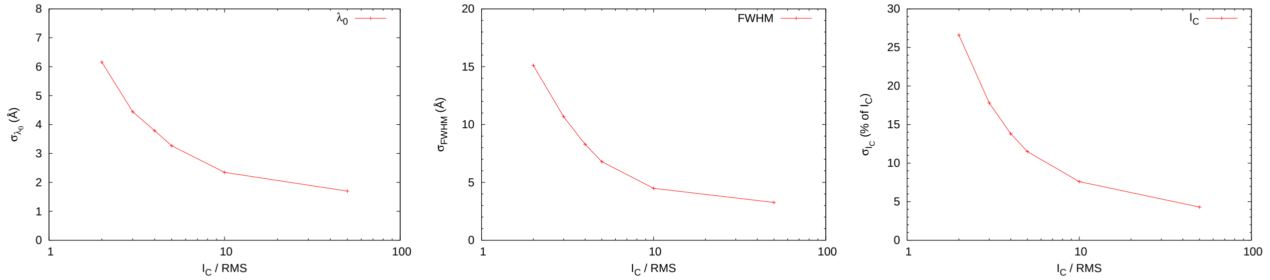

Figure 3.9: Evolution of the width of the distribution of the three fitted parameters as a function of the I_C/RMS parameter. *left:* evolution of the uncertainty on the position of the centroid λ_0 (in Å); *middle:* the same for the FWHM of the line (in Å) and *right:* the same for the line core, normalized to the value of I_C.

to which "real" noise is added, following the method presented in §3.2.3. The parameters of the simulations presented in this section are the following:

- $a = 5.0$ or 10.0, slightly changing the velocity field, from a smooth variation happening on $D \sim 60$ pixels to a more abrupt variation with $D \sim 30$ pixels (see Fig. 3.1).
- $b = 0.5$, we did not change the attenuation of the velocity field at the edge of the cube since this does not strongly impact the velocity field, compared to a. Moreover, the flux of the simulated galaxy is very low at the edge of the cube, where the effect of b is important, making it undetectable in most of our simulations.
- $V = 800$ km s^{-1}. We use only one value of large scale velocity gradients, representative of those observed in our real data.
- FWHM = 400 ; 800 or 1200 km s^{-1}. In order to investigate the effect of the ratio between bulk and turbulent motions, we produce simulations with velocity dispersions that have comparable, half value and half as much again value of the velocity gradient.
- $f = 0.2; 0.5; 0.8; 1.0; 1.2; 1.5$ and 2.0. We use many different relative sizes of the seeing disk compared to the galaxy in order to nearly continuously sample the effect of the seeing, which is the parameter that changes the most between our different observations.

3.4.1 Attenuation of velocity gradients

We first study how the effect of seeing attenuates the input velocity gradient, with simulated cubes that have $a = 5; 10$ and FWHM = 800 km s^{-1}. So only the relative size of the seeing disk varies significantly, from very good seeing, with $f = 0.2$, to very poor seeing with $f = 2.0$, *i.e.*, a seeing disk twice as large as the intrinsic size of the galaxy. The results are presented in Fig. 3.10 and Fig. 3.11.

Fig. 3.10 present the results as a velocity curve seen along a cut through the central horizontal axis. Indeed, as explained in §3.2.1, the velocity field varies only along the $x-$axis, meaning that we do not need both spatial coordinates to study the effect of the seeing on the input velocity field. This effect is obvious in Fig. 3.10: the input velocity curve is given by the black solid line while the results of our analysis tool are given by the different dotted lines, with a threshold at $I_C/\mathrm{RMS} = 5.0$. As explained in §3.2.4, the size of the observed galaxy is larger as the seeing disk becomes larger. This translates into a larger region over which the simulated galaxy can be detected, given in Fig. 3.10 by the arrows at the bottom, which color corresponds to the different PSF sizes simulated.

The green '+'-dotted line stands for the very good seeing simulation and the results follow nicely the input velocity curve, over a slightly less extended region than what is allowed by theory. The blue square-dotted line gives the results for the simulation in which the PSF is as large as the intrinsic size of the galaxy.

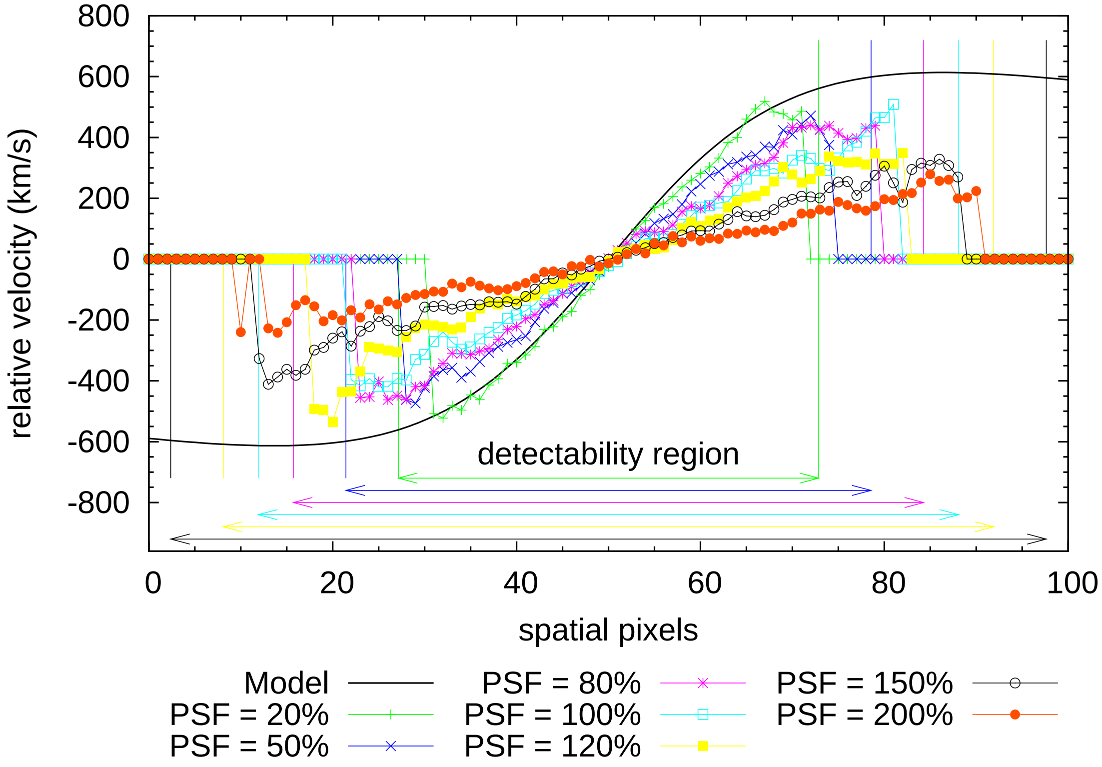

Figure 3.10: Results of the routine on cubes simulated with different PSF. The ratio f of the width of the PSF wrt the width of the 2D Gaussian shape of the flux is given as a percentage below the graph for the different curves. Since the convolution makes the flux spreads over a larger region, a “detectability region” is given for each simulation by the arrows and the two vertical lines (of the same color as the corresponding curve). The input parameters of the simulated cubes are: $a = 5.0$, $b = 0.5$, $V = 800$ km s^{-1} and FWHM $=$ 800 km s^{-1}.

While the shape of the velocity curve is still recovered, the intensity of the velocity gradient is reduced by 30%: from an input variation going from ~ -600 km s^{-1} to $+600$ km s^{-1}, the observed galaxy shows variations from ~ -400 km s^{-1} to $+400$ km s^{-1}. The relative extent over which the simulated galaxy is detected (compared to the theoritical detectability region) is also slightly reduced compared to the good seeing simulation. The very poor seeing simulation, with $f = 2.0$ and traced by the red circle-dotted line, sees its observed velocity gradient dramatically attenuated, by more than 60%: it goes from ~ -200 km s^{-1} to $+200$ km s^{-1}, while the input velicity curve spans the ~ -600 to $+600$ km s^{-1} range.

The right-hand side of Fig. 3.11 presents the same effect of attenuation of the observed velocity gradient compared to the input velocity curve, but using here 2-dimensional maps instead of curves across a predefined axis of the observed galaxy. Here the velocity is coded by the color and the full spatial information is present. Note that these results are obtained from simulations with slightly different parameters, since we use $a = 10.0$ (instead of $a = 5.0$ previously), *i.e.*, the velocity overturn happens on a smaller scale, as illustrated by Fig. 3.1.

The sharp velocity gradient is well recovered in the case of a good seeing simulation ($f = 20\%$) and the flux detected by the analysis routine is as extended as it can theoritically be, which is illustrated by the solid line circle. Moreover, the shape of the input velocity field is also well recovered, since both the central small scale overturn and the velocity plateau at the edge of the simulated galaxy are visible. When the size of the seeing disk becomes comparable to the intrinsic size of the simulated galaxy (*e.g.*, $f = 80\%$ or $f =$ 120%), the velocity gradient is strongly attenuated, the sharp overturn that happens over the central 2$-$3$''$

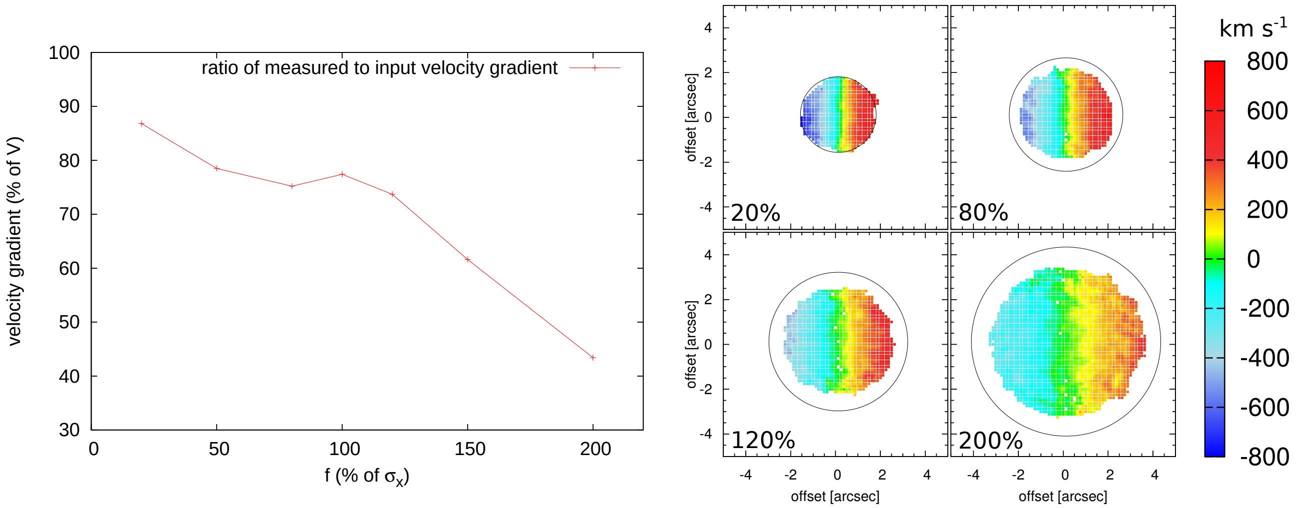

Figure 3.11: *Left*: Ratio of the measured maximum velocity offset to the input velocity gradient V as a function of the width of the seeing disk. The input parameters of the simulated cubes are: $a = 5.0$, $b = 0.5$, $V = 800$ km s^{-1} and FWHM $= 800$ km s^{-1}. *Right*: Results of the routine on cubes simulated with different PSF. The ratio f of the width of the PSF wrt the width of the 2D Gaussian shape of the flux is given as a percentage on each map. Since the convolution makes the flux spread over a larger region, a "detectability region" is given for each simulation by the circle. The input parameters of the simulated cubes are: $a = 10.0$, $b = 0.5$, $V = 800$ km s^{-1} and FWHM $= 800$ km s^{-1}.

of the model galaxy is diluted over the whole extent of the detected emission line region and the region where the simulated galaxy becomes smaller than what is theoritically possible. In the case of a very poor seeing simulation ($f = 200\%$), these effects are even more important: the observed velocity gradient that is only $\sim 1/3$ of the input value, the central details of the velocity field are completely washed out by the beam smearing and the size of the detected emission line region, although the largest of this set of simulation as explained in §3.2.4, is not as large as it could theoritically be.

The left-hand side of Fig. 3.11 summarizes one of the three effects of the seeing on the velocity field that we discussed previously. It presents the variation of the of the ratio of the measured maximum velocity offset to the input value as a function of the relative size of the seeing disk compared to the intrinsic size of the galaxy. The trend observed in the previous simulations appears here clearly: when the seeing disk is small compared to the intrinsic size of the galaxy ($f = 20\%$), the observed velocity field is very similar to the real one and the measured velocity offset is close to the input value (90% of it). Then, with the seeing disk roughly as large as the intrinsic size of the galaxy ($f = 80$, 100, 120%), this ratio plateaus around 75−80% of the input value, although the small scale variations are strongly diluted by the beam smearing. This ratio strongly decreases in case of very poor seeing (or intrinsically very small emission line region), reaching only half of the input value for $f = 200\%$.

3.4.2 Effects of beam smearing on velocity dispersions

In the previous section, we studied the effect of the seeing on the observed bulk motions, here we focus on the effects of the beam smearing on the velocity dispersion. We already showed that we could expect an increase of the velocity dispersion where the velocity field changes on scales similar to the size of the seeing disk. We discussed this effect in §3.2.2 and it is well illustrated by Fig. 3.2, which presents the spectrum of the simulated galaxy, integrated over the 5×5 central pixels, at the different steps of the creation of the simulated galaxy. The convolution process implies the leakage of the spectral information of the spatially surrounding regions into the central region causes the broadening and the attenuation of the line, especially in this case, where a quite large seeing disk ($f = 1.0$) is used.

The right-hand side of Fig. 3.12, we present the results regarding the observed velocity dispersion in simulations having the same parameters as previously: $a = 10.0$, $b = 0.5$, $V = 800$ km s^{-1}, FWHM $=$ 800 km s^{-1} and $f = 0.2; 0.5; 0.8; 1.0; 1.2; 1.5$ and 2.0. In the case of very good seeing ($f = 20\%$, *i.e.*, a seeing disk smaller than the scale of spatial variations of the velocity field), the observed velocity dispersion is equal to the input value, within the uncertainties estimated in the previous section. In particular, in the central region, the phenomenon of leakage explained in the previous paragraph happens on scales small enough that the observed velocity field does not significantly differ from the input model.

However, in cases of seeing disks comparable to the intrinsic size of the emission line region ($f = 0.8; 1.0$ or 1.2, *i.e.*, seeing disks with a size also comparable to the spatial scale of the velocity overturn) this effect of line broadening appears clearly. In the two examples of this kind given in Fig. 3.12 (top right and bottom left maps), there is a central vertical[4] region where we systematically measure a velocity dispersion of FWHM $\gtrsim$ 1000km s^{-1}, larger than the input value (FWHM$_{\text{input}}$ = 800 km s^{-1}). At larger radii, where the velocity field reaches a plateau, the measured velocity dispersion is back, within the uncertainties, to the input value. This is especially visible in the $f = 80\%$ simulation.

When the relative size of the seeing disk to the intrinsic size of the emission line region is too large (*e.g.*, $f = 200\%$), the leakage of the central information spreads over the whole extent of the observed emission line region, leading to observed velocity dispersions larger than the input value everywhere, and not only in the central regions as it is the case when smaller seeing disks are used for the simulation.

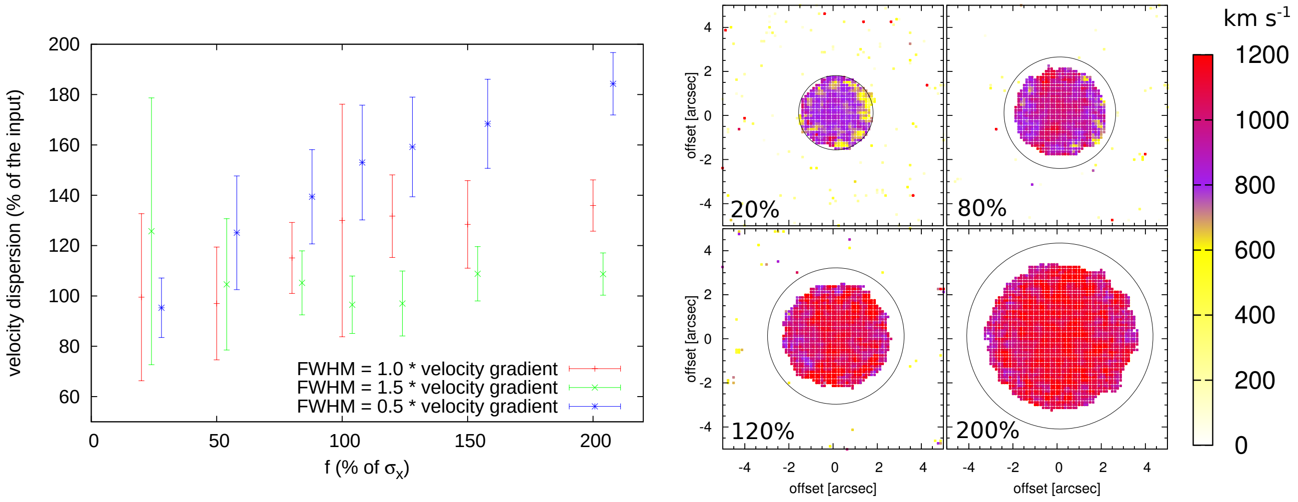

Figure 3.12: *Left*: Ratio of the mean measured velocity dispersion to the input velocity dispersion (which is the same in all spaxels) as a function of the width of the seeing disk. The error bars correspond to the RMS of the measured velocity dispersion accross the cube. All simulations are run with the same values of f, blue and green points are slightly shifted to the right only for readibility reasons. *Right*: Results of the routine on cubes simulated with different PSF. The ratio f of the width of the PSF wrt the width of the 2D Gaussian shape of the flux is given as a percentage on each map. Since the convolution makes the flux spreads over a larger region, a "detectability region" is given for each simulation by the circle. The input parameters of the simulated cubes are: $a = 10.0$, $b = 0.5$, $V = 800$ km s^{-1} and FWHM $= 800$ km s^{-1}.

The observed velocity dispersion can be influenced by another parameter that we have not studied yet: the relative importance of bulk-to-random motions of the gas. Observationally, these translate in the position of the centroid of the emission line (discussed in the previous section) and in the width of the line (discussed here), respectively. Indeed, if the velocity field varies more — or, equivalently, if the velocity dispersion is intrinsically smaller — on scales smaller or comparable to the seeing disk, then the leakage

---

[4] we remind that the velocity field does not vary along the $y-$axis.

effect is also sprectrally more dramatic. Conversely, if the velocity dispersion is large compared to the large scales velocity gradient, or if the size of the seeing disk is small compared to the typical scale over which the velocity field changes, then the effect of leakage on the observed line width is reduced.

The influence of this ratio is presented on the left-hand side of Fig. 3.12. For each value of the parameter f (from 0.2 to 2.0, all the other parameters are the same as before), we present the results of 3 simulations with different ratios of bulk-to-random motions: one in which the velocity dispersion is equal to the velocity gradient (FWHM = V = 800 km s^{-1}, called "simulation 1" and represented by the red '+'-shaped points), one in which it is half as much again as the velocity gradient (FWHM = $1.5 \times V$, called "simulation 2" and represented by the green '×'-shaped points) and one in which it is half as much as the velocity gradient (FWHM = $0.5 \times V$, called "simulation 3" and represented by the blue star-shaped points). The error bar associated with each point represents the dispersion in the measured velocity dispersion over the whole detected emission line region.

When the seeing disk is smaller than the spatial scale of the changes in the velocity field (*i.e.*, f = 20%), the observed velocity dispersion agrees with the input value. This is especially true for simulation 2 (with the lowest value of velocity dispersion), while the results for simulation 1 (with FWHM = V) shows larger error bars and those associated with simulation 3 (with FWHM = $1.5 \times V$) are even larger. This increase of the scatter of the measured velocity dispersion with the ratio of the bulk-to-random velocities can be understood since there is a larger power in the leakage, at a given wavelength (*i.e.*, at a given relative velocity), as the line gets broader.

When the seeing disk is comparable or greater than the spatial scale of the changes in the velocity field, the effects of the leakage of spectral information from the surrounding spaxels on to the observed one are important. However, if the velocity dispersion is large compared to the velocity gradient, flux is added to relative velocities that were already at a non-zero level. The theoritical net effect is a small increase in the measured velocity dispersion, as it is actually observed for large values of f (the right part of the left-hand side of Fig. 3.12) and low ratio of bulk-to-random velocities (green '×'-shaped points).

These effects explain why we observe that the measured velocity dispersion of simulation 3 (with FWHM = $1.5 \times V$) agrees with the input value for all values of seeing ; while the velocity dispersion measured in simulation 2 (with FWHM = $0.5 \times V$, traced by blue star-shaped points) increases with f, as more and more flux from neighbouring lines, having a different relative velocity, enters the line before we measure it, making it appearing broader. The situation of simulation 1 is intermediate, since velocity dispersions measured from this simulation agree with the input value up to intermediate value of $f \lesssim 120\%$. But for larger values of seeing, the leakage of flux leads to measured velocity dispersions larger than the input value.

3.4.3 Correcting the results derived from real observations

We have shown that the effect of seeing could be dramatic on the measured velocity gradients and velocity dispersions, compared to the intrinsic properties of the observed galaxy. The question is then: can the simulations that we created allow us to recover the real properties of our observations?

To answer this question, let's first take a step back and examine some assumptions that we used in our simulations, which, as with any modelling, are a simplification of reality.

- The shape of the PSF is assumed Gaussian: Although this is not rigorously exact in reality (*e.g.*, the PSF of SINFONI is not axisymetric), the main effects of the convolution proccess are grasped in our simulations, meaning that this assumption is adequate given the effects that we want to study.

- The noise used in our simulations: it can be Gaussian or coming from real observations. The set of simulations using Gaussian noise was mainly used to test the routines creating the simulated datacubes and as a benchmark against which we could compare simulations using more realistic noise. All of the simulations presented in this section were made with real noise, making this point as correct as possible.

- The simulated galaxies all have the same Gaussian surface brightness profile and the same kind of velocity field, and this is the main caveat of our simulations. Indeed, even if we changed the ratio of the intrinsic size of the galaxy compared to the size of the seeing disk (the f parameter) and if we tuned the velocity field through the a and b parameters, as well as varying the ratio of bulk-to-random motions, all the simulated galaxies are still quite similar to one another. Assuming that we can use them to deconvolve our observations implies that real galaxies are similar enough to our simulated objects. But the diversity of observed emission line regions, with their complex kinematics, especially those observable at high spatial resolutions, found around nearby active galaxies (*e.g.*, Fu & Stockton, 2009), strongly argues against such an assumption.

These simulations had many purposes: the first one (see section 3.3) was to estimate and justify the SNR threshold used in our routines, along with determining the uncertainties associated with the parameters of the fit at a given SNR. Also, we use these simulations to explore the effects of the beam-smearing, where the intrinsic properties of the galaxy (*e.g.*, the shape of its extended emission line region or its velocity field) are important. Therefore, an exact deconvolution of each observed galaxy and the recovery of its intrinsic parameters is beyond the scope of these simulations and of the present work. However, the results given previously will be important to mitigate our interpretations, depending on the relative size of the seeing disk and of the observed extended emission line regions.

Chapter 4

AGN feedback in high-redshift radio galaxies

Contents

This study will be submitted to A&A as Collet, Nesvadba, Lehnert, De Breuck et al. (2014a): Integral-field spectroscopy of moderately powerful radio galaxies at $z \geq 2$.

4.1 Motivation

As already discussed in the Introduction 1, one of the main open questions regarding the role of radio jets in regulating star formation in massive high-redshift galaxies, is whether or not jets with fairly moderate radio power are able to accelerate and heat the gas in their host galaxies. The most natural way to assess this is by studying samples of galaxies with more moderate radio power than those where signatures of AGN-driven winds have already been found, while employing similar observational techniques.

Namely, in this work, we focus on galaxies with radio powers of-order 10^{27-28} W Hz^{-1} (at 500 MHz in the rest-frame). They come from two different surveys, namely the Southern sample of distant radio galaxies of Broderick et al. (2007) and Bryant et al. (2009a,b) which we will refer to as the "NVSS sample" hereafter ; and the sample of radio galaxies within the EIS fields (ESO imaging survey) by Best et al. (2003a) and Brookes et al. (2006, 2008), the "CENSORS" sample. The main difference between the two is in the radio power, which is about an order of magnitude fainter for the CENSORS sources than the NVSS sources. Overall, these two samples straddle the range of radio powers that is intermediate between the most powerful radio galaxies studied previously, and the observed radio power found in the most intensely star-forming galaxies (of-order 10^{25} W Hz^{-1}). They allow thus to extrapolate from the most outstanding sources to ordinary, rapidly growing, high-redshift galaxies, while showing observationally very clear evidence for the presence of a radio-loud AGN. In high-redshift sources where the radio power can be explained by star formation, it is often entirely attributed to star formation, although distinguishing between centimeter emission from star forming regions and typical, steep-spectrum AGN at high redshift is not trivial to do in detail. By probing sources with this range in radio power, we also ensure that the energy output from the jet exceeds that from other processes, which should aid in producing signatures that can be uniquely identified even under the relatively severe limits imposed by observing galaxies in the distant Universe.

In this Chapter, we will present our analysis method, before dicussing the properties of individual galaxies, the overall properties of the sample, and the conclusions we can draw from this study for AGN feedback at high redshift.

4.2 Presentation of our analysis tools

For each galaxy we present integrated spectra (Fig. 4.5 and Table 4.3) and emission-line maps of the [OIII] surface brightness, relative velocities, and velocity dispersion (Fig. 4.6). Maps are only given for pixels where the signal-to-noise ratio of the line core exceeds 5. We used a Monte Carlo method to confirm that this was a good value to robustly measure the line properties (see Chapter 3), in spite of strong non-Gaussianities in the noise related to the imperfect night-sky line subtraction and bad pixels. Moreover, when fitting a line, we assess weights to spectral pixels depending on the presence and strength of night sky lines at this wavelength, as illustrated by Fig. 4.1.

Integrated spectra include all pixels where [OIII] is detected at a significant level. Before adding the spectrum of a pixel, we shift it to the systemic redshift in order to avoid artificial broadening of the line in the integrated spectrum by the large scale velocity gradient. We adopt the redshift estimated from the brightest pixels near the center of the galaxy as systemic (these are given in Table 4.3).

For each galaxy we also mapped the surface brightness, relative velocity to the systemic redshift and the velocity dispersion of [OIII] (Fig. 4.6) by fitting Gaussian profiles to the lines extracted from small apertures across the cube. Sizes are 3 pixels×3 pixels, corresponding to $0.4'' \times 0.4''$, or 5 pixels×5 pixels for the faintest regions of the cube. This helps improving the signal-to-noise ratio of the data, but still oversamples the seeing disk to avoid loss of spatial information. Contours on Fig. 4.6 show the line-free continuum emission for the galaxies where the continuum was detected. To measure the continuum, we mask all emission lines and the strongest night sky lines in the cube and interpolate the flux over these gaps. By doing this for all spatial pixels, we obtain continuum maps, that are shown as contours in Fig. 4.6.

We detect relatively bright continuum emission in NVSS J0024 and NVSS J2019, which we need to remove from the spectra before fitting the emission lines. To perform this subtraction, we mask strong

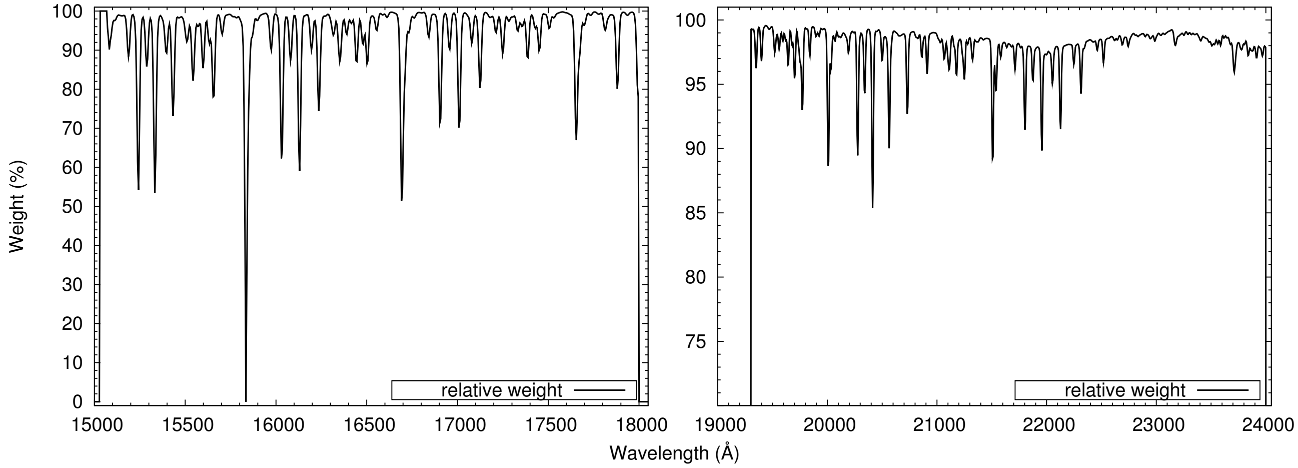

Figure 4.1: Relative weight given to spectral pixels when fitting an emission line a our datacubes, as a function of wavelength, depending on the presence and strength of night sky lines. $H-$band is given on the *left* and $K-$band is on the *right* (note the reduced scale for the $K-$band, since night sky lines are less intense there than in the $H-$band).

emission lines and strong night sky line residuals and fit a low-order polynomial over their whole spectrum, that we subtract afterwards. The other sources have only faint continuum emission which does not affect our line fits.

4.3 NVSS sample

4.3.1 Target selection

We selected our targets from the sample of 234 distant radio galaxies of Broderick et al. (2007) and Bryant et al. (2009a,b), following the pilot study of De Breuck et al. (2004, 2006). These sources have steep radio spectral indices $\alpha_{408-843} \leq -1.0$ between 408 MHz and 843 MHz, and fluxes at 408 MHz $S_{408} \geq 200$ mJy. From this catalogue, we selected 12 moderately low-power sources at z ≥ 2 with $P_{1.4\mathrm{GHz}} = \mathrm{few}\times 10^{27}$ W Hz^{-1}. They have sizes between $\sim 2''$ and $24''$, a typical range of radio sizes of powerful HzRGs, so that we suspect that the main biases in our sample selection are likely from requiring bright UV emission lines to obtain spectroscopic redshifts. Table 4.2 lists the radio properties of our targets. For the sake of simplicity, we will in the following truncate all source names after the 4^{th} digit. The full names of our targets are listed in Table 4.3. We will in the following describe our observations and data reduction in the cm radio and with near-infrared imaging spectroscopy, respectively.

4.3.2 Radio continuum observations

We also observed our sources with the Australian Telescope Compact Array (ATCA, project code: C2604 — PI: Nesvadba) at 5.5 GHz and 9.0 GHz (or wavelengths of 6 and 3 cm) in order to have observations at high enough spatial resolution, that can be compared with our SINFONI data.

The observation log is given in Table 4.1 and lists the date of observation, the total on source integration time and the secondary calibrator used for each source. The ATCA was in the 6A configuration (baselines from 337 m to 5939 m) during this period. During the run of 2012 January 28, we obtained for each source 13 snapshots of 5 min, spread over 8.5 hours in order to get a good $(u, v)-$coverage. During the run of 2012 Feb. 2, we obtained 14 snapshots of 5 min per source during 8.5 hours, except for NVSS J1449 which set earlier and for which we only had 5 snapshots taken over a little more than 3 hours. We used PKS B1934-638

Table 4.1: ATCA observing log for the NVSS sample.

Source ID	Date	TOT [1] [min]	Secondary Cal. [2]	beam (5.5 GHz) [arcsec×arcsec, deg.]	beam (9.0 GHz) [arcsec×arcsec, deg.]
NVSS J0024	28 Jan. 2012	65	2357-318	4.5×1.4, −0.1	2.9×0.9, −0.2
NVSS J0040	28 Jan. 2012	65	2357-318	4.5×1.4, −1.1	2.8×0.9, −1.3
NVSS J0129	28 Jan. 2012	65	0104-408	3.6×1.5, −6.4	2.3×0.9, −6.0
NVSS J0304	28 Jan. 2012	65	j0330-4014	4.2×1.6, −20.5	2.7×1.0, −18.5
NVSS J1449	02 Feb. 2012	25[3]	1458-391	6.3×1.5, −41.7	...
NVSS J2019	02 Feb. 2012	70	2054-377	3.9×1.5, 14.0	2.6×0.9, 13.2
NVSS J2046	02 Feb. 2012	70	2054-377	4.3×1.4, 10.0	2.8×0.9, 10.0
NVSS J2106	02 Feb. 2012	70	2054-377	4.5×1.4, −7.4	3.0×0.9, −8.0
NVSS J2342	28 Jan. 2012	65	2329-384	3.7×1.5, 3.4	2.3×0.9, 3.6

(1): Total on source integration time (in minutes). — (2): Secondary calibrator used. — (3): NVSS J1449 set before the end, hence the lower integration time and a poorer $uv-$coverage.

as bandpass and flux calibrator, which we observed at the beginning and the end of each session. These observations were done under bad wheather conditions, explaining the numerous noise features present in maps and the relatively large error bars of the derived fluxes.

The data reduction was done with Miriad (Sault et al., 1995), following the procedure presented in Chapter 2. This leads to typical beam sizes of $4'' \times 1.5''$ at 5.5 GHz and $2.5'' \times 0.9''$, with position angles between -6° and 13° (except for NVSS J1449, where PA = -40°). Details are given in Table 4.1.

In general, these observations confirm previous ones at 1.4 GHz and 2.8 GHz, *i.e.*, we confirm the morphology of previously already resolved sources and we put tighter upper limits on the spatial extension of compact sources. They are presented in Fig. 4.2. Only for NVSS J0024 we detect a second component to the Southwest of the main radio emission, this emission being too faint and below the detection threshold of previous observations ; and for NVSS J2342 we tentatively detect a radio core that is coincident with the galaxy. All other sources present very similar morphologies at 5.5 GHz and 9.0 GHz than at lower frequencies. All of our morphological measurements are given in Table 4.2: the largest angular scale (LAS) gives the separation between the two lobes, if the source is resolved, or the deconvolved size[1], if the source appears compact. The position angle (PA) traces the direction given by the two lobes of resolved sources, measured from North to East.

The measured fluxes at 5.5 GHz ($S_{5.5}$) and at 9.0 GHz ($S_{9.0}$), given in Table 4.2, extend nicely the radio spectral energy distribution towards higher frequencies. The radio SED is well fitted by power law with a steep index ($\alpha \simeq -1$, where $S_\nu = \nu^\alpha$), as illustrated by Fig. 4.3. From the fit to this SED, we extrapolate the flux of each source at 500 MHz restframe. Indeed, we use the 500 MHz restframe luminosity $\mathcal{L}_{500\mathrm{MHz}}$ of radiogalaxies to classify them according to their radio jet power.

4.3.3 IR imaging-spectrometry observations

Observations and data reduction

We observed these galaxies with the near-infrared imaging spectrograph SINFONI (Eisenhauer et al., 2003) between late 2009 and early 2010 in Service Mode (program ID 084.A-0324, PI De Breuck) at the Very Large Telescope of ESO under variable conditions. SINFONI is extensively described in Chapter 2, so we only briefly state the most important features of this instrument here. It is an image slicer which operates between 1.1 and 2.4μm. We used the seeing-limited mode with the largest available field of view of $8'' \times 8''$

---

[1] assuming that what is observed is the result of the convolution of two Gaussians: $\sigma^2_{\mathrm{obs}} = \sigma^2_{\mathrm{intrinsic}} + \sigma^2_{\mathrm{beam}}$

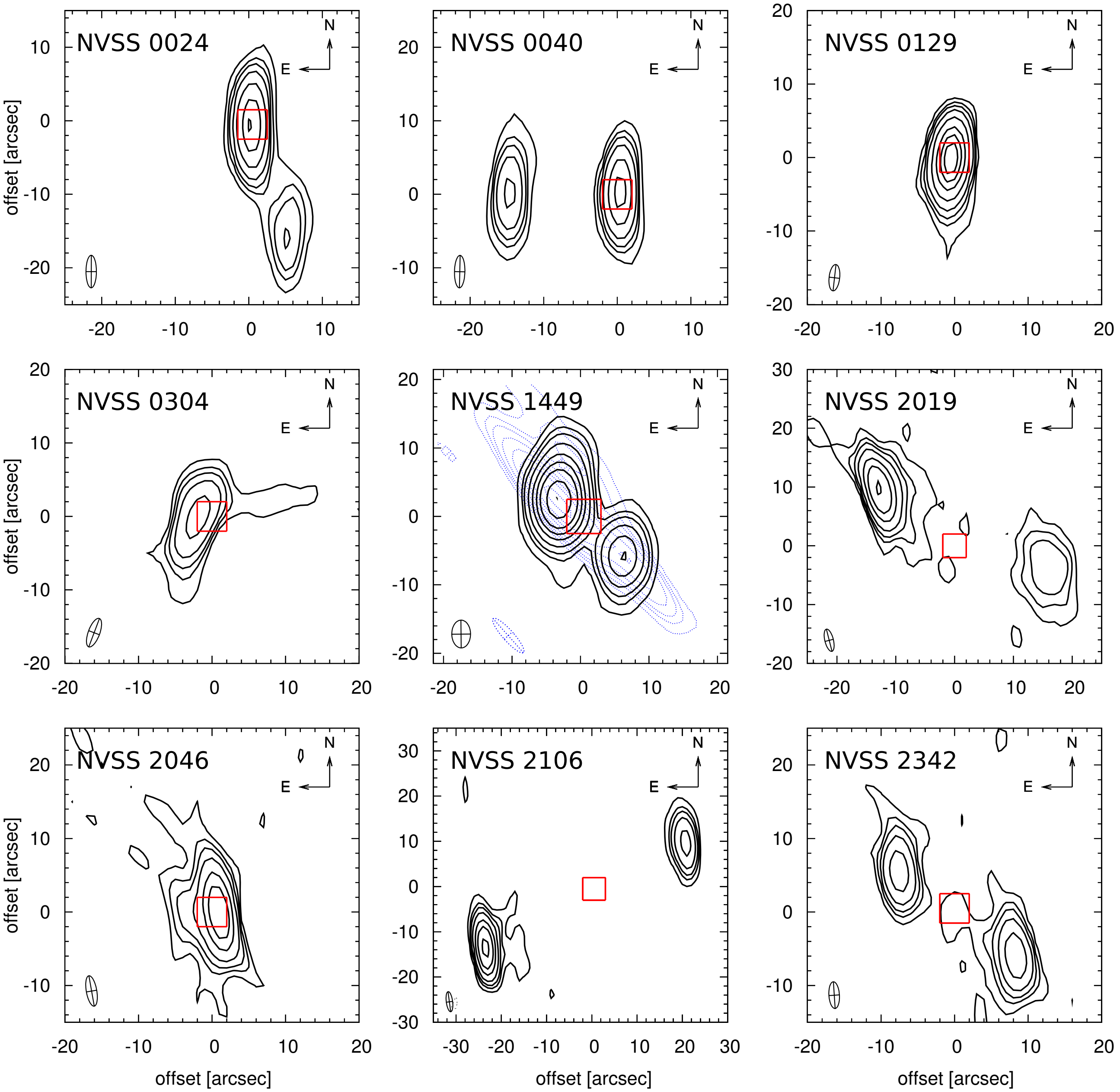

Figure 4.2: Radio morphologies at 5.5 GHz of the NVSS sample. The size and orientation of the restored beam is given in the bottom left of each panel. The red box indicates the size and location of the SINFONI maps presented in Fig. 4.5. For NVSS J1449, given the short observation time of this source and hence the deformed beam, we also present its 4.8 GHz observations from Bryant et al. (2009a), who observed a part of their sample at 4.8 GHz and 8.64 GHz. The contours are at levels (3, 6, 9, 15, 30, 50, 90)$\times\sigma$, where σ is the RMS level of each observation.

and a pixel scale of 250 mas. All data were taken with the $H + K$ grating which covers wavelengths between 1.45 μm and 2.4 μm at a spectral resolving power R $\sim$ 1500 ($\sim$ 200 km s^{-1}). We observed each galaxy for 180$-$230 min of on-source observing time, split into individual observations of 5 min length. Most of our galaxies are smaller than the field of view. We therefore adopted a dither pattern where the object is shifted between two opposite corners of the field of view, which allows us to use two subsequent frames for the sky subtraction and makes taking dedicated sky frames unnecessary. The spatial resolution of our data

Table 4.2: Results from the ATCA observations of the NVSS sample.

Source ID	$S_{5.5}$ [mJy]	$S_{9.0}$ [mJy]	LAS$^{(1)}$ [arcsec]	PA$^{(2)}$ [deg.]	$P_{500,rest}$ $^{(3)}$ [10^{28} W Hz^{-1}]	$P_{1.4}$ $^{(4)}$ [10^{27} W Hz^{-1}]
NVSS J0024	21.1	11.1	7.7 (7.7)	18.2 (19.0)	2.2	2.9
NVSS J0040	10.0	3.4	7.5 (7.2)	91.1 (89.1)	15.3	6.0
NVSS J0129	29.2	14.3	0.9 ; 0.7 (1.4)	… (3.1)	3.2	3.9
NVSS J0304	13.4	5.9	2.6 ; 1.8 (2.4)	… (27.4)	3.3	2.4
NVSS J1449	…	…	6.7 (6.8)	58.3 (48.0)	2.5	2.6
NVSS J2019	11.7	10.2	15.7 (14.7)	64.6 (63.6)	2.3	1.9
NVSS J2046	9.8	9.1	2.0 ; 1.8 (1.6)	… (-6.0)	3.3	3.0
NVSS J2106	19.8	22.4	25.0 (24.2)	97.6 (-62.4)	3.7	4.1
NVSS J2342	6.0	2.2	9.8 (9.4)	54.3 (55.3)	15.3	4.6

(1): Largest angular scale, corresponding to the separation between the two lobes, when detected, or to the deconvolved size, if the source appears compact. In this case, both deconvolved sizes at 5.5 and 9.0 GHz are given. We give previous measurements of Broderick et al. (2007); Bryant et al. (2009a) in brackets for comparison. — (2): Position angle of the source, measured from North to East, when two lobes are detected. — (3): Radio power at 500 MHz restframe (extrapolated from the radio spectrum of the sources). — (4): Radio power at 1400 MHz (observed).

is limited by the size of the seeing disk, which is typically around $1.0''$. The FWHM sizes of the PSFs of individual targets are given in Table 4.3. They are measured from a standard star observed at the end of each hour of data taking.

Data are dark-subtracted and flat-fielded. We then remove the curvature from the spectra in each slit and put them onto a common scale by using the bright night-sky lines superimposed on each frame, using arc lamp spectra only to set the absolute wavelength scale. We then sky subtract our data and rearrange them into three-dimensional data cubes, which are then combined. To account for the variability of the night sky we scale the total flux in each sky frame to the total flux in each object frame, after masking the target. We use the standard star observations to correct for telluric and instrumental effects, and to set the absolute flux scale.

In this analysis, we discuss the optical emission-line properties of 9 of the 12 galaxies we observed. Two of the other three, NVSS J004136-345046 and NVSS J103615-321659 have continuum, but no line emission at the redshifts previously measured in the rest-frame UV. NVSS J233034-330009 was identified as a star after our data were taken (Bryant et al., 2009b).

Relative alignment of the radio and SINFONI data

Studying the effects of the radio jet on the interstellar medium of high-redshift galaxies requires an accurate relative alignment between the radio and near-infrared data sets to better than an arcsecond, *i.e.*, better than the absolute astrometry of the VLT. Unfortunately, we did not detect the radio core of most of our galaxies with extended radio lobes. Moreover, owing to the small field of view of SINFONI, aligning our data cubes with the WCS is not trivial. We therefore register our cubes relative to the $K-$band imaging of Bryant et al. (2009a), which is well aligned with the WCS, and assume that the radio frame of the ATCA alignes well with the WCS, to better than $1''$ (Broderick et al., 2007). For compact radio sources (LAS $\lesssim 2.0''$ in Table 4.2), we assume that the $K-$band continuum is aligned with the radio source, corresponding to the assumption that the radio emission in compact sources originates from the galactic nucleus. The red box in each panel of Fig. 4.2, presenting the radio morphologies of the NVSS sample, gives the position of the SINFONI maps derived using this method.

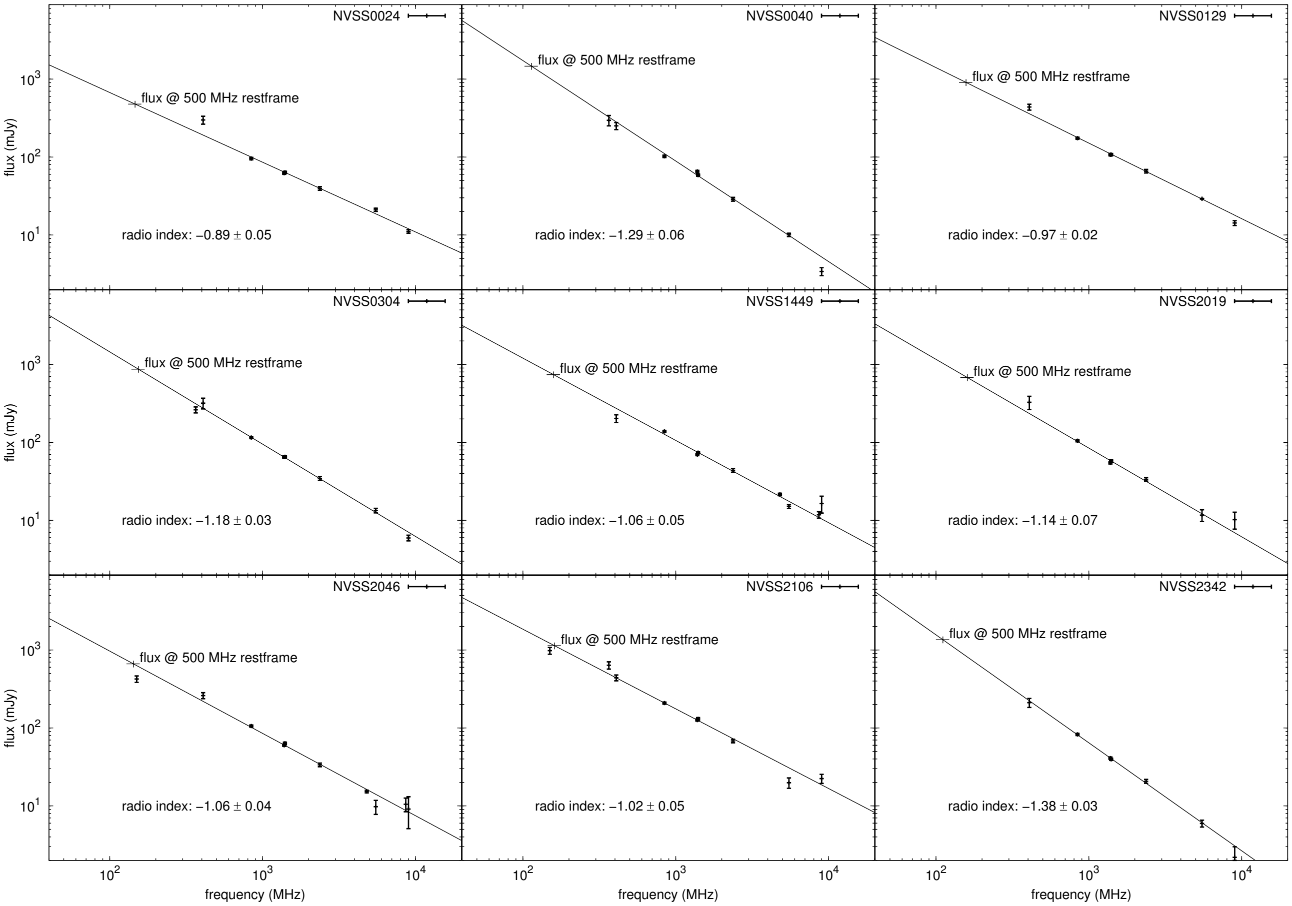

Figure 4.3: Spectral energy distribution in the radio for the 9 galaxies of the NVSS sample. They all display steep spectra (with $\alpha \simeq -1$, where $S_\nu = \nu^\alpha$), characteristic of HzRGs. We extrapolate the modelled power law to the 500 MHz restframe frequency in order to estimate their radio power.

4.3.4 Source description

NVSS J0024

We find this source at a redshift of $z = 2.415 \pm 0.001$, which is in good agreement with the previous estimate of J. Bryant (pers. comm.), who found $z_{\rm UV} = 2.416 \pm 0.001$. In the $H-$band, we detect the [OIII]$\lambda 4959, 5007$ doublet and Hβ. In the $K-$band, the Hα and [NII] emission lines are blended and Hα shows a broad component with FWHM = 3250 km s^{-1}.

In Fig. 4.6, we observe a strong continuum coincident with a bright emission line region with Hα surface brightness $\Sigma_{\rm H\alpha} \sim 5.0 - 9.0 \times 10^{-16}$ erg s^{-1} cm^{-2} arcsec^{-2}. The same region has very perturbed gas (FWHM $\sim$ 1200 km s^{-1}) and a perturbed velocity field that extends over $\sim 1.0'' \times 1.0''$, or $\sim$ 8 kpc at $z = 2.415$.

A fainter and extended part is in the Southwest, with $\Sigma_{\rm H\alpha} \sim 1.0 - 5.0 \times 10^{-16}$ erg s^{-1} cm^{-2} arcsec^{-2} and with much more quiescent gas (FWHM $\sim$ 400 km s^{-1}). It still shows a velocity field consistent with the systemic redshift. It extends over $1.0'' \times 2.0''$. To illustrate this difference, we present spectra of both regions in Fig. 4.7. Boxes in the dispersion map in Fig. 4.6 illustrate how these regions were selected. This extended emission line region to the Southwest is approximatively in the same direction as the seconnd radio lobe that we detect in our new radio observations.

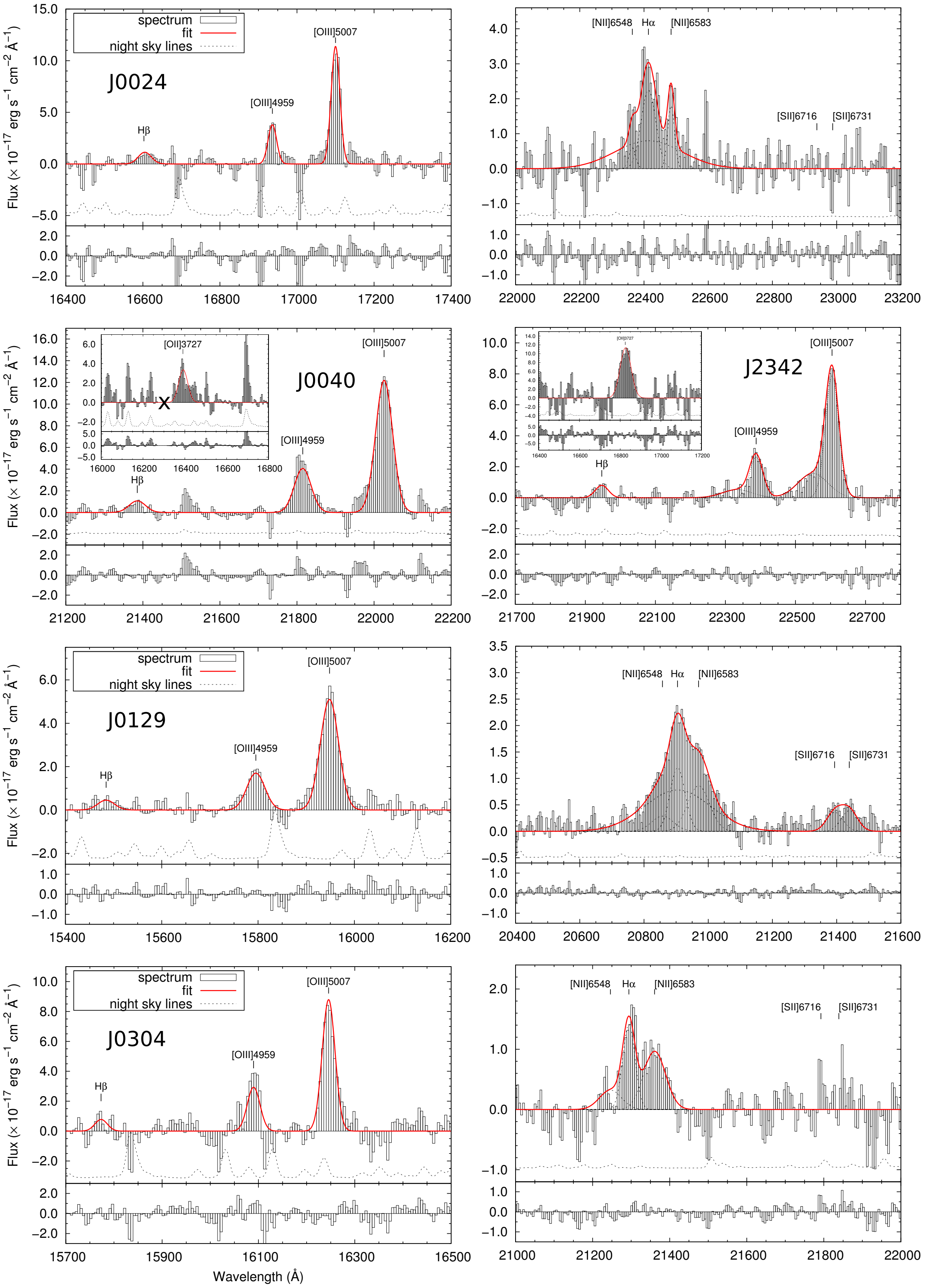

(a) Spectra of the NVSS sample

Figure 4.4: Spectra of the nine sources of our sample, corrected from velocity gradients. One is centered on the Hβ and the [OIII] emission lines and the second is centered on Hα and [NII]. Gaussian fits to detected lines are plotted as red, solid lines. Below each spectrum we show a typical night-sky spectrum (dashed lines), which we shifted by an arbitrary amount along the ordinate: night-sky residuals explain most of the noise spikes in our spectra.

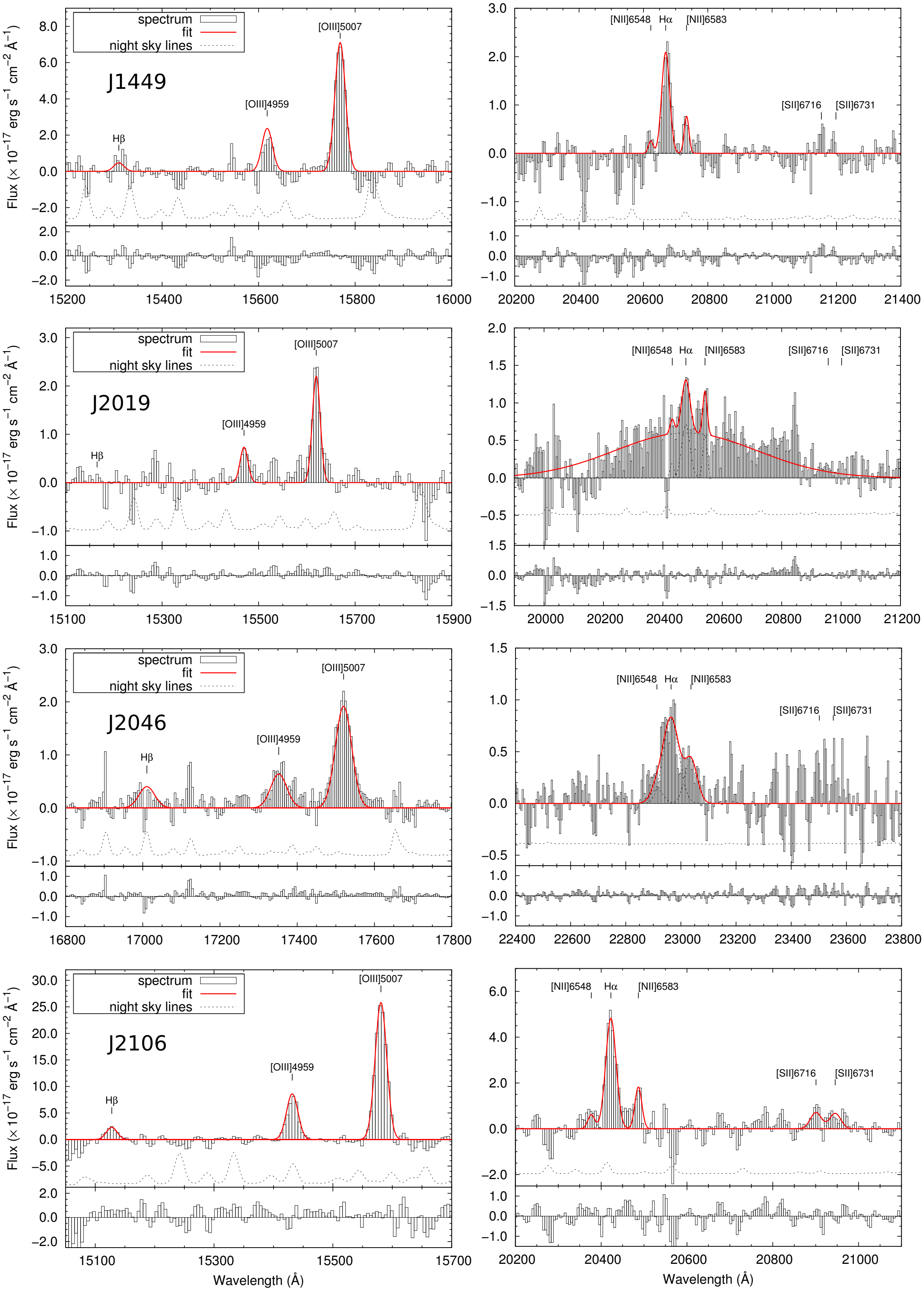

(a) Spectra of the NVSS sample

Figure 4.5: (*following*) We mark the bright rest-frame optical lines irrespecitve of whether they are detected or not. We also show the fit residuals below each spectrum. For NVSS J0040 and NVSS J2342 at $z \sim 3.5$, the only bright line in the $H-$band is the [OII] doublet, where both lines are blended. For these two galaxies we show [OII] as inset.

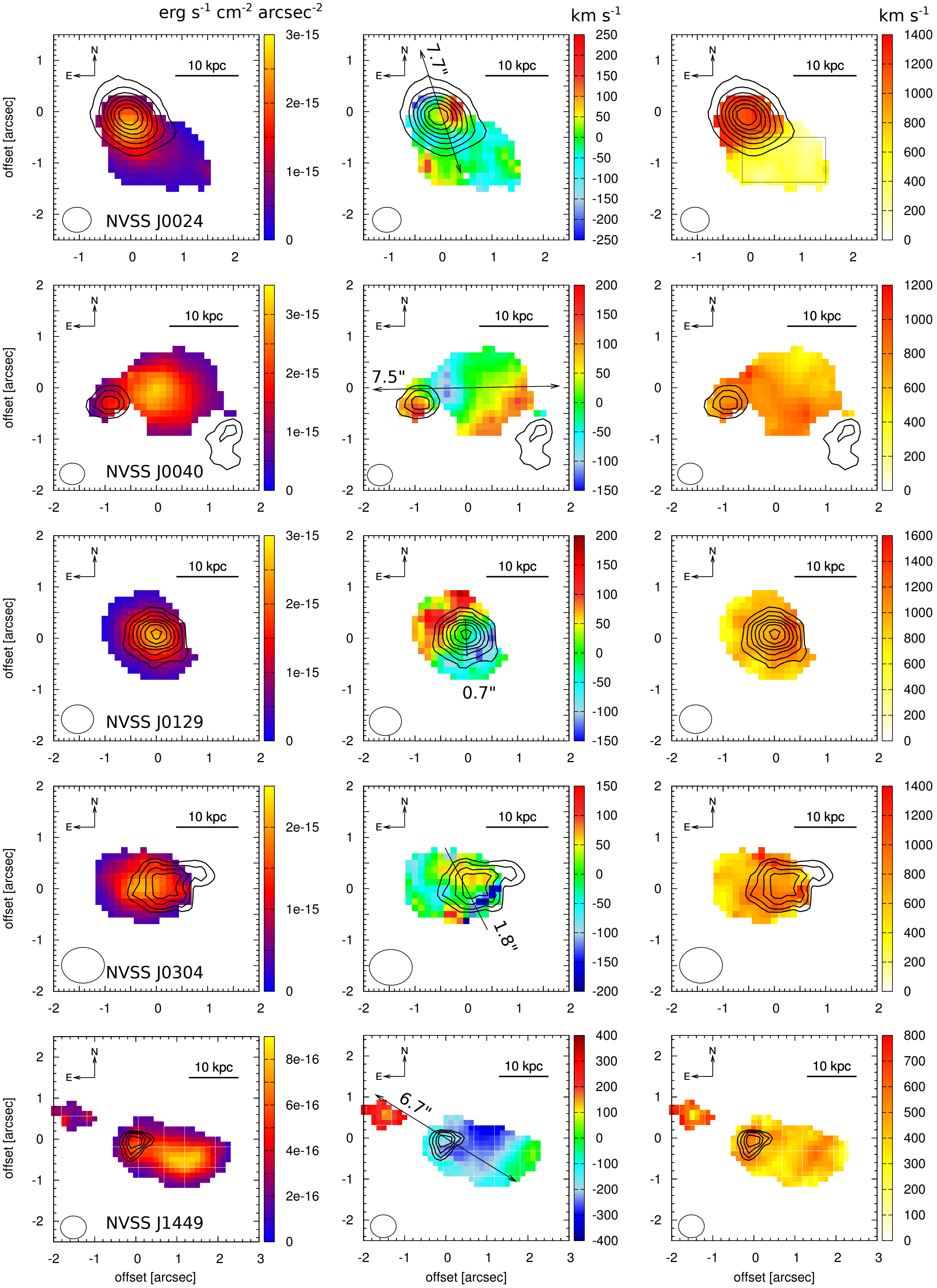

(a) Maps of the NVSS sample

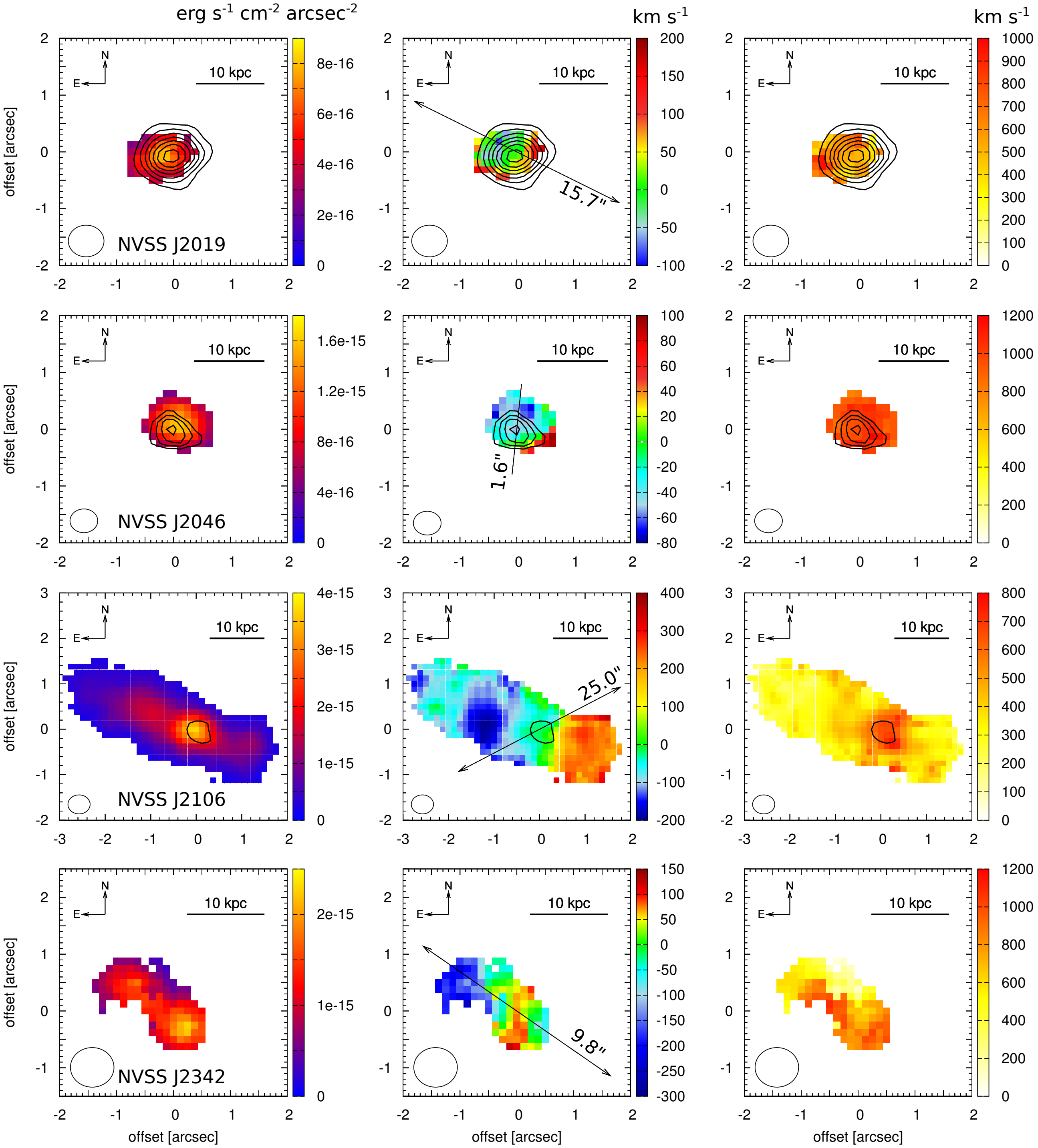

(b) Maps of the NVSS sample

Figure 4.6: Maps of [OIII] surface brightness (*left*), velocity (*center*) and velocity dispersion (*right*) of our 9 sources (from *top* to *bottom*). All maps are $4'' \times 4''$ wide, except for NVSS J1449 and NVSS J2106 for which they are $5'' \times 5''$ wide. The circle in the bottom left represents the FWHM size of the seeing disk. Contours mark the continuum where detected. Continuum levels begin at 3σ and then increase by step of 1σ, and are shown to ease orientation. The solid black line on the velocity maps indicates the axis of the radio emission that we measure, or of Broderick et al. (2007) if the source is observed compact. Numbers give the largest angular size in arcsec.

Table 4.3: IR imaging-spectrometry Observational information about our sources.

Source ID	RA (J2000)	Dec (J2000)	$z_{\rm UV}$ (1)	$z_{\rm IR}$	D_L (2) [Gpc]	ToT (3) [min]	Seeing [arcsec]	K_{img} (4) [mag]
NVSS J002431-303330	00:24:31.80	-30:33:28.6	2.416	2.415	19.56	230.0	0.8×0.7	18.8 ± 0.1
NVSS J004000-303333	00:40:00.01	-30:33:32.7	3.393	3.399	29.53	180.0	0.7×0.6	19.5 ± 0.2
NVSS J004136-345046	00:41:36.22	-34:50:46.8	2.635	...	21.74	180.0	0.8×0.7	19.2 ± 0.3
NVSS J012932-385433	01:29:32.92	-38:54:34.5	2.182	2.185	17.31	225.0	0.9×0.8	18.5 ± 0.1
NVSS J030431-315308	03:04:31.91	-31:53:08.4	2.250	2.245	17.89	190.0	1.2×1.0	18.7 ± 0.2
NVSS J103615-321659	10:36:15.26	-32:16:57.4	2.136	...	16.84	180.0	0.7×0.6	19.3 ± 0.2
NVSS J144932-385657	14:49:32.79	-38:56:57.5	2.149	2.149	16.97	220.0	0.9×0.8	19.8 ± 0.2
NVSS J201943-364542	20:19:43.54	-36:45:43.2	2.128	2.120	16.69	225.0	0.9×0.8	18.4 ± 0.3
NVSS J204601-335656	20:46:01.08	-33:56:57.1	2.502	2.499	20.39	180.0	0.7×0.6	19.7 ± 0.4
NVSS J210626-314003	21:06:25.90	-31:40:01.5	2.104	2.112	16.61	180.0	0.7×0.6	18.7 ± 0.2
NVSS J233034-330009	23:30:34.49	-33:00:11.5	2.675	...	22.14	180.0	0.8×0.8	17.2 ± 0.3
NVSS J234235-384526	23:42:35.04	-38:45:25.0	3.507	3.515	30.74	185.0	1.1×1.0	19.0 ± 0.1

(1): Spectroscopic redshift of Bryant et al. (2009b) and Johnston et al. (in prep.) measured from rest-frame UV emisson lines. — (2): Luminosity distance. — (3): On-source observing time. — (4): $K-$band magnitude of (Bryant et al., 2009a).

Table 4.4: Emission lines in NVSS J0024.

Line	λ_0 (1) [Å]	$\lambda_{\rm obs}$ (2) [Å]	FWHM (3) [km s^{-1}]	Flux (4) [10^{-16}erg s^{-1} cm^{-2}]
Hβ	4861.3	16603.4 ± 5.3	650 ± 70	4.8 ± 1.0
[OIII]	4958.9	16936.8 ± 5.4	350 ± 40	10.6 ± 2.1
[OIII]	5006.9	17100.7 ± 5.4	350 ± 40	32.2 ± 6.4
[NII]	6548.1	22364.6 ± 7.1	240 ± 25	1.6 ± 0.3
Hα	6562.8	22414.8 ± 7.1	680 ± 70	12.9 ± 2.6
Hα_b	6562.8	22414.8 ± 7.1	3270 ± 300	20.8 ± 4.2
[NII]	6583.4	22485.1 ± 7.1	240 ± 25	4.8 ± 1.0

(1): Rest-frame wavelength. — (2): Observed wavelength. — (3): Full-Width at Half Maximum, corrected for instrumental resolution (in km s^{-1}). — (4): Line flux deduced from the fit (in 10^{-16} erg s^{-1} cm^{-2}).

Table 4.5: Emission lines in NVSS J0040.

Line	λ_0 [Å]	$\lambda_{\rm obs}$ [Å]	FWHM [km s^{-1}]	Flux [10^{-16}]
[OII]	3727.5	16397.3 ± 4.0	900 ± 90	16.5 ± 3.3
Hβ	4861.3	21385.6 ± 3.7	670 ± 70	5.8 ± 1.2
[OIII]	4958.9	21814.9 ± 3.8	670 ± 70	22.3 ± 4.5
[OIII]	5006.9	22026.1 ± 3.8	670 ± 70	67.5 ± 13.5
[OIII]$_{\rm south}$	4958.9	21794.0 ± 3.8	760 ± 80	1.3 ± 0.7
[OIII]$_{\rm south}$	5006.9	22005.0 ± 3.8	760 ± 80	3.9 ± 1.9

NVSS J0040

We find this source at a redshift of $z = 3.399 \pm 0.001$ which means that the [OIII] doublet and Hβ fall in the $K-$band and the Hα and [NII] complexes are redshifted out of the atmospheric windows. In the $H-$band,

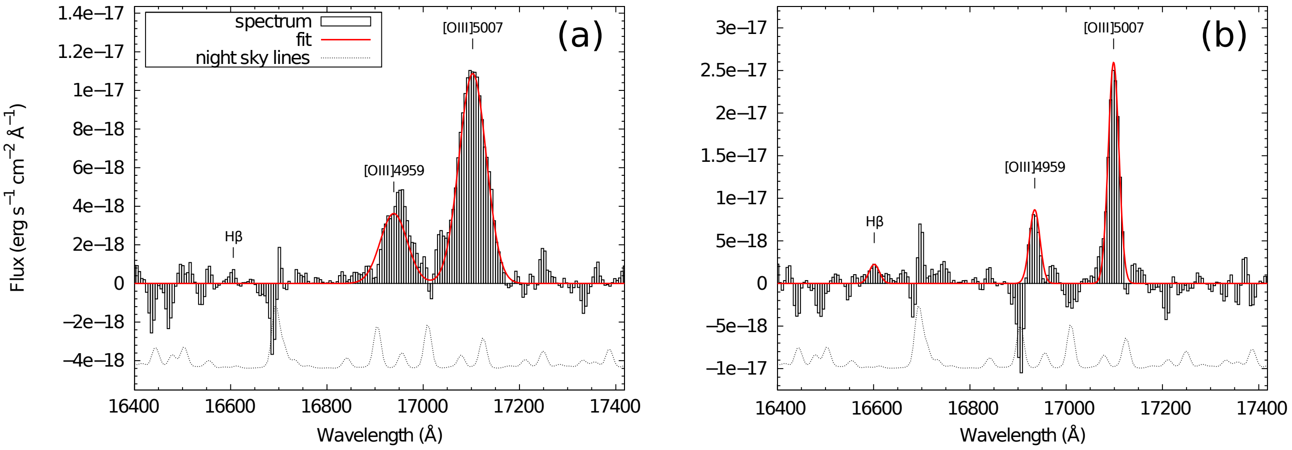

Figure 4.7: Spectra extracted from sub-regions of NVSS J0024 shown in Fig. 4.6. (a): Spectrum from the continuum region, with broad [OIII] lines (FWHM ∼ 1150 km s^{-1}). (b): Spectrum of the quiescent gas, with much more narrow lines (FWHM ∼ 450 km s^{-1}).

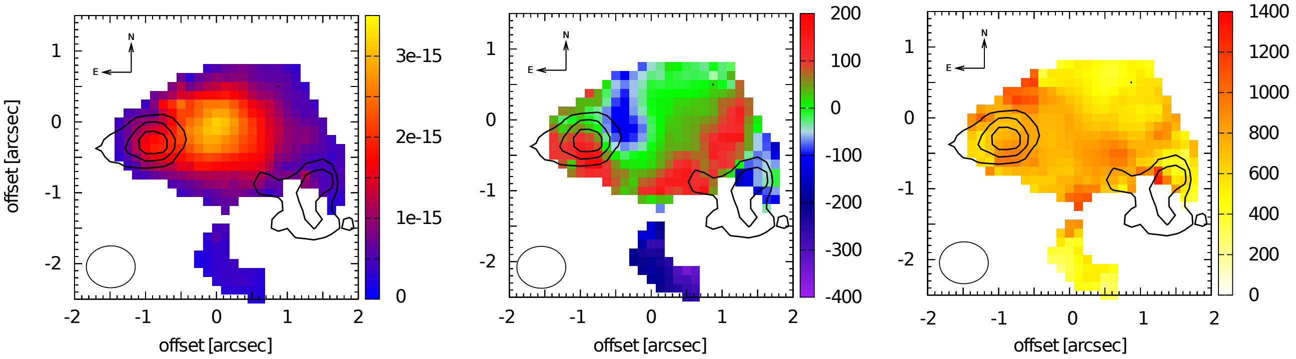

Figure 4.8: Maps of NVSS J0040 at SNR ≥ 3.0. A second emission line region clearly appears ∼ 2″ to the south of NVSS J0040, blueshifted by 350 ± 90 km s^{-1} relative to NVSS J0040. The integrated spectrum of this second region, given in Fig. 4.20, shows that the [OIII] doublet is clearly detected.

we only detect the [OII]λ3727 emission.

The emission line region extends over 2.5″×1.5″ with surface brightnesses between $\Sigma_{[\mathrm{OIII}]} \sim 4.0 \times 10^{-15}$ erg s^{-1} cm^{-2} arcsec^{-2} in the center and 1.0×10^{-15} erg s^{-1} cm^{-2} arcsec^{-2} in the periphery. We do not detect continuum in the center of this emission line region, but there is an extension in the east coincident with a faint continuum. We also detect continuum in the south west, but outside the EELR. The $K-$band image of Bryant et al. (2009a) shows very similar multi-component continuum emission, but likewise at low signal-to-noise ratio.

The velocity field is complex: the southwest region is redshifted by v ∼ 50−100 km s^{-1} and the eastern region is blueshifted by v ∼ 50−100 km s^{-1}. The extension in the east seems to have a proper velocity field as it is redshifted at v ∼ 80 km s^{-1}. The velocity dispersion is lower in the north (FWHM = 400−600 km s^{-1}) than in the south (FWHM = 700−800 km s^{-1}). In the radio, this source has two lobes along a west-east axis and 7.2″ away from one another.

We also observe faint line emission about 2″ to the south (about 15 kpc at z ∼ 3), at redshift $z_{\mathrm{south}} = 3.395 \pm 0.001$, *i.e.*, blueshifted by 350 ± 90 km s^{-1}. This is shown in Fig. 4.8 and further discussed in §4.7.

Table 4.6: Emission lines in NVSS J0129.

Line	λ_0 [Å]	$\lambda_{\rm obs}$ [Å]	FWHM [km s^{-1}]	Flux [10^{-16}]
Hβ	4861.3	15484.5 ± 3.5	720 ± 80	2.0 ± 0.4
[OIII]	4958.9	15795.4 ± 3.6	780 ± 80	8.0 ± 1.6
[OIII]	5006.9	15948.3 ± 3.6	780 ± 80	24.3 ± 4.9
[NII]	6548.1	20857.4 ± 4.7	1130 ± 110	2.5 ± 0.5
Hα	6562.8	20904.6 ± 4.7	750 ± 80	7.0 ± 1.4
Hα_b	6562.8	20904.6 ± 4.7	3470 ± 350	20.1 ± 4.0
[NII]	6583.4	20970.2 ± 4.7	1130 ± 110	7.4 ± 1.5
[SII]	6716.4	21393.9 ± 4.8	810 ± 80	2.9 ± 0.5
[SII]	6730.8	21439.8 ± 4.8	810 ± 80	3.1 ± 0.5

NVSS J0129

We find this source at a redshift $z = 2.185 \pm 0.001$. It is relatively spatially compact and has only weak continuum emission.

In the $H-$band, the [OIII] doublet is clearly detected and Hβ is marginally detected (at 5.6σ). In the $K-$band, Hα is strongly blended with [NII] and also presents a broad component (FWHM $\sim$ 3500 km s^{-1}). The [SII] doublet is well detected, but blended.

The emission line region is extended over $1.6'' \times 1.2''$, after deconvolving with the size of the seeing disk. It is brighter in the center with $\Sigma_{\rm H\alpha} \sim 1.0 - 1.7 \times 10^{-15}$ erg s^{-1} cm^{-2} arcsec^{-2} and fades toward the periphery. We detect continuum emission coincident with the emitting gas. The [OIII]λ4959,5007 lines show a clear velocity gradient of Δv $\sim$ 350 km s^{-1} along a northeast-southwest axis. The velocity dispersion is lower in the southeast region, with FWHM $\sim$ 700−800 km s^{-1}, whereas in the northwest, it is larger, with FWHM $\sim$ 900−1000 km s^{-1}.

The radio observations from Broderick et al. (2007) reveal a single component, with a deconvolved axis along the north-south direction and with a LAS of $1.4''$.

NVSS J0304

Table 4.7: Emission lines in NVSS J0304.

Line	λ_0 [Å]	$\lambda_{\rm obs}$ [Å]	FWHM [km s^{-1}]	Flux [10^{-16}]
Hβ	4861.3	15773.2 ± 2.8	480 ± 50	2.5 ± 0.5
[OIII]	4958.9	16089.9 ± 2.9	480 ± 50	9.7 ± 1.9
[OIII]	5006.9	16245.6 ± 2.9	480 ± 50	29.5 ± 5.9
[NII]	6548.1	21246.3 ± 3.8	910 ± 90	2.3 ± 0.5
Hα	6562.8	21294.0 ± 3.8	470 ± 50	5.7 ± 1.1
[NII]	6583.4	21360.8 ± 3.8	910 ± 90	6.9 ± 1.4

This very compact source at $z = 2.2446 \pm 0.0006$ is marginaly spatially resolved with a PSF of FWHM $= 1.2'' \times 1.0''$, the worst of this program. The emission line region extends over $1.5'' \times 1.5''$ and is dominated by the seeing disk. Faint continuum emission is also detected, at a slightly different position ($\sim 0.5''$ to the West) from the peaking [OIII]λ5007 surface brightness but at the same position as the peak of Hα surface brightness (where $\Sigma_{\rm H\alpha} \sim 7.0 \times 10^{-16}$ erg s^{-1} cm^{-2} arcsec^{-2}). The associated radio source is also compact: the largest angular size is $2.4''$, provided by Broderick et al. (2007).

The velocity map is uniform, as expected for a source which is marginaly resolved. Velocity offsets in the range of ~ 50 km s^{-1} are what is expected for our SNR. Velocity dispersions are in the range FWHM $= 500-1000$ km s^{-1}.

All line caracteristics are listed in Table 4.7. The [OIII] doublet is clearly detected in the $H-$band and is well fitted with single Gaussians. The same holds for the Hα + [NII] complex. The [SII] doublet is not detected.

NVSS J1449

Table 4.8: Emission lines in NVSS J1449.

Line	λ_0 [Å]	$\lambda_{\rm obs}$ [Å]	FWHM [km s^{-1}]	Flux [10^{-16}]
Hβ	4861.3	15310.4 ± 3.4	350 ± 40	1.3 ± 0.2
[OIII]	4958.9	15617.8 ± 3.5	360 ± 40	6.4 ± 1.3
[OIII]	5006.9	15769.0 ± 3.5	360 ± 40	19.5 ± 3.9
[NII]	6548.1	20622.9 ± 4.6	unres.	0.5 ± 0.1
Hα	6562.8	20669.2 ± 4.6	340 ± 35	6.6 ± 1.3
[NII]	6583.4	20734.1 ± 4.6	unres.	1.4 ± 0.3

NVSS J1449 has one of the larger radio sources in our sample, the lobes are offset by 7.5″ relative of each other. We find the [OIII] line at $z = 2.149 \pm 0.001$. NVSS J1449 has a very extended emission-line region of nearly 4″ (~ 30 kpc at $z \sim 2$) along a Northeast-Southwest axis. It is composed of two distinct parts: a bright southwestern part ($\Sigma_{\rm H\alpha} \lesssim 3.0 \times 10^{-16}$ erg s^{-1} cm^{-2} arcsec^{-2}), which is well covered by our data cube and extends over 2.0″×1.0″, and a fainter northeastern part ($\Sigma_{\rm H\alpha} \lesssim 1.5 \times 10^{-16}$ erg s^{-1} cm^{-2} arcsec^{-2}). Unfortunately, this region falls near the edge of the data cube, and we suspect it may extend well beyond. The two emission line regions are well aligned with the axis of the radio jet. We also detect continuum emission roughly in the middle between the two emission-line features.

There is a clear velocity offset of 800 km s^{-1} between the two emission-line regions. While the north-eastern part has a uniform velocity field (v ~ 400 km s^{-1}), the south-western part is more complex: the gas is roughly at the systemic redshift where the continuum emission is detected, is blueshifted by up to -400 km s^{-1}further in the Southwest and resumes the systemic redshift at the edge of this part. Line widths appear slightly more narrow in the Southwest (FWHM $\sim 400-500$ km s^{-1}) than in the Northeast (FWHM ~ 600 km s^{-1}).

In the $H-$band, we detect the [OIII] doublet and Hβ. In the $K-$band, Hα and [NII] are narrow enough not to be blended (FWHM=350 km s^{-1} for Hα. The width of the [NII] doublet is dominated by the spectral resolution of the instrument).

In Fig. 4.9, we present the Hα and [NII] surface brightness maps. They highlight the tail-like structure towards northwest seen in the relative velocity map, where the velocity drops to roughly systemic. These maps are obtained by fitting the Hα + [NII] complex simultaneously with 3 Gaussian line profiles and constraining their redshifts and line widths to be the same as for the [OIII] doublet. We also require that the flux ratio [NII]λ6583/[NII]λ6548 = 3.0, as given by quantum mechanics. There are only two remaining free parameters: line cores of Hα and [NII]. These constrains are necessary because of the relatively low signal-to-noise ratio of the three lines. But, as illustrated by the integrated spectra, these constrains are acceptable since the line properties of the [OIII] doublet and of the Hα + [NII] complex are very similar.

NVSS J2019

The radio source of NVSS J2019 is very extended, with LAS = 14.7″, corresponding to ~ 120 kpc at $z = 2.1$. In the $H-$band of our data cube, we detect the [OIII] doublet at a redshift of $z = 2.120 \pm 0.001$,

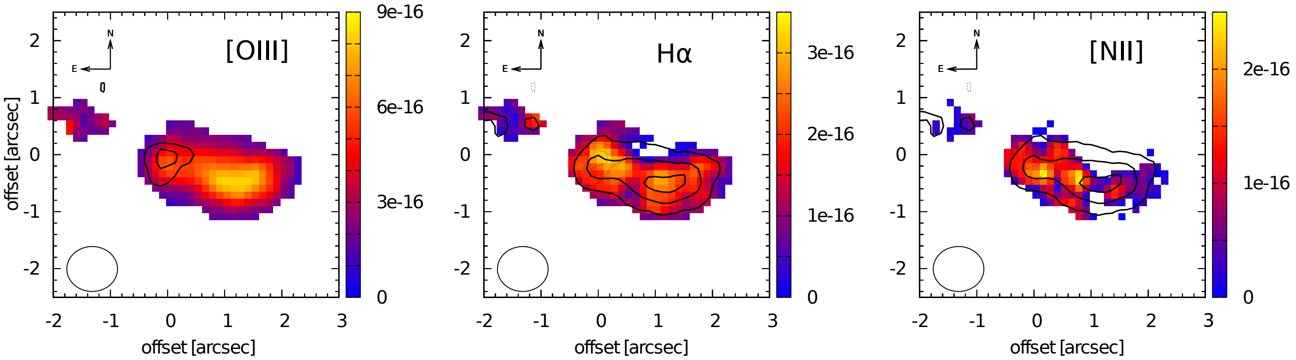

Figure 4.9: Surface brightness maps of NVSS J1449 at SNR ≥ 3.0 for [OIII]λ5007, Hα and [NII]λ6583 emission lines. The solid contours represent the [OIII] emission and the dashed contours the continuum. In the latters, the emission line morphology hilights the tail that goes to the north-west and that is not along the radio axis.

Table 4.9: Emission lines in NVSS J2019.

Line	λ_0 [Å]	$\lambda_{\rm obs}$ [Å]	FWHM [km s^{-1}]	Flux [10^{-16}]
Hβ	4861.3	15165.3 ± 4.4	150 ± 50	$\lesssim$ 0.5
[OIII]	4958.9	15469.8 ± 4.5	160 ± 30	1.5 ± 0.3
[OIII]	5006.9	15619.5 ± 4.5	160 ± 30	4.5 ± 0.9
[NII]	6548.1	20431.6 ± 5.9	unres.	0.4 ± 0.1
Hα	6562.8	20477.5 ± 5.9	410 ± 50	2.5 ± 0.5
Hα_b	6562.8	20477.5 ± 5.9	8250 ± 800	35.9 ± 7.0
[NII]	6583.4	20541.8 ± 5.9	unres.	1.1 ± 0.2
[OIII]$_{\rm south}$	4958.9	15450.9 ± 4.0	320 ± 30	0.5 ± 0.2
[OIII]$_{\rm south}$	5006.9	15600.4 ± 4.0	320 ± 30	1.6 ± 0.3

but not Hβ. This galaxy has compact emission line region of 1.0″ with an [OIII]λ5007 surface brightness $\Sigma_{\rm [OIII]} = 0.5 - 1.7 \times 10^{-15}$ erg s^{-1} cm^{-2} arcsec^{-2}. NVSS J2019 also has relatively bright continuum emission at the position of the emission-line gas. The velocity field shows a scatter of ≲ 50 km s^{-1}, consistent with a source that is at most marginally spatially resolved. The velocity dispersion is in the range FWHM = 400 − 700 km s^{-1} in most of the data cube.

In the $K-$band, in addition to narrow components of Hα and [NII], we find a broad Hα emission line (FWHM ≥ 8000 km s^{-1}) from a compact region aligned with the nucleus. We will come back to this line in §4.7.

About 3″ to the Southeast we marginally detect another compact line emitter at a very similar redshift $z_{\rm south} = 2.116 \pm 0.001$ (Fig. 4.20) . The proximity on the sky and in redshift suggests that both sources are physically related. We will discuss this source in more detail in §4.7.

NVSS J2046

NVSS J2046 at $z = 2.499 \pm 0.001$ is marginally spatially resolved with a FWHM size of 1″ compared to a 0.7″×0.6″ PSF. The emission line region is associated with a faint continuum source and roughly circular and extends over 1.0″, with $\Sigma_{\rm H\alpha} = 0.3 - 1.0 \times 10^{-15}$ erg s^{-1} cm^{-2} arcsec^{-2}. NVSS J2046 has a fairly compact radio source with LAS = 2.4″ along a Northeast-Southwest axis (Broderick et al., 2007).

Consistent with a marginally spatially resolved source, NVSS J2046 source has very uniform kinematics, with a scatter in the velocity map of ≲50 km s^{-1} as expected for the typcial SNR. Typical velocity dispersions

Table 4.10: Emission lines in NVSS J2046.

Line	λ_0 [Å]	$\lambda_{\rm obs}$ [Å]	FWHM [km s^{-1}]	Flux [10^{-16}]
Hβ	4861.3	17010.6 ± 5.5	790 ± 80	2.1 ± 0.2
[OIII]	4958.9	17352.1 ± 5.7	800 ± 80	3.4 ± 0.7
[OIII]	5006.9	17520.0 ± 5.7	800 ± 80	10.2 ± 2.0
[NII]	6548.1	22913.0 ± 7.5	670 ± 70	0.8 ± 0.2
Hα	6562.8	22964.4 ± 7.5	840 ± 80	5.8 ± 1.2
[NII]	6583.4	23036.5 ± 7.5	670 ± 70	2.4 ± 0.5

are in the range FWHM = $900 - 1100$ km s^{-1}.

Table 4.10 summarizes the line properties of NVSS J2046: in the $H-$band, the [OIII] doublet and Hβ are well detected and in the $K-$band, Hα and the [NII] doublet are blended but well fitted by a single Gaussian component. The [SII] doublet falls near the edge of the $K-$band (at ~ 2.36 μm) where the thermal emission of the Earth's atmosphere becomes important.

NVSS J2106

Table 4.11: Emission lines in NVSS J2106.

Line	λ_0 [Å]	$\lambda_{\rm obs}$ [Å]	FWHM [km s^{-1}]	Flux [10^{-16}]
Hβ	4861.3	15127.8 ± 3.3	240 ± 40	5.2 ± 1.1
[OIII]	4958.9	15431.6 ± 3.4	290 ± 40	21.0 ± 4.4
[OIII]	5006.9	15580.9 ± 3.4	290 ± 40	63.0 ± 13.2
[NII]	6548.1	20377.0 ± 4.4	100 ± 20	1.2 ± 0.2
Hα	6562.8	20422.7 ± 4.4	330 ± 35	14.7 ± 3.0
[NII]	6583.4	20486.8 ± 4.5	100 ± 20	3.7 ± 0.7
[SII]	6716.4	20900.7 ± 4.6	360 ± 40	2.3 ± 0.5
[SII]	6730.8	20945.5 ± 4.6	360 ± 40	2.2 ± 0.5

This galaxy shows a very large emission line region, larger than $4.5''$ (nearly 40 kpc at $z = 2.112 \pm 0.001$) along a Northeast-Southwest axis, with $\Sigma_{\rm H\alpha} = 0.2 - 1.1 \times 10^{-15}$ erg s^{-1} cm^{-2} arcsec^{-2}. Faint continuum emission is also detected, coincident with the brightest part of the emission line region. We observe a clear velocity gradient of ~ 600 km s^{-1}. Velocity dispersions are FWHM = $250 - 400$ km s^{-1} in most of pixels, except in the brightest central region, where they reach $500 - 700$ km s^{-1}. The radio structure of this source is also very extended (LAS = $24.2''$) and is along a Northwest-Southeast axis. Interestingly, it is mis-aligned with the extended emission-line region, this will be discussed in details in the Chapter 5.

In the integrated spectra, we detect the [OIII] doublet and Hβ in the $H-$band, each of them well fitted by a single Gaussian component. In the $K-$band, the [NII] doublet is narrower than the other sources in our sample, with FWHM = 120 km s^{-1}.

We note that Hα and [NII] emission-line regions are fainter and less extended than [OIII], as shown in Fig. 4.10. These maps were made in the same way as those of NVSS J1449.

NVSS J2342

NVSS J2342 is at a redshift $z = 3.515 \pm 0.001$, where the [OIII] doublet and the Hβ emission lines fall into the $K-$band. We find that the [OIII] doublet is better fitted with two Gaussian components: one with a

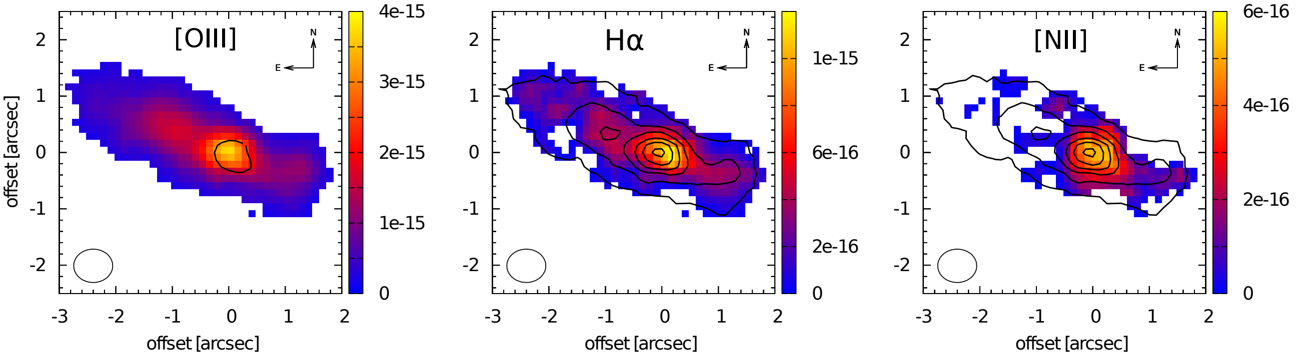

Figure 4.10: *Left to right:* Surface brightness maps of NVSS J2106 of [OIII], Hα and [NII]. Lines with SNR ≥ 3.0 are shown. Solid contours on the Hα and [NII] maps show the [OIII] morphology to ease comparison of the maps.

Table 4.12: Emission lines in NVSS J2342.

Line	λ_0 [Å]	$\lambda_{\rm obs}$ [Å]	FWHM [km s^{-1}]	Flux [10^{-16}]
[OII]	3727.5	16829.6 ± 5.0	1100 ± 110	7.7 ± 1.5
Hβ	4861.3	21947.0 ± 5.0	550 ± 60	3.7 ± 0.8
[OIII]	4958.9	22387.6 ± 5.2	550 ± 60	12.5 ± 2.5
[OIII]	5006.9	22604.3 ± 5.2	550 ± 60	37.8 ± 7.6
[OIII]$_{\rm blue}$	4958.9	22333.5 ± 5.2	1320 ± 130	5.6 ± 1.1
[OIII]$_{\rm blue}$	5006.9	22549.7 ± 5.2	1320 ± 130	16.9 ± 3.4

velocity dispersion of FWHM = 360 km s^{-1} and which gives the systemic redshift, and a blue wing, with more perturbed gas (FWHM = 1300 km s^{-1}) and blueshifted by 700 km s^{-1}. In the $H-$band, we only detect the [OII]λ3727 emission line.

The emission-line region extends over $2.0'' \times 1.0''$ along a Northeast-Southwest axis, with surface brightness $\Sigma_{\rm [OIII]} = 0.5 - 3.0 \times 10^{-15}$ erg s^{-1} cm^{-2} arcsec^{-2}. The velocity map shows a strong gradient of about 400 km s^{-1} between the north-eastern and the south-western parts, well aligned with the radio axis given by Broderick et al. (2007). The velocity dispersion is larger in the center of the galaxy (FWHM $\simeq$ 1000 – 1200 km s^{-1}) than in the periphery (FWHM $\simeq$ 600 km s^{-1}). We do not detect continuum emission and therefore we cannot measure the position of the stellar component of this source.

4.4 CENSORS sample

4.4.1 Target selection

The 6 galaxies with the lowest radio power ($\mathcal{L}_{\rm 1.4GHz} \sim 10^{26}$ W Hz^{-1}) come from the “Combined EIS-NVSS Survey Of Radio Sources” (CENSORS, Best et al., 2003a). This catalogue of 150 radio galaxies results from the cross-matching of the ESO Imaging Survey (EIS) patch D with the NVSS radio survey, already described at the beginning of this Chapter. The EIS patch D is a 3° × 2° field centered on the position RA = 09:51:36 and Dec = −21:00:00, with deep imaging in the $B-$, $V-$ and $I-$bands (with limiting magnitudes of 23 ; 24.5 and 25 respectively). This patch is far enough in the north to allow observations with the VLA under good conditions. The radio sources detected in the NVSS were reobserved at 1.4 GHz with the VLA in its BnA configuration, leading to a spatial resolution of $3''-4''$, compared to the initial NVSS spatial resolution of $45''$, and a survey complete to a flux density of 7.2 mJy. This allows the study of the structure of the radio sources and the likely identification of 102 optical counterparts.

$K-$band observations of the CENSORS sources was then performed by Brookes et al. (2006) in order to confirm the identification of host galaxies of radio emission found in the EIS imaging ; to further identify optical counterparts of the rest of the radio sources and to study the $K-$z relation. 142 optical-NIR counterparts are found out of the 150 CENSORS sources.

Finally, optical spectroscopy of most CENSORS sources with an optical-NIR counterpart was performed by Brookes et al. (2008). A total of 105 sources out of the 143 targeted have a redshift, among which 81 have a secure redshift estimate, *i.e.*, which is based on more than a single one emission line. We selected six sources with appropriate redshifts for follow-up observations with SINFONI, *i.e.*, the usual strong restframe visible emission lines will be redshifted in one of the IR atmospheric window accessible with SINFONI. Three of these six sources have extended radio morphologies and the three others are compact, unresolved radio cores.

4.4.2 Radio continuum observations

Table 4.13: ATCA observing log for the CENSORS sample.

Source ID	Date	TOT $^{(1)}$ [min]	Secondary Cal. $^{(2)}$	beam (5.5 GHz) [arcsec×arcsec, deg.]	beam (9.0 GHz) [arcsec×arcsec, deg.]
CEN 020	28 Jan. 2012	75	0925-203	5.5×1.5, −0.5	3.4×0.9, −0.5
CEN 072	28 Jan. 2012	75	0925-203	5.7×1.5, −0.1	3.5×0.9, −0.1
CEN 105	28 Jan. 2012	75	0925-203	5.5×1.5, −0.1	3.5×0.9, −0.1
CEN 118	28 Jan. 2012	75	0925-203	6.0×1.5, −0.7	3.7×0.9, −0.7
CEN 129	28 Jan. 2012	75	0925-203	6.2×1.5, −0.7	3.8×0.9, −0.6
CEN 134	28 Jan. 2012	75	0925-203	5.7×1.5, −0.5	3.5×0.9, −0.4

(1): Total on source integration time (in minutes). — (2): Secondary calibrator used.

As a part of our ATCA observing time, we also observed the CENSORS sample at 5.5 GHz and 9.0 GHz on the 2012 January 28. The weather was unstable, leading to relatively large error bars in the measured fluxes. The observation log is given in Table 4.13 and the results in Table 4.14. Note that we did not observe CENSORS 072, due to incorrect coordinates given for this source in Brookes et al. (2008).

These observations of the CENSORS sample were crucial if we want to compare the jet power of all HzRG with a single method, namely their 500 MHz restframe luminosity. Indeed, the CENSORS sample had only been observed at 1.4 GHz previously, contrary to the nine sources presented in the previous section (the "NVSS sample") that had radio fluxes measured at many other frequencies (coming both from radio surveys and observations by Broderick et al., 2007; Bryant et al., 2009a) that could allow the power law fit to the radio SED in any case. The ATCA observations also lead to a slightly better spatial resolution than the one achieved in previous observations: the clean beam of the ATCA is $\sim 5.5''\times1.5''$ at 5.5 GHz and $\sim 3.5''\times1.0''$ at 9.0 GHz, compared to the $3-4''$ resolution of the radio observations of Best et al. (2003a) with the VLA at 1.4 GHz. Moreover, the beam of our ATCA observations is elongated along a North-South direction, while the beam of the VLA observations of Best et al. (2003a) is rather elongated along an East-West direction, both sets of observations are therefore complementary.

This higher spatial resolution of our ATCA observations allows to separate some radio sources, previously observed to be compact, especially when the position angle between the two lobes is along an East-West direction, where our observations present their best spatial resolution.

Measured fluxes at 5.5 GHz and 9.0 GHz of the CENSORS sample indicate that those are steep spectrum sources, as is usually the case for HzRGs. Their extrapolated fluxes and luminosities at 500 MHz restframe confirm that they are fainter than sources in the NVSS sample by one order of magnitude (few $\times10^{27}$ W Hz^{-1} compared to few $\times10^{28}$ W Hz^{-1}). This shows that they have less powerful radio-loud AGN.

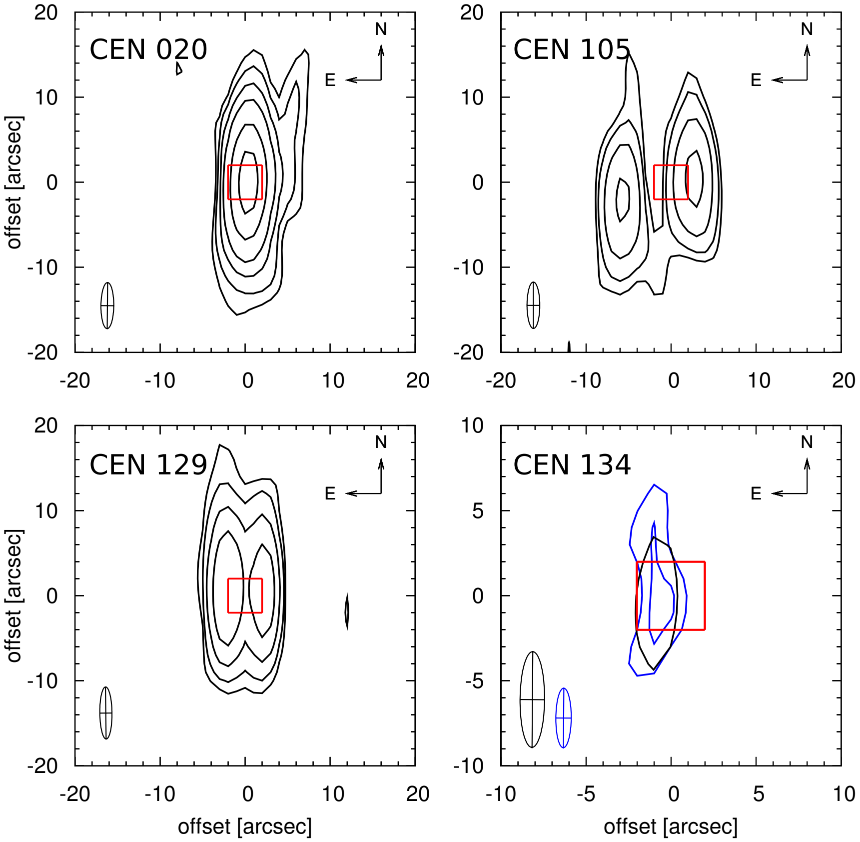

Figure 4.11: Radio morphologies of the CENSORS sources at 5.5 GHz, as derived from our ATCA observations. The size and orientation of the restored beam is given in the bottom left of each panel. The red box indicates the size and location of the SINFONI maps presented in Fig. 4.14. The contours are at levels (3, 5, 10, 20, 50, 100)×σ, where σ is the RMS level of each observation.

Table 4.14: Results from the ATCA observations of the CENSORS sample.

Source ID	$S_{5.5}$ [mJy]	$S_{9.0}$ [mJy]	LAS $^{(1)}$ [arcsec]	PA $^{(2)}$ [deg.]	$S_{500,rest}$ $^{(3)}$ [mJy]	P$_{1.4}$ $^{(4)}$ [10^{26} W Hz^{-1}]	P$_{500,rest}$ $^{(5)}$ [10^{27} W Hz^{-1}]
CEN 020	14.5	8.0	1.8 ; 1.2 (7.1)	… (163)	360.1	6.2	4.1
CEN 072$^{(6)}$	…	…	… ($\leq$ 0.7)	… (…)	…	7.6	…
CEN 105	2.2	0.8	4.3 ($\leq$ 6.8)	94.3 (…)	205.6	10.9	21.1
CEN 118	1.9	0.6	7.0 ; … (3.7)	… (157)	166.0	3.8	6.7
CEN 129	2.7	1.7	2.5 ($\leq$ 2.1)	94.6 (…)	50.4	3.8	2.3
CEN 134	2.4	1.0	21.9 (22.4)	131.1 (125)	88.4	3.4	3.8

(1): Largest angular scale, corresponding to the separation between the two lobes, when detected, or to the deconvolved size, if the source appears compact. In this case, both deconvolved sizes at 5.5 and 9.0 GHz are given. We give previous measurements of Best et al. (2003a) in brackets for comparison. — (2): Position angle of the source, measured from North to East, when two lobes are detected. — (3): Flux at 500 MHz restframe, extrapolated from the radio spectrum. — (4): Radio power at 1.4 GHz (observed). — (5): Radio power at 500 MHz restframe, extrapolated from the radio spectrum. — (6): We made an error in the pointing of CEN 072

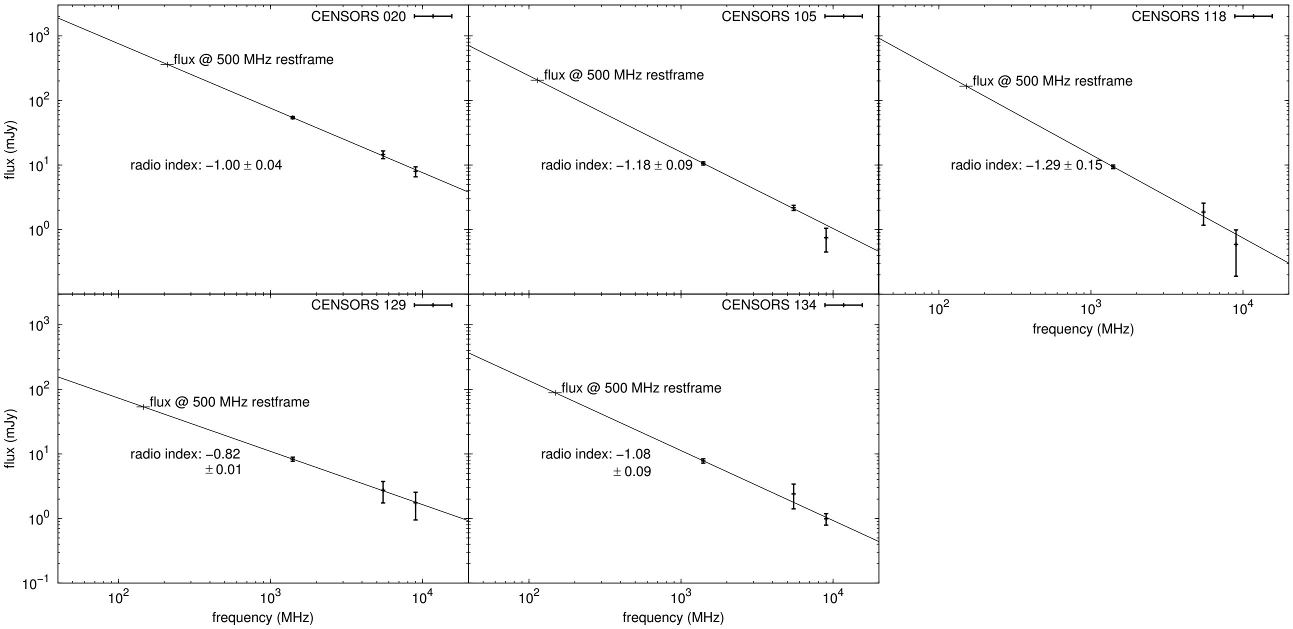

Figure 4.12: Spectral energy distribution in the radio for 5/6 galaxies of the CENSORS sample. They all display steep spectra (with $\alpha \simeq -1$, where $S_\nu = \nu^\alpha$), characteristic of HzRGs. We extrapolate the modeled power law to the 500 MHz restframe frequency to estimate their radio power.

4.4.3 IR imaging-spectroscopic observations

Observations and data reduction

We observed the galaxies of the CENSORS sample with SINFONI between late 2010 and early 2011 in Service Mode (program ID 086.B-0571, PI Nesvadba) at the Very Large Telescope of ESO under variable conditions. The observation strategy is the same as for the NVSS sample (see §4.3.3), the only difference is the observing time per target, which is longer to ensure a sufficient SNR of these sources for which we expected lower surface brightnesses. Therefore, the minimum on-source integration time is 300 min, but it reaches 440 min in the case of CENSORS 105. The spatial resolution of our data is limited by the size of the seeing disk, which is typically around $1.0''$. The FWHM sizes of the PSFs of individual targets are given in Table 4.15. They are measured from a standard star observed at the end of each hour of data taking.

In this analysis, we discuss the optical emission-line properties of 3 of the 6 galaxies we observed. In the 3 other cubes, we could not identify any emission line at the redshifts previously measured in the rest-frame UV.

Relative alignment of the radio and SINFONI data

Similarly to the NVSS sample, we do not detect the radio core of galaxies with extended radio lobes. We therefore register our cubes relative to the $K-$band imaging of Brookes et al. (2008), which is well aligned with the WCS, and assume again that the radio frame of the ATCA alignes well with the WCS, to better than $1''$ (Broderick et al., 2007). For compact radio sources (LAS $\lesssim 2.0''$ in Table 4.14), we assume that the $K-$band continuum is aligned with the radio source, corresponding to the assumption that the radio emission in compact sources originates from the galactic nucleus. The red box in each panel of Fig. 4.11, presenting the radio morphologies of the CENSORS sample, gives the position of the SINFONI maps derived using this method.

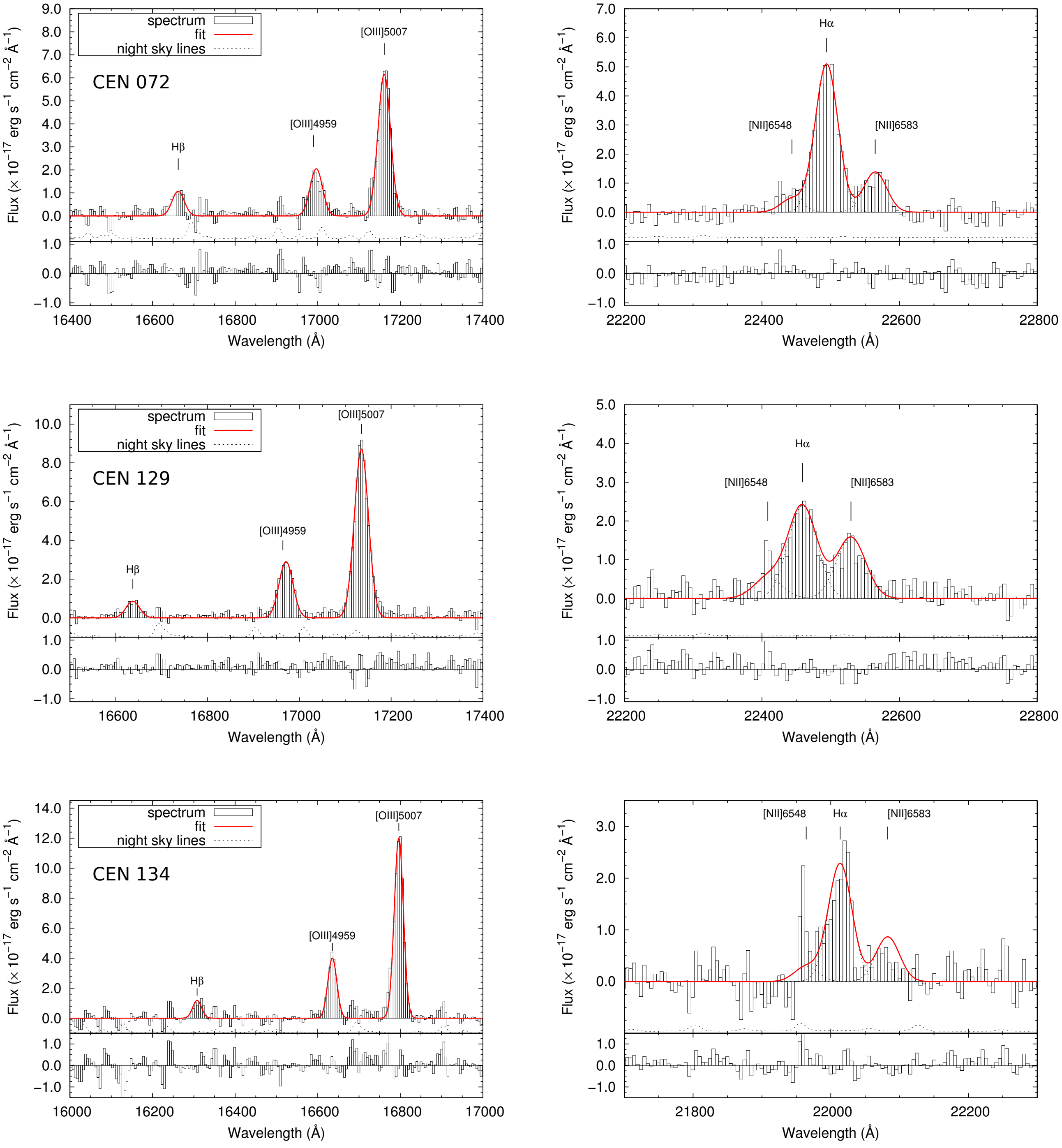

Figure 4.13: Spectra of the CENSORS sample, integrated over pixels where the [OIII] emission line is detected at SNR>5. The left column show spectra centered on the Hβ and [OIII] doublet emission lines and the right column is centered on the Hα + [NII] complex. All lines are well fitted by single Gaussians, which parameters can be found in Table 4.16, 4.17 and 4.18. Residuals to the fit are shown in the bottom panel.

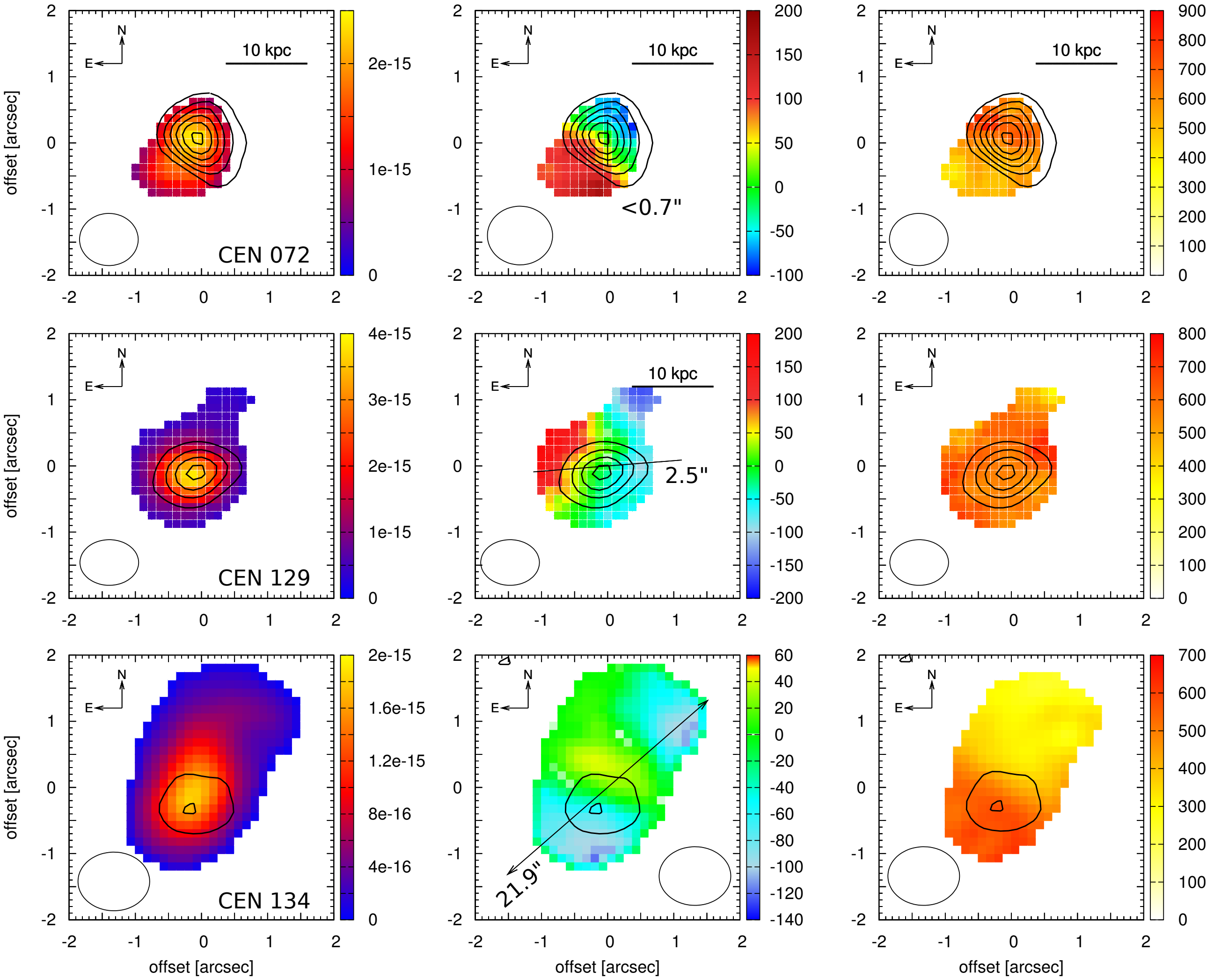

Figure 4.14: Maps of [OIII] surface brightness (*left*), velocity (*middle*) and velocity dispersion (*right*) of the 3 sources detected in our CENSORS sample. All maps are 4″×4″ and the ellipse in the bottom left represents the FWHM size of the seeing disk. Contours mark the stellar continuum emission, detected in the same datacube, beginning at the 3σ level and increasing by steps of 3σ.

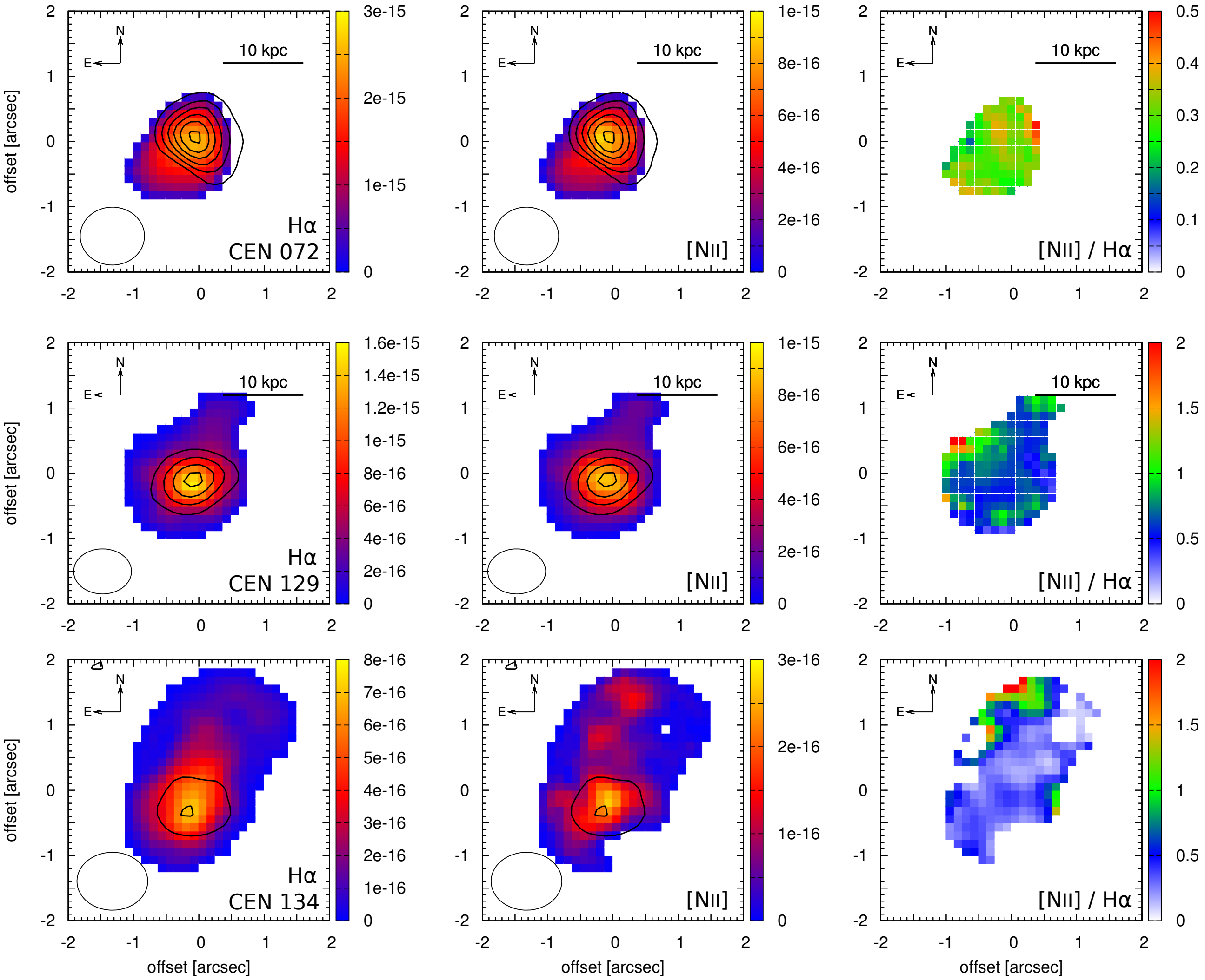

Figure 4.15: Maps of Hα surface brightness (*top*) and [NII]/Hα ratio (*bottom*) of the 3 sources detected in our CENSORS sample.

Table 4.15: IR imaging-spectrometry observational information about the CENSORS sample.

Source ID	alt. ID EISD ; NVSS	RA (J2000)	Dec (J2000)	$z_{\rm UV}$ $^{(1)}$	D_L [Gpc]	ToT $^{(2)}$ [min]	Seeing [arcsec]	K$_{img}$ $^{(3)}$ [mag]
CEN 020	30 ; J094604-211508	09:46:04.55	-21:15:04.8	1.377	9.815	345	...	> 19.4
CEN 072$^{(4)}$	97 ; J094925-203724	09:49:26.00	-20:37:23.7	2.427	19.672	320	1.0×0.9	18.88
CEN 105	138 ; J094724-210505	09:47:24.38	-21:05:02.3	3.377	29.295	440	...	20.70
CEN 118	161 ; J094748-204835	09:47:48.46	-20:48:35.2	2.294	18.369	295	...	19.82
CEN 129	170 ; J095226-200105	09:52:26.41	-20:01:07.1	2.421	19.613	305	0.9×0.7	19.51
CEN 134$^{(4)}$	182 ; J094949-213432	09:49:48.77	-21:34:28.2	2.355	18.965	390	1.1×0.9	20.24

(1): Spectroscopic redshift of Brookes et al. (2008) measured from rest-frame UV emisson lines. — (2): On-source observing time. — (3): $K-$band magnitude of Brookes et al. (2006) (1.0″ aperture), or 2σ limit. — (4): Coordinates provided in Brookes et al. (2008) are incorrect.

4.4.4 Source description

CENSORS 020

Best et al. (2003a) detected two lobes in their VLA observations of CENSORS 020, with a LAS = 7.1″ of and a PA =163°. It is observed compact in our ATCA observations, due to the orientation of the beam. But the extension of the source towards the Northwest is compatible with the observations of Best et al. (2003a). We do not detect any continuum or emission line source in our SINFONI observation of this galaxy.

CENSORS 072

Table 4.16: Emission lines in CENSORS 072.

Line	λ_0 [Å]	$\lambda_{\rm obs}$ [Å]	FWHM [km s^{-1}]	Flux [10^{-16} erg s^{-1} cm^{-2}]
Hβ	4861.3	16662.1 ± 4.0	530 ± 50	3.9 ± 0.8
[OIII]	4958.9	16989.8 ± 4.0	540 ± 50	7.7 ± 1.5
[OIII]	5006.9	17161.1 ± 4.0	540 ± 50	23.3 ± 4.5
[NII]	6548.1	22444.4 ± 5.2	470 ± 50	1.9 ± 0.4
Hα	6562.8	22494.8 ± 5.2	470 ± 50	21.1 ± 4.2
[NII]	6583.4	22565.4 ± 5.2	470 ± 50	5.8 ± 1.2

(1): Rest-frame wavelength. — (2): Observed wavelength. — (3): Full-Width at Half Maximum, corrected for instrumental resolution (in km s^{-1}). — (4): Line flux deduced from the fit (in 10^{-16} erg s^{-1} cm^{-2}).

This source is found at a redshift of z $= 2.427 \pm 0.001$, concording with the previous redshift based on restframe UV lines of Brookes et al. (2008). In its integrated spectrum, we detect the 6 usual lines: Hβ and the [OIII] doublet lies in the $H-$band and the Hα + [NII] complex is found in the $K-$band. The [SII] doublet is not detected. Unfortunately, we have no fluxes at 5.5 and 9.0 GHz due to a mismatch in coordinates, needed for high spatial resolution radio data for this source. However, from Best et al. (2003a), we know that its radio largest angular size is smaller than 0.7″, which is small enough to see that the extended emission line region is larger than the radio emission. Indeed, the emission line region extends over 1.7″×1.2″ (not correcting for the size of the seeing disk) along a Northwest to southeast axis. It presents a velocity gradient of $\sim$ 400 km s^{-1} along the same direction. The stellar continuum lies in the upper Northwest part of the EELR, where the velocity dispersion also tends to be larger (FWHM $\sim$ 700 km s^{-1}) than in the Southeast part (FWHM ∼ 550 km s^{-1}).

CENSORS 105

We detect two radio lobes, separated by 4.3″, nearly along a East-West direction (PA = 94.3°). This source was observed as a compact one by Best et al. (2003a) because of the orientation of the beam of their observations. We do not detect any continuum or emission line source in our SINFONI observation of this galaxy.

CENSORS 118

Similarly to CENSORS 020, this source is observed as a compact source in our ATCA observations. But Best et al. (2003a) detected two lobes, separated by 3.7″ and with a position angle PA = 157°, which is along the worst spatial resolution direction of our observations. We do not detect any continuum or emission line source in our SINFONI observation of this galaxy.

CENSORS 129

Table 4.17: Emission lines in CENSORS 129.

Line	λ_0 [Å]	$\lambda_{\rm obs}$ [Å]	FWHM [km s^{-1}]	Flux [10^{-16} erg s^{-1} cm^{-2}]
Hβ	4861.3	16637.0 ± 4.0	540 ± 60	3.2 ± 0.6
[OIII]	4958.9	16964.1 ± 4.0	550 ± 60	11.0 ± 2.2
[OIII]	5006.9	17135.2 ± 4.0	550 ± 60	33.4 ± 6.6
[NII]	6548.1	22408.6 ± 5.2	620 ± 70	2.8 ± 0.6
Hα	6562.8	22458.9 ± 5.2	620 ± 70	12.7 ± 2.5
[NII]	6583.4	22529.4 ± 5.2	620 ± 70	8.4 ± 1.6

This source is found at a redshift of z = 2.422 ± 0.001, in good agreement with the previous estimate of z = 2.421 based on restframe UV emission lines of Brookes et al. (2008). The integrated spectum of CENSORS 129 displays the usual emission lines: Hβ and the [OIII] doublet in the $H-$band and the strongly blended complex of the Hα line + [NII] doublet in the $K-$band. Its radio emission is resolved in our ATCA observations at 5.5 and 9.0 GHz (see Fig. 4.11), whereas it was found to be compact in previous observations at 1.4 GHz of Best et al. (2003a): it presents two radio lobes along an East-West axis (PA = 94.6°), separated by 2.5″ (20 kpc). It has a steep radio spectrum, with $\alpha = -0.82 \pm 0.01$, from which we extrapolate its flux at 500 MHz restframe: $S_{500,rest} = 50.4$ mJy.

CENSORS 129 has an extended emission line region with a small extension towards the Northwest, being otherwise circular, giving a size of 2.3″×1.7″ (not correcting for the size of the seeing disk) with its major axis along a Northwest-Southeast direction. A stellar continuum is detected at the center of the EELR. Its velocity field presents a gradient of ∼ 200 km s^{-1}, roughly aligned with the radio axis, along an East-West axis. The Northwest extension has the most strongly blueshifted emission (−200 km s^{-1}). The velocity dispersion is nearly constant over most of EELR, whith FWHM ∼ 600 km s^{-1}.

CENSORS 134

We find a redshift of z = 2.355±0.001 for CENSORS 134, again agreeing within the errors with the previous one estimated from restframe UV lines (Brookes et al., 2008). In the integrated spectrum of CENSORS 134, we detect Hβ and the [OIII] doublet in the $H-$band and the Hα and [NII] emission lines are present in the $K-$band. In the radio, this source is very extended at 1.4 GHz (LAS = 22.4″ and PA = 125° Best et al.,

Table 4.18: Emission lines in CENSORS 134.

Line	λ_0 [Å]	$\lambda_{\rm obs}$ [Å]	FWHM [km s^{-1}]	Flux [10^{-16} erg s^{-1} cm^{-2}]
Hβ	4861.3	16307.9 ± 1.9	330 ± 30	3.2 ± 0.6
[OIII]	4958.9	16635.4 ± 1.9	340 ± 30	11.0 ± 2.2
[OIII]	5006.9	16796.4 ± 1.9	340 ± 30	33.2 ± 6.6
[NII]	6548.1	21964.4 ± 2.5	490 ± 50	1.2 ± 0.2
Hα	6562.8	22013.7 ± 2.5	500 ± 50	9.8 ± 2.0
[NII]	6583.4	22082.8 ± 2.5	490 ± 50	3.7 ± 0.7

2003a) and at 5.5 GHz (LAS = 21.9″ and PA = 131°) but we do not detect the second lobe in our 9.0 GHz observations. It has a steep radio spectrum, with $\alpha = -1.08 \pm 0.09$, leading to an extrapolated flux at 500 MHz restframe of $S_{500,rest} = 88.4$ mJy.

The extended emission line region of CENSORS 134 spans 3.1″×1.8″ (not correcting for the size of the seeing disk), with its major axis aligned along a Northwest to Southwest direction. A stellar continuum is detected in the Southern part of the EELR. The velocity field is consistent with the systematic redshift, with most of the pixels being in the range ±50 km s^{-1} around the systemic velocity. The velocity dispersion is higher in the Southern part of the EELR, with FWHM ∼ 550 km s^{-1} and the gas is more quiescent in the Northern part, where FWHM ∼ 300 km s^{-1}.

4.5 Ensemble properties of the CENSORS and NVSS samples

After discussing each of our targets individually and in detail, we will now turn to characterizing the overall properties of our sample. The bright, rest-frame optical emission lines of the warm ionized gas of high-redshift galaxies contain important information about the gas properties of these galaxies, which taken together will enable us to draw conclusions about the nature and evolutionary state of these galaxies, and to search for putative signatures of AGN feedback. After summarizing the radio properties derived from our own observations and measurements from the literature, we will derive these properties in the reminder of this section for the NVSS and CENSORS samples together.

Although we do not have a complete sample in a strict statistical sense, this is a fairly common situation for studies of the spatially resolved properties of small to mid-sized samples of high-redshift galaxies (*e.g.*, Förster Schreiber et al., 2006, 2009), and our sample size is comparable to most of these studies. It is also important to note that our study is a parameter, not a population study. This means that we wish to analyze certain source properties as a function of the AGN characteristics of our sources. In other words, we ask for the "How", not for the "How many". Therefore, we have to sample the range of AGN properties as regularly as we can, and can put less emphasis on matching, *e.g.*, the shape of the radio luminosity function. For this reason, we do not require a statistically complete sample to identify global trends in our data.

4.5.1 Rest-frame optical continuum

We detect rest-frame optical continuum emission in eleven sources, eight from the NVSS, and three from the CENSORS sample. At redshifts z = 2−3, the observed $H-$ and $K-$bands correspond roughly to the rest-frame $V-$ and $R-$bands, and at redshifts z = 3−4, the rest-frame $B-$ and $V-$bands.

Since continuum fluxes in all sources are too faint to measure the detailed spectral profiles or even spectral slopes, we merely extract the spectrally integrated continuum image. We detect the continuum in 8/9 NVSS sources, and in all targets from the CENSORS sample. We generally find only one, spatially unresolved, continuum source, with one notable exceptions. In NVSS J0040 we find two very faint unresolved continuum emitters of about equal flux, perhaps indicating an on-going interaction of two galaxies, or AGN light scattered on extended dust (*e.g.*, Hatch et al., 2009). Both blobs are roughly along the radio jet axis, somewhat reminiscent of the "alignment effect" found in more powerful HzRGs (Vernet et al., 2001; Tadhunter et al., 1998).

4.5.2 Morphology of the extended emission line gas

Gas morphologies and kinematics are the two primary sets of constraints where the advantages of imaging spectrographs become particularly evident. Amongst our twelve targets, ten are spatially resolved into 2−10 spatial resolution elements along the major axis of the bright emission-line regions. The line images we obtain allow us to measure beam-matched isophotal sizes down to the 3σ detection limit of our data of typically $\sim 10^{-16}$ erg s^{-1} cm^{-2} arcsec^{-1} (see Table 4.20 for details).

One striking result of our SINFONI data is the great diversity in the gas morphology and kinematics of our targets. The sizes of emisson-line regions in our galaxies range from about 5−6 kpc, corresponding to our resolution limit, to very extended sources where line emission is detected over at least 30 kpc (*e.g.*, in NVSS J1449), and potentially more because we cannot exclude in all cases (*e.g.*, NVSS J1449) that parts of the emission-line region fall outside the $8'' \times 8''$ field of view of SINFONI. Resolved emission-line regions are often elongated with ellipticities between 0.2 and 0.7. We do find a correlation between elongation and size, as illustrated by Fig. 4.16, but this is likely an artifact from the relatively low spatial resolution. Typical emission-line surface brightnesses are comprised between $\sim 10^{-16}$ (our detection limit) and few $\times 10^{-15}$ erg s^{-1} cm^{-2} arcsec^{-2} (*e.g.*, see Fig. 4.6).

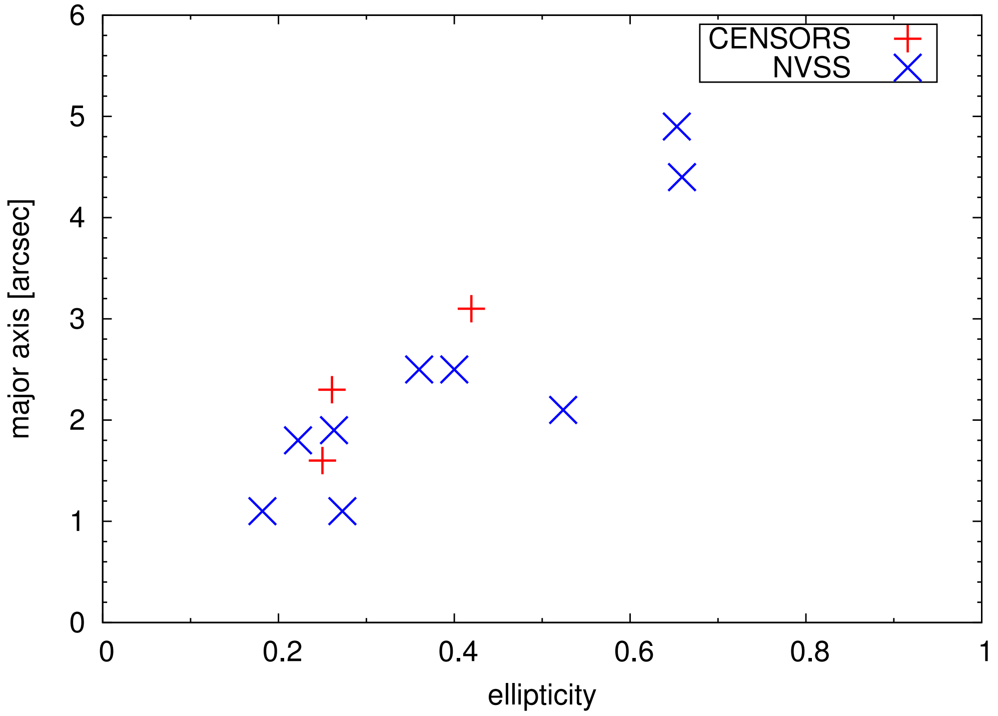

Figure 4.16: Major-axis of the extended emission line as a function of its ellipticity. Sources that are clearly resolved also tend to have higher ellipticities.

Since we consider the position of the continuum peak an approximate measure of the location of the central regions of our HzRGs (see Nesvadba et al., 2008, for a justification), we can evaluate for eight galaxies with spatially resolved gas and a single rest-frame optical continuum peak, whether the line emission extends symmetrically about the nucleus. It is interesting to note that this is not always the case, in particular we note a trend that the galaxies with the most regular velocity fields also appear to have gas that is well centered about the nucleus, as would be expected from a more dynamically relaxed system. (While lopsidedness does exist even in isolated low-z galaxies, it would need to reach extreme levels to be seen at a resolution of 5 kpc and more.) In NVSS J0040, the source with the two equally faint continuum emitters, most of the gas extends between the two continuum sources. This may somewhat favor the interpretation that the continuum is from two regions of scattered light rather than a merging galaxy pair, where we would expect at least some line emission to be associated with the nuclear regions of each interacting galaxy.

4.5.3 Kinematics

Our sample shows a diverse set of gas kinematics, where velocity fields range from very regular, dominated by a single, smooth large-scale velocity gradient, to very irregular velocity fields. The total velocity gradients are typically relatively small, of-order v $= 200-300$ km s^{-1}. Given that the spatial resolution of our data is not very high for many of our sources, this gradient may appear lower than the intrinsic velocity gradient owing to beam smearing effects (see Chapter 3). This may increase intrinsic values by up to about a factor two compared to what is measured, which is comparable or less than the unavoidable uncertainty from the unknown inclination of the gas relative to the line of sight. Visual inspection of Fig. 4.6 shows that at most two galaxies have regular velocity gradients without very obvious perturbations, NVSS J0129 and CEN 072, all other galaxies have significantly perturbed velocity fields. Even NVSS J0129 may have some irregularities in the blueshifted gas of the South-Western hemisphere, which may be blurred by the size of the seeing disk.

A good example for a galaxy with an irregular velocity field is CEN 134. CEN 134 and other galaxies with irregular velocity fields exhibit sudden velocity jumps at least in parts of the emission-line region, and at signal-to-noise levels where this irregularity must be intrinsic to our sources, over regions consistent with at least the size of the seeing disk (which is oversampled in the seeing-limited SINFONI mode, with $4-6$ pixels per FWHM of the PSF). This would not be the case for simple noise features. It is interesting that these velocity jumps are often associated with the continuum center, where we would expect the galaxy nucleus, and hence the AGN. While such gradients could be indicative of gravitational motion as well as outflows, it is immediately clear that the irregular fields of line widths are at variance with the interpretation that the gas in these galaxies is in an overall quiescently rotating disk configuration.

The line widths in our galaxies are overall relatively broad, FWHM $= 400-1000$ km s^{-1}, down to the spatial resolution limit of our data. This is more than what is attributed to the overall velocity gradients and beam smearing. We will come back to the interpretation of these kinematic properties in § 4.9.1.

Although all sources are dominated by the line emission from the radio galaxy itself, a few show additional emission-line components (*e.g.*, NVSS J0040, NVSS J2019 § 4.3.4), which may originate from the environment of the radio galaxy rather than that galaxy proper. We will further discuss these sources in § 4.7.

4.5.4 Extinction

The extended gas of powerful HzRGs is often very dusty (Nesvadba et al., 2008), leading to extinction of several magnitudes in the rest-frame $V-$band. We measure the Hα/Hβ decrement to estimate the extinction in the warm ionized gas of our sources, assuming an intrinsic Balmer decrement of Hα/H$\beta = 2.9$ and adopting the galactic extinction law of Cardelli et al. (1989). We detect Hα in all seven galaxies where it falls into the atmospheric windows (for NVSS J0040 and NVSS J2342, which are at z $\gtrsim 3.5$, we cannot observe Hα from the ground). Hβ is detected in 8/9 of the integrated spectra of the galaxies of our sample, and six galaxies have both lines in common. For NVSS J2019, we can only set an upper limit to the Hβ flux and consequently, we give lower limits to the extinction. We find typical extinctions between formally $A_{H\beta} = 0$ mag (in NVSS J0304 and NVSS J2106) and up to $A_{H\beta} = 2.2$ mag, where $A_{H\beta} = A_V - 0.14$ mag. Results of individual sources are listed in Table 4.19.

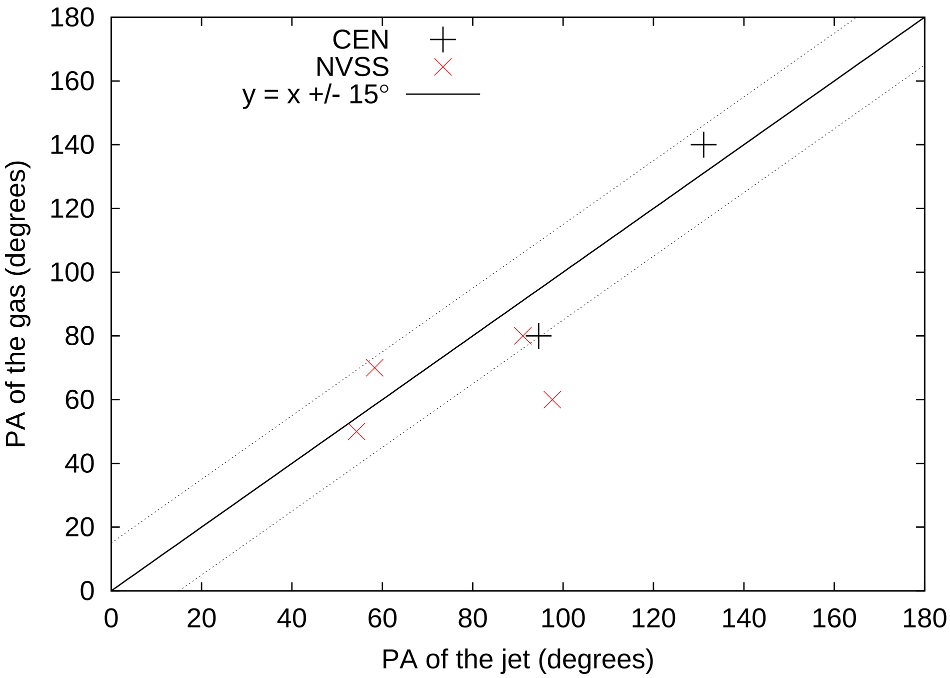

Figure 4.17: Position angle of the extended emission line region as a function of the position angle of the radio jet, when both are unambiguously determined. The red point that stands clearly off the correlation corresponds to NVSS J2106, which will be further studied in Chapter 5.

4.5.5 Electron densities

The ratio of the lines in the [S II]$\lambda\lambda$6716,6731 doublet is density-sensitive over large ranges in density from about 100 cm^{-3} to 10^5 cm^{-3} and can be used to estimate the electron density in the emission-line gas (see § 1.6.2 and Osterbrock, 1989). These lines are well detected in two galaxies: in NVSS J0129, where they are broad and blended and in NVSS J2106, where they are more accurately fitted (see Fig. 4.5). We find $n_e = 750$ cm^{-3} for NVSS J0129 and $n_e = 500$ cm^{-3} for NVSS J2106, assuming a temperature $T = 10^4$ K. Similar results were found in other HzRGs (*e.g.*, Nesvadba et al., 2006, 2008). We adopt a fiducial value of $n_e = 700$ cm^{-3} for the other galaxies of our sample.

4.5.6 Ionized gas mass

Estimating the mass of warm ionized gas in high-redshift galaxies is straight-forward, and can be done from measuring the flux of the bright Balmer lines and the electron density in the gas. The basic principle of the measurement is to count the number of recombining photons. Assuming case B recombination, we can estimate the ionized gas mass following Osterbrock (1989) by setting:

$$\mathrm{M_{ion}} = 9.73 \times 10^8 \, \frac{\mathcal{L}_{\mathrm{H}\alpha}}{10^{43}\,\mathrm{erg\,s^{-1}}} \, \frac{10^2\,\mathrm{cm}^{-3}}{n_e} \, \mathrm{M}_\odot$$

where $\mathcal{L}_{\mathrm{H}\alpha}$ is the Hα luminosity, corrected for extinction, and n_e is the electron density.

We find masses of ionized gas in our sample in the range $3-73 \times 10^8$ $\mathrm{M}_\odot$ when using extinction corrected luminosities and in the range $1 - 14 \times 10^8$ $\mathrm{M}_\odot$ when using the observed luminosities of Hα without taking extinction into account (see Table 4.19).

This is generally less than in previous studies of more powerful radio galaxies (*e.g.*, Nesvadba et al., 2006, 2008), which have masses of ionized gas from 10^9 to a few $\times 10^{10}$ $\mathrm{M}_\odot$.

4.5.7 Emission-line diagnostics

Table 4.19: Physical quantities derived from observations.

ID$^{(1)}$	A(Hβ)$^{(2)}$	$\mathcal{L}_{\mathrm{H}\alpha}$ $^{(3)}$	$\mathcal{L}^{\mathrm{corr}}_{\mathrm{H}\alpha}$ $^{(4)}$	$\mathcal{L}_{[\mathrm{O\,III}]}$ $^{(5)}$	n_e $^{(6)}$	M$_{\mathrm{ion}}$ $^{(7)}$	M$^{\mathrm{corr}}_{\mathrm{ion}}$ $^{(8)}$	Δv$^{(9)}$	FWHM$^{(10)}$
	[mag]	[$\times 10^{43}$ erg s^{-1}]			[cm^{-3}]	[10^8 M$_\odot$]		[km s^{-1}]	
NVSS J0024	0.0	5.9	5.9	14.8	(700)	8.2	8.2	(500)	600
NVSS J0040	...	...	$\geq$ 18.0	70.5	(700)	...	$\geq$ 25.1	(350)	700
NVSS J0129	0.7	2.5	4.4	8.7	750	3.5	6.1	350	940
NVSS J0304	0.0	2.2	2.2	11.3	(700)	3.0	3.0	(350)	680
NVSS J1449	1.9	2.3	10.9	6.7	(700)	3.1	15.2	800	440
NVSS J2019	$\geq$ 1.7	0.8	$\geq$ 3.6	1.5	(700)	1.2	$\geq$ 5.0	(300)	550
NVSS J2046	0.0	2.9	2.9	5.1	(700)	4.0	4.0	(180)	950
NVSS J2106	0.0	4.9	4.9	20.8	500	6.7	6.7	600	370
NVSS J2342	...	...	$\geq$ 12.7	42.7	(700)	...	$\geq$ 17.6	450	650
CEN 072	2.0	9.8	51.2	10.8	(700)	13.6	71.1	300	580
CEN 129	1.0	5.8	13.6	15.4	(700)	8.1	18.9	400	580
CEN 134	0.2	4.2	5.0	14.3	(700)	5.9	7.0	(200)	410

(1): Source ID. — (2): Extinction (in magnitude) at Hβ wavelength, deduced from the measured Hα/Hβ line ratio and assuming an intrisic Balmer decrement of 2.9. — (3): Hα luminosity (in 10^{43} erg s^{-1}), uncorrected from extinction. — (4): Hα luminosity (in 10^{43} erg s^{-1}), corrected from extinction. For NVSS J0040 and NVSS J2342, we give lower limit, from Hβ flux and assuming no extinction. — (5): [O III]λ5007 luminosity (in 10^{43} erg s^{-1}). — (6): Electron density (in cm^{-3}), deduced from the [S II]λ6716/[S II]λ6731 line ratio, assuming a temperature of 10^4 K. When the [S II] doublet is too faint to be measured, we choose a fudicial value of $n_e = 700$ cm^{-3}. — (7): Mass of ionized gas (in 10^8 M$_\odot$), assuming case B recombinaison and following Osterbrock (1989) and using observed Hα luminosities. — (8): Mass of ionized gas (in 10^8 M$_\odot$), assuming case B recombinaison and following Osterbrock (1989) and using extinction corrected luminosities. — (9): Value of the velocity gradient, Δv, across the ionized gas region (in km s^{-1}), if observed. — (10): Mean value of the velocity dispersion (in km s^{-1}).

Bright optical line emission in powerful quasars typically originates from gas that is photoionized by the comparably hard spectrum of the quasar rather than by star formation (*e.g.*, Kewley et al., 2001), however, in moderately powerful AGN, star formation can also play a role (Villar-Martín et al., 2008). The most powerful HzRGs are generally buried, radio-loud quasars (*e.g.*, Overzier et al., 2005) where the bright quasar emission very naturally plays a major role for the gas ionization. Our galaxies are somewhat less extreme in their radio properties (although still powerful compared to most low-redshift sources), which makes it worthwhile to investigate more explicitly, if their obscured AGN play a similar role in photoionizing the gas.

Baldwin, Phillips, & Terlevich (1981, see also Veilleux & Osterbrock 1987) introduced a set of diagnostic diagrams which allow for a simple, largely empirical analysis of diagnostic emission-line ratios of what dominates the ionization of the gas in galaxies, star formation or AGN (through photoionization and/or shocks). These diagrams compare the strength of low and high-ionization lines, most commonly [N II]λ6583 and [O III]λ5007, each normalized to the flux of a nearby Balmer line of hydrogen, *i.e.*, Hα and Hβ, respectively, to mitigate against the effects of extinction. Galaxies where most gas is in H II regions and heated by young stars falls along a sequence in this diagram, from which low-redshift AGN branch off towards higher [N II]/Hα and [O III]/Hβ ratios. The AGN branch is divided into LINERs with relatively low [O III]/Hβ ratios, and Seyfert-type AGN, where the line emission is mainly powered by photoionization. LINER-like spectra can be explained by shocks (although not necessarily uniquely), whereas the photoionization in Seyfert-like AGN may either come directly from the photons emitted by the AGN, or from X-ray emission produced by shocked gas in the sourrounding interstellar medium, in particular for fast shocks with velocities > 100 km s^{-1} (*e.g.*, Allen et al., 2008), or from a mixture of both.

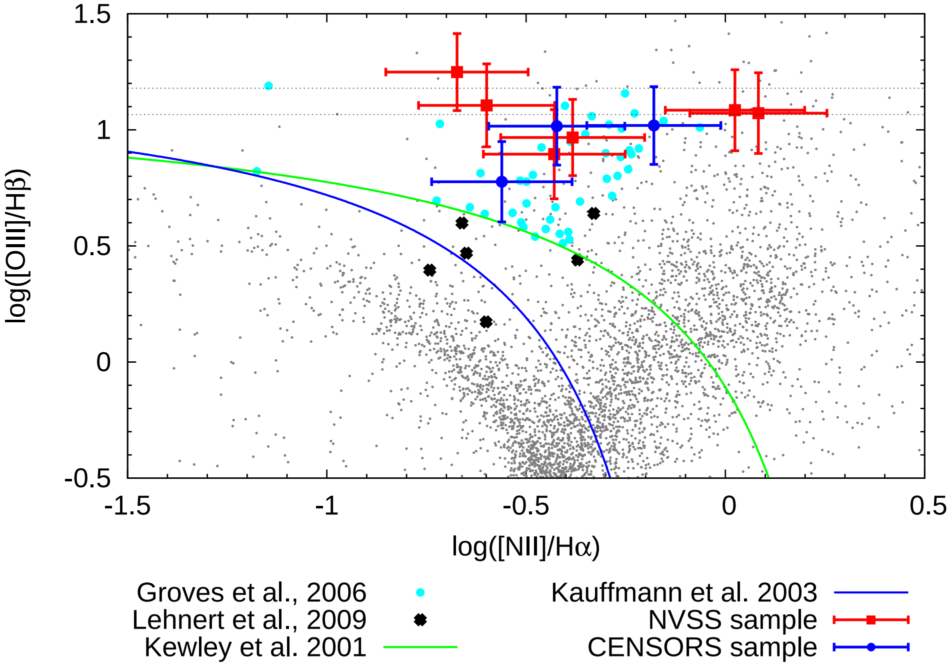

Figure 4.18: BPT diagram of all our sources for which Hα and Hβ are detected. All fall off the star-formation branch, however, they do not fall onto the "classical" AGN branch either, but have higher [OIII]/Hα ratios compared to their [NII]/Hα ratios. For NVSS J0040 and NVSS J2342, which Hα and [NII] emission do not fall in atmospheric windows, we just indicate their [OIII] to Hβ ratio by dashed lines. The comparison sample of Groves et al. (2006) is for low-metallicity AGN from the SDSS, whereas the Lehnert et al. (2009) sample consists of UV/optically selected z $\sim$ 2 galaxies with intermediate to high stellar mass and active star-formation.

Fig. 4.18 shows that our sources do not fall onto the star-formation branch in the diagram. They do not fall onto the branch of "classical" low-z AGN either, but have higher [OIII]/Hβ ratios for their measured [NII]/Hα ratios. Finding AGN in this region of the diagram may point towards relatively low gas-phase metallicities (Groves et al., 2006), relatively diffuse clouds that are highly ionized in their outer regions, but do not have very large partially ionized zones (Lehnert et al., 2009), high gas pressures (Lehnert et al., 2009), or towards a mixture of shocks and photoionization causing the line emission (Newman et al., 2013). This refers in particular to NVSS J1449, NVSS J2106, NVSS J2046 and NVSS J0024 (from top to bottom) which have $-0.7 \leq \log([\text{NII}]/\text{H}\alpha) \leq -0.4$. A detailed analysis of the emission-line properties of our galaxies is beyond the scope of our work, and would ideally be done with a combination of rest-frame optical and UV lines (Humphrey et al., 2009).

4.6 AGN and black-hole properties

We start this section by discussing the global AGN properties of our sources as they can be derived from the properties of the radio jets and extended emission-line regions. Subsequently, we will discuss the finding of broad (FWHM $\gg 1000$ km s^{-1}) Hα emission lines in some of our sources, in particular NVSS J2019, where we attribute the broad Hα line to nuclear broad-line emission from the direct vicinity of the supermassive black hole. These are very interesting probes of the active galactic nucleus itself, and very rare in high-redshift radio galaxies, in which the direct line of sight into the AGN is usually obscured.

4.6.1 Centimeter radio continuum

Within our broad survey of radio-selected AGN at redshifts $z \geq 2$, the role of the present sources is to bridge the gap of about 2−3 orders of magnitude in radio power between typical dusty starburst galaxies at these redshifts – the galaxy population where AGN feedback is supposedly at work – and the most powerful radio galaxies, in which AGN feedback signatures can be observed fairly easily, but which are also intrinsically very rare. At the reference frequency of 500 MHz in the rest-frame, which we mainly chose for compatibility with the sample of Miley & De Breuck (2008), they span a range from 2×10^{27} W Hz^{-1} to 1×10^{29} W Hz^{-1}, or from 3×10^{26} W Hz^{-1} to 6×10^{27} W Hz^{-1} at 1.4 GHz (observed ; see Tables 4.2 and 4.14). Radio spectral indices of our sources are between $\alpha = -0.8$ and -1.4 without evidence for spectral breaks (see Figs. 4.3 and 4.12). Finding suitable samples of radio-selected sources (or even radio-loud obscured AGN) at these redshifts with firm spectroscopic redshifts and good radio observations with of-order arcsec resolution and covering a good dynamic range becomes increasingly difficult.

For comparison, an intensely star-forming HyLIRG with $\mathcal{L}_{\rm FIR} = 1 \times 10^{13} \mathcal{L}_\odot$ of infrared luminosity would produce a rest-frame 1.4 GHz radio power of 10^{25} W Hz^{-1}, assuming a far-infrared-to-radio luminosity ratio of 2.0, as found for high-redshift sub-millimeter galaxies (*e.g.*, Michalowski et al., 2011), and a radio spectral index typical of star formation of $\alpha = -0.7 - -0.8$. The brightest individual, not gravitationally lensed high-redshift FIR emitting galaxies known are up to few $10^{13} \mathcal{L}_\odot$. Thus we do not expect significant contamination from centimeter radio emission from star formation in our sources.

Our sources cover a range of radio sizes and morphologies, ranging from single, compact sources at the size of the ATCA beam (typically $1''$−$3''$ at the highest frequencies of 9 GHz) to single compact sources which potentially have faint extended structures (if this is not dominated by residuals from the cleaning algorithm), to doubles with distances of up to $25''$. Only in one case do we potentially detect the radio core along with the lobes. Although this spatial resolution is lower by a factor 4−5 than what can be achieved with the JVLA at the highest resolutions and at similar frequencies, and is below the resolution of our SINFONI cubes, it is sufficient to distinguish between radio sources which have and have not yet broken out from the ISM of the host galaxy (*i.e.*, sources with sizes below or above of-order 10 kpc). This is the most important distinction for our purposes. Most of our targets are unfortunately too far South to be observed with the JVLA with a good, symmetric beam. At good signal-to-noise ratios and for unresolved sources, observed size estimates can of course contrain source sizes smaller than the beam.

4.6.2 Bolometric AGN emission

First of all, we consider the [OIII]λ5007 luminosity (Table 4.19) as a signature of the nuclear activity in our galaxies. Even if neglecting extinction, our measured [OIII]λ5007 line fluxes indicate line luminosities in the range of 0.1−few $\times 10^{44}$ erg s^{-1}, in the range of powerful quasars and only somewhat fainter than the [OIII]λ5007 luminosities of the most powerful HzRGs. Correcting the fluxes for extinction, which is relatively low in our targets (see § 4.5.4), increases these values by factors of a few. Using the relationship of Heckman et al. (2004), this would correspond to bolometric luminosities of the AGN of-order $\mathcal{L}_{\rm bol} = 3500 \times \mathcal{L}_{\rm [OIII]}$ or few 10^{46-47} erg s^{-1}. Although this estimate is known to overestimate the intrinsic bolometric luminosities of Quasars in radio-loud sources, this does not change the result at an order-of-magnitude-level as we are stating here.

4.6.3 Radio jet lifetime and mechanical energy

To compare the kinetic energy of the ionized gas seen in the EELR with the power of the radio jet, we have to assess the typical lifetime of the radio jet, τ, over which the radio jet power can be integrated in order to obtain its time-integrated energy. We calculate τ by dividing half of the largest angular scale of the radio emission of each source (see Tables 4.2 and 4.14) by the jet advance speed, that we assume to be $0.1 \times c$ (Wagner et al., 2012). This gives jet lifetimes in the range of $2 - 70 \times 10^5$ yrs and is in the general range

Table 4.20: Morphologies of the extended emission line regions of sources in our NVSS and CENSORS samples.

Source ID	major axis$^{(1)}$ [arcsec]	minor axis$^{(2)}$ [arcsec]	seeing$^{(3)}$ [arcsec]×[arcsec]	RMS($\Sigma_{[\mathrm{O\,III}]}$) $^{(4)}$ [$\times10^{-17}$ erg s^{-1}	RMS($\Sigma_{\mathrm{H}\alpha}$) $^{(5)}$ cm^{-2} arcsec^{-2}]
NVSS J0024	2.5	1.5	0.8×0.7	7.5	6.4
NVSS J0040	2.5	1.6	0.7×0.6	3.0	…
NVSS J0129	1.9	1.4	0.9×0.8	2.9	2.8
NVSS J0304	1.8	1.4	1.2×1.0	5.5	2.1
NVSS J1449	4.4	1.5	0.9×0.8	2.3	2.4
NVSS J2019	1.1	0.8	0.9×0.8	4.8	2.6
NVSS J2046	1.1	0.9	0.7×0.6	5.5	5.9
NVSS J2106	4.9	1.7	0.7×0.6	6.8	4.1
NVSS J2342	2.1	1.0	1.1×1.0	5.6	…
CEN 072	1.6	1.2	1.0×0.9	5.5	4.9
CEN 129	2.3	1.7	0.9×0.7	3.2	3.5
CEN 134	3.1	1.8	1.1×0.9	2.4	2.9

(1): Size of the major axis of the extended emission line regions (in arcsec). — (2): Size of the minor axis of the extended emission line regions (in arcsec). — (3): Seeing disk (at FWHM, in arcsec). — (4, 5): 1σ error on the surface brightness around the two main emission lines used in this work ([O III] and Hα), measured over a spectral window of 100−Å centered on the wavelength of the corresponding emission line (in units of $\times10^{-17}$ erg s^{-1} cm^{-2} arcsec^{-2}).

of few 10^6 yrs found by Blundell & Rawlings (1999) from spectral ageing considerations of powerful HzRGs (see also Kaiser & Alexander, 1997).

4.6.4 Jet kinetic energy

We estimate the power in the radio jet with the estimate of Willott et al. (1999), based on the 151 MHz restframe flux $\mathcal{L}_{151\ \mathrm{MHz}}$ of the galaxy:

$$\mathcal{L}_{\mathrm{jet}} = 3\times10^{45}\times f^{3/2}\times\left(\frac{\mathcal{L}_{151\ \mathrm{MHz}}}{10^{28}\ \mathrm{W\ Hz^{-1}\ sr^{-1}}}\right)^{6/7}\ \mathrm{erg\ s^{-1}}$$

where f represents the astrophysical uncertainties and is typically between 1 and 20. Here, we use $f = 10$. We use the fit to the radio SED of our sources to estimate their 151 MHz restframe flux, $S_{151\ \mathrm{MHz}}$, and then translate this flux into a luminosity by using their luminosity distance D_L, given by the cosmology:

$$\mathcal{L}_{151\ \mathrm{MHz}} = \frac{4\pi}{1+z}\times D_L^2\times S_{151\ \mathrm{MHz}}$$

Other estimates of the jet power exist in the literature, *e.g.*, by comparing the work needed to inflate the X-ray cavities observed in the hot plasma surrounding local BCGs with the radio flux of the BCG at 327 MHz restframe. With this approach, Bîrzan et al. (2008) find this relation:

$$\log\left(\frac{\mathcal{L}_{\mathrm{jet}}}{10^{42}\ \mathrm{erg\ s^{-1}}}\right) = (0.51\pm0.07)\times\log\left(\frac{\mathcal{L}_{327\ \mathrm{MHz}}}{10^{24}\ \mathrm{W\ Hz^{-1}}}\right) + (1.51\pm0.12)$$

If we use this relation, and still use our fit to the radio SED of our sources to estimate the 327 MHz restframe flux, we find radio jet powers much lower than with the expression given by Willott et al. (1999), especially for the most luminous sources. However, a more recent study by Cavagnolo et al. (2010), based on the same sample, but extended at lower radio luminosities, find an empirical relation in good agreement with the relation of Willott et al. (1999), provided that $f \simeq 10$. All the results are given in Table 4.21. However, this illustrates that the estimate of the mechanical jet power based on radio luminosity is reliable at the order of magnitude level only.

4.6.5 Broad line components and black-hole properties

Constraining the AGN properties of high-z radio galaxies is notoriously difficult, since it is the very nature of radio galaxies that the direct line of sight into the nucleus is obscured. However, in a few very powerful radio galaxies broad Hα lines have been observed (*e.g.*, Nesvadba et al., 2011b) that are likely to trace the gas kinematics within a few light-days from the supermassive black hole. Such lines can be used to constrain the mass of the black hole and its accretion rate (*e.g.*, Greene & Ho, 2005).

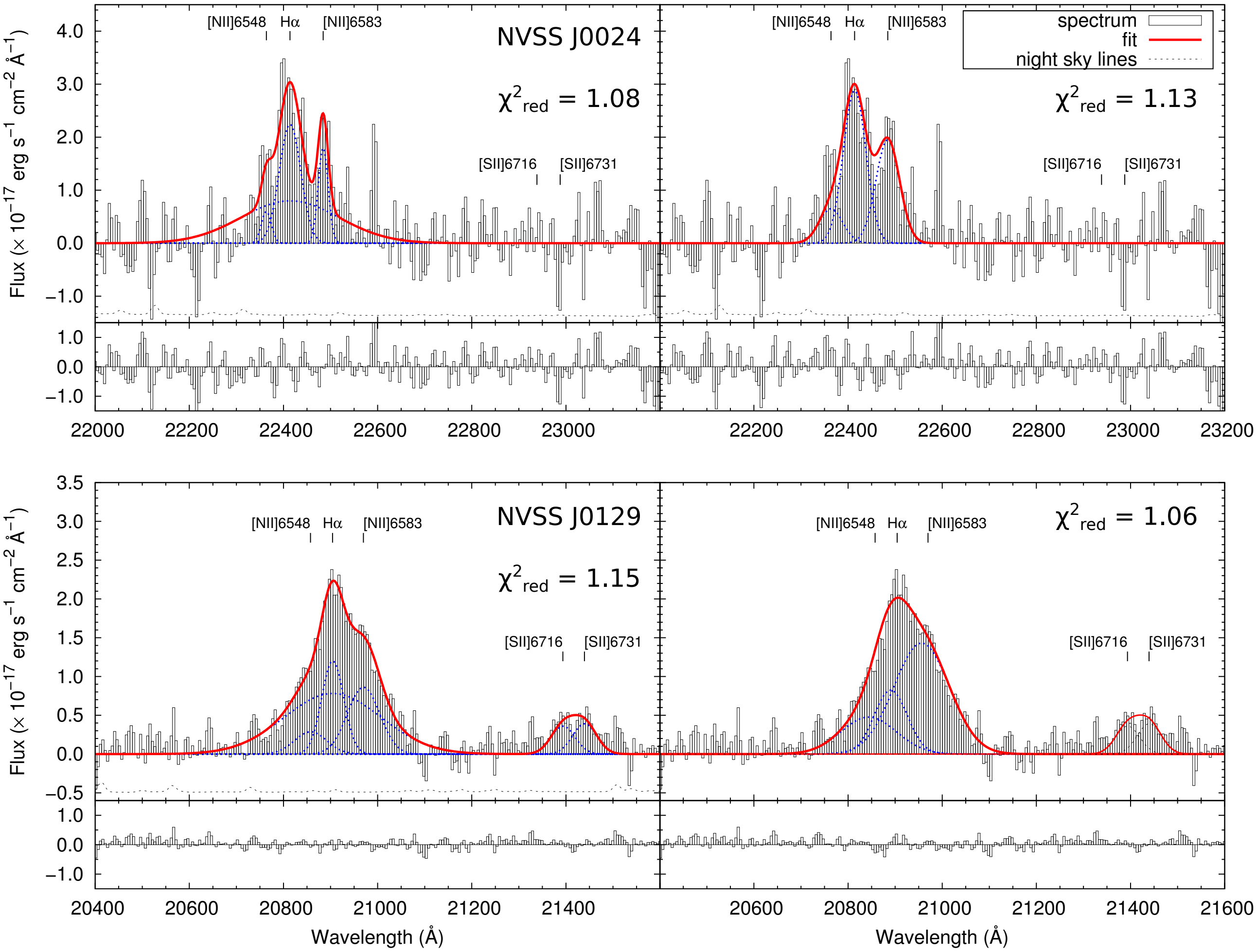

Figure 4.19: Comparison of the fits of the Hα + [NII] emission lines complex of NVSS J0024 and NVSS J0129, with (*left*) and without (*right*) an additional broad Hα component. While both fits are statistically acceptable, the additional broad Hα component is physically motivated (*e.g.*, for NVSS J0129, the [NII] flux is greater than the Hα flux if the fit does not include an additional component).

As discussed in § 4.2, we fitted the spectra of our sources with single Gaussian components. Within the uncertainties of our data this yields acceptable fits to the integrated spectra of most targets and for most emission lines. However, three of our targets, NVSS J0024, NVSS J0129 and NVSS J2019, require additional Hα components, as shown in Fig. 4.19. These components have FWHM $\geq$ 3000 km s^{-1}, significantly broader than the systemic line emission. Moreover, NVSS J2342 clearly shows a second [OIII]λ5007 component. Fainter, marginally detected broad [OIII]λ5007 components may also be present in NVSS J0024 and NVSS J0040.

The origin of broad (FWHM $\gg$ 1000 km s^{-1}) Hα line emission at high redshift has either been attributed to winds driven by starbursts (*e.g.*, Le Tiran et al., 2011; Shapiro et al., 2009; Nesvadba et al., 2007a) or active galactic nuclei on galaxy-wide scales (*e.g.*, Alexander et al., 2010; Nesvadba et al., 2011b; Harrison et al., 2012), or alternatively, to gas motions in the deep gravitational potential wells very near the supermassive black hole (*e.g.*, Alexander et al., 2008; Coppin et al., 2008; Nesvadba et al., 2011b). For galaxies like NVSS J2342, and perhaps NVSS J0024 and NVSS J0040, which have only relatively broad [OIII] components, it is clear that the broad line emission probes gas in the narrow-line region or outside, at larger galactocentric radii. This is similar to high-z quasars (*e.g.*, Harrison et al., 2012; Nesvadba et al., 2011c), since forbidden lines are collisionally de-excited at the high electron densities of the broad-line region (*e.g.*, Sulentic et al., 2000). The [OIII] emissivity is more sensitive to electron temperature and excitation conditions than the total gas mass, making it unlikely that blue [OIII] components trace significant fractions of the ISM.

For galaxies where we only observe broad components in the Hα + [NII]$\lambda\lambda$6548,6583 complex, with widths that make it difficult to uniquely associate the broad line emission with either line, the situation is less clear. Line widths of $\geq$ 3000 km s^{-1} have been considered as evidence of BLRs in submillimeter galaxies and quasars at z $\sim$ 2 (Alexander et al., 2008; Coppin et al., 2008), however, extended emission lines with FWHM $\sim$ 3500 km s^{-1} have been observed in very powerful radio galaxies at similar redshifts (*e.g.*, Nesvadba et al., 2006), and given the generally large line widths in our sources, it is clear that the ISM is experiencing a phase of strong kinetic energy injection.

Amongst our sources, NVSS J2019 clearly stands out in terms of line width and line luminosity. It is the only galaxy with a line as broad (FWHM = 8250 km s^{-1}) and as luminous ($\mathcal{L} = 1.1 \times 10^{44}$ erg s^{-1}) as the Hα emission from nuclear broad-line regions in powerful radio galaxies at similar redshifts (Nesvadba et al., 2011b), and exceeds the "typical" bona-fide AGN-driven winds by nearly an order of magnitude in line width. We do not find a broad component in [OIII] which would correspond to that seen in Hα.

Following Greene & Ho (2005) we can use the width and the luminosity of the Hα line to estimate the mass and accretion rate of the supermassive black hole (see Nesvadba et al., 2011b, for possible caveats of using these relationships for high-redshift radio galaxies) $\mathrm{M_{BH}} = 2.1^{+2.2}_{-1.1} \times 10^9$ M$_\odot$ and $\mathcal{L}_{\mathrm{bol,AGN}} = 1.4 \times 10^{12} \mathcal{L}_\odot$ and $\mathcal{L}_{\mathrm{bol}} = 5.3 \times 10^{45}$ erg s^{-1}. The Eddington luminosity of a $\mathrm{M_{BH}} = 2.1^{+2.2}_{-1.1} \times 10^9$ M$_\odot$ black hole is $\mathcal{L}_{\mathrm{Edd}} = 2.8 \times 10^{47}$ erg s^{-1}, corresponding to an Eddington ratio of 2%. These values are well within the range found for more powerful radio galaxies at z $\geq$ 2 (Nesvadba et al., 2011b), including the suspiciously low black-hole Eddington ratio compared to many bright high-redshift quasars (see Nesvadba et al., 2011b, for a detailed discussion). We caution however that we did not take into account that the extinction might be greater than that of optically selected quasars. Our non-detection of Hβ implies A(Hβ) $\geq$ 1.7, which, taken at face value, would correspond to a black-hole mass that exceeds our estimate by about a factor 2, with little impact on our overall results.

The more moderate line widths (FWHM $\geq$ 3000 km s^{-1}) and line luminosities of NVSS J0024 and NVSS J0129 make interpreting the nature of the broad line components in these galaxies more difficult, and it is not possible with the present data alone to clearly distinguish between the wind and the black-hole hypothesis. Under the hypothesis that these lines probe the AGN broad-line region, we find, with the same approach as above and using the measurements listed in Tables 4.4 and 4.6, $\mathcal{L}^{0129}_{\mathrm{bol,AGN}} = 6.4 \times 10^{44}$ erg s^{-1} and $\mathcal{L}^{0024}_{\mathrm{bol,AGN}} = 8.5 \times 10^{44}$ erg s^{-1} for NVSS J0129 and NVSS J0024, respectively, and black-hole masses of $\mathrm{M^{0129}_{BH}} = 2.8 \times 10^8$ M$_\odot$ and $\mathrm{M^{0024}_{BH}} = 2.4 \times 10^8$ M$_\odot$, respectively. The Eddington ratios would be as low as for NVSS J2019, about 2$-$3%. We caution however, that we have no firm observable to distinguish between AGN broad-line emission, and gas interacting with the radio jet on larger scales in these two sources. If confirmed to be tracing BLR gas, these two galaxies would have supermassive black holes with masses more akin to submillimeter galaxies than more powerful radio galaxies at z $\sim$ 2, although their accretion rates would be significantly lower than in submillimeter galaxies (which accrete near the Eddington limit Alexander et al., 2008). However, their kinetic jet power (5×10^{46} erg s^{-1} for both sources, using the Cavagnolo et al. (2010) approach), would slightly exceed their Eddington luminosities, $\mathcal{L}_{\mathrm{Edd}} = 3.6$ and

3.1×10^{46} erg s^{-1}, and their bolometric luminosities implied by Hα would be two orders of magnitude lower than those implied by their [OIII] luminosities. Although super-Eddington accretion is not impossible, it is very rarely observed, which is why we are doubtful that these are good bona-fide AGN broad-line regions.

4.7 Additional line emitters as tracers of environment and as dynamical probes of the mass of our HzRGs

High-redshift radio galaxies often do not exist in solitude. A large number of imaging and spectroscopic studies have demonstrated conclusively that many massive radio galaxies at z $\geq$ 2 are surrounded by galaxy overdensities at the same redshift, as well as significant reservoirs of molecular, atomic, and ionized gas, including diffuse intra-halo gas (Le Fèvre et al., 1996; Venemans et al., 2007; Hayashi et al., 2012; Galametz et al., 2012; van Ojik et al., 1997; Villar-Martín et al., 2003; De Breuck et al., 2003a; Nesvadba et al., 2009). With the small field of view of only $8'' \times 8''$, SINFONI can only constrain the very nearby environment of HzRGs out to few 10s of kpc ($8''$ correspond to 64 kpc at z $\sim$ 2), however, this small-scale environment is particularly interesting, *e.g.*, to study how accretion and merging may affect the evolutionary state of the radio galaxy. Given the presence of extended gas clouds well outside the radio galaxy itself, which we attribute to AGN-driven winds and bubbles, it may not be immediately clear how to identify a secondary line emitter within few 10s of kpc from the radio galaxy as another galaxy in each individual case.

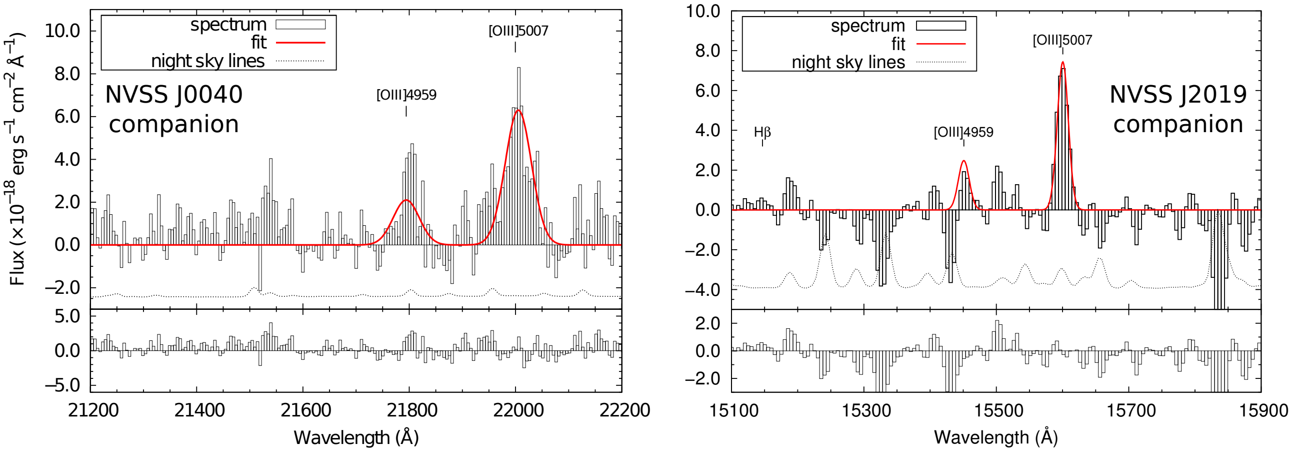

Figure 4.20: *Left*: Integrated spectrum of the southern part of the emission line region of NVSS J0040 that appears for SNR $\geq$ 3 and that is blueshifted at $z^{0040}_{\rm south} = 3.395 \pm 0.001$, as illustrated by Fig. 4.8. *Right*: Spectrum integrated over a $1.0'' \times 1.0''$ box situated $3.2''$ to the South-Southeast of NVSS J2019. The [OIII] emission is detected at the redshift: $z^{2019}_{\rm south} = 2.116 \pm 0.001$.

We have three such examples, NVSS J0040, NVSS J2019, and NVSS J1449. For the latter, we have already argued why we favor the interpretation of an AGN-driven bubble. For NVSS J0040 and NVSS J2019 the situation is more difficult. In either case, the line emission cannot be geometrically associated with the radio jet, which strongly disfavors a direct physical connection between jet and gas. The redshifts in both cases are significantly offset from those in the radio galaxy itself, moreover, in NVSS J2019, the line widths of this second component are very narrow, FWHM = 320 km s^{-1}, and the light is emitted from within about $1''$ (8 kpc at z = 2.1), as would be expected from a low-mass galaxy in the halo of NVSS J2019. High [OIII]/Hβ ratios as observed in this putative companion are consistent with what is observed in rest-frame UV selected, fairly low-mass galaxies like Lyman-break galaxies (LBGs) and other blue, intensely star-forming galaxies at high redshifts, and the [OIII] luminosity of our source, $\mathcal{L} = 5.3 \times 10^{42}$ erg s^{-1} does not stand out compared to, *e.g.*, the LBGs of Pettini et al. (2001), which typically have $\mathcal{L}$ = few $\times$ 10^{42} erg s^{-1}. In NVSS J0040, the line emission is closer to the HzRG, within about $1''$, and brighter, $\mathcal{L}([\text{OIII}]) = 4 \times 10^{43}$ erg s^{-1}. This may indicate that the gas is at least partially lit up by photons originating from the AGN of the radio galaxy. The proximity to the radio galaxy itself may also suggest that this gas is already dominated by the gravitational potential of the radio galaxy itself, either as part of a satellite galaxy being accreted (*e.g.*, Ivison et al., 2008; Nesvadba et al., 2007b), or perhaps because it is associated with an extended stellar envelope forming around the HzRG, as observed in other cases (Hatch et al., 2009, , chapter 5).

Under both hypotheses, the projected velocity of these additional line emitters would be dominated by gravitational motion, and can therefore be used as an order-of-magnitude measure of the dynamical mass of the central radio galaxy and its underlying dark-matter halo. Assuming that the system is approximately virialized, we set $M = v_c^2\ R/G$, where the circular velocity v_c is $v_c = v_{\rm obs}/\sin i$, and where R is the projected radius, and G the gravitational constant. With $v_{\rm obs} = 408$ km s^{-1} for the companion of NVSS J2019, $v_{\rm obs} = 350$ km s^{-1} for NVSS J0040, and projected distances of 24 kpc and 8 kpc, respectively, we find mass estimates of $9 \times 10^{11}\ \sin^{-1} i$ M$_\odot$ for NVSS J0040 and of $3 \times 10^{11}\ \sin^{-1} i$ M$_\odot$ for NVSS J2019, respectively. Both are in the range of stellar and dynamical masses estimated previously for the most powerful HzRGs (Seymour et al., 2007; De Breuck et al., 2010; Nesvadba et al., 2007a; Villar-Martín et al., 2003).

4.8 Comparison with other classes of high-z galaxies

4.8.1 Massive early-type galaxies at z $\sim$ 1.5

Given the relatively small velocity gradients we observe in our galaxies, it is worth asking in more detail what the possible contribution of rotational motion (and other gravitational processes like interactions or merging) to the observed gas kinematics of our sources might be. We decided to do this in an empirical way by comparing with a small sample of SINFONI Hα imaging spectroscopy of high-redshift galaxies (z = 1.4) in a similar mass range as our radio galaxies (Buitrago et al., 2014).

We have no stellar mass estimates for our sources specifically, but find dynamical masses for two sources in the range of few 10^{11} M$_\odot$ (see in the previous Section 4.7). Likewise, very powerful radio galaxies with similar radio spectral index but radio power about 1−2 orders of magnitude higher span a small range of about $3 - 5 \times 10^{11}$ M$_\odot$ of stellar mass (Seymour et al., 2007; De Breuck et al., 2010), and have similar dynamical mass estimates (Nesvadba et al., 2007a) as the targets we study here. $K-$band magnitudes of our sources, where detected, are in the range of 18 − 20 mag, consistent with these more powerful HzRGs. Although it would be dangerous to translate $K-$band magnitudes into stellar masses in a quantitative way, given the uncertainties in star-formation history, extinction, and the likely contribution from the AGN to the rest-frame optical continuum, it does highlight the similarity in the host properties of our sample and the very powerful HzRGs of Seymour et al. (2007); De Breuck et al. (2010).

All of this makes us believe that the best sample for this comparison is one of mass-selected galaxies of about 1−few $\times 10^{11}$ M$_\odot$ at redshifts of about z $\sim$ 2. Buitrago et al. (2014) obtained SINFONI imaging spectroscopy of ten M$_{\rm stellar} \geq 10^{11}$ M$_\odot$ at z $\sim$ 1.4, where they find fairly regular velocity fields and velocity gradients. They find velocity gradients of 190 km s^{-1} and 620 km s^{-1}, and line widths between about 100 km s^{-1} and 300 km s^{-1}. Their extended emission-line regions reach sizes of up to about 3″.

Our sources are thus within the lower part of the range in velocity gradient of equally massive high-z galaxies, and our sources with the least extended emission-line regions have roughly equal sizes. Unfortunately, Buitrago et al. (2014) do not state their surface-brightness detection limit, but since they have roughly similar on-source observing times, and used the same telescope and instrument, we may expect the depth of their data sets is about comparable to ours.

A significant difference we do find between the two samples is that the line widths of our galaxies are considerably higher, between 400 km s^{-1} and 1500 km s^{-1}. Accordingly, the ratio of turbulent to bulk kinetic motion is much lower, v/σ = 0.4 − 2.1 (see Table 4.19) compared to v/σ = 2 − 7 in the sample of Buitrago et al. (2014). Independent of the specific mechanism (or set of mechanisms) that drives the gas kinematics in either sample, we can conclude that the line widths in our targets are higher, and their velocity gradients comparable to, or even at the low end, of 'ordinary' mass-selected galaxies at high redshift within the same mass range. This suggests the systematic presence of an additional source which is injecting kinetic energy into our targets compared to the overall population of very massive high-z galaxies.

4.8.2 Dusty, obscured, radio-quiet submm-selected starbursts and AGN

Dusty, massive, intensely star-forming high-redshift galaxies selected in the sub-millimeter (SMGs) form another exquisite comparison sample for our study. Their immense far-infrared luminosities are likely powered by intense star formation, a rapidly accreting, obscured AGN, or a mixture of both. They are amongst the very well studied high-z galaxy populations observed with imaging spectroscopy. We base our comparison on three samples, the SINFONI and OSIRIS observations of SMGs, the sample of Alaghband-Zadeh et al. (2012) of SMGs without strong IR signatures of AGN, and the samples of Menéndez-Delmestre et al. (2013) and Harrison et al. (2012) which have weak and strong AGN contributions to the bolometric luminosity of the galaxy, respectively.

Although the gas kinematics are likely dominated by a major merger, it is interesting to note that the sample of Alaghband-Zadeh et al. (2012) has an average FWHM of Hα of 306 ± 111 km s^{-1}, with the exception of one galaxy with FWHM = 1740 km s^{-1}, likely a signature of an AGN that is weak or blue enough to not have been identified during their target selection in the IR. Velocity gradients are between 120 and 600 km s^{-1} observed over sizes of typically about $1''$, again excluding the AGN candidate with a size of $2.5''$ and 800 km s^{-1} velocity gradient. While the velocity gradients are comparable to the range we find in our sources, the line widths are much narrower, in spite of potentially substantial contributions of major mergers to the overall kinematics of these galaxies. The sources of Menéndez-Delmestre et al. (2013) have somewhat higher FWHMs in the range between FWHM = 200−500 km s^{-1}, although they are observed at higher spatial resolution with laser-guided adaptive optics, which may enhance the contrast between regions with higher and lower FWHM compared to seeing-limited data, and therefore lead to somewhat higher velocity dispersions. At any rate, the velocity dispersions in the sources of Menéndez-Delmestre et al. are also systematically smaller than in our galaxies.

Harrison et al. (2012, see also Alexander et al. 2010) discuss the kinematics of the warm ionized gas in 8 dusty, sub-mm selected starburst/AGN composites at z ∼ 1.4−3.4 as probed through imaging spectroscopy of [OIII]λ5007. The galaxies of Harrison et al. are detected at 1.4 GHz, albeit with low fluxes corresponding to luminosities in the range 10^{24-25} W Hz^{-1} which are too low to disentangle the relative contribution from star formation and radio jets in a unique way. Their obscured AGN infrared flux densities correspond to those of bright quasars and powerful radio galaxies, in the range of few 10^{46} erg s^{-1}.

Globally they find extended [OIII] line emission, in some cases with significant velocity offsets and/or broad line widths. Their line widths are in the range 200−1500 km s^{-1}, not very different from our targets, and velocity gradients are between 100 and 800 km s^{-1}. Their integrated gas properties appear therefore not very different from those in our targets, however, one striking difference are the integrated line profiles. Where signal-to-noise ratios permit, their lines show a narrow component superimposed onto a broad line, often with widths well in excess of FWHM ∼ 1000 km s^{-1}. Qualitatively very similar profiles were reported by Nesvadba et al. (2011c) in a z = 3.5 mid-IR selected obscured QSO, where a broad component with FWHM ∼ 1000 km s^{-1} was also found for the molecular gas. Likewise, the obscured quasar of Cano-Díaz et al. (2012) shows a distinctive broad and a narrow line component in the integrated spectrum.

Interpreting the ratios between broad and narrow [OIII] lines in terms of a mass ratio is prohibited by the strong dependence of the [OIII] brightness on gas density and ionization parameter (*e.g.*, Ferland et al., 2013), however, in a qualitative sense it is already interesting to note that such a clear distinction between broad and narrow component is absent in our sources. Generally speaking, these narrow components in SMGs have FWHM = 200−400 km s^{-1}, and Harrison et al. (2012) discuss that they may also show velocity gradients that are flattened at low surface brightnesses, which they attributed to the turnover of rotation curves. In constrast, all of our galaxies show FWHM $\gg$ 500 km s^{-1}, typically around FWHM = 800 km s^{-1} in the regions associated with radio emission, in particular in the central few kpc near the AGN, and we are not able to identify a more narrow line component. Extended, lower surface brightness emission with more quiescent kinematics is also observed, but in regions where a causal connection with the radio source is less obvious.

A detailed comparison of these sources with optically selected AGN covering a range in radio power will be presented in Chapter 6.

4.8.3 Very powerful HzRGs

One of the main goals of this thesis is to investigate how the impact of radio-loud AGN on their host galaxies changes with decreasing radio power. As can be seen from Tables 4.2 and 4.14, the radio power of our sources is about 2−3 orders of magnitude less than that of the most powerful sources in the sample of Miley & De Breuck (2008) and Nesvadba et al. (2006, 2008), 2014 in prep. Although the analysis of the full sample of these very powerful sources is still on-going, we can already conclude that the total velocity gradients and line widths of the full sample are in the range of those already discussed in the literature (Nesvadba et al., 2006, 2007a, 2008), although the detailed properties of course change from source to source. Overall, these sources have line widths of about 800−1500 km s^{-1} and velocity gradients of up to 1500 km s^{-1}, typically with the expected bipolar velocity maps of back-to-back outflows. Their ratios of bulk to turbulent gas motion are of-order unity.

One difference that becomes immediately clear are the velocity gradients, that are factors 3−5 lower in our sources than in the most powerful radio galaxies. In turn, however, the difference of FWHMs between our sources and the most powerful HzRGs are not very different, with typical ratios of >500 km s^{-1} and up to about 1500 km s^{-1} in parts of our sources. Likewise, in both samples we find regions with more quiescent gas kinematics. Nesvadba et al. find that the gas is generally elongated along the direction of the radio jet. This is not always the case here, but is nonethelss similar for 5/6 sources, where we find no monotonic, regular velocity gradient (see Fig. 4.17). In the 6^{th} source, NVSS J2106, we find a pronounced mismatch between the position angle of the radio jet and the bright, very elongated emission-line region of $\sim 60°$. We will discuss this source in more detail in Chapter 5.

Another difference between our sources and those of Nesvadba et al. appear to be the higher amounts of warm ionized gas in the latter, at least in the most extreme cases. As discussed in Section 4.5.6 and listed in Table 4.19, we find between 1 and 13 × 10^8 $M_\odot$ of warm ionized gas compared to typically ≥few ×10^9 and up to several 10^{10} $M_\odot$ in several of the very powerful sources. This cannot be due to extinction, the extinctions we measure from the observed Hα and Hβ fluxes in our targets are in fact lower than in the more powerful HzRGs, and sometimes even consistent with no extinction at all. While extinction estimates can only be sensitive to the gas that is not entirely obscured in both lines, as may be the case for dusty star-forming regions, it is consistent with globally lower gas column densities and lower total gas masses in the lower-power radio sources.

In the most powerful radio galaxies, the gas masses correspond within factors of a few to what would be expected to be observed in molecular gas in the most intensely star-forming, massive, dusty starburst galaxies at high redshift. However, we cannot postulate that this is also the case here, since it is well possible that only a small fraction of the ISM of an intrinsically gas-rich galaxy is photoionized by the AGN and/or star formation.

We are therefore currently carrying out a millimeter follow-up of CO(1−0) emission-line observations at ATCA to investigate whether we may have missed a reservoir of few 10^{10} $M_\odot$ of cold molecular gas in our sources. Although the detailed analysis is still on-going, we can already conclude that we did not detect any obvious line emission, which corresponds to an upper limit on the total molecular gas mass of few 10^{10} $M_\odot$ in the 4 sources of this sample that we observed. Of course it is possible that we may have missed substantial reservoirs of cold molecular gas of-order few 10^9 $M_\odot$. Since not all of the very powerful radio galaxies are easily detected in CO line emission either, likewise with upper limits in the same mass range (*e.g.*, Emonts et al., 2013), it is not immediately clear whether this constitutes a significant difference between the two samples or not. What we can however exclude is that these galaxies have similar molecular gas masses as the most intensely star-forming, dusty, massive starbursts at similar redshifts. Given that they appear to be already fairly massive, with few 10^{11} $M_\odot$ in dynamical mass, their total gas fractions are unlikely to exceed a few percent and are at most in the range of the most gas-rich radio galaxies in the nearby Universe (which have molecular gas masses of few $\times 10^9$ $M_\odot$; *e.g.*, Evans et al., 2005; Nesvadba et al., 2010).

4.9 The nature of the extended line emission and AGN feedback

In the previous sections we described the detailed properties of each individual source, of the overall sample, and extracted the astrophysical and physical parameters of the gas and radio source. We also searched for companion galaxies of our targets, major merger signatures like multiple continuum sources, and constrained the black-hole properties of the AGN, where possible. In the last section we compared with the most relevant samples of other types of high-z galaxies. We will now distill this set of empirical and physical constraints to conclude what we can learn from these targets about the role of moderately radio-loud AGN for the evolution of massive high-redshift galaxies.

First of all, our data sets do not provide much evidence that the most basic properties of the host galaxies themselves are significantly different from the most powerful HzRGs, apart from their possibly lower gas masses (see § 4.5.6 above). Although neither of the two samples are complete, and ours is also limited by the moderate sample size, we do find similar host galaxy and black-hole masses. The luminosity of the broad Hα line in NVSS J2019 is a factor 2 lower than that of the least luminous such line in the sample of Nesvadba et al. (2011b), a difference which is not necessarily significant.

It would be interesting to perform a narrow-band search for associated line emitters to infer whether some of these more moderately powerful radio galaxies are also signposts of dense regions in the high-redshift Universe like their more powerful counterparts.

A wide range of processes have been proposed to explain the kinematics of the warm ionized gas in high-redshift galaxies, ranging from disk rotation (*e.g.*, Förster Schreiber et al., 2006, 2009; Epinat et al., 2009, 2012) to mergers and galaxy interactions (Nesvadba et al., 2008; Epinat et al., 2012), to feedback from star formation (*e.g.*, Nesvadba et al., 2007b; Lehnert et al., 2009, 2013) and AGN (*e.g.*, Nesvadba et al., 2006, 2008; Harrison et al., 2012; Cano-Díaz et al., 2012), and the data sets do not always allow a unique distinction between the different possible mechanisms.

We will focus on disk kinematics and outflows as two possible interpretations, and discuss subsequently, what implications we can draw from these interpretations for our understanding of AGN feedback in these sources.

Disk hypothesis

The large velocity offsets in the most powerful radio sources make it relatively easy to conclude that the gas is driven by powerful, non-gravitational processes, and the only energy source that is strong enough to inject sufficient energy into the gas of these galaxies is the radio jet. In the sources we are studying here, the situation is not so clear. Although we do find velocity gradients of few 100 km s^{-1} in the 6 galaxies with resolved gas kinematics, in 4 cases they are relatively small, $\Delta v = 300-450$ km s^{-1}. For massive galaxies with stellar masses of few 10^{11} $M_\odot$, such velocity gradients may well originate from gravitational motion.

For example, assuming that the gas is in a (albeit perhaps not quiescently) rotating disk, we can derive the mass from the virial theorem by setting:

$$M = (v/\sin i)^2 R/G$$

where M is the dynamical mass of the galaxy, v the observed velocity, i the inclination angle between the disk normal and the line of sight, R the radius of the disk, and G the gravitational constant. Setting $v/\sin i = 150-225$ km s^{-1}, and R = 5 kpc (corresponding to a typical observed disk radius of 0.6″), we find masses in the range of $0.5 - 1.2 \times 10^{11}$ $M_\odot$, assuming an average inclination of 45°. This is not very different from the expected mass range of few 10^{11} $M_\odot$ of our targets derived from companion sources and the black-hole bulge mass relationship, as well as the stellar masses of more powerful HzRGs obtained by

Seymour et al. (2007) and De Breuck et al. (2010). Moreover, the existence of radio galaxies with not much weaker radio power at low redshift, and extended, massive gas disks (*e.g.*, Emonts et al., 2005), suggests that it is well possible to find signatures of rotation in our sources.

It is interesting, however, that the velocity offsets we find in our galaxies are lower than in the stellar mass-selected comparison sample of Buitrago et al. (2014), which are also in a range of 1− few 10^{11} $M_\odot$, whereas the gas in our sources extends over larger radii. If the velocity gradients we observe are indeed due to rotation, then this would imply that our radio galaxies have more shallow mass profiles than mass-selected samples of equally massive galaxies at the same redshift. This would point towards a different evolutionary history for both samples, however, a major, gas-rich merger, as is often considered to trigger powerful radio and quasar activity in high-redshift galaxies (*e.g.*, Sanders et al., 1988; Hopkins et al., 2006b), should make radio galaxy hosts more, not less concentrated, than galaxies in the field. It appears doubtful whether there has been sufficient time by z = 2 (only about 3 Gyrs after the Big Bang) for extended periods of minor, dry mergers, which would increase the effective radius of the mass profile as happening at lower redshifts.

Finding gas that is more extended than the galaxy, and has shallower velocity gradients is reminiscent of the radio-loud quasars at lower redshifts of Fu & Stockton (2006), which also show gas that is relatively extended compared to the size of the stellar component of their galaxies, and probes velocity ranges that are smaller than those expected from rotation, if stellar velocity dispersions are a good measure of the intrinsic galaxy kinematics. They conclude that the gas kinematics are likely not directly related to rotational motion. At high redshift, we cannot probe a similarly clear tracer of galaxy kinematics such as stellar absorption line widths, and therefore cannot address this question directly. It is therefore encouraging to find that the velocity gradients as observed do probe a similar range as our other estimates.

Radial motion and outflows

Regardless of whether the regular, monotonic velocity fields in our sources may or may not indicate rotation, they do show significant irregularities in their velocity maps, even at our relatively low spatial resolution of several kpc. Inspection of Figs. 4.6 and 4.14 show that all but perhaps three sources, NVSS J0129, NVSS J2046, and CEN 072, show significant residuals from simple, smooth, monotonic velocity gradients on those fairly large scales. This implies significant non-circular motion with sudden velocity jumps of up to several 100 km s^{-1}, over scales of few kpc. A good example is NVSS J0024, where we see two areas that are redshifted relative to the surrounding gas by about 200 km s^{-1}, or CEN 134, which shows two large blueshifted regions toward North-West and South-East, that are blueshifted by up to about 150−200 km s^{-1} relative to a central 'ridge' of more redshifted gas. It is clear that such kinematics cannot arise from simple disk rotation.

We also find very extended gas in some cases, in particular in NVSS J1449, where the line emission extends over 35 kpc, which is clearly larger than an individual galaxy. In addition, in CEN 134, NVSS 2342, NVSS J1449, and NVSS J0040, the gas is elongated along the radio jet axis, and in NVSS J0024, NVSS J0040, NVSS J0304, NVSS J1449, NVSS J2342, and CEN 134, the largest velocity offsets are also found near that direction (see Fig. 4.17). This is reminiscent of the "jet-cloud interactions" found in radio galaxies near and far (*e.g.*, Tadhunter, 1991) and even in AGN with low radio power (Fu & Stockton, 2006; Müller-Sánchez et al., 2011) in the nearby Universe.

In NVSS J1449 we find two emission-line regions along the jet axis, which we interpret as the two sides of a biconical jet-driven wind. Gas is found to extend over 35 kpc, which is clearly larger than an individual galaxy. The velocity offset between the two bubbles is 800 km s^{-1}, and the gas has FWHM line widths of up to about 800 km s^{-1}. The broad-band $K-$band image of Bryant et al. (2009a) shows fuzzy, clumpy structures at the sensitivity limit of the data near the eastern emission-line region, but no single, well pronounced continuum source consistent with a galaxy. At the depth of the image, we would have likely missed galaxies with masses significantly lower than that of the radio galaxy, however, it is not clear in this case how the lopsided morphology of the Southern bubble relative to the continuum of the radio galaxy, nor the fairly high gas surface brightness in this putative small galaxy could be explained. We therefore consider this source as an example of an AGN-driven wind, akin to other HzRGs. The eastern bubble is much smaller than the western bubble, however, similar asymmetries are found in more powerful radio galaxies at the same redshift (Nesvadba et al. 2014 in prep.). Moreover the eastern, blueshifted bubble is near the edge of our data cube and may extend further outside the field-of-view.

4.9.1 Implications for AGN feedback

Bulk motion

With the exception of NVSS J1449, our sources do generally not show unique evidence of coherent, large-scale outflows, like what we appear to witness in the most powerful radio galaxies at similar redshifts (Nesvadba et al., 2008), although it is not clear whether this is more of an observational interpretation, or implies the true absence of winds. But, as we just discussed, the irregularities in their velocity fields and overall large line widths and small v/σ ratios compared to the mass-selected sample of Buitrago et al. (2014) show nonetheless that gravitational motion alone is unlikely to be the sole driver of the gas kinematics. Likewise, observations like the co-alignment of jet and gas (Fig. 4.17), suggest that it might be too conservative to attribute even very regular velocity fields to rotation alone.

It is therefore interesting to ask whether at least it would be possible that the jets play a major role in producing the large-scale velocity gradients. To investigate whether the radio source could potentially be the main driver of the gas kinematics, it is therefore interesting to analyze the gas kinematics more closely, even though the observational signatures may not be as unique as in the more extreme cases. To elucidate this question, we compare the kinetic energy estimate of the radio jet from § 4.6.4 with the kinetic energy implied by the velocity gradients we find. Using simple classical mechanics, we set

$$\mathrm{E_{bulk}} = \frac{1}{2} \times \mathrm{M_{ion}^{corr}} \sum_{i\,\in\,\mathrm{EELR}} \frac{\Sigma(i)}{\Sigma_{\mathrm{tot}}} \times v(i)^2$$

where M_{ion} is the mass of warm ionized gas estimated in § 4.5.6, and corrected for extinction, and v is the estimate of the radial motion for a back-to-back outflow in the plane of the sky. We use the velocity offsets in each pixel from the central velocity, which we consider an acceptable approximation of the systemic velocity of the galaxy. To probe the disk kinematics out to faint surface brightnesses, we use the gas kinematics as measured from [OIII], and scale by the Hα/[OIII] line ratio in the integrated spectrum. Our direct observations of the velocity and surface-brightness distributions of both lines in the galaxies where both are bright enough to be probed out to large radii suggest that this does not introduce significant differences in the final estimate.

With the velocities and warm ionized gas masses in Table 4.19, we find values between $E_{\mathrm{bulk,min}} = 0.3$ and $E_{\mathrm{bulk,max}} = 2 \times 10^{56}$ erg in bulk kinetic energy in these galaxies. This corresponds to a small fraction of the mechanical energy carried by the radio jet, of-order a few percent or less (Table 4.21), if we assume typical jet lifetimes of-order 10^{6-7} yrs, as suggested by our data and with the arguments given in § 4.6.3. Thus, energetically, it would well be possible to accelerate the gas to the observed velocities with the radio power available.

This is in particular the case for NVSS J1449, where the bulk kinetic energy contributes to ~ 11 %.

Gas turbulence

The ratios of ordered to random motion in our galaxies (large-scale velocity gradients to line widths) are small, of-order v/$\sigma \simeq 0.5 - 1$ (where σ is the Gaussian line width, σ = FWHM/2.355), below what is found in mass-selected galaxies without AGN (Buitrago et al., 2014, see our previous comparison in § **??**). This implies that the gas, even if it is in a disk, cannot be in a stable configuration. Except for implausibly high inclination angles, gas in the line wings cannot be gravitationally bound to the disk because it reaches velocities exceeding the local escape velocity from the disk (however, the gas may remain bound to the

Table 4.21: Energetics of the galaxies of our sample.

ID(1)	$\mathrm{E}_{\mathrm{bulk}}$ (2)	$\mathrm{E}_{\mathrm{turb}}$ (3)	$\mathcal{L}_{\mathrm{jet}}^{\mathrm{W99}}$ (4)	$\mathcal{L}_{\mathrm{jet}}^{\mathrm{B08}}$ (4)	$\mathcal{L}_{\mathrm{jet}}^{\mathrm{C10}}$ (4)	τ (5)	$\mathrm{E}_{\mathrm{jet}}^{\mathrm{W99}}$ (6)	ϵ (7)
	$[10^{56}$ erg]			$[10^{45}$ erg s^{-1}]		$[10^{5}$ yrs]	$[10^{59}$ erg]	[%]
NVSS J0024	0.8	32.3	18.5	3.4	29.2	20.4	11.9	0.3
NVSS J0040	≥ 3.0	≥ 67.6	118.4	8.9	76.5	18.1	67.6	0.1
NVSS J0129	0.4	15.1	29.8	4.4	39.1	1.9	1.8	0.9
NVSS J0304	0.1	6.6	37.3	4.6	33.2	4.8	5.7	0.1
NVSS J1449	2.2	17.9	26.7	4.0	30.7	18.1	15.3	0.1
NVSS J2019	≥ 2.4	≥ 16.9	26.5	3.9	26.6	42.5	35.5	0.05
NVSS J2046	1.1	71.7	30.5	4.3	34.4	4.2	4.0	1.8
NVSS J2106	3.1	7.0	36.3	4.9	42.5	67.7	77.6	0.01
NVSS J2342	≥ 2.7	≥ 23.8	128.1	8.9	69.8	23.3	94.2	0.03
CENSORS 072	10.3	93.6	4.5	1.5	9.8	1.9	0.3	38.5
CENSORS 129	1.6	23.2	2.5	1.1	5.8	6.6	0.5	4.8
CENSORS 134	0.4	5.0	5.1	1.5	6.9	58.3	9.4	0.1

(1): Source name. — (2): bulk kinetic energy of the warm ionized gas. — (3): turbulent energy of the warm ionized gas. — (4): mechanical jet power, estimated from formulae given in Willott et al. (1999), Bîrzan et al. (2008) and Cavagnolo et al. (2010). — (5): fiducial age of the radio jet, assuming an advance speed of $0.1 \times c$. — (6): mechanical energy of the jet, $\mathcal{L}_{\mathrm{jet}}^{\mathrm{W99}} \times \tau$. — (7): ratio of the mechanical energy in the gas and jet

galaxy itself; see Nesvadba et al., 2011a, for the discussion of a similar example in a more nearby radio galaxy; another example is the nearby LINER NGC 1266 Alatalo et al. 2011).

Low v/σ values are one more commonality with the extended disks found in some low-redshift radio galaxies (Emonts et al., 2005; Nesvadba et al., 2011a), in particular the large line widths and irrregular line profiles. These disks appear very different from classical, thin disks in, *e.g.*, spiral galaxies. The gas in such disks appears overall filamentary and diffuse, and cannot form gravitationally bound clouds and stars. Densities even in the molecular gas traced by CO millimeter line emission are only of-order few 1000 cm^{-3} in the low-z sources, not very different from what we estimate here for the warm ionized gas. To understand the peculiar properties of these disks, in particular the absence of clear signatures of on-going and past star formation, Nesvadba et al. (2011a) proposed that the dense gas in these disks may have formed from a very diffuse ISM dominated by HI through the pressure enhancement in the cocoon inflated by the radio jet. Although this scenario is rather speculative and requires more observations to be confirmed, the broad properties of our targets may suggest that they may be fundamentally similar to these gas-rich radio galaxies in the more nearby Universe.

While we cannot infer whether these line widths reflect spatially unresolved velocity offsets on smaller scales, strong turbulent motion, or a mix of both, we do note that line widths are typically highest near the center of the galaxy (as probed by the continuum emission) where we would expect the impact of the AGN to be greatest.

It is interesting to compare the kinetic energy carried by bulk and by turbulent motion. As before, we set

$$\mathrm{E}_{\mathrm{turb}} = \frac{3}{2} \times \mathrm{M}_{\mathrm{ion}}^{\mathrm{corr}} \sum_{i \,\in\, \mathrm{EELR}} \frac{\Sigma(i)}{\Sigma_{\mathrm{tot}}} \times \sigma(i)^2$$

to estimate the turbulent energy, this time with velocity dispersion σ, *i.e.*, FWHM/2.355. With the line widths measured previously, we find values in the range $E_{\mathrm{turb,min}} = 1.3$ and $E_{\mathrm{turb,max}} = 38 \times 10^{57}$ erg in turbulent kinetic energy. For typical jet ages of few 10^{6-7} yrs, this corresponds to energy injection rates of few 10^{42} to 10^{44} erg s^{-1} (our precise numbers are for a fiducial 10^7 yrs). The turbulent energy corresponds to few 0.1% to few % of the mechanical energy carried by the radio jet.

Ratios between bulk and turbulent kinetic energy (under the assumption that bulk velocities are solely from radial motion) are typically between 0.2 and <10%, only NVSS J1449 has a ratio of 30%. The small contribution of the bulk kinetic energy to the total kinetic energy budget of the gas implies that the uncertainties owing to the unknown split between rotational and outflow motion does not have a large impact on the total budget of kinetic energy in the warm ionized gas.

The overall fraction of mechanical energy (in bulk and turbulent motion) of the jet which is deposited in the gas appears fairly similar to those in very powerful HzRGs, but a significant difference is that the turbulent energy appears here to be an order of magnitude greater than that in ordered motion (on kpc scales), whereas both are roughly equal in very powerful sources. Since turbulent energy is dissipating rapidly, on about a dynamical time of the gas (*e.g.*, Mac Low, 1999), this implies that even relatively high-velocity gas will unlikely escape, but will probably rain back onto the disk. This is at odds with the simple scenario whereby AGN feedback acts mainly by removing the gas (*e.g.*, Di Matteo et al., 2005). A cyclical model whereby gas is cooling down and accumulating at small radii near the supermassive black hole, before igniting another feedback episode, as has previously been suggested for the central galaxies of massive galaxy clusters (Pizzolato & Soker, 2005) may therefore be more appropriate here.

Above we did very simple, observational estimates of the putative energy transfer between radio jet and gas, finding that most of the gas is likely in turbulence. Far more detailed estimates have been performed on theoretical grounds in recent years with the aid of hydrodynamic models of ambient gas in radio host galaxies. Here we focus on the work of Wagner et al. (2012) who found that radio jet cocoons can transfer jet energy efficiently into the gas, assuming a clumpy, fractal two-phase medium with a density distribution set by interstellar turbulence like, *e.g.*, found by **?**. The range in jet power they cover with their 29 models is 10^{43-46} erg s^{-1}, well matched to our sources, and Eddington ratios $\eta = 10^{-4} \rightarrow 1$.

They find that a few 10% of the jet energy is transferred into the gas, mainly through the ram pressure transfer of partially thermalized gas streams occurring in low-density channels between denser clouds. This energy transfer corresponds at zeroth order to the ratio of gas kinetic to jet mechanical energy that we measure in our data. The values found in the simulations are somewhat higher than what we find in our data. However, our data can only be a lower limit to the actual energy transfer, since we do not observe all gas phases, in particular the hot, X-ray emitting gas and the molecular gas are missing. Likewise, uncertainties may arise from the details of the density distribution of the gas, filling factors, etc., since the ISM properties of high-redshift galaxies are not very well constrained yet. In particular cloud sizes – a parameter which is not observationally constrained at z $\sim$ 2 – appears to play a major role (Wagner et al., 2012). Overall, given all these uncertainties, we consider the correspondence between the model and data of an energy transfer in the percent range very encouraging.

This corresondence is also illustrated in Fig. 4.21, which was inspired by Fig. 11 of Wagner et al.. It shows the expected outflow speed of the gas as a function of radio power for a range of Eddington ratios. Our jets span the range of about 10^{46-47} erg s^{-1}, which for Eddington ratios of 0.1 to 0.01 corresponds to velocities of about 250−500 km s^{-1}. This is somewhat higher than the velocity offsets we observe, which might in parts be attributable to orientation effects and beam smearing. In particular in NVSS J2019, where we have a direct estimate of the Eddingtion ratio, we find a very good agreement between model and observations. However, what we plot in Fig. 4.21 are not the velocity offsets, but the widths of the integrated spectral lines after correcting for the velocity gradients, *i.e.*, the overall luminosity-weighted range of velocities from non-directed, presumably turbulent gas motion. This may further underline that a large part of the energy injected by the radio jet is transformed into turbulent, not bulk motion. The hatched area indicates the range of velocity dispersions measured by Buitrago et al. (2014) and illustrates that for jets less powerful that those of our sources, it will be difficult to identify the fingerprints of high-redshift AGN with observations of the kinematics of warm ionized gas in the presence of other processes. As Wagner et al. (2012) point out, estimating the long-term behavior of the gas kinematics over kpc scales is not possible with the current set of simulations, which only follow the evolution of the gas in the first 10^3 kyrs. As also cautioned by Wagner et al. (2012), finding that the gas is being accelerated to velocities of few 100 km s^{-1} does not automatically imply that the gas will ultimately escape, in particular in the presence of strong turbulent motion.

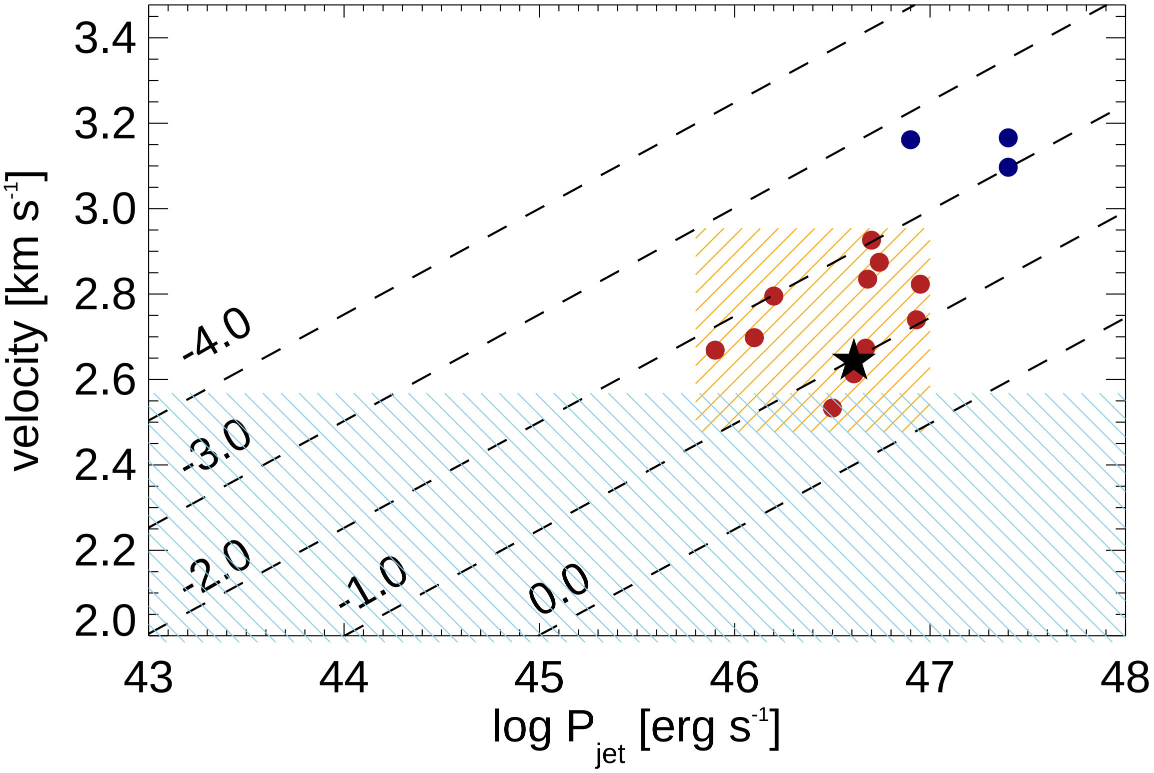

Figure 4.21: Widths of the integrated spectral lines (after correcting for the velocity gradients) as a function of radio power for a range of Eddington ratios (given by dashed lines, from $\log(\eta_{\rm Edd}) = -4.0 \rightarrow 0.0$)

Radiative quasar feedback?

Another possible feedback mechanism that has recently been widely discussed in the literature is radiative feedback from the bolometric energy output of AGN. From the cosmological point of view, radiative processes are attractive to explain, *e.g.*, the black-hole bulge scaling relationships, because the accretion rates implied by number counts of optically selected quasars appear to be a good match to the local black-hole demographics (*e.g.*, Yu & Tremaine, 2002). In spite of recent claims of AGN-driven bubbles and winds in bright, low-redshift quasars (*e.g.*, Liu et al., 2013a,b), statistical evidence is still rather scarce. For example, it has so far not been possible to find deviations in the star-formation rates of X-ray selected AGN hosts and galaxies without (*e.g.*, Mullaney et al., 2012).

One mode of radiation-driven feedback that has been particularly intensely discussed in recent years in the context of galaxy-wide outflows is radiation pressure. Each time a photons scatters on a dust (or gas) particle in the ISM it produces a small recoil in the ISM particle, with a net momentum transfer for fluxes that are high enough, in particular when the gas is optically thick, so that many interactions happen per photon. Murray et al. (2005) derived analytic equations to approximate the expected gas velocities as a function of quasar luminosity. Using their Equation 17, we set

$$V(r) = 2\sigma\sqrt{(\frac{\mathcal{L}}{\mathcal{L}_M} - 1)\ln\frac{r}{R_0}}$$

where σ is the stellar velocity dispersion of the host galaxy, and $\mathcal{L}$ is the quasar luminosity. R_0 is the launch radius of the outflow, and r the radius at which the velocity of the wind is measured. $\mathcal{L}_M = \frac{4\ f_g\ c}{G}\sigma^4$ is a critical luminosity that depends on the stellar velocity dispersion σ, the speed of light, c, gravitational constant, G, and the gas fraction, f_g. For $\mathcal{L} > \mathcal{L}_M$, radiation pressure may launch a wind. These equations are appropriate for the limiting case of an optically thick wind, in which case the interaction is most efficient. For these estimates we assume a launch radius of the wind, R_0, of a few 100 pc (the sizes of the circumnuclear molecular disks found in low-redshift ULIRGs Downes & Ray, 1998, and the lowest value in the AGN feedback models of Ciotti et al. 2009, 2010), and an outflow radius, r, of 5 kpc, roughly the radius that we spatially resolve.

We have an $\mathcal{L}_{\rm bol}$ estimate for NVSS J2019 from Hα, which gives 5×10^{45} erg s^{-1}. For a fiducial stellar mass of 5×10^{10} M$_\odot$ in a pressure-supported isothermal sphere, we find a velocity dispersion of $\sigma = \sqrt{M\ G/(5 \times R)}$ with stellar velocity dispersion σ, mass M, gravitational constant G, and radius R. We assume $R = 3$ kpc, which gives a velocity dispersion of $\sigma = 210$ km s^{-1}. The critical luminosity to launch a wind, $\mathcal{L}_M$ for this velocity dispersion and a gas fraction of 10% is $\mathcal{L}_M = 3.5 \times 10^{46}$ erg s^{-1}. This suggests that the AGN in our sources, unless NVSS J2019 is atypically weak, do not have sufficiently powerful quasars to launch fast outflows. We should also note that the Murray et al. estimate is, strictly speaking, only valid for buried quasars, whereas the overall low extinction in our sources (see § 4.5.4) suggests our sources are not very dusty.

4.10 Summary

This study aimed to assess the ability of moderately powerful radio jets to accelerate and heat the gas of their host galaxies in order to regulate the star formation, and the significance of this process in such a case. We already had clear signatures of efficient mechanical AGN feedback in the most powerful high redshift radio galaxies (*e.g.*, Nesvadba et al., 2006, 2008), hence we chose our sample to have radio luminosities $1-2$ orders of magnitude of magnitude fainter (with $\mathcal{L}_{\rm 500MHz} \sim 10^{27-29}$ W Hz^{-1}), but which energy budget is still clearly dominated by the AGN and not the star formation.

In our near-infrared imaging spectroscopy observations of our sample, we typically detect a faint, unresolved continuum emission around which we find extended emission line regions (clearly seen in [OIII] and Hα). The kinematics of this ionized gas is diverse among our sample: some sources (*e.g.*, NVSS J0129, CEN 072) show large scale and smooth velocity gradients, but of small magnitude (typically $\lesssim 400$ km s^{-1}) ; while other sources have very irregular velocity fields (*e.g.*, NVSS J0024). A common feature to all sources of our sample is their large velocity dispersions, with FWHM $= 400 - 1000$ km s^{-1}. The small ratios of bulk velocities to velocity dispersions indicate that the observed ionized gas cannot be in a stable rotating disk, even in cases where smooth velocity gradients are detected.

The measured emission line ratios clearly indicate that the observed gas is ionized by the central AGN. Our estimates of ionized gas masses are in the range of few 10^{8-9} M$_\odot$, which is at least one order of magnitude less than what was previously found in the most powerful radio galaxies. For a couple of sources, we found distinct emission line regions in the vicinity of the radio galaxy. Assuming they originate from satellite galaxies, we used them as proxies for the dynamical mass of the radio galaxy, and we found a few 10^{11} M$_\odot$, which is comparable to the typical mass of HzRGs (*e.g.*, Seymour et al., 2007; De Breuck et al., 2010). In one source (NVSS J2019), we find a broad component in its Hα emission line (with FWHM ~ 8250 km s^{-1}). We interpret this as the signature of the BLR and derive some properties of the black hole, such as its mass (M$_{\rm BH} \sim 2.1$ M$_\odot$) and its bolometric luminosity (5.3×10^{45} erg s^{-1}) which leads to an Eddington ratio of ~ 2 %.

We explore different possible sources of energy that can explain the large observed energies of the ionized gas: tranfer from the radio jet, radiative feedback from the large bolometric luminosity of the AGN or gravitational interactions. We show that a plausible scenario is the energy transfer from the radio jet to the ionized gas. Our estimations show that a fraction of the radio jet power is sufficient to power the kinematic of the ionized gas. Our observations are in agreement with the theoretical predictions of hydrodynamical models (see *e.g.*, Wagner et al., 2012).

Chapter 5

Focus on two intruiging HzRG

Contents

This study will be submitted to A&A as Collet, Nesvadba, De Breuck, Lehnert, et al. (2014b): The warm ionized gas in two peculiar high-redshift radio galaxies: Parallels to cluster central galaxies?

5.1 Motivation

In the previous chapter, we presented some results of our observing campaign led with the NIR integral field unit SINFONI, aiming to understand and quantify the effects of radio jets on the ISM of high-redshift radio galaxies. While it seems that radio jets have an impact on the ionized gas of nearly all the high-redshift radio galaxies (HzRG) of our sample, primarily traced by large velocity dispersions, extended, elongated emission-line regions along the radio jet axis, and in some cases large velocity offsets not reconcilable with virialized rotational motion, two objects displayed atypical features: NVSS J2106−314, that has already been introduced in §4.3.4 and TXS 2355−003, which has a higher radio power and is first described in this chapter.

Unlike all other galaxies of the sample, these two have extended warm ionized gas that has similar surface brightnesses to the other sources, but which show strong offsets in position angle to the radio jet axis. Gas associated with the radio jet axis, if present at all, is too faint to be seen in our SINFONI data. While gas seen in projection associated with the jet axis may or may not imply a physical association, it is clear that gas that is globally and significantly offset from the jet axis as projected on the sky is not reconcilable with a scenario where a cocoon inflated by the on-going jet activity is driving gas out of the host galaxy. In addition, these two sources have fairly low line widths in their extended gas, which is not typical for the rest of our sample as well. Line widths near the nucleus are higher, and may be affected by the radio core.

This chapter focuses on shedding light on these two sources. Close inspection of their properties suggests that the warm ionized gas may be less of a tracer of the black-hole activity than of the environment of HzRGs. Powerful radio galaxies in the early Universe are excellent tracers of dense environments, most likely massive galaxy clusters. This may be suggested by their high stellar masses (Seymour et al., 2007; De Breuck et al., 2010), their co-moving number density which matches expectations for massive dark-matter halos underlying rich galaxy clusters at low redshift (Venemans et al., 2007), and is directly seen through overdensities of high equivalent-width emission-line galaxies identified through narrow-band imaging (*e.g.*, Le Fèvre et al., 1996; Kurk et al., 2004c; Venemans et al., 2007) and of mid-infrared selected galaxies (Galametz et al., 2012), amongst others. Spectroscopy and narrow-band imaging also revealed extended halos of diffuse warm ionized gas seen in the form of extended Lyα halos (*e.g.*, Villar-Martín et al., 2003; Kurk et al., 2002), often interspersed with clouds, sheets, or filaments of denser, colder gas, that has previously been observed in the rest-frame UV through Lyα absorption from neutral gas (van Ojik et al., 1996), and even molecular gas (De Breuck et al., 2003b; Nesvadba et al., 2009). All of these are expected signatures of massive galaxy clusters, seen during a very early stage of their evolution. The radio galaxy is by far the most massive galaxy in these structures, and has all the characteristics expected from a young "brightest cluster galaxy" (*e.g.*, Hatch et al., 2008, 2009).

In this Chapter, we will present our study of the SINFONI observations of these two sources, but also include additional observations of one galaxy, TXS 2355−003, with the near-infrared imager ISAAC on the VLT, which I led as principle investigator. They complement our imaging spectroscopy in that they allow us to probe the environment of the radio galaxies out to radii of few 100 kpc. We start by highlighting why these two sources, as seen in the radio and with SINFONI, are so different from the rest of the sample, before describing our analysis of the broad-band images of both radio galaxies, and the narrow-band imaging centered on the Hα emission line of TXS 2355−003.

5.2 Two puzzling sources

5.2.1 Imaging spectroscopy of the warm ionized gas and rest-frame optical continuum

The SINFONI maps of NVSS J2106−314 and TXS 2355−003 are shown in Fig. 5.2 and 5.4, respectively. In NVSS J2106−314 at z = 2.104, [O III]$\lambda\lambda$4959,5007 and Hβ fall into the $H-$band, and Hα, [N II]$\lambda\lambda6548, 6583$ and [S II]$\lambda\lambda6716, 6731$ fall into the $K-$band, both of which we cover with our data set. In TXS 2355−003, we identify Hα and [N II]$\lambda\lambda6548, 6583$ at wavelengths corresponding to a redshift of z = 1.49. At this redshift, [O III]$\lambda\lambda4959, 5007$ and Hβ fall at redshifts below the lower wavelength cutoff of our grating, $\lambda_{\rm min} = 1.45$ μm.

Our redshift measurement does not agree with the previous redshift of z = 2.59 measured with longslit spectroscopy, which allegedly probed Lyα in the observed optical wavelength range (De Breuck et al., 2001). We did not identify any possible emission line consistent with the previous redshift z = 2.59, although [O III]$\lambda\lambda$4959,5007 and Hβ should fall into the $H-$band, and [N II]$\lambda\lambda$6548,6583, and Hα should fall into the $K-$band at that redshift. The optical spectrum shows no other line candidate consistent with z = 1.49, however, Lyα at that redshift falls well below the UV atmospheric cutoff.

Both galaxies have bright, spatially well resolved line emission. We fitted the extended line emission in both galaxies with single Gaussian profiles. Spectra were extracted from small apertures of $0.4'' \times 0.4''$, which helps to avoid the strongest pixel-to-pixel noise while safely oversampling the seeing disk so that no spatial information is lost. The data were also smoothed in spectral direction by three pixels, again, without loss of spectral resolution. Our fitting routine interpolates over wavelength ranges dominated by bright night-sky line residuals, and we only map spatial pixels where a line was detected at SNR > 3.

We also constructed line-free continuum images (shown as contours in Fig. 5.2 and Fig. 5.4) for both galaxies by collapsing the data cubes in spectral direction over all wavelengths free from emission lines and the most tenatious night-sky line residuals. The continuum is unresolved in either case, and we associate the continuum position in the cube with the central regions of the galaxy, regardless of whether the high surface-brightness stellar continuum around the galaxy center or the AGN dominates that continuum. At about $3''$ (24 kpc) of projected distance towards the north-east from TXS 2355−003, we find another, fainter $K-$band source, potentially a companion without bright line emission. NVSS J2106−314 appears to be an isolated source. Fig. 5.8 shows that there is a fainter, more extended continuum component not probed by SINFONI. This illustrates that spectral rebinning in the near-infrared does not allow to fully recover the continuum sensitivity of broad-band imaging, and highlights the importance of comparing deep broad-band imaging and imaging spectroscopy of high redshift galaxies when comparing line and continuum morphologies.

Line emission extends beyond the bright continuum seen in the SINFONI cubes (but not beyond the size of the lower surface-brightness continuum shown in Fig. 5.8). The size of the extended emission-line regions of NVSS J2106−314 and TXS 2355−003 is $5.3'' \times 2.0''$ (or 44.1 kpc×16.6 kpc) and $2.5'' \times 2.0''$ (or 21.1 kpc×16.9 kpc) along the major and minor axis, respectively, down to the surface-brightness detection limits given in Table 5.1. In NVSS J2106−314 the emission-line region is roughly centered on the continuum peak. In TXS 2355−003, the gas appears more lopsided. This is also seen in the continuum-subtracted ISAAC narrow-band imaging (Fig. 5.11). The integrated spectrum extracted from this fainter region, defined by the dashed rectangle in Fig. 5.4, clearly shows Hα and [N II]λ6583 (see Fig. 5.3). Fluxes and other line properties are listed for both galaxies in Table 5.1.

Both galaxies show velocity gradients of about 600 km s^{-1} over 25 kpc. In NVSS J2106−314, the gradient appears smooth on scales of 8 kpc and above, corresponding to the size of the seeing disk. In TXS 2355−003 we observe a more irregular velocity pattern, which could however be at least in parts due to the lower signal-to-noise ratio and irregular line profiles. In NVSS J2106−314, where we observe [O III]λ5007 and Hα at good signal-to-noise ratios, the gas kinematics and morphology are similar in either line.

The gas kinematics at larger radii is however more quiescent in both sources. Line widths in the extended gas of NVSS J2106−314 and TXS 2355−003 are FWHM = 300−400 km s^{-1}, more akin to those observed in a quasar illumination cone at z $\sim$ 2 (Lehnert et al., 2009) and Lyα blobs without powerful central radio source (*e.g.*, Wilman et al., 2005; Overzier et al., 2013). These FWHMs are thus significantly smaller than the higher-surface brightness gas in the central regions of these two galaxies themselves.

Table 5.1: Properties of the two galaxies discussed in this chapter.

	TXS 2355−003	NVSS J2106−314
Redshift	1.487	2.104
DL	10.792 Gpc	16.61 Gpc
radio power (500 MHz restframe)	3.7×10^{28} W Hz^{-1}	4.2×10^{28} W Hz^{-1}
radio size	38.8″ (328 kpc)	24.2″ (201 kpc)
jet timescale (advance speed 0.1*c*)	10.7×10^{6} yr	6.5×10^{6} yr
PA(jet, gas)	$\sim 90°$	$\sim 60°$
F([OIII]λ5007)$^{(1)}$	…	66.3 ± 13.2
F(Hβ)$^{(1)}$	…	5.2 ± 1.1
F([NII]λ6548)$^{(1)}$	2.8 ± 0.6	1.2 ± 0.2
F([NII]λ6583)$^{(1)}$	8.3 ± 1.7	3.7 ± 0.7
F([SII]λ6716)$^{(1,2)}$	1.4 ± 0.5	2.3 ± 0.5
F([SII]λ6731)$^{(1)}$	4.1 ± 1.0	2.2 ± 0.5
F(Hα)$^{(1)}$	12.0 ± 2.4	14.7 ± 3.0
$\mathcal{L}$(Hα)	1.7×10^{43} erg s^{-1}	4.8×10^{43} erg s^{-1}
ionized gas mass	2.4×10^{8} M$_\odot$	9.3×10^{8} M$_\odot$
RMS(SB,SINFONI map)$^{(3)}$	4.3	6.2

(1): All fluxes are given in units of $\times 10^{-16}$ erg s^{-1} cm^{-2}. — (2): [SII]λ6716 in TXS 2355−003 is affected by a night sky line residual. — (3): Surface brightness detection limit (in units of $\times 10^{-17}$ erg s^{-1} cm^{-2} arcsec^{-2})

Another stark difference to other HzRGs with similar data is that most of the emitting gas is at large position angles from the radio jet axis. Typically, jet and gas are aligned within about 20° − 30° (Fig. 5.1, see also Collet et al. 2013 in prep., Nesvadba et al. 2013 in prep.). Given the size of the minor axis of the extended line emission of up to $\sim 15-20$ kpc and beam smearing effects in the radio and near-infrared, this range is of-order of what would be expected if gas and jet were associated with each other. In NVSS J2106−314 and TXS 2355−003, however, the relative position angle between extended gas and radio jet axis is much larger, 60° and 90°, respectively. Fig. 5.1 shows that both galaxies clearly stand out from the overall sample of HzRGs with SINFONI observations.

5.2.2 Ancillary data and the need for complementary observations

Centimeter radio continuum

As presented in Fig. 5.2, NVSS J2106−314 has two lobes in the radio, separated by 24.2″ (nearly 200 kpc) along a Southeast to Northwest axis, but we do not detect any core in our ATCA observations, putting 3-σ upper limits on its putative flux of 13 μJy at 5.5 GHz and 61 μJy at 9.0 GHz.

TXS 2355−003 has a classic structure of 2 lobes, separated by 37″ (more than 300 kpc) along a Southeast to Northwest axis, and one bright core, as shown in the top left panel of Fig. 5.4. It has a steep spectrum in the radio ($\alpha = -1.18 \pm 0.06$), as is usual for HzRGs. Table 5.2 summarizes ancillary and our new VLA data for this source.

5.2.3 Complementary near infrared imaging with ISAAC

Finding extended line emission in powerful radio galaxies that is not related to the radio jet in an obvious way automatically poses the question whether the gas is more related to the radio galaxy itself, or to its environment, since many radio galaxies are known to trace massive dark-matter halos hosting galaxy overdensities as well as large quantities of diffuse and filamentary gas (*e.g.*, Venemans et al., 2007; van Ojik

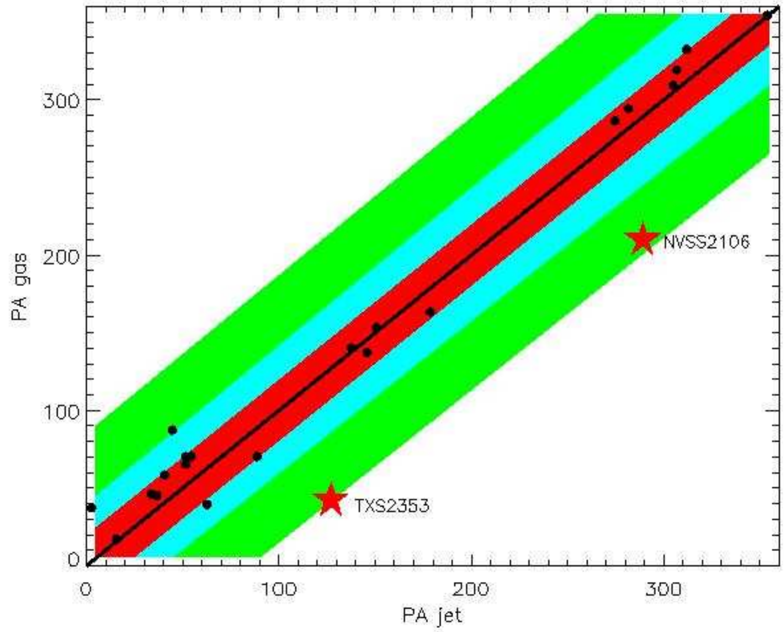

Figure 5.1: Illustration of the particularity of NVSS J2106−314 and TXS 2355−003. This graph presents the orientation of the extended emission line region (counted from North to the East) as a function of the orientation of the radio jets. For most of the sources, these two quantities agree to better than 25° for almost all the sources of our sample, with two noticeable exceptions: NVSS J2106−314 and TXS 2355−003.

Table 5.2: Ancillary radio measurements of TXS 2355−003

Frequency [MHz]	Flux(1) [mJy]		Reference
74	8060.0 ±	840	Cohen et al. (2007)
178	2900.0 ±	725	Gower et al. (1967)
365	1476.0 ±	61	Douglas et al. (1996)
408	1300.0 ±	80	Large et al. (1981)
1400	340.8 ±	11.1	Condon et al. (1998)
1400	357.0 ±	35.7*	White & Becker (1992)
2700	160.0 ±	16*	Wright & Otrupcek (1990)
3900	88.0 ±	8.8*	Larionov et al. (1994)
4850	89.0 ±	11.0	Griffith & Wright (1993)
4850	55.0 ±	8.3	Becker et al. (1991)
5000	29.4 ±	3.5 (SE lobe)	this work
—	26.6 ±	3.5 (NW lobe)	—
—	4.3 ±	0.5 (core)	—
8000	4.7 ±	0.5 (SE lobe)	—
—	2.6 ±	0.5 (NW lobe)	—
—	4.3 ±	0.5 (core)	—

(1): When no error is provided, we assume it corresponds to 10% of the flux and note it by an asterisk.

et al., 1997). This requires observations with much larger coverage than what can be obtained realistically

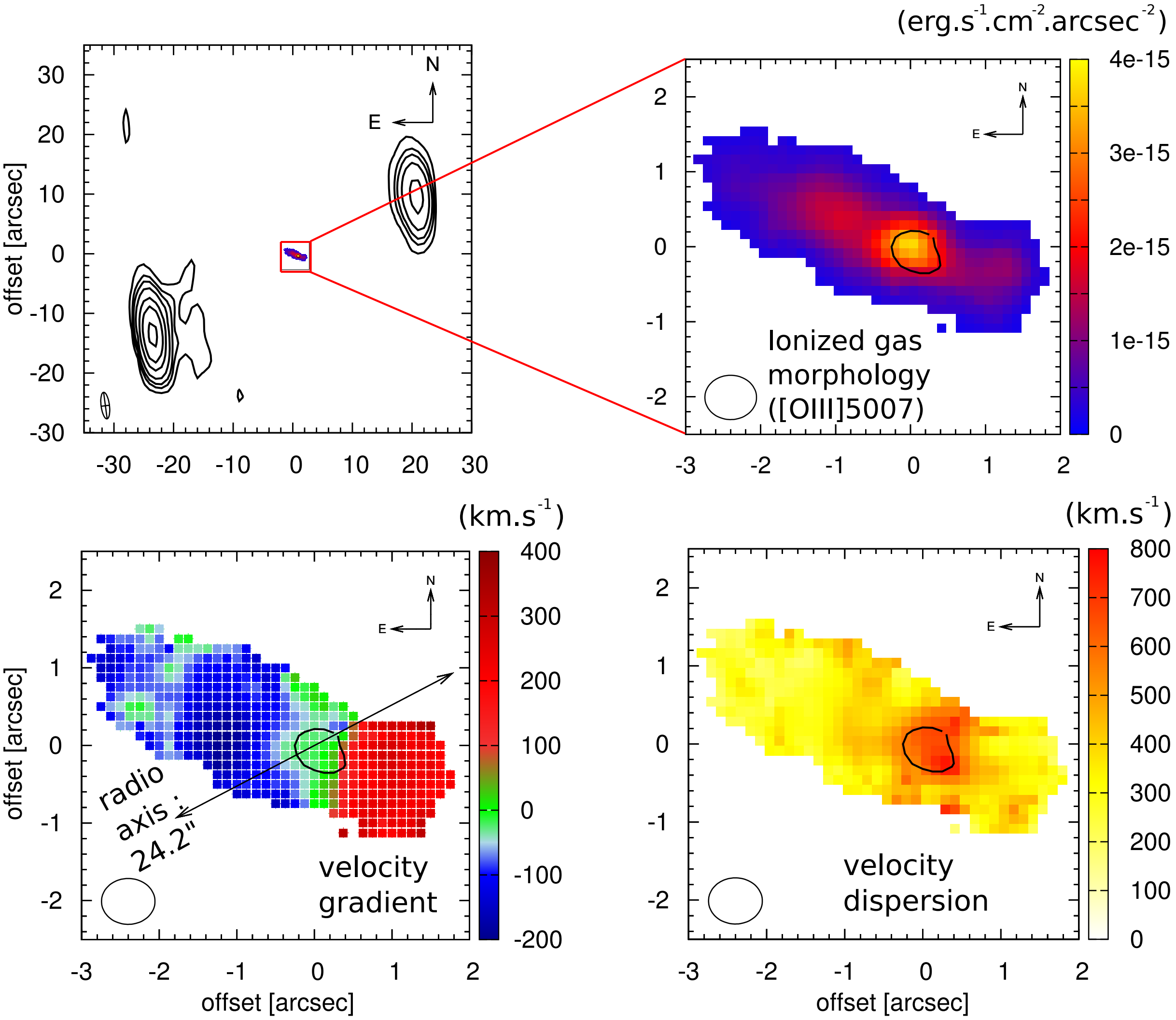

Figure 5.2: Radio observations of NVSS J2106−314 at 5.5 GHz (top left), coming from our ATCA observations. The relative size of the maps of the extended emission line region is given by the red square. The three others panels show the [OIII] surface brightness (top right), the relative velocity (bottom left) and the velocity dispersion (bottom right) of the ionised gas, as derived from our SINFONI observations.

Table 5.3: Emission lines in TXS 2355−003.

Line	λ_0 $^{(1)}$ [Å]	$\lambda_{\rm obs}$ $^{(2)}$ [Å]	FWHM $^{(3)}$ [km s^{-1}]	Flux $^{(4)}$ [10^{-16} erg s^{-1} cm^{-2}]
[NII]	6548.1	16289.1 ± 4.5	220 ± 25	1.8 ± 0.4
Hα	6562.8	16325.6 ± 4.5	220 ± 25	12.0 ± 2.4
[NII]	6583.4	16376.9 ± 4.5	220 ± 25	5.4 ± 1.1
[SII]	6716.4	16707.7 ± 4.5	220 ± 25	< 0.9
[SII]	6730.8	16743.5 ± 4.5	220 ± 25	2.6 ± 0.5

(1): Rest-frame wavelength. — (2): Observed wavelength. — (3): Full-Width at Half Maximum, corrected for instrumental resolution (in km s^{-1}). — (4): Line flux deduced from the fit (in 10^{-16} erg s^{-1} cm^{-2}).

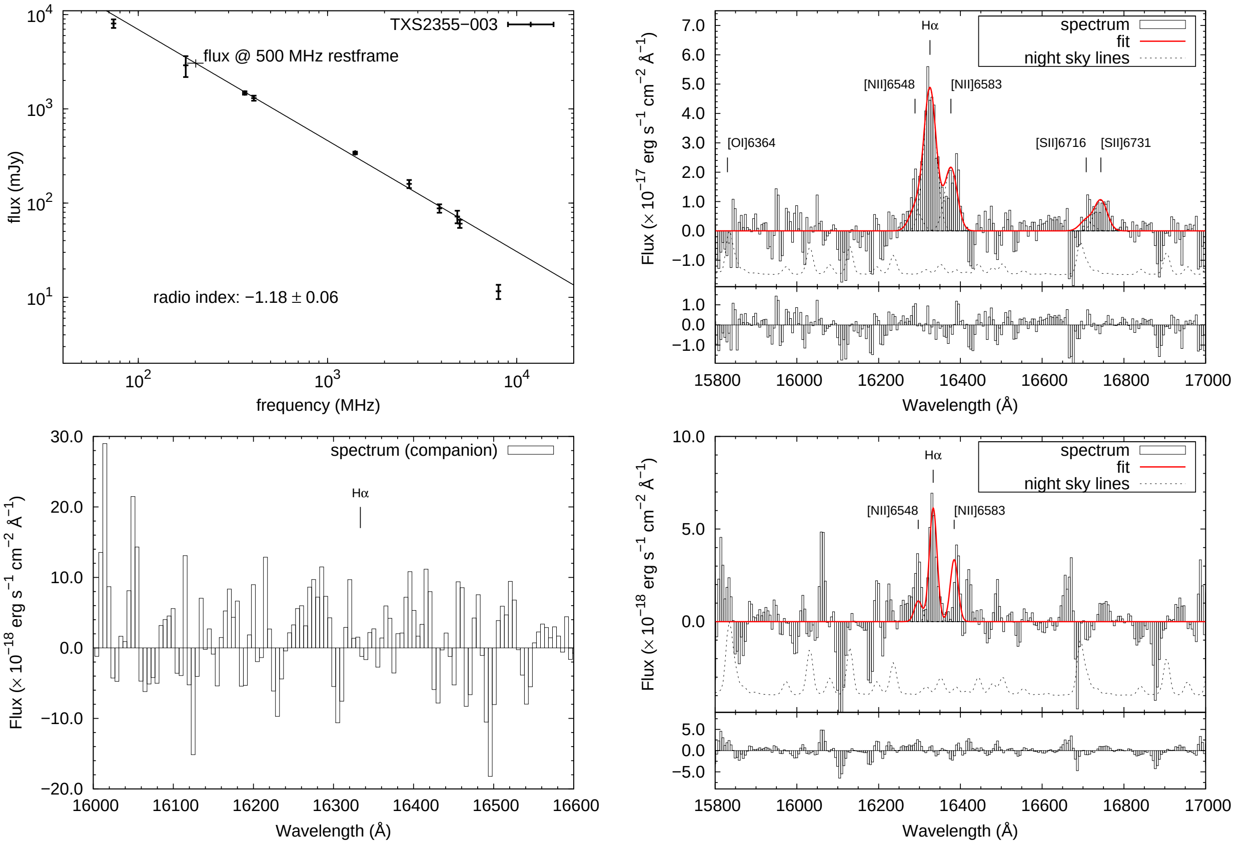

Figure 5.3: *Top left*: Spectral energy distribution of TXS 2355−003 in the radio, which follows a power law with a steep index, as is usual for HzRGs (*e.g.*, Miley & De Breuck, 2008). *Top right*: Spectrum of TXS 2355−003, integrated over all spaxels where the Hα emission from the galaxy is detected and corrected for velocity shifts. *Bottom left*: Integrated spectrum centered on the companion of TXS 2355−003. The wavelength of the Hα emission of TXS 2355−003 is indicated. *Bottom right*: Integrated spectrum of the Northeast part of the emission line region of TXS 2355−003, defined by the dashed rectangle in Fig. 5.4.

with the SINFONI field of view, and is the reason why we obtained narrow and broad-band imaging for TXS 2355−003, and broad-band imaging for NVSS J2106−314. The goal of this study is to search for overdensities of line emitters associated with the radio galaxy, and to investigate whether the extended emission line regions extend further out than the few tens of kpc covered by SINFONI.

Observations and data reduction

TXS 2355−003 was observed with ISAAC/VLT both in the $H-$band ($\lambda_0 = 1.65\ \mu$m and $\Delta\lambda = 3000$Å) and in the narrow-band filter NB1.64 ($\lambda_0 = 1.64\ \mu$m and $\Delta\lambda = 250$Å) on the nights 2012 September 30 and October 01. NVSS J2106−314 was observed on the 2012 October 02 in the K_s-band. The conditions were photometric during these 3 nights and the seeing disk in the reduced images is very good: $0.47''$ and $0.5''$ for the $H-$band and the NB images of TXS 2355−003 (respectively) and $0.43''$ for the K_s-band image of NVSS J2106−314.

For the NB imaging of TXS 2355−003, the observation was made of 99 integrations of 150 sec, repeated in blocks of $\sim$1 hour. Between each exposition, a dither pattern was adopted in order to avoid the systematic addition of bad-pixels at the same positions of the image and ease the subsequent sky subtraction (as it is usual in the IR). The $H-$band observation of TXS 2355−003 was made of 29 integrations of 12 sec and the K_s-band observation of NVSS J2106−314 was made of 25 integrations of 15 sec, both with a dither pattern

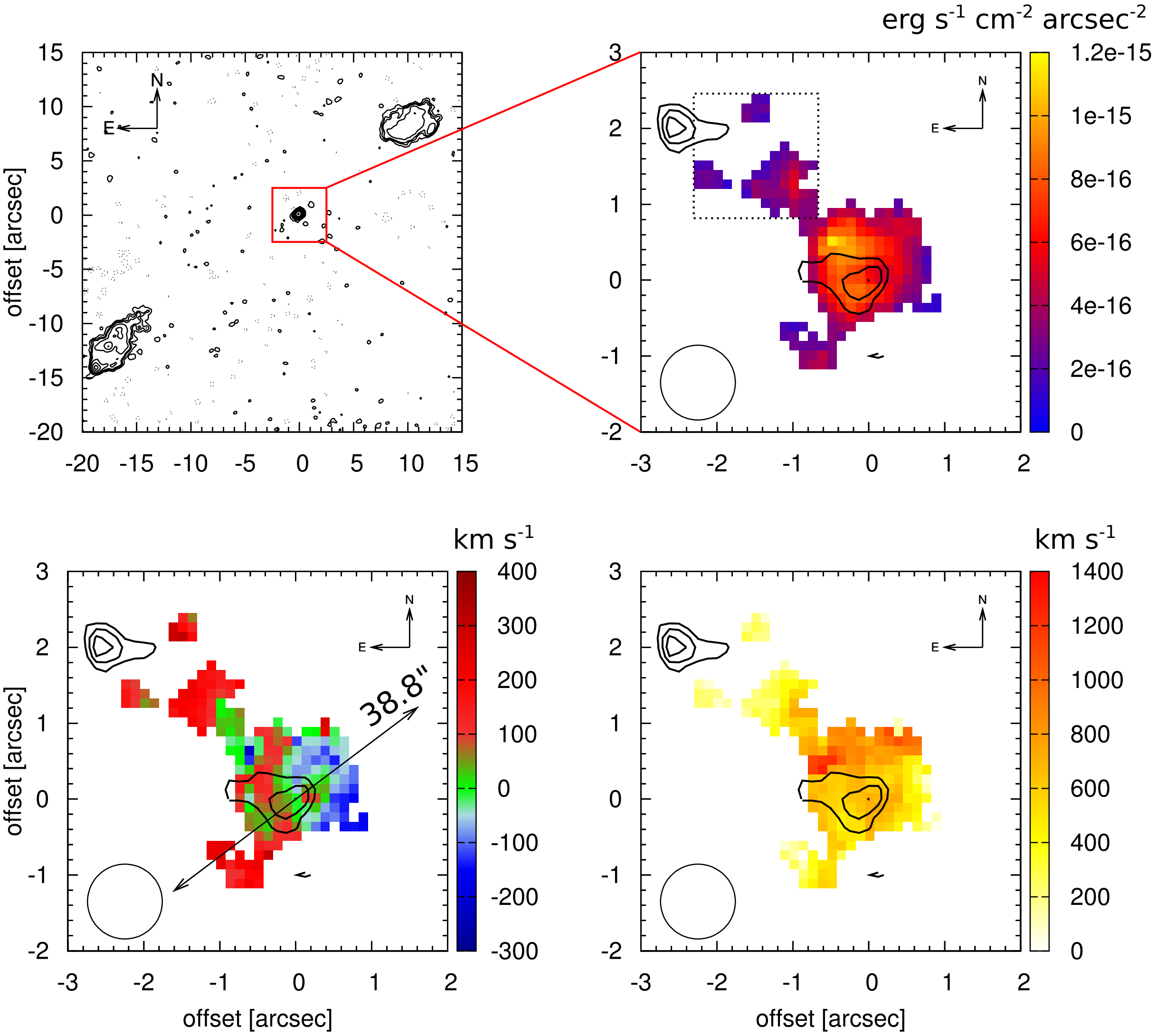

Figure 5.4: Radio observations of TXS 2355−003 at 5.0 GHz (top left) with the field of view of SINFONI in red ; and Hα surface brightness (top right), velocity (bottom left) and velocity dispersion (bottom right) from our SINFONI observations.

between each exposure.

After visual inspection, we discarded 17/99 frames in the the NB imaging of TXS 2355−003 because of a bright star in the corner that saturated the detector. We discarded 1/29 frame in the broad-band imaging of TXS 2355−003 because of a straight bright line (maybe a satellite).

Several stars detected in the 2-MASS survey are present in both fields. We used their coordinates (accurate to $\lesssim 0.1-0.2''$) to enhance the astrometry of our observations, using the software `gaia`. Indeed, we found that our observations were systematically shifted to the north-north-west by $1.73''$ (for TXS 2355−003) and by $1.06''$ (for NVSS J2106−314). The RMS of the fit to 2-MASS astrometry is of $0.07''$ for TXS 2355−003 (with 4 2-MASS objects in the field of view) and $0.32''$ (with 10 2-MASS objects in the field of view), so we estimate that the absolute astrometry of our observations is better than $0.3''$.

We also used these field stars to check our flux calibration and find that they agree to $\lesssim 20\%$:

- When using observations of standard stars, we find a conversion factor of 1.404×10^{-7} Jy/# (where # is the electrons number count) for the $H-$band observations of TXS 2355−003, and we find $1.537 \times$

Table 5.4: ISAAC observations log.

Object ID (1)	coordinates (2)	Date (3)	ToT (4)	Filter (5)	Std star (6)
TXS 2355−003	23:55:35.15 ; −00:02:41.9	30/09/2012	157.5 (200)	NB1.64	S234-E, S301-D
		01/10/2012	47.5 (47.5)	NB1.64	S071-D,
		01/10/2012	5.6 (5.8)	H	S677-D
NVSS J2106−314	21:06:25.90 ; −31:40:01.5	02/10/2012	6.25 (6.25)	K_s	S677-D

(1): Source identification. — (2): Coordinates of the source (J2000) — (3): Date of observation — (4): Time on Target (min) kept(observed) — (5): Filter used — (6): Standard star used

10^{-7} Jy/# when using the 2-MASS stars that are in the field.

- And for NVSS J2106−314, we find conversions factors of 1.791×10^{-7} Jy/# from the observations of standard stars and 2.232×10^{-7} Jy/# from stars in the field of NVSS J2106−314.

We used the flux calibration based on stars of the the field of view of the observations.

The combined frames give final images which depths reach, normalized to a 1 sec exposure time, $\sigma_{NB} = 5.83 \times 10^{-3}$ #, or $\sigma_{NB} = 1.16 \times 10^{-7}$ Jy arcsec^{-2} (or $m_{NB}^{min} = 26.24$ mag arcsec^{-2}) and $\sigma_H = 6.33 \times 10^{-2}$ #, or $\sigma_H = 1.452 \times 10^{-6}$ Jy arcsec^{-2} (or $m_H^{min} = 23.50$ mag arcsec^{-2}). For the K_s−band observations of NVSS J2106−314, we have $\sigma_{K_s} = 4.05 \times 10^{-2}$ #, or $\sigma_{K_s} = 1.186 \times 10^{-6}$ Jy arcsec^{-2} (or $m_{K_s}^{min} = 23.71$ mag arcsec^{-2}).

Completeness estimate

If we want to compare our observations with other works, and particularly sources counts, we need to take into account the difference of depth of the various images. In order to assess this completeness limit, we injected fake sources at empty positions in all individual frames of the NB observations before reducing them again. These artificial sources are located in the center of the final image. Their flux is chosen to be from 2 to 11 times the RMS level in the central part of the final image. Their size and morphology is the same as the seeing disk since we do not expect potential high-redshift sources to be much more extended than the seeing disk in our observations. By doing so, effects due to slight misalignments in the addition of individual frames, are also taken into account.

The results of this analysis are given in Fig. 5.5. It gives the number of artificial sources detected in the final image as a function of their input flux. From these results, we estimate that we detect 90% of sources with surface brightness above 5×10^{-7} Jy arcsec^{-2} (or above 24.7 mag$_{AB}$ arcsec^{-2}).

5.3 Continuum morphologies

5.3.1 Sérsic profiles

Lumimosity profiles can be a useful tool to have an idea of the morphology of these two unusual galaxies. Since it has been found that quiescent early-type galaxies at high-redshift tend to be more compact than local analogues (*e.g.*, Daddi et al., 2005; van Dokkum et al., 2008; Schawinski et al., 2011; Whitaker et al., 2012), luminosity profiles can also be used as evolutionary probes.

It is unquestionable that both galaxies are spatially resolved since their luminosity profiles are much more extended than the PSF of the observations, as illustrated in Fig. 5.6 and Fig. 5.7. The study of the luminosity profiles and of the two continuum images (Fig. 5.8) shows that these extended morphologies are due to the faint halos surrounding the galaxies. In the case of TXS 2355−003, it seems that the galaxy is only composed of this faint halo, without any stellar core or bulge as it is the case for NVSS J2106−314.

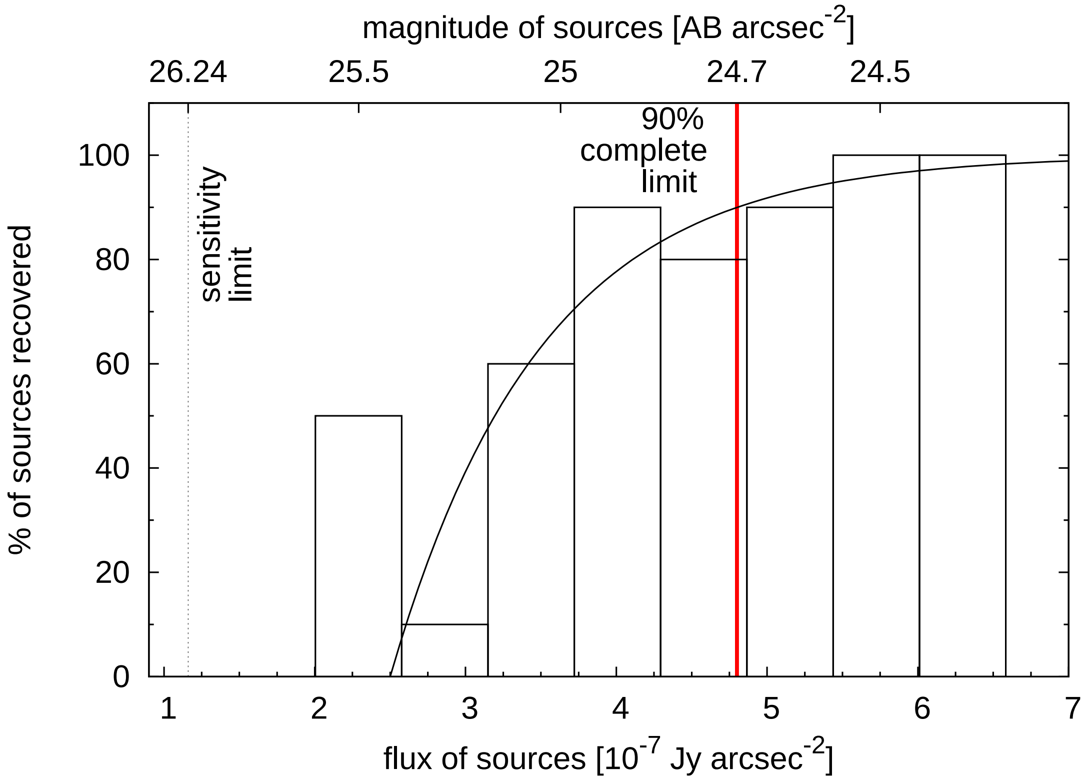

Figure 5.5: Percentage of sources recovered from those that were artificially included in individual frames for the narrow-band imaging. The "sensitivity limit" corresponds to the RMS in the central part of the final image. Our NB observations are 90% complete down to $\sim 5 \times 10^{-7}$ Jy arcsec^{-2}, or 24.7 mag$_{AB}$ arcsec^{-2}

Luminosity profiles are traditionnally well reproduced by Sérsic profiles (Sérsic, 1963, 1968) that have the form:

$$I(r) = I_e \ \exp\Big(- b_n \Big[\, (\frac{r}{R_e})^{1/n} - 1 \, \Big] \Big)$$

where I is the intensity as a function of the distance r from the (luminosity-)center of the galaxy. This model has 3 parameters:

- n is the Sérsic index and gives the shape of the luminosity profile. Typical values of n are $n = 1$, that gives an exponential profile ; $n = 4$ corresponds to the de Vaucouleurs (1948) profile, which usually well represents the shape of elliptical galaxies ; and disks of spiral galaxies are better represented by $n = 2$.
- R_e is the effective radius of the galaxy and gives an idea of the apparent size of the galaxy: half of the light from the galaxy is enclosed by the effective radius.
- I_e is the normalisation factor, taken here as the intensity at the effective radius.
- b_n is not a free parameter because it can be deduced from previous parameters and the total luminosity of the galaxy. Some approximation formulae exist and give an expression of b_n as a function of n (*e.g.*, Ciotti & Bertin, 1999; MacArthur et al., 2003).

We used two methods to study the morphology of TXS 2355−003 and NVSS J2106−314: Firstly, we obtained the luminosity profiles with the task `ellipse`, part of IRAF, which fits ellipses to isophotes of the object. Secondly, we used `Galfit` (Peng et al., 2002, 2010), a software that finds the Sérsic parameters that represent the better the morphology of the galaxy, based on a least-square algorithm.

Regarding the first method, based on the task `ellipse`, we kept only one point every $\sim 0.1''$ to performe the Sérsic profile fit, making sure that the ellipticity of these points is small enough ($\lesssim 0.05$ in the inner parts ; $\lesssim 0.40$ in the outer parts) as to approximate the major axis of the fitted ellipse by the radius of a circle. We then fit a Sérsic profile to these luminosity profiles. Some care needs to be taken here since the seeing (although it was very good by Paranal's standards) is of the same order of magnitude as the effective radius and therefore significantly affects the observed shape of the galaxy. In order to circumvent that effect, we convolved the Sérsic profile by the seeing of our observations, approximated by a Gaussian. This is a more robust method than, *e.g.*, deconvolving the image, which is an ill-posed problem.

Trying to directly fit the luminosity profiles by the convolved Sérsic profile is not satisfactory and gives unstable parameters solutions, depending on first guesses that are used. Instead, we decide to directly map the parameter space, since there are only two parameters difficult to estimate: n and R_e (the normalisation I_e is straightforward to derive). For n, we use steps of 0.01 from 0.10 (the lowest value of n for which the formula from MacArthur et al. (2003) can be used to estimate b_n) to 1.0 ; and for R_e, we use steps of $0.01''$ from $0.1''$ to $2.0''$.

Regarding `Galfit`, we use it on smoothed images of roughly the same size as those shown on Fig. 5.8. We use masks in order not to take into account the objects that are close to the galaxies, *i.e.*, the companion of TXS 2355−003 and the two sources to the Southeast of NVSS J2106−314. We leave all the parameters of the morphological model free to vary: the Sérsic parameters n and R_e, the position of the center of the model, the axis ratio (b/a) and the position angle. We also perform a De Vaucouleurs fit, *i.e.*, with $n = 4$. Residuals are inspected in each case and found to be reasonable for the Sérsic fits: they are shown in Fig. 5.9 and are within the $\pm 3\sigma$ range. In the case of the De Vaucouleurs fit of TXS 2355−003, the central region displays strong negative residuals, this is because of its extended structure lacking a strong peak, a feature impossible to reproduce with a Sérsic function having reasonnable parameters, hence the extreme value found for $R_e = 261$ kpc. The De Vaucouleurs fit to NVSS J2106−314 gives acceptable results, with residuals only slightly greater than the $\pm 3\sigma$ range. All the results are given in Table 5.5.

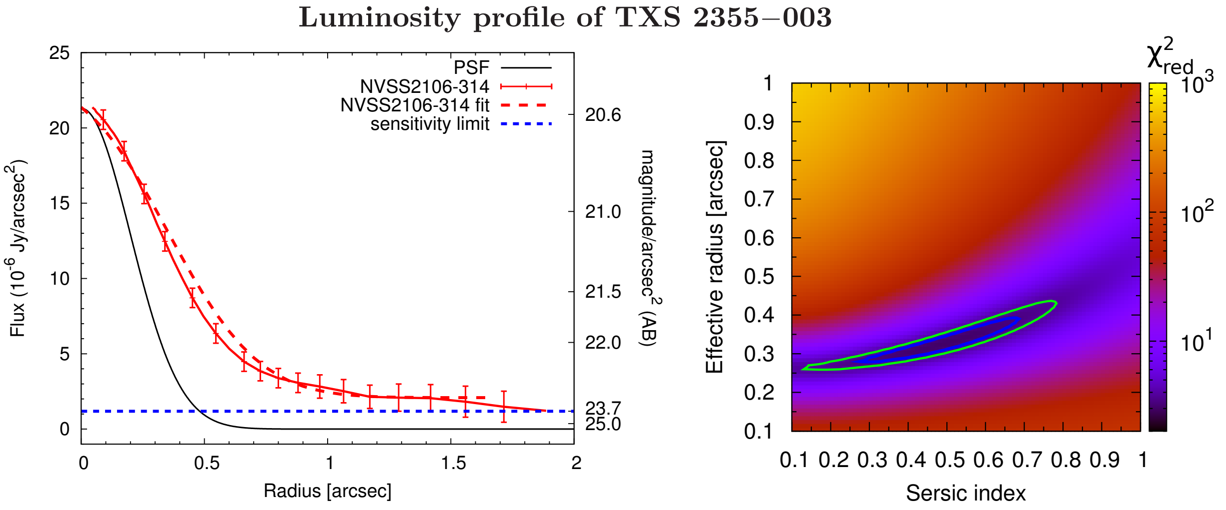
Luminosity profile of TXS 2355−003

Figure 5.6: *Left*: Luminosity profile of TXS 2355−003. The points with the errorbars are the points given by the task **ellipse** that are used for the fit (*i.e.*, one every $\sim 0.1''$). the solid red line is from the whole output of the task **ellipse**. The dashed red line is the best Sérsic profile that we find, based on our χ^2 mapping. *Right*: Map of the reduced χ^2 for the two parameters of the Sérsic function n and R_e that leads to the results given in the text. The blue contour gives the 1σ (68.3%) confidence level and the green contour gives the 99% confidence level.

We find that values of $n = 0.48 \pm 0.05$ and $R_e = 0.69 \pm 0.05''$ (5.8 ± 0.4 kpc) give the best representation of the luminosity profile of TXS 2355−003, with a reduced chi squared of $\chi^2_{red} = 2.4$ (see Fig. 5.6). The `Galfit` algorithm confirms our results and gives $n = 0.62$ and $R_e = 0.89''$ (7.5 kpc).

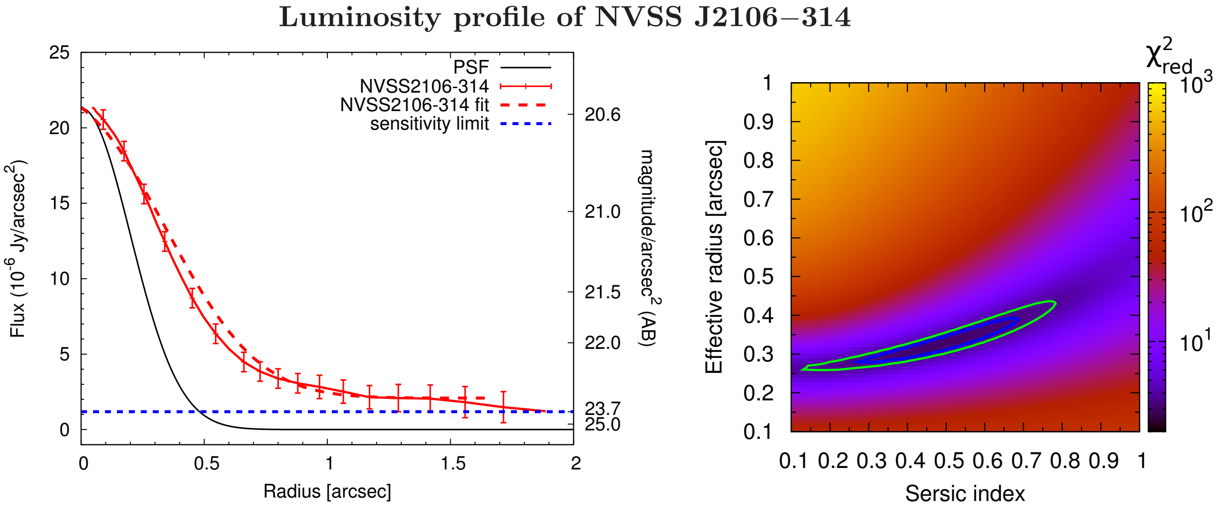

Figure 5.7: Same as Fig. 5.6 for NVSS J2106−314.

Regarding NVSS J2106−314, we find $n = 0.5 \pm 0.2$ and $R_e = 0.33 \pm 0.05''$ (2.7 ± 0.4 kpc), with a reduced chi squared of $\chi^2_{red} = 3.2$. The `Galfit` algorithm gives different results: $n = 1.3$ and $R_e = 0.85''$ (7.1 kpc). We note that these results lie in the same "valley" of the χ^2 map as ours, as illustrated by Fig. 5.7.

We summarize in Table 5.5 the values given by the different techniques that we use to fit the luminosity profiles of TXS 2355−003 and NVSS J2106−314.

Table 5.5: Values of Sérsic parameters given by our two analysis techniques.

Technique	TXS 2355−003				NVSS J2106−314			
	n	R_e	b/a	PA	n	R_e	b/a	PA
χ^2 mapping	0.48 ± 0.05	5.8 ± 0.4 kpc	—	—	0.50 ± 0.20	2.7 ± 0.4 kpc	—	—
Sérsic	0.78	9.6 kpc	0.85	62.6	1.32	7.1 kpc	0.56	74.1
De Vaucouleurs	4.0	260.8 kpc	0.83	45.1	4.0	9.8 kpc	0.50	72.6

5.4 Hα morphology of TXS 2355−003 and associated Hα-emitters

5.4.1 Narrow-band observations of TXS 2355−003

The situation of the NB imaging is illustrated by Fig. 5.10: if we assume that the galaxy has a flat underlying continuum (see Kurk et al., 2004a) at the level I_c (put at 0.1 on the figure) along with Hα + [NII] emission lines flux F_{el} (in red on the figure) and that our two filters have transmission functions $\tau_{NB}(\lambda)$ (for the NB1.64 filter) and $\tau_H(\lambda)$ (for the $H-$band filter), then the fluxes we observe are the sum of the emission lines flux and the continuum flux, $F_{c,NB}$ and $F_{c,H}$, expressed as:

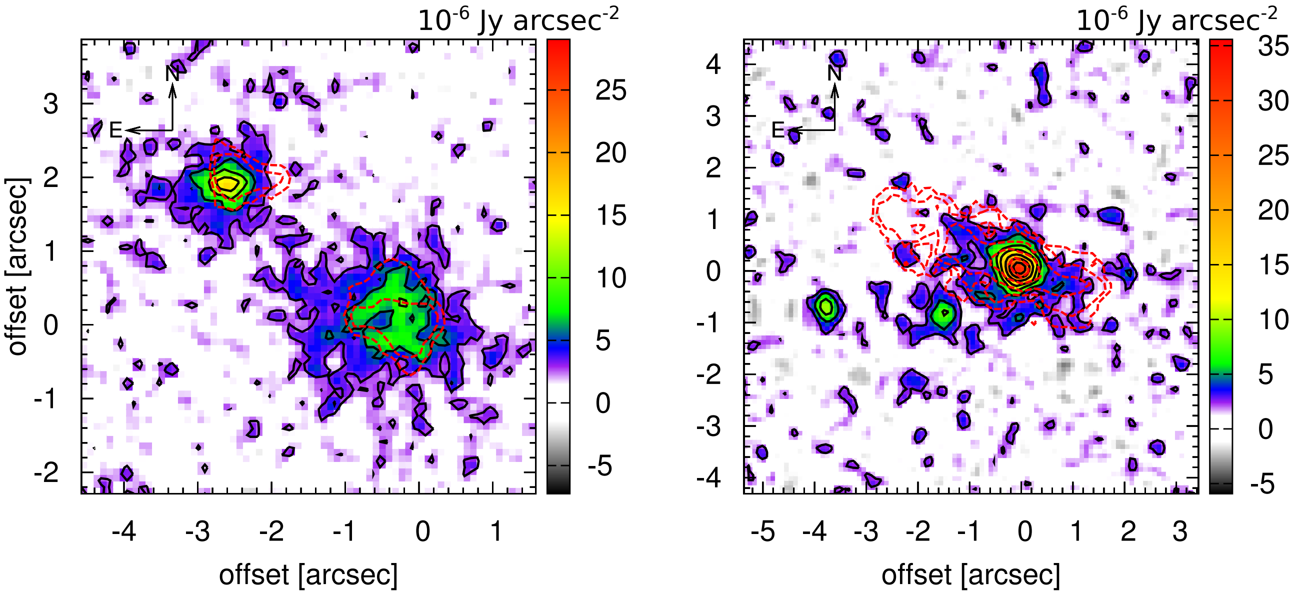

Figure 5.8: Continuum images of TXS 2355−003 ($H-$band, *left*) and NVSS J2106−314 (K_s-band *right*). The red dashed lines give the morphology of the continuum image of TXS 2355−003 or of the extended emission line region of NVSS J2106−314, as seen in our previous SINFONI observations. The black solid contours are at the 2, 4, 7, 10, 15, 20, 25 σ levels in each image, with $\sigma = 1.452 \times 10^{-6}$ Jy arcsec^{-2} for the $H-$band image of TXS 2355−003 and $\sigma = 1.186 \times 10^{-6}$ Jy arcsec^{-2} for the K_s-band image of NVSS J2106−314

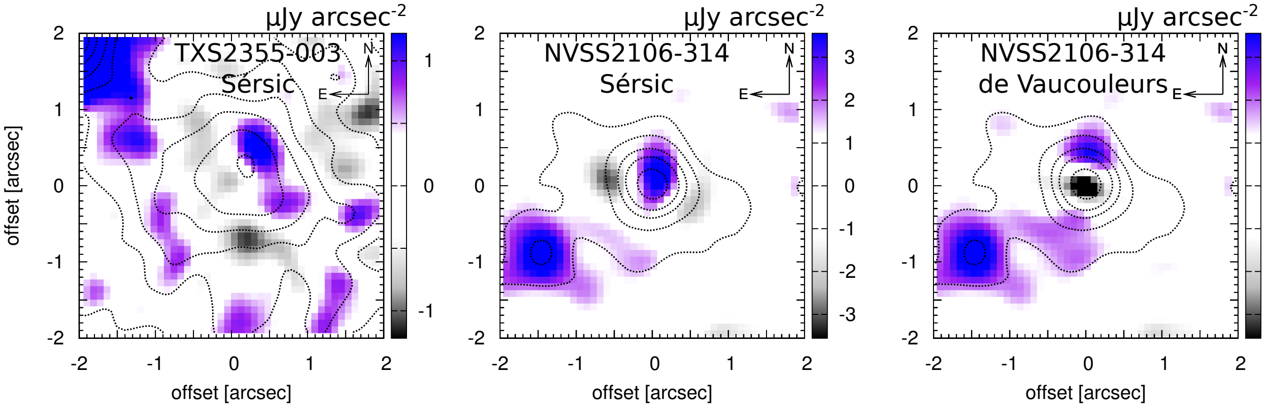

Figure 5.9: Residuals after subtraction of the morphological models found by the algorithm **Galfit**, assuming a Sérsic parametrization, for TXS 2355−003 ($H-$band, *left*) and NVSS J2106−314 (K_s-band *middle*). The residuals from the De Vaucouleurs fit to NVSS J2106−314 are shown on the *right*. The black dashed contours give the smoothed morphology of the source, at levels 2 ; 4 ; 7 ; 10 ; 15 ; 20 ; 25 σ, with $\sigma = 0.407\ \mu$Jy arcsec^{-2} for the $H-$band image of TXS 2355−003 and $\sigma = 1.186\ \mu$Jy arcsec^{-2} for the K_s-band image of NVSS J2106−314. The colorbar spans the $\pm 3\sigma$ range for both images and color saturates afterwards.

- in the $H-$band

$$F_H = \int \big(I_{el}(\lambda) + I_c(\lambda)\big) \times \tau_H(\lambda)\mathrm{d}\lambda$$
$$\simeq F_{el} \times \tau_H(\lambda_0) + I_c \times \int \tau_H(\lambda)\mathrm{d}\lambda$$

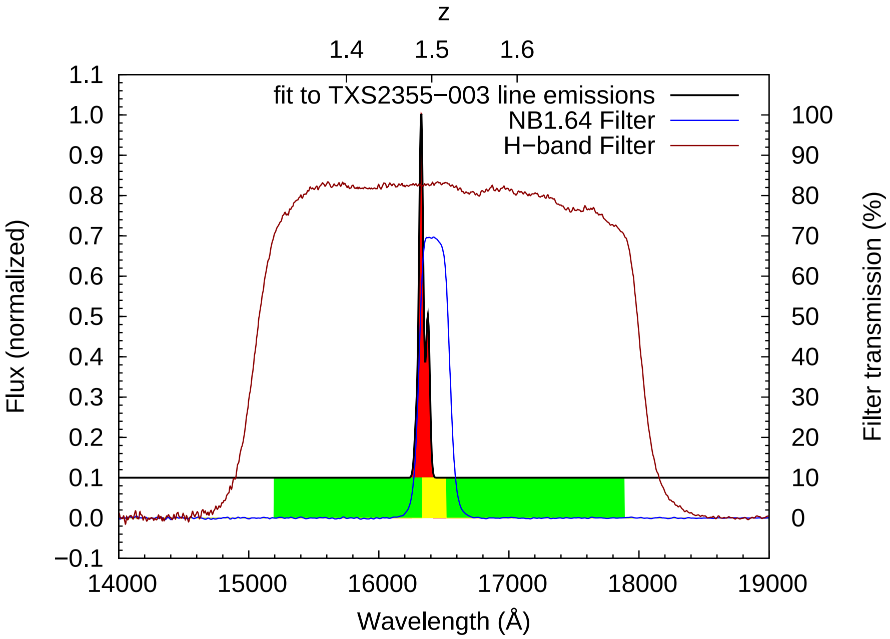

Figure 5.10: The transmission curves of the two filters used and the fit of the Hα + [NII] emission lines from the SINFONI data, with some continuum level added.

where λ_0 is the central wavelength of Hα (the main emission line). Here, we assumed that the transmission curve of the H filter is constant over the wavelength range where the emission lines are non-negligeable. We can also reasonably assume that the flux due to the continuum dominates the $H-$band flux: $F_{el} \times \tau_H(\lambda_0) \ll F_{c,H}$ and finally obtain:

$$F_H \simeq F_{c,H} = I_c \times \int \tau_H(\lambda)\mathrm{d}\lambda$$

- in the narrow-band

$$\begin{aligned} F_{NB} &= \int \big(I_{el}(\lambda) + I_c(\lambda)\big) \times \tau_{NB}(\lambda)\mathrm{d}\lambda \\ &\simeq F_{el} \times \tau_{NB}(\lambda_0) + I_c \times \int \tau_{NB}(\lambda)\mathrm{d}\lambda \end{aligned}$$

Here, the assumption that the transmission curve of the NB filter is constant over the wavelength range where the emission lines are non-negligeable can be challenged, since they lie at the edge of the filter. Using the spectrum of TXS 2355−003 from our SINFONI data, we assess that $\sim$ 20% of the emission lines light we could have expected if the lines were well-centered in the filter, is lost because of this. If taking only the Hα line into account, this effect increases to 25% (the [NII] line lies redwards and falls well at the maximum of the transmission of the filter).

We can obtain a continuum-subtracted image, in which most of the flux comes from the Hα + [NII] lines emission, by doing:

$$F_{el} \times \tau_{NB}(\lambda_0) = F_{NB} - I_c \times \int \tau_{NB}(\lambda)\mathrm{d}\lambda$$

$$F_{el} \times \tau_{NB}(\lambda_0) = F_{NB} - F_H \times \frac{\int \tau_{NB}(\lambda)\mathrm{d}\lambda}{\int \tau_H(\lambda)\mathrm{d}\lambda}$$

Numerically, we have $\tau_{NB}(\lambda_0) \simeq 0.7 \times 0.8$ (the 0.8 factor is to account for the position of the emission lines at the edge of the filter) and the ratio of the integral over the transmission of the two filters is 7.17%. This means that we should theoritically subtract 7.17% of the broad-band image from the narrow-band image in order to obtain solely the contribution of the Hα emission. When directly comparing fluxes from a dozen of stars in both images, we empirically find that a scaling factor of 7.61% gives better results, in particular that the residuals of objects in the center of the subtracted image were the closest to zero in this case.

5.4.2 Hα emitting gas associated with TXS 2355−003

Once we have the image of the Hα emission, we can study the distribution of the ionized gas around the radio galaxy and compare results obtained with ISAAC with previous ones coming from SINFONI. Fig. 5.11 (*left*) presents the extended Hα emission line region around TXS 2355−003 as seen in our ISSAC observations.

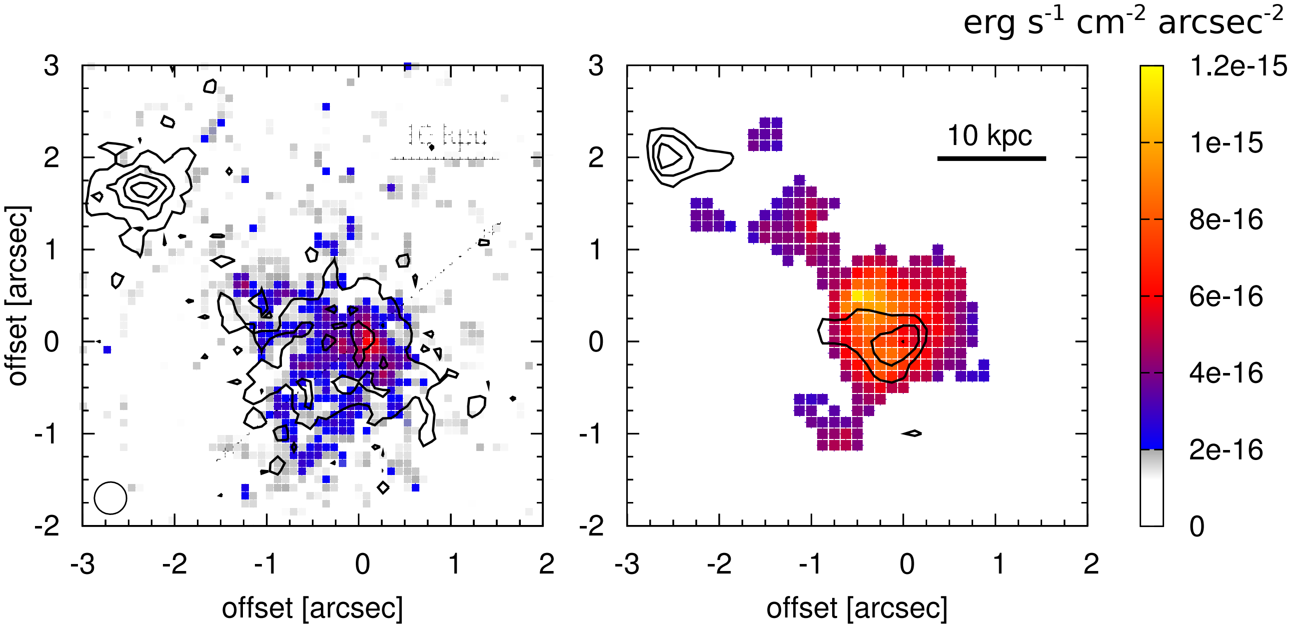

Figure 5.11: *Left*: NB image of TXS 2355−003, from which the scaled contribution of broad-band image is subtracted. This image therefore represents the contribution of the Hα + [NII] emitting gas. *Right*: Hα surface brightness of TXS 2355−003, as derived from our SINFONI observations. The scale is the same in both images and the solid coutour lines represent the continuum.

The morphology of the ionized gas is fairly consistent between both observations: a bright emission line region associated with the radio galaxy, more extended along two directions. Towards the Southeast, where the gas is clearly more extended than the continuum and towards the Northeast (*i.e.*, the companion) but without reaching it.

5.4.3 Finding Hα emitters associated with TXS 2355−003

The basic idea to find galaxies that lie at similar redshift as TXS 2355−003 is to look for objects that are "too" luminous in the NB image (compared to their BB image), this excess of light being due to the Hα + [NII] lines. Looking for objects that have color excess in the NB image can be seen in several ways. Here we use 2 of them: constructing a continuum subtracted image or by looking for color excesses, as did Bunker et al. (1995).

“Color”-magnitude diagram of the broad and narrow-band image

When plotting the color (*i.e.*, the quantity $m_H - m_{NB1.64}$) as a function of the magnitude $m_{NB1.64}$ of the objects that we observe, we expect Hα emitters to lie in the upper part of this diagram.

The first step is to extract the sources from our images. In this aim, we use sExtractor v2.5.0 (Bertin & Arnouts, 1996) on a sub-part of the final narrow-band image, in which the noise does not vary a lot. We set the parameters `DETECT_THRESH` = 2.0 and `ANALYSIS_THRESH` = 2.0 and the other ones are left to their default values. We then use the sources positions to perform aperture photometry (with an aperture diamater of 2″) on the narrow- and broad-band images.

The next step is to quantify the significance of excess of the Hα flux expected from the Hα emitters. Bunker et al. (1995) introduced a parameter, Σ, which measures the significance of the flux in excess. It is defined as “the number of standard deviations between the counts measured in the broad-band and the number expected on the basis of the narrow-band counts [assuming a flat spectrum]”, *i.e.*,:

$$\Sigma = \frac{F_H^{exp} - F_H}{\sigma}$$

where F_H^{exp} is the broad-band flux expected on the basis of the narrow-band flux and σ is the standard deviation, taken as the quadratic sum of the RMS level of broad- and narrow-band images: $\sigma = \sqrt{\sigma_H^2 + \sigma_{NB}^2}$.

We note that Bunker et al. (1995) used a fixed aperture for their photometry, therefore having a well-defined error, whereas sExtractor performs photometry on the whole extent of detected objects, leading to errors that depend on their sizes, among other parameters. In order to use relevant *constant* errors as Bunker et al. (1995) did, we can whether use median errors (*e.g.*, Kurk et al., 2004a), or use sources positions given by sExtractor and perform regular aperture photometry on sources detected. We chose this last option, with an aperture of 2″.

Using what we found previously, we have:

$$\Sigma = \left(\frac{\int \tau_H(\lambda)\mathrm{d}\lambda}{\int \tau_{NB}(\lambda)\mathrm{d}\lambda} \times F_{NB} - F_H \right) \times \frac{1}{\sigma}$$

With the idea of introducing a color term in this expression, it gives:

$$\begin{aligned}
\frac{F_H}{F_{NB}} &= \frac{\int \tau_H(\lambda)\mathrm{d}\lambda}{\int \tau_{NB}(\lambda)\mathrm{d}\lambda} - \frac{\sigma}{F_{NB}}\Sigma \\
m_H - m_{NB1.64} &\simeq -2.5 \log \left(\frac{\int \tau_H(\lambda)\mathrm{d}\lambda}{\int \tau_{NB}(\lambda)\mathrm{d}\lambda} - \frac{\sigma}{F_{NB}}\Sigma \right) \\
m_H - m_{NB1.64} &\simeq -2.5 \log \left(\frac{\int \tau_H(\lambda)\mathrm{d}\lambda}{\int \tau_{NB}(\lambda)\mathrm{d}\lambda} - \Sigma\sigma \, 10^{-0.4(8.9 - m_{NB1.64})} \right)
\end{aligned}$$

However, having red colors is not sufficient: the brightest sources of the field have fluxes much greater than σ and the previous constrain is not relevant for them. That is why we require that Hα candidates also have high enough equivalent width $\mathrm{EW_{H\alpha}}$, that is defined as (keeping previous notations):

$$\begin{aligned}
\mathrm{EW_{H\alpha,z}} &= \frac{F_{el}}{I_c} \\
&= \mathrm{EW_{H\alpha,0}} \times (1+z)
\end{aligned}$$

and that is insensitive to the flux of the sources. With what we showed previously:

$$\begin{aligned}
F_{el} &\simeq \frac{1}{\tau_{NB}(\lambda_0)} \left(F_{NB} - F_H \frac{\int \tau_{NB}(\lambda)\mathrm{d}\lambda}{\int \tau_H(\lambda)\mathrm{d}\lambda} \right) \\
I_c &\simeq \frac{F_H}{\int \tau_H(\lambda)\mathrm{d}\lambda}
\end{aligned}$$

we obtain:

$$\mathrm{EW}_{\mathrm{H}\alpha,\mathrm{z}} \simeq \frac{F_{NB}}{F_H} \times \frac{\int \tau_H(\lambda)\mathrm{d}\lambda}{\tau_{NB}(\lambda_0)} - \frac{\int \tau_{NB}(\lambda)\mathrm{d}\lambda}{\tau_{NB}(\lambda_0)}$$

Then, to express this as a function of the color $m_H - m_{NB1.64}$:

$$\frac{F_{NB}}{F_H} \simeq \frac{1}{\int \tau_H(\lambda)\mathrm{d}\lambda}\left(\tau_{NB}(\lambda_0) \times \mathrm{EW}_{\mathrm{H}\alpha,\mathrm{z}} + \int \tau_{NB}(\lambda)\mathrm{d}\lambda\right)$$

$$m_H - m_{NB1.64} \simeq 2.5\log\left(\frac{\tau_{NB}(\lambda_0) \times \mathrm{EW}_{\mathrm{H}\alpha,\mathrm{z}}}{\int \tau_H(\lambda)\mathrm{d}\lambda} + \frac{\int \tau_{NB}(\lambda)\mathrm{d}\lambda}{\int \tau_H(\lambda)\mathrm{d}\lambda}\right)$$

Taking typical values of our observations ($\mathrm{EW}_{\mathrm{H}\alpha,0} = 25-50$ Å ; $\tau_{NB}(\lambda_0) \simeq 0.7$; $\int \tau_H(\lambda)\mathrm{d}\lambda \simeq \tau_H(\lambda_0)\Delta\lambda_H \simeq 0.8 \times 3000$ Å ; $\int \tau_{NB}(\lambda)\mathrm{d}\lambda \simeq \tau_{NB}(\lambda_0)\Delta\lambda_{NB} \simeq 0.7 \times 250$ Å), we find:

$$m_H - m_{NB1.64}\ (\mathrm{EW}_{\mathrm{H}\alpha,0} = 25\ \text{Å}) = -2.63$$
$$m_H - m_{NB1.64}\ (\mathrm{EW}_{\mathrm{H}\alpha,0} = 50\ \text{Å}) = -2.42$$
$$m_H - m_{NB1.64}\ (\mathrm{EW}_{\mathrm{H}\alpha,0} = 100\ \text{Å}) = -2.11$$

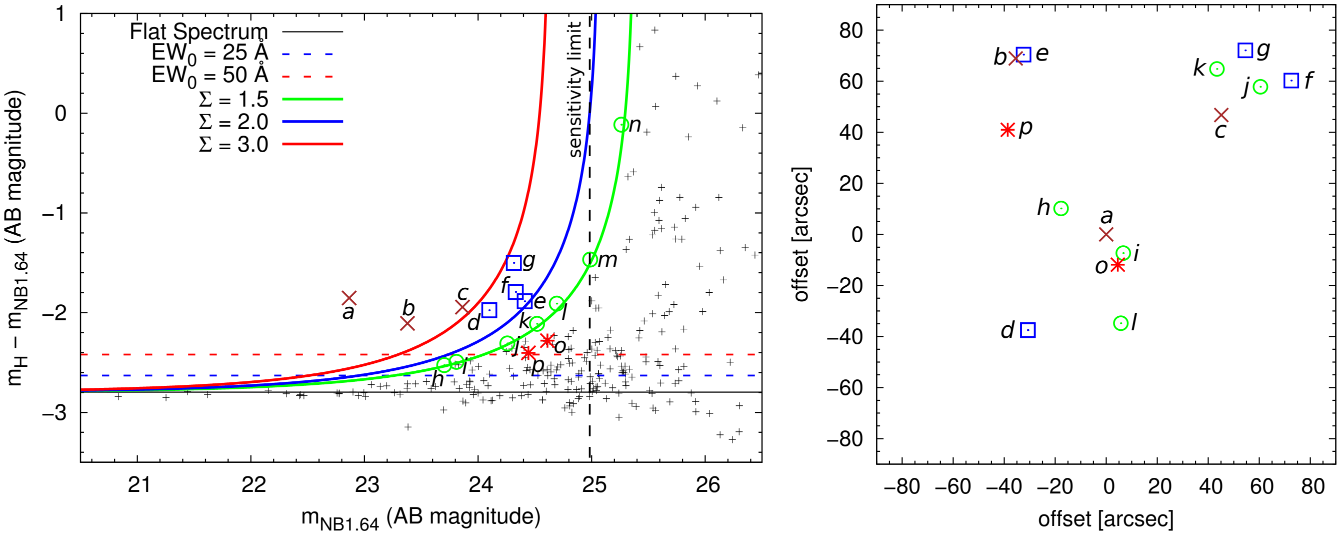

Figure 5.12: *Left*: The color-magnitude diagram of the sources detected in our observations. The HzRG is identified by the "a". The sensitivity limit corresponds to the RMS level of our observations in the 2″ aperture used for the photometry of objects. Hα emitters candidates are indicated by colored symbols, depending on the significance of their detection. *Right*: Positions of the Hα emitters candidates, with the HzRG at (symbol"a") lying at the center of the field.

The resulting color-magnitude diagram is shown on Fig. 5.12, with different selection criteria that can be used ($\Sigma = 3$; 2 or 1.5) and two equivalent widths levels ($\mathrm{EW}_{\mathrm{H}\alpha,0} = 25; 50$Å). With loose criteria, we find 14 Hα emitters candidates in total. Among them, 3, including the radiogalaxy TXS 2355−003, have a strong probability of being genuine high-redshift objects. 4 other objects have $\Sigma \geq 2$ and $\mathrm{EW}_{\mathrm{H}\alpha,0} \geq 50$Å and are also probably Hα emitters at z ∼ 1.5. The remaining 7 objects are less securely identified, and we confirm their reality by visually inspecting their appearance in the continuum-subtracted narrow-band imaging, to investigate whether systematic effects may lead to 'fake' sources. We thus discard two objects, one (object n) with a flux that is below the sensitivity limit and appears to have an extraordinarily high high equivalent width. Likewise, object m is not robust, having a flux comparable with the RMS level found in random empty 2″ apertures.

In order to confirm the results coming from our color-magnitude study, we inspect selected objects in the NB image. Fig. 5.13 presents thumbnails images of 12 out of the 14 candidate Hα emitters (objects a to l). Note that the radio galaxy TXS 2355−003 is labeled with the letter a.

Indeed, when inspecting the continuum subtracted NB image, it appears that these 2 objects (m and n) are not detected. They were selected by sExtractor only because they were lying at the periphery of the image, where the signal-to-noise ratio is lower due to the adopted dither pattern.

Subtraction of scaled images

When inspecting the continuum subtracted NB image, it appears that some objects that were looking like possible Hα emitters were missed by the previous selection. In order to cope with this issue, we run sExtractor on this image and then on its negative version. This strategy takes advantage of an artefact of this image that cannot be completely accounted for: the astrometry and the seeing of the NB image differ from the one of the BB image by a fraction of an arcsecond. Although this can be considered as a negligeable amount, it is large enough to produce a negative spot due to an oversubtraction next to a bright spot where the object is undersubtracted in the operation of subtracting the BB image from the NB image.

However, because our Hα emitters have large equivalent widths, their line flux boosts their flux in the narrow-band image at a level that they should lack this negative feature. The idea is then to crossmatch objects detected in the continuum subtracted NB image with those of its negative. Objects in the continuum subtracted NB image that lack counterparts should be plausible Hα candidates. When applying this method, we find 50 such objects, among which 11 out of the 14 previous candidates are selected (objects b, i and m miss). Thumbnails of these candidates from the continuum subtracted NB image are shown in Fig. 5.13. Visual inspection of the others reveals that 2 of them seem serious candidates, our main rejection criteria for the other objects being that the negative feature is just below the 2σ detection level that we use in sExtractor, or made of several little pieces. These two other candidate Hα emitters, denoted by letters o and p in the different selection methods, are also well detected in the NB image.

5.4.4 An overdensity of Hα emitters around TXS 2355−003

Given the relatively good seeing of our data of $0.5''$, most Hα candidates are marginally spatially resolved (Fig. 5.13(a) shows their postage stamps in the continuum-subtracted narrow-band image) and we estimate Hα equivalent widths of 50−250Å in the rest-frame, corresponding to Hα fluxes of about 1−few $\times 10^{-16}$ erg s^{-1} cm^{-2}. The properties of these 14 candidates (the radio galaxy and 13 more emitters) are given in Table 5.6. We did not correct the Hα flux and equivalent widths for [NII] emission, which should fall into the same filter, as observations of optically broad and narrow-band selected galaxies at high redshift typically show very low [NII]/Hα line ratios of-order 10% (*e.g.*, Förster Schreiber et al., 2009; Lehnert et al., 2009; Queyrel et al., 2012). We note for the sake of completeness that using the conversion of Kennicutt (1998) with a $1-100$ M$_\odot$ Salpeter initial mass function, the total Hα flux for all candidate Hα emitters except the radio galaxy corresponds to a rather moderate total SFR = 215 M$_\odot$ yr^{-1}.

With an effective field-of-view of 5.4 arcmin^2 (neglecting the trimmed edges where our data did not reach the full depth), our overall source count of 14 Hα emitting candidates with fluxes $> 7\times10^{-17}$ erg s^{-1} cm^{-2} and significances $\Sigma \geq 1.5$ therefore corresponds to a density of 2.6 arcmin^{-2}, corresponding to an overdensity of a factor 33. If we only consider the 6 narrow-band excess sources above $\Sigma = 2$ (and excluding the radio galaxy itself), we find a source density of 1.1 arcmin^{-2}, and an overdensity of a factor 16 relative to the field. Kurk et al. (2004c) found a source density of 3.2 arcmin^{-2} for $\Sigma \geq 2$ and EW$_0 >$ 25Å around the z = 2.16 radio galaxy MRC1138-262.

This is comparable to the densities of Hα emitters found around other HzRGs: Kurk et al. (2004c) detected 40 HAE in two ISAAC pointings around PKS1138-262 at z = 2.16, leading to $\Sigma_{HAE} \simeq 3.2$ HAE arcmin^{-2}. Matsuda et al. (2011) found 137 Hα candidates in a large area of 0.56 deg^2, made of 4 fields, containing 5 QSOs and one HzRG, and centered on z = 2.23. This gives a mean value of $\Sigma_{HAE} \simeq 0.07$ HAE arcmin^{-2}, but with large variations across the observed field.

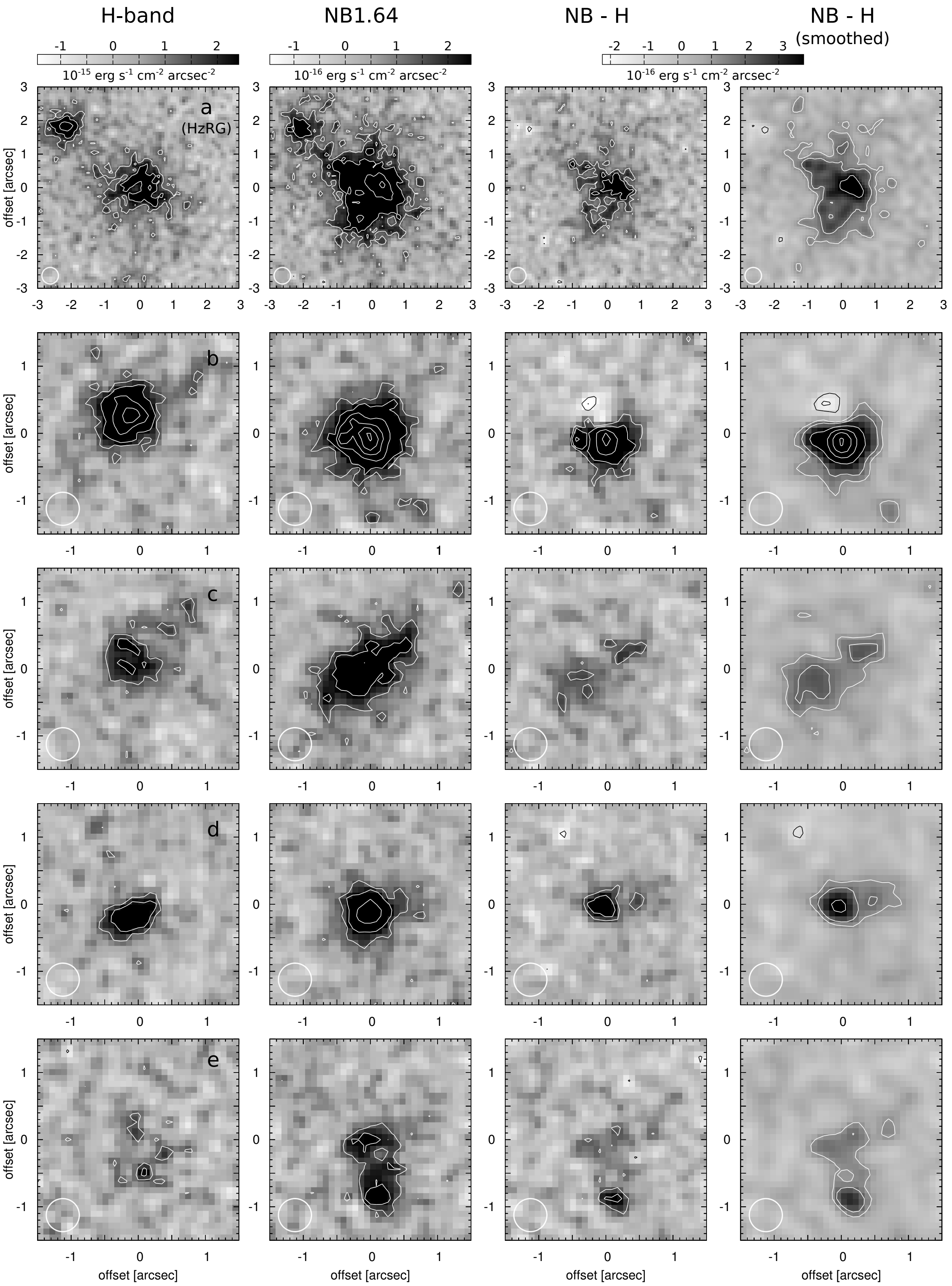

(a) Thumbnails of HAE candidates

Figure 5.13: Caption is under the last part of the image.

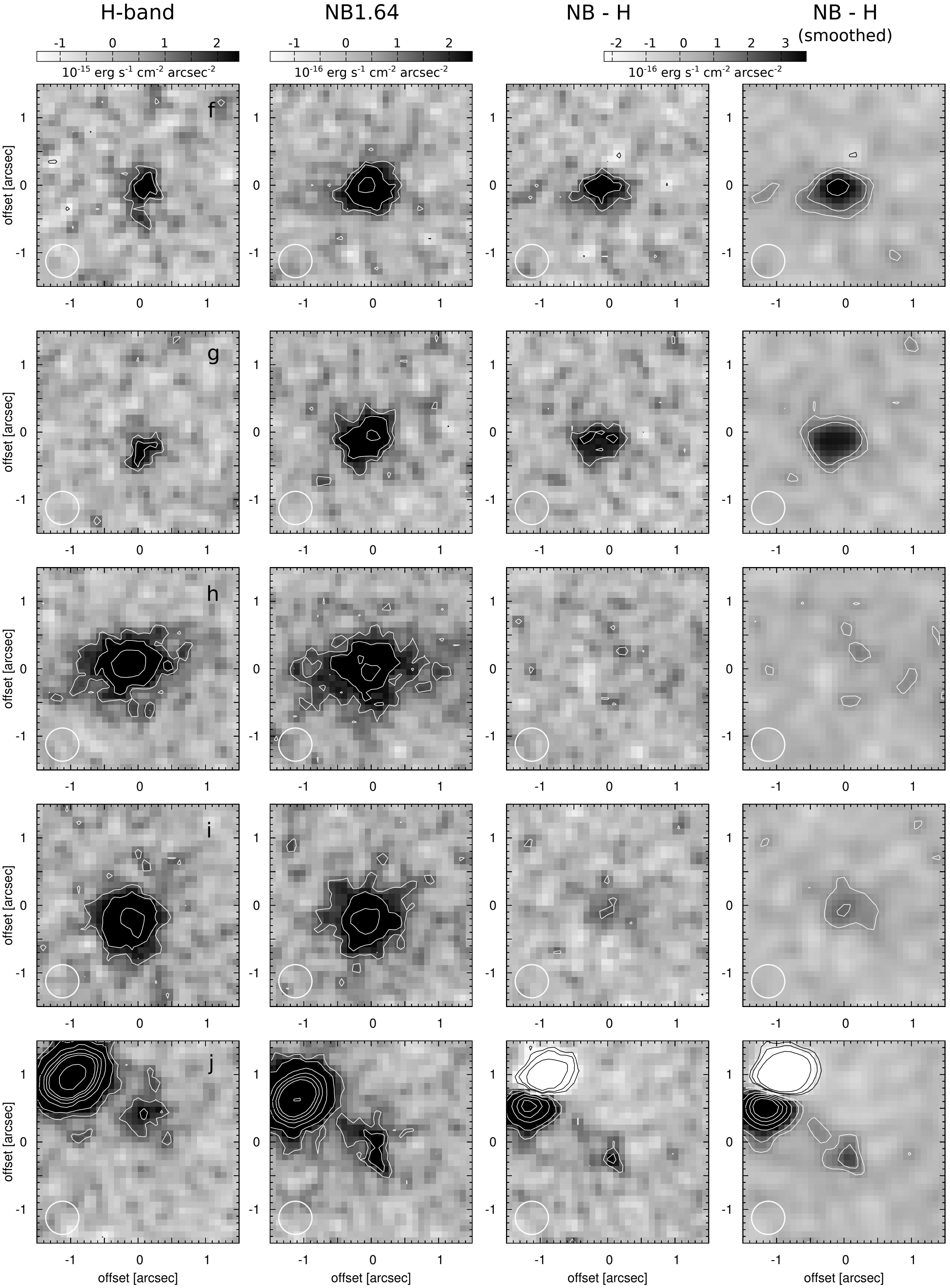

(b) Thumbnails of HAE candidates

Figure 5.13: Caption is under the last part of the image.

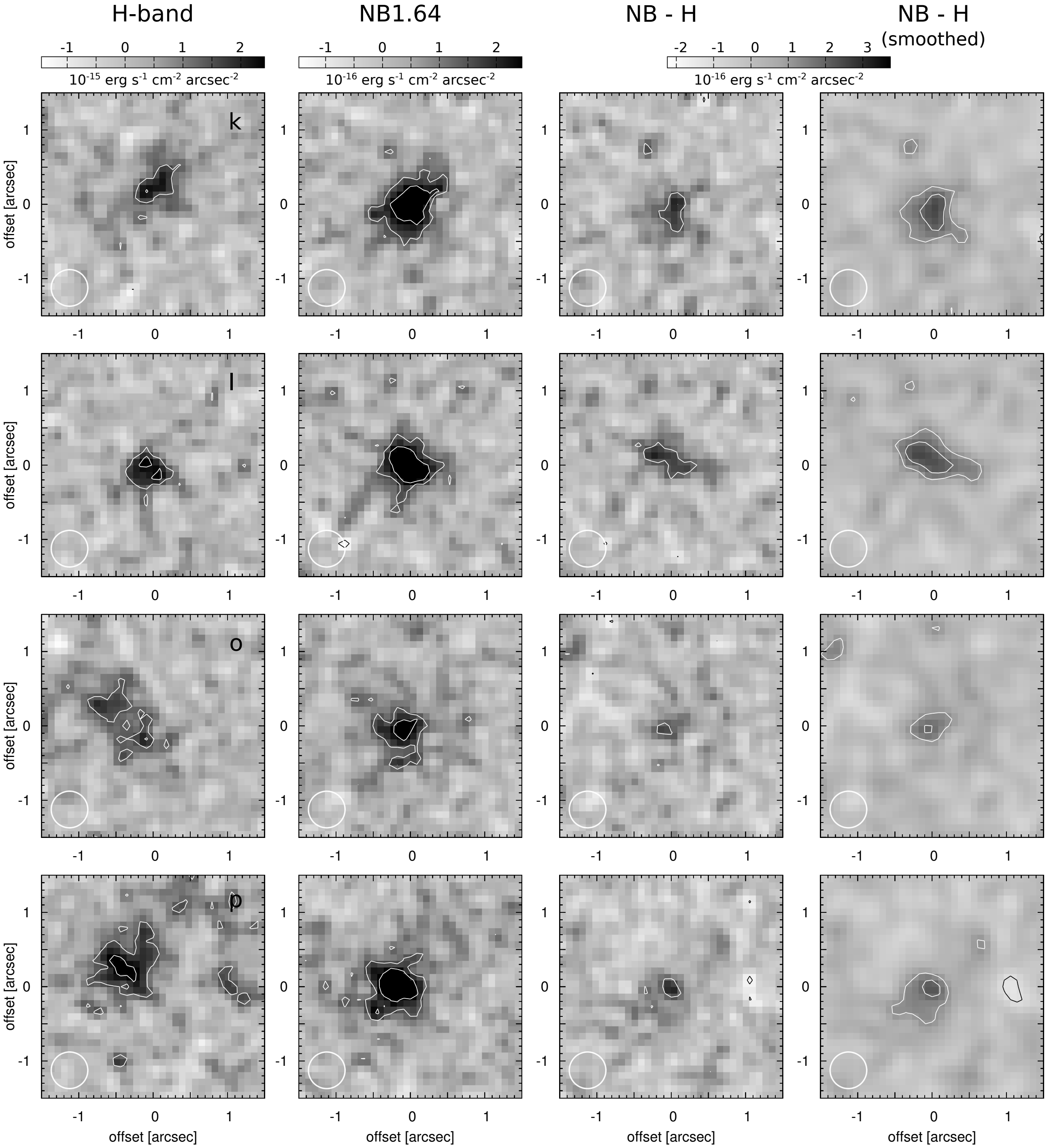

(c) Thumbnails of HAE candidates

Figure 5.13: Thumnails of the Hα emitters selected by the Bunker plot and confirmed when subtracting the continuum in the NB image. *Left column*: $H-$band images of the candidates. *Middle column*: NB1.64 images of the candidates. *Right columns*: Continuum-subtracted NB images of the candidates, the last column showing them smoothed with a Gaussian kernel of $\sigma = 1$ pixel. The color palette spans the -3σ to $+5\sigma$ in each case, in order to highlight the faint features of these HAE candidates. The contours give the morphology of the sources at larger surface brightnesses: white contours are at levels 3 ; 5 ; 10 ; 15 ; 20 σ and the black contours are at levels -10 ; -5 ; -3σ. The RMS levels for each type of image are the following: $\sigma_{BB} = 4.8 \times 10^{-16}$ erg s^{-1} cm^{-2} arcsec^{-2} ; $\sigma_{NB} = 4.9 \times 10^{-17}$ erg s^{-1} cm^{-2} arcsec^{-2} ; $\sigma_{NB,cont-sub} = 7.5 \times 10^{-17}$ erg s^{-1} cm^{-2} arcsec^{-2} and $\sigma_{NB,cont-sub,smoothed} = 2.2 \times 10^{-17}$ erg s^{-1} cm^{-2} arcsec^{-2}

Table 5.6: Parameters of the putative Hα emitters found in our observations.

ID (1)	coordinates (2)	distance (3)	NB flux (4)	BB flux (5)	color (6)	EW (7)	Hα flux (8)	SFR (9)
a	23:55:35.58 -00:02:46.2	0.0	25.9 (22.9)	14.3 (21.0)	-1.85	152.4	63.6	17.5
b	23:55:37.95 -00:01:36.8	1.29	16.2 (23.4)	11.3 (21.3)	-2.11	100.2	32.1	8.8
c	23:55:32.56 -00:01:59.2	1.08	10.3 (23.9)	6.2 (21.9)	-1.94	132.3	23.8	6.6
d	23:55:37.64 -00:03:23.9	0.81	8.3 (24.1)	5.4 (22.1)	-2.04	112.7	18.7	5.1
e	23:55:37.74 -00:01:35.3	1.29	6.2 (24.4)	3.5 (22.5)	-1.89	145.1	20.1	5.5
f	23:55:31.92 -00:01:33.8	1.51	6.7 (24.3)	3.5 (22.5)	-1.79	166.8	17.1	4.7
g	23:55:30.72 -00:01:45.7	1.57	6.8 (24.3)	2.7 (22.8)	-1.50	248.2	15.0	4.1
h	23:55:35.14 -00:02:53.7	0.17	12.0 (23.7)	12.3 (21.2)	-2.49	41.0	11.2	3.1
i	23:55:36.77 -00:02:36.0	0.34	10.9 (23.8)	10.8 (21.3)	-2.53	36.9	11.2	3.1
j	23:55:31.53 -00:01:48.2	1.39	7.2 (24.2)	6.0 (21.9)	-2.31	66.7	11.0	3.0
k	23:55:32.67 -00:01:41.1	1.30	5.7 (24.5)	3.9 (22.4)	-2.11	99.3	11.2	3.1
l	23:55:35.21 -00:03:21.2	0.59	4.8 (24.7)	2.8 (22.8)	-1.91	139.7	11.4	3.1
o	23:55:35.28 -00:02:58.1	0.21	5.2 (24.6)	4.2 (22.3)	-2.28	71.0	8.3	2.3
p	23:55:38.17 -00:02:04.9	0.94	6.1 (24.4)	5.5 (22.0)	-2.40	52.9	7.8	2.1

(1): Source identification (cf Bunker plot and thumbnails). — (2): Coordinates of the source (J2000). — (3): Distance from the HzRG (in arcmin). — (4): $2''$ diameter aperture NB flux (in 10^{-7}Jy). The corresponding AB magnitude is given in brackets. — (5): $2''$ diameter aperture BB flux (in 10^{-6}Jy). The corresponding AB magnitude is given in brackets. — (6): Color of the source. — (7): Rest-frame equivalent width of the Hα emission, assuming that all the excess flux in the NB image comes from this line (in Å). — (8): Derived Hα flux, assuming that all the color excess in the NB image is due to line emission (in 10^{-17} erg s^{-1} cm^{-2}). — (9): Star formation rate derived from our Hα flux, following Kennicutt (1998) (in M$_\odot$ yr^{-1}).

A blind redshift search for Hα emitters in the field at z = 1.48 has recently been performed by Sobral et al. (2013) through the NB 1.617 filter at UKIRT, which has a very similar width of 210 Å (compared to 250 Å for our ISAAC filter), and which we will use as reference for the expected source density in the field. The HiZEL survey (Sobral et al., 2009, 2010, 2012, 2013) gives an estimate of the Hα emitters that we can expect in a blank field: Sobral et al. (2012) concentrated on Hα emitters at z $\simeq$ 1.47, *i.e.*, at the same epoch as TXS 2355−003 is observed, z = 1.487. They found 295 NB emitters over the 0.67 deg^2 field of their main analyses, and 411 over the entire 0.79 deg^2 field of their NB observations. Among them, 190 objects also show an excess in deep NB imaging centered on the [OII]λ3727 emission line and have colors compatible with a photometric redshift z $\simeq$ 1.47. This leads to densities of HAE in the field of $\Sigma_{HAE} \simeq 0.14$ HAE arcmin^{-2} (with all NB emitters) ; $\Sigma_{HAE} \simeq 0.12$ HAE arcmin^{-2} (with NB emitters in their main field for analyses) and $\Sigma_{HAE} \simeq 0.08$ HAE arcmin^{-2} (with NB emitters having an adequate photometric redshift). These values include galaxies down to a 3σ flux level of 7×10^{-17} erg s^{-1} cm^{-2}, compared to 1×10^{-17} erg s^{-1} cm^{-2} in our case.

Although our source densities at z = 1.5 are lower than those in the z = 2.16 overdensity around MRC 1138-262, the best studied candidate galaxy cluster around a HzRG, the significance of the overdensity relative to the field at the same epoch is high, because the star-formation rate density at z = 1.5 in the field is already strongly declining for the highest Hα luminosities (*e.g.*, Sobral et al., 2013). This might, but does not necessarily imply a general redshift dependence in the star-formation activity around high-z galaxies, but may just reflect intrinsic differences between the two structures).

5.4.5 A search for extended gaseous filaments

Given that we observe high surface-brightness gas that extends to the periphery of our SINFONI data cube, it is only natural to ask whether we may have missed more extended filaments outside the small SINFONI field of view of $8'' \times 8''$. Our narrow-band imaging of TXS 2355−003 does not reveal any such line emission outside the SINFONI field of view. With our 3σ detection limit of 6×10^{-20} erg s^{-1} cm^{-2} Å^{-1} in the continuum subtracted narrow-band imaging, and taking into account the 250Å filter width and cosmological surface-brightness dimming $\propto (1+z)^4$, *i.e.*, 39 at z = 1.5, we would have been sensitive to the equivalent of line emission with surface brightness $\geq 6 \times 10^{-16}$ erg s^{-1} cm^{-2} for nearby clusters, more than an order of magnitude fainter than the surface brighness observed, *e.g.*, in parts of the filaments in the Perseus cluster (Hatch et al., 2007). While it is possible that our good, but nonetheless limited spatial resolution of $0.4''$, corresponding to 3.2 kpc at z = 1.5 will smear out very thin filamentary emission, this does not imply the absence of diffuse warm ionized gas in the halo of our sources, as Villar-Martín et al. (2003) have shown with deeper Lyα observations that high-z radio galaxies are quite commonly surrounded by faint halos of warm ionized gas. It is unfortunate that we have no narrow-band imaging of NVSS J2106−314, which has the brighter, more extended emission line region of the two galaxies in our SINFONI data.

5.5 The nature of the extended ionized gas

5.5.1 Comparison with other HzRGs

As already discussed in §5.2, TXS 2355−003 and NVSS J2106−314 are unusual in several respects. One of the prime arguments of Chapter 4 and of Nesvadba et al. (2006, 2008) that jet and gas are physically related in their HzRGs was the good alignment between the position angle of jet and gas in their 4 sources. They also found very large, super-gravitational velocity gradients of up to > 1000 km s^{-1}, and roughly equally large line widths, which are clearly super-gravitational and require energy input rates that can plausibly only be provided by the AGN.

Neither of these findings apply to our two galaxies presented here. Velocity gradients and line widths are smaller, few 100 km s^{-1} in both sources, and the mismatch in position angle between jet and gas is striking. The more moderate gas kinematics in NVSS J2106−314 and TXS 2355−003 could perhaps also be due to the lower radio power of these sources compared to those of Nesvadba et al. (2006, 2008), as other HzRGs with similar radio power have also been found to have smaller velocity gradients, however, the line widths in these other galaxies are invariably high, of-order FWHM = 800−1000 km s^{-1}, which indicates that the gas is still strongly kinematically perturbed by kinetic energy injection from the radio jet, even in galaxies with lower radio power than that of NVSS J2106−314 (Collet et al. 2013a, §**??**).

Although we are unaware of other examples of high-redshift galaxies without powerful radio-loud AGN in the literature, that would resemble the extended warm ionized gas found in NVSS J2106−314 or TXS 2355−003 (the sub-millimeter selected obscured AGN SMM J1636+4057 may however exhibit a certain resemblance Harrison et al., 2012), we therefore do not favor the interpretation that the gas kinematics are directly related to the energy injection from the radio jets in these two cases. To postulate that jet cocoons are driving the gas out as they expand through the ambient gas like in other HzRGs, it appears unavoidable that cocoon (and hence, jet) and gas are cospatial, both in three dimensions and in projection.

In the cm radio continuum, TXS 2355−003 and NVSS J2106−314 are amongst the most extended sources, with sizes of ∼ 310 kpc and 190 kpc, respectively. Compared to other HzRGs, which often show extended, irregular, knotty, and sometimes bent synchrotron morphologies (*e.g.*, van Breugel et al., 1986; Carilli et al., 1997; Pentericci et al., 2000a), their cm morphologies are very "dull", their jets terminate simply in two unresolved hotspots, which is certainly consistent with the absence of strong interactions between jets and surrounding gas, but also implies that an ambient gaseous component is present out to large radii from the radio galaxy, where the hotspots are.

What makes the presence of extended, kinematically rather quiescent gas interesting in our two targets is also the absence of such gas in the other HzRGs. This includes galaxies with compact radio sources, where the jet cannot (yet) have expanded enough to affect gas at large radii from the nucleus. This cannot be a mere observational effect, since the depths of these data are within the range of the overall sample, and the line emission of our targets is not significantly fainter than in other HzRGs with SINFONI data. TXS 2355−003 has relatively low surface-brightness gas and is at the lower-redshift end of our sample, z = 1.5. Given that surface-brightness dimming is a strong function of redshift, scaling as $(1+z)^4$ for line emission, similar features may have gone unnoticed in our higher-redshift objects. However, from the line ratios of NVSS J2106−314, where we detect Hα and [OIII] with a ratio of [OIII]λ5007/Hα = 4.5 (see §4.5.7), we would expect to see similar features at least in [OIII]$\lambda\lambda$4959,5007, but those lines are unfortunately not covered by our data set. NVSS J2106−314 is at a more typical redshift of our sample and has higher gas surface brightness, making it even more unlikely that we may have missed similar features in other galaxies of our overall SINFONI sample.

The absence of such features in other HzRGs does certainly not imply the absence of diffuse emission-line gas in their halos. Villar-Martín et al. (2003) found faint, diffuse Lyα emission surrounding 10 HzRGs at z $\sim$ 2.5, with typical surface brightnesses of few 10^{-17} erg s^{-1} cm^{-2} arcsec^{-2}, however, for typical Lyα/Hα ratios = 7−13 in HzRGs (Villar-Martín et al., 2003), this would imply Hα and [OIII]$\lambda\lambda$4959,5007 surface brightnesses about one to two orders of magnitude lower than the few $10^{-(16-15)}$ erg s^{-1} cm^{-2} arcsec^{-2} that we observe in our sources (Fig. 4.6(a)). While we observe extended gas with fairly quiescent kinematics in some cases around other HzRGs (Collet et al. 2013, Nesvadba et al. 2013), this gas has lower surface-brightness than the gas associated with the jets, and is clearly not the component of extended line emission that dominates our data.

We also emphasize that we not only see the presence of bright gas at large position angles from the jet axis in our sources, but also the absence of a pronounced component that would be along the direction of the radio jet. This does not imply, of course, that there is no line emission at all along the radio jet axis. This could not be expected given the limited spatial resolution of our data, and intrinsically large, kpc extend of the gas. The narrow-band image of TXS 2355−003 does in fact suggests a faint, not well spatially resolved emission-line component along the jet axis. This component, however, does not stand out compared to the rest of the gas, does not extend beyond the radius of the bright galaxy continuum seen with SINFONI, and is very difficult to isolate in the SINFONI data cube observed at lower spatial resolution from the remaining emission-line regions. It is therefore difficult to considere this feature as a specific component that could uniquely be associated with the jet.

A merger?

Ivison et al. (2008) argued on the example of the HzRG 4C60.07 at z = 3.8 that extended molecular gas and dust near the radio galaxy originates from a satellite galaxy that is being accreted onto the HzRG, which itself is not gas rich.

We do not believe that such a scenario would be appropriate here. Only TXS 2355−003 has a clear companion continuum emitter associated with the emission-line region, at the far end of the line emission. Since this companion has no line emission, it is not clear whether it is physically associated with TXS 2355−003 or simply seen in projection along a nearby line of sight. NVSS J2106−314 has the more pronounced gas flow of our two galaxies, but no companion seen in the continuum down to K = 23.7 mag. If the gas seen in NVSS J2106−314 was originating from an on-going merger with a single, massive galaxy, then this merger would already need to be sufficiently advanced so that the stellar component of the galaxy has either been sufficiently dispersed to have continuum surface brightnesses below our detection limit, which is unlikely for massive high-z galaxies, which have often highly centrally concentrated light profiles (*e.g.*, Daddi et al., 2005). Alternatively, this galaxy would already be near coalescence with NVSS J2106−314 so that we do not resolve the pair spatially (*i.e.*, both galaxies would be within $\leq$ 5 kpc). Observations of radio-loud quasars at less challenging redshifts suggest that such merger debris would be orders of magnitude lower in surface brightness (Stockton et al., 2002; Fu & Stockton, 2007b).

We do not consider it very likely that the companion of TXS 2355−003 is the source of the gas seen.

Apart form the simple fact that even intensely star-forming galaxies have much lower masses of warm ionized gas than the 1−few $\times 10^9$ $M_\odot$ in our two sources, it would not be clear how the accretion of a gas-rich galaxy would produce a spectacular tail of 10^9 $M_\odot$ of high surface-brightness gas extending over 30 kpc without engendering significant star formation. The example of MRC 1138-262 at z = 2.16, perhaps the best studied HzRG on the sky, shows that HzRGs can have nearby companion galaxies within few 10s of kpc, which are already on the red sequence and devoid of gas (Kodama et al., 2007), but unequivocally demonstrating that they are physically associated with the HzRG is of course difficult without bright line emission that would facilitate obtaining spectroscopic redshifts. Imaging spectroscopy of MRC 1138-262 has shown that these galaxies are co-spatial with bright, extended optical line emission in the gaseous halo around the HzRG, without being the source of the line emission themselves (Nesvadba et al., 2006; Kuiper et al., 2011).

Merger models and observations suggest that tidal forces not only produce extended (but, at least at low redshift, relatively low-surface-brightness) tails, but also funnel gas towards the nuclei of the interacting galaxies (*e.g.*, Barnes & Hernquist, 1996), fueling intense nuclear starbursts. While the putative companion of TXS 2355−003 is clearly detected in the continuum, we detect no line emission from Hα down to fluxes of 3.3×10^{-18} erg s^{-1} cm^{-2}. Using the calibration of Kennicutt (1998), and neglecting extinction, this would correspond to star-formation rates of-order 10 $M_\odot$ yr^{-1}, well below those found in many gas-rich, isolated star-forming galaxies at high redshift. Since the source is well detected in the $K-$band continuum (rest-frame $I-$band for z = 1.5), extinction from dusty star formation cannot resolve this contradiction, as the Hα equivalent widths would be invariably very low, at odds with the hypothesis of an intense starburst, even if hidden behind dust.

Broadly similar arguments apply to the hypothesis of a tail stripped by ram-pressure, which could appear to fall between the radio galaxy and companion for certain viewing angles. It has been suggested in the literature (Elmegreen & Elmegreen, 2010; Rauch et al., 2013) that ram-pressure stripping of gas-rich galaxies falling into dense environments at high redshift may produce spectactular tidal tails owing to their high gas fractions. Numerical simulations would make us expect in this case that gas at the head of the infalling gas would be compressed, enhancing the gas surface brightness within the galaxy, and potentially enhanced star formation (Kapferer et al., 2008). This may be the case for the galaxies discussed by Elmegreen & Elmegreen (2010), which have tails with surface-brightnesses factors of a few lower than in our targets, and bright line emission in their central regions pwoered by their active star formation (*e.g.*, Förster Schreiber et al., 2006; Lehnert et al., 2009). The putative ram-pressure stripped tails in the galaxies recently presented by Rauch et al. (2013) are see in Lyα with much lower surface-brightness (of-order 10^{-20} erg s^{-1} cm^{-2}) than what we may hope to detect with SINFONI. Likewise, the low-redshift cluster central galaxy NGC4696 appears to have extended filaments of warm ionzied gas shock-heated by the ram pressure of infalling clouds (Farage et al., 2010). However, the Hα flux and surface brightness is several orders of magnitude greater than in NGC4696, and our emission-line diagnostics does not support the shock hypothesis (see below), hence we discard this interpretation for TXS 2355−003 and NVSS J2106-314.

In the next section we will use our observational results for TXS 2355−003 and NVSS J2106−314, as well as the considerable set of observations showing that HzRGs are generally brightest cluster galaxies, to argue that the our targets show many similarities with brightest cluster galaxies at lower redshifts.

Extended gas disks?

The smooth, monotonous velocity gradient that we see in particular in NVSS J2106−314 may either be indicative of back-to-back outflows, of gas infall, or gas rotation in a flattened, disk-like or ellipsoidal configuration. The low spatial resolution that can be achieved for high redshift galaxies is a major hindrance in distinguishing between these scenarios. For powerful radio galaxies, the large amplitudes of velocity offsets and line widths makes rotating gas disks and infall implausible (Nesvadba et al., 2006, 2008), as the gas appears to be not gravitationally bound to the gravitational potential of the host galaxy, but given the lower velocity dispersions and gradients we observe in TXS 2355−003 and NVSS J2106−314, this is not the case here. In fact, extended gas disks and filaments are not unusual in radio galaxies in the more nearby Universe, in particular at high radio powers (for low-z radio galaxies, *i.e.*, of-order 10^{25-26} W Hz^{-1} at 1.4 GHz and 2−3 orders of magnitude lower than in our HzRGs).

We note that HzRGs are not good sites to search for signatures of "cold accretion" a galaxy-growth mode through replenishment of the ISM with pristine gas (*e.g.*, Dekel et al., 2009) that has recently received much attention in the literature. The reason is that the diffuse, warm ionized halo gas already shows evidence for metallicities up to about solar (Villar-Martín et al., 2003).

Gas-rich radio galaxies are rare in the low-redshift Universe (as are powerful radio galaxies *per se*), but those that are known, are amongst the galaxies with the highest (molecular) gas masses known. *e.g.*, 3C293 at z = 0.045 has $M_{gas,mol} = 7 \times 10^9$ $M_\odot$ (Evans et al., 1999, 2005), nearly reaching the 10^{10} $M_\odot$ of molecular gas more typical for intensely star-forming high-redshift galaxies (*e.g.*, Greve et al., 2005). Ogle et al. (2010) found from Spitzer observations of warm H_2 that 30% of nearby radio galaxies have large amounts of molecular gas, many of which are also rich in cold gas seen in CO (Nesvadba et al., 2010). It is unlikely that this gas originates from a massive, on-going merger in all cases. At least in some galaxies, secular processes like gas accretion and the mass return from evolved stellar populations appears more plausible (Nesvadba et al., 2011a, see also Ciotti et al. 1991; Mathews & Brighenti 2003).

In spite of these interesting resemblences of the gas disks in TXS 2355−003 and NVSS J2106−314 with isolated low-redshift radio galaxies, the most outstanding examples of such disks in the nearby Universe are in the central galaxies of nearby cool-core clusters, where gas masses can reach values of up to few 10^{10} $M_\odot$, that are otherwise only encountered in the early Universe (*e.g.*, Hatch et al., 2006; Wilman et al., 2009; Farage et al., 2010; Hamer et al., 2012), including many powerful radio galaxies (*e.g.*, Papadopoulos et al., 2000; De Breuck et al., 2005; Emonts et al., 2011b,a). We will explore this resemblence in more detail in the following section.

5.6 Parallels to cluster central galaxies

Evidence has grown in recent years that many powerful high-redshift radio galaxies are progenitors of brightest cluster galaxies (BCGs). Many HzRGs reside amidst overdensities of galaxies (*e.g.*, Le Fèvre et al., 1996; Venemans et al., 2007; Galametz et al., 2012) and in gas-rich environments with diffuse Lyα emission from warm ionized gas (Villar-Martín et al., 2002, 2003) with embedded denser filaments of neutral atomic and molecular gas (van Ojik et al., 1997; Nesvadba et al., 2009). Their co-moving number density corresponds to that of young, massive galaxy clusters (Venemans et al., 2007; Nesvadba et al., 2008). Best (2000) point out that in particular galaxies with very extended radio sources are likely to be central cluster galaxies. The reason is that the pressure from the Mpc-scale intracluster medium is boosting the luminosity of the radio source even for comparably extended jets. Our two sources are amongst the most extended radio sources in our SINFONI sample, and amongst the largest radio sources known at high redshift, in broad agreement with this hypothesis. Of course, finding an overdensity of emission-line galaxies with high Hα equivalent widths around TXS 2355−003 (§5.4.4) is direct evidence that in terms of their environments, at least one of our two sources is a typical HzRGs. We will in the following discuss additional arguments, based on our SINFONI and ISAAC data, why both our sources have much in common with what may plausibly be expected from "young" BCGs, and why extended emission-line regions akin to those found in our two sources, may actually arise very naturally in such a scenario.

5.6.1 Continuum magnitudes, sizes and light profiles

K−band magnitudes

Integrated magnitudes are the simplest way of characterizing our sources photometrically. The observed K−band is a reasonably good proxy of stellar mass out to redshifts $z \geq 2$ (*e.g.*, Kauffmann & Haehnelt, 2000), and it may therefore not be surprising that the most massive galaxies follow a relatively tight relationship between observed K−band magnitude and redshift (the well-known "K-z" relationship of radio galaxies

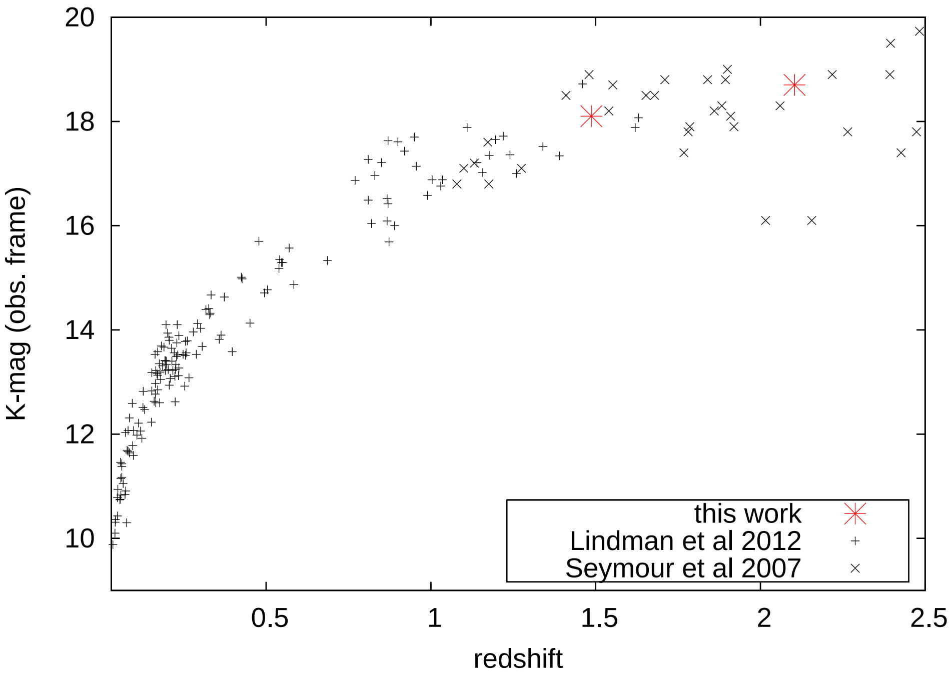

Figure 5.14: Observed $K-$band luminosity of brightest-cluster galaxies as a function of redshift, the black dotted line shows the expectation for passive luminosity evolution (plot reproduced from Lidman et al., 2012, and slightly extrapolated to z=2.1). The large, red stars illustrate that TXS 2355−003 and NVSS J2106−3140 fall well into the expected range of $K-$band magnitude, and also have typical $K-$band magnitudes for HzRGs at their redshifts (The black crosses symbols show the $K-$band magnitudes of the sample of Seymour et al., 2007, and are of course equivalent to the well-known K-z relationship of radio galaxies De Breuck et al. 2002; Willott et al. 2003).

De Breuck et al., 2002; Willott et al., 2003). Lidman et al. (2012) recently studied the same relationship for BCGs specifically. In Fig. 5.14 we show where TXS 2355−003 and NVSS J2106−314 fall relative to both relationships. Light and dark blue dots show the Lidman et al. (2012) sample of BCGs and the Seymour et al. (2007) HzRGs, respectively, illustrating the good agreement of our targets with both samples, as well as that of both samples with each other (a prerequisite if HzRGs are to be the progenitors of BCGs seen during their final stages of active star formation). The black line shows expectations for passive luminosity evolution of massive galaxies, and is taken from Lidman et al. (2012).

Finding that our sources have typical $K-$band magnitudes for HzRGs in their redshift range suggests that they also have typical stellar masses. Measuring stellar masses of HzRGs is notoriously difficult, because the obscured AGN makes significant contributions to the continuum in nearly all relevant wavebands (Seymour et al., 2007; De Breuck et al., 2010). Using their stellar mass estimates derived from comprehensive observations in the observed optical, NIR, and MIR as measured with Spitzer, we performed a simple calibration of stellar mass, $\mathrm{M}_{stellar}$, as a function of absolute $K-$band magnitude, M_K, finding a purely empirical relationship of $\log{(M_{stellar}/M_{\odot})} = 6.18 - 0.189\ \mathrm{M}_K$, with a 1-$\sigma$ scatter of about 0.3 dex in mass. For TXS 2355−003 and NVSS J2106−314, this suggests stellar masses in the range $\log{(M^{2353}/M_{\odot})} = 11.1 - 11.4$ and $\log{(M^{2106}/M_{\odot})} = 11.2 - 11.5$, respectively.

Isophotal sizes and surface-brightness profiles

In Section 5.3 we presented our Sérsic and De Vaucouleurs fits to the light profiles of our two radio galaxies, and will now discuss these properties in the context of HzRGs and other high-redshift galaxy populations.

One of the outstanding characteristics of massive, passively evolving high-redshift galaxies is that their rest-frame UV and optical continua are more strongly centrally concentrated than those in more nearby galaxies (Daddi et al., 2005; van Dokkum et al., 2008, , who found $R_e \leq 1$ kpc and 0.9 kpc, respectively). A decrease in R_e by a factor ≥ 2 compared to the local value has also been found for HzRGs (Pentericci et al., 2001) at $z \geq 2$.

Typically, these galaxies are only resolved with high-resolution HST imaging, and deep photometry shows no deviations from Sérsic laws with indices of typically ≥ 2, including the $n \sim 4$ expected for disk galaxies ($n \sim 2$ would be characteristic of disks; *e.g.*, Szomoru et al., 2010; Cassata et al., 2010). We note that it is important to focus on massive, intensely star-forming systems in this context, which are forming stars near their maximally allowed rate (*e.g.*, Elmegreen, 1999). For all we know, these are the parent population of HzRGs (*e.g.*, Blain & Phillips, 2002). Fairly diffuse, extended stellar structures have been found in lower-mass, UV/optically selected galaxies at high redshift with more moderate star formation properites (*e.g.*, the 6 "BM/BX" galaxies of Förster Schreiber et al., 2011), with $R_e = 2.7 - 6.2$ kpc, but these are very different galaxy populations whose evolutionary history is unlikely to have much in common with the radio galaxies we investigate here.

As for the stellar morphologies of HzRGs generally, their broad-band surface-brightness profiles in the optical and near-infrared are often extended in high-resolution HST imaging, and very irregular. Only few are well fitted with $r^{1/4}$ profiles (*e.g.*, Pentericci et al., 2001, see also Waddington et al. 2002, who find $R_e = 2.7$ and 2.9 kpc in two radio galaxies at $z \simeq 1.5$). This has been attributed to galaxy interactions or mergers, although the bright emission-line nebulae of HzRGs make it often difficult to distinguish between faint continuum features and emission-line contamination (Nesvadba et al., 2008).

Our two galaxies are neither well fitted with $r^{1/4}$ laws (see §5.3) nor are they the 'typical' distorted HzRGs, but they do show faint, extended wings surrounding a higher surface-brightness region around the nucleus. Both are clearly spatially resolved (Fig. 5.8), at least in the low surface-brightness wings. These wings dominate thus the light profile fits, giving Sérsic profiles of $n = 0.5$ in both cases and at all radii. Although high-redshift galaxies do not cluster around the typical values of $n = 2$ for disks and $n = 4$ for spheroidal galaxies like galaxies at low redshift, but show a large range of possible Sérsic indices (from $n < 1$ to 10 Daddi et al., 2005; van Dokkum et al., 2008; Förster Schreiber et al., 2011), finding $n = 0.5$ is at the extreme end of the distribution. It is however interesting that the inner regions of NVSS J2106−314, and neglecting the extended stellar envelope, are also adequately fit with an $r^{1/4}$ law, because this may imply that parts of the stellar component of the galaxy have already established the structural properties of a relaxed early-type galaxy. This would be in agreement with other arguments why powerful radio galaxies are very near the end of their active formation period (see also Nesvadba et al., 2011c; Seymour et al., 2012).

A galaxy class that is characterized by extended stellar envelopes are the central galaxies of massive galaxy clusters (cD galaxies; *e.g.*, Schombert, 1987). These envelopes are likely to be formed from the debris of repeated accretion of several satellite galaxies. Whereas the standard hierachical model of galaxy formation posits that those envelopes should build slowly over time (*e.g.*, De Lucia & Blaizot, 2007), Hatch et al. (2008, 2009) discussed a similar envelope around the z = 2.16 HzRG MRC 1138−262 (the "Spiderweb", Miley et al., 2006) in detail, finding that the rest-frame UV colors of the faint continuum emission are consistent with an envelope formation history that is by and large co-eval with that of the high-surface brightness central regions.

To our knowledge MRC 1138−262 is the only HzRG with such an analysis currently in the literature. However, McDonald et al. (2012) suggest a broadly similar scenario for the extended continuum emission surrounding the FIR-luminous BCG of the "Phoenix Cluster", SPT−CL J2344−4243 at z = 0.6. The radii of these envelopes appear to be smaller in our case than those found around BCGs, which can extend out to up to about 100 kpc. In MRC 1138-262, the envelope is detected out to an isophotal size of $11'' \times 6''$, *i.e.*, 90 kpc × 50 kpc at the surface-brightness limit of the deep ACS F814W imaging of Miley et al. (2006). For comparison, the halo in the "Phoenix cluster", like a BCG that is currently growing very rapidly owing to intermittent fueling by a large gas reservoir (McDonald et al., 2012), has a halo of about 40 kpc. This may potentially indicate that these structures are not yet well evolved in our two sources, but given the limited depth of our sources, which is further aggravated by surface brightness dimming scaling in the continuum as $(1+z)^5$, observational effects are likely to dominate.

We note that for the time being, the interpretation that these halos are indeed stellar envelopes in TXS 2355−003 and NVSS J2106−314 is merely one hypothese amongst several, although one that is supported by the close analogy between our sources and MRC 1138-262. Alternatives include in particular scattering of AGN light on dust surrounding the radio galaxy (see Hatch et al., 2008, for a discussion of how these scenarios can be distinguished). At any rate, this highlights the interest of obtaining deep, high-resolution, multi-wavelength imaging of our two galaxies.

5.6.2 Warm ionized gas

As we already mentioned in §5.4.5, cluster central galaxies host some of the most magnificent examples of extended disks and filaments of warm ionized gas in the relatively nearby Universe.

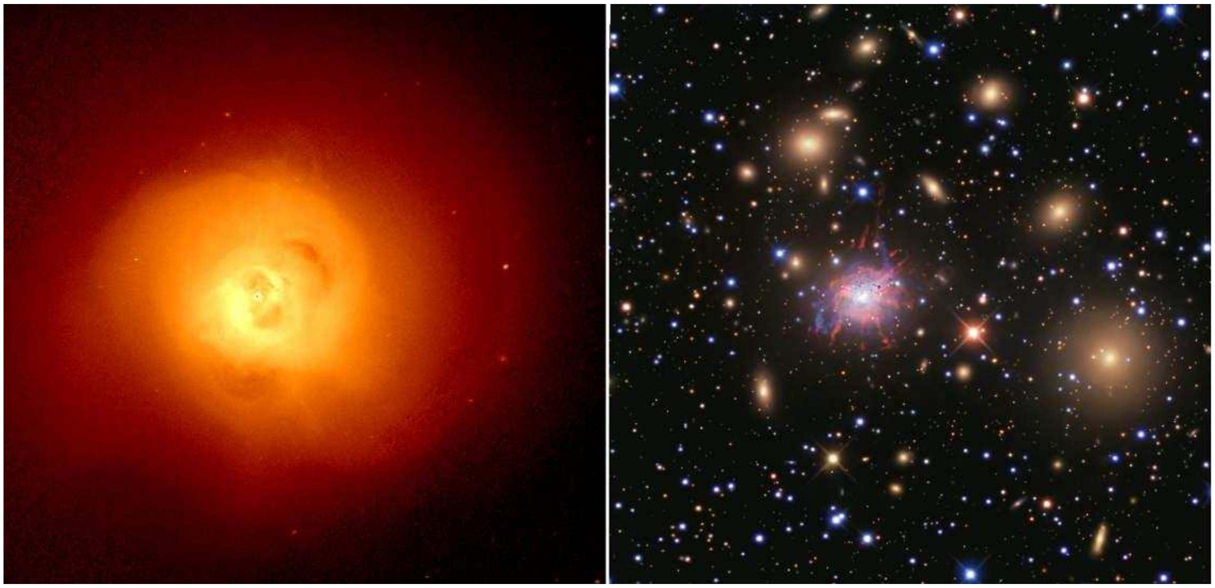

Figure 5.15: The Perseus cluster, as seen in X-rays (*left*) and in the visible (*right*), where the complex system of Hα filaments is clearly visible (Fabian et al., 2011).

Following McDonald et al. (2010), about 30% of cooling flow clusters have such Hα extended filaments. The most impressive example of these filamentary structures seen in Hα is found around NGC 1275, as visible on the right of Fig. 5.15, the BCG of the Perseus cluster (Conselice et al., 2001). These filaments of filaments can alos be rich in molecular gas, as observed, again, in the Perseus cluster (see Salomé & Combes, 2003; Salomé et al., 2006, 2011). The origin of these filaments is not clear and many hypotheses are proposed to explain them. One of these hypotheses is that hot gas condenses in the trail of radio bubbles, as they rise in the cluster atmosphere, as predicted by hydrodynamical models (Reynolds et al., 2005; Revaz et al., 2008). They can also originate from the cooling of some regions of the hot, X-ray emitting gas, that is then ionized, either by conduction from the surrounding hot gas, by star formation occuring inside the cold filament or by the AGN (see the discussion in McDonald et al., 2010, 2011, for more details). Although it is not clear whether HzRGs like TXS 2355−003 and NVSS J2106−314 already have fully established halos of X-ray gas (Overzier et al., 2005), such halos were likely formed around z ∼ 2, potentially through AGN feedback from the radio jets of the central galaxy (McCarthy et al., 2008). Over an AGN lifetime, HzRGs emit similar kinetic energies to the most powerful radio sources in cluster central galaxies in the more nearby Universe (Nesvadba et al., 2009). This and the observational finding, that the environs of HzRGs do contain large amounts of diffuse gas with embedded clouds and filaments makes it at least plausible that fundamentally similar filaments may already exist, although their formation and cooling may be very different, depending on the detailed evolutionary state of the gaseous halos at high redshift.

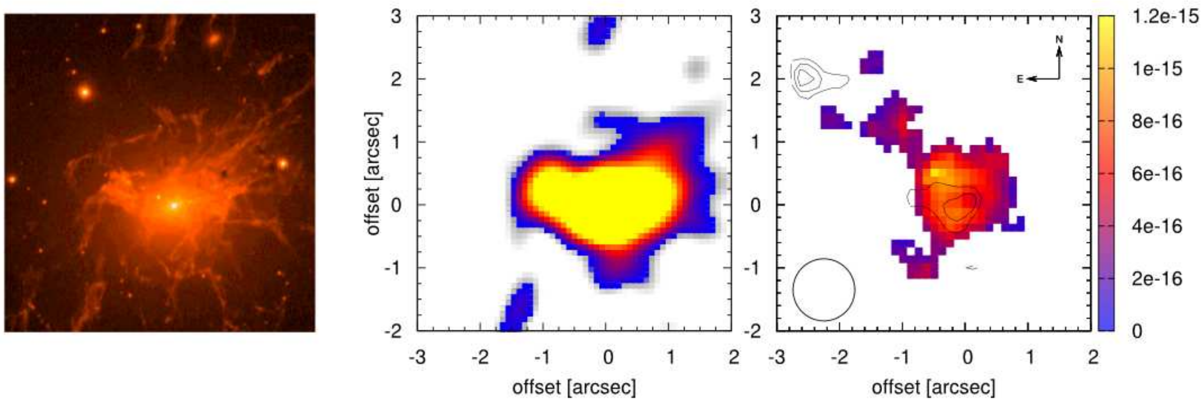

Figure 5.16: *Left*: The Hα filaments of the Perseus cluster, as observed by Conselice et al. (2001). *Center*: The same Hα filaments, as they would be observed if the system was at the redshift of TXS 2355−003 (z = 1.487). *Right*: Hα surface brightness of TXS 2355−003, as derived from our SINFONI observations. Surface brightness scales in the two last images are the same (in units of erg s^{-1} cm^{-2} $arcsec^{-2}$).

In this context, it is certain interesting that in a system such as NGC 1275, if it were observed at the redshift of TXS 2355−003, the Hα filaments would become nearly indistinguishable, from those observed, as can be seen from Fig. 5.16. The similarity in morphologies between the distant Perseus filamentary system and the Hα emission from TXS 2355−003 certainly makes it plausible that the extended gas we see in our SINFONI observations of TXS 2355−003 could be part of extended filaments that are fundamentally very similar to those found in the central regions of cool-core clusters like the Perseus cluster. Taking all phases of warm and cold neutral and ionized gas together with $T \leq 10^4$ K, these structures can include up to few 10^{10} $M_\odot$ (*e.g.*, Salomé et al., 2006) of gas. The mass of warm ionized gas derived from the Hαrecombination flux in our two sources, few $\times 10^8$ $M_\odot$ (Table 5.1), is however several orders of magnitudes greater than the masses estimated in more nearby clusters (Heckman et al., 1989). The same has been found for other HzRGs (Nesvadba et al., 2008).

A number of nearby galaxy clusters have had spectacular imaging spectroscopy published in recent years, see for example Hatch et al. (2006, 2007), Wilman et al. (2006, 2009), and Farage et al. (2010, 2012). In BCGs with bright, extended emission-line regions the gas has typical FWHM $\sim 100-300$ km s^{-1} outside the near-nuclear regions, with a characteristic broadening towards the center, with typical FWHM ≥ 500 km s^{-1} and up to the values we find near the center of NVSS J2106−314 and TXS 2355−003 (§5.2.1 and Figs. 5.2 & 5.4). Regular velocity gradients of few 100 km s^{-1}, like what we observe in our sources, are also found in some of the BCGs of the more nearby clusters, *e.g.*, Abell 262 (Hatch et al., 2007) or 2A 0335+096 (Farage et al., 2012).

Unlike the remaining sample of Nesvadba et al. of a total of 50 HzRGs, the warm ionized gas in cluster cores is not always spatially associated with the non-thermal radio emission (although counter examples exist, at least seen in projection Heckman et al., 1989), and the extended gas may or may not show largely monotonous velocity gradients. Abell 1795 is an exquisite example, where the gas appears to avoid the radio jet axis in these galaxies, in particular at the highest emission-line surface brightnesses (van Breugel et al., 1984). Likewise, extended disks in nearby BCGs, *e.g.*, Hydra-A, can be even near-orthogonoal to the radio jet axis, while showing a monotounous velocity gradient most likely dominated by rotation (Hamer et al. 2013, in prep., see also Hamer et al., 2012, for a discussion of a sub-sample). This is quite unlike what we observe in most HzRGs, with the notable exception of TXS 2355−003 and NVSS J2106−314.

A more quantitative comparison of the optical emission-line properties in low-z clusters and our two sources reveals some similarities, but also significant differences between our two galaxies and low-redshift BCGs. Line ratios within inidividual filaments of BCGs vary over large ranges (*e.g.*, Hatch et al., 2007), and still make it very challenging to identify a unique gas heating mechanism. However, given the serious limitations in surface-brightness in our data, such detailed analyses are beyond what we may hope to achieve, and we must therefore restrict ourselves to observationally more simple comparisons. We therefore compared with the sample of longslit spectra of Crawford et al. (1999), who analyzed the global optical emission-line properties of a large sample of the brightest galaxies in 215 well developed, X-ray selected clusters at moderate redshifts, most taken from the ROSAT Brightest Cluster Sample (Ebeling et al., 1998). They find Hα with a range of luminosities between 10^{38} erg s^{-1} and 10^{43} erg s^{-1}, as well as other bright optical line emission in about 1/3 of their sample, and present a number of scalings of the size, Hα luminosity and surface brightness with each other and with several diagnostic line ratios of the bright optical emission lines.

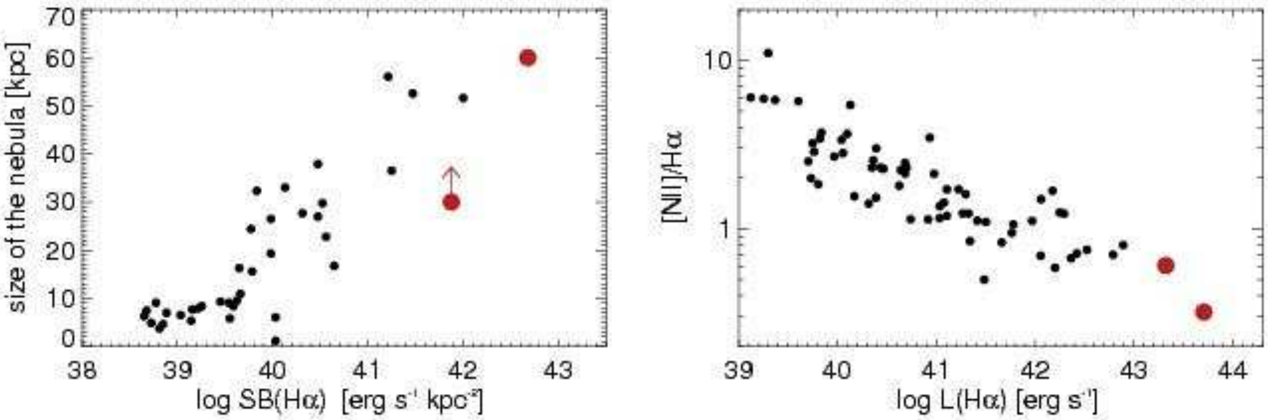

Figure 5.17: *Left*: Size of the extended emission line region as a function of its Hα surface brightness. *Right*: [NII]/Hα ratio as a function of Hα luminosity. Black points denote sources of Crawford et al. (1999) and TXS 2355−003 and NVSS J2106−314 are red points.

Figs. 5.17 show where TXS 2355−003 and NVSS J2106−314 fall in their diagrams. Fig. 5.17 shows that both of our galaxies are factors of a few more extreme than the local galaxies in terms of their Hα luminosity as well as Hα surface luminosity. The galaxy of the Crawford et al. sample that is most akin to our sources, in fact, is the central galaxy of the cluster Zw 3146, a LIRG with $\mathcal{L}_{\rm FIR} = 4 \times 10^{11} \mathcal{L}_{\odot}$, and surrounded by a cluster environment particularly rich in cold gas (10^{11} $M_{\odot}$ Egami et al., 2006), and thereby reminiscent of HzRGs. Although our galaxies are more luminous in Hα and have higher Hα surface brightnesses than the Crawford et al. sample, they do follow the trends of that sample well in terms of their Hα properites, size, low-ionization line ratio ([NII]/Hα for both; [NII]/Hα and [SII]/Hα for NVSS J2106−314), and, with the exception of the much higher [OIII] flux.

Although this comparison highlights a broad similarity between our two sources and the central galaxies of cool-core clusters, it also shows that the gas excitation mechanism is likely different. Given the bright [OIII] flux and surface brightness in our two sources, we favor AGN photoionization over other potential mechanisms. This can be reconciled with a simple BPT-type analysis of the emission-line ratios (Fig. 4.18), which places both sources into the Seyfert part of the digram. The [NII]/Hα and [SII]/Hα ratios are however lower than in nearby Seyfert galaxies, which could either indicate clouds with low column densities with highly ionized envelopes, but no extensive partially ionized zone (Lehnert et al., 2009), or low metallicity (Groves et al., 2006). Newman et al. (2013) just presented an analysis of blue star-forming galaxies at $z \sim 2$ which fall into broadly similar parts of the BPT diagram, explaining them by a mixture of shocks and photoionization. In our case, however, line luminosities are so high that shocks are unlikely to produce the line emission (Le Tiran et al., 2011, see also Farage et al. 2010).

The high [OIII] luminosity of 66.3×10^{-16} erg s^{-1} that we measure in NVSS J2106−314 further highlights AGN photoionization as most likely heating source of the gas (see Villar-Martín et al., 2008, 2011; Nesvadba et al., 2011b, for similar cases). This is also supported by the fact that we find NVSS J2106−314 to be indistinguishable from our other HzRGs (see Chapter 4), at least when probed in the few bright lines that we have access to with our data sets. AGN photoionization is the prime gas heating mechanism suggested by more comprehensive analyses of longslit spectra of HzRGs in the rest-frame UV/optical (*e.g.*, Humphrey et al., 2007, 2009; Villar-Martín et al., 1999).

5.6.3 Origin of the gas in the BCG scenario and a note on AGN feedback

What is the origin of the gas in our two sources? One possibility is certainly that we are seeing clouds within the halo of the radio galaxy as they are being illuminated by the light cone from the AGN. Similar effects have previously been seen in less powerful, radio-quiet AGN at similar redshifts (Lehnert et al., 2009). In this case, we may be seeing one of the same clouds in emission, which are otherwise (and more commonly) seen in absorption (*e.g.*, van Ojik et al., 1997), as its emission-line flux is boosted by the illumination from the AGN. From an empirical viewpoint, however, a caveat may be that neutral absorbers associated with HzRGs are otherwise only seen in galaxies with compact radio sources (van Ojik et al., 1997) , which may be disrupted by the cocoon as the radio source expands through the gas surrounding the radio galaxy (Krause, 2005). TXS 2355−003 and NVSS J2106−314 however have very extended radio sources of sizes of-order 100 kpc, amongst the largest currently known at redshifts $z \geq 2$. It would also not be clear a priori, why we see no similar effects in other HzRGs, where the gas is found to be either compact (in galaxies with compact radio sources) or aligned with the jet axis. Why would only these two galaxies have a quasar ionization cone that is misaligned relative to the axis of the radio jet? Would we not expect to see clouds away from the jet axis predominantly in compact radio sources (where absorption is detected) in this scenario, rather than in two of the most extended radio sources at these redshifts?

With projected velocities of few 100 km s^{-1}, and sizes of up to about 30 kpc, these structures should be as long-lived, or even longer-lived than the extended gas that we see at higher velocities, and typically similar sizes in the more common HzRGs. One possibility of reconciling this with the absence of large numbers of such sources amongst HzRGs is that TXS 2355−003 and NVSS J2106−314 are in an evolutionary phase that is normally not accompanied by bright radio emission, *i.e.*, a selection effect would explain why these sources are so unusual. This could be the case if the radio source in these two galaxies would be particularly long-lived, for example, because the jets remain confined by the ambient gas out to large radii from the radio galaxy, if these two galaxies are embedded in particularly rich environments. In this case, it could perhaps be expected that TXS 2355−003 and NVSS J2106−314 are just the first two examples of a class of high-redshift brightest cluster galaxies with extended emission-line gas. This is not in contradiction with the finding of **?** that distant cluster appear to exhibit bright optical line emission less frequently than more nearby clusters. The redshift range spanned by these studies extends out to $z \leq 1$, an epoch where galaxy clusters were already much more mature than those surrounding high-redshift radio galaxies.

It is also interesting to note that, contrary to what may be suggested by the SINFONI cubes, which suggest a more compact continuum, the ISAAC images do show that the continuum envelopes extend out to similar radii as the extended warm ionized gas. If the wings in the continuum surface brightness profiles of our two sources indeed represent extended stellar envelopes originating from a phase of rapid accretion of many satellite galaxies in the very early evolution of the HzRGs, then it is unlikely that all of this gas has been consumed by star formation, given that the efficiency with which gas is transformed into stars is only a few percent per free-fall time. Left-over gas from this period may still be present in the surroundings of the radio galaxy. Alternatively, jet-driven winds associated with the large radio jets we observe may have dispersed the ISM of these galaxies just a few 10^7 yrs ago, and it may be parts of this gas that is cooling and has already started to rain back onto the galaxy. perhaps fueling a new feedback cycle, as has been proposed for nearby galaxy clusters (*e.g.*, Pizzolato & Soker, 2005; Antonuccio-Delogu & Silk, 2010).

Nesvadba et al. (2010) estimated that mechanical heating may keep massive, turbulent gas disks 'stirred-up' for only few 10^7 yrs and perhaps up to 10^8 yrs, until the kinetic energy has been dissipated and radiated away through line emission. This would happen regardless of the heating mechanism indicated by our emission-line analysis, as shocks would not produce high enough surface brightnesss to make an observable contribution to the observed line emission (Le Tiran et al., 2011; Nesvadba et al., 2006). The age of the radio size, as losely constrained by their size, of few 10^7 yrs (Table 5.1) would be of the same order as this cooling time.

In either scenario, weak shocks driven through the gas, *e.g.*, caused by the passage of a companion galaxy (McDonald et al., 2010), as may be suggested by the secondary $K-$band companion source in TXS 2355−003, or from the expanding cocoon around the radio jet, may then contribute to sweeping up these gaseous vestiges, confining them at least temporarily into gas that is dense enough to give rise to bright rest-frame optical line emission (Nesvadba et al., 2011b).

If the of-order 10^8 $M_\odot$ of warm ionized gas mass represent the bulk of the warm ($T \leq 10^4 - 5$ K) and cold gas in this system, then this would correspond to only a small fraction of the total gas mass of massive, intensely star-bursting high-z galaxies, which have few 10^{10} $M_\odot$ and more of gas (albeit mostly in molecular gas). It would also correspond to only a few percent or less of the baryonic mass of these two galaxies, with their likely stellar masses in the typical range for HzRGs of few 10^{11} $M_\odot$. Even if this gas was to form stars, the resulting stellar mass would not have a measurable impact on the star-formation history of the descendents of these galaxies at $z \sim 0$. CO molecular studies of both galaxies would be very interesting to explore this hypothesis further.

Chapter 6

AGN feedback in high-redshift quasars

Contents

This study will be submitted to A&A as Collet, Nesvadba, Lehnert, De Breuck, et al. (2014c): Feedback signatures in a radio-selected sample of distant Quasars

6.1 Scientific motivation

In the previous chapters, we discussed AGN feedback on the example of radio galaxies with a range of moderately strong radio power. We will now turn to powerful, optically selected quasars at z $\sim$ 2, which are complementary in that they have about equal bolometric luminosities as the most powerful radio galaxies, of order 10^{46} erg s^{-1}, but their central AGN are not obscured by large amounts of dust and possibly gas, as is the case for the radio galaxies. In the radio, at centimeter wavelengths, they have a range of radio power, from 2.7×10^{28} W Hz^{-1} at 1.4 GHz (observed) to below 10^{25} W Hz^{-1} at 1.4 GHz, as implied by their non-detection in FIRST. Specifically, we selected two subsamples, one with detected radio emission ("radio-loud sample", see below) and one with FIRST non-detections (the "radio-quiet sample" below). In total, we have 11 galaxies, 6 with radio detections, and 5 without (Tables 6.1 and 6.2). Our goal is to investigate the systematic changes in gas mass, and turbulent and bulk kinetic energy as a function of object class (quasars vs. radio galaxies) and radio power. When considering their pure radio properties, we can also view them as an extension of our radio-selected sample at higher radio powers (the radio galaxies) towards fainter and fainter radio power, while keeping in mind that their host galaxies are likely to be drawn from different populations, as it is not clear, for example, whether blue, optically selected quasars are really hosted by the most massive dark-matter halos (*e.g.*, Lehnert et al., 1999b; Hyvönen et al., 2007). Trends in gas masses and kinematics with radio power and between the radio galaxy and quasar samples should nonetheless show clearly in a simple, well constrained, and empirical way, whether both populations show equally clear signatures of AGN feedback, as could be expected if both take on similar roles in galaxy evolution.

In many ways, optically selected quasars are "the" classical AGN sub-population. Kellermann et al. (1989) found from following up bright quasars from the Palomar-Green survey with the VLA in the cm radio, that AGN are likely to form a bimodal population with only 1/10 of all sources being radio loud (*i.e.*, at least 10× brighter in the radio than in the optical). Although it is now known that X-ray selected AGN outnumber the blue quasar population (*i.e.*, most AGN are obscured in the optical), and it is not clear whether the blue quasar phase is most closely associated with the most intensely star-forming phase in the merger scenario of Sanders et al. (1988) and Hopkins et al. (2006b), they do remain a major reference sample for studies of AGN feedback. For example, Soltan (1982) found based on statistical arguments that most black-hole growth in the nuclei of galaxies occured during bright Quasar-like phases (see also Yu & Tremaine, 2002). This clearly attributes an important role to blue Quasars in explaining the correlations between black hole mass and bulge properties of their host galaxies, one of the prime arguments motivating AGN feedback studies (see Chapter 1). When, if not during the main phases of black-hole growth, should such a relationship be established?

Finding observational evidence of outflows in optical AGN has long been challenging due to the presence of a bright point source in the nucleus of the galaxy – the AGN itself – and observational limitations. Given the difficulty of handling the AGN emisson and the unknown morphology and axis of the possible AGN wind, the first claims of rest-frame optical emission lines from warm ionized gas are very recent. Lately, claims have been made of optically selected AGN at redshifts z $\sim$ 0.5 to host large, AGN-driven bubbles and emission-line kinematics indicative of ouflows (Liu et al., 2013a,b; Greene et al., 2012). The QSOs of Liu et al. and Greene et al. are obscured, but likely because of their orientation relative to the line of sight (the opening of the torus surrounding the AGN is not aligned with the line of sight), and not because of the specific properties of their host galaxies. This is not to say that optically selected AGN do not show evidence of outflows. About 10% of these AGN have blueshifted broad absorption lines in their rest-frame UV spectra (broad absorption-line quasars; BAL Arav et al., 2001; Crenshaw et al., 2003; Ganguly et al., 2007), with velocity widths of up to about 10,000 km s^{-1}. These likely indicate outflows in the near vicinity of the black hole, but the fate of this gas as it moves outwards is less clear. If BAL-type winds do lead to kpc-scale outflows of significant fractions of the ISM of a quasar host galaxy, similar to what has been observed in powerful radio galaxies, then we should see them in imaging spectroscopy observations.

At redshift z $\sim$ 2, Cano-Díaz et al. (2012) analyzed the SINFONI data cube of a z = 2.4 quasar selected for its high [OIII]λ5007 luminosity (another empirical measure of bolometric quasar luminosity), but without finding equally large ionized gas masses as in powerful HzRGs, or velocity offsets in excess of about 100 km s^{-1}. Likewise, Nesvadba et al. (2011c) presented SINFONI observations of two obscured QSOs selected in the mid-infrared with the Spitzer/SWIRE survey (Polletta et al., 2008), finding that the effects of the AGN onto the gas, although clearly present, are restricted to the inner few kpc of the galaxy corresponding to the point spread function of their data. Harrison et al. (2012) recently presented an analysis of sub-millimeter-selected galaxies in the same redshift range, finding evidence of extended gas, sometimes with perturbed kinematics, but again with kinematic properties that appear much less extreme than those in radio galaxies, including the very broad line widths we found in the samples we discussed previously.

In the remainder of this Chapter, we will present our analysis of the SINFONI data cubes of optically selected quasars. As in the radio galaxies before, our goal is to identify extended emission-line regions of warm ionized gas, and to quantify the kinematic properties of this gas. We will compare the properties of these sources with those of the radio galaxies trying to disentangle the effects of the AGN radiation and radio source. As compared to the radio galaxies, however, we do encounter a major hindrance in the case of the Quasars, which is their aforementioned bright line emission from the AGN itself, which dominates the rest-frame optical spectrum, and which must be carefully subtracted before the fainter, more narrow line emission originating from larger regions within the Quasar host galaxy can be studied. We will present my method to perform this subtraction before turning to the scientific results of this study.

6.2 Separating broad and narrow-line component

6.2.1 Typical spectrum of a quasar

Typical quasar spectra are dominated by very bright, very broad optical emisson lines with FWHM of-order 1,000−10,000 km s^{-1} (*e.g.*, Shen et al., 2011) and up to $\sim$ 15,000 km s^{-1}, superimposed on a bright power-law continuum. In the classical picture of the central region of the AGN, the accretion disk, which is made of material that becomes hotter and hotter as it comes closer to the supermassive black hole, gives rise to a non-thermal continuum radiation. At somewhat larger, but still near-nuclear radii, dense clouds of gas (with $n_H \sim 10^{10-11}$ cm^{-3} Snedden & Gaskell, 1999) constituting the broad-line region (BLR), reach relativistic velocities as they rotate within the deep gravitational potential well of the black hole, giving rise to the characteristic broad line emission. We have made use of this paradigm of rotation of virialized gas in §4.6.5 when estimating the mass of the supermassive black hole in NVSSJ2019. The large densities are required to explain why broad-line emission is not observed in forbidden lines, which have much lower critical densities to collisional de-excitation. Quasar variability studies (reverberation measurements) have shown that this region is relatively small ($R_{BLR} \sim 10 - 100$ light-days Kaspi et al., 2005). It cannot be spatially resolved with our observations. In recent years, more and more authors favor a scenario where the broad-line emission is in fact due to the accretion disk itself (*e.g.*, Down et al., 2010), although a mix of both scenarios is also possible, for example, if material is being lifted from the surface of the accretion disk, forming a population of broad-line emitting clouds (*e.g.*, Proga & Kallman, 2003). A typical Quasar spectrum is shown in Fig. 6.1 from Vanden Berk et al. (2001). The continuum can be modelled by two power laws, with a break at $\sim$ 5000Å.

However, here we are rather interested in the kinematics of the gas at larger scales. Superimposed on the nuclear broad-line emission, quasar spectra often show narrower line components, lines coming from the so-called narrow-line region (NLR). The spectral properties of these lines suggest this gas is outside the gravitational potential well of the supermassive black hole. While the classical narrow-line region is less than a kpc in size, bright narrow line emission in particular in high-redshift quasars has been found to

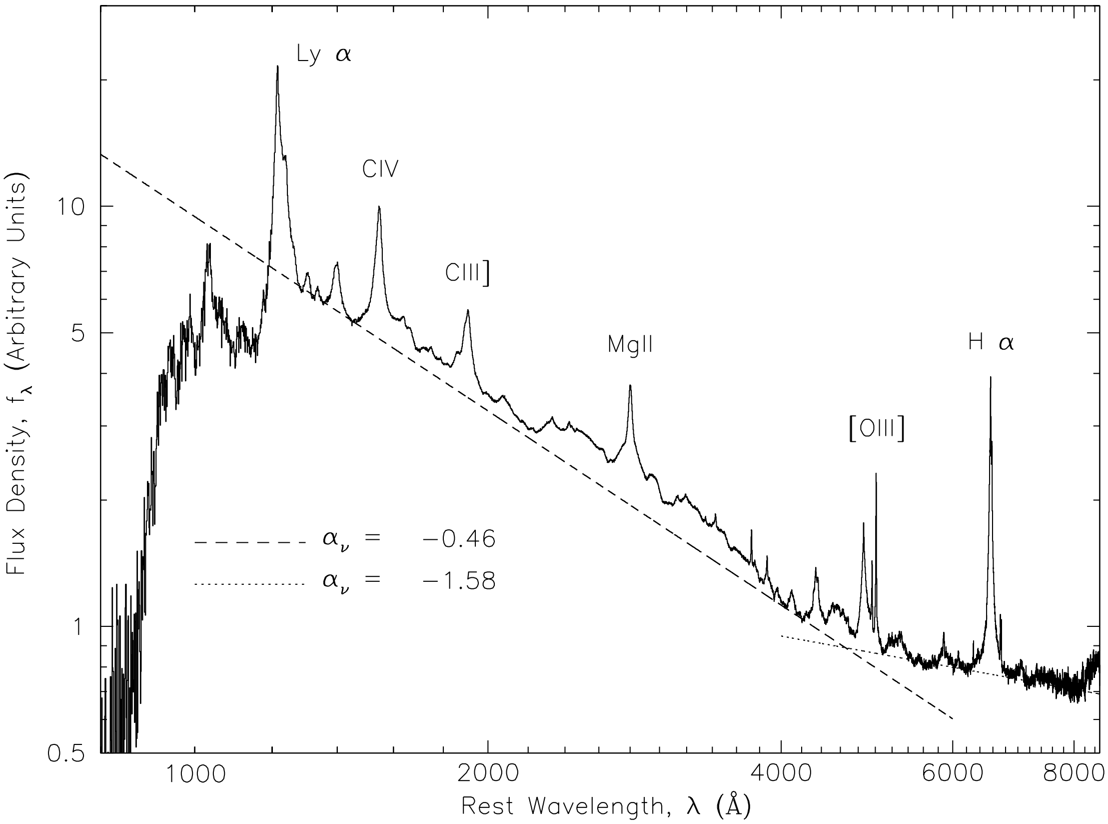

Figure 6.1: Composite QSO spectrum from Vanden Berk et al. (2001), made from more than 2200 QSOs spectra observed with the SDSS.

be extended over kpc scales (*e.g.*, Harrison et al., 2012), and these lines may therefore be tracers of many different kinematic processes, including gas outflows or infall, or even rotation in the gravitational potential of the host galaxy (as has also been found for the smaller narrow-line regions in nearby Seyfert galaxies, Nelson & Whittle, 1996).

One of the main characteristics of the high-redshift radio galaxies we have studied previously is that their nuclear broad-line regions are highly obscured. This is not the case for quasars, and in fact, the nuclear broad lines are often the by far dominant spectral component, to the point where the narrow lines is identified by eye with difficulty in the spectrum. This means that, in order to assess the gas kinematic information provided by the narrow emission lines in imaging spectroscopy data sets, we will need to accurately subtract the broad-line emission at a level of a few percent of the total broad line flux or better. Only this allows us to study the behaviour of the gas over the whole extent of the galaxy.

At present, there is no good 'standard' technique to do this, several methods have been presented in the literature, but they typically leave strong residuals. Existing methods subtract either Gaussian fits to the broad component (Cano-Díaz et al., 2012), or exploit the fact that the broad-line region, which itself is spatially unresolved, must also be identical in all spatial pixels, so that its intrinsic spectral shape must be identical in all spatial pixels, except for a scaling factor. Christensen et al. (2006) investigated three different methods based on this simple principle, by either (1) subtracting a theoretical model of the point-spread function of their instrument (PMAS at the 3.6 m telescope at Calar Alto), (2) extracting and subtracting two narrow-band images that were on and off the narrow line component. Previous to the subtraction, they re-scaled the "off-line" component to the peak flux of a Gaussian fit to the unsubtracted spectrum of their source to obtain a measure of the peak flux coming from the BLR. (3) They extracted the spectra of individual spatial pixels from within a 2″ aperture around the nucleus, and subtracted re-scaled versions of the integrated spectrum bracketing the expected emission-line from these individual spectra in an iterative way. After 3 iterations, they typically reached stable results, but still found equally large residuals in the resulting line images.

Having high spatial resolution is certainly helpful, *e.g.*, with adaptive optics-assisted observations from the ground or the Hubble Space Telescope in space. Our quasar observations are in fact adaptive-optics assisted, using bright nearby stars as natural reference for the guide probe. Their spatial resolution is therefore limited by the spatial sampling rather than their resolution (we observed with the 250 mas pixel scale to maximize our sensitivity to low surface-brightness emission). However, even the highest spatial resolutions that can be achieved at high redshift, of-order $0.1''-0.2''$ at redshift $z \sim 2$, still correspond to about 1 kpc, and the wings of line profile of the bright broad-line region emission are easily traced over several times the FWHM size of the point spread function, which makes it challenging nonetheless to isolate any possible narrow-line emission in these cases.

The strategy we developed as part of this thesis to access the information contained in the narrow-line emission extends the various methods investigated by Christensen et al. (2006) and results in residuals that are of-order of 1% of the original broad-line flux, small enough to investigate the narrow-line component which is of-order of $1-20$% of the broad-line flux. We will present this method in more detail in the next subsection.

6.2.2 Isolating the narrow and broad emission-line components

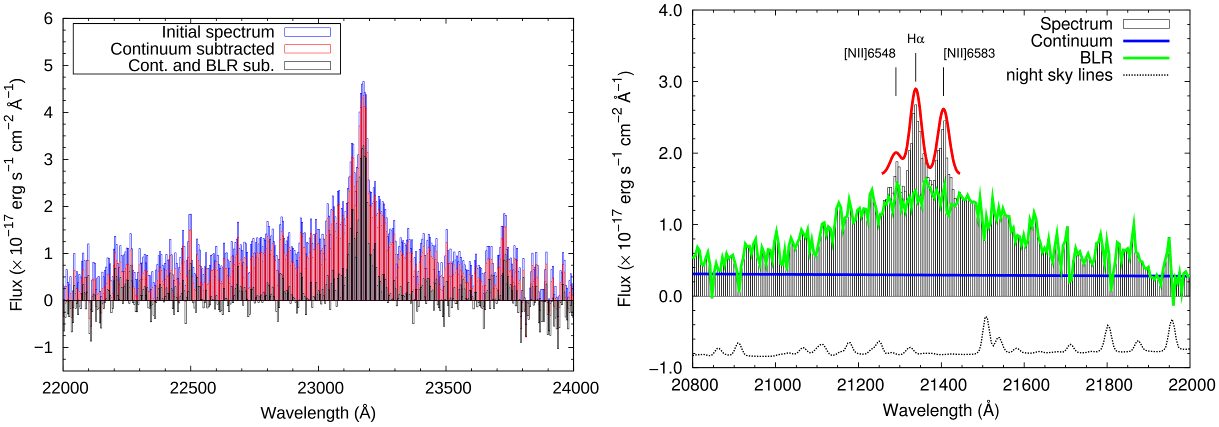

Figure 6.2: *Left*: Illustration of the subtraction of the continuum and the broad component from the integrated spectrum of MRC 1558−003. The blue spectrum is the initial one, the red histograms correspond to the continuum-subtracted spectrum and the the black spectrum is the final one, subtracted from the BLR. *Right*: The same for the QSO SDSS J0035+010, which has the most obvious narrow-line emission in the integrated spectrum of our quasar sample (but the line emission is not spatially resolved). In each case, following the algorithm presented below, we first substract the continuum (assumed to be a power law), we then roughly fit a single Gaussian to the broad line component, masking the central part of the spectrum. The residual from the previous step essentially contains the narrow component(s), which are assumed to be well represented by single Gaussian(s). The residuals from the fit of the narrow component(s) of the line are added back to the rough estimate of the BLR in order to obtain the final BLR model, that is scaled and subtracted from each spaxel.

Most of the QSOs that we observed have redshifts around $z \sim 2.5$, meaning that we observe the Hβ and [OIII] emission lines in the $H-$band, while the Hα emission line falls into the $K-$band. We start by subtracting the continuum. The continuum in all our sources is dominated by the Quasar emission, with little, if any, contribution from the stellar population of the host galaxy, and is therefore well represented by a simple power law. The slope index is determined by a fit to the integrated spectrum of the source and is then used for all spaxels, only the normalization is left free.

Once the continuum is subtracted, we still have to correctly subtract the component originating from the BLR. This can be challenging, since the broad emission of QSOs is often rather badly fitted with a single Gaussian fit, and given the intrinsic brightness of the spectral features of the AGN, it is critical that our subtraction method uses a representation of the shape of the AGN spectrum that is as accurate as possible. In addition, since we do not know the redshift or width of the narrow line component a priori, we do not want to use multi-Gaussian components in order not to 'overfit' the spectrum. Eventually, we have no theoretical reason to expect that the broad AGN emission lines have profiles that are intrinsically Gaussian (*e.g.*, Down et al., 2010). We therefore decide to rely on a method which measures the spectral shape of the spectrum itself, and is therefore somewhat related to the strategy adopted by Christensen et al. (2006).

Our strategy follows the subsequent steps:

1. We visually identify the spectral position of the narrow component of the line, which is possible for our sources through careful visual inspection. Alternatively, one of the methods proposed by Christensen et al. (2006) could be used for a first-pass visualization of potential emission lines.

2. We fit a single Gaussian to the broad component as a preliminary "first-guess" model of the line profile.

3. We create a 0^{th}-order model of the broad component by taking the line itself in spectral regions where the narrow component is not detected and the single Gaussian model produced at the previous step where it is.

4. We subtract this 0^{th}-order model from the line. If previous steps were correctly performed, the narrow component of the line should be the main feature in the residuals.

5. We fit the residuals of the previous step, *i.e.*, the NLR, by a single Gaussian.

6. The residuals from this last step are added to 0^{th}-order model of the BLR to give the final model of the broad component of the line.

7. This model of BLR is subtracted in each spaxel of our SINFONI data cube. The scaling of the BLR model is performed thanks to the line core of a single Gaussian component fit to the broad line of this spaxel, which avoids the narrow-line component.

The outcome of this procedure is illustrated for two sources in Fig. 6.2, presenting their spatially integrated spectra. Both sources were used to develop the algorithm described above. Note that the source shown in the left panel of this example is in fact a radio galaxy from the sample of Nesvadba et al. (2011b), not a QSO. The reason is that this source has a BLR which is easily seen in the input spectrum, but also known superimposed narrow lines coming from extended gas on kpc scales, which are clearly seen in all steps of the process (including the total spectrum), and therefore allows to assess the systematics introduced at each step of the broad-line subtraction. The other source is the radio-loud quasar (SDSS J0035+010) of our present sample that has the most obvious narrow lines, which therefore illustrates the perfomance of our algorithm well.

Although this subtraction leaves unavoidable residuals, when integrating over the residuals we find that the uncertainties that are clearly attributable to the AGN subtraction correspond to 1−2% of the intrinsic line flux, a value that we consider entirely acceptable.

6.2.3 Subtracting the narrow line component associated with the nucleus

Another possible source of contamination to the emission of the ionized gas present at large scales is the narrow line region (NLR). The NLR is composed of clouds in the central regions of the host galaxy (typically at radii $\lesssim 100$ pc) which are strongly influenced by the AGN. Spectrally, the NLR is very similar to the rest of the large scales ionized gas. Thus, we have to take advantage of the unresolved nature of the NLR in our observations and we decide to subtract the spectrum of the central pixel in our source, scaled as the PSF. The central pixel is identified as the pixel where the BLR is the brightest. The PSF is also defined from the spatial variations of the intensity of the BLR.

With this method, we tend to overestimate the contribution of the narrow line region, since we integrate all the flux along the line of sight that goes through the nucleus, *i.e.*, potentially also from emission line regions not associated with the nucleus. One noticable artifact that it creates is the hole at the center of the maps of these sources (see Fig. 6.9 for example). This hole is of course not real and is due to our method to subtract the spectrally narrow component coming from the nucleus. However, this method gives strict lower limits to the line fluxes of sources that are still detected ans therefore allows intrepretations regarding the extended emission line region, whereas fluxes encompassing the emission from the nucleus would be difficult to interpret.

6.3 Sample properties, observations and data reduction

In order to allow for a good subtraction of the AGN light, we restricted ourselves to observing sources that have bright stars (R < 17 mag) within 30″, which we used as natural guide stars to obtain adaptive-optics assisted observations. Our sources come from two samples, the Quasar catalog extracted by Shen et al. (2009) from the Sloan Digital Sky Survey data release 5, and the complete “Quarter-Jansky sample” of 178 Southern radio-selected quasars by Jackson et al. (2002); Hook et al. (2003); Wall et al. (2005).

All sources have high-quality spectroscopic redshifts obtained in the observed optical from their bright rest-frame UV lines, and are at redshifts z = 2.0 to 2.6. This means that for all sources Hα and the [NII] doublet fall into the $K-$band, whereas [OIII]$\lambda\lambda$4959,5007 and Hβ fall into the $H-$band. For the five sources drawn from the Quarter-Jansky sample, we use the redshift provided by Hook et al. (2003) and for the sources coming from the Quasar catalog of Shen et al. (2009), we used the most recent available spectroscopy, presented in Pâris et al. (2012). The redshift based on the Lyα emission line of SDSS quasars differs slightly from the redshift based on the other detected emission lines (*e.g.*, NIV, CIV, CIII], see Fig. 6.3). Therefore, when we provide the redshift of the SDSS sources based on restframe UV, $z_{\rm UV}$, we refer to the redshift given by the NIV, CIV and CIII] emission lines. The discrepancy between the redshifts based on Lyα and on the other emission lines can be due to the strong absorption features observed just blueward of the Lyα emission line (see Fig. 6.3) and which are caused by intervening clouds of neutral gas.

The bolometric power of these quasars, which was initially estimated from their $B-$band magnitude as the sample was selected, is of-order 10^{46-47} erg s^{-1}, comparable to the bolometric power of powerful HzRGs. Their radio flux spans however a large range including 5 sources without radio detection in the VLA 1.4 GHz survey of the Northern sky, FIRST. We used all available radio observations to measure the radio spectral index for those 6 sources that are detected in FIRST and other surveys (Fig. 6.4), finding indices between −0.5 and 0.2. This is a significant difference to powerful HzRGs, which are today mostly selected based on their steep spectral indices in the radio. We will come back to this point below.

6.3.1 Centimeter radio properties

The radio-loud quasars of our sample were first catalogued as quasars by Veron-Cetty & Veron (1983) and detected in the radio by Quiniento et al. (1988), except for B 0227−369, which already appeared in the study of Savage et al. (1977). They are all part of the “Parkes quarter-Jansky flat-spectrum sample” (Jackson et al., 2002; Hook et al., 2003; Wall et al., 2005) which provides their fluxes at 2.7 GHz and 5 GHz, as well as spectroscopic redshifts. Except for B 0524−433 which has a too low declination, all sources are detected in the NVSS (Condon et al., 1998) as well. Moreover, two sources (B 0113−283 and B 0227−369) are also detected in the Australia Telescope 20 GHz Survey (Murphy et al., 2010), which also provides updated fluxes at 5 GHz and 8 GHz. Taken together with their detections in other surveys (Large et al., 1981; Bennett et al., 1986; Wright & Otrupcek, 1990; Griffith et al., 1994; Douglas et al., 1996; Wright et al., 1996; Bock et al., 1999; Kovalev et al., 2007; Healey et al., 2007; Mao et al., 2010), we can approximate their fluxes at 500 MHz restframe, as illustrated by Fig. 6.4. Note that B 0227−369 is also detected with Fermi (Kovalev, 2009; Mahony et al., 2010).

Table 6.1: Ancillary information regarding our sample of radio-loud quasars.

Source ID	RA (J2000)	Dec (J2000)	$z_{\rm UV}$ (1)	D_L (2) [Gpc]	S_{500} (3) [mJy]	α (4)	P_{327} [$\times10^{27}$ W Hz^{-1}]	P_{500} [$\times10^{27}$ W Hz^{-1}]	P_{1400} (5) [$\times10^{27}$ W Hz^{-1}]
B 0113−283	01:15:23.88	−28:04:55.2	2.555	20.938	486	-0.01 ± 0.11	25.6	25.5	25.2
B 0227−369	02:29:28.47	−36:43:56.8	2.115	16.636	124	$+0.19 \pm 0.13$	3.8	4.1	5.0
B 0524−433	05:25:54.50	−43:18:11.0	2.164	17.108	1159	-0.53 ± 0.08	50.9	40.6	23.6
B 1657+022	16:59:45.00	+02:13:07.0	2.039	15.909	615	-0.24 ± 0.07	20.6	18.6	14.6
SDSS J0035+010	00:35:12.90	+01:04:30.7	2.2538	17.978	181	-0.26 ± 0.00	7.9	7.1	5.4
SDSS J2226+005	22:26:46.53	+00:52:11.5	2.2520	17.960	1460	-0.34 ± 0.04	65.7	57.0	40.3

(1): Spectroscopic redshift of Hook et al. (2003), measured from rest-frame UV emisson lines, or given by the SDSS-DR9 (Pâris et al., 2012). — (2): Luminosity distance, derived from the redshift based on restframe UV lines. — (3): Estimated flux at 500 MHz restframe. — (4): Radio spectral index. — (5): Estimated luminosity at 327 MHz, 500 MHz and 1.4 GHz restframe, as extrapolated from the power law fit to the radio SED.

For the sources which are not detected in the radio we can only give upper limits on their radio luminosity. The FIRST catalog includes sources down to 0.78−1.03 mJy in the same region as our sources, and when retrieving images from the FIRST survey centered on our sources, we find an RMS level of 0.1−0.2 mJy. Assuming fiducial radio spectral indices of 0.0 (*i.e.*, literally a flat-spectrum source) or −0.8 (a typical value for steep-spectrum sources), this corresponds to upper limits to their radio powers of, at most, few 10^{25} W Hz^{-1} at our reference frequency of 500 MHz in the rest-frame.

Table 6.2: Ancillary information regarding our sample of radio-quiet QSOs.

Source ID	RA (J2000)	Dec (J2000)	$z_{\rm UV}$ (1)	D_L (2) [Gpc]	$\rm RMS_{1400}$ (3) [μJy]	P_{327} [$\times10^{24}$ W HZ^{-1}]	P_{500} [$\times10^{24}$ W HZ^{-1}]	P_{1400} (4) [$\times10^{24}$ W HZ^{-1}]
SDSS J0035+002	00:35:21.62	00:19:41.0	2.3602	19.016	104	4.5 ; 38.0	4.5 ; 27.1	4.5 ; 11.9
SDSS J0839+045	08:39:01.92	04:53:45.6	2.3564	18.979	138	5.9 ; 50.2	5.9 ; 35.7	5.9 ; 15.7
SDSS J1306+025	13:06:08.07	02:59:43.7	2.4323	19.724	144	6.7 ; 57.6	6.7 ; 41.0	6.7 ; 18.0
SDSS J1434+010	14:34:36.51	01:05:22.2	2.1959	17.416	137	5.0 ; 40.3	5.0 ; 28.7	5.0 ; 12.6
SDSS J1435+035	14:35:00.28	03:54:03.5	2.4938	20.331	145	7.2 ; 62.5	7.2 ; 44.5	7.2 ; 19.5

(1): Spectroscopic redshift from the SDSS-DR9 (Pâris et al., 2012) (from all detected lines except Lyα). — (2): Luminosity distance, derived from the redshift based on restframe UV lines. — (3): RMS level in FIRST images at the position of the source. — (4): Upper limits on the radio luminosities, assuming a spectral index $\alpha = 0.0$ and $\alpha = -0.8$ (respectively).

6.3.2 NIR imaging-spectroscopy

We observed these quasars with SINFONI at the Very Large Telescope of ESO between late 2008 and early 2009 in Service Mode (program ID 082.A-0602, PI Nesvadba) for a first part of the SDSS quasars, and between early and the middle of 2010 for the radio loud quasars drawn from the “Quarter-Jansky sample” and the rest of the SDSS quasars (program ID 085.A-0065, PI Nesvadba ; see the observation logs in the Appendixes A.2 and A.3 to obtain all the details). The observation strategy is very similar to the one adopted for the observation of the sample of radio galaxies (see Chapter 4). Specifically, the on-source integration time was set to 5 min, repeated in blocks of 1 hr, at the end of which a standard star was observed. We chose the large field of view of $8'' \times 8''$ (*i.e.*, with a pixel scale of $0.25''$/pix) in order to be able to probe the full extent of putative emission line regions. We used the $H+K$ band in order to be able to observe the Hβ and [O III]$\lambda 4959, 5007$ emission lines in the $H-$band and the Hα, [N II]$\lambda 6548, 6583$ and [S II]$\lambda 6716, 6731$ emission lines in the $K-$band, given the redshift of our targets. In order to avoid taking dedicated sky frames, we adopted a dither pattern in which the target is successively offset in two opposite corners of the field of view. The main difference to our previous observations is that these one are assisted by adaptive-optics, which leads to spatial resolution better than $\lesssim 0.5''$. Supplementary information about these observations is given in Table 6.3, and all the details can be found in Table A.3 and A.4.

The data reduction is done in the same way as for the previous sample of high-redshift radio galaxies (see §2.1.4 for all the details of the data reduction): individual frames are dark-subtracted, flat-fielded and wavelength-calibrated (with a spectral lamp for a first estimate and then enhanced thanks to the OH emission lines). Individual frames are then sky subtracted, corrected for telluric absorptions and combined and re-arranged in a single cube before flux calibration is finally performed.

The redshift of these quasars are estimated with two different methods: the first redshift estimate is based on the centroid of the fit to the narrow component of emission lines, *i.e.*, we use the same technique as for high-redshift radio galaxies (see Chapter 4). The second estimate is based on the broad component of the Hα emission line: it is calculated from the wavelength that divides in two the flux of the broad Hα line. Both estimates are given in Table 6.3 and are usually in agreement (the only noticeable discrepancy is for B 0113−283). The estimate of the velocity dispersion of the broad component of the Hα and Hβ emission lines is performed empirically, since they are hard to model. We therefore use the Full-Width at Half Maximum (FWHM) of the line, calculated from the wavelengthes at which the line reaches between 45 and 55% of its maximum: we obtain two groups of wavelengthes, one blueward and one redward of the peak wavelength. The FWHM is set to be the mean difference between these two groups and the error is defined from the wavelength differences between the maximum and the minimum wavelengthes in each group, namely we add these two differences and take the half of this sum. This is illustrated on the first spectrum of Fig. 6.5(a): the two dashed blue lines (nearly horizontal) represent the levels at 45 and 55% of the peak of the emission line. The black vertical dashed lines mark wavelengthes at which the flux density is between the two levels: these define two groups of wavelength, one blueward and one redward of the peak wavelength. The FWHM of the line is then the difference between the average wavelengthes of the two groups. Note also that we produce emission line maps (presenting the NLR surface brightness, relative velocities and velocity dispersions) for 5 of the 6 radio-loud quasars and for 3 of the 5 radio-quiet quasars that we observed. In all the other cubes, we cannot obtain these maps due to the faintness of the narrow component compared to the broad component in the Hα line.

6.4 Results

We detected bright emission lines, including broad nuclear lines with FWHM $\gg 1000$ km s^{-1} and/or narrow-line components with typical line widths FWHM $\sim 100-1000$ km s^{-1} in all data cubes. In order to analyze the narrow-line emission in more detail we subtracted the broad component with a method described above (§ 6.2). In 1/6 sources with (B 0113−283) and in 2/5 sources without (SDSS J0839+045 and SDSS J1435+035) radio counterpart, we did not detect significant residuals after the broad-line subtraction, and we will not consider these sources for our subsequent analysis of the spatially-resolved emission line properties. For the remaining 8 sources (5/6 with, 3/5 without radio detection) we typically identified [O III], Hβ, Hα, and [N II] lines, including broad components of Hα and Hβ.

We used two methods to obtain redshifts of these sources from their integrated spectra: First, the redshift estimate is based on the centroid of the fit to the narrow component of emission lines, *i.e.*, we use the same

Table 6.3: Basic observations log of the radio-loud (first part of the Table) and radio-quiet (second part of the Table) quasars.

Source ID	ToT (1) [min]	PSF (2) [arcsec]	$z_{\rm IR}^{\rm NLR}$ (3)	$z_{\rm IR}^{\rm BLR}$ (4)	Δv (5) [km s^{-1}]
B 0113−283	180	0.4 ×0.3	2.563	2.571	-673
B 0227−369	175	0.35×0.25	2.122	2.121	+96
B 0524−433	175	0.4 ×0.25	2.168	2.167	+95
B 1657+022	180	0.3 ×0.2	2.043	2.041	+197
SDSS J0035+010	135	0.5 ×0.4	2.251	2.254	-277
SDSS J2226+005	180	0.3 ×0.2	2.247	2.251	-370
SDSS J0035+002	100	0.5 ×0.4	2.355	2.351	+358
SDSS J0839+045	180	0.35×0.3	2.368	2.372	-356
SDSS J1306+025	250	0.4 ×0.3	2.414	2.419	-439
SDSS J1434+010	250	0.45×0.4	2.201	2.202	-94
SDSS J1435+035	175	0.4 ×0.3	2.505	2.505	0.0

(1): Total on source exposure time (in minutes). — (2): PSF of the observation, measured from the standard stars observed at the end of each 1 hr observation block. — (3): Redshift of the source, estimated from the narrow emission line(s) seen in our SINFONI observations (with a typical uncertainty of ±0.001). — (4): Redshift of the source, defined as the median wavelentgh of the broad Hα line (with a typical uncertainty of ±0.002). — (5): Velocity offset between the two redshift estimates.

Table 6.4: Properties of the quasars and of their Hα broad line.

Sources	z (1)	D$_L$ (2) [Gpc]	α_λ (3)	ext. (4) [A_V]	FWHM (4) [km s^{-1}]	$\mathcal{F}_{\rm BRL}$ (5) [10^{-15} erg s^{-1} cm^{-2}]	res. (6) [% of $\mathcal{F}_{\rm BRL}$]
B 0113−283	2.563	21.017	-1.88	0.6	4250 ± 300	17.0	3.0
B 0227−369	2.122	16.704	-0.26	1.7	6650 ± 100	18.5	1.2
B 0524−433	2.168	17.147	-0.97	0.0	4400 ± 200	47.0	1.6
B 1657+022	2.043	15.947	-1.37	. . .	2550 ± 250	32.5	1.2
SDSS J003513+010430	2.251	17.951	-1.91	. . .	4350 ± 500	5.0	3.2
SDSS J222646+005211	2.247	17.912	-0.68	0.7	2100 ± 100	12.5	1.0
SDSS J003522+001941	2.355	18.965	-1.00	0.0	5950 ± 450	17.4	2.8
SDSS J083902+045345	2.370	19.112	-5.08	0.2	4650 ± 400	13.6	0.6
SDSS J130608+025943	2.415	19.554	-1.14	2.8	3700 ± 350	8.5	1.8
SDSS J143436+010522	2.203	17.485	-1.49	1.3	3650 ± 150	27.5	0.8
SDSS J143500+035403	2.506	20.452	-1.15	0.0	4800 ± 450	20.5	1.4

(1): Redshift estimated from our SINFONI observations. — (2): Luminosity distance derived from our redshift estimate. — (3): Index of the power law fitted to the quasar continuum. — (4): FWHM of the broad component of the Hα emission line. The uncertainties are derived from the width of the line at 45% and 55% of its line core. — (5): Flux of the broad component of the Hα emission line (in 10^{-15} erg s^{-1} cm^{-2}). — (6): Relative intensity of residuals in the integrated spectrum after the subtraction of the broad and narrow components of the emission line. These residuals are integrated over ±50Å around the redshift of the source.

technique as for high-redshift radio galaxies (see Chapter 4). The second estimate is based on the broad component of the Hα emission line: it is calculated from the wavelength at which the blue and the red part of the broad Hα line profile are equal. Both estimates are given in Table 6.3 and are in agreement for all sources but B 0113−283.

The velocity dispersions of the broad Hα and Hβ line profiles are not estimated from Gaussian fits, but directly from the measured line profile, since we have no reason to posit that our line profiles are intrinsically Gaussian. We simply use the Full-Width at Half Maximum (FWHM) of the line, calculated from the wavelengths at which the line reaches between 45 and 55% of its maximum. We determine average wavelength where these fluxes are reached on the blue and red line wing, and take the wavelength difference between the two wings to approximate the FWHM (see the spectrum of B 0113−283 in Fig. 6.5).

6.4.1 Description of individual sources: Quasars with radio counterparts

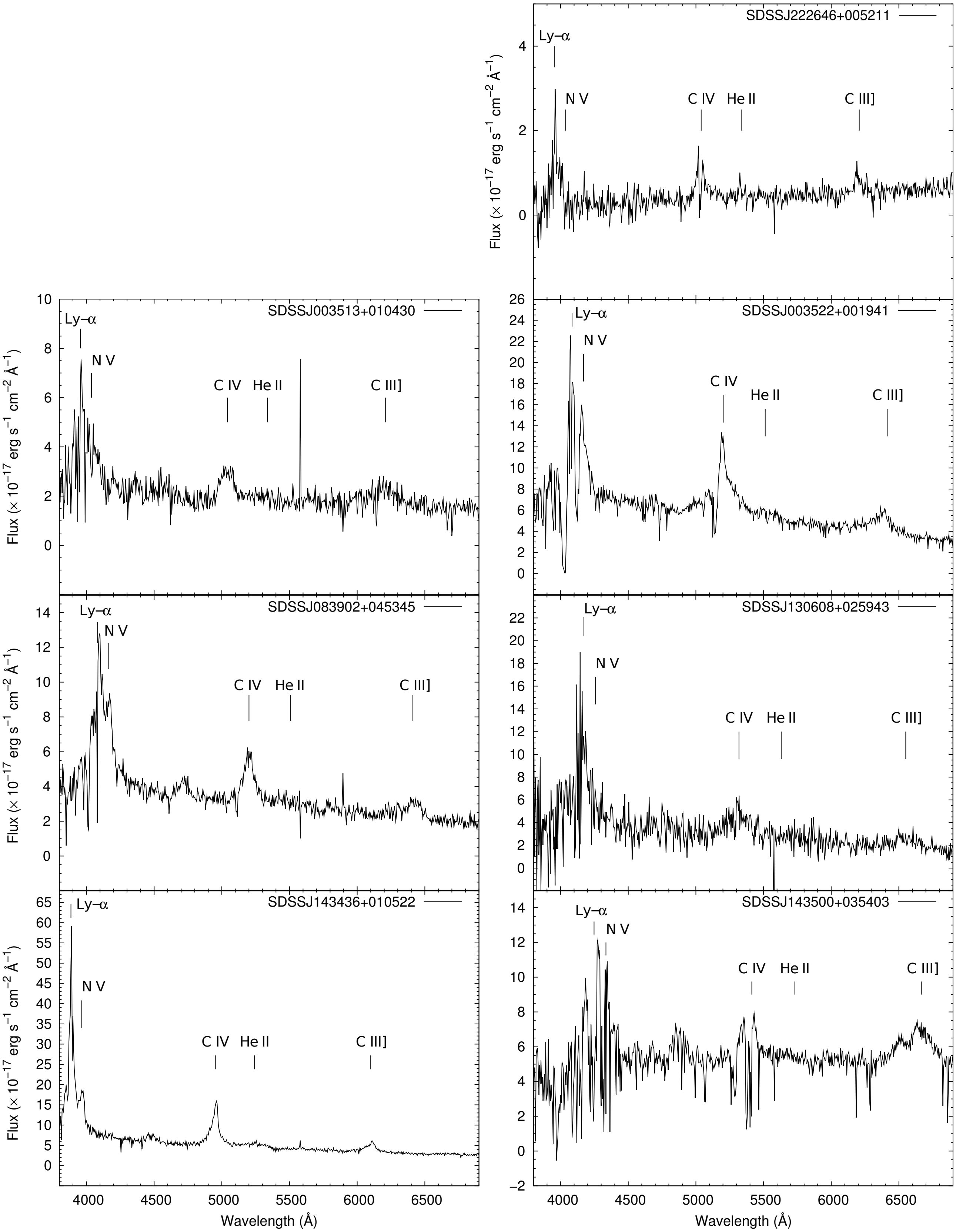

Figure 6.3: Restframe UV spectra of some sources of our sample of quasars (those drawn from the sample of Shen et al., 2009) as observed by the SDSS to date (Pâris et al., 2012). The redshift that we quote for these sources is based on all detected emission lines except Lyα. Indeed, this line shows important absorption features, due to intervening neutral gas, and this makes Lyα a less reliable redshift estimate.

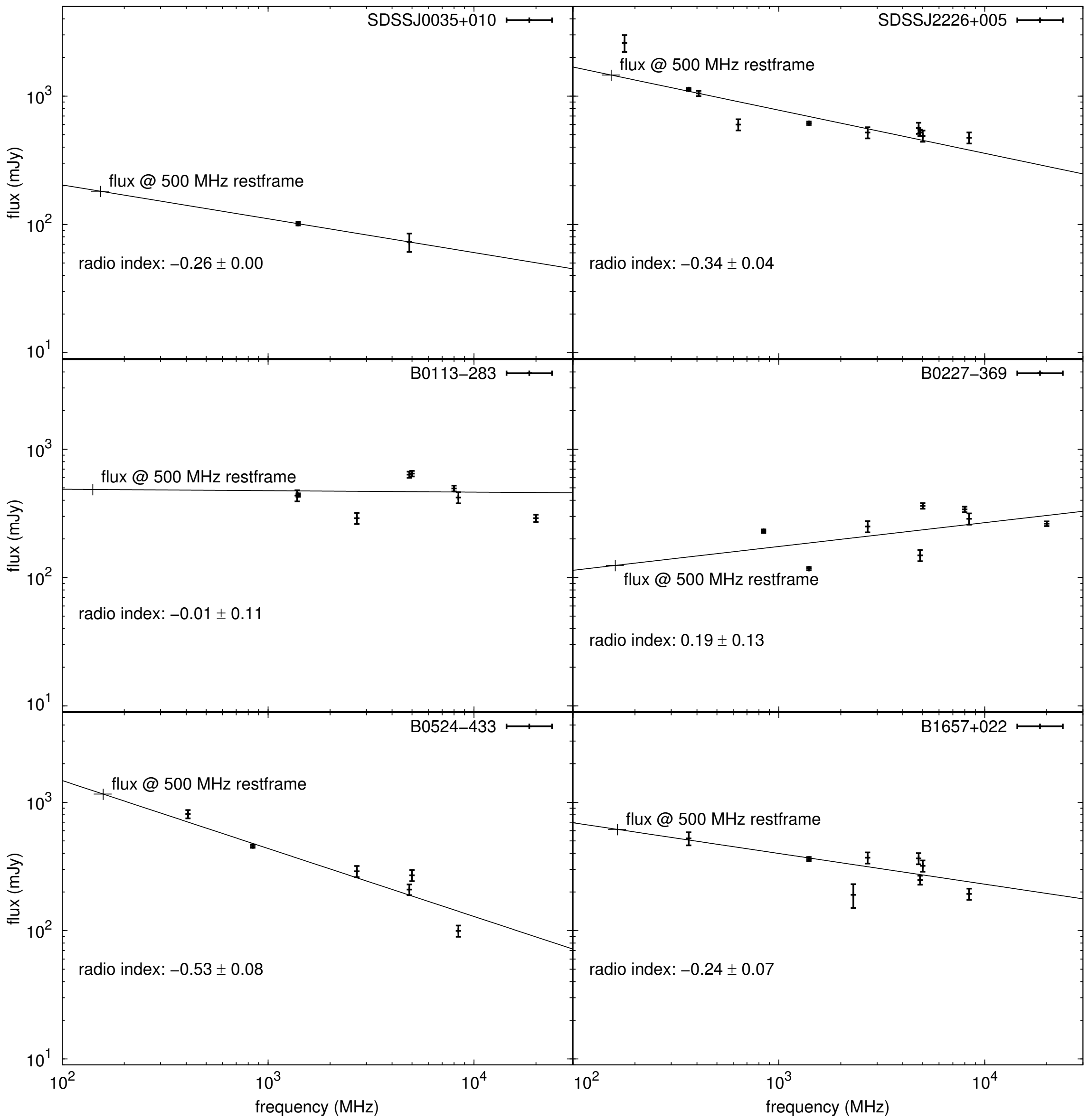

Figure 6.4: Spectal energy distribution in the radio domain of our sample of radio-loud quasars. Contrary to HzRGs that tend to have steep spectra, those of quasars are more or less flat. The same technique (extrapolation from the power-law fitted to the SED) is used to derived their luminosity at 500 MHz restframe.

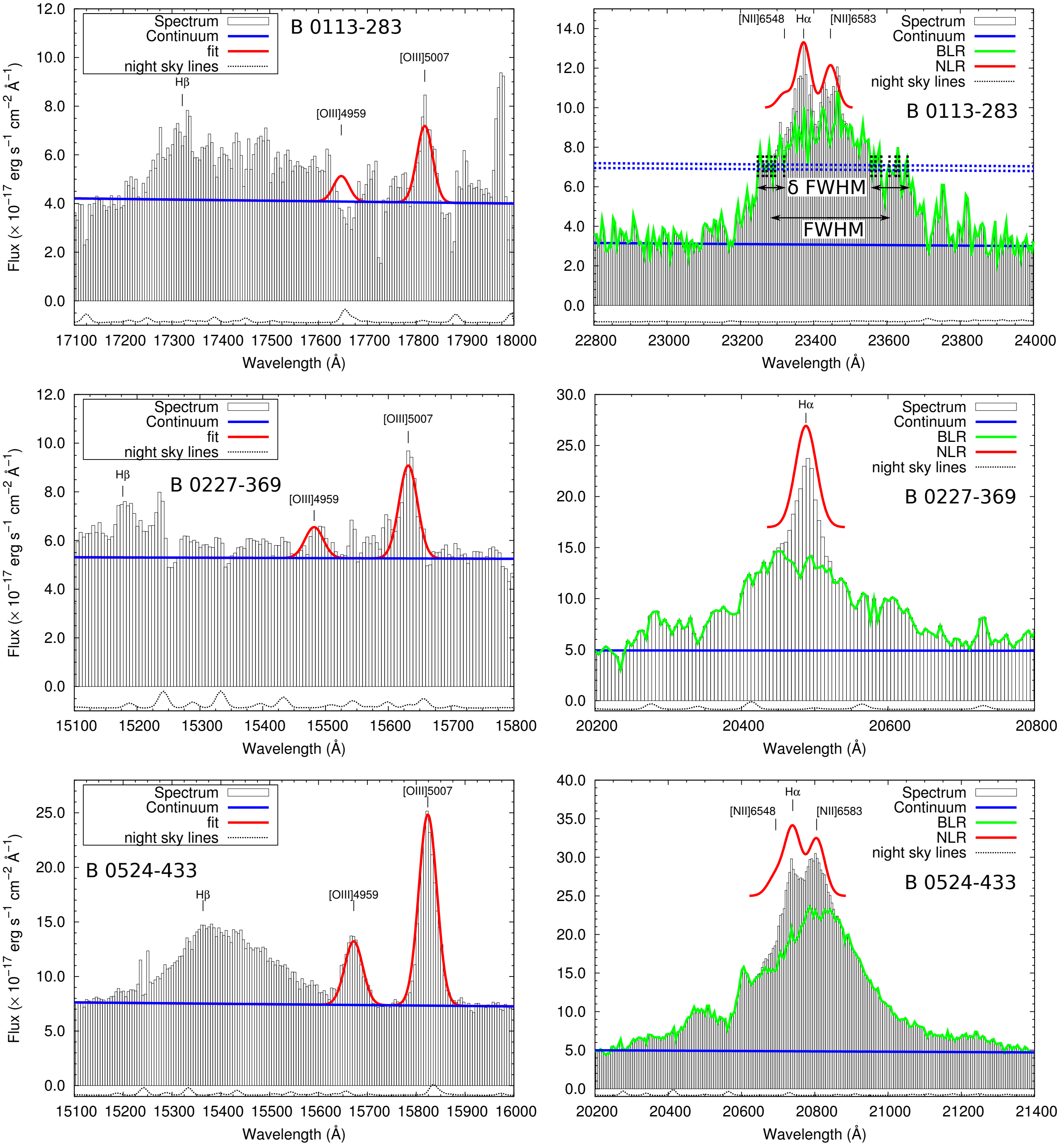

(a) Spectra of the radio loud quasars sample (1/2)

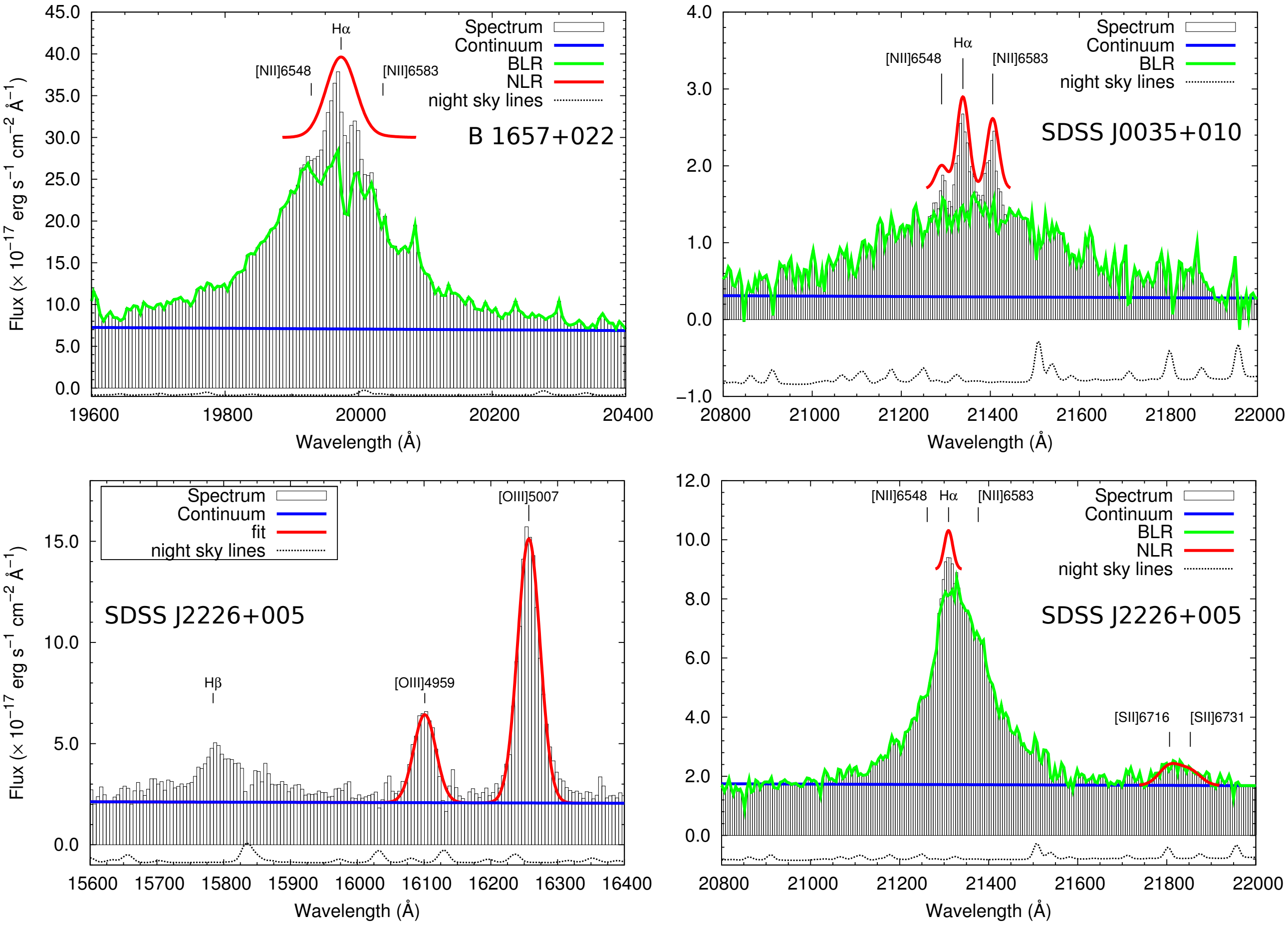

(b) Spectra of the radio loud quasars sample (2/2)

Figure 6.5: Integrated spectra of the six radio-loud quasars in our sample. One is centered on the Hβ and the [OIII] doublet lines, when detected, and the second is centered on Hα and [NII]. Continuum level is given by the blue line and the green line gives the estimate that we made of the broad line component, as explained in the text. The line emission on top of the broad component is assumed to be part of the narrow component, well represented by a Gaussian curve.

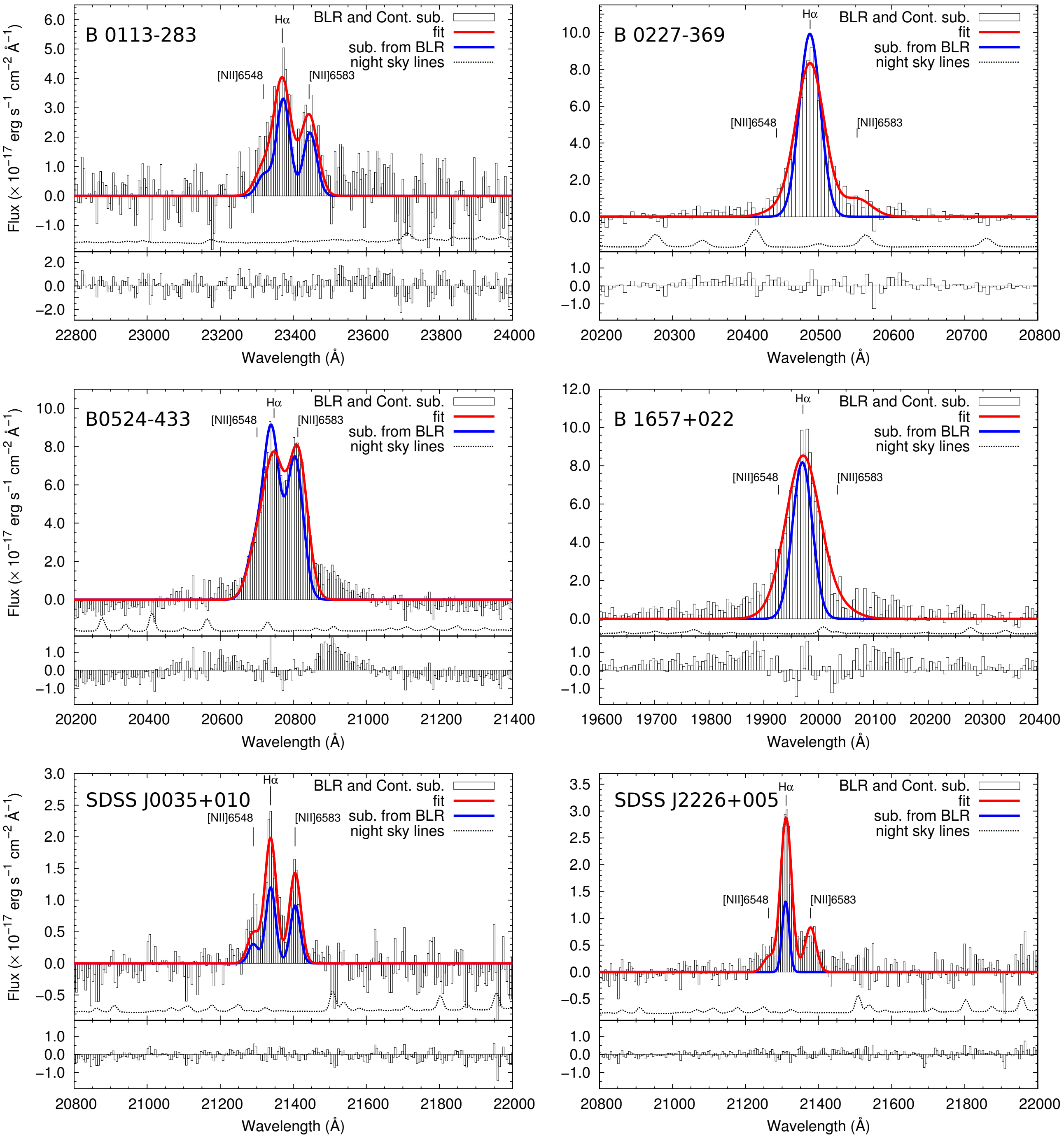

Figure 6.6: Spectra of the six BLR-subtracted radio-loud quasars in our sample, integrated over the same region as those shown in Fig. 6.5. Some sources (*e.g.*, B 0524−433 or B 1657+022) show important residuals at the position of the Hα emission line, due to incorrect subtraction of the BLR in individual spaxels. The blue line shows the model of the narrow lines emission that we subtracted from the integrated spectrum to obtain the model of the broad component of the Hα emission line. The red line shows the fit to the narrow components of the Hα and [NII] emission line in the integrated spectrum of the BLR-subtracted cube.

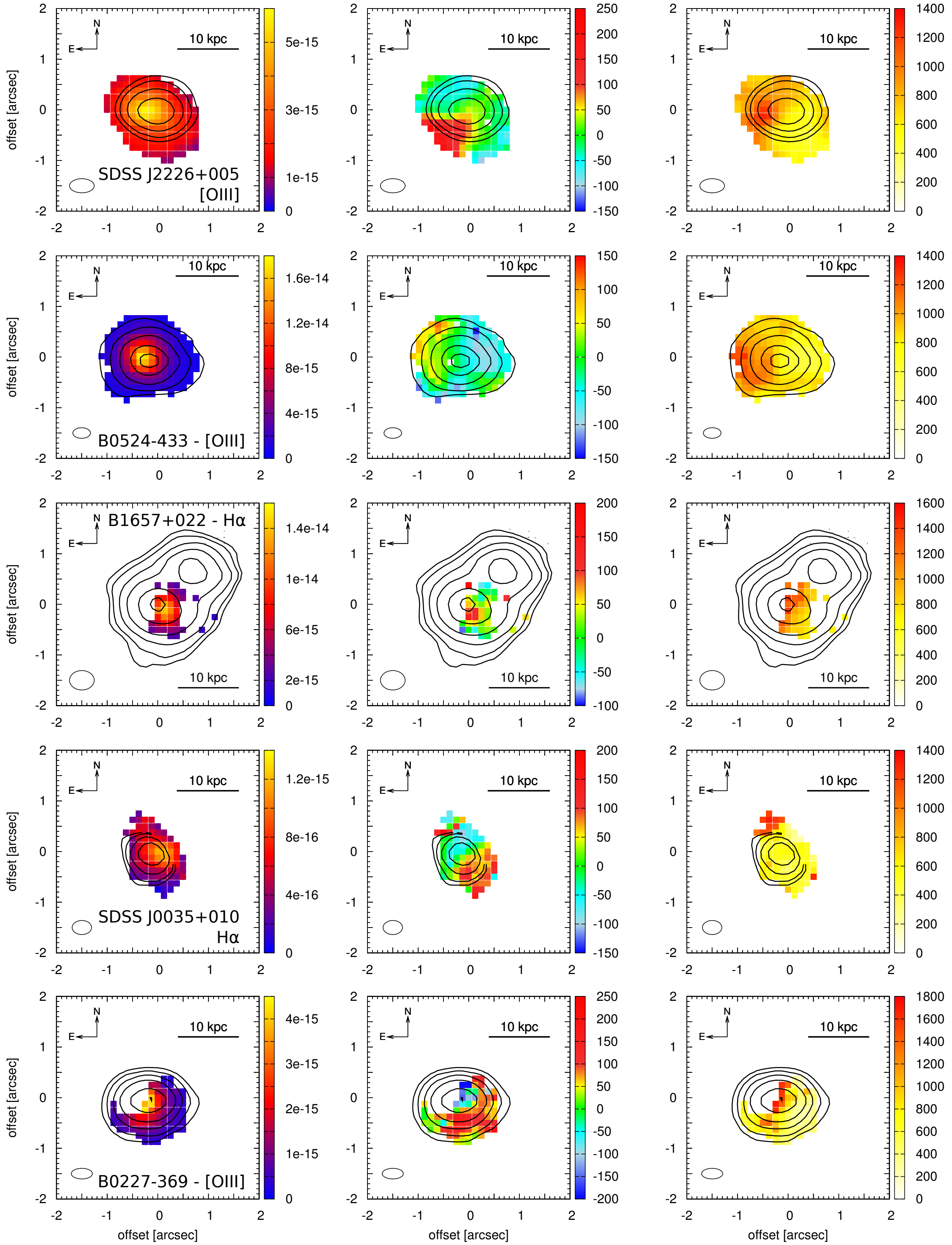

Figure 6.7: Maps tracing the emission and kinematics of *all* (*i.e.*, both circum-nuclear and extended) the ionized gas in the the radio loud quasar sample, based whether on the [OIII] emission line (when present) or the narrow component of the Hα emission line (when detected). Sources are shown in order of increasing radio power at a frequency of 500 MHz in the rest-frame, with the most powerful on the top of the figure. Strong night-sky line residuals just redward of the [OIII]λ5007 emission line prevented us from analyzing the line emission in the NE part of B 0227−369.

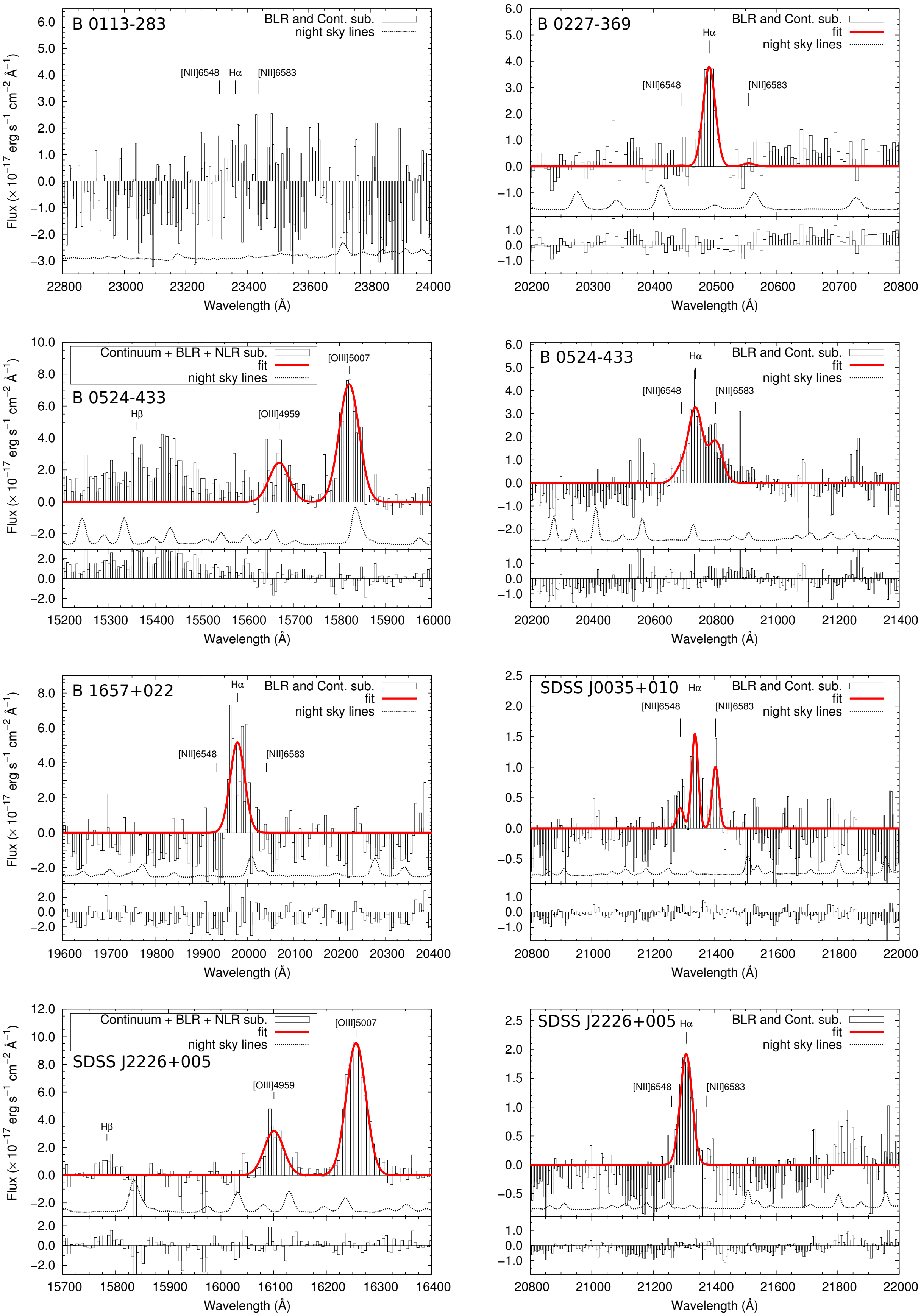

Figure 6.8: Spectra of the six radio-loud quasars in our sample, subtracted from the broad Hα emission line and from the nuclear narrow emission lines, and integrated over the same region as those shown in Fig. 6.5.

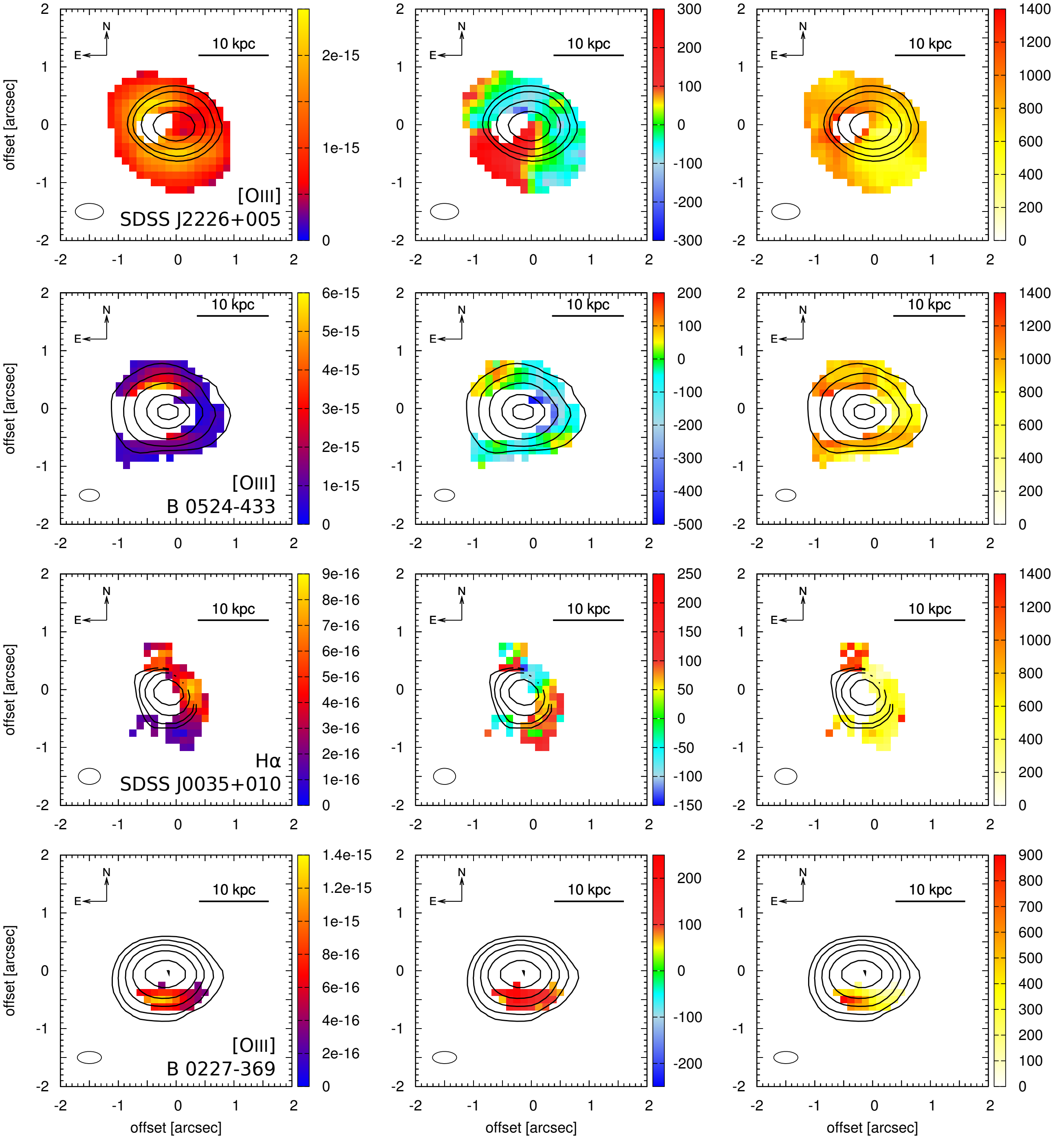

Figure 6.9: Maps tracing the emission and kinematics of only the extended ionized gas in the the radio loud quasar sample (*i.e.*, the nuclear narrow component has been subtracted, as explained in § 6.2.3). They are based whether on the [OIII] emission line (when present) or the narrow component of the Hα emission line (when detected).

B 0113−283

Table 6.5: Emission lines in B 0113−283.

			only BLR subtracted		BLR and scattered NLR subtracted	
Line	λ_0 $^{(1)}$ [Å]	$\lambda_{\rm obs}$ $^{(2)}$ [Å]	FWHM $^{(3)}$ [km s^{-1}]	Flux $^{(4)}$ [10^{-16} erg s^{-1} cm^{-2}]	FWHM $^{(3)}$ [km s^{-1}]	Flux $^{(4)}$ [10^{-16} erg s^{-1} cm^{-2}]
Hβ_{br}	4861.3	17321.2 ± 5.0	3100 ± 200	49.0 ± 10.0	…	…
[OIII]	4958.9	17646.6 ± 2.5	560 ± 60	4.2 ± 0.8	…	≤ 0.8
[OIII]	5006.9	17817.4 ± 2.5	560 ± 60	12.7 ± 2.6	…	≤ 0.8
[NII]	6548.1	23317.7 ± 5.0	670 ± 70	5.4 ± 1.0	…	≤ 0.7
Hα	6562.8	23370.0 ± 5.0	670 ± 70	23.0 ± 5.0	…	≤ 0.7
[NII]	6583.4	23443.4 ± 5.0	670 ± 70	16.1 ± 3.0	…	≤ 0.7

The left-hand side of this Table gives the characteristics of the narrow component of the emission lines subtracted only from the broad component, while the left-hand side gives the characteristics of the narrow component of the emission lines also subtracted from the scattered narrow component.
(1): Rest-frame wavelength. — (2): Observed wavelength. — (3): Full-Width at Half Maximum, corrected for instrumental resolution (in km s^{-1}). — (4): Line flux deduced from the fit (in 10^{-16} erg s^{-1} cm^{-2}).

We find this source at redshift $z = 2.563 \pm 0.001$, measured from the spectral position of the narrow components of the Hα and [NII] lines. This is quite different from the redshift estimated from the broad component of the Hα emission line, $z = 2.571 \pm 0.002$. This value also differs from the restframe UV estimate ($z_{\rm UV} = 2.555$) provided by Hook et al. (2003), which is based on three emission lines (blended Lyα and NV, and a clearly detected CIV). This offset of ~ 700 km s^{-1} could be explained by gas motions near the AGN in the UV and/or by absorption features blueward of the Lyα wavelength due to intervening clouds of atomic gas. The broad component of the Hα emission line is clearly detected in the $K-$band (with FWHM $= 4250 \pm 300$ km s^{-1}), with a faint narrow Hα and [NII] doublet on top of it. In the $H-$band, a broad Hβ line is clearly detected, as well as the [OIII] doublet, although it is faint. Line parameters are listed in Table 6.5. Given the faintness of the narrow component of the Hα and [OIII] lines, we are not able to produce maps of the dynamics of the ionized gas in this quasar.

B 0227−369

Table 6.6: Emission lines in B 0227−369.

			only BLR subtracted		BLR and scattered NLR subtracted	
Line	λ_0 [Å]	$\lambda_{\rm obs}$ [Å]	FWHM [km s^{-1}]	Flux [10^{-16} erg s^{-1} cm^{-2}]	FWHM [km s^{-1}]	Flux [10^{-16} erg s^{-1} cm^{-2}]
Hβ_{br}	4861.3	15177.2 ± 8.0	1290 ± 400	38.3 ± 9.0	…	…
[OIII]	4958.9	15481.9 ± 5.3	570 ± 60	4.6 ± 1.0	…	≤ 0.4
[OIII]	5006.9	15631.7 ± 5.3	570 ± 60	14.1 ± 3.0	…	≤ 0.4
[NII]	6548.1	20442.4 ± 4.0	630 ± 70	1.6 ± 0.7	…	≤ 0.5
Hα	6562.8	20488.3 ± 4.0	630 ± 70	41.0 ± 7.0	220 ± 30	9.4 ± 2.0
[NII]	6583.4	20552.6 ± 4.0	630 ± 70	4.8 ± 2.0	…	≤ 0.5

This source is detected at redshift $z = 2.122 \pm 0.001$, based on its [OIII] and Hα emission lines, and we find the same estimate when using the broad component of the Hα emission line, with $z = 2.121 \pm 0.002$. But these values are quite different from the redshift based on restframe UV lines ($z_{UV} = 2.115$) of Hook et al. (2003), which comes from two well detected emission lines (Lyα, blended with NV, and CIV) and three other fainter emission lines (NV, SiIV/OIV] and CIII]). We detect the [OIII] doublet in the $H-$band, along with a broad Hβ emission line (see Fig. 6.5(a)). In the $K-$band, we clearly detect the broad component of the Hα emission line (with FWHM = 6650 ± 100 km s^{-1}), as well as its narrow component. However, no [NII] emission line is observed. All the information about the detected emission lines is given in Table 6.6. The [OIII] line is used to produce the maps of the dynamics of the ionized gas (see Fig. 6.7) and it is well fitted by a single Gaussian over most of the extended emission line region, although no acceptable fit can be found in the North-eastern part of the extended emission line region because of strong night sky residuals in this region. In the Southwest, the [OIII] emission line is redshifted by ∼ 200 km s^{-1}and is relatively quiescent, with FWHM ∼ 300 km s^{-1}. The velocity dispersion increases to high values (FWHM ∼ 1500 km s^{-1}) where the continuum is the brightest and where the velocity field also changes and becomes blueshifted. The emission line region is as extended as the continuum and they are observed over $1.5'' \times 1.4''$.

B 0524−433

Table 6.7: Emission lines in B 0524−433.

			only BLR subtracted		BLR and scattered NLR subtracted	
Line	λ_0 [Å]	λ_{obs} [Å]	FWHM [km s^{-1}]	Flux [10^{-16} erg s^{-1} cm^{-2}]	FWHM [km s^{-1}]	Flux [10^{-16} erg s^{-1} cm^{-2}]
Hβ_{br}	4861.3	15363.5 ± 5.0	4500 ± 200	169.0 ± 34.0	...	...
[OIII]	4958.9	15672.0 ± 2.0	760 ± 80	27.3 ± 3.1	910 ± 100	13.3 ± 3.0
[OIII]	5006.9	15823.7 ± 2.0	760 ± 80	81.8 ± 9.3	910 ± 100	40.0 ± 9.0
[NII]	6548.1	20700.9 ± 4.0	970 ± 100	19.0 ± 3.8	720 ± 80	3.4 ± 1.0
Hα	6562.8	20747.4 ± 4.0	970 ± 100	48.1 ± 9.6	720 ± 80	17.9 ± 3.5
[NII]	6583.4	20812.5 ± 4.0	970 ± 100	57.1 ± 11.2	720 ± 80	10.2 ± 2.5

We find B 0524−433 at a redshift $z = 2.160 \pm 0.001$, not too different from the previous estimate based on restframe UV emission lines ($z_{UV} = 2.164$) of Hook et al. (2003) and also similar to the value found when using the broad component of the Hα emission line, $z = 2.167 \pm 0.002$. In the $K-$band, we detect a broad Hα emission line (with FWHM = 4400±200 km s^{-1}) on top of which narrow [NII] and Hα emission lines are also detected. The [OIII] emission is clearly detected in the $H-$band, together with a broad Hβ emission line, whose properties are similar to the broad Hα emission line. All the information about the detected emission lines is given in Table 6.7. From the [OIII] emission line we construct maps of the emission line region, which is found to be as extended as the continuum, and observed over $1.9'' \times 1.6''$, with a major axis along a East-West axis. The ionized gas presents a velocity gradient of ∼ 150 km s^{-1}along a Northeast to Southwest axis. The velocity dispersion is less important in the western region, with FWHM = 600 − 800 km s^{-1}, while it reaches FWHM ∼ 1000 km s^{-1}in the eastern regions (see Fig. 6.7).

B 1657+022

We find this quasar at a redshift of $z = 2.043 \pm 0.001$, not too different from the restframe UV estimate ($z_{UV} = 2.039$) of Hook et al. (2003) and also in agreement with the redshift based on the broad component of the Hα emission line ($z = 2.041 \pm 0.002$). In the $K-$band, the narrow component of the Hα emission line can be easily identified, together with a norrow[NII] component, on top of the dominant broad component of the Hα emission line (with FWHM = 2250 ± 250 km s^{-1}). All the information about the detected emission lines is given in Table 6.8. Maps of the ionized gas are based on the narrow Hα component and therefore do not extend very far from the central emission (where the SNR is sufficient) and cover about

Table 6.8: Emission lines in B 1657+022.

Line	λ_0	$\lambda_{\rm obs}$	only BLR subtracted FWHM	 Flux	BLR and scattered NLR subtracted FWHM	 Flux
	[Å]	[Å]	[km s^{-1}]	[10^{-16} erg s^{-1} cm^{-2}]	[km s^{-1}]	[10^{-16} erg s^{-1} cm^{-2}]
Hβ_{br}	4861.3	...	...	≤ 2.3	...	...
[OIII]	4958.9	15063.1 ± 3.0	570 ± 60	2.0 ± 0.5	...	≤ 0.6
[OIII]	5006.9	15208.9 ± 3.0	570 ± 60	5.9 ± 1.2	...	≤ 0.6
[NII]	6548.1	19926.6 ± 4.0	1070 ± 110	1.5 ± 0.3	...	≤ 1.2
Hα	6562.8	19971.4 ± 4.0	1070 ± 110	65.5 ± 13.1	490 ± 60	20.5 ± 4.5
[NII]	6583.4	20034.0 ± 4.0	1070 ± 110	4.5 ± 0.9	...	≤ 1.2

1.1″ from one side to the other. This is much less extended than the continuum (observed over 2.9″×2.0″, along a Southeast-Northwest axis), which is comprised of two components, separated by ∼ 1″, along the same Southeast-Northwest axis. The emission line region is coincident with the brightest continuum source, situated in the Southwest. The velocity field is complex and does not display any ordered large scale movement. The velocity dispersion increases from the outer pixels (with FWHM ∼ 800 km s^{-1}) towards the center of the continuum where it reaches FWHM ∼ 1200 km s^{-1}.

SDSS J0035+010

Table 6.9: Emission lines in SDSS J003513+010430.

Line	λ_0	$\lambda_{\rm obs}$	only BLR subtracted FWHM	 Flux	BLR and scattered NLR subtracted FWHM	 Flux
	[Å]	[Å]	[km s^{-1}]	[10^{-16} erg s^{-1} cm^{-2}]	[km s^{-1}]	[10^{-16} erg s^{-1} cm^{-2}]
Hβ_{br}	4861.3	...	...	≤ 1.6	...	...
[OIII]	4958.9	...	...	≤ 0.9	...	≤ 0.3
[OIII]	5006.9	...	...	≤ 0.9	...	≤ 0.3
[NII]	6548.1	21290.2 ± 4.5	470 ± 50	1.9 ± 0.2	250 ± 40	0.9 ± 0.3
Hα	6562.8	21338.0 ± 4.5	470 ± 50	7.9 ± 0.8	250 ± 40	4.1 ± 0.9
[NII]	6583.4	21405.0 ± 4.5	470 ± 50	5.7 ± 0.6	250 ± 40	2.7 ± 0.6

We find this source at a redshift of $z = 2.251 \pm 0.001$, similar to the value obtained from the broad Hα emission line ($z = 2.254 \pm 0.002$) and also close to the value given by the SDSS ($z_{\rm UV} = 2.2538$), based on restframe UV emission lines (Pâris et al., 2012, see also Fig. 6.3). In the $K-$band, narrow components in the Hα and [NII] emission lines are clearly detected on top of the broad Hα component (with FWHM = 4350 ± 500 km s^{-1}), as illustrated in Fig 6.5(b)). The most obvious narrow emission lines components of our sample are actually those of this source, this is why we used it to test and validate the code subtracting the broad component in the emission line complexes (presented in §6.2.2). In the $H-$band, we do not detect any [OIII] or Hβ emission because of the important noise due to strong night sky line residuals, as illustrated by Fig. 6.10. Emission-line properties are summarized in Table 6.9.

Thanks to the relatively important narrow Hα emission line and the good subtraction of the BLR, we can probe the the ionized gas over 1.5″×1.1″ (or ∼ 12 kpc×8.5 kpc), the emission line region being extended along a Northeast-Southwest axis. In the velocity map, a gradient of ∼ 150 km s^{-1} is also present along the same direction. The velocity dispersion is relatively quiescent over most of the extended emission line region, compared to the rest of the sample, with FWHM ∼ 500 km s^{-1}. A few pixels at the Northeast end

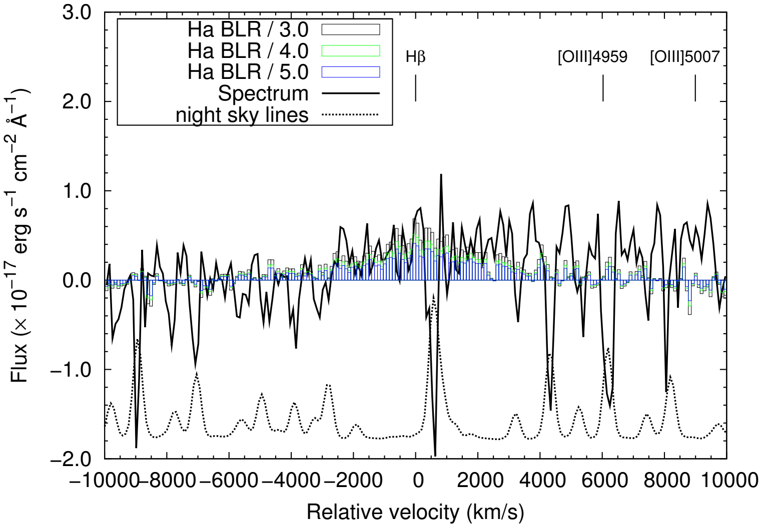

Figure 6.10: Broad component of the Hα emission line shifted to the Hβ spectral zone and scaled to potential Hβ fluxes ; *i.e.*, scaled by factors 1/3, 1/4 and 1/5, represented by black, green and blue histograms respectively. The observed spectrum around the Hβ spectral zone is given by the black solid line, which shows several strong spikes, due to night sky line residuals. This illustrates the fact that the spectrum of SDSS J0035+010 is too noisy to allow the detection of the Hβ line.

have much higher velocity dispersions (FWHM $\sim$ 1200 km s^{-1}), and some of them have systemic redshifts imcompatible with those of neighbouring pixels (given the size of the PSF) and it happens that in these pixels the Hα + [NII] complex is fitted as a single broader Gaussian. The continuum is less extended than the emission line region, but is nonetheless extended along the same direction as the EELR over $0.9'' \times 1.1''$.

SDSS J2226+005

Table 6.10: Emission lines in SDSS J222646+005211.

Line	λ_0	$\lambda_{\rm obs}$	only BLR subtracted		BLR and scattered NLR subtracted	
			FWHM	Flux	FWHM	Flux
	[Å]	[Å]	[km s^{-1}]	[10^{-16} erg s^{-1} cm^{-2}]	[km s^{-1}]	[10^{-16} erg s^{-1} cm^{-2}]
Hβ_{br}	4861.3	15784.1 ± 5.0	2100 ± 150	35.0 ± 7.0	...	...
[OIII]	4958.9	16101.0 ± 3.0	650 ± 70	18.2 ± 3.4	740 ± 80	14.9 ± 3.5
[OIII]	5006.9	16256.9 ± 3.0	650 ± 70	55.0 ± 10.0	740 ± 80	44.6 ± 10.0
[NII]	6548.1	21263.1 ± 4.5	440 ± 50	1.1 ± 0.2	...	$\leq$ 0.4
Hα	6562.8	21310.8 ± 4.5	440 ± 50	11.0 ± 2.2	590 ± 70	9.3 ± 2.0
[NII]	6583.4	21377.7 ± 4.5	440 ± 50	3.2 ± 0.7	...	$\leq$ 0.4
[SII]	6716.4	21806.1 ± 4.0	740 ± 70	3.9 ± 0.8	...	...
[SII]	6730.8	21852.9 ± 4.0	740 ± 70	2.8 ± 0.6	...	...

We find this source at a redshift of z = 2.247 ± 0.001, slightly smaller than the value found from the broad component of the Hα emission line (z = 2.251 ± 0.002). The latter value is however consistent with redshift coming from the SDSS (*i.e.*, z = 2.252 Pâris et al., 2012). The redshift difference corresponds to a velocity offset of -370 km s^{-1} between the narrow and broad optical and UV lines. The broad Hα emission line (with FWHM = 2100 ± 100 km s^{-1}) is predominant in the $K-$band, with faint narrow components of the Hα and [NII] emission lines on top of it. Note that the [SII] doublet is also detected. In the $H-$band, the [OIII] doublet is clearly detected, along with a broad Hβ emission line (with FWHM = 2100 ± 150 km s^{-1}, the same value as for the broad component of the Hα emission line). Emission-line properties are summarized in Table 6.10.

The emission line region, as traced by the [OIII] emission line, is extended over $2.0'' \times 1.4''$ (15.5 kpc×11.5 kpc) along a Northeast to Southwest direction. The Southeast part of the EELR is redshifted by ~ 150 km s^{-1}, while the rest of it is compatible with the systematic redshift quoted before. The velocity dispersion is higher in the Northeast part of the EELR, with FWHM ~ 900 km s^{-1}, while it is more quiescent in the Southwest part, with FWHM ~ 500 km s^{-1}. The continuum is less extended than the emission line region, over $1.6'' \times 1.3''$, and along a East-West axis, different from the axis defined by the emission line region.

6.4.2 Description of individual sources: QSOs without radio counterpart

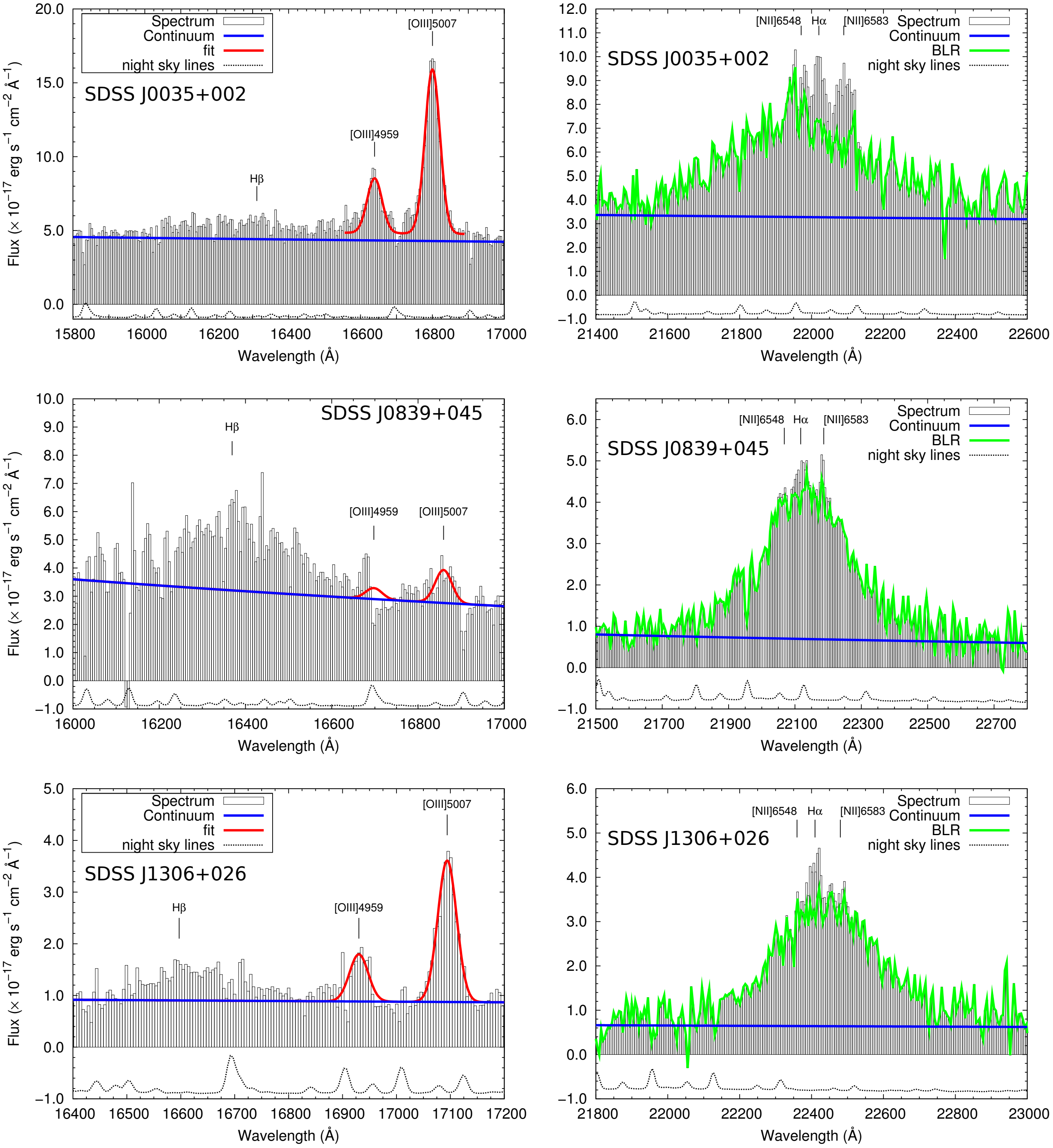

(a) Spectra of the radio quiet quasars sample (1/2)

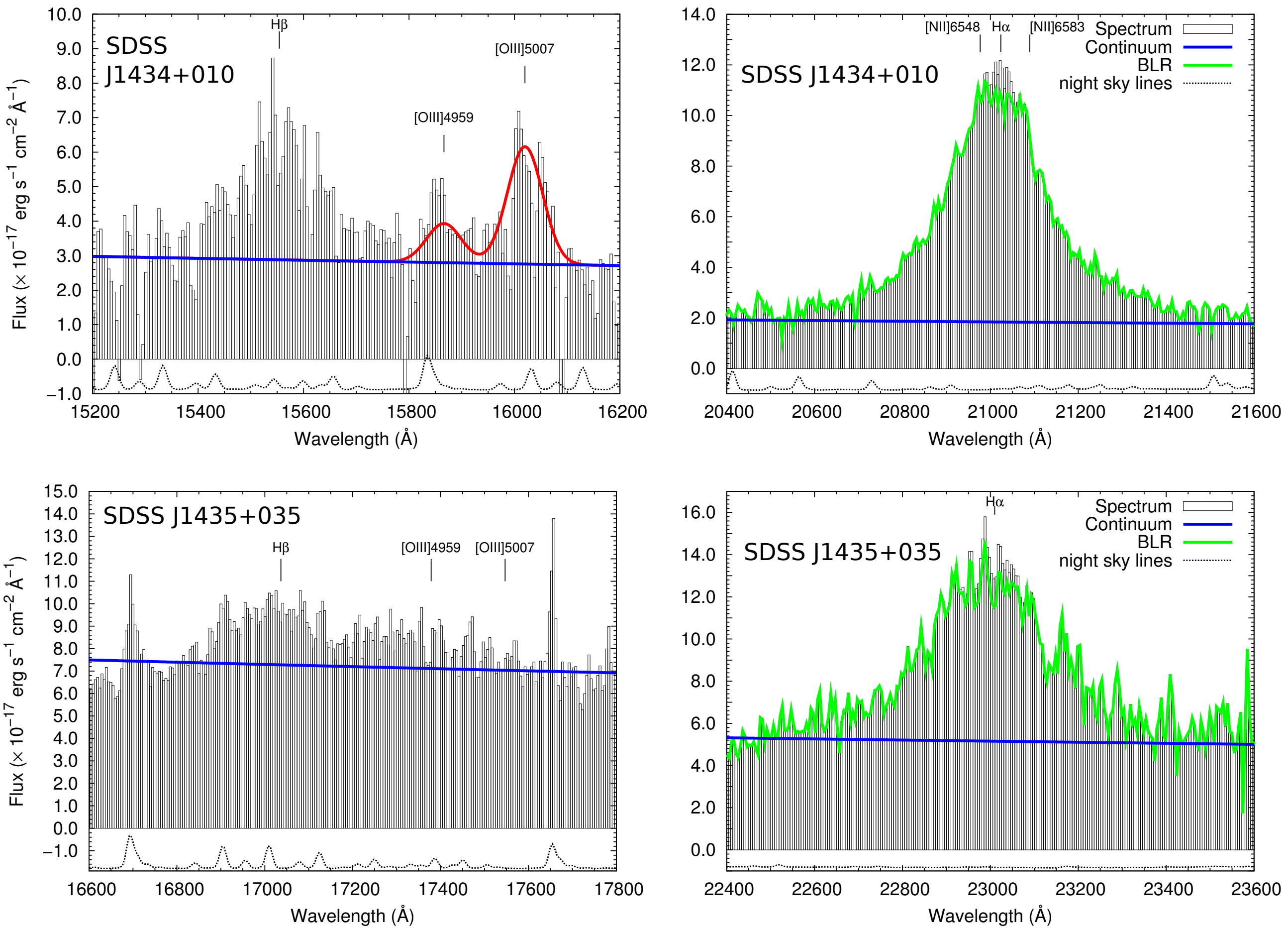

(b) Spectra of the radio quiet quasars sample (2/2)

Figure 6.11: Integrated spectra of the five radio-quiet quasars in our sample. One is centered on the Hβ and the [OIII] doublet lines, when detected, and the second is centered on Hα and [NII]. Continuum level is given by the blue line and the green line gives the estimate that we made of the broad line component, as explained in the text. The line emission on top of the broad component is assumed to be part of the narrow component, well represented by a Gaussian line.

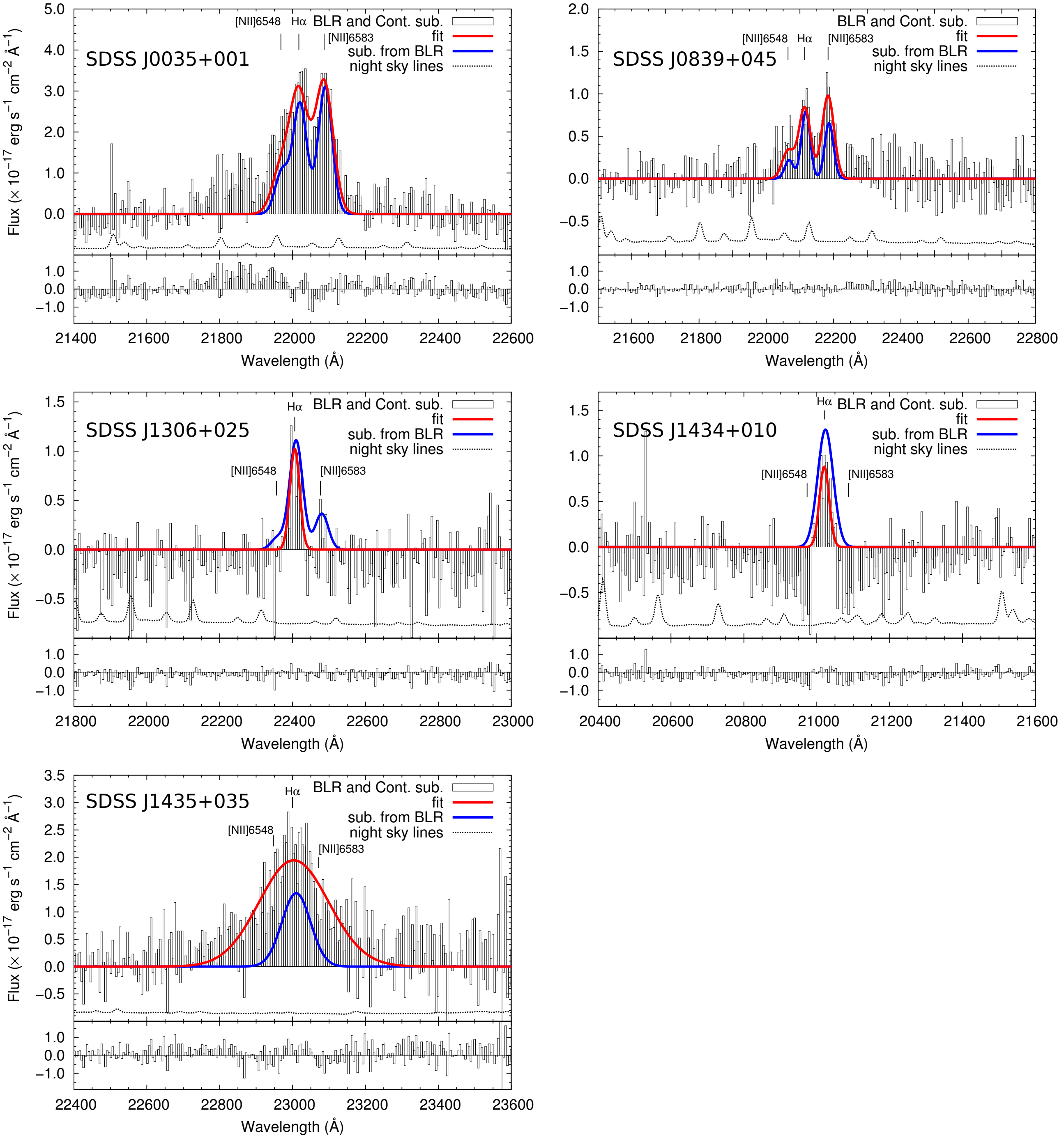

Figure 6.12: Spectra of the five BLR-subtracted radio-quiet QSOs in our sample, integrated over the same region as those shown in Fig. 6.11. Some sources (*e.g.*, SDSS J1434+010) show residuals, probably coming from incorrectly subtracting the BLR in individual spaxels. The blue line shows the model of the narrow lines emission that we subtracted from the integrated spectrum to obtain the model of the broad component of the Hα emission line. The red line shows the fit to the narrow components of the Hα and [NII] emission line in the integrated spectrum of the BLR-subtracted cube.

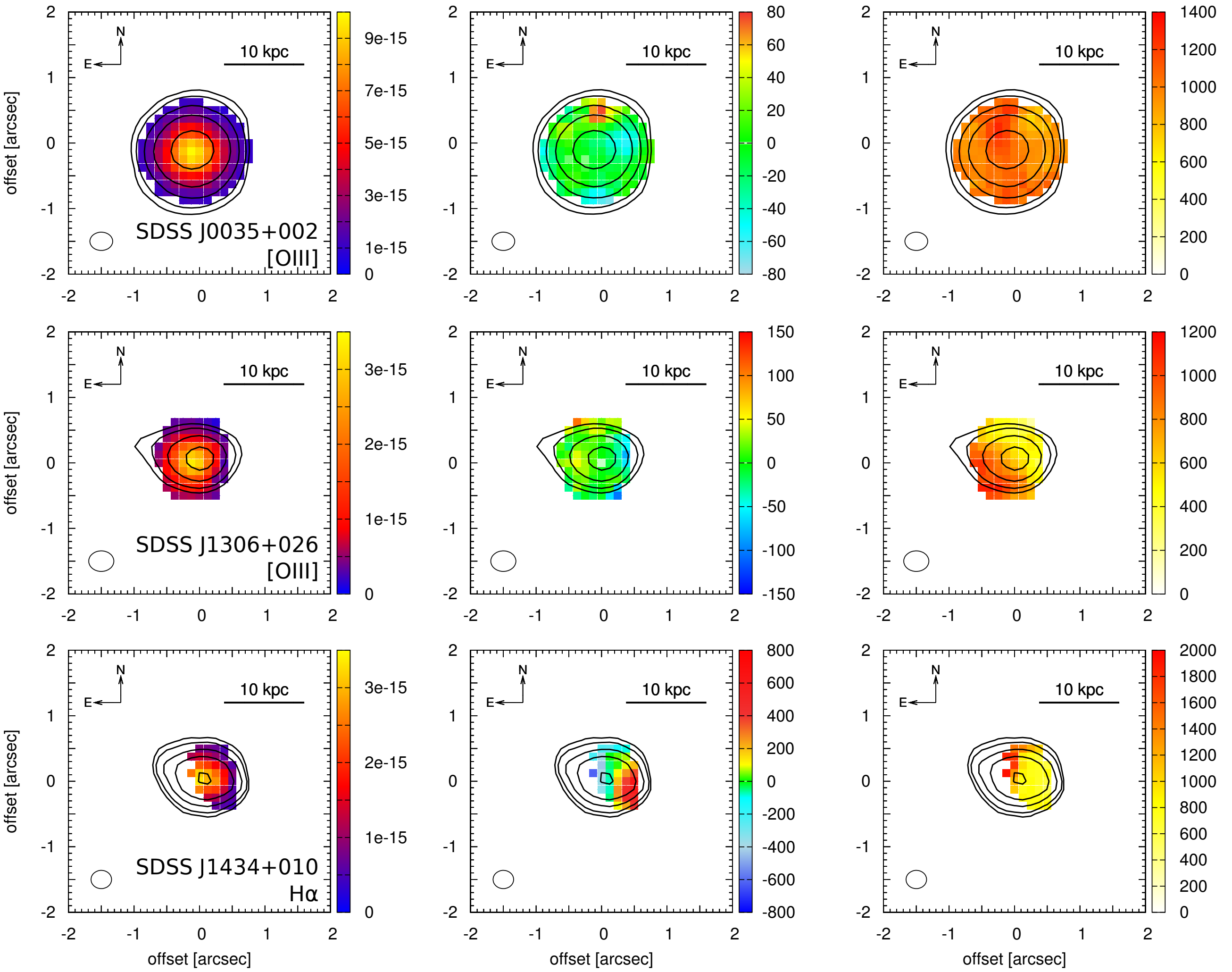

Figure 6.13: Maps tracing the emission and kinematics of *all* (*i.e.*, both circum-nuclear and extended) the ionized gas in the the radio-quiet quasars sample, based either on the [OIII] emission line (where present) or the narrow component of the Hα emission line (where detected).

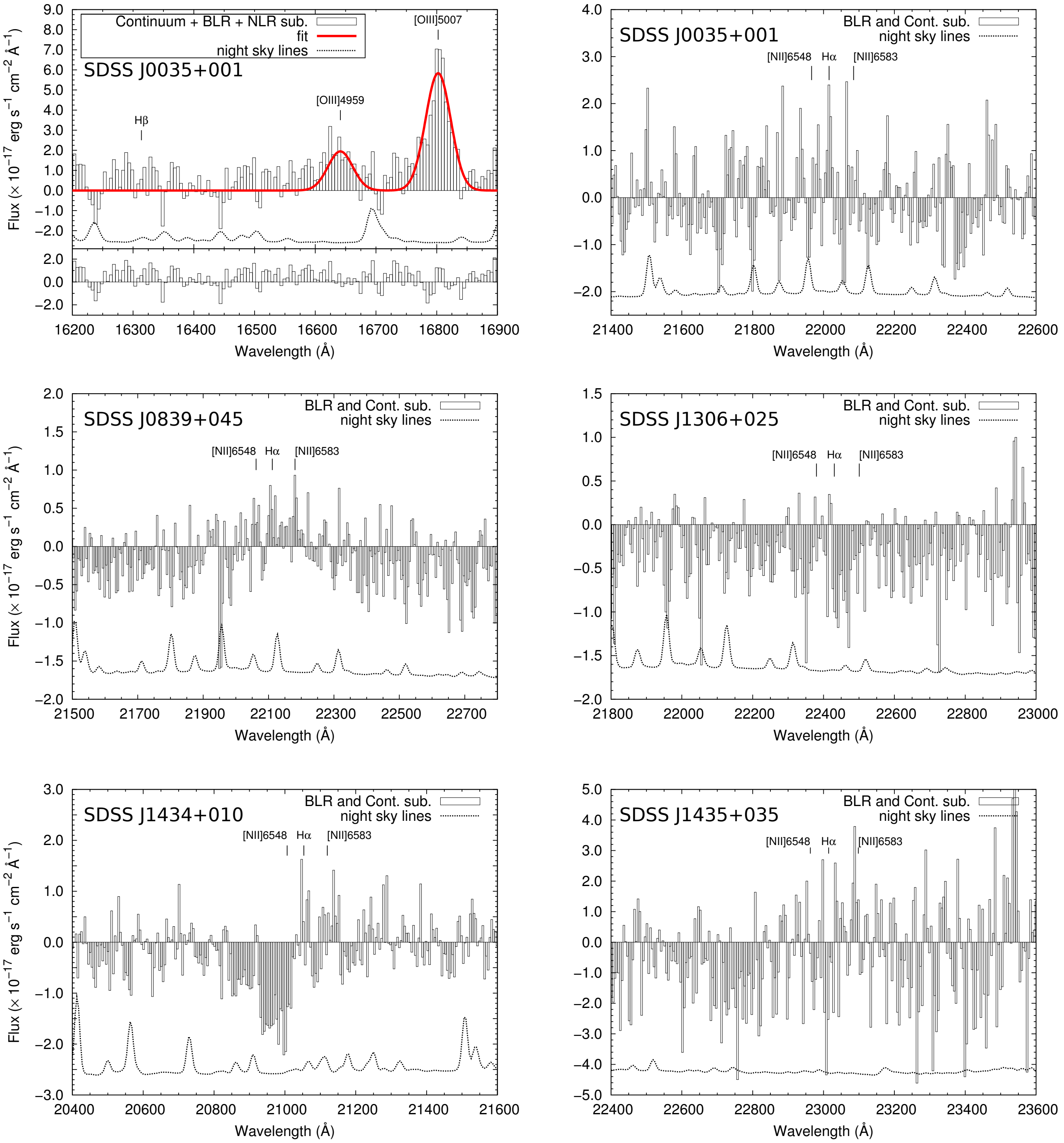

Figure 6.14: Spectra of the five radio-quiet quasars in our sample, subtracted from the broad Hα emission line and from the central narrow emission lines, and integrated over the same region as those shown in Fig. 6.11.

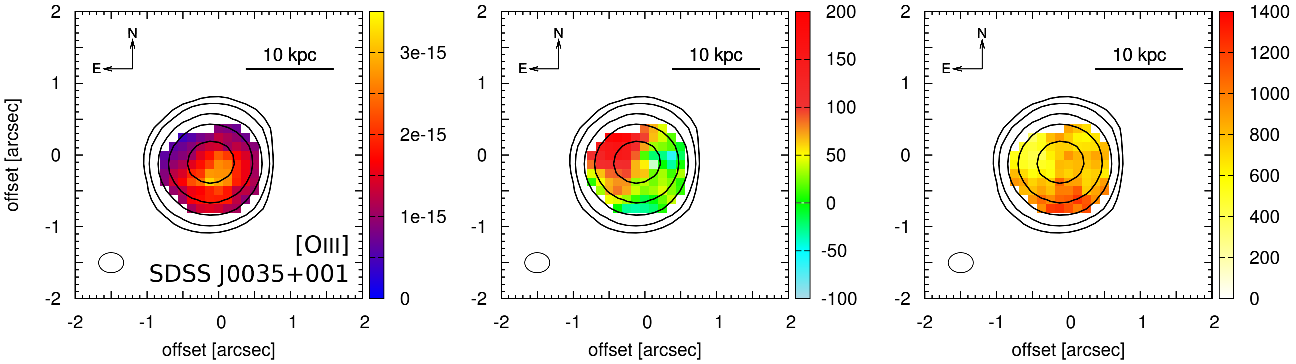

Figure 6.15: Maps tracing the emission and kinematics of only the extended ionized gas in the the radio-quiet quasars sample (*i.e.*, the nuclear narrow component has been subtracted, as explained in § 6.2.3). They are based either on the [OIII] emission line (where present) or the narrow component of the Hα emission line (where detected).

SDSS J0035+002

Table 6.11: Emission lines in SDSS J003522+001941.

			only BLR subtracted		BLR and scattered NLR subtracted	
Line	λ_0 [Å]	$\lambda_{\rm obs}$ [Å]	FWHM [km s^{-1}]	Flux [10^{-16} erg s^{-1} cm^{-2}]	FWHM [km s^{-1}]	Flux [10^{-16} erg s^{-1} cm^{-2}]
Hβ_{br}	4861.3	16309.7 ± 5.0	5500 ± 550	72.9 ± 20.5	...	...
[OIII]	4958.9	16639.1 ± 1.5	820 ± 80	19.2 ± 3.0	...	10.1 ± 2.5
[OIII]	5006.9	16800.2 ± 1.5	820 ± 80	58.3 ± 9.0	...	30.3 ± 7.0
[NII]	6548.1	21968.0 ± 4.0	750 ± 80	6.7 ± 1.4	...	$\leq$ 0.5
Hα	6562.8	22017.4 ± 4.0	750 ± 80	18.0 ± 3.6	...	$\leq$ 0.5
[NII]	6583.4	22086.5 ± 4.0	750 ± 80	20.0 ± 4.0	...	$\leq$ 0.5

The left-hand side of this Table gives the characteristics of the narrow component of the emission lines subtracted only from the broad component, while the left-hand side gives the characteristics of the narrow component of the emission lines also subtracted from the scattered narrow component.
(1): Rest-frame wavelength. — (2): Observed wavelength. — (3): Full-Width at Half Maximum, corrected for instrumental resolution (in km s^{-1}). — (4): Line flux deduced from the fit (in 10^{-16} erg s^{-1} cm^{-2}).

This source is found at a redshift of z = 2.355 ± 0.001, with an excellent agreement between redshifts given by the [OIII] and Hα emission lines. The redshift estimate based on the broad component of the Hα emission line is slightly smaller (z = 2.351 ± 0.002), while the redshift provided by the SDSS is slightly larger (with $z_{\rm UV} = 2.3602$ Pâris et al., 2012). In the $H-$band, the [OIII] doublet is clearly detected, over a very broad Hβ emission line (with FWHM = 5500 ± 550 km s^{-1}). Because the Hβ is so broad, it slightly contaminates the [OIII] doublet, hence the small offset (of $\sim 5.0 \times 10^{-18}$ erg s^{-1} cm^{-2} Å^{-1}) visible in Fig. 6.11(a) between the fit to the [OIII] emission lines and the continuum level. In the $K-$band, the narrow Hα + [NII] complex is detected on top of the broad Hα emission line component (with FWHM = 5950 ± 450 km s^{-1}). All the information about the detected emission lines is given in Table 6.11.

The extended emission line region has a nearly circular shape, with a diameter of $\sim 1.6''$ (or $\sim$ 13 kpc). The EELR is as extended as the continuum emission from the QSO. The velocity map based on the [OIII] doublet shows very little variation over the extended emission line region: most of the spaxels are within

$\pm$ 30 km s^{-1}around the systematic redshift, which is in the range of the uncertainties. The velocity dispersion is also fairly constant over the EELR, with most of the spaxels having FWHM $\sim$ 900$-$1100 km s^{-1}.

SDSS J0839+045

Table 6.12: Emission lines in SDSS J083902+045345.

Line	λ_0	$\lambda_{\rm obs}$	only BLR subtracted FWHM	 Flux	BLR and scattered NLR subtracted FWHM	 Flux
	[Å]	[Å]	[km s^{-1}]	[10^{-16} erg s^{-1} cm^{-2}]	[km s^{-1}]	[10^{-16} erg s^{-1} cm^{-2}]
Hβ_{br}	4861.3	16368.9 $\pm$ 5.0	3550 $\pm$ 400	70.5 $\pm$ 17.5	...	...
[OIII]	4958.9	16697.6 $\pm$ 3.5	750 $\pm$ 70	1.9 $\pm$ 1.0	...	$\leq$ 0.4
[OIII]	5006.9	16859.2 $\pm$ 3.5	750 $\pm$ 70	5.7 $\pm$ 1.2	...	$\leq$ 0.4
[NII]	6548.1	22064.6 $\pm$ 4.0	510 $\pm$ 30	1.4 $\pm$ 0.3	...	$\leq$ 0.2
Hα	6562.8	22114.2 $\pm$ 4.0	510 $\pm$ 30	3.7 $\pm$ 0.8	...	$\leq$ 0.2
[NII]	6583.4	22183.6 $\pm$ 4.0	510 $\pm$ 30	4.3 $\pm$ 0.9	...	$\leq$ 0.2

We find this source at a redshift of z = 2.368 ± 0.001, which is slightly smaller than the estimate found with the broad component of the Hα emission line (z = 2.372 ± 0.002). However, these two values are significantly larger than the redshift provided by the SDSS (*i.e.*, $z_{\rm UV}$ = 2.3564 Pâris et al., 2012). In the $H-$band, we observe a strong and broad Hβ emission line (with FWHM = 3550 ± 400 km s^{-1}). The [OIII] doublet is also marginally detected: although the [OIII]λ4959 is affected by a strong night sky line residual and potentially also by the red wing of the strong Hβ line, the [OIII]λ5007 is reasonnably well detected. In the $K-$band, the broad Hα emission line dominates (with FWHM = 4650 ± 450 km s^{-1}), on top of which we detect faint and narrow Hα and [NII] components. All the information about the detected emission lines is given in Table 6.12. Both the [OIII] and the narrow Hα components are too faint to provide maps of the extended emission line region.

SDSS J1306+025

Table 6.13: Emission lines in SDSS J130608+025943.

Line	λ_0	$\lambda_{\rm obs}$	only BLR subtracted FWHM	 Flux	BLR and scattered NLR subtracted FWHM	 Flux
	[Å]	[Å]	[km s^{-1}]	[10^{-16} erg s^{-1} cm^{-2}]	[km s^{-1}]	[10^{-16} erg s^{-1} cm^{-2}]
Hβ_{br}	4861.3	16597.0 $\pm$ 5.0	2750 $\pm$ 400	12.5 $\pm$ 3.5	...	...
[OIII]	4958.9	16930.3 $\pm$ 1.6	650 $\pm$ 60	4.0 $\pm$ 0.8	...	$\leq$ 0.3
[OIII]	5006.9	17094.1 $\pm$ 1.6	650 $\pm$ 60	12.0 $\pm$ 2.4	...	$\leq$ 0.3
[NII]	6548.1	...	...	$\leq$ 0.5	...	$\leq$ 0.3
Hα	6562.8	22406.0 $\pm$ 4.0	350 $\pm$ 40	3.4 $\pm$ 0.7	...	$\leq$ 0.3
[NII]	6583.4	...	...	$\leq$ 0.5	...	$\leq$ 0.3

This source is found at a redshift of z = 2.414 ± 0.001, slightly smaller than the value found with our method based on the broad component of the Hα emission line (z = 2.419 ± 0.002). These two estimates are also much smaller than the redshift based on restframe UV lines and coming from the SDSS (which gives $z_{\rm UV}$ = 2.4323 Pâris et al., 2012). The [OIII] doublet is well detected in the $H-$band, as well as a broad Hβ

component (with FWHM = 2750 ± 400 km s^{-1}). In the $K-$band, a clear narrow Hα component together with a faint [NII] doublet is detected on top of the broad Hα line (with FWHM = 3700 ± 350 km s^{-1}). All the information about the detected emission lines is given in Table 6.13.

The [OIII] emission line region extends over $1.1'' \times 1.0''$ along a North-South direction, while the continuum rather extends along a East-West axis, over $1.5'' \times 1.1''$. The velocity field is mostly consistent with the systematic redshift, with a marginal velocity gradient along a North-South axis. The velocity dispersion goes from ~ 400 km s^{-1}in the Northwest region to ~ 1000 km s^{-1} in the Southeast part of the EELR.

SDSS J1434+010

Table 6.14: Emission lines in SDSS J143436+010522.

			only BLR subtracted		BLR and scattered NLR subtracted	
Line	λ_0 [Å]	$\lambda_{\rm obs}$ [Å]	FWHM [km s^{-1}]	Flux [10^{-16} erg s^{-1} cm^{-2}]	FWHM [km s^{-1}]	Flux [10^{-16} erg s^{-1} cm^{-2}]
Hβ_{br}	4861.3	15554.0 ± 5.0	2500 ± 200	64.0 ± 15.0	...	...
[OIII]	4958.9	15866.3 ± 2.0	1440 ± 150	9.4 ± 1.9	...	≤ 0.6
[OIII]	5006.9	16019.9 ± 2.0	1440 ± 150	28.5 ± 5.5	...	≤ 0.6
[NII]	6548.1	...	...	≤ 0.5	...	≤ 0.4
Hα	6562.8	21020.7 ± 4.5	370 ± 40	2.9 ± 0.6	...	≤ 0.4
[NII]	6583.4	...	...	≤ 0.5	...	≤ 0.4

We find this source at a redshift of z = 2.201 ± 0.002, in agreement with the estimate based on the broad component of the Hα emission line (z = 2.202 ± 0.002), but slightly higher than the value given by the SDSS (*i.e.*, $z_{\rm UV} = 2.1959$ Pâris et al., 2012), based on restframe UV lines. In the $H-$band of the integrated spectrum, the [OIII] doublet is detected, as well as a broad Hβ component (with FWHM = 2500 ± 200 km s^{-1}). In the $K-$band, on top of the prominent broad Hα emission line (with FWHM = 3650 ± 150 km s^{-1}), only a narrow Hα emission line is found and no [NII] emission line. All the information about the detected emission lines is given in Table 6.14.

The [OIII] doublet being too faint to produce maps of the extended emission line region, we use the narrow Hα line to probe it. It extends over $1.0'' \times 0.6''$ (or 8.0 kpc×5 kpc) with the main axis being along a Northeast to Southwest direction. The continuum emission is larger (extended over $1.6'' \times 1.3''$, with a major axis along a East-West direction) and the EELR lies mainly in the western part of the continuum emission. The velocity map presents a gradient of ~ 900 km s^{-1}, along a Northeast to Southwest axis. The velocity dispersion is between FWHM = 700−1000 km s^{-1}over most of the EELR, except in the Northeast region, where it reaches FWHM $\gtrsim 1300$ km s^{-1}.

SDSS J1435+035

This source is found at a redshift of z = 2.505 ± 0.001, which is in excellent agreement with the redshift estimate based on the broad component of the Hα emission line (z = 2.505 ± 0.002). However, these values are larger than what is provided by the SDSS (with $z_{\rm UV} = 2.4938$ Pâris et al., 2012), based on restframe UV lines. No [OIII] doublet can be detected in the $H-$band, but we observe a broad Hβ emission line (with FWHM = 2600 ± 300 km s^{-1}). In the $K-$band, a broad Hα emission is found (with FWHM = 4800 ± 450 km s^{-1}), on top of which a narrow component of the Hα emission line is detected, along with a faint [NII] doublet. All the information about the detected emission lines is given in Table 6.15. The non-detection of the [OIII] emission line and the relative faintness of the narrow component of the Hα emission line mean that no map of a putative extended emission line region can be constructed.

Table 6.15: Emission lines in SDSS J143500+035403.

Line	λ_0	$\lambda_{\rm obs}$	only BLR subtracted FWHM	 Flux	BLR and scattered NLR subtracted FWHM	 Flux
	[Å]	[Å]	[km s^{-1}]	[10^{-16} erg s^{-1} cm^{-2}]	[km s^{-1}]	[10^{-16} erg s^{-1} cm^{-2}]
Hβ_{br}	4861.3	17036.6 ± 6.5	2600 ± 300	86.8 ± 15.5	...	...
[OIII]	4958.9	...	...	$\leq$ 0.9	...	$\leq$ 0.8
[OIII]	5006.9	...	...	$\leq$ 0.9	...	$\leq$ 0.8
[NII]	6548.1	22948.0 ± 4.5	2390 ± 250	1.7 ± 0.4	...	$\leq$ 0.8
Hα	6562.8	22999.5 ± 4.5	2390 ± 250	35.9 ± 7.2	...	$\leq$ 0.8
[NII]	6583.4	23071.7 ± 4.5	2390 ± 250	5.2 ± 1.0	...	$\leq$ 0.8

6.4.3 Overall sample properties

Following the subtraction of the broad-line component as described above, and keeping all the narrow-line flux found in our sources, we analyzed our data cubes in precisely the same way as previously for the radio galaxies (see Section 4.2).

We show the emission-line morphologies, and maps of relative gas velocities and FWHM line widths in our sources in Fig. 6.7 and 6.9 for the radio-loud quasars (maps of all the ionized gas emitting the narrow emission line component, and maps of only the extended ionized gas, respectively) ; and in Fig. 6.13 and 6.15 for the radio-quiet QSOs (in the same order as the radio-loud quasars). These maps are created by fitting Gaussian profiles to the lines extracted from small apertures across the cube. The size of the aperture is set to 3 pixels×3 pixels, corresponding to $0.4''\times0.4''$. This helps improving the signal-to-noise ratio of the data, and is still comparable to the seeing disk to avoid loss of spatial information. Maps are only given for pixels where the signal-to-noise ratio of the line core exceeds 5 and, when fitting a line, we assess weights to spectral pixels depending on the presence and strength of night sky lines at this wavelength. The line-free continuum morphologies are shown as contours. All line fluxes (or upper limits), line widths and redshifts of the residual lines as measured from integrated spectra are listed in Tables 6.5 to 6.15. Integrated spectra are presented in Fig. 6.5, 6.6 and 6.8 for the radio-loud quasars. The first Figure corresponds to integrated spectra of the sources as they are observed, the second one corresponds to the BLR-subtracted sources and the third one to sources for which both the BLR and circum-nuclear-NLR components have been subtracted. The integrated spectra of the radio-quiet QSOs are presented in Fig. 6.11, 6.12 and 6.14, in the same order as for the radio-loud quasars.

The bright continuum emission from our sources is generally compact or marginally resolved, with spectral slopes that are adequately fitted by blue power laws, as expected from the accretion disks in bright, optically-selected quasars. Only in B 1657+033 do we detect a second continuum emitter at $1''$ offset from the QSO, which has however no obvious associated line emission within our data cube. The brightness of the continuum, and absence of line emission would be unexpected for a physically related, perhaps interacting source at a similar redshift, we therefore suspect this is an interloper of foreground star, but didn't pursue this question further.

Emission-line morphologies and surface-brightness profiles

The emission-line morphologies shown in Figs. 6.7 and 6.13 show that, following the subtraction of the broad, nuclear components of Hα, nearly all sources have bright residual line emission with relatively narrow widths akin to the FWHM $\sim$ 100$-$1000 km s^{-1} of typical narrow-line regions around AGN. Exceptions are one radio-loud (B 0113$-$283) and two radio-quiet quasars (SDSS J0839+045 and SDSS J1435+035), where the additional narrow-line component could not be mapped. Since all of our sources were observed down to fairly similar surface-brightness limits, this is not an observational artifact, but a genuine spread in the properties of our objects.

Most sources are dominated by a bright central point source, and line emission is detected over 3−4 resolution elements along the major axis. Liu et al. (2013a) found that at low redshifts, z = 0.3−0.5, powerful quasars have isophotes that appear rounder than those of radio-loud quasars. We find that 2/3 sources without, and 1 or 2 sources with radio counterpart have circular isophotes consistent with the morphology of the broad-line region and continuum. In particular SDSS J1434+010 is very elongated, with a ratio of major-to-minor axis of $a/b = 1.7$; however, comparison with Fig. 1 of Liu et al. (2013a) shows that this is also the case in two of their sources at similar surface-brightness levels as we can reach at z $\sim$ 2, although their morphologies at fainter isophotes are becoming rounder.

We caution that (as is often done at high-z) finding extended line emission beyond the FWHM size of the point spread function or seeing disk is alone not sufficient to consider a source to be spatially resolved, in particular for bright targets, where the large dynamic range of the line images makes it possible to trace the light profiles over several FWHM. We must also show that the light profiles are significantly different from that of a point source.

Fig. 6.16 shows the azimuthally averaged surface-brightness profiles of the bright optical narrow-line emission (either [OIII] or Hα) in the sources where emission lines are bright enough to make such an analysis possible. The surface brightness profiles of the line emission are shown as red lines. All sources show an excess at radii between about 0.5 and 1$''$. The Figure shows clearly that none of the sources, except perhaps SDSS J0035+010, strictly follows the expected surface-brightness profile of a point source. However, the spatially resolved analysis below will show that SDSS J0035+010 has residual line emission that is spatially resolved.

However, the genuine nuclear AGN tracers like the light profiles from the pure broad-line components of Hα (black dotted line in Fig. 6.16), and the bright quasar continuum (blue solid line in Fig. 6.16) also do not strictly follow the surface-brightness profiles of unresolved stars. This may either indicate that our estimate of the size or the shape of the PSF (derived from calibration stars at the end of each one-hour observing sequence) may be too inaccurate. Possible reasons include different observing conditions during the quasar observations and those of the stars, or because the natural guide stars used in these observations have offsets of typical 10$''$−20$''$ from the quasar (the quasars themselves were too faint to use as guide probe), or because the AGN light itself is not strictly a point source. While a detailed analysis of the SINFONI PSF during natural-guide-star observations is beyond the scope of this thesis, it is well known from polarimetry and other studies that quasars can have important amounts of light from circum-nuclear regions that is scattered off dusty clouds at larger radii (*e.g.*, Borguet et al., 2008), thereby mimicking extended gas. We somewhat favor this astrophysical interpretation, although this distinction is of minor practical importance for our subsequent analysis.

Inspection of Fig. 6.16 shows that only SDSS J2226+005, B 0524−433 and SDSS J1434+010 have emission-line surface brightness profiles that are significantly different from those of the broad line and continuum emission.

Emission line diagnostics

As in previous chapters, we used the emission-line diagnostics based on the BPT diagram (Baldwin, Phillips, & Terlevich, 1981) to identify the source of ionization of the narrow emission line regions detected around the quasars of our sample, as illustrated in Fig. 6.17. Amongst the several diagnostic diagrams that were proposed by these authors, we only use that with [NII]/Hα vs. [OIII]/Hβ, because [NII] is easier to measure than [SII] or even [OI], which were not detected in most targets.

A major difficulty, and hence source of error, for our quasars, lies in estimating the Hα and Hβ fluxes, since the broad component of these emission lines must not be taken into account when constructing the BPT diagram. For the Hα flux, we use the results of our algorithm that substract the BLR, with the results stated in the individual sources description. However, for the Hβ flux, running this algorithm does not provide valuable results, for the following reasons: First, the flux of Hβ is smaller than the one of Hα,

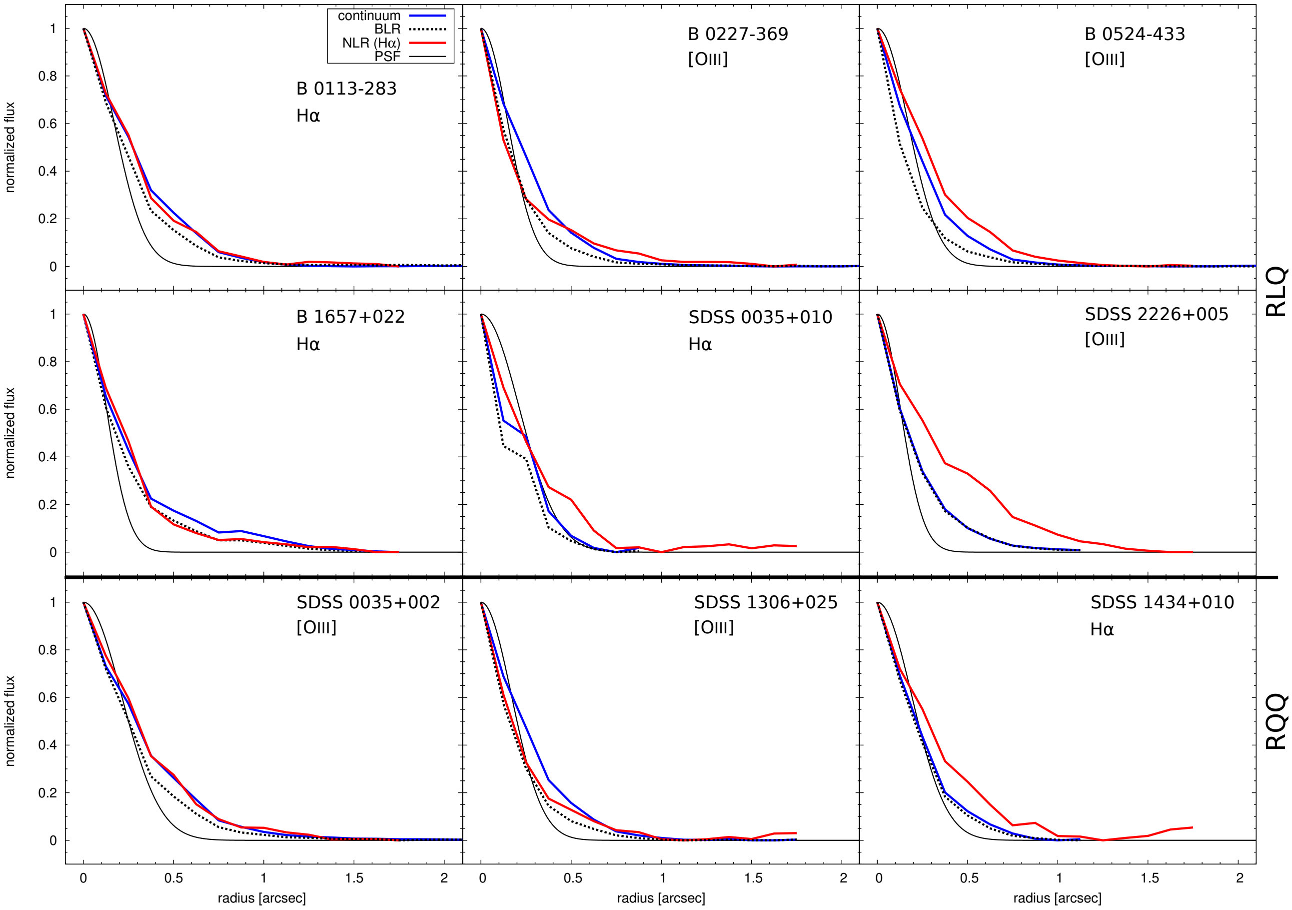

Figure 6.16: Normalized surface brightness profiles of our sources. The blue solid lines show the profile of the contiuum and the black dotted lines show the profile of the BLR component of Hα, respectively. The red lines show the narrow component of Hα ([OIII] for sources where it is detected, as listed in each panel).

making this exercice intrinsically harder. The extinction also affects the Hβ emission line more strongly than Hα. Second, the intensity of night sky lines residuals is more important in the $H-$band, where Hβ is observed, than in the $K-$band, where Hα is observed. This means that the narrow component of the Hβ emission line is expected to be at the same level as the noise. To circumvent this difficulty, we use the Hα flux as a proxy for the Hβ flux, with a canonical ratio value of 3.0, further corrected for the extinction of each source.

The results of this analysis are shown in Fig. 6.17, where red and blue squares indicate the radio-loud and radio-quiet subsamples, respectively. Small grey dots show the low-redshift quasars and star-forming galaxies from Kauffmann et al. (2003a), with the two characteristic branches, one of HII regions in star-forming galaxies (at low [NII]/Hα ratios), and the AGN branch at high [NII]/Hα ratios. As is to be expected for powerful quasars, all sources are consistent with photoionization by the AGN, although two sources (B 0227−369 and B 1657+022) falls very near the dividing lines of Kauffmann et al. (2003b) and Kewley et al. (2001), at least when considering the lower limit of [OIII]/Hβ of B 1657+022 at face value. However, [OIII] fluxes of 5 and 2×10^{43} erg s^{-1}, respectively, appear very high to be explained with star-formation (Villar-Martín et al., 2008). The line ratios would imply high ionization parameters corresponding to $q =$ few 10^8 s^{-1} (Kewley et al., 2001), and very low metallicities of $0.2-0.4\times$ the solar value, which appears relatively unexpected for high-z quasars, in particular in the near-nuclear regions which dominate the the overall emission from our galaxies, and for which, *e.g.*, Vernet et al. (2001) report solar or even super-solar metallicities. Given that we already know that these galaxies host radio-loud quasars with rapidly accreting supermassive black holes, quasar ionization appears to be the less speculative explanation in both cases.

However, following Groves et al. (2006), even for AGN photoionization, the 5/8 of our sources in this Figure with very low [NII]/Hα ratios may still have low metallicities (about 0.5 of the solar value, if taking the results and assumptions of Groves et al. (2006) at face value). A more thorough emission-line analysis with a photoionization code like Cloudy Ferland et al. (2013), and using additional diagnostic lines would be necessary to explore this possibility further. A plausible, major caveat of attributing low [NII]/Hα ratios to low metallicities is that the critical density to collisional de-excitation of the [NII] lines is very low, only few 100 cm^{-3} (compared to, *e.g.*, 3,800 cm^{-3} for [OIII]λ5007) which may cause the [NII] lines to be abnormally faint in these galaxies (*e.g.*, Osterbrock, 1989). Similar effects have previously been demonstrated to be at work in UV/optically selected starburst gaxies at z $\sim$ 2 (Lehnert et al., 2009, 2013).

Source	major axis (1) [arcsec]	minor axis (2) [arcsec]	PSF (3) [arcsec×arcsec]	RMS [OIII](4) [10^{-17} erg s^{-1}	RMS Hα(5) cm^{-2} arcsec^{-2}]
B 0113	...	...	0.4 × 0.3	4.8	7.0
B 0227	1.4	0.9	0.35 × 0.25	9.1	5.3
B 0524	1.9	1.5	0.4 × 0.25	8.5	7.1
B 1657	1.0	0.6	0.3 × 0.2	12.0	20.9
SDSS 0035+010	1.6	1.1	0.5 × 0.4	6.6	4.5
SDSS 2226	2.1	1.4	0.3 × 0.2	4.0	1.7
SDSS 0035+002	1.6	1.5	0.5 × 0.4	3.8	5.5
SDSS 0839	...	...	0.35 × 0.3	15.0	3.9
SDSS 1306	1.1	1.0	0.4 × 0.3	4.5	5.5
SDSS 1434	1.0	0.6	0.45 × 0.4	14.3	4.3
SDSS 1435	...	...	0.4 × 0.3	3.0	6.8

(1): Size of the extended emission line region along its major axis. — (2): Size of the extended emission line region along its minor axis. — (3): PSF of the observation. — (4): RMS of the [OIII] surface brightness for each source. — (5): RMS of the Hα surface brightness for each source.

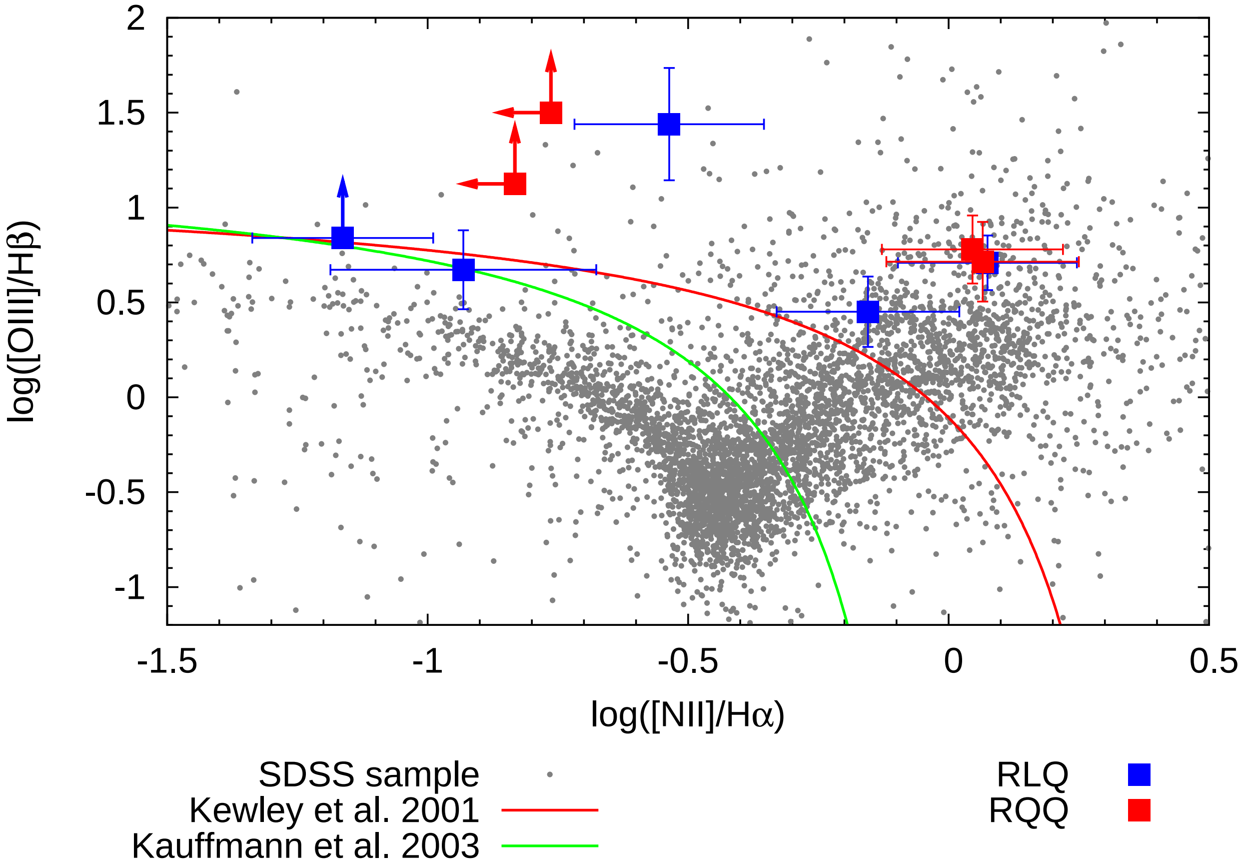

Figure 6.17: The BPT diagram of our sample of quasars. Radio-loud sources are in blue and radio-quiet sources are in red. Arrows indicate lower or upper limits, usually on the [NII] and/or on the Hβ flux.

Gas kinematics

As already discussed above, we have performed separate analyses of the total narrow-line emission in our sources, including the component where the narrow-line surface brightness profiles follow those of the broad-line and continuum emission, and subsequently subtracted this component from the extended narrow-line data cubes to obtain the component that is genuinely observed only in the gas. Here we will discuss the kinematics as observed in the total narrow-line cubes, as well as the kinematics of the cubes where we only have kept the line component that is distinct from the BLR and continuum emission (for the sources where this was possible). We will refer to these two as "total" and "distinct" NLR data sets hereafter.

Estimating systemic redshifts for high-redshift galaxies is notoriously difficult, but here we can exploit the empirical finding from low-redshift studies that the broad-line region of the AGN, in spite of some caveats in individual cases, typically match the systemic redshift of the host galaxy within 200 km s^{-1} (Sulentic et al., 2000). We can therefore use the offsets between the redshifts obtained from the broad Hα lines and the integrated narrow-line profiles to approximate the overall velocity offsets between the warm ionized gas and the host galaxy for our quasars. Results are listed in Tab. 6.3. Overall, we find offsets between -670 km s^{-1} and $+360$ km s^{-1} between narrow and broad emission lines in our sample, with no clear difference between radio-loud and radio-quiet objects. Four sources (two with radio source and two without) have offsets < 100 km s^{-1} which we consider as insignificant. These values provide global velocity estimates of the gas, and given that the line images of our sources are generally dominated by their bright, central components, are most likley to originate from the central few kpc of the narrow-line regions in our targets.

The total range of velocity offsets within individual galaxies is between <100 km s^{-1} and 1,100 km s^{-1} (in SDSS J1434+010). Maps for individual galaxies are given in Figs. 6.7 and 6.13, and the detailed properties of each individual sources have already been discussed above. Here we only describe the global trends.

The typical range for the radio sample is between 250 and 350 km s^{-1}. The spatially-resolved velocity maps of our targets range from very regular and featureless (SDSS J0035+002, SDSS J1306+026, to sources with regular, monotonous velocity gradients along the major axis of an elongated emission-line region (SDSS J1434+010) to irregular sources with several regions of different velocity (SDSS J2226+005, B 0227−369, B 0524−433 and SDSS J0035+010). In B 1657+022 the emission-line region is too compact for a clear classification. It is interesting that the one source (without radio counterpart) with a regular velocity gradient has also the largest (but monotonous) velocity gradient (SDSS J0035+002), whereas the sources in the radio-sample have generally more irregular velocity maps with non-monotonous gradients (*e.g.*, SDSS J2226+005).

6.4.4 Circum-Nuclear and genuinely extended emission

Interpreting the properties of the warm ionized gas in optically selected, unobscured quasar host galaxies is often challenging, because the observed line emission can originate from several environments. In the classical AGN picture, the narrow-line region (NLR) is the bright line emission produced by the very blue, steep ionizing spectrum of the AGN. These lines typically originate from a relatively compact circum-nuclear region with sizes of few 10s to few 100 pc around the AGN, where electron densities are lower than the critical density for collisional de-excitation, and which is typically unresolved with all but the highest-resolution observations (Osterbrock, 1989). This region, although intrinsically unresolved, produces sufficiently bright line emission that the wings in the surface brightness profile of this region and scattered light can dominate the emission from the overall galaxy, as we saw in Fig. 6.16. However, more recent work has emphasized that the size of NLRs scales with bolometric AGN luminosity (Hainline, 2008; Husemann et al., 2013), and that the brightest QSOs can have narrow-line regions with sizes of up to 10s of kpc (*e.g.*, Bennert et al., 2002). Some authors refer to these as extended narrow-line regions, others as extended emission-line regions (*e.g.*, Husemann et al., 2013), reserving the term “NLR” only to the brightest innermost regions of the AGN photoionization zones.

Our main interest here is to identify gas that forms distinct components on galaxy-wide scales, which could be attributed to bubbles or winds swept up by the energy emitted by the AGN, and would be the analogs of powerful high-z radio galaxies (Chapter 4, see also Nesvadba et al., 2006, 2008). Given that our objects have projected sizes of only a few spatial resolution elements, we must be particularly careful to distinguish such components from the quasar illumination zones. Another complication is that emission produced in the unresolved circum-nuclear zone might be scattered off clouds at larger radii (*e.g.*, Borguet et al., 2008), so that intrinsically unresolved emission regions may in fact appear to be spatially resolved.

To account for these possibilities, we will in the following refer to “narrow-line region” as the total AGN photoionization zones as probed by the narrow emission lines in the integrated spectrum, and will otherwise distinguish between “circum-nuclear” gas at radii less than our spatial resolution, about $0.4''$ or 3 kpc at $z = 2$ and gas that is “extended” (corresponding to the two parts in Tab. 6.5 to 6.15). We will identify gas as “circum-nuclear” when it has a surface-brightness distribution which is comparable to that of the quasar continuum and broad emission lines, both of which are known to be intrinsically unresolved in our targets, and irrespective of whether the emission formally has a surface-brightness profile that is shallower than the PSF. This also circumvents uncertainties in our PSF estimate derived from stars.

As already discussed in § 6.4.3, only narrow-line components that have distinct surface-brightness distributions will be considered as genuinely “extended” gas. This may be too restrictive for some purposes, but since our main goal is to compare with powerful radio galaxies, where such genuinely extended components are observed regularly, and where the central source is obscured, we believe that this is an appropriate way to proceed here. We will of course also use the total narrow-line emission (without removal of the circum-nuclear component) where relevant for our scientific arguments.

6.4.5 Subtraction of the circum-nuclear narrow-line component

To further search for genuinely extended emission-line regions in our sources we have subtracted the circum-nuclear component from the narrow-line cube. We used the spectrum of the central pixel of each source as templates to approximate the intrinsic spectral shape of the AGN spectrum (continuum, broad, and narrow line emisson). We scale this spectrum by a factor, which corresponds to the ratio of line-free continuum flux between the central pixel and every other pixel in the data cube where line emission was previously detected, and subtract this scaled nuclear spectrum from the surrounding pixels. The results for all cubes are shown in Fig. 6.9 for radio-loud quasars and in Fig. 6.15 for radio-quiet QSOs.

Consistent with our previous result that the azimuthally averaged surface-brightness profiles of broad lines, continuum, and narrow lines are indistinguishable for most sources, we find that the residuals in most of our cubes are negligible, and consistent with residuals from the fitting routine. Integrated spectra of our sources extracted from the cubes after subtraction are shown in Figs. 6.8 and 6.14.

Only in five sources do we detect a line component that appears to be a genuinely separate component of emission-line gas, including four radio-detected AGN. Only two sources, SDSS J0035+010 and SDSS J2226+005 have emission line regions that are well detected over extended areas.

The emission-line morphologies, velocities, and line width distributions of these galaxies are shown in Figs. 6.9 and 6.15. For the corresponding integrated spectra see Fig. 6.8 and 6.14. In addition to the integrated spectra of sources with extended components, we also show the spectra of those without, to demonstrate that the non-detections are not due to the systematics introduced by line subtraction. The spectrum of B 0113−283 shows that there may be a faint Hα component, which is however formally below our significance cutoff, so that we use the upper limit instead.

Comparing the gas kinematics before and after the subtraction of the circum-nuclear component, we find differences in particular in the radio-undetected source SDSS J0035+002, which has a clear velocity offset of about 200 km s^{-1} after removal of the central component, and much lower line widths, of-order 300 km s^{-1} in most of the source. Prior to the removal, the velocity gradient was hidden under the bright central component, and the lines were broadened to 1000 km s^{-1}.

The changes in the maps of the AGN with radio counterpart are less obvious, apart from stronger residuals of the line removal process in the very central regions. For example, in SDSS J2226+005, we only find a slight increase in the velocity offset of the redshifted area to the east (by $\lesssim$ 100 km s^{-1} over most of this area) and the line widths do not change significantly. The same is true for the other four sources, B 0524−433, SDSS J0035+010, and B 0227−369, although the regions of extended ionized gas are smaller in these targets than in SDSS J2226+005.

6.4.6 Electron densities and ionized gas masses

As already discussed in § 1.6.2, ionized gas masses can be estimated from Hα line luminosities, once that electron densities are known. Unfortunately, we have no direct density estimates for most of our targets here. SDSS J2226+005 is our source with the most powerful radio counterpart, and the only source where we have a (heavily blended) observation of the [SII] doublet of $\mathcal{F}(6716)/\mathcal{F}(6731)=1.4 \pm 0.4$, which corresponds to a density range of 100−1000 cm^{-3}. Although formally, this source falls into the same range in electron density as the radio galaxies in § 4.5.5 and of Nesvadba et al. (2008), if we take our density estimate at face value, we find densities of about 100 cm^{-3} near the low-density limit, hence lower by factors of a few.

We will now provide rough mass estimates of our sources from the Hα fluxes and electron densities, scaled to an electron density of 500 cm^{-3}, to account for the uncertainties from the poorly constrained electron densities. Using the relation of Osterbrock (1989), introduced previously in § 1.6.2, we find masses between 2 and $17 \times 10^7 n_{e,500}^{-1}$ M$_\odot$ in our quasars with radio sources, and upper limits of $2 - 6 \times 10^7 n_{e,500}^{-1}$ M$_\odot$ in those without.

We only use the extended emission-line gas, which remains after the subtraction of the circum-nuclear emission, for our estimates of the gas mass in putative outflows. The reason we discard this circum-nuclear emission (*i.e.*, narrow-line emission with the same surface-brightness profile as the nuclear tracers) is that we suspect that electron densities may take a wide range of values, including much higher densities, at which narrow-line emission will be suppressed, as done previously in more nearby quasars (*e.g.*, Fu & Stockton, 2008). This would imply that density estimates based on forbidden lines would not be good representatives for the global emission-line spectrum. To the extent where those sources may serve as low-redshift analogs of our targets, we would also expect electron densities in the range of one to a few 100 cm^{-3}. Likewise, the low [NII]/Hα ratios we find in our targets (the critical density to depopulate the $^3P_2$ level corresponding to the [NII]λ6583 line is 310 cm^{-3}), and perhaps even the faintness of [OIII] in one target (the critical density is 3800 cm^{-3}) may be at least partially attributed to this (§ 6.4.3). A more detailed emission-line analysis including fainter diagnostic lines would be an interesting approach to further persue this question.

6.4.7 The AGN: Black-hole masses, bolometric luminosities and Eddington ratios

Having the BLR component of Hα and the rest-frame optical continuum measured for all of our sources, we are also able to constrain the properties of the central supermassive black hole of our sources. As done previously in Chapter 4 we will use the line width of the broad component of the Hα emission line and the luminosity of this line to do this estimate, using the calibration of Greene & Ho (2005). Since we also have observed optical spectra available, including [CIV] and the far-UV continuum around 1350Å (either through optical broad-band photometry or spectroscopy) we would in principle also be able to use the calibration of Vestergaard (2002) to translate the luminosity of the Hα broad-line region into an AGN continuum luminosity at a rest-frame wavelength of 5100Å,

$$\mathcal{L}_{5100}/10^{44} = (\mathcal{L}_{\mathrm{H}\alpha}/5.25 \times 10^{42}\ \mathrm{erg\,s^{-1}})^{0.86}, \tag{6.1}$$

where $\mathcal{L}_{\mathrm{H}\alpha}$ and $\mathcal{L}_{5100}$ are the luminosity at 5100Å of the quasar continuum, and that of the Hα component originating in the AGN broad-line region, respectively. $\mathcal{L}_{5100}$ has previously been calibrated by Kaspi et al. (2000) against the bolometric luminosity of nearby AGN with reverberation measurements to be

$$\mathcal{L}_{\mathrm{bol}} = 9 \times \mathcal{L}_{5100}$$

Another empirical relation between the bolometric luminosity of type-I AGNs and their optical continuum luminosities is given by Heckman et al. (2004) and is obtained from the study of a large sample of local SDSS quasars:

$$\mathcal{L}_{\mathrm{bol}} = 10.9 \times \mathcal{L}_{5000}$$

With these relationships, and using our measurements listed in Table 6.16, we can estimate black-hole masses from the observed Hα broad-line properties of our sources. Table 6.16 gives estimates of black-hole masses and bolometric luminosities for individual objects, which overall fall into the range 0.3×10^9 to 3.4×10^9 M$_\odot$ and 1.1×10^{46} to 19.0×10^{46} erg s^{-1}, respectively.

As previously already discussed in the context of NVSS J2019, the radio galaxy with a broad-line region seen in Hα (see § 4.6.5), the Eddington luminosity is a measure of the maximal accretion rate onto a supermassive black hole which can be reached for a spherically symmetric accretion flow before radiation pressure will balance gravitational attraction. For a given radiative efficieny of the accretion flow (which is typically set to 10%), the Eddington luminosity depends only on black-hole mass, $\mathcal{L}_{\mathrm{Edd}} = 10^{38} \times \mathrm{M_{BH}}$ [erg s^{-1}], where the black-hole mass M$_{\mathrm{BH}}$ is given in M$_\odot$. Assuming that all Quasars have the same canonical radiative efficiency, the ratio of bolometric to Eddington luminosity of a black hole provides therefore a measure of "accretion activity" of the quasar.

Using the estimates of Kaspi et al. (2000) and Heckman et al. (2004), we find Eddington luminosities between 10 and 100%. For B 1657+022, we find nominally a ratio of 200% when using the Heckman et al. (2004) estimate, which is strictly speaking unphysical, if the simple spherical accretion model applies. However, rare examples of super-Eddington accretion do exist in the literature, and can be explained by non-spherical accretion geometries (as would naturally arise from disk-like configurations of the accretion flow), as well as with uncertainties in the black-hole mass estimates, radiative efficiency, and measurement uncertainties. In particular, it is well known that radio-loud AGN can show [OIII] luminosities that are higher than those of radio-quiet AGN, and B 1657+02 is amongst our radio-loud sources.

Table 6.16: Properties of the black holes of our sample of quasars.

Source	$\mathcal{L}_{\rm bol}$ $^{\rm H04,\ (1)}$	$\mathcal{L}_{\rm bol}$ $^{\rm K00,\ (2)}$	$\mathcal{L}_{\rm Edd}$ $^{(3)}$	$\mathcal{L}_{\rm BLR}$ $^{(4)}$	$M_{\rm BH}$ $^{(5)}$	$\epsilon_{\rm Edd}^{\rm H04}$ $^{(6)}$	$\epsilon_{\rm Edd}^{\rm K00}$ $^{(7)}$
		$[10^{46}$ erg s$^{-1}]$		$[10^{44}$ erg s$^{-1}]$	$[10^{9}$ M$_\odot]$		
B 0113−283	11.5	7.5	22.0	8.98	$1.6^{+1.4}_{-0.7}$	0.34	0.52
B 0227−369	9.5	5.4	46.9	6.18	$3.4^{+2.3}_{-1.3}$	0.2	0.11
B 0524−433	12.1	12.7	34.5	16.53	$2.5^{+1.9}_{-1.0}$	0.35	0.36
B 1657+022	16.8	8.1	8.3	9.89	$0.6^{+0.5}_{-0.3}$	2.0	0.97
SDSS J0035+010	1.1	2.0	9.7	1.93	$0.7^{+0.7}_{-0.4}$	0.11	0.2
SDSS J2226+005	4.3	4.4	4.1	4.80	$0.3^{+0.2}_{-0.1}$	0.95	0.93
SDSS J0035+002	10.1	4.8	34.5	5.38	$2.5^{+2.2}_{-1.1}$	0.29	0.14
SDSS J0839+045	6.5	7.8	27.6	9.40	$2.0^{+1.8}_{-1.0}$	0.24	0.28
SDSS J1306+025	2.2	3.6	11.0	3.89	$0.8^{+0.7}_{-0.4}$	0.20	0.33
SDSS J1434+010	5.5	8.3	17.9	10.06	$1.3^{+0.9}_{-0.5}$	0.31	0.46
SDSS J1435+035	19.0	8.4	31.7	10.26	$2.3^{+2.1}_{-1.1}$	0.46	0.26

(1): Bolometric luminosity of the quasar, derived with the estimate of Heckman et al. (2004): $\mathcal{L}_{\rm bol} = 10.9 \times \mathcal{L}_{5000}$ [in 10^{46} erg s^{-1}]. — (2): Bolometric luminosity of the quasar, derived with the estimate of Kaspi et al. (2000) and estimating $\mathcal{L}_{5100}$ from the broad component of the Hα emission line (Vestergaard, 2002): $\mathcal{L}_{\rm bol} = 9.0 \times \mathcal{L}_{5100}$ [in 10^{46} erg s^{-1}]. — (3): Eddington luminosity, derived from our estimate of the SMBH mass [in 10^{46} erg s^{-1}]. — (4): Luminosity of the broad component of the Hα emission line. — (5): Mass of the central black hole, derived with the formula of Greene & Ho (2005): $M_{\rm BH} = 2\,(\mathcal{L}_{\rm BLR}/10^{42}\ {\rm erg\ s^{-1}})^{0.55}\,({\rm FWHM}/10^{3}\ {\rm km\ s^{-1}})^{2.06} \times 10^{6}\ {\rm M_\odot}$ — (6, 7): Eddington ratios, using the prescriptions of Heckman et al. (2004) and Kaspi et al. (2000), respectively, to estimate $\mathcal{L}_{\rm bol}$.

6.5 Discussion

6.5.1 Comparison with high-redshift radio galaxies

Supermassive black holes and AGN

We selected our quasar sample initially to have a good comparison with high-redshift radio galaxies at redshifts $z \sim 2$, which have radio power at 500 GHz in the rest-frame in the range few $10^{26} - 10^{29}$ W Hz^{-1}, and bolometric AGN luminosities mainly in the range of 10^{46-47} erg s^{-1}. Most of their bolometric AGN emission is obscured, and these bolometric luminosities are estimated from the FIR emission measured with Herschel (Drouart et al. 2014, submitted), taking into account that $\mathcal{L}_{\rm bol} = 6 \times \mathcal{L}_{\rm FIR,AGN}$ (see Drouart et al. 2014, and references therein).

Apart from their similar bolometric power, the AGN in the two samples are very different. Most obviously, of course, our sources are selected in the optical, which may either imply they are seen under a different inclination angle (if the unified model applies) or at a different stage of their evolution, if the scheme of Sanders et al. (1988); Hopkins et al. (2006b) is approximately correct, that intense, dusty starbursts triggered by major mergers are first evolving into obscured, then unobscured quasars, as AGN feedback is blowing out the remaining gas at a certain point in the starburst phase. While it is unlikely that this scenario applies at all cosmic epochs and in all types of AGN (*e.g.*, Wild et al., 2007; Dicken et al., 2012), it is not ruled out per se in our sources.

It is therefore interesting that we find significantly lower line widths of the AGN broad lines in the quasars (radio loud and radio quiet) than in the HzRGs. Our SMBH mass estimates are of-order 10^{8-9} $M_\odot$ compared to 10^{9-10} $M_\odot$ for HzRGs, including NVSS J2019 discussed in Chapter 4, which has a similarly high black-hole mass estimate as the most powerful radio galaxies, but a relatively moderate radio power more comparable to those in our present radio-detected subset. Our optically selected quasars have lower black-hole masses than HzRGs. This immediately rules out that the two samples are probing the same class of high-redshift AGN host galaxies seen during the same AGN activity phase as could be expected in the evolutionary scenario of Sanders et al. (1988) and Hopkins et al. (2006b). Given that the Salpeter or e-folding time of supermassive black hole growth is short, $t_s = M/\dot{M} = 4.5 \times 10^7 \epsilon/0.1(\mathcal{L}/\mathcal{L}_{\rm Edd})^{-1}$ yrs (Salpeter, 1964), and with the high accretion rates we found in § 6.4.7, it may be possible for the black holes in our quasars to grow by an order of magnitude in mass within one to few 10^8 yrs, *i.e.*, one star-formation timescale. However, if these AGN have already blown out the gas and dust with which fuled the star formation in their host, then their black-hole masses should be higher than in powerful radio galaxies, not lower. This does of course not preclude our targets from becoming radio galaxies if they will undergo another merger event.

Host galaxies

It is notoriously difficult to probe the properties of the host galaxies of type-1 quasars, even in the nearby Universe. The quasar emission is simply outshining the host galaxy too strongly. This is even the case for the extended gas that we find in some of our sources. By analogy with the nearby quasars of Fu & Stockton (2008), we may worry that the morphology and kinematics of the extended gas in our sources may not be closely related to the properties of the host galaxy. This worry is further substantiated by the irregular velocity fields in many, in particular the radio-loud sources (see Fig. 6.9).

We therefore use an empirical relationship between [OIII] line width and stellar velocity dispersion to at least provide an order-of-magnitude estimate of the dynamical mass of the host galaxy. Nelson & Whittle (1996) found for nearby Seyfert galaxies that there is a relationship between the line widths in the narrow-line region and the stellar velocity dispersion of the host galaxy as measured from absorption lines. Greene & Ho (2005) established that a similar relationship exists for powerful quasars in the SDSS as well. The astrophysical origin of this relationship is not intuitively clear, because the stellar velocity dispersions are probed over much larger radii than the narrow-line region, which have typical sizes of few 100 pc. Typical turnover radii of the rotation curves in nearby galaxies are about 1 kpc or greater, so it is not a priori clear whether narrow-line regions indeed sample the rotation curve out to large enough radii to provide a direct measure for the large-scale rotation velocity. The similarity of line profiles could therefore also be related to a mix of gravitational and non-gravitational processes. For example, over extended timescales, gas with velocities that exceed the circular velocity of the galactic bulge may preferentially escape (see Nesvadba et al., 2011c, for a related nearby example of an AGN host where this might happen).

The central line widths of radio-loud AGN tend to be somewhat higher than those of the stellar absorption lines by about 20% whereas those of radio-quiet quasars are about 20% more narrow. Taking into account that mass scales with the square of the velocity dispersion, this amounts to an uncertainty of a factor ∼ 2, comparable to the uncertainties, *e.g.*, introduced by the unknown inclination angle and acceptable for an order-of-magnitude estimate. (Greene & Ho, 2005) also note that the uncertainty is in fact less, even for radio-loud targets, if we use the velocity width of the line core of the [OIII] line, and not the full line profile, which can be affected by broad line wings. Our lines however appear to be well fitted by Gaussian profiles ; an effect that might be due to the lower signal-to-noise ratios of our data, and presence of night-sky lines, which makes us even less sensitive to faint, broad features in our spectra.

If we use the circum-nuclear [OIII] component to estimate the line width (which corresponds best to the 'classical' narrow-line regions in low-redshift AGN hosts), then we find that most galaxies fall into a range FWHM = 570−820 km s^{-1}. Two galaxies have generally narrow-line widths with FWHM $\gg$ 1000 km s^{-1}, which we supsect are too large to be plausibly dominated by gravitational motion. For the other galaxies, we set

$$M = 5 \times (FWHM/2.355)^2 \times R/G, \tag{6.2}$$

where R is the radius and G the gravitational constant. The factor 5 is a scaling that is appropriate for an isothermal sphere (Bender et al., 1992). For a rotationally supported disk galaxy this factor would be unity, however, projection effects would lower the observed velocity gradient compared to the intrinsic circular velocity. For average inclinations this would imply a correction factor of about 2.8 for v^2.

With these considerations, assuming an effective radius R=1 kpc, and the [OIII] FWHMs given in Tables 6.5 to 6.15, we find a broad mass range for our galaxies of $0.2 - 1 \times 10^{11}$ $M_\odot$. The uncertainties are generally large, but it is nonetheless interesting that these masses are somewhat lower than the stellar masses of HzRGs measured by Seymour et al. (2007); De Breuck et al. (2010), most of which fall into a narrow range of $(3 \pm 1) \times 10^{11}$ $M_\odot$.

We add that, if we use the velocity gradients in the two sources with fairly regular, monotonously rising velocities instead, SDSS J0035+010 and SDSS J1434+010, which have very different total velocity offsets of 300 km s^{-1} and 800 km s^{-1}, respectively, (*i.e.*, circular velocities of $0.5 \times \Delta v = 150$ km s^{-1} and 400 km s^{-1}, respectively) we find a velocity range of 1×10^{10} and 1×10^{11} $M_\odot$, not correcting for inclination. This overall mass range is comparable to that derived from the [OIII] velocity dispersions above. We note that 800 km s^{-1} are at the extreme high end of expected gravitational motion. The largest stellar velocity dispersion measured in the SDSS in massive elliptical galaxies are 435 km s^{-1} (Bernardi et al., 2008), and velocities from gaseous disks are likely to be smaller, because of smaller radii probed by the gas, inclination effects, and dissipation, all of which tend to decrease, not increase the observed velocity gradient. An important component of radial motion is therefore likely in SDSS J1434+0101.

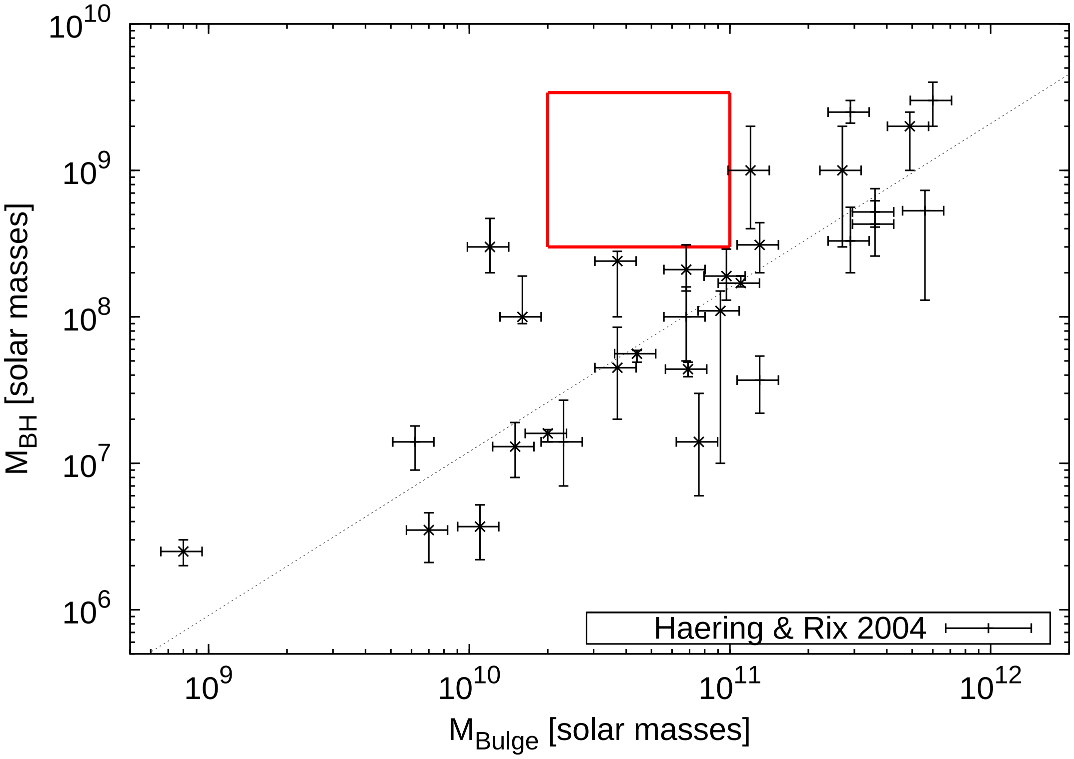

Figure 6.18: $M_{BH} - M_{bulge}$ relation of Häring & Rix (2004) with the global region occupied by our sample of radio-loud quasars and radio-quiet QSOs denoted by the red rectangle. M_{BH} is estimated using the broad component of the Hα emission line and the relation of Greene & Ho (2005) (see § 6.4.7). M_{bulge} is estimated using the FWHM of the [OIII] emission line (see § 6.5.1).

6.5.2 Comparison with low-redshift quasars

Although the basic physics of AGN feedback is unlikely to have changed from redshifts z $\sim$ 2 until today, there is mounting evidence of profound evolutionary changes in the properties of massive galaxies between these two redshift ranges. In particular, massive high-redshift galaxies appear to be very gas-rich, with considerable star-formation rates (*e.g.*, Caputi et al., 2006; Tacconi et al., 2008). This is particularly true for high-redshift "radio galaxies" which show substantial differences to classical radio galaxies in the nearby Universe (see Introduction and Chapter 4). All these reasons make it worthwhile to compare our sources with low-redshift quasars with roughly similar AGN properties.

An excellent comparison sample is that of Fu & Stockton (2009) of 8 radio-selected quasars at redshifts z=0.1−0.3, and one radio galaxy, 3C79 at z=0.26. They obtained Keck/GMOS imaging spectroscopy for those sources, which were selected for having particularly luminous extended emission-line regions. Their main findings are that the extended gas is extended over sizes between 10 and 60 kpc, and often strongly kinematically distorted, with individual regions reaching velocities of up to 500−1100 km s^{-1}. However, global velocity offsets as seen in their maps, corresponding to the global offsets we have derived for our data, are more in the range of $\sim$ 50−200 km s^{-1}, similar to those we find in our sources. More localized perturbations would be smoothed out at the scales that we resolve spatially in the distant Universe.

Likewise, the velocity dispersions are relatively low, of-order FWHM = 200−300 km s^{-1}. Overall, regions with the largest velocity gradients, and line widths exceeding the FWHM = 200−300 km s^{-1} range, are associated with the synchrotron emission from extended radio jets. [OIII]λ5007 luminosities of their sources are in the range of 1−few $\times 10^{43}$ erg s^{-1}, factors of a few lower than ours, which reach up to 3×10^{44} erg s^{-1}, however, line ratios are fairly similar, placing their galaxies in a similar region of the BPT diagram as ours. They attribute this to low metallicities in the extended gas, however, they do not comment on the generally high gas densities that they find from [SII] and [OI] of few 100 cm^{-3} which can lower [NII]/Hα ratios, and thereby mimic low metallicites (Lehnert et al., 2009).

Fu & Stockton (2007a) point out that their Hβ luminosity in their most extreme source, 4C37.43 at z = 0.45, of 1×10^{-14} erg s^{-1} implies a mass of 3×10^{10} $M_{\odot}$, which would be a factor $\sim 10^{2-3}$ larger than our estimates. However, this value was obtained for an assumed density of 1 cm^{-3}, as postulated in their two-phase emission-line model, without direct density measurement. Since M_{HII} is proportional to n_e^{-1}, and if using the same approach and assumptions in both cases, our gas-mass estimates are in fact broad agreement with theirs. While it is likely that the extended emission-line regions in our targets have a wide range of gas density, as would also be expected from a turbulent multi-phase medium (*e.g.*, Guillard et al., 2012; Nesvadba et al., 2010), it does appear to us to be more conservative to restrict ourselves to the directly observed values, although these will be biased towards the relatively dense gas with the highest emissivity. For the most powerful radio galaxies, where gas masses in galaxies with measured electron densities of 500-700 cm^{-3} have been derived in the same way, the assumption of Fu & Stockton (2007a) would imply extremely high ionized gas masses of up to 4×10^{13} $M_{\odot}$, which appear implausibly high to us. Current estimates of up to few 10^{10} $M_{\odot}$ already imply that the mass of warm ionized gas is roughly similar to that of the molecular gas. The molecular gas is typically the dominant gas component of intensely star-forming, massive high-redshift galaxies, and may therefore serve as a rough approximation to the total gas content of gas-rich, massive high-z galaxies.

In light of the strong differences between powerful high-redshift radio galaxies and radio galaxies at low redshifts in terms of their dust and molecular gas masses, radio and quasar power, and star-formation rates, it is interesting that the extended emission-line regions in the high-redshift quasars we have analyzed appear to be so broadly similar to the low-redshift quasars of Fu & Stockton (2009). In particular, the line luminosities in low-redshift radio galaxies appear to be lower by 2−3 orders of magnitude than those at high redshift (*e.g.*, Holt et al., 2008), and implied gas mass estimates would be accordingly lower.

Table 6.17: [OIII] and Hβ luminosities of our sources and masses of extended ionized gas.

Source	$\mathcal{L}_{[\mathrm{OIII}]}$ $^{(1)}$	$\mathcal{L}_{\mathrm{H}\beta}$ $^{(2)}$	$\mathrm{M}_{\mathrm{ion\ gas}}$ $^{(3)}$
	[10^{43} erg s^{-1}]		[10^{8} M$_{\odot}$]
B0113-283	6.6	4.0	<0.5
B0227-369	4.7	4.5	17.1
B0524-433	29.0	5.6	8.7
B1657+022	1.9	6.6	8.6
SDSS J0035+010	22.0	1.0	2.2
SDSS J2226+005	21.0	1.4	8.7
SDSS J0035+002	25.0	2.6	<0.3
SDSS J0839+045	2.4	5.3	<0.2
SDSS J1306+026	5.6	5.3	<0.2
SDSS J1434+010	10.0	0.4	<0.2
SDSS J1435+035	<0.4	5.9	<0.6

(1, 2): [OIII] and Hβ luminosities of our sources (in [10^{43} erg s^{-1}]). Hβ luminosities were estimated from setting $\mathcal{L}_{\mathrm{H}\beta} = \mathcal{L}_{\mathrm{H}\alpha}/3$ and further correcting for extinction. — (3): Mass of ionized gas in the extended emission line regions (in [10^{8} M$_{\odot}$]).

6.5.3 Implications for AGN feedback

The main goal of this thesis is to explore in a uniform way and with the aid of imaging spectroscopy a range of AGN radio and bolometric power at similar high redshifts as the most powerful radio galaxies previously studied in a similar way by Nesvadba et al. (2006, 2007a, 2008), and to elucidate by comparison whether AGN feedback leaves similar signatures in these types of objects. In this section, we are focusing on optically, not radio-selected quasars, i.e. sources with an unobscured sightline into the central regions of the AGN, although they purposefully do probe a range of radio power.

In the most powerful high-z radio galaxies, the main signatures of AGN-driven winds were the high ionized gas masses of up to few 10^{10} M$_{\odot}$, large, abrupt velocity offsets of up to ~2500 km s^{-1} (Nesvadba et al., 2006), and broad FWHMs of-order 1000 km s^{-1}. We also found a correlation between the position angle of the extended emission-line regions of warm ionized gas and the axis of the radio jet, and between the size of jet and nebulosity, in the sense that the gas is always less extended than the radio jet, although a one-to-one relationship cannot be found.

The sources we studied here are significantly different. Their ionized gas masses are lower, mostly in the range of few 10^{8} M$_{\odot}$ for radio-detected sources, and few 10^{7} M$_{\odot}$ (upper limits) for sources without radio counterpart. Although we do find extended emission-line regions in some cases, these extend only over diameters of $1''-2''$, similar to the sizes of other high-z galaxies without prominent AGN (*e.g.*, Förster Schreiber et al., 2009; Swinbank et al., 2006). We find velocity gradients in a subset of sources, but these are smaller than those of powerful radio galaxies, in the range of 100−200 km s^{-1} what can also be explained with gravitational motion in galaxies with few 10^{10-11} M$_{\odot}$ in mass. Even if these were dominated by radial outward motion rather than rotation or merger-driven kinematics, it would not be clear at all that the gas is indeed outflowing. An interesting exception is SDSS J1434+010, which has a very high total velocity gradient of 800 km s^{-1}, albeit a very low ionized gas mass ($\leq$ few 10^{7} M$_{\odot}$).

What makes this comparison important in the context of the mechanisms underlying AGN feedback is that the bolometric power, regardless of the mechanical power of their radio source, is comparable to that in powerful radio galaxies, few 10^{46-47} erg s^{-1}, although the black-hole masses are lower. The simple observational fact that we do note see very extended, high-surface brightness outflows like in very powerful radio sources, although both samples have bolometric power in the same range, already shows that having a bolometrically luminous AGN is not a sufficient pre-requisite for efficiently producing AGN-driven winds.

This also adds to the evidence that the jets play a critical role in driving the gas out in the very powerful radio sources. High dust and gas column densities may also play a role, in particular for radiation pressure (Murray et al., 2005), but as discussed by Nesvadba et al. (2011c) this does not appear empirically to be sufficiently efficient to accelerate large fractions of the ISM over kpc scales to the velocities observed, even in very powerful obscured quasars.

Our galaxies tend to show larger velocity offsets between the broad nuclear emission lines and the narrow line emission in the circum-nuclear gas (with offsets of up to 700 km s^{-1},see Table 6.3) than between the broad nuclear emission lines and the genuinely extended velocity component. One possible explanation is that the gas in the circum-nuclear regions is being accelerated by the energy output from the AGN, presumably due to the high radiative energy output, but that this gas is subsequently decelerated, perhaps in broad analogy with low-redshift narrow-line Seyfert I galaxies (Komossa et al., 2008), which are also characterized by high accretion rates of $0.5 - 1\times$ Eddington, and where a decelelation appears to happen between the inner and outer narrow-line region. Another possibility is that the AGN inflates bubbles in the ISM, but only in the central regions, and that outflows are too dispersed for the gas to reach very high surface brightnesses further out, perhaps because the pressure confinement from a cocoon, as produced in very powerful radio galaxies, is less efficient (in galaxies with less powerful radio sources) or absent (if the absence of measureable radio emission implies the absence of a radio nucleus). Projection effects could in this scenario explain why the gas shows a range in line widths in the radio detected subset, and the one galaxy without radio detection that has an extended emission-line component.

Although, like already argued previously in Chapter 4, our lower-power radio-detected objects do not generally show very clear signatures of large-scale outflows, like in very powerful radio galaxies, they do appear to be intermediate between these and the quasars without radio counterparts. First, quasars without radio detection have lower amounts of extended warm ionized gas that those with a detection. This does not necessarily imply they have also lower gas masses overall, for example, Omont et al. (2003) find that 30% of optically selected high-z AGN are detected with the IRAM/Mambo bolometer at 1.3 mm, *i.e.*, they have significant amounts of dust and presumably also molecular gas. We have no direct measurements of molecular gas in our sources, but even if large amounts of molecular gas were present, this gas would be shielded from the AGN radiation. It is interesting that also in low-redshift sources with very weak radio emission, extreme gas kinematics appear to be restricted to the gas near the radio jet (Husemann et al., 2013).

Of course, it is also well possible that these galaxies are overall less gas-rich, in which case the host galaxies themselves would be less obvious candidates for AGN feedback to play a decisive evolutionary role, at least at the epoch probed by our observations.

Although our constraints on the black-hole bulge mass relationship are limited because of the difficulty of probing quasar host masses at high redshift, they do suggest that the black holes in our sources are too massive for their host galaxies, like previously found for very powerful radio galaxies (Nesvadba et al., 2011b), but opposite to the dust-selected sub-millimeter galaxies of Alexander et al. (2008) and quasars of Coppin et al. (2008) at similar redshifts, where black hole growth seems to lag behind the growth of the host. If this is not due to selection effects (Alexander et al., 2008, and Coppin et al. 2008 use CO line widths to constrain the host mass, not ionized gas lines like Nelson & Whittle 1996), then this might suggest that the hosts of optically selected quasars at high-z are themselves in a different evolutionary stage. To fall onto the local black-hole bulge mass relationship, they would need to grow predominantly in bulge, not black-hole mass. Such growth can be assured even after the main formation period of the galaxy bulge is terminated, in particular through repeated accretion of lower-mass satellite galaxies, which can lead to mass increase by factors 2−4 (Nesvadba et al., 2011b, and references therein). The bright optical continuum emission somewhat disfavors rapid bulge growth, since large-scale obscuration through extended star formation in the host galaxy should lead at least to some reddening of the quasar emission. Likewise, the radio spectral indices of our radio-loud AGN are generally smaller than those in powerful radio galaxies. If the radio sources were expanding into a dense circum-nuclear medium, we would expect a steepening of the radio spectral index, since high-energy particles in the jet would predominantly loose their energy. It would in fact be very interesting to obtain direct measurements of the dust in these systems, for example with ALMA, to see whether their host galaxies are growing along with the black holes.

All of this highlights that high-redshift AGN with similar bolometric power can probe very different populations of host galaxies. For example, Juneau et al. (2013) argue that many distant AGN are hosted by 'normal' star-forming galaxies that have average stellar growth rates compared to the ensemble of star-forming galaxies overall. Not all appear to be directly related to the 'classical' starburst galaxies that would be associated with the Sanders-Hopkins evolutionary scale, at least during evolutionary stages near coalescence of the merging galaxies. In turn, AGN activity – radio and bolometric – appears to be triggered in a range of hosts during different stages of AGN and black-hole (co-) evolution, as has also been recently argued in the nearby Universe (Dicken et al., 2012). Exploring this diversity will be an interesting endeavor for years to come.

6.5.4 Summary

In Chapter 6, we present the results of our SINFONI observations of a sample of eleven high redshift quasars, some of them are radio-loud (6/11) and the rest of them are radio-quiet (5/11). Our aim was to test whether the large bolometric luminosity of quasars could impact the ISM at the scale of the whole host galaxy and drive outflows of ionized gas.

The first step of this study is to carefully subtract the broad component of the Hα emission line. We take advantage of the unresolved nature of the broad line region and of the spectral shape of the *narrow* component — which is easier to model than the broad component — to create a model of the nuclear broad Hα emission line, using a method similar to one developped by Christensen et al. (2006). We then subtract this model in our observations and detect emission line regions around five of the six radio-loud quasars and around three of the five radio quiet quasars. However, these emission line regions still encompass the component from the narrow line region, the circum-nuclear region around the AGN with bright line emission. This emission therefore does not originate from extended narrow line components and is not relevant in our research of large scale winds produced by the energy emitted by the AGN. We then also subtract this component from our observations and detect truly extended emission line regions around four out of the six radio-loud quasars and one out of the five radio-quiet QSOs.

From the broad component of the Hα emission line, we can estimate the mass of the supermassive black hole, following the relation of Greene & Ho (2005). We find SMBH masses between 0.3 and 3.4×10^9 $M_\odot$. The bolometric luminosities of the AGN can be estimated from monochromatic luminosities (with relations provided by Kaspi et al., 2000; Heckman et al., 2004, for example) and our results are in the range $1 - 19 \times 10^{46}$ erg s^{-1}. This gives Eddington ratios (*i.e.*, ratios of bolometric to Eddington luminosities) in the range $10 - 100$ %, which is a typical value for blue quasars. We use the [OIII] line width to derive the dynamical mass of the galaxy. Although this is only an order of magnitude estimate, we find that our sources tend to lie above the local $M_{BH} - M_{bulge}$ relationship (Häring & Rix, 2004).

When comparing the extended emission line regions of our sample of high-redshift quasars with a sample of local ones (of **?**, for instance), we find that they are broadly similar in term of gas content and kinematics. We interpret the absence of extended emission line regions around radio-quiet QSOs as a suggestion that whether the bolometric luminosity of the AGN is less efficient in driving large scale winds or that the hosts of luminous quasars are less gas rich than HzRGs.

Chapter 7

Summary and Outlook

7.1 Summary

We carried out observations of a large number of active galaxies in the high redshift Universe in order to assess the significance and the mode of AGN feedback. Mechanisms of AGN feedback can be elegant ways to solve some problems or puzzles of current models of galaxy formation and evolution, such as the overcooling problem or the $M-\sigma$ relation, detailed in the introductory Chapter 1. To this end, we mainly used the instrument SINFONI at the VLT, complemented in some cases with radio observations with the ATCA and infrared imaging performed with ISAAC. We presented all of these instruments and telescopes in Chapter 2. In Chapter 3, we presented Monte Carlo simulations that allowed us to analyse our data in a comprehensive way. These data were presented in the following Chapters: in the Chapter 4, we give the results of our SINFONI and ATCA observations of twelve high redshift radio galaxies (HzRGs). We know that the radio jets of the most powerful HzRGs are able to drive large outflows of ionized gas out their host galaxy (*e.g.*, Nesvadba et al., 2006, 2008) and we wanted to see if radio jets of lower and lower powers could do the same. In Chapter 6, we present the results of our SINFONI observations of a sample of eleven high redshift quasars, some of them are radio-loud (6/11) and the rest of them are radio-quiet (5/11). We wanted to see what impact the large bolometric luminosity of quasars could have on the ISM at the scale of the whole host galaxy. Finally, in the Chapter 5, we studied the results of near infrared imaging (both broad- and narrow-band) with ISAAC of two high redshift radio galaxies that do not follow the usual trend observed in the rest of our sample: their extended emission line regions are not aligned with their radio jets.

7.1.1 Summary of our study of mechanical AGN feedback in moderately powerful high redshift radio galaxies

This study aimed to assess the ability of moderately powerful radio jets to accelerate and heat the gas of their host galaxies in order to regulate the star formation, and the significance of this process in such a case. We already had clear signatures of efficient mechanical AGN feedback in the most powerful high redshift radio galaxies (*e.g.*, Nesvadba et al., 2006, 2008), hence we chose our sample to have radio luminosities $1-2$ orders of magnitude of magnitude fainter (with $\mathcal{L}_{500\mathrm{MHz}} \sim 10^{27-29}$ W Hz^{-1}), but which energy budget is still clearly dominated by the AGN and not the star formation.

In our near-infrared imaging spectroscopy observations of our sample, we typically detect a faint, unresolved continuum emission around which we find extended emission line regions (clearly seen in [OIII] and Hα). The kinematics of this ionized gas is diverse among our sample: some sources (*e.g.*, NVSS J0129, CEN 072) show large scale and smooth velocity gradients, but of small magnitude (typically $\lesssim 400$ km s^{-1}) ; while other sources have very irregular velocity fields (*e.g.*, NVSS J0024). A common feature to all sources of our sample is their large velocity dispersions, with FWHM $= 400-1000$ km s^{-1}. The small ratios of bulk velocities to velocity dispersions indicate that the observed ionized gas cannot be in a stable rotating disk, even in cases where smooth velocity gradients are detected.

The measured emission line ratios clearly indicate that the observed gas is ionized by the central AGN. Our estimates of ionized gas masses are in the range of few 10^{8-9} $M_{\odot}$, which is at least one order of magnitude less than what was previously found in the most powerful radio galaxies. For a couple of sources, we found distinct emission line regions in the vicinity of the radio galaxy. Assuming they originate from satellite galaxies, we used them as proxies for the dynamical mass of the radio galaxy, and we found a few 10^{11} $M_{\odot}$, which is comparable to the typical mass of HzRGs (*e.g.*, Seymour et al., 2007; De Breuck et al., 2010). In one source (NVSS J2019), we find a broad component in its Hα emission line (with FWHM $\sim$ 8250 km s^{-1}). We interpret this as the signature of the BLR and derive some properties of the black hole, such as its mass ($M_{BH} \sim 2.1$ $M_{\odot}$) and its bolometric luminosity (5.3×10^{45} erg s^{-1}) which leads to an Eddington ratio of ~ 2 %.

We explore different possible sources of energy that can explain the large observed energies of the ionized gas: tranfer from the radio jet, radiative feedback from the large bolometric luminosity of the AGN or gravitational interactions. We show that a plausible scenario is the energy transfer from the radio jet to the ionized gas. Our estimations show that a fraction of the radio jet power is sufficient to power the kinematic of the ionized gas. Our observations are in agreement with the theoretical predictions of hydrodynamical models (see *e.g.*, Wagner et al., 2012).

7.1.2 Summary of our study of radiative AGN feedback in high redshift quasars

In Chapter 6, we present the results of our SINFONI observations of a sample of eleven high redshift quasars, some of them are radio-loud (6/11) and the rest of them are radio-quiet (5/11). Our aim was to test whether the large bolometric luminosity of quasars could impact the ISM at the scale of the whole host galaxy and drive outflows of ionized gas.

The first step of this study is to carefully subtract the broad component of the Hα emission line. We take advantage of the unresolved nature of the broad line region and of the spectral shape of the *narrow* component — which is easier to model than the broad component — to create a model of the nuclear broad Hα emission line, using a method similar to one developped by Christensen et al. (2006). We then subtract this model in our observations and detect emission line regions around five of the six radio-loud quasars and around three of the five radio quiet quasars. However, these emission line regions still encompass the component from the narrow line region, the circum-nuclear region around the AGN with bright line emission. This emission therefore does not originate from extended narrow line components and is not relevant in our research of large scale winds produced by the energy emitted by the AGN. We then also subtract this component from our observations and detect truly extended emission line regions around four out of the six radio-loud quasars and one out of the five radio-quiet QSOs.

From the broad component of the Hα emission line, we can estimate the mass of the supermassive black hole, following the relation of Greene & Ho (2005). We find SMBH masses between 0.3 and 3.4×10^{9} $M_{\odot}$. The bolometric luminosities of the AGN can be estimated from monochromatic luminosities (with relations provided by Kaspi et al., 2000; Heckman et al., 2004, for example) and our results are in the range $1-19\times10^{46}$ erg s^{-1}. This gives Eddington ratios (*i.e.*, ratios of bolometric to Eddington luminosities) in the range $10-100$ %, which is a typical value for blue quasars. We use the [OIII] line width to derive the dynamical mass of the galaxy. Although this is only an order of magnitude estimate, we find that our sources tend to lie above the local $M_{BH}-M_{bulge}$ relationship (Häring & Rix, 2004).

When comparing the extended emission line regions of our sample of high-redshift quasars with a sample of local ones (of **?**, for instance), we find that they are broadly similar in term of gas content and kinematics. We interpret the absence of extended emission line regions around radio-quiet QSOs as a suggestion that whether the bolometric luminosity of the AGN is less efficient in driving large scale winds or that the hosts of luminous quasars are less gas rich than HzRGs.

7.1.3 Summary of our study of two peculiar high redshift radio galaxies

Finally, in the Chapter 5, we studied the results of near infrared broad-band imaging with ISAAC of two high redshift radio galaxies that do not follow the usual trend observed in the rest of our sample: their extended emission line regions are not aligned with their radio jets. This broad-band imaging revealed extended stellar enveloppes in these systems, whose effective radii are larger than those of usually compact high redshift galaxies (*e.g.*, Daddi et al., 2005; van Dokkum et al., 2008). We also took advantage of the availability with ISAAC of a narrow-band filter centered on the redshifted Hα emission line of one of the two HzRGs. We could then probe the ionized at larger distances than what was initially allowed by SINFONI and its small field of view. We confirm the unusual morphology of the Hα emission line region around this source. We also detected thirteen Hα-emitters around the high redshift radio galaxy, meaning that this region is denser than the field by a factor of ~ 30.

7.2 Outlook: What are the remaining open questions?

In the few last years, a lot of new telescopes and intruments came into service, which will allow much more precise and sensitive observations. The most important of them for galaxy formation and evolution is arguably the Atacama Large Millimeter/submillimeter Array (ALMA), which will routinely observe the cold molecular gas in high redshift galaxies, although it was already feasible, but challenging, with previous facilities. LOFAR and other SKA pathfinders are also coming to maturity. Furthermore, in the next few years, new telescopes are planned to come into service. Two of them can be of particular interest in the study of the role of the AGN in the evolution of galaxies: The Square Kilometer Array (SKA, Carilli & Rawlings, 2004; Taylor, 2013) and the James Webb Space Telescope (JWST, Gardner et al., 2006), in particular with its Mid-InfraRed Instrument (MIRI, Wright et al., 2010). In the next sections, we discuss some open questions that can possibly be tested with these new facilities.

7.2.1 What happen to other phases of the ISM?

In this thesis, we focused on the warm ionized phase of the interstellar medium, but, in principle, AGN feedback should be able to affect the gas in all its phases. For instance, Nesvadba et al. (2010, 2011a) observed the molecular gas of the local radio galaxy 3C 326: it appears that this galaxy has a large reservoir of molecular gas, nearly equally divided between the warm and cold phases (with $\mathrm{M_{cold\ mol\ gas}} \simeq 1.5 \times 10^9\ \mathrm{M_\odot}$ and $\mathrm{M_{warm\ mol\ gas}} \simeq 2.0 \times 10^9\ \mathrm{M_\odot}$) but does not form star at a rate as high as galaxies without radio jets, but with similar content of molecular gas do. Another example of AGN feedback due to the effects of radio jets is given in Morganti et al. (2005) and focuses on the neutral atomic gas in a sample of seven local radio galaxies. They observed strong absorption feature against the bright radio continuum, that they interpret as the blueshifted absorptions of the 21 cm transition of neutral gas, outflowing from the host galaxy. With the advent of ALMA, studies of the cold molecular gas, through the CO molecule, are becoming common. This kind of study has already been conducted in a local Seyfert galaxy, NGC 1433, by Combes et al. (2013), who detected an outflow of molecular gas of $\sim 3.6 \times 10^6\ \mathrm{M_\odot}$ at a rate of $\sim 7\ \mathrm{M_\odot\ yr^{-1}}$ and which is thought to be powered by the radio jet coming from the AGN of the galaxy.

However, the content in gas and the physical conditions of the gas are different between local and high redshift radio galaxies and direct comparisons are therefore dangerous. These studies of low redshift radio galaxies are rather examples of the "maintenance phase", which role is to keep the unescaped and returned gas from stellar evolution unsuitable for star formation (see §1.3.3) in order to keep local massive galaxies "red and dead". Observations of the hot phase of the gas associated with local radio galaxies also reveal this "maintenance phase" at work: cavities are observed in the X-ray emitting gas and are filled with radio emitting plasma from the jets (see McNamara & Nulsen, 2007, 2012, for a recent review on this subject). Nonetheless, those local examples of the impact of radio jets shows that they are able to couple themselve and to deposit a fraction of their mechanical energy in all the phases of the interstellar medium. These works now need to be extended to high redshift radio galaxies in order to test if their jets are also able to act on all the phases of the instellar medium and not just on the warm ionized gas as we showed it is the case in this thesis. Instruments that will allow the study of these other phases of the interstellar medium include:

- The Atacama Large Millimeter/submillimeter Array (ALMA, *e.g.*, Kurz & Shaver, 1999; Kurz et al., 2002; Zwaan et al., 2013) has been available to the community for couple of years now. It allows observations of unprecedented sensibility and spatial and spectral resolution in the millimeter/submillimeter window. This wavelength range is perfectly suited to observe cold processes ($T \sim 10 - 100$ K), in particular the star formation that occurs from cold molecular gas. Observing the content in this cold molecular gas of our samples is therefore very important to test whether AGN feedback is efficient in perturbing the molecular gas of their host galaxy, and possibly even driving outflows encompassing a molecular phase. It is crucial to lead these observations to test whether AGN feedback is able to perturbe the reservoir of material from which star formation occurs and if it is therefore able to stop star formation in their host galaxy. This kind of study was already conducted in the local Seyfert galaxy NGC1433 by Combes et al. (2013), who detected an outflow of molecular gas of $\sim 3.6 \times 10^6$ $M_\odot$ at a rate of ~ 7 $M_\odot$ yr^{-1}, which is powered by the radio jet coming from the AGN of the galaxy. Now it needs to be extended at higher redshifts and to span a large range of radio powers.

- The "Low Frequency Array" (LOFAR, van Haarlem et al., 2013) is reaching its full capabilities, with its first call for proposal that closed this September. This telescope opens a new window on our Universe, at very low radio frequencies, in the range 30−240 MHz (with the possibility to observed down to 10 MHz). This new telescope is fully presented by van Haarlem et al. (2013) and here we just give some of its key characteristics: The core of the array is in the Netherlands, with 40 "stations", and eight other LOFAR stations spread over Europe (France, Germany, Sweden and the UK so far), leading to high sensitivity (the noise level reaches ∼ 1 mJy in ∼ 1 hrs of observing time) and high spatial resolution (it easily reaches the arcsec level if the most remote stations are used).

  LOFAR is therefore the ideal instrument to investigate radio relics, due to previous AGN activity (*e.g.*, Schoenmakers et al., 2000a,b; Kaiser et al., 2000; Konar et al., 2012; Sirothia et al., 2013). Indeed, the spectral index of radio lobes steepens as the halo is getting older. There are several theoretical models of how ageing acts on the spectral index (*e.g.*, Kardashev, 1962; Pacholczyk, 1970; Jaffe & Perola, 1973; Harwood et al., 2013), but they all predict its steepening. This could also give some hints about the "duty cycle" of radio AGN, *i.e.*, the fraction of time during which the black hole is active (*e.g.*, Dong et al., 2010; Bîrzan et al., 2012). Finally, LOFAR should also be a good tool to test of the "maintenance phase" (*e.g.*, Croton et al., 2006; Somerville et al., 2008; Dubois et al., 2010) of AGN feedback. Radio jets are already thought to be responsible for cavities observed in X-rays (*e.g.*, McNamara et al., 2000; Fabian et al., 2000), but some of these cavities are devoid of high-frequency radio emission (*e.g.*, McNamara et al., 2001), although observations at lower frequency reveal more complex radio structures (*e.g.*, Clarke et al., 2005). Finally, LOFAR should be sensible enough to carry studies similar to the one of Morganti et al. (2005) and to search for outflows of neutral gas in high redshift radio galaxies.

- The SKA will be built in South Africa and in Australia by 2020 and will allow high sensitivity (with a noise down to the mJy level in just a few minutes of observation), high spatial resolution radio observations of the southern sky. Similarly to LOFAR, it will open the very low frequency window (with observations down to 50 MHz) and up to higher frequencies (20 GHz), already reached by current radio telescopes (*e.g.*, the ATCA, see §2.3), although with lower sensitivities and spatial resolutions. The SKA will therefore allow to tackle the same issues as LOFAR, already discussed before.

- The Chandra (Weisskopf et al., 2002) and XMM-Newton (Jansen et al., 2001) satellites could allow observations at high energies of our samples of AGN. First, measures of the X-ray flux of our sources would give the least biased estimate of the AGN power (*e.g.*, Brandt & Hasinger, 2005; Page et al., 2012) and we could avoid using order of magnitude measures, based on empiric relations, such as the relations given by Willott et al. (1999) or by Bîrzan et al. (2008) that allows to estimate the power in radio jets from the radio luminosity of the source, but with a large scatter ; or to estimate the bolometric luminosity of quasars from a monochromatic flux density (*e.g.*, Kaspi et al., 2000; Vestergaard, 2002) or from the flux of some emission lines (such as Hα or [OIII], *e.g.*, Greene & Ho, 2005; Dicken et al., 2009). X-ray observations could also be interesting regarding the two regions with unsual extended emission line sources described in Chapter 5. Indeed, we interpreted them as putative cooling flows at high redshift and it would be very interesting to check if they are actually embedded in a cocoon of hot (T $\sim 10^{7-8}$ K) X-ray emitting gas, as cooling flow clusters are.

- The James Webb Space Telescope (JWST, Gardner et al., 2006) is planned to be launched in space in 2018 and to observe the sky in the infra-red (from 0.6 to 28 μm) from the Lagrangian point L2. Beyond the unprecedented sensibility and spatial and spectral resolution that should be reached by the JWST in the near infra-red, its Mid-InfraRed Instrument (MIRI, Wright et al., 2010) will also re-open the mid infra-red window (from $\sim 3\mu$m to $\sim 30\mu$m) that has not been accessible since the Spitzer satellite ran out of helium in 2009. In particular, the observation in high redshift galaxies of the warm dust, supposedly heated by the AGN, and of warm molecular gas emission lines, potentially excited by shocks, could potentially bring interesting information about this phase of the gas (*e.g.*, Guillard et al., 2012). On the other hand, the level of the mid infra-red continuum can give constraints on the AGN contribution in dust heating, as explained before in the previous paragraph regarding ALMA.

7.2.2 Are these systems actively forming stars?

In this thesis, we studied the observational signatures of possible mechanisms of AGN feedback, which prime physical motivation is to solve the overcooling problem in massive galaxies (see §1.2.3), *i.e.*, to prevent them from converting too much of their gas into stars and hence from forming too many stars. It would therefore be very interesting to measure their star formation rates and to see if it is affected by the AGN, whether because of mechanical or radiative energy that is deposited in the system. However, measuring star formation rates is a difficult exercice, especially in high redshift active galaxies. Indeed, signatures of star formation (such as photoionization of the interstellar medium because of bright massive stars, heating of the dust or the form of the continuum emitted by the sum of all the stars of the galaxy) are all contaminated (at best) or dominated (at worst) by the AGN. It is arguably in the infrared that effects due to star formation and to AGN can be best disentangled: the harder spectrum of AGN heats more the dust than radiation coming from stars, meaning that the far infrared emission of galaxy can be assumed to originate from cold dust heated solely by stars (see Seymour et al., 2012, for an application of this hypothesis).

With the new receptors recently installed on the Karl Jansky Very Large Array (JVLA), we can have the high sensitivity, on top of high spatial resolution (sub-arcsecond), needed to probe the small-scales structures of the jets of the radio galaxies in our sample. Coupling the morphology of the jet with the kinematic of the gas, *e.g.*, observed with SINFONI, could allow us to better understand how the mechanical energy of the jet is deposited in the interstellar medium. With the high sensitivity of the JVLA, we could also possibly distinguish regions of star formation from the jet, although both are expected to have similar steep spectra and making this distinction would therefore rely more on the morphology of the emission.

7.2.3 What is the stellar morphology of these galaxies?

In Chapter 5, we studied the stellar morphology of two of the high-redshift radio galaxies in our sample. We found that they already had large effective radii, at contrast with what is generally observed for early type high redshift galaxies that tend to be very compact. Observations with high spatial resolution of the rest of the sample could allow us to see if these two galaxies are peculiar or if most of HzRG also have already evolved stellar morphologies. The Hubble Space Telescope (HST) or with the upcoming generation of 30 meters telescopes (*e.g.*, the European Extremely Large Telescope — E-ELT — or the Thirty Meters Telescope — TMT) would be well suited to this kind of study. These observations could also lead to a better understanding of the environment of high redshift radio galaxies and of the epoch of formation of clusters of galaxies. Radio galaxies are already known to lie in overdense regions of the Universe, so observing their surroundings at different epochs might give us some hints on how and when clusters of galaxies formed.

This study could be well assisted by the second generation of IFUs that are now being delivered at the VLT and that could observe in details individual galaxies that are associated with the radio galaxy. These two new IFUs are MUSE (the Multi Unit Spectroscopic Explorer Bacon et al., 2006), that will work in the optical (from 4650Å to 9300Å), and KMOS (Sharples et al., 2005, 2013), that will work in the near infra-red (from 0.8μm to 2.5μm). They are actually both made of several (24) IFUs, each of them working on a small region (*e.g.*, $2.8'' \times 2.8''$ in the case of KMOS) of the whole field of view of the instrument (which is $1' \times 1'$, AO assisted, in the case of MUSE, and $7.2'$ in diameter, non-AO assisted, in the case of KMOS). In the case of KMOS, these individual IFUs can be moved on the field of view, leading to the possibility of observing several objects in a single exposure (which would be very interesting for the study of individual galaxies that seem to be part of a single structure), while in the case of MUSE, individual IFUs are fixed. Note that because of the configurable nature of the individual IFUs of KMOS, they cannot be positionned as to form a continuous mosaic, so the observation of a large field of view requires to adopt a dither pattern. The spectral resolution of both instrument is a few thousand (from 2000 to 4000 for MUSE and from 1800 to 4200 for KMOS). These new instruments will also allow the observation of the warm ionized gas, especially the redshifted Lyα emission line in the case of MUSE, in large samples of galaxies. Generalizing the kind of study presented in this thesis to a few hundreds (maybe even thousand) galaxies will be possible with these new instruments.

7.2.4 Energy loss from the jet

Polarization from radio observations, *e.g.*, with the JVLA, can bring many constraints on the radio jets morphology and on the way mechanical energy from the radio jets is deposited in the interstellar medium, which is presently not fully understood. Faraday rotation causes the receding jet to be more depolarized than the approaching jet, which is known as the Laing-Garrington effect (Laing, 1988; Garrington et al., 1988). Moreover, the Faraday rotation can be used to measure the density of the medium between the two jets since it can be expressed from the rotation measure, which is sensitive to the electron density and the magnetic field along the line of sight. So, by comparing the polarization angle of each jet and assuming some typical value for the magnetic field and the fact that the emission of both jets goes through the same medium once it has left the radio galaxy, we can estimate the electron density integrated over the scale of the host galaxy. Another possibility offered by high resolution radio observations is to directly spot the energy deposit from the radio jet into the interstellar medium. This would result in the depolarization of the radio emission in region where the gas would appear more perturbed (*e.g.*, Best et al., 1998).

Bibliography

Alaghband-Zadeh, S., Chapman, S., Swinbank, A., et al. 2012, Monthly Notices of the Royal Astronomical Society, 424, 2232

Alatalo, K., Blitz, L., Young, L. M., et al. 2011, Astrophysical Journal, 735, 88

Alexander, D., Swinbank, A., Smail, I., McDermid, R., & Nesvadba, N. 2010, Monthly Notices of the Royal Astronomical Society, 402, 2211

Alexander, D., Brandt, W., Smail, I., et al. 2008, Astrophysical Journal, 135, 1968

Allen, M. G., Groves, B. A., Dopita, M. A., Sutherland, R. S., & Kewley, L. J. 2008, Astrophysical Journal Supplement Series, 178, 20

Antonucci, R. 1993, Annual Review of Astronomy & Astrophysics, 31, 473

Antonuccio-Delogu, V., & Silk, J. 2008, Monthly Notices of the Royal Astronomical Society, 389, 1750

—. 2010, Monthly Notices of the Royal Astronomical Society, 405, 1303

Arav, N., & Li, Z.-Y. 1994, Astrophysical Journal, 427, 700

Arav, N., Li, Z.-Y., & Begelman, M. C. 1994, Astrophysical Journal, 432, 62

Arav, N., de Kool, M., Korista, K. T., et al. 2001, Astrophysical Journal, 561, 118

Archibald, E., Dunlop, J., Hughes, D., et al. 2001, Monthly Notices of the Royal Astronomical Society, 323, 417

Bacon, R., Adam, G., Baranne, A., et al. 1995, Astronomy & Astrophysics Supplement Series, 113, 347

Bacon, R., Bauer, S., Böhm, P., et al. 2006, The Messenger, 124, 5

Baldwin, J. A., Phillips, M. M., & Terlevich, R. 1981, Astronomical Society of the Pacific, 93, 5

Barnes, J. E., & Hernquist, L. 1996, Astrophysical Journal, 471, 115

Barvainis, R. 1987, Astrophysical Journal, 320, 537

Becker, R., White, R., & Edwards, A. 1991, Astrophysical Journal Supplement, 75, 1

Begelman, M., Blandford, R., & Rees, M. 1984, Reviews of Modern Physics, 56, 255

Bender, R., Burstein, D., & Faber, S. M. 1992, Astrophysical Journal, 399, 462

Bennert, N., Falcke, H., Schulz, H., Wilson, A. S., & Wills, B. J. 2002, Astrophysical Journal, 574, L105

Bennett, C., Lawrence, C., Burke, B., Hewitt, J., & Mahoney, J. 1986, Astrophysical Journal Supplement Series, 61, 1

Benson, A., Bower, R., Frenk, C., et al. 2003, Astrophysical Journal, 599, 38

Bernardi, M., Hyde, J., Fritz, A., et al. 2008, Monthly Notices of the Royal Astronomical Society, 391, 1191

Bertin, E., & Arnouts, S. 1996, Astronomy & Astrophysics Supplement, 117, 393

Best, P., Arts, J., Röttgering, H., et al. 2003a, Monthly Notices of the Royal Astronomical Society, 346, 627

Best, P., Carilli, C., Garrington, S., Longair, M., & Röttgering, H. 1998, Monthly Notices of the Royal Astronomical Society, 299, 357

Best, P., Kaiser, C., Heckman, T., & Kauffmann, G. 2006, Monthly Notices of the Royal Astronomical Society, 368, L67

Best, P., Kauffmann, G., Heckman, T., et al. 2005, Monthly Notices of the Royal Astronomical Society, 362, 25

Best, P., Lehnert, M., Miley, G., & Röttgering, H. 2003b, Monthly Notices of the Royal Astronomical Society, 343, 1

Best, P., von der Linden, A., Kauffmann, G., Heckman, T., & Kaiser, C. 2007, Monthly Notices of the Royal Astronomical Society, 379, 894

Best, P. N. 2000, Monthly Notices of the Royal Astronomical Society, 317, 720

Bianchi, S., Corral, A., Panessa, F., et al. 2008, Monthly Notices of the Royal Astronomical Society, 385, 195

Bîrzan, L., McNcNamara, B., Nulsen, P., Carilli, C., & Wise, M. 2008, Astrophysical Journal, 686, 859

Bîrzan, L., Rafferty, D., McNamara, B., Wise, M., & Nulsen, P. 2004, Astrophysical Journal, 607, 800

Bîrzan, L., Rafferty, D., Nulsen, P., et al. 2012, Monthly Notices of the Royal Astronomical Society, 427, 3468

Blain, A., & Phillips, T. 2002, Monthly Notices of the Royal Astronomical Society, 333, 222

Blandford, R. 1976, Monthly Notices of the Royal Astronomical Society, 176, 465

Blandford, R., & Begelman, M. 1999, Monthly Notices of the Royal Astronomical Society, 303

Blandford, R., & Rees, M. 1974, Monthly Notices of the Royal Astronomical Society, 169, 395

Blandford, R., & Znajek, R. 1977, Monthly Notices of the Royal Astronomical Society, 179, 433

Blundell, K. M., & Rawlings, S. 1999, Nature, 399, 330

Bock, D., Large, M., & Sadler, E. 1999, Astrophysical Journal, 117, 1578

Böhringer, H., Voges, W., Fabian, A., Edge, A., & Neumann, D. 1993, Monthly Notices of the Royal Astronomical Society, 264, L25

Bonnet, H., Conzelmann, R., Delabre, B., et al. 2004, Society of Photo-Optical Instrumentation Engineers (SPIE) Conference Series, 5490, 130

Borguet, B., Hutsemékers, D., Letawe, G., Letawe, Y., & Magain, P. 2008, Astronomy and Astrophysics, 478, 321

Bouché, N., Murphy, M., Kacprzak, G., et al. 2013, Science, 341, 50

Brandt, W., & Hasinger, G. 2005, Annual Review of Astronomy & Astrophysics, 43, 827

Broderick, J., Bryant, J., Hunstead, R., Sadler, E., & Murphy, T. 2007, Monthly Notices of the Royal Astronomical Society, 381, 341

Brookes, M., Best, P., Peacock, J., Röttgering, H., & Dunlop, J. 2008, Monthly Notices of the Royal Astronomical Society, 385, 1297

Brookes, M., Best, P., Rengelink, R., & Röttgering, H. 2006, Monthly Notices of the Royal Astronomical Society, 366, 1265

Bryant, J., Broderick, J., Johnston, H., et al. 2009a, Monthly Notices of the Royal Astronomical Society, 394, 2197

Bryant, J., Johnston, H., Broderick, J., et al. 2009b, Monthly Notices of the Royal Astronomical Society, 395, 1099

Buitrago, F., Conselice, C., Epinat, B., et al. 2014, Monthly Notices of the Royal Astronomical Society, 439, 1494

Bunker, A., Warren, S., Hewett, P., & Clements, D. 1995, Monthly Notices of the Royal Astronomical Society, 273, 513

Burns, J. O. 1990, Astronomical Journal, 99, 14

Busca, N., Delubac, T., Rich, J., et al. 2013, Astronomy and Astrophysics, 552, 96

Cano-Díaz, M., Maiolino, R., Marconi, A., et al. 2012, Astronomy and Astrophysics, 537, L8

Caputi, K., Dole, H., Lagache, G., et al. 2006, Astrophysical Journal, 637, 727

Cardelli, J., Clayton, G., & Mathis, J. 1989, Astronomical Journal, 345, 245

Carilli, C., Perley, R., & Harris, D. 1994, Monthly Notices of the Royal Astronomical Society, 270, 173

Carilli, C., & Rawlings, S. 2004, New Astronomy Reviews, 48, 11

Carilli, C., Röttgering, H., van Ojik, R., Miley, G., & van Breugel, W. 1997, Astrophysical Journal Supplement, 109, 1

Carilli, C., & Taylor, G. 2002, Annual Review of Astronomy & Astrophysics, 40, 319

Cassata, P., Giavalisco, M., Guo, Y., et al. 2010, Astrophysical Journal Letters, 714, L79

Cavagnolo, K., McNamara, B., Nulsen, P., et al. 2010, Astrophysical Journal, 720, 1066

Chajet, L., & Hall, P. 2013, Monthly Notices of the Royal Astronomical Society, 429, 3214

Christensen, L., Jahnke, K., Wisotzki, L., & Sánchez, S. 2006, Astronomy and Astrophysics, 459, 717

Ciotti, L., & Bertin, G. 1999, Astronomy and Astrophysics, 352, 447

Ciotti, L., D'Ercole, A., Pellegrini, S., & Renzini, A. 1991, Astrophysical Journal, 376, 380

Ciotti, L., Ostriker, J. P., & Proga, D. 2009, Astrophysical Journal, 699, 89

—. 2010, Astrophysical Journal, 717, 708

Clark, B. 1980, Astronomy and Astrophysics, 89, 377

Clarke, T., Sarazin, C., Blanton, E., Neumann, D., & Kassim, N. 2005, Astrophysical Journal, 625, 748

Cohen, A., Lane, W., Cotton, W., et al. 2007, Astronomical Journal, 134, 1245

Cohen, M. H., Ogle, P. M., Tran, H. D., Goodrich, R. W., & Miller, J. S. 1999, Astronomical Journal, 118, 1963

Cole, S., Aragon-Salamanca, A., Frenk, C., Navarro, J. F., & Zepf, S. 1994, Monthly Notices of the Royal Astronomical Society, 271, 781

Collins, C. A., Stott, J. P., Hilton, M., et al. 2009, Nature, 458, 603

Combes, F., García-Burillo, S., Casasola, V., et al. 2013, Astronomy and Astrophysics, 558, 124

Condon, J. J., Cotton, W. D., Greisen, E. W., et al. 1998, Astronomical Journal, 115, 1693

Conselice, C., Gallagher, III, J., & Wyse, R. 2001, Astronomical Journal, 122, 2281

Coppin, K., Swinbank, A., Neri, R., et al. 2008, Monthly Notices of the Royal Astronomical Society, 389, 45

Cowie, L. L., Songaila, A., Hu, E. M., & Cohen, J. 1996, Astronomical Journal, 112, 839

Crawford, C., Allen, S., Ebeling, H., Edge, A., & Fabian, A. 1999, Monthly Notices of the Royal Astronomical Society, 306, 857

Crenshaw, D. M., Kraemer, S. B., & George, I. M. 2003, Annual Review of Astronomy & Astrophysics, 41, 117

Croom, S., Richards, G., Shanks, T., et al. 2009, Monthly Notices of the Royal Astronomical Society, 399, 1755

Croom, S., Lawrence, J., Bland-Hawthorn, J., et al. 2012, Monthly Notices of the Royal Astronomical Society, 421, 872

Croton, D., Springel, V., White, S., et al. 2006, Monthly Notices of the Royal Astronomical Society, 365, 11

Daddi, E., Renzini, A., Pirzkal, N., et al. 2005, Astrophysical Journal, 626, 680

De Breuck, C., Downes, D., Neri, R., et al. 2005, Astronomy and Astrophysics, 430, L1

De Breuck, C., Hunstead, R. W., Sadler, E. M., Rocca-Volmerange, B., & Klamer, I. 2004, Monthly Notices of the Royal Astronomical Society, 347, 837

De Breuck, C., Klamer, I., Johnston, H., et al. 2006, Monthly Notices of the Royal Astronomical Society, 366, 58

De Breuck, C., Neri, R., & Omont, A. 2003a, New Astronomy Reviews, 47, 285

De Breuck, C., van Breugel, W., Stanford, S., et al. 2002, Astronomical Journal, 123, 637

De Breuck, C., van Breugel, W., Röttgering, H., et al. 2001, Astronomical Journal, 121, 1241

De Breuck, C., Neri, R., Morganti, R., et al. 2003b, Astronomy and Astrophysics, 401, 911

De Breuck, C., Seymour, N., Stern, D., et al. 2010, Astrophysical Journal, 725, 36

De Lucia, G., & Blaizot, J. 2007, Monthly Notices of the Royal Astronomical Society, 375, 2

de Vaucouleurs, G. 1948, Annales d'Astrophysique, 11, 247

De Young, D. S., & Heckman, T. M. 1994, Astrophysical Journal, 431, 598

Dekel, A., Sari, R., & Ceverino, D. 2009, Astrophysical Journal, 703, 785

Di Matteo, T., Springel, V., & Hernquist, L. 2005, Nature, 433, 604

Dicken, D., Tadhunter, C., Axon, D., et al. 2009, Astrophysical Journal, 694, 268

—. 2012, Astrophysical Journal, 745, 172

Done, C., Jin, C., Middleton, M., & Ward, M. 2013, Monthly Notices of the Royal Astronomical Society, 434, 1955

Dong, R., Rasmussen, J., & Mulchaey, J. S. 2010, Astrophysical Journal, 712, 883

Donzelli, C., Muriel, H., & Madrid, J. 2011, Astrophysical Journal Supplement, 195, 15

Douglas, J., Bash, F., Bozyan, F., Torrence, G., & Wolfe, C. 1996, Astronomical Journal, 111, 1945

Down, E., Rawlings, S., Sivia, D., & Baker, J. 2010, Monthly Notices of the Royal Astronomical Society, 401, 633

Downes, T., & Ray, T. 1998, Astronomy and Astrophysics, 331, 1130

Draine, B., & Lee, H. 1984, Astrophysical Journal, 285, 89

Dubois, Y., Devriendt, J., Slyz, A., & Teyssier, R. 2010, Monthly Notices of the Royal Astronomical Society, 409, 985

Ebeling, H., Edge, A., Böhringer, H., et al. 1998, Monthly Notices of the Royal Astronomical Society, 301, 881

Efstathiou, G. 1992, Monthly Notices of the Royal Astronomical Society, 256, 43

Egami, E., Rieke, G., Fadda, D., & Hines, D. 2006, Astronomy and Astrophysics, 652, L21

Eisenhauer, F. Abuter, R., Bickert, K., Biancat-Marchet, F., et al. 2003, Society of Photo-Optical Instrumentation Engineers (SPIE) Conference Series, 4841, 1548

Elmegreen, B. G. 1999, Astrophysical Journal, 517, 103

Elmegreen, B. G., & Elmegreen, D. M. 2010, Astrophysical Journal, 722, 1895

Emmering, R. T., Blandford, R. D., & Shlosman, I. 1992, Astrophysical Journal, 385, 460

Emonts, B., Morganti, R., Tadhunter, C., et al. 2005, Monthly Notices of the Royal Astronomical Society, 362, 931

Emonts, B., Norris, R., Feain, I., et al. 2011a, Monthly Notices of the Royal Astronomical Society, 415, 655

Emonts, B., Feain, I., Mao, M., et al. 2011b, ApJ Letters, 734, L25

Emonts, B., Feain, I., Röttgering, H., et al. 2013, Monthly Notices of the Royal Astronomical Society, 430, 3465

Epinat, B., Contini, T., Le Fèvre, O., et al. 2009, Astronomy and Astrophysics, 504, 789

Epinat, B., Tasca, L., Amram, P., et al. 2012, Astronomy and Astrophysics, 539, 92

Evans, A., Mazzarella, J., Surace, J., et al. 2005, Astrophysical Journal Supplement Series, 159, 197

Evans, A., Sanders, D., Surace, J., & Mazzarella, J. 1999, Astrophysical Journal, 511, 730

Fabian, A., Vasudevan, R., & Gandhi, P. 2008, Monthly Notices of the Royal Astronomical Society, 385, L43

Fabian, A., Sanders, J., Ettori, S., et al. 2000, Monthly Notices of the Royal Astronomical Society, 318, L65

Fabian, A., Sanders, J., Allen, S., et al. 2011, Monthly Notices of the Royal Astronomical Society, 418, 2154

Farage, C., McGregor, P., & Dopita, M. 2012, Astrophysical Journal, 747, 28

Farage, C., McGregor, P., Dopita, M., & Bicknell, G. 2010, Astrophysical Journal, 724, 267

Fasano, G., Bettoni, D., Ascaso, B., et al. 2010, Monthly Notices of the Royal Astronomical Society, 404, 1490

Ferland, G., Porter, R., van Hoof, P., et al. 2013, Revista Mexicana de Astronomía y Astrofísica, 49, 137

Ferrarese, L., & Ford, H. 2005, Space Science Reviews, 116, 523

Ferrarese, L., & Merritt, D. 2000, Astrophysical Journal, 539, 9

Förster Schreiber, N., Shapley, A. E., Erb, D., et al. 2011, Astrophysical Journal, 731, 65

Förster Schreiber, N., Genzel, R., Bouché, N., et al. 2009, Astrophysical Journal, 706, 1364

Förster Schreiber, N. M., Genzel, R., Lehnert, M. D., et al. 2006, Astrophysical Journal, 645, 1062

Fu, H., & Stockton, A. 2006, Astrophysical Journal, 650, 80

—. 2007a, Astrophysical Journal, 664, L75

—. 2007b, Astrophysical Journal, 666, 794

—. 2008, Astrophysical Journal, 677, 79

—. 2009, Astrophysical Journal, 690, 953

Gaibler, V., Krause, M., & Camenzind, M. 2009, Monthly Notices of the Royal Astronomical Society, 400, 1785

Galametz, A., Vernet, J., De Breuck, C., et al. 2010, Astronomy and Astrophysics, 522, 58

Galametz, A., Stern, D., De Breuck, C., et al. 2012, Astrophysical Journal, 749, 169

Galametz, A., Stern, D., Pentericci, L., et al. 2013, Astronomy and Astrophysics, 559, 2

Ganguly, R., Brotherton, M. S., Cales, S., et al. 2007, Astrophysical Journal, 665, 990

Gardner, J. P., Mather, J. C., Clampin, M., et al. 2006, Space Science Reviews, 123, 485

Garrington, S., Leahy, J., Conway, R., & Laing, R. 1988, Nature, 331, 147

Gebhardt, K., Bender, R., Bower, G., et al. 2000, Astrophysical Journal, 539, L13

Gendre, M., Best, P., & Wall, J. 2010, Monthly Notices of the Royal Astronomical Society, 404, 1719

Gott, J. Richard, I., Jurić, M., Schlegel, D., et al. 2005, Astrophysical Journal, 624, 463

Gower, J., Scott, P., & Wills, D. 1967, Memoirs of the Royal Astronomical Society, 71, 49

Graham, A., Lauer, T. R., Colless, M., & Postman, M. 1996, Astrophysical Journal, 465, 534

Graham, A. W., Onken, C. A., Athanassoula, E., & Combes, F. 2011, Monthly Notices of the Royal Astronomical Society, 412, 2211

Greene, J., & Ho, L. 2005, Astrophysical Journal, 630, 122

Greene, J. E., Zakamska, N. L., Ho, L. C., & Barth, A. J. 2011, Astrophysical Journal, 732, 9

Greene, J. E., Zakamska, N. L., & Smith, P. S. 2012, Astrophysical Journal, 746, 86

Greve, T., Bertoldi, F., Smail, I., et al. 2005, Monthly Notices of the Royal Astronomical Society, 359, 1165

Griffith, M., & Wright, A. 1993, Astronomical Journal, 105, 1666

Griffith, M. R., Wright, A. E., Burke, B., & Ekers, R. 1994, Astrophysical Journal Supplement Series, 90, 179

Groves, B. 2007, in Astronomical Society of the Pacific Conference Series, Vol. 373, The Central Engine of Active Galactic Nuclei, 511

Groves, B. A., Heckman, T. M., & Kauffmann, G. 2006, Monthly Notices of the Royal Astronomical Society, 371, 1559

Guillard, P., Ogle, P. M., Emonts, B. H. C., et al. 2012, Astrophysical Journal, 747, 95

Gültekin, K., Richstone, D., Gebhardt, K., et al. 2009, Astrophysical Journal, 698, 198

Hainline, L. J. 2008, PhD thesis, California Institute of Technology

Hamer, S., Edge, A., Swinbank, A., et al. 2012, Monthly Notices of the Royal Astronomical Society, 421, 3409

Häring, N., & Rix, H.-W. 2004, Astrophysical Journal, 604, L89

Harrison, C., Alexander, D., Swinbank, A., et al. 2012, Monthly Notices of the Royal Astronomical Society, 426, 1073

Harwood, J. J., Hardcastle, M. J., Croston, J. H., & Goodger, J. L. 2013, Monthly Notices of the Royal Astronomical Society, 435, 3353

Hatch, N., Overzier, R., Röttgering, H., Kurk, J., & Miley, G. 2008, Monthly Notices of the Royal Astronomical Society, 383, 931

Hatch, N. A., Crawford, C., & Fabian, A. 2007, Monthly Notices of the Royal Astronomical Society, 380, 33

Hatch, N. A., Crawford, C., Johnstone, R., & Fabian, A. 2006, Monthly Notices of the Royal Astronomical Society, 367, 433

Hatch, N. A., Overzier, R., Kurk, J., et al. 2009, Monthly Notices of the Royal Astronomical Society, 395, 114

Hayashi, M., Kodama, T., Tadaki, K.-i., Koyama, Y., & Tanaka, I. 2012, Astrophysical Journal, 757, 15

Healey, S. E., Romani, R. W., Taylor, G. B., et al. 2007, Astrophysical Journal Supplement Series, 171, 61

Heavens, A., Panter, B., Jimenez, R., & Dunlop, J. 2004, Nature, 428, 625

Heckman, T., Baum, S., van Breugel, W., & McCarthy, P. 1989, Astrophysical Journal, 338, 48

Heckman, T. M., Armus, L., & Miley, G. K. 1990, Astrophysical Journal Supplement Series, 74, 833

Heckman, T. M., Kauffmann, G., Brinchmann, J., et al. 2004, Astrophysical Journal, 613, 109

Högbom, J. A. 1974, Astronomy and Astrophysics Supplement, 15, 417

Holt, J., Tadhunter, C. N., & Morganti, R. 2008, Monthly Notices of the Royal Astronomical Society, 387, 639

Hook, I., Shaver, P., Jackson, C., Wall, J., & Kellermann, K. 2003, Astronomy and Astrophysics, 399, 469

Hopkins, A., & Beacom, J. 2006, Astrophysical Journal, 651, 142

Hopkins, P. F., Hernquist, L., Cox, T. J., et al. 2006a, Astrophysical Journal Supplement Series, 163, 1

Hopkins, P. F., Somerville, R. S., Hernquist, L., et al. 2006b, Astrophysical Journal, 652, 864

Hubble, E. 1929, Proceedings of the National Academy of Science, 15, 168

Humphrey, A., Iwamuro, F., Villar-Martín, M., et al. 2007, Monthly Notices of the Royal Astronomical Society, 382, 1729

Humphrey, A., Iwamuro, F., Villar-Martín, M., Binette, L., & Sung, E. C. 2009, Monthly Notices of the Royal Astronomical Society, 399, L34

Husemann, B., Wisotzki, L., Sánchez, S. F., & Jahnke, K. 2013, Astronomy and Astrophysics, 549, A43

Hyvönen, T., Kotilainen, J., örndahl, E., Falomo, R., & Uslenghi, M. 2007, Astronomy and Astrophysics, 462, 525

Ichimaru, S. 1977, Astrophysical Journal, 214, 840

Ivison, R., Morrison, G., Biggs, A., et al. 2008, Monthly Notices of the Royal Astronomical Society, 390, 1117

Ivison, R., Smail, I., Amblard, A., et al. 2012, Monthly Notices of the Royal Astronomical Society, 425, 1320

Jackson, C., Wall, J., Shaver, P., et al. 2002, Astronomy and Astrophysics, 386, 97

Jaffe, W. J., & Perola, G. C. 1973, Astronomy and Astrophysics, 26, 423

Jansen, F., Lumb, D., Altieri, B., et al. 2001, Astronomy and Astrophysics, 365, L1

Jones, C., & Forman, W. 1984, Astrophysical Journal, 276, 38

Juneau, S., Dickinson, M., Bournaud, F., et al. 2013, Astrophysical Journal, 764, 176

Jungwiert, B., Combes, F., & Palous, J. 2001, Astronomy and Astrophysics, 376, 85

Kacprzak, G. G., Churchill, C. W., Barton, E. J., & Cooke, J. 2011a, Astrophysical Journal, 733, 105

Kacprzak, G. G., Churchill, C. W., Evans, J. L., Murphy, M. T., & Steidel, C. C. 2011b, Monthly Notices of the Royal Astronomical Society, 416, 3118

Kaiser, C. R., & Alexander, P. 1997, Monthly Notices of the Royal Astronomical Society, 286, 215

Kaiser, C. R., Schoenmakers, A. P., & Röttgering, H. J. 2000, Monthly Notices of the Royal Astronomical Society, 315, 381

Kapferer, W., Kronberger, T., Ferrari, C., Riser, T., & Schindler, S. 2008, Monthly Notices of the Royal Astronomical Society, 389, 1405

Kardashev, N. S. 1962, Soviet Astronomy, 6, 317

Kaspi, S., Maoz, D., Netzer, H., et al. 2005, Astrophysical Journal, 629, 61

Kaspi, S., & Netzer, H. 1999, Astrophysical Journal, 524, 71

Kaspi, S., Smith, P., Netzer, H., et al. 2000, Astrophysical Journal, 533, 631

Kauffmann, G., Colberg, J. M., Diaferio, A., & White, S. D. 1999, Monthly Notices of the Royal Astronomical Society, 303, 188

Kauffmann, G., & Haehnelt, M. 2000, Monthly Notices of the Royal Astronomical Society, 311, 576

Kauffmann, G., Heckman, T., White, S. D. M., et al. 2003a, Monthly Notices of the Royal Astronomical Society, 341, 54

Kauffmann, G., Heckman, T., Tremonti, C., et al. 2003b, Monthly Notices of the Royal Astronomical Society, 346, 1055

Kellermann, K., Sramek, R., Schmidt, M., Shaffer, D., & Green, R. 1989, Astronomical Journal, 98, 1195

Kennicutt, R. 1998, Annual Review of Astronomy and Astrophysics, 36, 189

Kewley, L., Dopita, M., Sutherland, R., Heisler, C., & Trevena, J. 2001, Astrophysical Journal, 556, 121

Kodama, T., Tanaka, I., Kajisawa, M., et al. 2007, Monthly Notices of the Royal Astronomical Society, 377, 1717

Komossa, S., Xu, D., Zhou, H., Storchi-Bergmann, T., & Binette, L. 2008, Astrophysical Journal, 680, 926

Konar, C., Hardcastle, M., Jamrozy, M., Croston, J., & Nandi, S. 2012, Monthly Notices of the Royal Astronomical Society, 424, 1061

Kormendy, J., & Gebhardt, K. 2001, in American Institute of Physics Conference Series, Vol. 586, 20th Texas Symposium on relativistic astrophysics, 363–381

Kormendy, J., & Richstone, D. 1995, Annual Review of Astronomy and Astrophysics, 33, 581

Kovalev, Y. 2009, Astrophysical Journal Letters, 707, L56

Kovalev, Y., Petrov, L., Fomalont, E., & Gordon, D. 2007, Astronomical Journal, 133, 1236

Krause, M. 2005, Astronomy and Astrophysics, 431, 45

Kuiper, E., Hatch, N., Miley, G., et al. 2011, Monthly Notices of the Royal Astronomical Society, 415, 2245

Kurk, J., Cimatti, A., di Serego Alighieri, S., et al. 2004a, Astronomy and Astrophysics, 422, L13

Kurk, J., Pentericci, L., Overzier, R., Röttgering, H., & Miley, G. 2004b, Astronomy and Astrophysics, 428, 817

Kurk, J., Pentericci, L., Röttgering, H., & Miley, G. 2002, in Revista Mexicana de Astronomia y Astrofisica Conference Series, Vol. 13, Revista Mexicana de Astronomia y Astrofisica Conference Series, 191–195

Kurk, J., Pentericci, L., Röttgering, H., & Miley, G. 2004c, Astronomy and Astrophysics, 428, 793

Kurk, J., Röttgering, H., Pentericci, L., et al. 2000, Astronomy and Astrophysics, 358, L1

Kurz, R., Guilloteau, S., & Shaver, P. 2002, The Messenger, 107, 7

Kurz, R., & Shaver, P. 1999, The Messenger, 96, 7

Labbé, I., Franx, M., Rudnick, G., et al. 2003, Astronomical Journal, 125, 1107

Laing, R. 1988, Nature, 331, 149

Large, M., Mills, B., Little, A., Crawford, D., & Sutton, J. 1981, Monthly Notices of the Royal Astronomical Society, 194, 693

Larionov, M., Parijskij, Y., Zhuravlev, V., et al. 1994, Astronomy and Astrophysics Supplement, 106, 119

Le Fèvre, O., Deltorn, J. M., Crampton, D., & Dickinson, M. 1996, Astrophysical Journal Letters, 471, L11

Le Tiran, L., Lehnert, M., van Driel, W., Nesvadba, N., & Di Matteo, P. 2011, Astronomy and Astrophysics, 534, L4

Lehnert, M., & Heckman, T. 1996a, Astrophysical Journal, 462, 651

Lehnert, M., Le Tiran, L., Nesvadba, N., et al. 2013, Astronomy and Astrophysics, 555, 72

Lehnert, M., Nesvadba, N., Tiran, L., et al. 2009, Astrophysical Journal, 699, 1660

Lehnert, M., Tasse, C., Nesvadba, N., Best, P., & van Driel, W. 2011, Astronomy and Astrophysics, 532, L3

Lehnert, M. D., & Heckman, T. M. 1995, Astrophysical Journal Supplement Series, 97, 89

—. 1996b, Astrophysical Journal, 472, 546

Lehnert, M. D., Heckman, T. M., & Weaver, K. A. 1999a, Astrophysical Journal, 523, 575

Lehnert, M. D., van Breugel, W. J., Heckman, T. M., & Miley, G. K. 1999b, Astrophysical Journal Supplement Series, 124, 11

Léna, P., Rouan, D., Lebrun, F., Mignard, F., & Pelat, D. 2008, L'observation en astrophysique (EDP Sciences / CNRS Éditions)

Lidman, C., Suherli, J., Muzzin, A., et al. 2012, Monthly Notices of the Royal Astronomical Society, 427, 550

Liu, F. S., Mao, S., & Meng, X. M. 2012, Monthly Notices of the Royal Astronomical Society, 423, 422

Liu, G., Zakamska, N. L., Greene, J. E., Nesvadba, N. P., & Liu, X. 2013a, Monthly Notices of the Royal Astronomical Society, 430, 2327

—. 2013b, Monthly Notices of the Royal Astronomical Society

Ludwig, R. R., Greene, J. E., Barth, A. J., & Ho, L. C. 2012, Astrophysical Journal, 756, 51

Mac Low, M.-M. 1999, Astrophysical Journal, 524, 169

MacArthur, L., Courteau, S., & Holtzman, J. 2003, Astrophysical Journal, 582, 689

Magnelli, B., Lutz, D., Santini, P., et al. 2012, Astronomy and Astrophysics, 539

Magorrian, J., Tremaine, S., Richstone, D., et al. 1998, Astronomical Journal, 115, 2285

Mahony, E. K., Sadler, E. M., Murphy, T., et al. 2010, Astrophysical Journal, 718, 587

Mao, S., Gaensler, B., Haverkorn, M., et al. 2010, Astrophysical Journal, 714, 1170

Marcolini, A., Brighenti, F., & D'Ercole, A. 2004, Monthly Notices of the Royal Astronomical Society, 352, 363

Marconi, A., & Hunt, L. K. 2003, Astrophysical Journal, 589, 21

Mathews, W. G., & Brighenti, F. 2003, Astrophysical Journal, 590, L5

Matsuda, Y., Nakamura, Y., Morimoto, N., et al. 2009, Monthly Notices of the Royal Astronomical Society, 400, L66

Matsuda, Y., Richard, J., Smail, I., et al. 2010, Monthly Notices of the Royal Astronomical Society, 403, L54

Matsuda, Y., Smail, I., Geach, J., et al. 2011, Monthly Notices of the Royal Astronomical Society, 416, 2041

Matteucci, F., & Recchi, S. 2001, Astrophysical Journal, 558, 351

Matthews, T. A., & Sandage, A. R. 1963, Astrophysical Journal, 138, 30

Mayo, J., Vernet, J., De Breuck, C., et al. 2012, Astronomy and Astrophysics, 539, A33

McCarthy, I., Babul, A., Bower, R., & Balogh, M. 2008, Monthly Notices of the Royal Astronomical Society, 386, 1309

McDonald, M., Veilleux, S., & Mushotzky, R. 2011, Astrophysical Journal, 731, 33

McDonald, M., Veilleux, S., Rupke, D., & Mushotzky, R. 2010, Astrophysical Journal, 721, 1262

McDonald, M., Bayliss, M., Benson, B., et al. 2012, Nature, 488, 349

McNamara, B., & Nulsen, P. 2007, Annual Review of Astronomy & Astrophysics, 45, 117

—. 2012, New Journal of Physics, 14, 055023

McNamara, B., Wise, M., Nulsen, P., et al. 2000, Astrophysical Journal, 534, L135

—. 2001, Astrophysical Journal, 562, L149

Menéndez-Delmestre, K., Blain, A. W., Swinbank, M., et al. 2013, Astrophysical Journal, 767, 151

Michalowski, M., Murphy, E., Hjorth, J., et al. 2011, in Astronomical Society of the Pacific Conference Series, Vol. 446, Galaxy Evolution: Infrared to Millimeter Wavelength Perspective, 387

Mihos, J. C., & Hernquist, L. 1996, Astrophysical Journal, 464, 641

Miley, G., & De Breuck, C. 2008, Astronomy and Astrophysics Review, 15, 67

Miley, G. K., Overzier, R. A., Zirm, A. W., et al. 2006, Astrophysical Journal, 650, L29

Moe, M., Arav, N., Bautista, M. A., & Korista, K. T. 2009, Astrophysical Journal, 706, 525

Moorwood, A., Cuby, J., Ballester, P., et al. 1999, The Messenger, 95, 1

Morganti, R., Tadhunter, C., & Oosterloo, T. 2005, Astronomy and Astrophysics, 444, L9

Mullaney, J., Pannella, M., Daddi, E., et al. 2012, Monthly Notices of the Royal Astronomical Society, 419, 95

Müller-Sánchez, F., Prieto, M., Hicks, E., et al. 2011, Astrophysical Journal, 739, 69

Murphy, M., Webb, J., & Flambaum, V. 2003, Monthly Notices of the Royal Astronomical Society, 345, 609

Murphy, T., Sadler, E. M., Ekers, R. D., et al. 2010, Monthly Notices of the Royal Astronomical Society, 402, 2403

Murray, N., Chiang, J., Grossman, S., & Voit, G. 1995, Astrophysical Journal, 451, 498

Murray, N., Quataert, E., & Thompson, T. A. 2005, Astrophysical Journal, 618, 569

Nelson, C. H., & Whittle, M. 1996, Astrophysical Journal, 465, 96

Nesvadba, N., Boulanger, F., Lehnert, M., Guillard, P., & Salomé, P. 2011a, Astronomy and Astrophysics, 536, L5

Nesvadba, N., De Breuck, C., Lehnert, M., et al. 2011b, Astronomy and Astrophysics, 525, 43

Nesvadba, N., Lehnert, M., De Breuck, C., Gilbert, A., & Van Breugel, W. 2008, Astronomy and Astrophysics, 491, 407

Nesvadba, N., Lehnert, M., Eisenhauer, F., et al. 2006, Astrophysical Journal, 650, 693

Nesvadba, N., Polletta, M., Lehnert, M., et al. 2011c, Monthly Notices of the Royal Astronomical Society, 415, 2359

Nesvadba, N., Neri, R., De Breuck, C., et al. 2009, Monthly Notices of the Royal Astronomical Society, 395, L16

Nesvadba, N., Boulanger, F., Salomé, P., et al. 2010, Astronomy and Astrophysics, 521, A65

Nesvadba, N. P. H., Lehnert, M. D., De Breuck, C., Gilbert, A., & van Breugel, W. 2007a, Astronomy and Astrophysics, 475, 145

Nesvadba, N. P. H., Lehnert, M. D., Genzel, R., et al. 2007b, Astrophysical Journal, 657, 725

Newman, S. F., Genzel, R., Förster Schreiber, N. M., et al. 2013, Astrophysical Journal, 767, 104

Ogle, P., Boulanger, F., Guillard, P., et al. 2010, Astrophysical Journal, 724, 1193

Omont, A., Beelen, A., Bertoldi, F., et al. 2003, Astronomy and Astrophysics, 398, 857

Osterbrock, D. E. 1989, Astrophysics of Gaseous Nebulae and Active Galactic Nuclei (University Science Books)

Overzier, R., Harris, D., Carilli, C., et al. 2005, Astronomy and Astrophysics, 433, 87

Overzier, R., Nesvadba, N., Dijkstra, M., et al. 2013, Astrophysical Journal, 771, 89

Pacholczyk, A. 1970, Radio astrophysics. Nonthermal processes in galactic and extragalactic sources

Page, M., Symeonidis, M., Vieira, J., et al. 2012, Nature, 485, 213

Panter, B., Jimenez, R., Heavens, A. F., & Charlot, S. 2007, Monthly Notices of the Royal Astronomical Society, 378, 1550

Papadopoulos, P. P., Röttgering, H. J. A., van der Werf, P. P., et al. 2000, Astrophysical Journal, 528, 626

Pâris, I., Petitjean, P., Aubourg, É., et al. 2012, Astronomy and Astrophysics, 548, A66

Peng, C., Ho, L., Impey, C., & Rix, H. 2002, Astronomical Journal, 124, 266

—. 2010, Astronomical Journal, 139, 2097

Pentericci, L., McCarthy, P. J., Röttgering, H. J. A., et al. 2001, Astrophysical Journal Supplement Series, 135, 63

Pentericci, L., Röttgering, H., Miley, G., Carilli, C., & McCarthy, P. 1997, Astronomy and Astrophysics, 326, 580

Pentericci, L., Röttgering, H., Miley, G., et al. 1998, Astrophysical Journal, 504, 139

Pentericci, L., Van Reeven, W., Carilli, C., Röttgering, H., & Miley, G. 2000a, A&A Supp, 145, 121

Pentericci, L., Kurk, J., Röttgering, H., et al. 2000b, Astronomy and Astrophysics, 361, L25

Perlmutter, S., Aldering, G., Goldhaber, G., et al. 1999, Astrophysical Journal, 517, 565

Pettini, M., Shapley, A. E., Steidel, C. C., et al. 2001, Astrophysical Journal, 554, 981

Pizzolato, F., & Soker, N. 2005, Astrophysical Journal, 632, 821

Polletta, M., Omont, A., Berta, S., et al. 2008, Astronomy and Astrophysics, 492, 81

Press, W. H., & Schechter, P. 1974, Astrophysical Journal, 187, 425

Proga, D., & Kallman, T. R. 2003, Astrophysical Journal, 616, 688

Queyrel, J., Contini, T., Kissler-Patig, M., et al. 2012, Astronomy and Astrophysics, 539, 93

Quiniento, Z., Cersosimo, J., & Colomb, F. 1988, Astronomy and Astrophysics Supplement Series, 76, 21

Rauch, M., Becker, G. D., Haehnelt, M. G., Carswell, R. F., & Gauthier, J.-R. 2013, Monthly Notices of the Royal Astronomical Society, 431, L68

Rees, M., Begelman, M., Blandford, R., & Phinney, E. 1982, Nature, 295, 17

Reuland, M., Röttgering, H., van Breugel, W., & De Breuck, C. 2004, Monthly Notices of the Royal Astronomical Society, 353, 377

Revaz, Y., Combes, F., & Salomé, P. 2008, Astronomy and Astrophysics, 477, 33

Reynolds, C. S., McKernan, B., Fabian, A. C., Stone, J. M., & Vernaleo, J. C. 2005, Monthly Notices of the Royal Astronomical Society, 357, 242

Richards, G., Strauss, M., Fan, X., et al. 2006, Astronomical Journal, 131, 2766

Robinson, D. C. 1975, Physical Review Letters, 34, 905

Rocca-Volmerange, B., Le Borgne, D., De Breuck, C., Fioc, M., & Moy, E. 2004, Astronomy and Astrophysics, 415, 931

Rocca-Volmerange, B., Drouart, G., De Breuck, C., et al. 2013, Monthly Notices of the Royal Astronomical Society, 429, 2780

Ross, N. P., McGreer, I. D., White, M., et al. 2013, Astrophysical Journal, 773, 14

Rousselot, P., Lidman, C., Cuby, J.-G., Moreels, G., & Monnet, G. 2000, Astronomy and Astrophysics, 354, 1134

Sajina, A., Yan, L., Armus, L., et al. 2007a, Astrophysical Journal, 664, 713

Sajina, A., Yan, L., Lacy, M., & Huynh, M. 2007b, Astrophysical Journal, 667, L17

Sajina, A., Yan, L., Lutz, D., et al. 2008, Astrophysical Journal, 683, 659

Salomé, P., & Combes, F. 2003, Astronomy and Astrophysics, 412, 657

Salomé, P., Combes, F., Revaz, Y., et al. 2011, Astronomy and Astrophysics, 531, A85

Salomé, P., Combes, F., Edge, A., et al. 2006, Astronomy and Astrophysics, 454, 437

Salpeter, E. 1964, Astrophysical Journal, 140, 796

Salpeter, E. E. 1955, Astrophysical Journal, 121, 161

Sanders, D., Soifer, B., Elias, J., et al. 1988, Astrophysical Journal, 325, 74

Saripalli, L., Hunstead, R., Subrahmanyan, R., & Boyce, E. 2005, Astronomical Journal, 130, 896

Sault, R., Teuben, P., & Wright, M. 1995, in Astronomical Society of the Pacific Conference Series, Vol. 77, Astronomical Data Analysis Software and Systems IV, 433

Savage, A., Bolton, J. G., & Wright, A. E. 1977, Monthly Notices of the Royal Astronomical Society, 179, 135

Saxton, C. J., Bicknell, G. V., Sutherland, R. S., & Midgley, S. 2005, Monthly Notices of the Royal Astronomical Society, 359, 781

Schawinski, K., Treister, E., Urry, C. M., et al. 2011, The Astrophysical Journal Letters, 727, L31

Schechter, P. 1976, Astrophysical Journal, 203, 297

Scheuer, P. 1974, Monthly Notices of the Royal Astronomical Society, 166, 513

Schmidt, M. 1959, Astrophysical Journal, 129, 243

—. 1963, Nature, 197, 1040

Schoenmakers, A. P., de Bruyn, A., Röttgering, H., & van der Laan, H. 2000a, Monthly Notices of the Royal Astronomical Society, 315, 395

Schoenmakers, A. P., de Bruyn, A., Röttgering, H., van der Laan, H., & Kaiser, C. 2000b, Monthly Notices of the Royal Astronomical Society, 315, 371

Schombert, J. M. 1987, Astrophysical Journal Supplement Series, 64, 643

Sérsic, J. 1963, Boletin de la Asociacion Argentina de Astronomia La Plata Argentina, 6, 41

—. 1968, Atlas de galaxias australes

Seymour, N., Stern, D., De Breuck, C., et al. 2007, Astrophysical Journal Supplement, 171, 353

Seymour, N., Altieri, B., De Breuck, C., et al. 2012, Astrophysical Journal, 755, 146

Shakura, N. I., & Sunyaev, R. A. 1973, Astronomy and Astrophysics, 24, 337

Shapiro, K. L., Genzel, R., Quataert, E., et al. 2009, Astrophysical Journal, 701, 955

Sharples, R., Bender, R., Bennett, R., et al. 2005, The Messenger, 122, 2

Sharples, R., Bender, R., Agudo Berbel, A., et al. 2013, The Messenger, 151, 21

Shen, Y., Strauss, M. A., Ross, N. P., et al. 2009, Astrophysical Journal, 697, 1656

Shen, Y., Richards, G. T., Strauss, M. A., et al. 2011, Astrophysical Journal Supplement, 194, 45

Silk, J. 1997, Astrophysical Journal, 481, 703

Silk, J., & Rees, M. 1998, Astronomy and Astrophysics, 331, L1

Sirothia, S., Gopal-Krishna, & Wiita, P. J. 2013, Astrophysical Journal Letters, 765, L11

Skrutskie, M., Cutri, R., Stiening, R., et al. 2006, Astronomical Journal, 131, 1163

Smajić, S., Fischer, S., Zuther, J., & Eckart, A. 2012, Astronomy and Astrophysics, 544, 105

Snedden, S. A., & Gaskell, C. M. 1999, Astrophysical Journal, 521, L91

Sobral, D., Best, P. N., Geach, J. E., et al. 2010, Monthly Notices of the Royal Astronomical Society, 404, 1551

Sobral, D., Best, P. N., Matsuda, Y., et al. 2012, Monthly Notices of the Royal Astronomical Society, 420, 1926

Sobral, D., Smail, I., Best, P. N., et al. 2013, Monthly Notices of the Royal Astronomical Society, 428, 1128

Sobral, D., Best, P., Geach, J., et al. 2009, Monthly Notices of the Royal Astronomical Society, 398, 75

Soltan, A. 1982, Monthly Notices of the Royal Astronomical Society, 200, 115

Somerville, R. S., Hopkins, P. F., Cox, T. J., Robertson, B. E., & Hernquist, L. 2008, Monthly Notices of the Royal Astronomical Society, 391, 481

Springel, V., Di Matteo, T., & Hernquist, L. 2005, Astrophysical Journal, 620, L79

Steer, D., Dewdney, P., & Ito, M. 1984, Astronomy and Astrophysics, 137, 159

Steigman, G. 2007, Annual Review of Nuclear and Particle Systems, 57, 463

Stern, D., Holden, B., Stanford, S., & Spinrad, H. 2003, Astrophysical Journal, 125, 2759

Stockton, A., MacKenty, J. W., Hu, E. M., & Kim, T.-S. 2002, Astrophysical Journal, 572, 735

Sulentic, J., Marziani, P., & Dultzin-Hacyan, D. 2000, Annual Review of Astronomy and Astrophysics, 38, 521

Swinbank, A., Chapman, S., Smail, I., et al. 2006, Monthly Notices of the Royal Astronomical Society, 371, 465

Szomoru, D., Franx, M., van Dokkum, P. G., et al. 2010, Astrophysical Journal Letters, 714, L244

Tacconi, L., Genzel, R., Smail, I., et al. 2008, Astrophysical Journal, 680, 246

Tadhunter, C., Morganti, R., Robinson, A., et al. 1998, Monthly Notices of the Royal Astronomical Society, 298, 1035

Tadhunter, C., Wills, K., Morganti, R., Oosterloo, T., & Dickson, R. 2001, Monthly Notices of the Royal Astronomical Society, 327, 227

Tadhunter, C. N. 1991, Monthly Notices of the Royal Astronomical Society, 251, 46

Tanaka, I., Breuck, C. D., Kurk, J. D., et al. 2011, Publications of the Astronomical Society of Japan, 63, 415

Taylor, A. 2013, in IAU Symposium, Vol. 291, IAU Symposium, 337–341

Thomas, D., Maraston, C., Bender, R., & Mendes de Oliveira, C. 2005, Astrophysical Journal, 621, 673

Thomas, D., Maraston, C., Schawinski, K., Sarzi, M., & Silk, J. 2010, Monthly Notices of the Royal Astronomical Society, 404, 1775

Thoul, A. A., & Weinberg, D. H. 1995, Astrophysical Journal, 442, 480

Tombesi, F., Cappi, M., Reeves, J., et al. 2010, Astronomy and Astrophysics, 521, 57

Uzan, J.-P. 2011, Living Reviews in Relativity, 14, 2

van Breugel, W., Heckman, T., & Miley, G. 1984, Astrophysical Journal, 276, 79

van Breugel, W. J., Heckman, T. M., Miley, G. K., & Filippenko, A. V. 1986, Astrophysical Journal, 311, 58

van Dokkum, P., Franx, M., Kriek, M., et al. 2008, Astrophysical Journal — Letters, 677, L5

van Haarlem, M., Wise, M., Gunst, A., et al. 2013, Astronomy and Astrophysics, 556, 2

van Ojik, R., Röttgering, H., Carilli, C., et al. 1996, Astronomy and Astrophysics, 313, 25

van Ojik, R., Röttgering, H., Miley, G., & Hunstead, R. 1997, Astronomy and Astrophysics, 317, 358

Vanden Berk, D. E., Richards, G. T., Bauer, A., et al. 2001, Astronomical Journal, 122, 549

Veilleux, S., & Osterbrock, D. E. 1987, Astrophysical Journal Supplement Series, 63, 295

Venemans, B., Kurk, J., Miley, G., et al. 2002, Astrophysical Journal, 569, L11

Venemans, B., Röttgering, H., Overzier, R., et al. 2004, Astronomy and Astrophysics, 424, L17

Venemans, B., Röttgering, H., Miley, G., et al. 2005, Astronomy and Astrophysics, 431, 793

—. 2007, Astronomy and Astrophysics, 461, 823

Vernet, J., Fosbury, R., Villar-Martín, M., et al. 2001, Astronomy and Astrophysics, 366, 7

Veron-Cetty, M. P., & Veron, P. 1983, stronomy and Astrophysics Supplement Series, 53, 219

Vestergaard, M. 2002, Astrophysical Journal, 571, 733

Vikhlinin, A., Kravtsov, A., Forman, W., et al. 2006, Astrophysical Journal, 640, 691

Villar-Martín, M., Fosbury, R. A. E., Binette, L., Tadhunter, C. N., & Rocca-Volmerange, B. 1999, Astronomy and Astrophysics, 351, 47

Villar-Martín, M., Humphrey, A., Delgado, R. G., Colina, L., & Arribas, S. 2011, Monthly Notices of the Royal Astronomical Society, 418, 2032

Villar-Martín, M., Humphrey, A., Martínez-Sansigre, A., et al. 2008, Monthly Notices of the Royal Astronomical Society, 390, 218

Villar-Martín, M., Vernet, J., di Serego Alighieri, S., et al. 2003, Monthly Notices of the Royal Astronomical Society, 346, 273

—. 2002, Monthly Notices of the Royal Astronomical Society, 336, 436

von der Linden, A., Best, P. N., Kauffmann, G., & White, S. D. 2007, Monthly Notices of the Royal Astronomical Society, 379, 867

Wada, K. 2012, Astrophysical Journal, 758, 66

Waddington, I., Windhorst, R., Cohen, S., et al. 2002, Monthly Notices of the Royal Astronomical Society, 336, 1342

Wagner, A. Y., & Bicknell, G. V. 2011, Astrophysical Journal, 728, 29

Wagner, A. Y., Bicknell, G. V., & Umemura, M. 2012, Astrophysical Journal, 757, 136

Wagner, A. Y., Umemura, M., & Bicknell, G. V. 2013, Astrophysical Journal, 763, L18

Wall, J., Jackson, C., Shaver, P., Hook, I., & Kellermann, K. 2005, Astronomy and Astrophysics, 434, 133

Wandel, A., Peterson, B., & Malkan, M. 1999, Astrophysical Journal, 526, 579

Weisskopf, M., Brinkman, B., Canizares, C., et al. 2002, Publications of the Astronomical Society of the Pacific, 114, 1

Werner, M., Roellig, T., Low, F., et al. 2004, Astrophysical Journal Supplement Series, 154, 1

Whitaker, K., Kriek, M., van Dokkum, P., et al. 2012, Astrophysical Journal, 745, 179

White, R., & Becker, R. 1992, Astrophysical Journal Supplement, 79, 331

White, S., & Rees, M. 1978, Monthly Notices of the Royal Astronomical Society, 183, 341

White, S. D., & Frenk, C. S. 1991, Astrophysical Journal, 379, 52

Wild, V., Kauffmann, G., Heckman, T., et al. 2007, Monthly Notices of the Royal Astronomical Society, 381, 543

Willott, C., Rawlings, S., Blundell, K., & Lacy, M. 1999, Monthly Notices of the Royal Astronomical Society, 309, 1017

Willott, C., Rawlings, S., Blundell, K., Lacy, M., & Eales, S. 2001, Monthly Notices of the Royal Astronomical Society, 322, 536

Willott, C., Rawlings, S., Jarvis, M., & Blundell, K. 2003, Monthly Notices of the Royal Astronomical Society, 339, 173

Wilman, R., Edge, A., & Swinbank, A. 2006, Monthly Notices of the Royal Astronomical Society, 371, 93

—. 2009, Monthly Notices of the Royal Astronomical Society, 395, 1355

Wilman, R., Gerssen, J., Bower, R., et al. 2005, Nature, 436, 227

Wilson, W. E., Ferris, R., Axtens, P., et al. 2011, Monthly Notices of the Royal Astronomical Society, 416, 832

Wright, A., & Otrupcek, R. 1990, in PKS Catalog (1990), 0

Wright, A. E., Griffith, M. R., Hunt, A. J., et al. 1996, Astrophysical Journal Supplement, 103, 145

Wright, G., Rieke, G., Boeker, T., et al. 2010, in Society of Photo-Optical Instrumentation Engineers (SPIE) Conference Series, Vol. 7731, Society of Photo-Optical Instrumentation Engineers (SPIE) Conference Series

Yan, L., Chary, R., Armus, L., et al. 2005, Astrophysical Journal, 628, 604

York, D., Adelman, J., Anderson, Jr., J., et al. 2000, Astronomical Journal, 120, 1579

Yu, Q., & Tremaine, S. 2002, Monthly Notices of the Royal Astronomical Society, 335, 965

Zwaan, M., Andreani, P., Biggs, A., et al. 2013, The Messenger, 151, 20

Appendix A

Observing logs

A.1 CENSORS sources

A.2 Radio-quiet QSOs

A.3 Radio-loud quasars

Table A.1: Log of the CENSORS sources observations. (1/2)

Source ID (1)	Date (2)	ToT (3)	Dist (4)	Std star (5)
CEN020	24/11/2010	90	24/11/2010	Hip040105† (B5v)
				Hip040053* (B5v)
	25/11/2010	90		Hip044099† (B7v)
				Hip026694* (B5v)
				Hip048128* (B2V)
	15/01/2011	45	27/01/2011	Hip047868* (B0.5iiin)
				Hip054970* (B5iii)
	31/01/2011	40		Hip048128* (B2v)
				(Hip040105* (B5v))
	01/02/2011	80		Hip033288† (B3v)
				Hip033288* (B3v)
CEN072	09/02/2011	85	27/02/2011	Hip049269† (B9v)
				Hip049619* (B3v)
	14/02/2011	45		Hip045411* (B9iii)
	20/02/2011	110		Hip048128† (B2v)
				Hip045145† (B5v)
	22/02/2011	80		Hip042665† (B8v)
CEN105	04/02/2011	265	27/01/2011	Hip026785** (B2v)
				Hip058128** (B2v)
				Hip049201† (B2v)
				Hip035413† (B3v)
				Hip043473† (B3v)
				Hip055051†,* (B1v)
	05/02/2011	45		(Hip047137** (B3v))
				(Hip037597** (B3v))
				(Hip039446** (B4v))
				Hip055051**,* (B1v)
				(Hip081214* (B3v))
	12/02/2011	90		Hip049042† (B9v)
				Hip064491* (B8v)
	13/02/2011	40		Hip049269* (B9v)

(1) - Source identification
(2) - Dates of observation
(3) - Time on Target (min)
(4) - Date of the distorsion file used
(5) - Standard star used ($\star\star$: observed at the beginning of the run ; $\dagger$: observed in the middle of the run ; $\star$: observed at the end of the run)

Table A.2: Log of the CENSORS sources observations. (2/2)

Source ID (1)	Date (2)	ToT (3)	Dist (4)	Std star (5)
CEN118	05/02/2011	90	27/01/2011	(Hip047137** (B3V))
				(Hip037597** (B3V))
				(Hip039446** (B4V))
				Hip055051**,† (B1V)
				Hip081214* (B3V)
	06/02/2011	125		Hip029387† (B3V)
				Hip037439† (B3V)
				Hip043464* (B3V)
	08/02/2011	40		(Hip028649** (B2V))
				(Hip033300** (B2V))
				(Hip048128** (B2V))
				Hip048128** (B2V)
				Hip030739* (B3V)
				(Hip042322* (B3V))
	10/02/2011	40		Hip050162* (B3V)
CEN129	01/02/2011	55	27/02/2011	Hip033288** (B3V)
	17/02/2011	130		(Hip041463** (B2V))
				Hip051927**,† (B6V)
				Hip077206* (B8V)
	(22/02/2011)	5		No std star observed
	23/02/2011	45		Hip048383* (B9V)
	06/03/2011	20		Hip047397* (B5V)
	10/03/2011	15		No std star observed
	19/03/2011	40		Hip054970* (B5III)
CEN134	29/11/2010	40	24/11/2010	Hip044462* (B6/B7IV/V)
	24/02/2011	90	27/02/2011	Hip063541† (B5III)
				Hip055938* (B3V)
	27/02/2011	85		Hip025881† (B3V)
				Hip044317* (B5V)
	01/03/2011	60		Hip043566† (B6V)
	02/03/2011	75		Hip045145† (B5V)
				(Hip087030* (B6V))
	04/03/2011	40		Hip028220* (B5)
				Hip041640* (B4V)
				(Hip050135* (B4V))

(1) - Source identification
(2) - Dates of observation
(3) - Time on Target (min)
(4) - Date of the distorsion file used
(5) - Standard star used ($\star\star$: observed at the beginning of the run ; $\dagger$: observed in the middle of the run ; $\star$: observed at the end of the run)

Table A.3: Log of the radio-quiet QSOs observation.

Source ID (1)	Date (2)	ToT (3)	Dist (4)	Std star (5)
B0113-283	06/07/2010	90	09/07/2010	(Hip086951**) (B3V)
				Hip106474** (B3IV)
				Hip082658** (B5V)
				Hip093458* (B5III)
	12/07/2010	90		(Hip076434**) (B2III/IV)
				(Hip093849**) (B7II)
				Hip082254** (B4V)
				Hip095952* (B5III)
				Hip013441* (B5Vn)
				(Hip111397*) (B7III)
B0227-369	12/07/2010	45	08/07/2010	(Hip076434**) (B2III/IV)
				(Hip093849**) (B7II)
				(Hip082254**) (B4V)
				Hip095952** (B5III)
				Hip013441* (B5Vn)
				Hip111397* (B7III)
	20/07/2010	45		(Hip084475**) (B7V)
				(Hip099265**) (B5)
				Hip083861** (B2V)
				Hip013441* (B5Vn)
	22/07/2010	85		Hip109927** (B8)
				Hip008951† (B9)
				Hip000349* (B9Vn)
B0524-433	23/09/2010	175	06/09/2010	Hip100196** (B8V)
				Hip023919† (B8V)
				Hip025931† (B9V)
				Hip025480† (B2V)
				Hip032193* (B5V)
B1657+022	13/04/2010	45	14/04/2010	Hip081214* (B3V)
	13/07/2010	90	08/07/2010	Hip081214† (B3V)
				Hip082670* (B5V)
				Hip083498* (B8III)
				(Hip092470*) (B2IV)
	18/07/2010	45		Hip082734** (B2III)
				Hip089677* (B5V)

(1) - Source identification
(2) - Dates of observation
(3) - Time on Target (min)
(4) - Date of the distorsion file used
(5) - Standard star used ($\star\star$: observed at the beginning of the run ; †: observed in the middle of the run ; $\star$: observed at the end of the run)

Table A.4: Log of the radio-loud quasars observations. (1/2)

Source ID (1)	Date (2)	ToT (3)	Dist (4)	Std star (5)
SDSSJ003513+010430	04/10/2008	90	01/10/2008	Hip094265† (B5III)
				Hip015188* (B3V)
	16/10/2008	45		Hip000744* (B5V)
				(Hip014898*) (B3V)
				(Hip001115*) (B4V)
SDSSJ003522+001941	16/10/2008	10	27/10/2008	Hip000744** (B5V)
				Hip014898* (B3V)
				(Hip001115*) (B4V)
	29/10/2008	45		Hip118055* (G2V)
	01/11/2008	45		Hip115729* (B3III)
SDSSJ083902+045345	05/02/2009	90	03/02/2009	Hip045742† (B5V)
				Hip047397* (B5V)
	15/02/2009	45		(Hip042322*) (B5V)
				(Hip073345*) (B5V)
				(Hip072983*) (B5V)
	17/02/2009	45		Hip046296* (B2/B3IV)
SDSSJ130608+025943	18/04/2010	45	14/04/2010	(Hip047868**) (B0.5IIIn)
				(Hip054970**) (B5III)
				(Hip067111**) (B5IV)
				Hip065303** (B6IV)
				Hip085803* (B6V)
	10/05/2010	115	12/05/2010	Hip067279† (B2V)
				Hip074680* (B3V)
	28/05/2010	45		Hip067279* (B2V)
				(Hip082652*) (B3III)
				(Hip070506*) (B3IV)
	09/06/2010	45	11/06/2010	Hip055051* (B1V)
				Hip070506* (B3IV)

(1) - Source identification
(2) - Dates of observation
(3) - Time on Target (min)
(4) - Date of the distorsion file used
(5) - Standard star used ($\star\star$: observed at the beginning of the run ; †: observed in the middle of the run ; $\star$: observed at the end of the run)

Table A.5: Log of the radio-loud quasars observations. (2/2)

Source ID (1)	Date (2)	ToT (3)	Dist (4)	Std star (5)
SDSSJ143436+010522	28/05/2010	85	12/05/2010	Hip067279** (B2V)
				Hip082652* (B3III)
				Hip070506* (B3IV)
	10/06/2010	90	10/06/2010	Hip055051** (B1V)
				Hip070506† (B3IV)
				Hip070506* (B3IV)
	13/06/2010	40		Hip057628* (B3II/III)
				(Hip088201*) (B3V)
				(Hip084435*) (B3V)
				(Hip092470*) (B2IV)
				(Hip001115*) (B4V)
	23/07/2010	35	08/07/2010	Hip080496* (B9V)
				(Hip079470*) (B9V)
				(Hip095229*) (B8V)
				(Hip094079*) (B8)
				(Hip112798*) (B9.5/A0V)
				(Hip003082*) (B9)
SDSSJ143500+035403	24/06/2010	85	10/06/2010	Hip066298† (B9V)
				Hip083764* (B9)
	08/08/2010	90	08/08/2010	Hip068124† (B2/B3IV)
				Hip070506* (B3IV)
SDSSJ222646+005211	13/10/2008	90	27/10/2008	Hip108215† (B3Vn)
				Hip108215* (B3Vn)
	28/10/2008	45		Hip110659* (G2V)
	22/07/2010	45	08/07/2010	Hip109927* (B8)
				(Hip008951*) (B9)
				(Hip000349*) (B9Vn)

(1) - Source identification
(2) - Dates of observation
(3) - Time on Target (min)
(4) - Date of the distorsion file used
(5) - Standard star used ($\star\star$: observed at the beginning of the run ; †: observed in the middle of the run ; $\star$: observed at the end of the run)